ABSTRACT

Title of dissertation: PROBING FUNDAMENTAL PHYSICS WITH GRAVITATIONAL WAVES FROM INSPIRALING BINARY SYSTEMS

Noah Sennett
Doctor of Philosophy, 2021

Dissertation directed by: Professor Alessandra Buonanno
Department of Physics

The mergers of black holes and/or neutron stars in binary systems produce the most extreme gravitational environments in the local universe. The first direct detections of gravitational waves by Advanced LIGO and Virgo provide unprecedented observational access to the highly dynamical, strong-curvature regime of gravity. These measurements allow us to test Einstein's theory of General Relativity in this extreme regime. This thesis examines how the gravitational-wave signal produced during the inspiral—the earliest phase of a binary's coalescence—can better inform our understanding of the fundamental nature of gravity.

My work addressing this topic is comprised of two major components. First, I examine the behavior of binary black-hole and neutron-star systems in various possible extensions of General Relativity, constructing analytic models of their orbital motion and gravitational waveform—their gravitational-wave signature—during their inspiral. The majority of alternative theories I consider modify General Relativity by introducing a new scalar component of gravity. In many of these theories,

standard perturbative techniques are used to model the inspiral of binary systems. However, I also examine in depth the non-perturbative phenomenon of *scalarization* for which such methods fail. I show that this phenomenon occurs due to a second-order phase transition in the strong-gravity regime and develop an analytic framework to model the effect across a range of alternative theories of gravity.

The other component of this thesis is the development of a statistical infrastructure suitable for testing General Relativity using gravitational-wave observations. I adopt a more flexible and modular approach than existing alternatives, allowing this infrastructure to be immediately applied with a wide range of waveform models. In work done in conjunction with the LIGO Scientific and Virgo Collaborations, I use this statistical framework to place bounds on phenomenological deviations from General Relativity using the binary black-hole and neutron-star events detected during LIGO's first and second observing runs—no evidence for deviations from Relativity is found.

These two research directions outlined above are complementary; the type of statistical inference discussed here requires models for the gravitational-wave signal produced by inspiraling systems that allow for deviations from General Relativity, and the analytic models I construct are suitable for this task. In this thesis, I carry out the complete procedure of building and employing analytic models of gravitational waveforms to place constraints on specific alternative theories of gravity with observations by LIGO and Virgo.

PROBING FUNDAMENTAL PHYSICS WITH GRAVITATIONAL WAVES FROM INSPIRALING BINARY SYSTEMS

by

Noah Sennett

Dissertation submitted to the Faculty of the Graduate School of the
University of Maryland, College Park in partial fulfillment
of the requirements for the degree of
Doctor of Philosophy
2021

Advisory Committee:
Professor Alessandra Buonanno, Chair/Advisor
Professor Theodore Jacobson
Professor Julie McEnery
Professor Peter Shawhan
Professor Raman Sundrum

Preface

The following several hundred pages comprise my Ph.D. dissertation, the culmination of over half a decade of scientific research. Compiling work on this scale is a sensible means of justifying one's qualification for an advanced degree to a committee (and the institution they represent) that could not directly observe the completion of said work. Yet this monolithic focus on one individual's research is in many way at odds with the pace and practice of modern science, where work is often finished on much shorter timescales and in collaboration with several others. The work I present in this dissertation is original and my own but in many cases has been published previously with several co-authors in peer-reviewed journals. But, as this dissertation is intended as a measure of *my* scientific achievement, in this preface I explicitly delineate the portions of work done with collaborators to which I was the primary contributor. This preface is not intended as a summary of the material covered in these chapters; such an overview is reserved until after a pedagogical introduction to the scientific topics at hand in Section 1.4. Chapters to which I am the sole contributor employ the pronouns I/my, whereas those that include work done with collaborators use we/our.

Chapter 1 provides an introduction to the scientific topics covered in this thesis, a review of relevant literature, and an overview of the remainder of the dissertation. I was the sole author of this chapter.

Chapter 2 contains work published in Ref. [1]. In this work, I was the primary contributor to the analysis of non-perturbative phenomena in Einstein-Maxwell-dilaton gravity (Section 2.2.4). Additionally, I provided the discussion on the

prospects of constraining this theory with gravitational-wave observations of binary black holes by analyzing bounds on dipole energy flux (Section 2.3.2) and the estimated fraction of signal-to-noise ratio these deviations from general relativity would provide for ground-based detectors (Section 2.3.4).

Chapter 3 contains work published in Ref. [2]. I contributed significantly to every component of this chapter. At many points in the chapter, extended calculations were carried out independently by myself and collaborator Sylvain Marsat and then compared as a means of verifying the results; as such, he and I contributed approximately equally to the work.

Chapter 4 contains work published in Ref. [3]. I was the primary contributor to and author of all of the work in this chapter.

Chapter 5 contains work published in Ref. [4]. This work serves as a recapitulation, reinterpretation, and extension of many of the results presented in the previous chapter (and Ref. [3]). As such, I was the primary contributor and was primarily responsible for all text and figures in the work.

Chapter 6 contains work published in Ref. [5]. Though the overarching ideas contained in the work arose through discussion between all the co-authors, I was the primary contributor to all results, text, and figures presented in the chapter with the exception of the discussion of critical exponents of phase transitions of compact objects in alternative theories of gravity (Section 6.4.2).

Chapter 7 contains work published in Ref. [6]. This work represents a collaboration between co-authors from the pulsar timing and gravitational-wave communities; my primary contribution was to the components of the publication focused on

gravitational-wave observations. Specifically, I was the primary contributor to the discussion of projected constraints on dynamical scalarization given pulsar-timing observations at the time of publication (Section 7.4.2).

Chapter 8 contains work published in Ref. [7]. Though my co-authors had carried out analogous calculations in previous work, and thus offered invaluable insight in carrying out the calculations here, I was primarily responsible for the results and discussion presented in this chapter. The only component of the work to which I was not the primary contributor was the discussion of waveform approximants (Section 8.6.1, specifically Figure 8.4).

Chapter 9 contains work published in Refs. [8–10] as well as unpublished work [11]. While the results presented in this chapter have appeared elsewhere, the discussion given in this chapter is restricted to results to which I was the primary contributor, with the following qualifications. In certain places, e.g. Figure 9.1, additional results from Refs. [9, 10] are included to provide comparison between others' work and my own; the discussion in the text explicitly distinguishes between these results and those to which I contributed directly. Additionally, the investigation done to place constraints on higher-order curvature corrections from binary black hole observations (Section 9.5) was split primarily between myself and collaborator Richard Brito. We each made approximately equal contributions to these results—e.g. I produced results for the left panel of Figure 9.5 while he produced results for the right. However, I was primarily responsible for all text and figures presented in this chapter.

Chapter 10 serves as a conclusion for the dissertation, providing a recapitula-

tion of important results from the previous chapters as well as directions for future work. I was the sole author for this chapter.

Acknowledgments

First and foremost, I would like to thank my advisor, Alessandra Buonanno, for her help and guidance throughout my graduate career. She provided me with ideas and advice on several challenging and timely projects while still allowing me the flexibility to carve out my own niche in our burgeoning field. She has taught me the care and patience needed to produce my highest-quality work and helped me bolster the impact of such work on the scientific community at large. And, simply put, this dissertation would not exist if not for her unwavering confidence and support.

I would like to thank all of my co-authors of the papers that comprise this dissertation: Richard Brito, Alessandra Buonanno, László Gergely, Victor Gorbenko, Tanja Hinderer, Maximiliano Isi, Mohammed Khalil, Michael Kramer, Sylvain Marsat, Serguei Ossokine, Bangalore Sathyaprakash, Leonardo Senatore, Lijing Shao, Jan Steinhoff, Justin Vines, and Norbert Wex. I am grateful to the LIGO Scientific and Virgo Collaborations, specifically the Testing General Relativity subgroup, for facilitating much of the work presented here.

I owe my gratitude to that entire Astrophysical and Cosmological Relativity division of the Albert Einstein Institute, comprised of too many wonderful scientists and friends for me to list here; I've learned more about our field through discussions over lunch and coffee than I ever could on my own. There are a few people I would like to individually recognize: Sylvain Marsat, for his countless lessons in post-Newtonian theory and using Mathematica to its fullest; Jan Steinhoff, for revealing

the wonderful theoretical basis behind waveform modeling and our many invaluable conversations on testing relativity without relying on phenomenonlogy; and Vivien Raymond, for introducing me to parameter estimation with LAL and constantly helping when my runs would invariably crash. I would also like to heartfully thank the staff and international office at the AEI for their invaluable help in getting situated upon moving from the US.

I would like to thank my friends and peers at UMD—Bill, Kyle, Seokjin, and Yidan—for sharing the ups and downs of the start of graduate school, and I would like especially to thank my friends and fellow students at the AEI—Andrea, Daniel, Kyohei, Mohammed, Nils, Riccardo, and Roberto—for helping transform my stay in Germany from an extended expedition into a home away from home.

And lastly, I would like to thank my parents for their constant support, acting as a solid foundation and sounding board throughout the trials and tribulations of my Ph.D.

Table of Contents

Preface ii

Acknowledgements vi

List of Tables xiv

List of Figures xv

List of Abbreviations xviii

1 Introduction 1
- 1.1 Einstein's theory of general relativity . . . 1
- 1.2 Gravitational-wave science with compact binaries . . . 7
  - 1.2.1 Generation by compact binary coalescence . . . 7
    - 1.2.1.1 Early inspiral . . . 7
    - 1.2.1.2 Late inspiral and merger . . . 12
    - 1.2.1.3 Ringdown . . . 16
  - 1.2.2 Observation with ground-based detectors . . . 17
    - 1.2.2.1 Laser-interferometric detectors . . . 17
    - 1.2.2.2 Bayesian inference with gravitational waves . . . 21
- 1.3 Testing general relativity with gravitational waves . . . 28
  - 1.3.1 Motivations for modifying general relativity . . . 28
  - 1.3.2 The menagerie of modified gravity . . . 30
    - 1.3.2.1 Additional fields . . . 31
    - 1.3.2.2 Broken diffeomorphism invariance . . . 36
    - 1.3.2.3 Non-locality . . . 37
  - 1.3.3 Tests of gravity with gravitational waves . . . 39
    - 1.3.3.1 Testing various facets of gravitational wave signals . 39
    - 1.3.3.2 Designing gravitational-wave tests of general relativity 42
- 1.4 Overview of this thesis . . . 46
  - 1.4.1 Post-Newtonian and effective-one-body descriptions of binary black holes in Einstein-Maxwell-dilaton gravity . . . 47
  - 1.4.2 Post-Newtonian waveforms in massless scalar-tensor theories . 49

1.4.3 Dynamical scalarization as a non-perturbative phenomenon . . 50
1.4.4 Dynamical scalarization as a second-order phase transition . . 53
1.4.5 Theory-agnostic modeling of dynamical scalarization 56
1.4.6 Projected constraints on scalarization by combining pulsar-timing and gravitational-wave observations 58
1.4.7 Tidal signature of boson stars in binary systems 61
1.4.8 Parameterized tests of general relativity with generic frequency-domain waveform models 64

2 Hairy binary black holes in Einstein-Maxwell-dilaton theory and their effective-one-body description 69
2.1 Introduction 70
2.2 Einstein-Maxwell-dilaton theory 74
2.2.1 Setup 74
2.2.2 Black-hole solution 77
2.2.3 Dynamics of a test black-hole in a background black-hole space-time 80
2.2.4 Compact objects in Einstein-Maxwell-dilaton and scalar-tensor theories 85
2.3 Post-Newtonian approximation in Einstein-Maxwell-dilaton theory . . 88
2.3.1 Two-body dynamics 88
2.3.2 Gravitational energy flux 94
2.3.3 Gravitational-wave phase in the stationary-phase approximation 100
2.3.4 Number of useful gravitational-wave cycles 107
2.4 Effective-one-body framework 109
2.4.1 Effective-one-body Hamiltonian in Garfinkle-Horowitz-Strominger gauge 111
2.4.2 Effective-one-body Hamiltonian in Schwarzschild gauge 118
2.4.3 Comparison of two effective-one-body Hamiltonians in Einstein-Maxwell-dilaton theory 122
2.5 Conclusions 128

3 Gravitational waveforms in scalar-tensor gravity at 2PN relative order 132
3.1 Introduction 133
3.2 Gravitational waves in scalar-tensor gravity 137
3.2.1 Binary systems of compact objects 137
3.2.2 Generic constraints on scalar-tensor gravity 140
3.2.3 Detector response 144
3.3 Dynamics for quasi-circular orbits 146
3.4 Radiative coordinates and hereditary contributions 149
3.4.1 Radiative coordinates 150
3.4.2 Tail contributions 152
3.4.3 Memory contributions 153
3.5 Balance equation and phase evolution 155
3.5.1 The dipole-driven regime 158

3.5.2 The quadrupole-driven regime . . . 159
3.6 Spin-weighted spherical modes of the waveform . . . 162
3.7 Stationary phase approximation . . . 167
3.7.1 The dipole-driven regime . . . 169
3.7.2 The quadrupole-driven regime . . . 170
3.8 Conclusions . . . 172
3.9 Acknowledgements . . . 174

4 Modeling dynamical scalarization with a resummed post-Newtonian expansion 175
4.1 Introduction . . . 176
4.2 Non-perturbative phenomena in scalar-tensor gravity . . . 179
4.2.1 Spontaneous scalarization: single neutron star . . . 183
4.2.2 Dynamical scalarization: neutron-star binaries . . . 186
4.3 The post-Dickean expansion . . . 191
4.3.1 Action and field equations . . . 191
4.3.2 Relaxed field equations . . . 193
4.4 Structure of the near-zone fields . . . 196
4.5 Two-body Equations of motion . . . 200
4.5.1 Newtonian order . . . 200
4.5.2 Post-Dickean order . . . 203
4.6 Structure of the far-zone fields . . . 205
4.6.1 Near-zone contribution to the scalar field . . . 206
4.6.2 Radiation-zone contribution to the scalar field . . . 208
4.7 Two-body Scalar mass . . . 211
4.8 Validity of the Post-Dickean expansion . . . 217
4.8.1 Quasi-equilibrium configurations . . . 219
4.8.2 Earlier analytic models . . . 223
4.9 Conclusions . . . 226
4.10 Acknowledgements . . . 229

5 Effective action model of dynamically scalarizing binary neutron stars 230
5.1 Introduction . . . 231
5.2 Nonperturbative phenomena in scalar-tensor gravity . . . 233
5.2.1 Spontaneous scalarization . . . 236
5.2.2 Dynamical and induced scalarization . . . 238
5.3 Effective action with a dynamical scalar charge . . . 241
5.3.1 The effective point-particle action . . . 244
5.3.2 Dynamics of a binary system . . . 248
5.4 Results . . . 253
5.4.1 Computing $c^{(i)}$ . . . 253
5.4.2 Comparison against previous models . . . 255
5.5 Dynamical scalarization as a phase transition . . . 261
5.5.1 Spontaneous scalarization of an isolated body . . . 263
5.5.2 Dynamical scalarization of equal-mass binaries . . . 264

5.5.3 Scalarization of unequal-mass binaries . . . 266
5.6 Conclusions . . . 269
5.7 Acknowledgments . . . 271

6 Theory-agnostic modeling of dynamical scalarization in compact binaries 272
6.1 Introduction . . . 273
6.2 Linear mode instability and effective action close to critical point . . . 278
6.3 Matching strong-field physics into black-hole solutions . . . 284
6.4 Modeling strong-gravity effects within the theory-agnostic framework 289
6.4.1 Spontaneous scalarization . . . 290
6.4.2 Critical exponents of phase transition in gravity . . . 292
6.4.3 Dynamical scalarization . . . 295
6.5 Conclusions . . . 300
6.6 Acknowledgements . . . 303

7 Constraining nonperturbative strong-field effects in scalar-tensor gravity by combining pulsar timing and laser-interferometer gravitational-wave detectors 304
7.1 Introduction . . . 305
7.2 Nonperturbative strong-field phenomena in scalar-tensor gravity . . . 307
7.3 Constraints from binary pulsars . . . 312
7.4 Projected sensitivities for laser-interferometer gravitational-wave detectors . . . 324
7.4.1 Dipole radiation for binary neutron-star inspirals . . . 325
7.4.2 Dynamical scalarization . . . 336
7.5 Conclusions . . . 344
7.6 Acknowledgments . . . 348

8 Distinguishing boson stars from black holes and neutron stars from tidal interactions in inspiraling binary systems 349
8.1 Introduction . . . 350
8.2 Boson star basics . . . 354
8.3 Tidal perturbations of spherically-symmetric boson stars . . . 358
8.3.1 Background configuration . . . 358
8.3.2 Tidal perturbations . . . 360
8.3.3 Extracting the tidal deformability . . . 362
8.4 Solving the background and perturbation equations . . . 364
8.5 Results . . . 369
8.5.1 Massive Boson Stars . . . 369
8.5.2 Solitonic boson stars . . . 372
8.5.3 Fits for the relation between M and Λ . . . 374
8.6 Prospective constraints . . . 375
8.6.1 Estimating the precision of tidal deformability measurements . 375
8.6.2 Distinguishability with a single deformability measurement . . 383
8.6.3 Distinguishability with a pair of deformability measurements . 386

8.7 Conclusions . . . 392
8.8 Acknowledgments . . . 397

9 Parameterized tests of general relativity with generic frequency-domain waveform models 398
9.1 Introduction . . . 399
9.2 The FTA construction of generalized waveform models . . . 402
9.3 Theory-agnostic inspiral tests with LIGO/Virgo events . . . 405
9.4 Constraints on Jordan-Fierz-Brans-Dicke gravity from GW170817 . . . 410
9.4.1 Gravitational-wave signature of Jordan-Fierz-Brans-Dicke gravity . . . 413
9.4.1.1 Isolated neutron star solutions in Jordan-Fierz-Brans-Dicke gravity . . . 414
9.4.1.2 Polynomial fits of the neutron star scalar charge . . . 416
9.4.2 Constraining α_0 with GW170817 . . . 418
9.5 Constraints on higher-order curvature corrections from GW151226 and GW170608 . . . 423
9.5.1 Gravitational-wave signature of higher-order curvature corrections . . . 425
9.5.1.1 Conservative dynamics . . . 426
9.5.1.2 Dissipative dynamics . . . 427
9.5.1.3 Gravitational waveform in the stationary phase approximation . . . 428
9.5.1.4 On the validity of the post-Newtonian waveform model 429
9.5.2 Constraining d_Λ with GW151226 and GW170608 . . . 430

10 Conclusions and future work 436

A The 1PN two-body Lagrangian in Einstein-Maxwell-dilaton theory 442
A.1 Expanding the metric and connection coefficients . . . 442
A.2 Expanding the action . . . 443
A.3 The field equations . . . 446
A.4 The 1PN Lagrangian . . . 449

B Energy flux to next-to-leading PN order in Einstein-Maxwell-dilaton theory 450
B.1 Scalar energy flux . . . 450
B.2 Vector energy flux . . . 457
B.3 Tensor energy flux . . . 461
B.4 Energy flux for circular orbits . . . 464

C Translating between scalar-tensor theory notations 466

D Explicit formulas for the Fourier-domain phasing of waveforms in scalar-tensor theories 468

E Post-Dickean expansion of mass and scalar charge 478

F Two-body potentials at post-Dickean order 480

G A closer look at the dynamical scalarization model of *Palenzuela et. al.* 482

H Effective action for compact objects away from critical point 488

I Numerical calculation of the effective point-particle action $V(q)$ 493

J Ingredients for the Fisher matrix analysis 495

K Dynamical scalarization in ultra-relativistic binary neutron stars 498

List of Tables

2.1 Effective-one-body Hamiltonians in Einstein-Maxwell-dilaton theory . 124

3.1 Scalar-tensor parameters 138
3.2 Weak-field constraints on scalar-tensor parameters 142

4.1 Resummation schemes of the post-Dickean expansion 193
4.2 Orbital and gravitational-wave frequency of dynamical scalarization . 222

7.1 Parameters of binary pulsar used to constrain scalar-tensor theories . 313
7.2 Constraints on scalar-tensor parameters from binary-pulsar observations 320
7.3 Limits from binary-pulsar observations on number of gravitational-wave cycles in binary neutron stars in scalar-tensor theories 326
7.4 Dynamical scalarization frequency of equal mass binary neutron stars 337
7.5 Dynamical scalarization of binary neutron stars given binary pulsar constraints 341

9.1 One-dimensional polynomial fits of neutron star coupling in Jordan-Fierz-Brans-Dicke gravity 416
9.2 Multivariate polynomial fits of neutron star coupling in Jordan-Fierz-Brans-Dicke gravity 417

E.1 Resummed component of mass and scalar charge for various resummation schemes 479

List of Figures

1.1 Theory-specific/agnostic and top-down/bottom classification of thesis contents . . . 45
1.2 Projected constraints on Einstein-Maxwell-dilaton gravity . . . 49
1.3 Scalar charge of dynamically scalarized binary neutron star . . . 52
1.4 Hamiltonian of dynamically scalarized binary neutron star . . . 54
1.5 Scalarization phase space for binary black holes in Einstein-Maxwell-scalar gravity . . . 57
1.6 Projected constraints on scalar dipole . . . 60
1.7 Tidal deformability of boson stars . . . 62
1.8 Constraints on higher-order curvature corrections . . . 67

2.1 Scalar charge of isolated black hole in Einstein-Maxwell-dilaton gravity 80
2.2 Scalar charge of test black hole in Schwarzschild background in Einstein-Maxwell-dilaton gravity . . . 81
2.3 Validity of post-Newtonian expansion in various alternative theories of gravity . . . 87
2.4 Scalar charge of binary black hole with equal electric charge . . . 92
2.5 Scalar charge of binary black hole with equal mass . . . 93
2.6 Energy flux of binary black holes in Einstein-Maxwell-dilaton gravity 96
2.7 Energy flux of binary black holes in Einstein-Maxwell-dilaton gravity 97
2.8 Projected constraints on Einstein-Maxwell-dilaton gravity . . . 98
2.9 Phase difference between Einstein-Maxwell-dilaton gravity and General Relativity . . . 106
2.10 Number of useful cycles in Einstein-Maxwell-dilaton gravity . . . 110
2.11 Effective-one-body binding energy in Einstein-Maxwell-dilaton gravity 123
2.12 Innermost stable circular orbit of effective spacetime in Einstein-Maxwell-dilaton gravity . . . 124

4.1 Scalar charge of isolated neutron star in scalar-tensor theories . . . 184
4.2 Analytic approximations of scalar-tensor theories . . . 186
4.3 Breakdown of post-Newtonian expansion at onset of dynamical scalarization . . . 190

4.4 Scalar mass of dynamically scalarized binary neutron star 218
4.5 Resummed scalar charge of binary neutron star 223
4.6 Comparison of models of dynamical scalarization 224

5.1 Effective point-particle potential for neutron stars in scalar-tensor theories 254
5.2 Dynamical scalarization of binary neutron stars 256
5.3 Binding energy of dynamically scalarized binary neutron stars 259
5.4 Hamiltonian of dynamically scalarized binary neutron star 265
5.5 Binding energy of binary neutron stars undergoing spontaneous, induced, and dynamical scalarization 266

6.1 Theory-agnostic approach to model scalarizing compact objects . . . 280
6.2 Effective point-particle potential for black holes in Einstein-Maxwell-scalar theory 285
6.3 Critical behavior of black-hole scalar charge near the onset of scalarization 294
6.4 Scalar charge of dynamically scalarized black holes in Einstein-Maxwell-scalar theory 298
6.5 Scalarization phase space of binary black holes in Einstein-Maxwell-scalar theory 300

7.1 Spontaneous scalarization in scalar-tensor theories 309
7.2 Neutron-star mass and radius for several equations of state 314
7.3 Posterior distributions of scalar-tensor parameters from binary-pulsar observations 319
7.4 Constraints on scalar-tensor parameters from binary-pulsar observations 321
7.5 Allowed scalar coupling of isolated neutron stars given binary-pulsar observations 322
7.6 Noise spectral density of ground-based gravitational-wave detectors . 330
7.7 Sensitivity of ground-based gravitational-wave detectors to scalar dipole in binary neutron stars 331
7.8 Correlations between binary neutron-star parameters 332
7.9 Projected upper limits on scalar-tensor parameters from gravitational-wave observations 335
7.10 Dynamical scalarization of binary neutron stars given binary pulsar constraints 340

8.1 Boson star tidal perturbations 367
8.2 Tidal deformability of massive boson stars 369
8.3 Tidal deformability of solitonic boson stars 372
8.4 Phase difference between tidal waveform models 379
8.5 Projected tidal-parameter measurement uncertainty for binary black holes with Advanced LIGO 385

8.6 Projected tidal-parameter measurement uncertainty for binary neutron stars with Advanced LIGO . . . 387
8.7 Discriminating neutron stars from boson stars with projected measurement precision of Advanced LIGO . . . 390
8.8 Discriminating black holes from boson stars with projected measurement precision of current and planned gravitational-wave detectors . 393

9.1 Posterior distributions of deviations from post-Newtonian predictions in binary black hole and neutron star events observed by LIGO and Virgo . . . 407
9.2 Upper bounds on deviations from post-Newtonian predictions in binary black hole and neutron star events observed by LIGO and Virgo 408
9.3 Prior distributions on Jordan-Fierz-Brans-Dicke parameter . . . 420
9.4 Posterior distributions on Jordan-Fierz-Brans-Dicke parameter from GW170817 . . . 421
9.5 Independent constraints on higher-order curvature corrections from GW151226 and GW170608 . . . 433
9.6 Combined constraints on higher-order curvature corrections from both GW151226 and GW170608 . . . 434

G.1 Ambiguities in the dynamical scalarization model of *Palenzuela et al.* due to derivatives of scalar charge . . . 483
G.2 Ambiguities in the dynamical scalarization model of *Palenzuela et al.* due to post-Newtonian corrections to feedback loop . . . 485

K.1 Dynamical scalarization of neutron stars with ultra-relativistic cores . 499

List of Abbreviations

ADM	Arnowitt-Deser-Misner
BBH	Binary black hole
BH	Black hole
BNS	Binary neutron star
BS	Boson star
DD	Dipole-driven
EA	Einstein-Æther
EFT	Effective field theory
EMd	Einstein-Maxwell-dilaton gravity
EMS	Einstein-Maxwell-Scalar gravity
EOB	Effective-one-body
ESGB	Einstein-Scalar-Gauss-Bonnet gravity
GR	General relativity
GW	Gravitational wave
JFBD	Jordan-Fierz-Brans-Dicke gravity
NS	Neutron star
PN	Post-Newtonian
QD	Quadrupole-driven
SPA	Stationary phase approximation
ST	Scalar-tensor

Chapter 1: Introduction

1.1 Einstein's theory of general relativity

Formulated by Albert Einstein over a century ago [12, 13], general relativity (GR) remains one of the most successful physical theories of the modern era. At its core, the theory embodies the equivalence principle—the notion that a local observer cannot distinguish the effects of gravity from the "fictitious forces" expected in a non-inertial frame of reference. Mathematically, this stipulation requires that (locally) the equations that describe the laws of physics including gravity can be reduced to their non-gravitational analogs through an appropriate choice of coordinate system. The underlying structure of such a coordinate system was established by Minkowski a decade prior [14]: space and time come fused together as a four-dimensional spacetime that is covariant under Lorentz transformations. Combining these two ideas, the natural canvas for a relativistic theory of gravity is curved spacetime, represented by a differentiable manifold $\mathcal{M}$ equipped with a metric $g_{\mu\nu}$ and the unique torsion-free, affine connection compatible with that metric. Gravity is described entirely by the curvature of this connection, as encapsulated by

the Riemann tensor $R_{\lambda\mu\sigma\nu}$.[1] At any point in spacetime, one can construct normal coordinates in which (locally) the metric reduces to that of Minkowski spacetime $\eta_{\mu\nu} = \text{diag}(-1, 1, 1, 1)$, and thus all laws of physics appear as they would in special relativity, i.e. in their form absent gravity.

In GR, the metric $g_{\mu\nu}$ dynamically responds to matter (or energy) as described by the Einstein field equations

$$R_{\mu\nu} - \frac{1}{2} g_{\mu\nu} R + \Lambda g_{\mu\nu} = 8\pi T_{\mu\nu}, \tag{1.1}$$

where $R_{\mu\nu} \equiv g^{\lambda\sigma} R_{\lambda\mu\sigma\nu}$ is the Ricci tensor, $R \equiv g^{\mu\nu} R_{\mu\nu}$ is the Ricci scalar, Λ is a cosmological constant, and $T_{\mu\nu}$ is the stress-energy tensor of the matter in the spacetime, which I collectively represent by the field(s) ψ. As most concisely put by Misner, Thorne, and Wheeler, these differential equations determine the manner in which "matter tells space how to curve [and] space tells matter how to move," [15]. The latter statement can be more clearly seen using the Bianchi identity in conjunction with Eq. (1.1) to show

$$\nabla_\mu T^{\mu\nu} = 0, \tag{1.2}$$

which, when $T_{\mu\nu}$ describes a point particle minimally coupled to gravity, reduces to the geodesic equation for that particle's worldline. Solutions to the Einstein field

[1] Throughout this thesis, I adopt the sign conventions of Ref. [15] for the Riemann tensor and its associated covariant derivatives ∇_μ. Additionally, unless explicitly stated otherwise, I work in geometric units where $G = c = 1$. Greek indices represent temporal and spatial components (e.g. $\mu = 0, 1, ...$) whereas Latin indices represent only spatial components (e.g. $i = 1, 2, ...$).

equations are local extrema of the Einstein-Hilbert action

$$S[g_{\mu\nu}, \psi] = \frac{1}{16\pi} \int d^4x \sqrt{-g} \, (R - 2\Lambda) + S_m[g_{\mu\nu}, \psi], \tag{1.3}$$

where S_m is the action of the matter ψ on the curved spacetime specified by $g_{\mu\nu}$, which determines the stress-energy tensor via

$$T_{\mu\nu} = \frac{-2}{\sqrt{-g}} \frac{\delta S_m}{\delta g^{\mu\nu}}. \tag{1.4}$$

For example, in the aforementioned case of a point particle of mass m minimally coupled to the metric, the appropriate matter action and stress-energy are

$$S_m = -m \int d\tau \sqrt{-g_{\mu\nu} u^\mu u^\nu}, \qquad T_{\mu\nu} = \frac{m}{\sqrt{-g}} \int d\tau \, u_\mu u_\nu \delta^{(4)}(\gamma^\alpha(\tau) - x^\alpha), \tag{1.5}$$

where $u^\mu \equiv d\gamma^\mu/d\tau$ is the four-velocity of the particle's worldline γ^μ, parameterized by an arbitrary affine parameter τ.

Compared to its non-relativistic predecessors, GR represents a massive repudiation in our understanding of the nature of gravity. Accompanying this paradigm shift, the theory predicts novel phenomena absent in Newtonian gravity. This thesis primarily contends with two such predictions: black holes (BHs) and gravitational waves (GWs). I provide a brief introduction to each topic in the remainder of this subsection.

First predicted only one year after the advent of GR [16], BHs are localized regions of curvature. The defining feature of BH spacetimes is the presence of an event horizon. This hypersurface divides the spacetime into interior and exterior regions such that future-oriented timelike and lightlike curves originating in the former cannot cross into the latter. Physically, the event horizon represents a one-way

boundary for the flow of information; any matter or radiation that enters the BH interior can never escape. Black holes primarily form through the gravitational collapse of matter. Whether a collapsing matter configuration will form a BH depends primarily on its compactness, i.e. the ratio of its mass to its (linear) size; though still unproven, the Hoop conjecture [17] posits that a BH forms only when matter of mass M fits within a spherical shell with the Schwarzschild radius $R_S = 2M$. In our local universe, the densities needed to form a BH can only occur during the final stage of the evolution of very massive stars. However, in the very early universe, critically over-dense regions could have also collapsed to form primordial BHs that may have survived to the present [18–20]. Current observations point to the existence of astrophysical BHs of two distinct varieties, distinguished by their mass: stellar-mass BHs ($10^0 M_\odot \lesssim M \lesssim 10^2 M_\odot$) and supermassive BHs ($10^5 M_\odot \lesssim M \lesssim 10^9 M_\odot$).[2] This thesis focuses on the former class, as they represent viable sources for ground-based GW detectors.

A number of properties of BHs predicted in GR offer compelling targets for both theoretical and observational study. For example, BH spacetimes in GR appear only to come in a relatively limited variety—this property is often categorized as the "no-hair conjecture." This property posits that all isolated BHs coupled to electromagnetism are uniquely specified by their mass, spin, and electric charge; contrast this scenario to that of composite systems of charged baryons, which can differ by any of an infinite number of independent multipole moments. This prop-

[2] The latter class is sometimes further subdivided into "massive" and "supermassive" BHs; this distinction is not needed for this thesis, so I categorize those two classes together.

erty has also been shown to hold for BHs coupled to other fields [21–23] (though not all [24]). Another intriguing property of BHs in GR is their connection to spacetime singularities. Penrose famously showed that BHs formed through gravitational collapse will generically host a singularity in their interior region, provided that the imploding matter obeys the null energy condition [25]. The presence of such a singularity indicates that GR is non-predictive in such a region and highlights the need for new physical insight to complete the theory.

Besides BHs, another of the earliest predictions of GR was the existence of GWs [26, 27]—wavelike perturbations of the metric that propagate energy and momentum at the speed of light. Their basic structure can be seen by considering gravity linearized around a flat background, wherein the metric takes the form $g_{\mu\nu} = \eta_{\mu\nu} + h_{\mu\nu}$ with $|h_{\mu\nu}| \ll 1$. Inserting this ansatz into Eq. (1.1) and dropping terms non-linear in the metric perturbation $h_{\mu\nu}$ reveals that its trace-reverse $\bar{h}_{\mu\nu} \equiv h_{\mu\nu} - \frac{1}{2}\eta_{\mu\nu}\eta^{\lambda\sigma}h_{\lambda\sigma}$ obeys a wave equation provided that one works in the Lorenz gauge $\partial_\mu \bar{h}^{\mu\nu} = 0$:

$$\Box \bar{h}_{\mu\nu} = -16\pi T_{\mu\nu}, \tag{1.6}$$

where $\Box$ is the flat-space D'Alambertian operator. In vacuum, one can use gauge symmetries to eliminate all but two independent components of this tensor, which correspond to the two polarizations of GWs predicted in GR. In the appropriate gauge, these non-trivial components are spatial ($h_{0\mu} = 0$), transverse ($\eta^{ij}\partial_i h_{jk} = 0$) and traceless ($\eta^{ij}h_{ij} = 0$). These physical components can be distilled from $\bar{h}_{\mu\nu}$ with

an appropriate projection operator that depends on the direction of propagation $\hat{\mathbf{n}}$

$$h_{ij}^{\mathrm{TT}} = \Lambda_{ij}{}^{kl}(\hat{\mathbf{n}})\bar{h}_{kl}, \tag{1.7}$$

where the superscript denotes the "transverse-traceless" gauge described above; a complete expression for $\Lambda_{ij}{}^{kl}$ is given in Eq. (1.39) of Ref. [28].

The central theme of this thesis is to motivate and improve tests of the fundamental nature of gravity using GWs. I focus on GWs produced by compact binary systems, i.e. binaries comprised of objects with compactness $C = M/R \gtrsim 10^{-2}$; the only known astrophysical objects that surpass this threshold are BHs and neutron stars (NSs). In the remainder of this chapter, I outline the phenomenology of such GWs and discuss the techniques used to model these predictions. I outline how these waveform models are employed to detect GWs and to infer the properties of the signals' sources and the underlying fundamental physics that govern their behavior. Next, I discuss motivations for and examples of modified theories of gravity, highlighting the potential imprint of such modifications in GW signals observable with detectors. I describe various considerations involved in formulating tests of gravity with GW observations. Finally, I end with a more detailed overview of the work contained in this thesis.

1.2 Gravitational-wave science with compact binaries

1.2.1 Generation by compact binary coalescence

The GWs produced by coalescing compact binary systems can be divided into three phases: inspiral, merger, and ringdown. In this section, I provide a brief overview of each of these phases, highlighting the techniques used to study the two-body problem in each regime. This thesis primarily focuses on the inspiral behavior of binary systems, and so I discuss that topic in the greatest detail. However, I include an abbreviated review of the other phases as a foundation for discussions of inspiral-merger-ringdown (IMR) models that synthesize information from all regimes and also to establish the broader context for the inspiral results presented here.

1.2.1.1 Early inspiral

The inspiral phase of a binary system begins with the two bodies well-separated. The binary is characterized by three independent distance scales: the size of each body R_1 and R_2 and their separation r. For compact objects, to which I restrict my attention, the bodies' masses satisfy $m_i \sim R_i$; for convenience, I label the bodies such that $m_1 \geq m_2$. The inspiral begins in the regime in which there is a clear hierarchy between these various scales, meaning that $m_2 \ll m_1$ and/or $m_1 \ll r$. The gravitational radiation produced by the binary during the early inspiral can differ significantly between these two cases. Accordingly, the computational techniques used to predict this radiation differ as well. Analytic approaches to the two-body

problem attempt to solve the field equations (1.1) perturbatively in the appropriate small parameter: $q \equiv m_2/m_1$ or $\epsilon \equiv M/r$, respectively, where $M \equiv m_1 + m_2$. The former approach relies on computing the so-called gravitational self-force of the smaller body moving in a background spacetime associated with the larger body; see Ref. [29] and references therein for a pedagogical review of this approach. The latter approach is known as the post-Newtonian (PN) approximation, which serves as the foundation for much of the modeling efforts described in the thesis. I outline a few basic results derived using the PN approximation below, but refer the reader to Ref. [30] for a detailed review of the subject.

Within the PN approach, the motion of the binary is solved order-by-order in a power series expansion in the small parameter ϵ around the Newtonian prediction. Equivalently, because I consider bound orbits, this is a low-velocity expansion with $\epsilon \sim v^2$. The quadrupole formula, computed first in Einstein's original paper on GWs [26] , describes the leading-order PN prediction for the GWs observed far from a compact source. Despite its simplicity, this result offers key insights into the gravitational radiation from compact binaries that remain true at higher PN orders. I provide a brief derivation below.

Working within linearized gravity (a valid assumption when working at leading PN order), Eq. (1.6) can be formally inverted leaving

$$\begin{aligned} \bar{h}_{ij}(x^\alpha) =& 4 \int d^4x' \, \delta \left(x^0 - x'^0 - |\mathbf{x} - \mathbf{x}'| \right) \frac{T_{ij}(x')}{|\mathbf{x} - \mathbf{x}'|}, \\ =& \frac{4}{d} \int d^3x' \, T_{ij}(t_{\rm ret} + \mathbf{x}' \cdot \hat{\mathbf{n}}, \mathbf{x}'), \end{aligned} \tag{1.8}$$

where I have used that at distances $d \equiv |\mathbf{x}| \gg r$ far from the binary, the denominator

can be approximated by $|\mathbf{x}-\mathbf{x}'| = d - \mathbf{x}'\cdot\hat{\mathbf{n}} + \mathcal{O}(r^2/d)$ and defined the unit vector $\hat{\mathbf{n}} \equiv \mathbf{x}/d$ and the retarded time $t_{\rm ret} \equiv x^0 - d$. Then, one can Taylor expand the integrand in Eq. (1.8) to

$$T_{ij}(t_{\rm ret} + \mathbf{x}'\cdot\hat{\mathbf{n}}, \mathbf{x}') = T_{ij}(t_{\rm ret}, \mathbf{x}') + (\mathbf{x}'\cdot\hat{\mathbf{n}})\,\partial_0 T_{ij}(t_{\rm ret}, \mathbf{x}') + \frac{(\mathbf{x}'\cdot\hat{\mathbf{n}})^2}{2}\partial_0^2 T_{ij}(t_{\rm ret}, \mathbf{x}') + \ldots, \tag{1.9}$$

The most relevant time scale of the binary's motion is its orbital period $\tau_{\rm orb} = r/v$; thus we see that each time derivative above introduces a power of v to the final result, and so Eq. (1.9) corresponds to a PN expansion. Keeping only the first term, I insert Eq. (1.9) into Eq. (1.8). Because I am working within the regime of linearized gravity, the non-linearities in Eq. (1.2) can be neglected, leaving the identity $\partial_\mu T^{\mu\nu} = 0$; by repeatedly employing this identity, one can integrate Eq. (1.8) by parts to show that

$$\bar{h}_{ij} = \frac{2}{d}\left(\ddot{M}_{ij}(t_{\rm ret}) + \mathcal{O}(v^3)\right), \tag{1.10}$$

where $M_{ij} \equiv \int d^3x'\, T^{00} x_i x_j$ is the quadrupole moment of the source. Finally, the physical (non-gauge) components representing the GWs are extracted by applying the operator $\Lambda_{ij}{}^{kl}$ to Eq. (1.10). Note that by simplifying Eq. (1.2) as done above, I have implicitly assumed that the sources are weakly self-gravitating, i.e. the gravitational field does not comprise a major component of their stress-energy. Given that I wish to study the behavior of compact objects, whose self-gravity is non-negligible, this assumption may seem unfounded. However, the property of effacement in GR guarantees that the strong internal gravitational fields of the compact bodies influence the dynamics of a binary only at comparatively high PN order: at 2PN for

spinning bodies and 5PN for non-spinning bodies [31].

I highlight a few important consequences of Eq. (1.10). First, the dominant component of GWs arises from quadrupolar radiation, i.e. radiation produced by a time-varying quadrupole moment. Though the derivation above was done only at leading PN order, in fact, monopolar and dipolar radiation (which dimensional arguments would suggest enter at lower order) are absent in GR even when non-linear gravitational interactions are considered. These dissipative channels are protected due to the diffeomorphism invariance of the theory and the fact that gravity is mediated solely by the metric; these conditions guarantee that GWs behave as massless, spin-2 gauge fields, which cannot be be excited by a purely monopolar or dipolar source (see Secs. 2.2.3 and 3.3.1 of Ref. [28] for more detail). However, as we shall see in Section 1.3, many possible extensions of GR violate these two conditions; the additional dissipative channels available in these theories can dramatically affect the rate at which compact binaries coalesce.

A second key observation is that GWs produced during the inspiral are directly linked to the motion of the binary. Using two copies of Eq. (1.4) as the stress-energy for a binary system, one sees that the quadrupole moment oscillates at twice the orbital frequency. Hence, for binaries on circular orbits, the dominant GW frequency is precisely two times the orbital frequency. However, the GW signal produced by binaries following eccentric orbits is comprised of a more complex spectrum of Fourier modes. Throughout this thesis, I restrict my attention to systems on non-eccentric orbits. This assumption is valid for stellar-mass binaries that form in isolation, as they are expected to have radiated nearly all eccentricity before

reaching orbital frequencies observable with ground-based GW detectors [28, 32]. However, binaries that form through dynamical processes, such as by dynamical capture in dense stellar environments [33] or through three-body interactions like the Kozai-Lidov mechanism [34, 35], may not have time to circularize before becoming observable with ground-based detectors; in these scenarios, the binaries can retain eccentricity up to $e \lesssim 10^{-1}$ upon entering the frequency band of Advanced LIGO/Virgo. Work to detect and measure such eccentric systems is underway [36], but I do not pursue it further in this dissertation.

Without eccentricity, the inspiral evolution of a binary is well-described by a circular orbit whose radius slowly decreases—such a binary is said to follow quasi-circular orbits. Using the quadrupole formula (1.10) and dimensional analysis, one can formulate this statement more precisely by comparing the orbital period $\tau_{\rm orb}$ to the radiation-reaction timescale $\tau_{\rm RR}$, which is the timescale over which the dissipation of energy through GWs alters the circular orbit. One can approximate $\tau_{\rm RR}$ as the ratio of the binding energy $E \sim Mv^2$ and the rate at which energy is emitted by the system dE/dt. The energy flux $\mathcal{F}$ propagated by gravitational radiation is encapsulated in the Landau-Lifshitz pseudotensor [37]; in the transverse-traceless gauge, this is given by $\mathcal{F} \sim \dot{h}^{\rm TT}_{ij}\dot{h}^{ij}_{\rm TT} \sim v^{10}/d^2$. Integrating the flux over a sphere of size d, one finds $\tau_{\rm RR} \sim E/(dE/dt) \sim M/v^8$, which differs from the orbital timescale $\tau_{\rm orb} \sim r/v \sim M/v^3$ by a factor of v^{-5}. Thus, during the early inspiral, where $v \ll 1$ by assumption, the evolution of the binary is said to be (approximately) adiabatic.

Extending the GW prediction (1.10) to higher PN order requires utilizing the hierarchy of timescales in the problem. In addition to the the orbital and

radiation-reaction timescales discussed above, spinning bodies will also precess on the timescale $\tau_{\rm prec}$, with $\tau_{\rm orb} \ll \tau_{\rm prec} \ll \tau_{\rm RR}$. One begins by determining the orbital dynamics of the binary, working on short enough timescales that precession and radiation-reaction enter as sub-leading effects; I carry out this procedure in the context of two modified theories of gravity in Chapters 2 and 4. Inserting this solution into the stress-energy tensor, one then computes the gravitational radiation at the given PN order (see Chapter 2 for an example). The precessional dynamics, which I do not consider in this thesis, are then determined by averaging the previous solutions over the orbital timescale, while still treating radiation-reaction as subdominant. Finally, by relating the energy carried away by this outgoing radiation to a commensurate shift in the energy of the orbit, one determines the rate at which the quasi-circular orbits shrink. All of these pieces are combined to produce the most accurate prediction for the GWs at a given PN order; I carry out these last steps in Chapters 2 and 3 for two alternative theories of gravity.

1.2.1.2 Late inspiral and merger

As the orbit of a compact binary shrinks, the perturbative PN approximation becomes increasingly inaccurate. Ultimately, the description of the system as two separate bodies breaks down, and one must contend with the non-linearities in the field equations (1.1) in a non-perturbative way. In this subsection, I discuss the phenomenology at the end of the inspiral and introduce the effective-one-body (EOB) formalism [38, 39], a resummation of the PN approximation that extends its

validity further into the non-linear regime. Finally, I outline how numerical relativity (NR) is used to compute the GW signal in the highly non-linear regime, and how these predictions can be incorporated into the previous analytic approaches.

To better understand the behavior of a binary as the PN approximation breaks down, I first consider the low mass-ratio limit $q \ll 1$. To zeroth order in this small parameter, the smaller mass M_2 simply evolves along geodesics of the spacetime determined by M_1. For simplicity, let us assume that the larger mass is a BH. Then, the quasi-circular orbits that characterize the PN inspiral can only extend up to the innermost stable circular orbit (ISCO) of the background spacetime. For a Schwarzschild background, the last (stable) circular orbit has a radius of $r_{\rm ISCO} = 6M_1 \sim 6M$; if the larger BH has spin, the ISCO radius decreases (increases) for prograde (retrograde) orbits of the smaller body. After passing through this orbit, the smaller body plunges into the larger BH on a geodesic with non-negligible radial velocity. This evolution is quite distinct from the earlier quasi-circular orbits, in which the velocity was primarily tangential; thus the passage through the ISCO and the start of the plunge offers a clear indication that the inspiral has ended.

The EOB formalism uses results derived in the PN regime to extend the test-particle limit used above to non-zero values of q. The overarching aim of this approach is to map the dynamics of a binary to that of a test body moving in an effective background spacetime determined by the binary's characteristics. This goal is realized by mapping the Hamiltonians and radiation-reaction forces (which describe the conservative and dissipative sectors of the system, respectively) for test particle motion to a resummation of PN description of the two-body problem.

For demonstrative purposes, I simply focus on the conservative sector and ignore the effect of spins. Schematically, one maps the real and effective spacetimes by identifying conserved action angle variables in the orbits of each. This identification, in turn, determines a mapping between the 2-body Hamiltonian $H_{\rm real}$ describing the PN motion of two bodies and the Hamiltonian $H_{\rm eff}$ describing the motion of a test particle moving through the effective spacetime, i.e. $H_{\rm eff} = f(H_{\rm real})$. The energy map, first derived in Ref. [38] is given by

$$\frac{H_{\rm eff} - \mu}{\mu} = \frac{H_{\rm real} - M}{\mu}\left[1 + \frac{\eta}{2}\frac{H_{\rm real} - M}{\mu}\right], \tag{1.11}$$

where $\mu = M_1 M_2/M^2$ is the reduced mass and $\eta = \mu/M$ is the symmetric mass ratio, or equivalently,

$$H_{\rm real} - M = M\sqrt{1 + 2\eta\left(\frac{H_{\rm eff} - \mu}{\mu}\right)} - M. \tag{1.12}$$

The effective spacetime is constructed by first considering generic deformations to a background Kerr spacetime (or Schwarzschild for non-spinning binaries). From this ansatz for the effective geometry, one constructs the suitable effective Hamiltonian $H_{\rm eff}$ that describes test-body motion in that spacetime. Then, one identifies a suitable choice of effective spacetime by requiring that $H_{\rm eff}$ satisfy Eq. (1.12) for an appropriate PN estimate of $H_{\rm real}$. I carry out this procedure in Chapter 2 in the context of a modified theory of gravity. Note that the knowledge of the real Hamiltonian is incomplete, e.g. the expression is only known up to some finite PN order, which leaves some flexibility in how the effective spacetime is defined. Oftentimes, one leverages this ignorance by calibrating the model to include information from other sources, such as from gravitational self-force calculations [40–43] or from

NR [44, 45]. This extra tuning, particularly from NR simulations, allows the analytic EOB formalism to track the evolution of a binary through merger, where highly non-linear interactions arise.

Even discounting its impact on the calibration of EOB models, the advent of NR simulations of binary systems over the last decade and a half has played a crucial role in furthering our understanding of compact binary mergers. Numerical relativity is based on the 3+1 decomposition of spacetime first described within the Arnowitt-Deser-Misner (ADM) formalism [46, 47], which divides the Einstein equations into a set of four constraint equations, to be solved on a spacelike hypersurface, and 12 first order evolution equations, which conserve the constraint equations, i.e. if the constraint equations are satisfied on one spacelike hypersurface, then they are also satisfied on nearby slices. However, the first successful numerical evolutions of BBHs was not achieved until much later [48–50] using multiple different formulations of the Einstein equations. Today, several NR codes actively produce numerical evolutions of BBHs and BNSs and extract the GW signals they generate, using various formulations of the Einstein equations, numerical schemes, and computational techniques; see Refs. [51, 52] and references therein for details. However, such simulations can be very computationally expensive, taking months to finish even when parallelized over several hundred cores on supercomputers. Thus, analytic models remain necessary as a fast and efficient supplement to numerical simulations to detect GW events with LIGO/Virgo and infer properties of their corresponding sources.

1.2.1.3 Ringdown

After merger, the system continues to emit GWs as it relaxes into its final equilibrium configuration. Sufficiently long after the merger, the system is well-described by perturbations of the background solution to (1.1) corresponding to the final remnant object. When the remnant is just given by a vacuum configuration, e.g. after the merger of a stellar-mass binary black hole (BBH) or neutron-star black-hole (NSBH) binary, the system is completely described by tensor perturbations on a Kerr background

$$g_{\mu\nu} = g^{(\mathrm{Kerr})}_{\mu\nu} + h_{\mu\nu}, \tag{1.13}$$

with $h_{\mu\nu} \ll 1$. I focus on this simple case, but similar phenomenology can occur after the formation of a hypermassive NS from a binary neutron star (BNS) merger [53, 54], though in that case, the system is described by perturbations to both the metric and matter fields.

Working within the linear regime, that is ignoring any backreaction of $h_{\mu\nu}$ on $g^{(\mathrm{Kerr})}_{\mu\nu}$, and assuming physical boundary conditions, the late-time behavior of $h_{\mu\nu}$ is given by a sum of quasinormal modes whose time-dependence takes the form $e^{i\omega_n t}$ with a complex frequency ω_n [55, 56]. Thus, any distant observer would measure a GW signal composed of damped sinusoids. Fully non-linear NR simulations of merging BHs confirm that in astrophysical systems, the post-merger GW signal is indeed well reproduced by a sum of exponentially decaying sinusoids.

1.2.2 Observation with ground-based detectors

In the following subsections, I provide an overview of laser-interferometric GW detectors and how they are used to measure GW. Other techniques for detecting GWs have been devised (e.g. Weber bars [57–59] and atom interferometry [60–62]), but I focus only on laser interferometry for the remainder of the thesis.

1.2.2.1 Laser-interferometric detectors

The measurement of GWs involves tracking the motion of freely-falling test masses, which, absent any external forces, simply follow geodesics of spacetime. Incident GWs, which are wave-like perturbations of curvature, will induce deviations to the background geodesic motion of the masses. The equivalence principle guarantees that the response of a single test mass cannot be disentangled from the gauge freedom in defining a reference frame; however, the *relative motion* of a system of (separated) test masses does provide a signature for GWs. In the limit that the separation of the masses is much smaller than the curvature scale, the relative separation $\xi^\mu(\tau)$ of the two bodies is given by the geodesic deviation equation

$$T^\alpha \nabla_\alpha (T^\beta \nabla_\beta \xi^\mu) = R^\mu{}_{\nu\rho\sigma} T^\nu T^\rho \xi^\sigma + \mathcal{O}\left(\xi^2\right) \tag{1.14}$$

where $T^\mu = d\gamma^\mu/d\tau$ is the four-velocity of one of the bodies. For weak perturbations $\delta R_{\mu\nu\rho\sigma}$ that vary over different timescales than the background $R^{(0)}_{\mu\nu\rho\sigma}$ (e.g., a static background curvature produced by the Earth and an incident GW with only non-zero frequency content), one sees that the change in relative separation of two test

masses initially at rest scales as $\delta\xi \sim h\,\xi^{(0)}$, where $h \ll 1$ is the magnitude of the perturbation and $\xi^{(0)}$ is the separation of the background geodesics. Thus, the success of a GW detector relies on its ability to resolve small distance variations between test masses located at long relative distances.

Laser interferometry is an ideal technique for achieving this goal. In its simplest form, a phase-coherent beam of light (e.g., from a laser) is passed through a beam splitter, and the subsequent beams are directed through two orthogonal arms. The beams are reflected off mirrors at the end of each arm, and then are recombined back at the source. The difference in the path length for each beam (modulo the wavelength of the light) determines the intensity of the combined light, allowing for relative distance measurements on the sub-wavelength scale. Absent any other forces, the mirrors in each arm follow geodesics, and so a GW passing through the detector changes the proper length of each cavity and thus the intensity of the recombined beam. In reality, other external forces are applied to the mirrors; some, like the vertical force to suspend the mirrors in the cavities, do not impact the response of the interferometer to an incident GW, whereas others, such as those from radiation pressure, thermal and seismic fluctuations carried through the suspension system, or time-varying (Newtonian) gravitational gradients from the external environment, are more difficult to disentangle from GWs, and thus serve as sources of noise in the detector.

The LIGO [63] and Virgo [64] instruments refine this basic principle using more complex optical systems; I outline a few such improvements, but direct the interested reader to Refs. [63–66] for more detail. Rather than simply recombining

the laser light after a single transit through the detector, Fabry-Perot cavities are used for the arms, allowing one to increase the effective path length of the photons by $\sim \mathcal{O}(100)$, with an equivalent increase in sensitivity to GWs. A similar technique is used to increase the effective power of the laser by another factor of $\sim \mathcal{O}(100)$; a power recycling mirror is coupled to the system to capture light emitted from the beam splitter back to the laser. Increasing the laser power helps to reduce quantum shot noise in the system, described below.

Experimental noise ultimately determines the sensitivity of a detector, and consequently the quantity and quality of the GW science for which it can be used. In the remainder of this section, I outline the major sources of noise in the LIGO and Virgo instruments. Each source of noise impacts the frequency-dependent response of the detector differently, and thus techniques to mitigate noise over some frequency bands may worsen sensitivity at other frequencies. The calibration of the detectors involves balancing the various sources of noise to construct the most effective instrument for the desired science. I discuss two broad categories of noise sources below: optical read-out noise and displacement noise [28]. The former class of noise arises from the quantum nature of the optical system, whereas the latter represents classical disturbances that impact the motion of the test masses.

Optical read-out noise in an interferometer is comprised of quantum shot noise and radiation-pressure noise. Shot noise occurs due to the quantized nature of light; because the beam traveling through the detector arms is composed of a finite number of photons, the intensity of light measured by the interferometer fluctuates following Poisson counting statistics. This noise impacts the detector's sensitivity at high

frequencies, and can be mitigated by increasing the power of laser light. The photons in the interferometer exert radiation pressure on the test masses; because the intensity of photons incident on the test masses fluctuates, so too does this pressure, inducing another source of stochastic noise in the detector. Radiation pressure noise impacts the low-frequency sensitivity of the detector, and (conversely to shot noise) can be mitigated by decreasing the amount of laser light in the interferometer. Thus, a tradeoff between these two sources of noise must be made in the design of an interferometric GW detector

The two dominant sources of displacement noise are seismic and thermal fluctuations. At very low frequencies, the dominant source of noise comes from seismic activity, both from anthropogenic (e.g. nearby technicians, cars, etc.) and natural sources (e.g. surface waves in the Earth's crust). Some components of this noise can be mitigated through the complex isolation systems [63], but others, such as the time-varying gravity-gradients [67] are unavoidable. Thermal fluctuations in the test masses and the systems used to suspend them also cause small displacements in the faces of the mirrors, which in turn induce small displacements in the effective length of the detector arms. The impact of thermal noise on the detector's sensitivity decreases with frequency, but does so at a lesser rate than seismic and radiation pressure noise; thus thermal noise plays the most significant role at moderate frequencies [63].

1.2.2.2 Bayesian inference with gravitational waves

Laser interferometers are designed to resolve the minute relative distance fluctuations caused by a passing GW. However, as discussed above, instrumental and environmental noise are unavoidable; typically, noise has a much larger impact on the detector output than any incident GW. Fortunately, the characteristics of both the noise and underlying signal are well understood; this knowledge is leveraged to extract the signal from noise. In this section, I outline the strategies used by the LIGO and Virgo collaborations to detect GWs and subsequently estimate the properties of their sources.

For concreteness, I consider the time-dependent output of a single detector $d(t) \equiv h(t) + n(t)$ where $h(t)$ arises from an incident GW and $n(t)$ from noise; typically, $|h(t)| \ll |n(t)|$. Note that $h(t)$ is a contraction of the GW $h_{ij}(t - \hat{\mathbf{n}} \cdot \mathbf{x})$ (traveling in the $\hat{\mathbf{n}}$ direction) and a detector tensor $D^{ij}(\hat{\mathbf{n}})$, which encapsulates the directional dependence of the detector's sensitivity [28]. In anticipation of work to come, it is often convenient to project the incident GW into a polarization basis. In the limit that the wavelength of the GW is much larger than the detector, one can drop the spatial dependence of h_{ij} measured at the detector, and thus decompose the signal into

$$h_{ij}(t) = \sum_A h_A(t) e^A_{ij}(\hat{\mathbf{n}}), \tag{1.15}$$

where $\{e^A_{ij}\}$ are a complete set of polarization tensors. Then the detector response

is given by

$$h(t) = \sum_A F^A(\hat{\mathbf{n}}) h_A(t), \tag{1.16}$$

where $F^A(\hat{\mathbf{n}}) \equiv D^{ij} e^A_{ij}(\hat{\mathbf{n}})$ is the antenna pattern of the detector, which represents the directional-dependence of the detector's sensitivity to each GW polarization.

The noise in the LIGO and Virgo detectors is approximately stationary, meaning its statistical properties (e.g. mean, variance, etc.) are nearly constant over time. Without loss of generality, I can assume the mean of the noise $\langle n(t) \rangle = 0$, where $\langle \ldots \rangle$ represents an ensemble average of noise realizations or, assuming ergodicity, an average over a long time interval. In the Fourier domain, the correlation function for a stationary stochastic process takes a particularly simple form

$$\langle \tilde{n}^*(f) \tilde{n}(f') \rangle = \frac{1}{2} \delta(f - f') S_n(f), \tag{1.17}$$

where $S_n(f)$ is the noise spectral density of the detector; due to this simplicity, it is often more convenient to work in the Fourier domain. The noise is also approximately Gaussian, meaning that the probability of a particular noise realization n is given by

$$P(n) = \mathcal{N} \exp\left[-\frac{1}{2} (n|n) \right], \tag{1.18}$$

where $\mathcal{N}$ is an overall normalization and I have introduced the inner product

$$(a|b) \equiv \int_{-\infty}^{\infty} df \, \frac{\tilde{a}^*(f) \tilde{b}(f)}{S_n(f)/2} = 4 \, \mathrm{Re} \left(\int_0^{\infty} df \, \frac{\tilde{a}^*(f) \tilde{b}(f)}{S_n(f)} \right). \tag{1.19}$$

Matched filtering is one approach adopted by the LIGO and Virgo teams to identify the presence of a GW produced by a coalescing binary system in the data

stream $d(t)$.[3] This technique involves applying a filter to $d(t)$ that amplifies the presence of the GW $h(t)$ relative to the noise $n(t)$. The optimal (Wiener) filter for such a task is given in the Fourier domain by [28]

$$\tilde{W}_h(f) = \frac{\tilde{h}(f)}{S_n(f)}, \tag{1.20}$$

where the subscript highlights the dependence of the filter on h. This choice maximizes the (averaged) measured signal-to-noise ratio of the signal $\langle\rho\rangle$, where ρ is defined for a generic filter W as

$$\rho \equiv \frac{\int_{-\infty}^{\infty} df\, \tilde{s}(f)\tilde{W}^*(f)}{\left(\int_{-\infty}^{\infty} df\, \frac{1}{2}S_n(f)|\tilde{W}(f)|^2\right)^{1/2}}. \tag{1.21}$$

Using the filter in Eq. (1.20) gives the optimal signal-to-noise ratio SNR $\equiv (h|h)^{1/2}$. For stationary, Gaussian noise, ρ^2 follows a χ^2 distribution with two degrees of freedom whose mean is determined by the optimal SNR of the underlying GW. Thus, for a particular noise realization $n(t)$, the magnitude of ρ allows one to determine the statistical significance of the presence of a non-zero GW in the data. Larger ρ corresponds to a higher statistical significance, and thus lower false-alarm probability—the probability of such a value of ρ being achieved only through noise. A segment of data is said to contain a GW provided that ρ exceeds some predetermined threshold, which corresponds to a desired maximum false-alarm rate. In practice, the noise in an actual detector is non-stationary and non-Gaussian, and so ρ^2 does not follow a χ^2 distribution and serves as a poor test statistic for determining

[3] Other, more model-independent strategies are also employed to detect GWs, particularly for short signals. These include the coherent WaveBurst [68, 69] and omicron-LALInference-Burst [70] pipelines and BayesWave [71] searches.

the presence of a GW in the data. More sophisticated test statistics are used in its place to mitigate these non-ideal aspects of the noise. However, I restrict my attention to the idealized case here, noting that the same overall strategy can be applied using test statistics better adapted to the noise. Additional statistical significance is gained by folding into the analysis the fact that a true GW signal should be observable coincidentally across a network of detectors; I ignore this added complication here.

Gravitational-wave detection requires one to assess whether a GW is present in a stretch of data. Unlike in the discussion above, the precise form of h (and thus optimal choice of W_h) is not known ahead of time. To circumvent this problem, one approach instead uses a large bank of template waveforms $\{\tilde{h}(f;\boldsymbol{\theta})\}$, each with different intrinsic parameters (masses, spins, etc.) and/or extrinsic parameters (distance, sky location, etc.), represented by $\boldsymbol{\theta}$. The signal-to-noise ratio ρ is computed using each waveform in the template bank, representing a goodness-of-fit of the waveform to the data. Using a finite template bank reduces the signal-to-noise ratio (and thus the statistical significance of a detection) compared to when the optimal matched filter W_h is used; this reduction can be mitigated using a sufficiently dense bank of templates. Consider the case where the incident GW is given by $\tilde{h}(f;\hat{\boldsymbol{\theta}})$, whereas the best-fit waveform in the template bank is $\tilde{h}(f;\boldsymbol{\theta})$. Then $\hat{\rho}$ computed using the optimal filter is related to the maximum ρ recovered with the template

bank by

$$\rho \approx \hat{\rho}\left(1 - \frac{(h(\hat{\boldsymbol{\theta}})|h(\boldsymbol{\theta}))}{\left[(h(\hat{\boldsymbol{\theta}})|h(\hat{\boldsymbol{\theta}}))(h(\boldsymbol{\theta})|h(\boldsymbol{\theta}))\right]^{1/2}}\right), \tag{1.22}$$

where the second term in parentheses is called the mismatch between the two waveforms. LIGO and Virgo use template banks constructed such that any possible waveform in the parameter space of its search has a mismatch of less than 3% with respect to at least one template; for more detail see Refs. [72–74]. However, one can also appreciate from Eq. (1.22) the importance of accurate waveform models for GW detection: inaccuracies in waveform models will further reduce the recovered signal-to-noise ratio.

The matched-filtering strategies outlined above are optimized to quickly determine whether a stretch of data d contains a GW. However, they do not guarantee that parameters $\boldsymbol{\theta}$ of the best-fit template accurately match the parameters $\hat{\boldsymbol{\theta}}$ of the true underlying signal. Instead, once a GW is detected, parameter estimation is carried out within a more comprehensive Bayesian framework. The ultimate goal of this procedure is to estimate the posterior probability of the parameters of the signal given the observed data $p(\boldsymbol{\theta}|d)$; this probability is given by Bayes' theorem as

$$p(\boldsymbol{\theta}|d) = \frac{p(\boldsymbol{\theta})p(d|\boldsymbol{\theta})}{p(d)}, \tag{1.23}$$

where $p(d|\boldsymbol{\theta})$ is the likelihood of the data given the parameters, $p(\boldsymbol{\theta})$ is the prior probability on the model parameters, and $p(d)$ is the evidence for the data. I detail the significance of each of these terms below.

Again assuming stationary Gaussian noise, the likelihood can be inferred directly from Eq. (1.18): if the total signal is modeled by $d = h(\boldsymbol{\theta}) + n$, then this

equation becomes

$$p(d|\boldsymbol{\theta}) = \mathcal{N} \exp\left[-\frac{1}{2}\left(d - h(\boldsymbol{\theta})|d - h(\boldsymbol{\theta})\right)\right]. \tag{1.24}$$

Note that this is the likelihood corresponding to detection in a single interferometer, but under the assumption that the noise in each detector in a network is uncorrelated with the others', the joint likelihood is simply the product of the likelihood in each detector.

The prior probability represents the *a priori* expectation for the distribution of the model parameters. The particular choice of prior distribution becomes less relevant if the likelihood is much more sharply peaked with respect to $\boldsymbol{\theta}$; in this limit, the prior can be treated as approximately constant, and thus only contributes to the normalization of the posterior. This situation arises for GW signals with high SNR: if the data corresponds to a loud GW signal with parameters $\hat{\boldsymbol{\theta}}$, i.e. $d = h(\hat{\boldsymbol{\theta}}) + n$, then the likelihood takes the approximate form

$$p(d|\boldsymbol{\theta}) = \mathcal{N} \exp\left[-\frac{1}{2}\Gamma_{ij}(\theta - \hat{\theta})^i(\theta - \hat{\theta})^j \times \left(1 + \mathcal{O}((\mathrm{SNR})^{-1}\right)\right], \tag{1.25}$$

where $\Gamma_{ij} = \left(\frac{\partial h}{\partial \theta^i}|\frac{\partial h}{\partial \theta^j}\right)$ is the Fisher information matrix evaluated at $\hat{\boldsymbol{\theta}}$. The posterior probability distribution is well approximated by the likelihood provided that $|\nabla_{\boldsymbol{\theta}} p(\hat{\boldsymbol{\theta}})| \times |\sqrt{\Gamma^{-1}_{ij}}| \ll 1$, i.e. the prior varies more slowly than the likelihood near its peak.

Finally, the evidence $p(d)$ does not meaningfully inform the posterior probability—given the prior and the likelihood, the evidence simply represents the overall normalization of the posterior distribution (which must integrate to unity to be a proper probability distribution). However, the evidence is a key component in Bayesian

model selection: given two competing hypotheses (or models) $\mathcal{H}_1$ and $\mathcal{H}_2$, the odds ratio between the hypotheses is given by

$$\mathcal{O}^{\mathcal{H}_1}_{\mathcal{H}_2} = \frac{p(\mathcal{H}_1|d)}{p(\mathcal{H}_2|d)} = \frac{p(\mathcal{H}_1)}{p(\mathcal{H}_2)} \frac{p(d|\mathcal{H}_1)}{p(d|\mathcal{H}_2)}, \tag{1.26}$$

where the last term is the Bayes factor, i.e. the ratio of the evidence for each model.

In principle, the posterior distribution can be computed directly from Eq. (1.23) (up to normalization) over the full parameter space of $\boldsymbol{\theta}$ given a particular set of priors, waveform model $h(\boldsymbol{\theta})$ and data stream d. In practice, this direct approach is infeasible due to the high dimensionality of the parameter space and the computational expense of evaluating the likelihood function Eq. (1.24). Instead, stochastic sampling methods are used to efficiently and adaptively choose points in the parameter space for which to evaluate the likelihood and reconstruct the posterior distribution. The two methods employed in this thesis are Markov chain Monte Carlo (MCMC) and nested sampling. The MCMC methods employ the Metropolis-Hastings algorithm [75, 76]: a Markov chain of points in parameter space is constructed through a sequence of jump proposals such that the stationary distribution of the chain matches the posterior probability distribution $p(\boldsymbol{\theta}|d)$. The acceptance or rejection of each proposal (which determines whether the next element of the chain is the proposed point or current point, respectively) is decided randomly with a probability related to the relative posterior probability of the proposed and current points. Nested sampling uses the algorithm of Skilling [77] to estimate a sequence of likelihood contours and the prior volume within each by picking points in parameter space with progressively higher likelihood. Then, the posterior distribution

is reconstructed by re-sampling this sequence of points according to their posterior probabilities. In conjunction with the LSC Algorithm Library (LAL), I use the `LALInference` [78] software package to perform parameter estimation with either of the sampling techniques mentioned above.

1.3 Testing general relativity with gravitational waves

One of the primary goals of GW science is to probe the fundamental nature of gravity and test whether it is best described by GR. I begin this section by presenting theoretical motivations for undertaking this endeavor. I then discuss the form in which modifications to GR could appear, both at the fundamental level (e.g. in the action) and as differences in GW phenomenology. Finally, I outline some strategies used to place constraints on deviations from GR with GWs.

1.3.1 Motivations for modifying general relativity

General relativity has passed every experimental test of the past hundred years [79]. These tests convincingly validate the predictions of GR over scales of $1\mu\text{m} \lesssim \ell \lesssim 1\text{AU}$. Yet, there remain several compelling reasons to continue to explore alternative theories that modify GR on different scales.

As discussed in Sec. 1.1, singularities naturally arise in GR. In addition to the case of gravitational collapse mentioned earlier, singularities also occur in the early-time limit of many cosmological models. Singularities point to a deficiency in the theory; GR becomes non-predictive for the causal future of a singularity.

However, by appropriately modifying the Einstein-Hilbert action, one can resolve the interior singularity of BHs [80] or the early-time singularity in cosmological spacetimes [81, 82].

Ignorance of the fundamental physics underpinning current cosmological models provides another reason to consider modifications to GR. The ΛCDM model remains the most successful cosmological model to date, yet it posits that the majority of the energy in the Universe today is comprised of dark energy and dark matter. While many proposals beyond the Standard Model have been put forth to explain these dark sectors, none have been confirmed to date. Moreover, the ΛCDM model seems to require very precise fine-tuning: the value of the cosmological constant Λ consistent with cosmological observations differs from the vacuum energy expected via dimensional analysis by 120 orders of magnitude. As an alternative to extending the Standard Model, modified theories of gravity can also explain some of the phenomena for which these dark sectors are invoked.

Finally, GR is a strictly classical theory, whereas a complete theory of everything will presumably also incorporate quantum effects into gravity. In principle, deviations from GR could persist even as one takes the classical limit of such a theory. For example, in string theory—the most well-known quantum-gravity theory—the scalar dilaton naturally accompanies the tensor graviton; this additional field could (in principle) play a role in the classical limit of the theory. Reversing this line of reasoning, classical modifications to GR could potentially make the theory easier to quantize. For example, adding higher-order curvature terms to GR makes the theory renormalizable [83]; though this property is not strictly necessary to construct

a quantum theory of gravity, it would make the quantization of the classical theory much more straightforward.

In this thesis, I primarily focus on potential deviations from relativity in the "strong-field" regime, defined as where the (dimensionless) Newtonian potential $\Phi_{\rm Newt} \sim M/R$ and (dimensionful) curvature scale $\xi \sim M/R^3$ are both large. Corrections in this regime can potentially alleviate each of the issues discussed above, either directly (e.g. to resolve singularities or improve renormalizability) or indirectly (e.g. via corrections to behavior on cosmological scales induced by deviations on much shorter distance scales).

1.3.2 The menagerie of modified gravity

As outlined in Sec. 1.1, GR directly embodies the equivalence principle. However, it is not the only possible theory of gravity to do so; the same fundamental tenants are encoded into all metric theories of gravity—theories in which the non-gravitational fields ψ couple minimally to the metric. Yet, out of all possible metric theories, GR remains exceptionally simple. This sentiment is made more precise through Lovelock's theorem [84, 85]: the Einstein field equations are the only second-order field equations that respect the equivalence principle and whose action is diffeomorphism-invariant, local, and dependent only on the four-dimensional metric.

Lovelock's theorem singles out GR as the unique metric theory that satisfies all of the aforementioned conditions. Conversely, all alternative theories of gravity

must violate at least one of these requirements. From this perspective, each of the conditions of Lovelock's theorem can be viewed as a fundamental pillar on which GR is based; if any of these pillars are removed, GR is no longer the only possible gravity theory. In the remainder of this subsection, I discuss examples of alternative theories that are allowed by relaxing each of these conditions in turn, focusing specifically on the modifications to GR that impact the GW signal observable with ground-based detectors. However, I restrict my attention to metric theories (which satisfy the equivalence principle by construction) and ignore the possibility of field equations containing derivatives higher than second order, as these would generally manifest an Ostrogradsky instability [86]. The remaining pillars that one can relax are: (i) gravity is mediated solely by the metric, (ii) gravity is diffeomorphism invariant, (iii) gravity is local, and (iv) spacetime is four-dimensional. For brevity, I discuss only one or two alternative theories of gravity for each condition to highlight the new GW phenomenology that can occur outside of GR; for a more representative survey of the landscape of modified gravity, see Refs. [79, 87–89]. Because the phenomenology manifested in higher-dimensional theories (iv) can be found in the other alternatives I present, I will not discuss this final type of modification in detail.

1.3.2.1 Additional fields

Perhaps the simplest way to extend GR is to include additional fields that mediate gravity. In a metric theory, these new fields cannot couple directly to matter, as this would prevent the universal coupling of the non-gravitational sector

to the metric. The prototypical example of such an extension are scalar-tensor (ST) theories, which include a scalar field non-minimally coupled to the metric. The action in such theories is given by

$$S_{\rm ST}[g_{\mu\nu},\varphi,\psi] = \frac{1}{16\pi}\int d^4x\sqrt{-g}\,e^{\varphi}\left(R-\omega(\varphi)g^{\mu\nu}\partial_\mu\varphi\partial_\nu\varphi-U(\varphi)\right)+S_m[g_{\mu\nu},\psi], \tag{1.27}$$

where I have restricted my attention to the case of zero cosmological constant (which I continue to do for the remainder of the thesis). Written this way, the scalar field takes the same form as a dilaton, which arises in many theories of quantum gravity, e.g. string theory. ST theories are used to incorporate modifications to GR in both the strong- and weak-gravity regimes. I work within the former class of theories in several places in this thesis; see Chapters 3-7. For weak-field (i.e. cosmological) modifications, ST theories are often expressed instead as $f(R)$ theories, whose action

$$S_{f(R)}[g_{\mu\nu},\psi] = \frac{1}{16\pi}\int d^4x\sqrt{-g}f(R)+S_m[g_{\mu\nu},\psi]. \tag{1.28}$$

can be mapped to Eq. (1.27) via $e^{\varphi}=f'(R)$, $\omega(\varphi)=0$, and $U(\varphi)=e^{\varphi}R-f(R)$.

The class of theories described by Eq. (1.27) is actually a very restricted subset of viable scalar extensions of GR. Horndeski theories [90] cover all possible alternative theories with a single scalar field whose field equations are second order, so as to avoid Ostragradsky instabilities. More recently, an even larger classes of "beyond Horndeski" theories have been established [91–93] whose equations of motion are higher than second order, but that remain free of ghosts.

The GWs produced from compact binary systems in ST theories differ from those produced in GR in a number of ways. First, the orbital evolution of a binary

is impacted by the introduction of the new scalar degree of freedom. The most dramatic change occurs when the Compton wavelength of the scalar is significantly larger than the separation of the binary; in this case, the binary can emit dipole radiation, sourced by a time-varying scalar dipole moment. Recall that dipole radiation is prohibited in GR and, from dimensional analysis, expected to scale with a weaker power of $1/c$ (i.e. enter at lower PN order) than quadrupole radiation. Thus, binaries with non-zero scalar dipole moment can emit significantly more energy and thus evolve more rapidly than the equivalent system in GR, particularly at large orbital separations. If the Compton wavelength of the scalar is much smaller than the orbital separation, then the field will be effectively screened away through a Yukawa-like potential [94] such that the dynamics much more closely resemble GR (e.g. no dipole radiation will be emitted). Nevertheless, even in this case, the structure of the compact objects in the binary can significantly differ from GR, which can offer another signature of deviations; for example, in massive ST theories, the mass [95] and tidal deformability [96] of neutron stars can differ from the equivalent star in GR, which would be imprinted in the GWs produced.

Besides modifications to their source, GWs in ST theories also contain additional polarization content. Beyond the two transverse-traceless polarizations modes found in GR, ST theories predict a third transverse breathing-mode that is isotropic in the plane orthogonal to its wave vector; this new mode corresponds to a helicity-0 state of the graviton. Massive ST theories contain an additional fourth, longitudinal polarization [97]. With just a single detector, the polarization content of a GW signal is degenerate with the wave's direction of propagation (or equivalently,

the relative orientation of the detector and the source), and thus cannot be determined. However, with a network of N non-coaligned detectors, one can, in principle, discriminate between N polarization states of the incident wave.

Scalar-tensor theories are a standard first example of modified gravity because they predict a wide variety a phenomena that are relatively easy to compute. However, no-hair theorems guarantee that isolated BHs are no different in ST theories than in GR (although there may be certain astrophysical contexts in which these theorems can be circumvented [98]). Yet, there exist other extensions of gravity in which BHs do behave differently than in GR. For completeness, I discuss one such example: Einstein-Æther (EA) theory. This theory allows for breaking of the local boost symmetry of GR (i.e. violations of Lorentz invariance) by introducing a unit vector u^μ known as the æther field that represents a preferred timelike direction. This is a particularly compelling alternative theory because it has recently been shown to have a well-posed Cauchy formulation [99].

The action for EA theory is given by

$$S_{\rm EA} = \frac{1}{16\pi}\int d^4x\sqrt{-g}\left[R + \mathcal{L}_u + \lambda(u^\mu u_\mu + 1)\right] + S_m[g_{\mu\nu}, \psi], \tag{1.29}$$

where

$$\mathcal{L}_u \equiv - K^{\mu\nu}{}_{\rho\sigma}\nabla_\mu u^\rho \nabla_\nu u^\sigma, \tag{1.30}$$

$$K^{\mu\nu}{}_{\rho\sigma} \equiv c_1 g^{\mu\nu}g_{\rho\sigma} + c_2\delta^\mu_\rho\delta^\nu_\sigma + c_3\delta^\mu_\sigma\delta^\nu_\rho - c_4 u^\mu u^\nu g_{\rho\sigma}, \tag{1.31}$$

and u^μ is constrained to be a unit timelike vector through the Lagrange multiplier λ. If u^μ is hypersurface orthogonal, then it can be rewritten as the normal vector

to a preferred time-foliation ϕ of the spacetime, i.e. $u^\mu = \nabla^\mu\phi/\sqrt{(\nabla^\nu\phi\nabla_\nu\phi)}$, where $\phi = \text{const}$ are spacelike hypersurfaces. In this special case, EA theory coincides with Khronometric theory [100], which is the low-energy limit of Hořava gravity [101], a proposed theory of quantum gravity more amenable to standard quantum field theory techniques than GR.

As with ST theories, the introduction of a new field in EA theory impacts the evolution of compact binary systems and the propagation of the GWs that they emit. There exist five propagating modes in EA theory: the two standard tensor modes found in GR, two transverse vector modes and a single scalar mode [102]. The existence of scalar and vector modes allows for the emission of dipole radiation. The amount of dipole radiation emitted by a binary is determined by the relative motion of the binary and the æther field and the structure of each body. In the limit that each body moves slowly relative to the æther and at leading PN order, the emission of scalar and vector radiation is determined by the so-called "sensitivity" of each body, which depends on the composition of that object. While the sensitivities of spherically symmetric NSs are known [103], the analogous computation for BHs has not been undertaken in EA theory[4]. Nevertheless, spherically symmetric BH solutions have been constructed in EA theory [105], and their sensitivity is known to be non-zero [106].

[4]Note that the calculation of BH sensitivities has been recently computed in Khronometric theory [104], which corresponds to EA theory for a restricted set of æther field configurations.

1.3.2.2 Broken diffeomorphism invariance

Massive gravity is a commonly studied alternative to GR that violates diffeomorphism invariance. A fully non-linear theory of massive gravity free of ghosts was derived fairly recently by de Rham, Gabadadze, and Tolley (dRGT) [107, 108]. The action for dRGT massive gravity is given schematically by

$$S_{\mathrm{dRGT}}[g_{\mu\nu},\psi] = \frac{1}{16\pi}\int d^4x\sqrt{-g}\left[R + \frac{1}{2}m_g^2\sum_{n=0}^{4}\alpha_n\mathcal{L}_n(\mathcal{K}^{\mu}{}_{\nu})\right] + S_m[g_{\mu\nu},\psi], \quad (1.32)$$

where α_n are constant coefficients, m_g is the mass of the graviton, $\mathcal{L}_n[X^{\mu}{}_{\nu}]$ is a function containing n contractions of X, and $\mathcal{K}^{\mu}{}_{\nu} \equiv \delta^{\mu}_{\nu} - \sqrt{g^{\mu\alpha}f_{\alpha\nu}}$ where $f_{\mu\nu}$ is a non-dynamical, reference metric; see Ref. [108] for more detail. The appearance of the reference metric breaks the diffeomorphism invariance of the theory.

A massive graviton has five possible polarization states, as is expected for a massive, spin-2 particle. In addition to the two helicity-2 transverse traceless modes also present in GR, the theory predicts a helicity-0 transverse breathing mode and two spin-1 longitudinal modes [109]. However, the two helicity-1 modes do not couple directly to matter, and thus are not expected to be produced through binary coalescence, and the remaining helicity-0 mode is suppressed by Vainshtein screening [110] in the presence of matter (e.g. within the dark matter halo of a galaxy) [109]; hence, GWs observed on Earth will typically be of only the polarizations expected in GR. However, the presence of non-zero graviton mass causes these GWs to propagate subluminally. This modification of the dispersion relation induces a frequency-dependent shift in the overall phase of the incident GW [111].

Constraining this deviation from the signal predicted in GR allows one to constrain the mass of the graviton using GWs; I discuss this type of test in more detail below.

1.3.2.3 Non-locality

Adding non-local corrections to GR can both help resolve singularities that appear in solutions of collapsing matter or evolving cosmologies and potentially explain the accelerated expansion of our universe. For illustrative purposes, I consider the theory proposed in Ref. [112], where non-local corrections appear over long distance scales; these terms could arise as corrections from quantum gravity in the infrared regime. The action for this theory is given by

$$S_{\text{non-local}} = \frac{1}{16\pi}\int d^4x\sqrt{-g}\left[R - \frac{1}{6}m^2 R\left(\Box^{-1}\right)^2 R\right], \tag{1.33}$$

where m represents the mass scale of new physics. Cosmological solutions in this theory have been constructed with self-accelerating expansion in which the effective dark energy is generated by these non-local terms [112]. These solutions are consistent with current Solar System and cosmological observations [113], indicating that this theory provides a compelling alternative to the current ΛCDM paradigm.

The primary GW signature of this theory is associated with the propagation of GWs. The non-local terms in Eq. (1.33) dynamically generate a mass for the conformal mode of the metric; however this mode is non-radiative, and does not comprise part of the observable GW signal generated in this theory. In fact, unlike the massive gravity theory discussed in the previous subsection, the only propagating degrees of freedom in this non-local theory are two spin-2 modes that propagate at

the speed of light (as in GR) [114]. However, unlike GR, the *damping* of these modes as they propagate over cosmological distances differs from that in GR [115].

The amplitude of GWs is inversely proportional to the luminosity distance to the source d_L; this quantity reduces to the distance d in Eq. (1.10) in the special case that the background spacetime is Minkowskian. However, in more generic cosmological backgrounds, the luminosity distance will depend on the redshift of the signal z observed today due to the cosmological evolution of the Universe. In GR, the luminosity distance for GWs takes the same familiar form as for electromagnetic waves; for a spatially flat, Friedmann–Lemaitre–Robertson–Walker universe with an evolving scale factor $a(t)$, I have

$$d_L(z) = \frac{1+z}{H_0} \int_0^z \frac{dz' \rho_0}{\sqrt{\rho_R (1+z')^4 + \rho_M (1+z')^3 + \rho_{\rm DE}(z)}}, \tag{1.34}$$

where $H_0 \equiv \dot{a_0}/a_0$ is the Hubble constant (measured today), ρ_R, ρ_M, $\rho_{\rm DE}$ are the density of radiation, matter, and dark energy, respectively, and $\rho_0 \equiv 3H_0^2/(8\pi)$ is the critical density needed to ensure a flat spatial metric. However, in the non-local extension of GR considered here, the luminosity distance for GWs no longer takes this form, and so discrepancies can emerge between the luminosity distance recovered with the electromagnetic signal $d_L^{\rm EM}$ and with the GW signal $d_L^{\rm GW}$ from the same source. This type of analysis has been carried out using the coincident electromagnetic and GW observations of GW170817 [116]; however, only weak bounds on this theory could be placed due to the poor measurement of H_0 from those observations.

1.3.3 Tests of gravity with gravitational waves

1.3.3.1 Testing various facets of gravitational wave signals

The previous subsection outlined the range of phenomenology that can arise in modified theories of gravity. In this section, I discuss how to formulate tests of GR given these predictions. I detail three classes of tests, corresponding to various types of deviations from GR that could be imprinted on the GW signal from a compact binary inspiral. I first consider deviations to the *GW generation* by the system, e.g. modifications to orbital motion of the binary. Next, I formulate tests of *GW propagation*. Finally, I discuss tests of the *GW polarizations* present in an emitted signal. Though many alternative theories of gravity predict deviations from GR in more than one of these categories, it is often convenient to consider these various phenomena independently.

As we have seen in the previous sections, the inspiral portion of the an observed GW signal contains a direct imprint of the orbital motion of the binary that sources it. Accordingly, deviations to the binary's evolution due to modifications to GR impact the inspiral portion of the GW. To measure (or constrain) these deviations, one performs Bayesian inference employing the techniques of Sec. 1.2.2.2. This approach relies on a waveform model to reproduce the observed GW signal; however, to capture potential deviations from GR, this model must be "generalized" to include parameterized deviations away from the GR prediction. The additional modifications are controlled through a set of *deviation parameters* $\{\delta\hat{\varphi}_n\}$. Though

there are several possible ways in which to introduce parameterized deviations to a GR signal, a common choice for tests of the inspiral evolution is to consider independent modifications of each series coefficient in a PN-expanded prediction for the signal [73, 117–123]—in this case, each $\delta\hat{\varphi}_n$ represents the extent of deviation from the GR prediction at a particular PN order. This particular approach for constructing generalized waveform models can be easily related to the predictions of many alternative theories of gravity; provided that an alternative theory admits a low-velocity expansion and that deviations from GR are small, then the signal predicted in this alternative theory can be mapped to the model outlined above. Then, using Bayesian inference, one attempts to measure/constrain the deviation parameters in this model for a given GW observation to determine whether that signal is consistent with the predictions of GR (i.e. consistent with no deviations in the waveform model). Chapter 9 focuses on this type of test using observations made by LIGO and Virgo.

Tests of GW propagation can be designed in much the same way as tests of GW generation: modifications to the propagation of GWs are introduced to a GR waveform model through a set of parameterized deviations. For example, Refs. [9, 10, 111, 122, 124–126] considered corrections to the graviton dispersion relation in GR, which, in the Fourier domain, is simply $E^2 = p^2$, where E and $\mathbf{p}$ are the temporal and spatial components of the wavevector of a propagating plane wave. These references considered deviations that were polynomial in $|\mathbf{p}|$; as before the deviation parameters represent the magnitude of the correction at each polynomial order. Modifications to the dispersion relation modify the phase evolution of the

GW signal (see Ref. [126]), and these deviations can be constrained in a similar manner to deviations to GW generation discussed above. Other types of tests of GW propagation are possible with coincident observations of electromagnetic and GW signals from a single source. For example, simply computing the difference in time of arrival between γ-rays and GWs produced by the BNS coalescence GW170817 provided strong constraints on many alternative theories of gravity [127–134].

Tests of GW polarizations differ significantly from those of GW generation or propagation. They rely on the fact that the directional sensitivity of a given detector differs for each possible polarization. The directional dependence of the sensitivity of interferometer I to a GW of polarization A incident from a particular position in the sky $\mathbf{\Omega}$ can be expressed as an antenna pattern $F_{(I)}^{(A)}(\mathbf{\Omega})$. With only a single detector, the polarization and amplitude of a GW signal are completely degenerate; it requires a network of detectors to disentangle these quantities. If the sky location of the source of GWs is known (e.g. from the a coincident electromagnetic observation), then one approach to identify non-GR polarization content in the signal employs so-called *null streams* [135]. With a network of three or more independent detectors, one can project out the tensorial (GR) modes present in the data stream from each interferometer via straightforward algebraic manipulation. Then, if any coherent signal remains across the resulting null streams, this indicates the presence of non-GR polarization content in the signal. An alternative approach uses Bayesian model selection (as described in Section 1.2.2.2) to differentiate between different polarizations [136]. One considers the relative odds that an observed GW can be described by polarization A versus polarization B by computing the Bayesian evi-

dence in support of the following hypotheses: the GW signal at detector I is given by $h^{(A)}_{(I)} = {F^{(A)}_{(I)}}^{ij} h_{ij}$ or the GW signal at detector I is given by $h^{(B)}_{(I)} = {F^{(B)}_{(I)}}^{ij} h_{ij}$. Unlike the null stream approach, this method requires some waveform model h_{ij} for the incident GW; in Refs. [9, 122], this analysis was conducted using waveforms constructed with a morphology-independent sum of sine-Gaussians [71, 137] to constrain the polarization content in observed GW signals. However, note that, at present, the hypotheses used in this test are somewhat artificial; GW sources generate multiple polarizations of GWs in most modified theories of gravity, whereas the hypotheses assumed here assume the entire signal is of only one polarization.

1.3.3.2 Designing gravitational-wave tests of general relativity

Tests of GR are commonly classified into one of two contrasting categories: *theory-specific* and *theory-agnostic* tests [88] (or equivalently, *direct* and *parameterized* tests [89]). These two types of tests differ conceptually in the underlying assumptions they require. Theory-specific tests are based on the supposition that a specific theory (or set of theories) correctly describes the classical behavior of gravity, and then use GW observations to better inform our understanding of these theories. In contrast, theory-agnostic tests do not rely wholly on any particular theory of gravity, but rather consider the predictions in a parameterized neighborhood of theories around GR.

The choice of theory-specific or theory-agnostic approach guides the ultimate design of GW tests (such as those outlined in the previous subsection) one performs.

For concreteness, let us consider a specific example: suppose I wish to test the inspiral dynamics (GW generation) in a observed signal produced by a coalescing BNS. A theory-specific test would consider a specific class of theories—for example, ST theories—in which the GW signal from such a system would differ from the predictions of GR. The dominant non-GR effect in such theories arise from the emission of dipole radiation, which contributes a -1PN correction to the phase evolution of the frequency-domain GW signal. The magnitude of this effect is governed by a set of theory parameters, which, in the case of ST theories, simply characterize the functions $\omega(\varphi)$ and $U(\varphi)$ in Eq. (1.27). In fact, if I assume that $U(\varphi) = 0$, then the dominant non-GR effect is determined only by the constant ω_0—the first term in the PN expansion of $\omega(\varphi) = \omega_0 + \omega_0'\varphi + \ldots$. Thus, a theory-specific test could use a waveform model generalized to incorporate this -1PN effect (as characterized by ω_0) in hopes of measuring this fundamental parameter of the assumed theory. Or, one could use Bayesian model selection to compare the relative odds that this ST theory is favored/disfavored versus a GR model.

In contrast, a theory-agnostic test of similar deviations could be used to constrain generic -1PN deviations to the GW signal produced by a BNS in GR. Again, one must use a waveform model generalized from a GR prediction to include the possibility of such a -1PN effect. However, unlike in the theory-specific case, the magnitude of this correction would not be regulated by any fundamental constant of a theory; instead, one could simply introduce a generic deviation parameter $\delta\hat{\varphi}$ that represents a free coefficient that dictates the size of this -1PN term. One could then employ many of the same statistical techniques in hopes of measuring/constraining

$\delta\hat{\varphi}$. The information inferred on this deviation parameter offers a measure of consistency between the observed data and the predictions of GR.

As this example illustrates, the actual procedure for carrying out theory-specific and theory-agnostic tests can be remarkably similar. And yet, the statistical questions addressed in each of the outlined tests are fundamentally different. Within a Bayesian framework, this distinction is inherently manifested in the choice of prior distribution [$p(\boldsymbol{\theta})$ in Eq. (1.23)] one employs. In fact, as long there exists a bijection relating ω_0 to $\delta\hat{\varphi}$, one can convert the posterior distribution measured on either quantity (in the theory-specific or theory-agnostic test outlined above, respectively) to a posterior on the other; then all differences in the two results stem from the corresponding choices of priors.

A complementary dichotomy distinguishing different types of GW tests of GR are the notions of *top-down* and *bottom-up* designs [88].[5] A top-down approach begins from some fundamental physical principle, e.g. an action or set of symmetries, and then translates this foundation to a set of observables that can be tested against data. Conversely, a bottom-up approach starts from some phenomenological model of observables, then, through comparison against data, infers properties about the underlying physics at play. The two example tests laid out above would be classified as top-down (starting from a particular action) and bottom-up (starting from a phenomenological feature in the GW signal), respectively. However, these two

[5]Reference [88] presents theory-specific and top-down tests as one and the same, and similarly with theory-agnostic and bottom-up tests. As laid out in this subsection, I believe that two categorizations are largely orthogonal, not redundant.

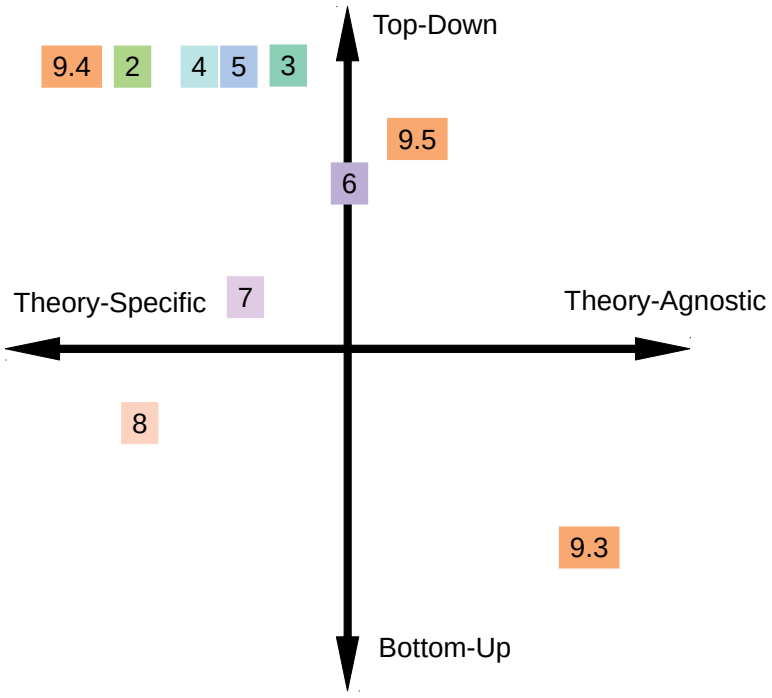

Figure 1.1: Schematic representation of how the contents of each chapter could be categorized as theory-specific vs. theory-agnostic and top-down vs. bottom-up tests of GR. For chapters for which additional work is required to formulate a test of GR (e.g. additional PN computations are needed), I assume the corresponding missing pieces can be completed with similar techniques as existing work.

dichotomies are independent, e.g. one can design a top-down, theory-agnostic test. To help guide the reader, I present a schematic representation in Fig. 1.1 of how the various chapters of this thesis (discussed in detail below) would be classified according to these two categorizations.

1.4 Overview of this thesis

The remainder of the thesis is organized so as to loosely follow the spectrum from theory-specific to theory-agnostic tests of gravity using GW observations of binary inspirals. I begin in Chapters 2 and 3 with perturbative calculations of waveform models in particular classes of alternative theories of gravity, which could serve as the foundation for theory-specific tests [1, 2]. In Chapters 4-8, I turn to models of specific phenomenology that can occur in a range of potential modifications of GR. Chapters 4-6 contend with a particular phenomenon known as *scalarization* that occurs in several alternative theories, culminating in a theory-agnostic analytic model of the phenomenon [3–5]. Chapter 7 demonstrates how such a model could be employed to test GR, focusing on a specific alternative theory of gravity [6]. Chapter 8 examines the potential to test gravity with an even more widespread phenomenon—the tidal deformations of the compact bodies in inspiraling binaries—using various *boson star* models as benchmarks to determine whether exotic compact objects could be distinguished from BHs or NSs [7]. Chapter 9 contends with an even broader range of phenomenology, developing an infrastructure to allow parameterized deviations to be incorporated into the inspiral phase of a

generic waveform model and then using this construction to perform various tests of GR with existing GW observations by LIGO and Virgo. This chapter discusses theory-agnostic tests performed as part of the LIGO Scientific Collaboration [9, 10] as well as tests of specific alternative theories of gravity [11, 138]. Finally, Chapter 10 provides some concluding remarks and possible directions for future work.

I briefly summarize the findings documented in each chapter below, highlighting certain specific results and figures that reappear later.

1.4.1 Post-Newtonian and effective-one-body descriptions of binary black holes in Einstein-Maxwell-dilaton gravity

In Chapter 2, I study the inspiral of BBHs in Einstein-Maxwell-dilaton gravity (EMd) [1]. In this theory, gravity contains an additional scalar component (a dilaton), which is sourced by electromagnetism. Due to its simplicity, this is a convenient toy model for generic modified theories in which the no-hair theorems of GR no longer hold: the theory is characterized by a single parameter a, which determines the coupling strength between the dilaton and Maxwell field. In EMd specifically, electrically charged BHs also host an additional scalar charge absent in GR. In this work, I examine BBHs with electric (and scalar) charge, and contrast their behavior with electrically charged binaries in GR. Though astrophysical BHs are expected to be electrically neutral[6], EMd serves as a useful proxy for more generic no-hair violations. This work provides a foundation for modeling and testing more generic

[6]Certain dark matter proposals have been made that would allow BHs to attain significant electric charge [139–144], which would allow for viable tests of EMd.

such phenomena using GW detections of BBHs.

Working within the PN approximation, I compute the dynamics and energy flux of BBHs at next-to-leading order. I use these results to compute ready-to-use Fourier-domain waveforms for the inspiral in EMd. The key feature that distinguishes charged BBHs in EMd from their counterparts in GR is the emission of scalar dipole radiation (discussed in Sec. 1.2). I study in detail the impact of this additional energy flux to the gravitational waveform, relative to both charged and uncharged BBHs in GR. Figure 1.2 depicts the projected constraints that can be set on the EMd coupling parameter a given a GW measurement of dipole flux consistent with the current best dipole constraint from X-ray binary systems [145]. Here I parameterize the dipole emission as a dipole-flux ratio B relative to the quadrupolar flux predicted in GR $\mathcal{F}_{\rm GR}$

$$\mathcal{F} = \mathcal{F}_{\rm GR}\left(1 + Bv^{-2}\right), \tag{1.35}$$

Current measurements of low-mass X-ray binaries provide a constraint of $|B| \lesssim 2\times10^{-3}$ [145] and combined bounds from BBH events observed during the first and second observing runs of LIGO and Virgo constrain $|B| \lesssim 3\times10^{-3}$ [10], so I use $|B| \lesssim 10^{-3}$ as a rough benchmark for my analysis.

As discussed in Section 1.2, the PN approximation becomes increasingly inaccurate towards the end of the inspiral of BBHs, and more sophisticated tools are required to model the waveform (and thus test the nature of gravity) beyond this phase. Following the analogous approach used in GR, I construct an EOB formalism for binaries in EMd to resum the PN results discussed above. This extends

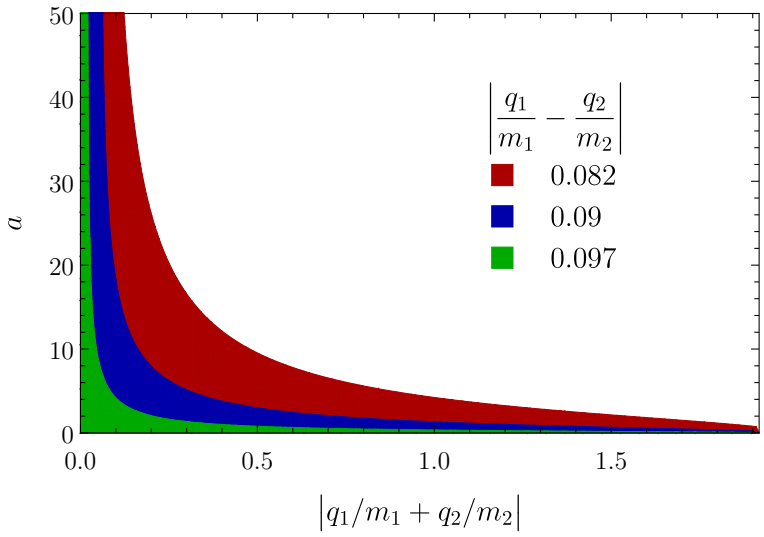

Figure 1.2: Projected constraints on EMd from dipole flux measurements with GW detectors. Allowed values of EMd coupling a consistent with a dipole flux ratio of $|B| \leq 10^{-3}$ are indicated by the shaded regions as a function of mass-weighted total electric charge. Colors indicate various possible electric dipoles consistent with the bound on B. Figure taken from Ref. [1].

the validity of the EMd model to a more relativistic regime and more accurately reproduces the test-particle limit. I explore the gauge freedom inherent to any EOB construction, examining two possible generalizations of the gauge used in GR models for EMd. This discussion is invaluable as one explores potential EOB formulations of more generic alternative theories of gravity.

1.4.2 Post-Newtonian waveforms in massless scalar-tensor theories

In Chapter 3, I consider the inspiral dynamics in a broader class of scalar extensions of GR [2]. I focus on a popular class of ST theories in which an additional massless scalar field couples non-minimally to the metric [146, 147]. Unlike in EMd,

all matter couples (indirectly) to this scalar field, but isolated BHs do not because of no-hair theorems [23, 148]. Thus, the class of theories considered in this chapter can be tested through the GW observation of BNSs or neutron-star black-hole systems.

Using previously derived PN results [149–151], in this chapter I compute ready-to-use frequency-domain inspiral waveforms for non-spinning, non-eccentric binary systems. I use the most accurate (highest PN order) results known at the time of writing, which correspond to 2PN relative order. As with many scalar extensions of GR, the primary observational signatures of this theory arise from the emission of scalar-dipole radiation. I discuss in detail two regimes of the inspiral: the dipole-driven regime, which occurs at very low-frequencies where dipole radiation dominates quadrupolar radiation, and the quadrupole-driven regime, which occurs later in the inspiral where quadrupolar radiation is dominant. Given current observational constraints, ground-based and space-based GW detectors are likely only sensitive to binaries in the latter stage, but binary pulsar measurements could potentially probe the former.

1.4.3 Dynamical scalarization as a non-perturbative phenomenon

Scalarization of compact objects (BHs and NSs) arises from spontaneous symmetry breaking of an additional scalar component of gravity [4, 152]. Scalarization can significantly alter the evolution of a binary system, hastening the inspiral and leading to a dramatically different GW signal. *Spontaneous scalarization*—the scalarization of a single, isolated object—has been found in several scalar exten-

sions of GR [147, 153–168]. In contrast, *dynamical scalarization*—scalarization that occurs during the coalescence of a binary system—has been demonstrated only for BNSs in ST theories [169–172]. Chapters 4 and 5 explicitly focus on these theories known to exhibit dynamical scalarization, while Chapter 6 examines new theories in which the phenomenon is likely to occur.

In Chapter 4, I show that dynamical scalarization is a *non-perturbative phenomenon* in the sense that its appearance coincides with the breakdown of the PN approximation [3]. A similar result was known already for spontaneous scalarization [153]; thus, my work places the two phenomena on equal footing. I develop a diagnostic to test the convergence of the PN expansion in the context of scalarization, which in turn, can be used to estimate the onset of dynamical scalarization.

To model dynamical scalarization, I construct a semi-analytic method that resums the PN expansion at the level of the action—I denote this resummation as the post-Dickean (PD) expansion. I perform this resummation by introducing a new dynamical variable to the Lagrangian of the theory that tracks the non-perturbative growth of the scalar field near each compact body. Working at next-to-leading order (1PD, analogous to 1PN), I compute the early-inspiral dynamics of BNSs before and after dynamical scalarization.

An example of such a result is shown in Fig. 1.3; I plot the scalar mass M_S—a measure of scalarization—of a BNS as a function of orbital and GW frequency. The blue and green curves depict two models of dynamical scalarization constructed in Chapter 4. I compare these semi-analytic results against previous phenomenological models [173] (black with pink shading) and quasi-equilibrium configuration (QE)

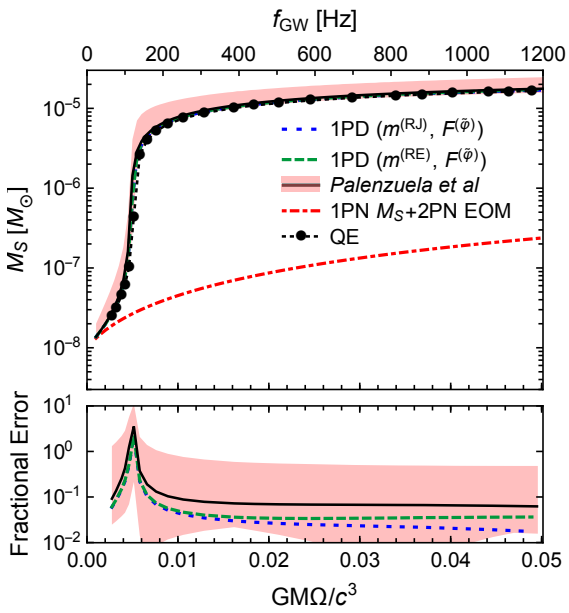

Figure 1.3: Scalar mass M_s as a function of orbital frequency Ω and gravitational wave frequency $f_{\rm GW}$ for a BNS that undergoes dynamical scalarization. The blue and green curves correspond to two PD formulations constructed in Chapter 4. These semi-analytic models reproduce the numerical quasi-equilibrium (QE) configuration calculations of [174] (dashed black) to within a few percent; the fractional error is shown in the bottom panel. The PD models achieve comparable accuracy to the phenomenological model of Ref. [173] (solid black curve with estimated systematic uncertainty in pink). Because dynamical scalarization is a non-perturbative phenomenon, it cannot be captured using only the PN approximation, whose prediction is shown in red. Figure taken from Ref. [3].

calculations (dashed black) made with NR [174]. The red dot-dashed curve shows the PN prediction for the scalar mass of the system; the discrepancy between this perturbative prediction and the QE results confirms that dynamical scalarization is a non-perturbative phenomenon.

1.4.4 Dynamical scalarization as a second-order phase transition

Building on the observation in Chapter 4 that the onset of dynamical scalarization coincides with the loss of analyticity of the PN expansion, in Chapter 5, I aim to explain the physical origin behind the breakdown of the standard perturbative approach. I show explicitly that dynamical scalarization is a second-order phase transition [4]. Given this perspective, the breakdown of the PN expansion found previously is unsurprising. Recall that the PN formalism provides an approximate solution to the Einstein equation expanded perturbatively around a Newtonian solution; in the context of the two-body problem, the evolution of a binary system is formulated in terms of its behavior at very large separations (the Newtonian limit). However, because dynamical scalarization is a second-order phase transition, the order parameters that describe a binary system exhibit discontinuous derivatives at the onset of scalarization. The PN expansion is blind to phenomenology that arises spontaneously in the relativistic regime (e.g. a new scalarized phase), and thus cannot sensibly reproduce dynamical scalarization. Note that despite the similarities between spontaneous and dynamical scalarization, only the latter phenomenon poses such an obstacle to the standard PN approach; in contrast, spontaneous scalarization remains present in a binary system even at very large separations, and thus can be integrated seamlessly into the PN formalism.

Besides providing a better conceptual understanding of the phenomenon, the connection between dynamical scalarization and phase transitions offers some insight as to how to best construct analytic models of binary systems that undergo

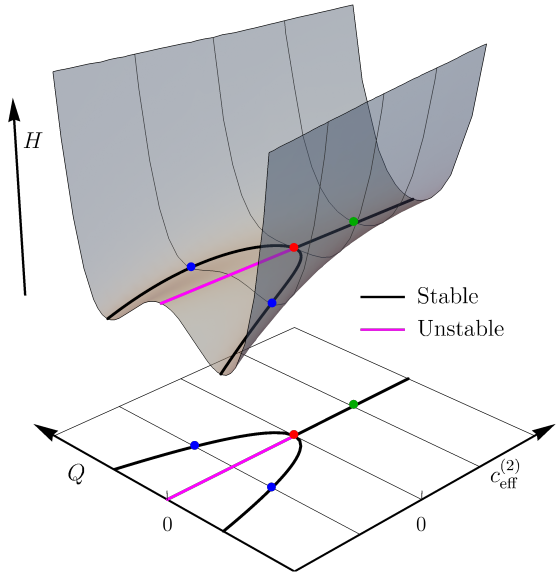

Figure 1.4: The Hamiltonian H of an equal-mass BNS (vertical axis) as function of scalar charge Q and effective parameter $c_{\rm eff}^{(2)} = c^{(2)} - 1/r$. When $c_{\rm eff}^{(2)}$ becomes negative, stable equilibrium scalarized configurations ($Q \neq 0$) emerge and unscalarized configurations ($Q = 0$) become unstable. The bottom lower plane shows the phase space of equilibrium configurations, with the critical point separating the unscalarized and scalarized phases indicated with the red point. Both H and Q are given in units of $M_\odot$, whereas $c_{\rm eff}^{(2)}$ is shown with units of $M_\odot^{-1}$. Figure adapted from Ref. [4].

scalarization. In Chapter 5, I construct such a model for binaries in the ST theories considered in Chapter 4. Like the approach adopted in Chapter 4, I introduce new dynamical variables that track the scalarization of each body during the evolution of the inspiral. Unlike the previous approach, which incorporated a large degree of freedom in how these variables were defined, the construction in Chapter 5 explicitly uses the scalar charge Q of each body as dynamical variables; these quantities are a natural choice, as they also serve as order parameters characterizing the second-order phase transition of dynamical scalarization.

With this approach, I construct an analytic model of dynamical scalarization at leading (Newtonian) order. I compute the conservative dynamics of a binary system at this order and calculate the Hamiltonian that governs its motion. This measure of energy allows us, for the first time, to estimate the stability of dynamically scalarized systems and draw connections to the Landau model of phase transitions. For example, Fig. 1.4 depicts the appearance of a Mexican-hat shaped potential (characteristic of a second-order phase transition) during dynamical scalarization of a binary system. In this diagram, the translucent sheet depicts the Hamiltonian (vertical axis) of a BNS as a function of scalar charge Q and an effective parameter $c^{(2)}_{\rm eff}$, defined as the difference between a coefficient $c^{(2)}$ that depends on the structure of the NSs and the inverse of their separation $1/r$. At large distances (positive $c^{(2)}_{\rm eff}$), the energy is minimized in an unscalarized configuration ($Q = 0$). However, below a critical separation ($c^{(2)}_{\rm eff} = 0$), the local minima shift to scalarized configurations ($Q \neq 0$), while the unscalarized configuration becomes unstable. These two phases are indicated with the green and blue points in Fig. 1.4, respectively, with the critical point at which scalarization begins marked in red. The equilibrium solutions are projected onto the bottom plane to depict the phase space of binary configurations; the bifurcation of stable solutions at the critical point demonstrates the discontinuous first derivative of the order parameter Q expected in a second-order phase transition.

1.4.5 Theory-agnostic modeling of dynamical scalarization

Chapters 4 and 5 examined the conceptual and technical challenges of constructing an analytic model of dynamical scalarization, yet restricted their scope to a narrow class of ST theories [153] in which scalarization has been previously been shown to occur [169–172]. However, the recent discovery of spontaneously scalarized BH solutions in other scalar extensions of GR [158–168] has renewed interest in such non-perturbative phenomena in a broader context. Chapter 6 examines scalarization (spontaneous and dynamical) from a theory-agnostic perspective that encompasses all theories in which the phenomena are known to occur [5]. I show that any theory that admits spontaneous scalarization must also admit dynamical scalarization. Additionally, I establish a robust parameterization that completely characterizes scalarization at Newtonian order that is suitable for searches for deviations from GR with GW observations.

In keeping with this theory-agnostic direction, I begin by identifying the key criteria needed for scalarization to occur around a compact object in any modified theory of gravity: (i) the theory must admit a GR solution, i.e. one in which the scalar field vanishes and (ii) this unscalarized solution must be unstable to scalar perturbations. Working in the regime close to the critical point at which the first scalar mode instability arises (i.e. near the onset of scalarization), I use effective field theory (EFT) techniques to construct an effective point-particle action describing each compact object in a binary system. Using this ansatz, I compute the conservative dynamics governing the inspiral of binary systems at Newtonian

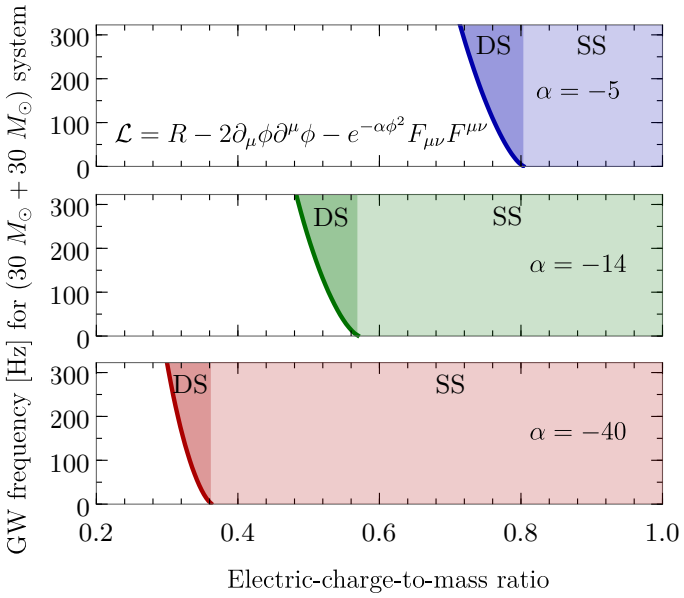

Figure 1.5: The phase space of scalarization that occurs for BBHs in EMS gravity. The parameter α modulates the coupling strength between the Maxwell and scalar fields; three choice are depicted here. Black holes with substantial electric charge will spontaneously scalarize (SS) across all orbital/GW frequencies, shown here with light shading. Below the threshold for spontaneous scalarization, dynamical scalarization (DS) can still occur, shown with darker shading. The frequency at which dynamical scalarization occurs is greater for less electrically-charged BBHs, as depicted with the dark boundary of the shaded region. Figure adapted from Ref. [5].

order; this calculation closely resembles the results of Chapter 5.

I demonstrate how this model can be applied to a generic alternative theory using Einstein-Maxwell-scalar (EMS) gravity as a proxy. In EMS theory, BHs with sufficient electric charge can spontaneously manifest scalar charge [158]. Starting from sequences of static, spherically-symmetric solutions, I use this EFT approach to reconstruct the effective action governing the dynamics of the critical scalar mode that leads to scalarization; I find close agreement with independent calculations of

the mode dynamics from linear perturbation analyses of GR solutions. Then, I use this effective action to explicitly predict the onset of dynamical scalarization across the parameter space of EMS theory, shown in Fig. 1.5. This result represents the first prediction of dynamical scalarization in a BBH, and because it is made for a theory whose formulation in NR has already been established [158], numerical confirmation would be quite straightforward. Though substantial effort is expended exploring the full phase space of scalarization in EMS theory, I emphasize throughout Chapter 6 how this same procedure can be straightforwardly applied to other alternative theories of gravity.

1.4.6 Projected constraints on scalarization by combining pulsar-timing and gravitational-wave observations

Though GW detectors offer the best hope of detecting phenomenology like dynamical scalarization, the best constraints on many theories that manifest such effects come from radio observations of binary pulsars. In Chapter 7, I investigate the constraints that pulsar timing can set on a popular ST theory that admits spontaneous and dynamical scalarization in NSs and determine the degree to which future GW observations can improve these constraints [6]. Finally, I examine whether the constraints set on this ST theory rule out the possibility of detecting dynamical scalarization with GWs; I find that current bounds on the theory are unable to do so.

I consider the specific class of ST theories introduced in Ref. [153], which was

also used in Chapters 4 and 5. The strongest bounds on this theory come from binary NS-white dwarf (WD) systems. The relativistic densities required to trigger scalarization can be found in NSs but not in WDs, and thus NS-WD systems can potentially host larger scalar dipoles (and thus greater dipole radiation) than BNSs. I place constraints on the ST theories of [153] using timing measurements of five NS-WD systems; prior to this work, constraints had only been set using individual binary pulsars.

Additionally, in this work, I examine the dependence of these constraints on the NS equation of state (EOS), i.e. the internal structure of the NS. The constraints that can be set from a single binary pulsar depend crucially on this unknown nuclear physics; fortunately, by combining observations from several pulsars, this variance can be mitigated. Figure 1.6 highlights some of the constraints set using this method: I plot with colored lines the upper bounds on the dimensionless scalar dipole $|\Delta\alpha|$ of a hypothetical BNS consistent with current binary pulsar measurements for different possible EOSs. The system considered here has a fixed secondary mass of $m_A = 1.25 M_\odot$ while the primary mass is allowed to vary.

After establishing the most stringent (at the time of writing) constraints from binary pulsars, I examine the degree to which future GW detections could improve these bounds. Working in the limit of large SNR, for which the posterior distribution is well-approximated by Eq. (1.25), I estimate the precision with which current—Advanced LIGO (aLIGO)—and planned—Cosmic Explorer (CE) and Einstein Telescope (ET)—ground-based GW detectors can measure the scalar dipole of a BNS at a luminosity distance of 200 Mpc. The bounds achievable with these detectors are

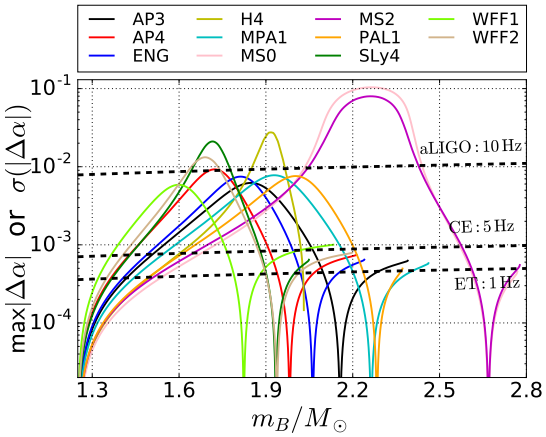

Figure 1.6: *(Colored lines)*: Upper bound on dimensionless scalar dipole $|\Delta\alpha|$ at a 90% confidence level from binary pulsar observations as a function of primary NS mass for several possible EOSs—the secondary NS has a fixed mass of $m_A = 1.25M_\odot$ and the same EOS as the primary. *(Dashed lines)*: Projected statistical uncertainty for $|\Delta\alpha|$ measured for a BNS at a luminosity distance of 200 Mpc for current and planned ground-based GW detectors. Figure taken from Ref. [6].

depicted with dashed lines in Fig. 1.6. Because the theoretical values of scalar dipole constrained by binary pulsars (colored lines) exceed the statistical uncertainty expected in such a measurement with GWs (dashed lines), I can conclude that current detectors could potentially extend bounds for a narrow range of mass configurations, but next-generation detectors will offer much broader improvements. Furthermore, I investigate whether dynamical scalarization could be observed by GW detectors given the theory constraints set by binary pulsars; detecting this phenomenon would provide smoking-gun evidence in support of deviations from GR. Using an identification criterion established in the literature [175], I use the model constructed in Chapter 4 to demonstrate several possible binary configurations for which dynamical scalarization could potentially be detected with Advanced LIGO, thereby validating

continued study and future searches for the phenomenon.

1.4.7 Tidal signature of boson stars in binary systems

In Chapter 8, I shift my attention from phenomenology that can only occur in scalar extensions of GR to that which occurs in much broader contexts [7]. Specifically, I explore how tidal interactions between inspiraling bodies can be used to probe new physics. These interactions are directly linked to the structure of the compact objects in the binary, and thus may be able to distinguish BHs and NSs from other exotic alternatives in binary systems. During the adiabatic inspiral, the dominant tidal interaction is characterized entirely by the tidal deformability Λ of each body, which describes the linear response of a spherical body's quadrupole moment $\mathcal{Q}_{ij}$ to an externally imposed quadrupolar tidal field $\mathcal{E}_{ij}$, i.e.

$$\mathcal{Q}_{ij} = M^5 \Lambda \mathcal{E}_{ij}, \tag{1.36}$$

where the body's mass M has been factored out so that Λ is dimensionless.

In this chapter, I investigate whether tidal effects in a GW signal can differentiate BHs and NSs from boson stars (BSs), a compelling toy model for exotic compact objects. Boson stars are simply self-gravitating clouds of (classical) scalar field. They are an exemplary class of exotic compact objects because they have been shown to form dynamically through gravitational collapse and, by tuning the mass μ of the fundamental boson field, can be constructed with any astrophysical mass. Various families of BSs have been postulated, each differentiated by the type of scalar self-interaction they consider. In this thesis, I consider two common choices:

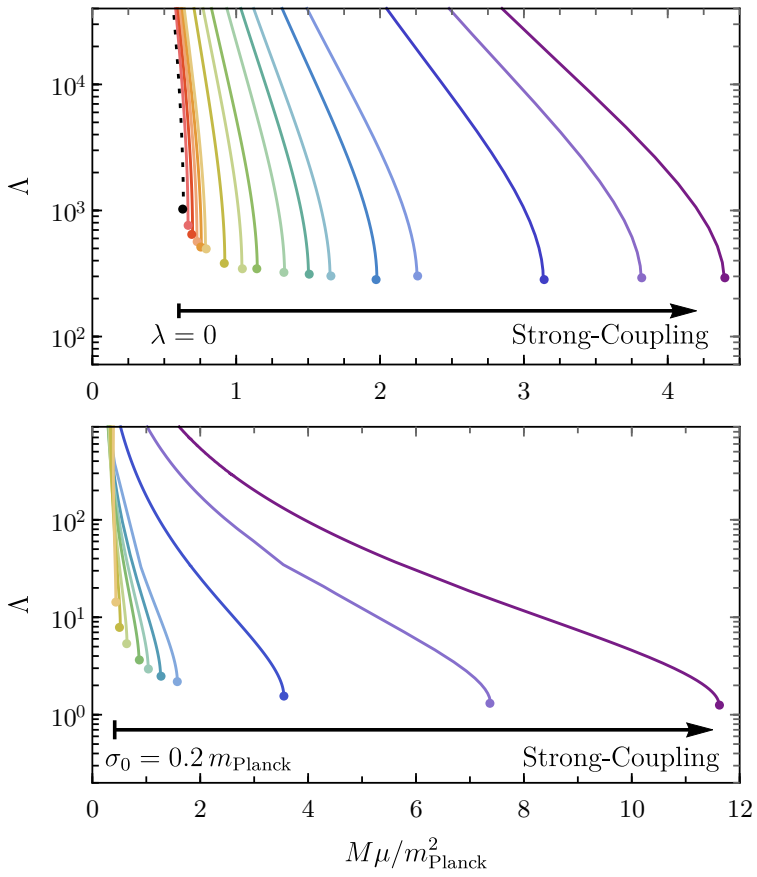

Figure 1.7: Tidal deformability Λ for massive (top panel) and solitonic (bottom panel) BSs as a function of mass M, rescaled by boson mass μ. Colors represent various choices of self-interaction strength, given by λ and σ_0 for massive and solitonic BSs, respectively. Figure adapted from Ref. [7].

massive BSs, characterized by a quartic interaction $V(\phi) = \mu^2|\phi|^2 + \lambda|\phi|^4/2$, and *solitonic* BSs, with the interaction potential $V(\phi) = \mu^2|\phi|^2(1 - 2|\phi|^2/\sigma_0^2)^2$.

I begin by computing the tidal deformability of each family of BSs across a broad range of parameter space. This procedure involves first constructing numerical solutions for spherically-symmetric scalar configurations, and then solving the first-order perturbation equations describing static, tidal deformations of these backgrounds. Finally, the quantities of interest, i.e. the mass M and tidal deformability Λ, are extracted from the asymptotic behavior of each of these solutions. Figure 1.7 presents the results of these calculations, in which the tidal deformability is shown as a function of mass for various choice of self-interaction strength (depicted with different colors) for massive (top panel) and solitonic (bottom panel) BSs.

I next turn to the question of whether GW detectors can measure tidal deformabilities with enough precision to differentiate these classes of BSs from BHs or NSs. Similar to the approach in Chapter 7, I use the Fisher information matrix, in conjunction with Eq. (1.25), to estimate the statistical uncertainty expected for these tidal parameters for canonical systems with aLIGO, ET, and CE. I outline two strategies for differentiating binary BHs and NSs from binary BSs with a GW inspiral, the first relying on only a measurement of the tidal deformability of a single body and the second combining measurements of each body's deformability. I find that massive BSs can be distinguished from BHs with current GW detectors, but that future detectors would be needed to differentiate solitonic BSs and BHs. Matters are slightly more complicated for the case of NSs, as they have their own inherent (non-zero) tidal deformability; however even using current detectors, I find

that one can differentiate between BNSs and binary BSs.

1.4.8 Parameterized tests of general relativity with generic frequency-domain waveform models

Chapter 9 introduces new tools to enable tests of GR with GW inspirals across a variety of contexts. Here I focus on parameterized tests, that is, statistical tests that aim to measure (or constrain) a set of "deviation parameters" that quantify discrepancies in an observed GW signal and the predictions of GR. These types of tests rely on "generalized" waveform models—models in which the parameter space of a baseline GR waveform is extended to include potential deviations from GR; these modifications are controlled by a set of deviation parameters. For example, in a theory-specific test, these new parameters could represent the physical constants, masses, couplings, etc. that define a particular theory that one aims to measure. In contrast, for a theory-agnostic test, these parameters would describe the phenomenological features in the waveform one wishes to constrain.

The chapter describes a new infrastructure for constructing generalized waveforms from any non-precessing[7], frequency-domain GR baseline model. Given its flexibility, this new framework is denoted as the flexible theory-agnostic (`FTA`) approach. Prior to the introduction of the `FTA` framework, parameterized tests of GW inspirals only employed the small subset of waveform models with known, an-

[7]The restriction to non-processing waveform models is made for simplicity; extending the approach documented here to precessing models is relatively straightforward and represents a possible direction for future work.

alytic representations in the frequency-domain (e.g. Refs. [73, 118, 120, 122, 176]). With this new tool, I am now able to extend these tests to new waveform models, and determine the systematic biases that arise due to the choice of underlying GR waveform.

I begin Chapter 9 by detailing the construction of the `FTA` infrastructure and the statistical framework in which it can be employed. Then, I use this approach to perform three different tests of GR using GW observations made during the first and second observing runs of LIGO and Virgo. Unlike in previous chapters, here I carry out Bayesian inference using the full suite of statistical tools outlined in Sec. 1.2.2.2.

First, as part of the LIGO Scientific Collaboration, I place theory-agnostic constraints on phenomenological deviations to the inspiral phase from the catalog of BBH [10] and BNS [9] observations made by LIGO and Virgo. All tests that I perform indicate consistency with the predictions of GR. Additionally, I find good agreement between the bounds recovered using a generalized waveform constructed with the `FTA` infrastructure and those constructed with an earlier approach [120, 176] with a different baseline GR model. This agreement suggests that no significant systematic errors arise from the choice of waveform model, thereby solidifying the claim that no deviations from GR are present.

Next, I use the `FTA` framework to place constraints on Jordan-Fierz-Brans-Dicke gravity (JFBD) [177–179] from the BNS observation GW170817 [11]. This ST theory represents one of the oldest and most well-known alternative relativistic theories of gravity. Although the constraints I place are ultimately not competitive

with existing bounds from Solar System experiments, this analysis provides a useful benchmark for GW tests of GR that can be easily understood by a large segment of the physics community. Jordan-Fierz-Brans-Dicke gravity is characterized by a single parameter α_0, which represents the coupling of the scalar field to test particles, with $\alpha_0 = 0$ corresponding to GR.[8] I perform two complementary analyses on GW170817 to constrain α_0: the first using a waveform model generalized to include phenomenological deviations from GR (akin to that used in the theory-agnostic tests described above) and the second using a generalized waveform model adapted specifically to JFBD. Taking the more conservative bounds from these two analyses, I find that the observed BNS can set the constraint $|\alpha_0| \lesssim 4 \times 10^{-1}$; for comparison the strongest bounds from weak-field tests are $|\alpha_0| \leq 4 \times 10^{-3}$ [180].

Finally, I examine the constraints that can be placed on certain higher-order curvature corrections that generically arise in many possible extensions of GR [138]. For definiteness, I examine the particular model proposed in [181], which uses EFT techniques to construct the generic extension to GR—subject to a number of reasonable assumptions—whose effects are potentially observable by ground-based GW detectors. Starting from the results of [181], I compute the leading-order PN corrections to a frequency-domain GR waveform predicted in this theory. These deviations are parameterized by the energy scale Λ (or its equivalent distance scale $d_\Lambda \equiv \Lambda^{-1}$) at which higher-order curvature corrections appear. I use the `FTA` framework to construct a generalized waveform model including these effects, and then use Bayesian

[8] For historical reasons, this parameter is often expressed instead as $\omega_{\rm BD} \equiv \frac{1}{2}\alpha_0^{-2} - \frac{3}{2}$, where GR is recovered in the limit that $\omega_{\rm BD} \to \infty$.

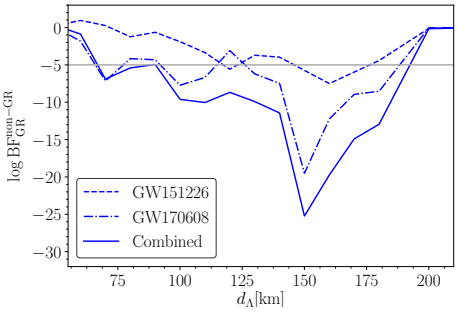

Figure 1.8: The logarithm of the Bayes factor (BF) between the competing hypotheses that higher-order curvature corrections do (non-GR) or do not (GR) arise at a fixed scale distance d_Λ. Dashed and dot-dashed lines depict the BFs recovered using GW151226 and GW170608, respectively, and the solid line indicates the BF achieved by combining both events. By imposing a conservative significance threshold to select one hypothesis over the other $|\log \mathrm{BF} \geq 5|$ (shown with a horizontal gray line), I translate these results into a bound on d_Λ: I rule out the appearance of higher-order curvature corrections at scales of $\sim 70 - 200$ km. Figure adapted from Ref. [138].

inference to constrain the energy scales at which new physics could appear. My results are summarized in Fig. 1.8: I plot the Bayes factor (BF) [the last term in Eq. (1.26)] between the competing hypotheses that higher-order curvature corrections do/do not arise at a given distance scale d_Λ. The dashed and dot-dashed curves respectively depict the BFs recovered using BBH events GW151226 [182] and GW170608 [183]—the two lowest-mass (longest) BBH events observed during the first two observing runs of LIGO and Virgo; the solid curves show the BFs achieved by combining information from both events. The magnitude of the logarithm of the BF indicates how strongly one hypothesis is preferred over the other. By setting a conservative significance threshold of $|\log \mathrm{BF}| \geq 5$, I can translate these result into bounds on d_Λ. I find that these GW events can rule out the appearance of

higher-order curvature corrections arising on distance scales of $\sim 70 - 200$ km.

Chapter 2: Hairy binary black holes in Einstein-Maxwell-dilaton theory and their effective-one-body description

Authors: *Mohammed Khalil, Noah Sennett, Jan Steinhoff, Justin Vines, and Alessandra Buonanno*[1]

Abstract: In General Relativity and many modified theories of gravity, isolated black holes (BHs) cannot source massless scalar fields. Einstein-Maxwell-dilaton (EMd) theory is an exception: through couplings both to electromagnetism and (non-minimally) to gravity, a massless scalar field can be generated by an electrically charged BH. In this work, we analytically model the dynamics of binaries comprised of such scalar-charged ("hairy") BHs. While BHs are not expected to have substantial electric charge within the Standard Model of particle physics, nearly-extremally charged BHs could occur in models of minicharged dark matter and dark photons. We begin by studying the test-body limit for a binary BH in EMd theory, and we argue that only very compact binaries of nearly-extremally charged BHs can manifest non-perturbative phenomena similar to those found in certain scalar-tensor theories. Then, we use the post-Newtonian approximation to study the dynamics of binary BHs with arbitrary mass ratios. We derive the equations

[1]Originally published as Phys. Rev. **D98**, 104010 (2018).

governing the conservative and dissipative sectors of the dynamics at next-to-leading order, use our results to compute the Fourier-domain gravitational waveform in the stationary-phase approximation, and compute the number of useful cycles measurable by the Advanced LIGO detector. Finally, we construct two effective-one-body (EOB) Hamiltonians for binary BHs in EMd theory: one that reproduces the exact test-body limit and another whose construction more closely resembles similar models in General Relativity, and thus could be more easily integrated into existing EOB waveform models used in the data analysis of gravitational-wave events by the LIGO and Virgo collaborations.

2.1 Introduction

The first observations of gravitational waves (GWs) from coalescing binary black holes (BHs) [123, 182–185] and neutron stars [186] offer unprecedented opportunities to test the highly dynamical, strong-field regime of General Relativity (GR) [79, 89, 187]. Leveraging the extraordinary precision of GW detectors to test gravity requires waveform models that incorporate potential deviations from GR. One can construct such models in a theory-independent way by considering phenomenological deviations to waveform models in GR and then constraining the magnitude of these corrections, see, e.g., the constructions of [117–120]. Such an approach has been used by the LIGO and Virgo collaborations to test GR with binary BHs [73, 122, 123]. Alternatively, one can compute the waveform produced in a particular alternative theory, which can then be used to measure directly the fundamental

quantities that define that modified theory of gravity [79].

Here, we adopt the latter approach, focusing on the dynamics of binary BHs in Einstein-Maxwell-dilaton (EMd) theory. This theory originated as a low-energy limit of string theory [188, 189]. In EMd theory, a scalar field (the dilaton) couples to a vector field (the photon) such that BHs with electric charge also source the scalar; the BH develops a scalar charge, or hair. It has been shown that in GR (and some scalar extensions) isolated BHs cannot carry such a charge [23, 148]; these results are often referred to as "no-hair theorems." Analytic solutions exist in EMd theory for spherically symmetric BHs parameterized by the dilaton coupling constant a [see Eqs. (2.1) and (2.2) below for the action]. For $a = 0$, the theory reduces to Einstein-Maxwell (EM) theory and the BH solution is the Reissner-Nordström metric. For $a = 1$, the solution corresponds to the low energy limit of heterotic string theory. For $a = \sqrt{3}$, the solution corresponds to Kaluza-Klein BHs [190], and an analytic solution for charged spinning BHs in EMd theory is only known for that value of a [191].

In the absence of electric charge, isolated BHs in EMd theory behave as in GR. Within the Standard Model, astrophysical BHs are expected to be electrically neutral; however, there exist various theoretical mechanisms beyond the Standard Model that would allow BHs to accumulate non-negligible charge. For a BH with charge Q and mass M to accrete a particle with the same-sign charge q and mass m, gravitational attraction between the two bodies must overpower their electrostatic repulsion, i.e., $q\,Q \lesssim m\,M$, or equivalently $Q/M \lesssim m/q$.[2] Furthermore, a charged

[2]Throughout this work, we use geometric units, in which $G = c = 4\pi\epsilon_0 = 1$, where G is the

BH will neutralize via spontaneous pair production [192] or interactions with astrophysical plasmas [193] over timescales that grow with the mass-to-charge ratio of the available fundamental particles. For electrons, the dimensionless mass-to-charge ratio $m_e/q_e \sim 10^{-22}$ severely limits the charge that BHs can develop through accretion, and guarantees that any BH charged through other means will discharge quickly. However, particles with much larger mass-to-charge ratios are predicted in models of minicharged dark matter [139–141] and would allow BHs to acquire and retain a much larger electric charge [194]. Similarly, models in which dark matter is charged under a hidden U(1) gauge field [142–144], a "dark photon," would allow for BHs to develop significant hidden charge, provided that the ratio of the dark-matter particle's mass to its (hidden) charge is sufficiently large [194]. These two types of dark matter models are consistent with laboratory experiments and cosmological observations [195–197]; current constraints restrict the new particles' mass to 1 GeV $\lesssim m \lesssim$ 10 TeV [144] and its charge to $\lesssim 10^{-14}(m/\mathrm{GeV})q_e$ [198] (see also Fig. 1 in Ref. [194]).

The dynamical evolution of binary BHs in EMd theory has been studied in various contexts. Numerical-relativity simulations of single and binary BHs were performed in Ref. [199]. The authors considered small electric charges and found that the resulting gravitational waveforms are difficult to distinguish from those in GR. Numerical-relativity simulations of the collision of charged BHs with large electric charges in EM theory were performed in Refs. [200, 201], where it was found that a significant fraction of the energy is carried away by electromagnetic radiation.

bare gravitational constant.

In this work, we compute the conservative and dissipative dynamics of a binary BH, and the resulting gravitational waveform, in EMd theory, to first order in the (weak-field and slow-motion) post-Newtonian (PN) approximation. We also construct an effective-one-body (EOB) Hamiltonian description [38, 39] of the conservative dynamics, which provides an analytical resummation of the PN dynamics to exactly recover the test-body limit. In late 2017, the 1PN Lagrangian for a two-body system in EMd theory was derived independently in Ref. [202] using a method different from our own. In that work, the author also discussed an abrupt transition in the scalar charge of a BH as the external scalar field is varied. However, we show here that this transition occurs only in binaries composed of nearly-extremal charged BHs and only near the end of their coalescence. Although extremally charged BHs are excluded when restricting to the Standard Model of particle physics, they are still viable in minicharged dark matter and dark photons models, as we have discussed above.

The paper is structured as follows. In Sec. 2.2, we study the behavior of a small BH in the background of a much more massive companion. By exploring the response of this test BH to its external environment, we discuss whether non-perturbative, strong-field phenomena, akin to those seen in binary neutron stars in scalar-tensor (ST) theories, can occur in binary BHs in EMd theory. In Sec. 2.3, we use the PN approximation to study the dynamics of a binary system with an arbitrary mass ratio. We derive the two-body 1PN Lagrangian and Hamiltonian (with details relegated to Appendix A) and calculate the scalar charge of the two bodies. Further, we derive (with details in Appendix B) the next-to-leading order

PN scalar, vector, and tensor energy fluxes emitted by the binary. Restricting our attention to quasi-circular orbits, we compute the Fourier-domain gravitational waveform at next-to-leading-order using the stationary-phase approximation. In Sec. 2.4, we work out an EOB description of the PN Hamiltonian in EMd theory. We construct two EOB Hamiltonians: one based on the exact BH solution, and the other based on an approximation to that solution. The former is more physical in the strong-gravity regime because it exactly reproduces the dynamics in the test-body limit; the latter uses the same gauge as EOB models in GR, and thus would be easier to integrate into existing data-analysis infrastructure. We compare these two EOB Hamiltonians by calculating the binding energy and the innermost stable circular orbit to determine the region of the parameter space in which they agree. Finally, we present some concluding remarks in Sec. 2.5.

2.2 Einstein-Maxwell-dilaton theory

2.2.1 Setup

We consider a generalization of EMd theory presented in Refs. [188, 189] in the Jordan frame

$$S = \int d^4x \, \frac{\sqrt{-\tilde{g}}}{16\pi} e^{-2a\varphi} \left(\tilde{R} + (6a^2 - 2)\tilde{g}^{\mu\nu}\tilde{\nabla}_\mu\varphi\tilde{\nabla}_\nu\varphi - F_{\mu\nu}F^{\mu\nu} \right) + S_m(\tilde{g}_{\mu\nu}, A_\mu, \psi), \tag{2.1}$$

where φ is a scalar field (the dilaton), a is the dilaton coupling constant, $F_{\mu\nu} \equiv \tilde{\nabla}_\mu A_\nu - \tilde{\nabla}_\nu A_\mu$ is the electromagnetic field tensor, and tildes signify quantities in the Jordan frame. We also include some matter fields ψ, which couple minimally

to $\tilde{g}_{\mu\nu}$ and, through some fundamental electric charge, to A_μ; we represent this total matter action schematically with S_m. By construction, electrically neutral, non-self-gravitating matter configurations will follow geodesics of $\tilde{g}_{\mu\nu}$, and thus this theory respects the weak equivalence principle. However, self-gravitating systems are bound (in part) through non-linear interactions of the scalar field. The back-reaction of the scalar field on the metric exerts an additional force on such systems, causing them to no longer follow geodesics; thus, this theory violates the strong equivalence principle.

The Einstein frame provides a more convenient representation of EMd theory. Performing the conformal transformation $g_{\mu\nu} = \mathcal{A}^{-2}(\varphi)\tilde{g}_{\mu\nu}$ with $\mathcal{A} = e^{a\varphi}$, the action becomes

$$S = \int d^4x \, \frac{\sqrt{-g}}{16\pi} \left(R - 2g^{\mu\nu}\partial_\mu\varphi\partial_\nu\varphi - e^{-2a\varphi}F_{\mu\nu}F^{\mu\nu} \right) + S_m(\mathcal{A}^2(\varphi)g_{\mu\nu}, A_\mu, \psi), \quad (2.2)$$

where $g_{\mu\nu}$ is the Einstein-frame metric. Here, we primarily work in the Einstein frame, but occasionally use quantities in the Jordan frame, denoted with tildes. For a discussion of the equivalence between the two frames see Ref. [203].

For the matter action S_m, we adopt the approach introduced by Eardley [204], in which each body is treated as a delta function and the dependence on the scalar field is incorporated into the masses. For charged monopolar point particles, neglecting dipoles/spins and higher multipoles, the matter action in the Einstein frame can be written as [147]

$$S_m = -\sum_A \int dt \left[\mathfrak{m}_A(\varphi)\sqrt{-g_{\mu\nu}\, v_A^\mu v_A^\nu} - q_A A_\mu v_A^\mu \right], \quad (2.3)$$

where $\mathfrak{m}_A(\varphi)$ is the field-dependent mass of particle A, q_A is the electric charge,

$v_A^\mu \equiv u_A^\mu/u_A^0$ where u_A^μ is its four-velocity, and the fields are evaluated at the particle's location. The mass in the Einstein frame $\mathfrak{m}(\varphi)$ is related to the mass in the Jordan-Fierz frame $\tilde{\mathfrak{m}}(\varphi)$ by

$$\mathfrak{m}(\varphi) = \mathcal{A}(\varphi)\tilde{\mathfrak{m}}(\varphi), \tag{2.4}$$

where $\tilde{\mathfrak{m}}(\varphi)$ is generally not a constant except for bodies with negligible self-gravity.

In most cases, a closed-form expression for the field-dependent mass $\mathfrak{m}(\varphi)$ cannot be found. Instead, one expands the mass about the external/background value φ_0 of the scalar field

$$\ln \mathfrak{m}(\varphi) = \ln \mathfrak{m}(\varphi_0) + \left.\frac{d\ln \mathfrak{m}(\varphi)}{d\varphi}\right|_{\varphi_0} \delta\varphi + \frac{1}{2}\left.\frac{d^2 \ln \mathfrak{m}(\varphi)}{d\varphi^2}\right|_{\varphi_0} \delta\varphi^2 + \mathcal{O}\left(\frac{1}{c^6}\right), \tag{2.5}$$

where $\delta\varphi \equiv \varphi - \varphi_0$. The mass expansion can be parameterized in terms of

$$\alpha(\varphi) \equiv \frac{d\ln \mathfrak{m}(\varphi)}{d\varphi}, \qquad \beta(\varphi) \equiv \frac{d\alpha(\varphi)}{d\varphi}, \tag{2.6}$$

where α is referred to as the (dimensionless) scalar charge. With these parameters, the mass expansion can be written as

$$\mathfrak{m}(\varphi) = m\left[1 + \alpha\delta\varphi + \frac{1}{2}(\alpha^2+\beta)\delta\varphi^2 + \mathcal{O}\left(\frac{1}{c^6}\right)\right], \tag{2.7}$$

where the field-dependent mass is denoted by the Gothic script $\mathfrak{m}$, while the mass evaluated at the background value of the scalar field is denoted by m. We also drop the dependence of the parameters on the background value to simplify the notation, i.e., $\alpha \equiv \alpha(\varphi_0)$, and $\beta \equiv \beta(\varphi_0)$. For the field-dependent parameters, we always explicitly write $\alpha(\varphi)$ and $\beta(\varphi)$. The expression for $\alpha(\varphi)$ depends on the structure of the body; for static BHs, it depends only on the charge-to-mass ratio, whereas for baryonic matter, it also depends on the body's composition.

We note that Eq. (2.3) together with the expansion of the mass (2.7) provide a systematic construction of an effective source or action for an extended object in a PN expansion. We neglect couplings to derivatives of the field, which would correspond to dipole/spin and higher multipole interactions. Due to invariance under gauge transformations $A_\mu \to A_\mu + \partial_\mu \epsilon$, the charges q_A must be constant; they cannot depend on the scalar field like the masses.

2.2.2 Black-hole solution

The metric for an electrically-charged non-rotating BH in EMd theory is given by [188, 189]

$$ds^2 = -A(r)dt^2 + B(r)dr^2 + r^2 C(r) d\Omega^2, \tag{2.8}$$

with

$$A(r) = \left(1 - \frac{r_+}{r}\right)\left(1 - \frac{r_-}{r}\right)^{\frac{1-a^2}{1+a^2}}, \tag{2.9a}$$

$$B(r) = \frac{1}{A(r)}, \tag{2.9b}$$

$$C(r) = \left(1 - \frac{r_-}{r}\right)^{\frac{2a^2}{1+a^2}}, \tag{2.9c}$$

where the constants r_+ and r_- are given in terms of the Arnowitt-Deser-Misner mass M and electric charge Q by

$$M = \frac{r_+}{2} + \left(\frac{1-a^2}{1+a^2}\right)\frac{r_-}{2}, \tag{2.10}$$

$$Q^2 = \frac{r_+ r_-}{1+a^2} e^{-2a\varphi_0}. \tag{2.11}$$

The constant r_+ corresponds to the outer horizon, and r_- corresponds to the inner horizon. The surface area of the horizon (entropy of the BH) is proportional to

$r_+^2 C(r_+)$. Here, we refer to the metric (2.8) as the GHS metric, after Garfinkle, Horowitz and Strominger who found the solution in that form in Ref. [189].

The electromagnetic four-potential A_μ, for an electrically-charged BH, is given by

$$A_0(r) = -\frac{Q}{r} e^{2a\varphi_0}, \qquad A_i(r) = 0\,, \tag{2.12}$$

and the scalar field φ is given by

$$\varphi(r) = \varphi_0 + \frac{a}{1+a^2} \ln\left(1 - \frac{r_-}{r}\right). \tag{2.13}$$

While we consider only electric charges here, we note that the solution for a magnetically charged BH can be obtained from the above solution via the duality rotation that sends $F_{\mu\nu} \to \frac{1}{2} e^{-2a\varphi} \epsilon_{\mu\nu}{}^{\lambda\rho} F_{\lambda\rho}$ and $\varphi \to -\varphi$. [3] In addition to the electric charge, BHs in EMd theory can acquire scalar charge, also called dilaton charge, defined by [189]

$$D \equiv \frac{1}{4\pi} \int d^2\Sigma^\mu \nabla_\mu \varphi, \tag{2.14}$$

where the integral is over a two-sphere at spatial infinity, leading to

$$D = \frac{a}{1+a^2} r_-\,. \tag{2.15}$$

Far from the BH, we have $\varphi(r) \simeq \varphi_0 - D/r + \mathcal{O}(1/r^2)$, which means that D acts as the monopole charge sourcing the scalar field.

[3] The results of Sec. 2.2 hold also for magnetic charges if we flip the sign of φ. However, the PN and EOB results in the following sections would change in non-trivial ways for the magnetic case, since the BH's $F_{\mu\nu}$ is given by $F_{\theta\phi} = Q_m \sin\theta$ with a magnetic charge Q_m, as opposed to $F_{tr} = Q/r^2$ with an electric charge Q (all other components being zero in each case).

The constants r_+ and r_- can be expressed in terms of the mass and the dilaton charge, or the mass and electric charge, as

$$\begin{aligned} r_- &= \frac{1+a^2}{a} D \\ &= \frac{1+a^2}{1-a^2}\left(M - \sqrt{M^2 - (1-a^2)Q^2 e^{2a\varphi_0}}\right), \end{aligned} \tag{2.16a}$$

$$\begin{aligned} r_+ &= 2M - \frac{1-a^2}{a} D \\ &= M + \sqrt{M^2 - (1-a^2)Q^2 e^{2a\varphi_0}}\,. \end{aligned} \tag{2.16b}$$

Expressing quantities in terms of the dilaton charge D, rather than the electric charge Q, makes most equations simpler as it avoids the square root. Therefore, in most of the equations below, we use D instead of Q. The relation between Q and D can be read off from Eq. (2.16a), or Eq. (2.16b),

$$Q^2\, e^{2a\varphi_0} = \frac{2M}{a} D - \frac{1-a^2}{a^2} D^2\,. \tag{2.17}$$

The maximum electric charge of the BH occurs when $r_+ = r_-$, which leads to

$$Q_{\max}\, e^{a\varphi_0} = \sqrt{1+a^2}\, M. \tag{2.18}$$

Hence, for nonzero values of a, an EMd BH can be more charged than an extremal Reissner-Nordström BH with the same mass. Since the dilaton charge is related to the electric charge via Eq. (2.17), the maximum electric charge (2.18) corresponds to the maximum dilaton charge $D_{\max} = aM$.

Without loss of generality, we set the background scalar field to zero, i.e., $\varphi_0 = 0$. To recover the dependence on φ_0, one can simply rescale all electric charges by the factor $e^{a\varphi_0}$, and add the constant φ_0 to the scalar field.[4] We also consider

[4] To see why this is true, consider the action (2.2) with the transformation $Q \to Qe^{a\varphi_0}$ and

only non-negative values of a since the action (2.2) is invariant under $a \to -a$ and $\varphi \to -\varphi$, so the predictions for negative dilaton couplings are given by changing the sign of the scalar field.

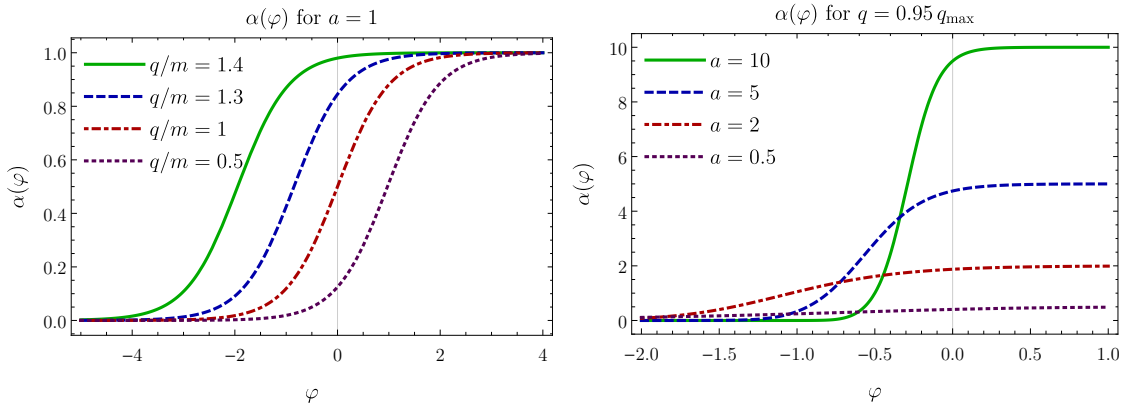

Figure 2.1: $\alpha(\varphi)$ for $a = 1$ with different charge-to-mass ratios (left), and for different values of a with $q = 0.95\, q_{\max}$ (right).

2.2.3 Dynamics of a test black-hole in a background black-hole space-time

Before turning to the dynamics of a generic two-BH system in EMd theory, it will be useful to study the test-body limit of such a system, i.e., the limit in which one body's mass is negligible compared to the other's. In EM theory (without the

$\varphi \to \varphi + \varphi_0$. The vacuum part of the action is symmetric under that transformation, and in the matter action (2.3), the mass $\mathfrak{m}(\varphi)$ is parameterized in terms of the difference $\varphi - \varphi_0$. The electromagnetic part of the matter action is more subtle; it depends on $qv^\mu A_\mu \propto Qqe^{2a\varphi_0}/r$, and hence, one can absorb a factor of $e^{a\varphi_0}$ into each of the two charges. However, since $A_0 = -Qe^{2a\varphi_0}/r$, the transformation $Q \to Qe^{a\varphi_0}$, $\varphi \to \varphi + \varphi_0$ is not valid in equations that depend on A_μ; one first needs to express A_μ in terms of the charges before performing that transformation.

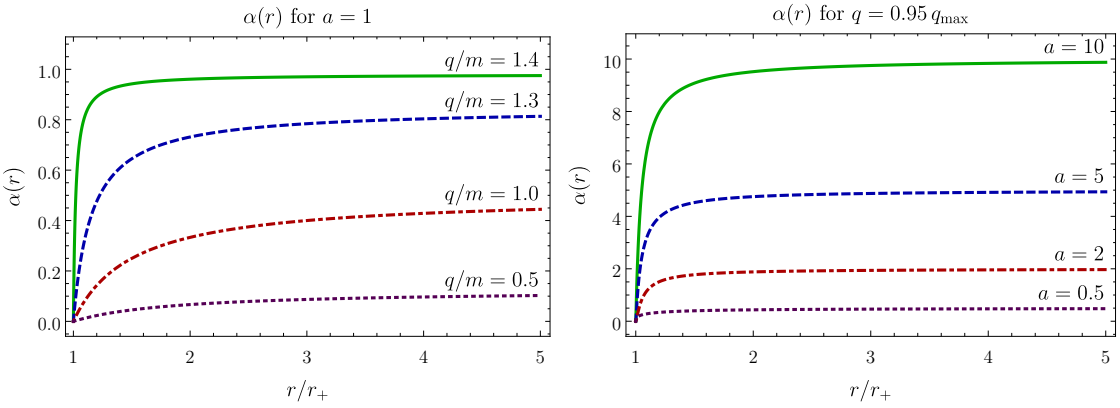

Figure 2.2: $\alpha(r)$ for $a = 1$ with different charge-to-mass ratios (left), and for different values of a (right). In both plots, the charge of the large BH is extremal $Q = \sqrt{1 + a^2}M$, and r is scaled by the horizon radius, which is given by Eq. (2.16b). For $a = 1$, the horizon radius is $2M$ independently of the charge or the coupling constant.

dilaton), the test-body limit of a charged BH corresponds simply to a monopolar point-mass with constant mass and constant charge. In EMd theory, however, a BH's mass must retain a dependence on the dilaton field even as its size goes to zero. In the zero-size limit, we can use the local value of the (background) dilaton field φ, at the small BH's location, to determine its mass $\mathfrak{m}(\varphi)$ in the same way that a lone finite-size BH's mass would be determined by the asymptotic value of the field (as in the previous subsection). This defines what we mean by a "test BH" in EMd theory.[5]

Let us suppose a test BH with mass $\mathfrak{m}(\varphi)$, electric charge q, and dilaton charge d moves in the fixed background spacetime of a larger BH with mass M, electric

[5] This is not to be confused with some uses of the phrase "test body" in the context of ST theories, where one means a body with negligible self-gravity (unlike a BH), so that the mass in the Jordan-Fierz frame is constant and the scalar charge is zero.

charge Q, and dilaton charge D. The mass of the test BH $\mathfrak{m}(\varphi)$ depends on the scalar field φ generated by the larger BH. The expansion of $\mathfrak{m}(\varphi)$ is given in terms of the parameters α and β by Eq. (2.7), and the scalar field φ is given by Eq. (2.13).

To find how α and β depend on the mass and charge of the BH, one needs to find the dependence of the mass on the scalar field. We can get a differential equation for $\mathfrak{m}(\varphi)$ from Eq. (2.16a), or Eq. (2.16b), by identifying the mass M and charge Q with those of the test BH, i.e., $M \to \mathfrak{m}(\varphi)$ and $Q \to q$. The background value of the scalar field can be identified with the field from the more massive BH $\varphi_0 \to \varphi$, and the scalar charge by $D \to d\mathfrak{m}(\varphi)/d\varphi$, as was shown by the matching conditions in Ref. [202]. This leads to the equation

$$\frac{d\mathfrak{m}(\varphi)}{d\varphi} = \frac{a}{1-a^2}\left[\mathfrak{m}(\varphi) - \sqrt{\mathfrak{m}(\varphi)^2 - (1-a^2)q^2e^{2a\varphi}}\right], \tag{2.19}$$

which, as far as we know, has no analytic solution for arbitrary values of a. Nevertheless, we can still obtain an expression for the dimensionless scalar charge, which is defined by Eq. (2.6),

$$\alpha(\varphi) = \frac{a}{1-a^2}\left[1 - \sqrt{1-(1-a^2)\frac{q^2e^{2a\varphi}}{\mathfrak{m}^2(\varphi)}}\right], \tag{2.20}$$

and

$$\beta(\varphi) = \frac{a^2q^2e^{2a\varphi}}{(1-a^2)\mathfrak{m}^2(\varphi)}\left[1 - \frac{a^2}{\sqrt{1-(1-a^2)\frac{q^2e^{2a\varphi}}{\mathfrak{m}^2(\varphi)}}}\right], \tag{2.21}$$

in agreement with Ref. [202].

It is interesting to note that an exact analytic solution to the differential equation (2.19) can be found when the coupling constant $a = 1$, that is

$$\mathfrak{m}(\varphi) = \sqrt{\text{const.} + \frac{1}{2}q^2e^{2\varphi}}\,. \tag{2.22}$$

Since the above expression should give m when $\varphi = 0$, the integration constant is found to be $m^2 - \frac{1}{2}q^2$. Hence,

$$\mathfrak{m}(\varphi) = \sqrt{m^2 - \frac{1}{2}q^2 + \frac{1}{2}q^2 e^{2\varphi}}\,. \tag{2.23}$$

By differentiating $\mathfrak{m}(\varphi)$, we get the parameters

$$\alpha = \frac{q^2}{2m^2}\,, \qquad \beta = \frac{q^2}{m^2} - \frac{q^4}{2m^4}\,. \tag{2.24}$$

In Fig. 2.1, we plot $\alpha(\varphi)$ as a function of φ. We see that the test BH's $\alpha(\varphi)$ transitions between two values: zero and a. The function $\alpha(\varphi)$ reaches its maximum value when the quantity $q^2\, e^{2a\varphi}/\mathfrak{m}^2$ approaches $1 + a^2$, which means that in the Jordan-Fierz frame, the charge q approaches the extremal value $\sqrt{1+a^2}\tilde{\mathfrak{m}}$, where the mass in the Jordan-Fierz frame $\tilde{\mathfrak{m}}$ is given by Eq. (2.4). Changing the charge-to-mass ratio shifts the curve on the horizontal axis, while changing a changes the maximum value of α and determines how quickly this transition occurs.

We emphasize that the scalar field φ generated by the more massive BH is always negative, as can be seen from Eq. (2.13), so the test BH always descalarizes. Further, because of the logarithm, the magnitude of φ increases slowly with decreasing separation until r approaches the inner horizon r_-, where it diverges. For the scalar charge of the test BH to change dramatically before merging with its much larger companion, both BHs must be close to extremally charged. As discussed in Sec. 2.1, extremally-charged BHs can exist in minicharged dark matter and dark photon models. If the test BH is not sufficiently charged, its scalar charge is close to zero when well separated from its companion, and then monotonically decreases

toward zero as the binary evolves. The total shift in the scalar field that the test BH experiences prior to crossing the outer horizon is given by

$$\varphi(r_+) - \varphi(\infty) = \frac{a}{1+a^2} \ln \left[\frac{1 - D/D_{\rm max}}{1 - (1-a^2)D/2D_{\rm max}} \right] . \tag{2.25}$$

Thus, if the large BH is not also sufficiently charged, then the test BH's scalar charge does not change dramatically.

In Fig. 2.2, we substitute the expression for the scalar field of the larger BH $\varphi(r)$ into that for the scalar charge of the test BH $\alpha(\varphi)$, and plot $\alpha(r)$ versus the separation r scaled by the horizon radius. When setting the charge of the large BH to its extremal value, $Q = \sqrt{1+a^2}M$, we see that the charge of the test BH also needs to be near extremal for the descalarization transition to occur. Yet, the transition only occurs very close to the horizon of the background BH. Hence, we expect this descalarization to drastically affect the GW signature only during the late inspiral and plunge of a test BH into a more massive BH and only when the BHs are nearly-extremally charged, when the horizon, the innermost-stable circular orbit, and the divergence in φ coincide. This result is analogous to extremal Kerr BHs, where the plunge occurs at significantly smaller separations [205]. However, a comparable-mass binary does not perform many orbits at small separations due to stronger radiation reaction, and thus we expect that the transition in the scalar charge would have a negligible effect on GWs from the inspiral of a comparable-mass binary.

We note that, while the descalarization transition occurs for near-extremal BHs, the largest change in the value of α from infinity until, e.g., $r = 2r_+$ occurs

when the electric charge is $q/m \sim 1$, as can be seen in the left panel of Fig. 2.2. This is due to the slope of $\alpha(\varphi)$ at the background value of the scalar field $\varphi_0 = 0$. So, in order to increase the change in the scalar charge to observe descalarization, it is important to have a maximal $\beta(\varphi) \equiv d\alpha(\varphi)/d\varphi$.

2.2.4 Compact objects in Einstein-Maxwell-dilaton and scalar-tensor theories

Certain ST theories can exhibit non-perturbative phenomena, known as induced or dynamical scalarization, in binary systems of neutron stars [169–172]. Having established how a BH responds to its scalar environment, we now investigate whether such effects could arise in binary BHs in EMd theory. In Ref. [199], the authors suggested that dynamical and induced scalarization are much less significant in EMd theory than in ST theories. In this subsection, we support this claim using more quantitative arguments by directly comparing the behavior of BHs and neutron stars in the respective theories.

In Ref. [3], the authors argued that the onset of induced and dynamical scalarization coincide with a breakdown of the PN approximation. Specifically, these non-perturbative phenomena indicate that the scalar field has grown beyond the validity of a PN expansion of $\mathfrak{m}$, e.g., Eq. (2.7). A useful diagnostic for determining the onset of such phenomena is to compare the relative size of the coefficients of such a power series to the small parameter with which one constructs the expansion.

While both EMd theory and ST theories include an additional scalar field,

the non-minimal coupling of that field to the Jordan-Fierz (physical) metric can differ substantially. To facilitate comparisons between these theories, we consider an expansion of $\mathfrak{m}$ in $G_{\rm N}(\varphi)$, the parameter that characterizes the gravitational force felt between two test bodies placed in the scalar background φ. In both EMd theory and ST theories, this Newton's "constant" is given by

$$G_{\rm N}(\varphi) \equiv \mathcal{A}^2(\varphi)\left[1+\left(\frac{d\log\mathcal{A}}{d\varphi}\right)^2\right]. \tag{2.26}$$

We expand $\mathfrak{m}$ in terms of this quantity

$$\mathfrak{m}(G_{\rm N}) = m\left[1+C_1\left(\frac{G-G_{\rm N}^0}{G_{\rm N}^0}\right)+C_2\left(\frac{G-G_{\rm N}^0}{G_{\rm N}^0}\right)^2+\dots\right], \tag{2.27}$$

where we have defined

$$G_{\rm N}^0 \equiv G_{\rm N}(\varphi=0), \tag{2.28a}$$

$$C_1 \equiv \left[\frac{d\log\mathfrak{m}}{d\log G_{\rm N}}\right]_{G_{\rm N}=G_{\rm N}^0}, \tag{2.28b}$$

$$C_2 \equiv \frac{1}{2}\left[\frac{d^2\log\mathfrak{m}}{(d\log G_{\rm N})^2}+\left(\frac{d\log\mathfrak{m}}{d\log G_{\rm N}}\right)^2-\frac{d\log\mathfrak{m}}{d\log G_{\rm N}}\right]_{G_{\rm N}=G_{\rm N}^0}. \tag{2.28c}$$

We compare these coefficients for BHs in EMd theory to that of neutron stars in Brans-Dicke gravity [177–179], defined by the coupling

$$\mathcal{A}_{\rm BD}(\varphi) = e^{-\alpha_0\varphi}, \tag{2.29}$$

and theories first considered by Damour and Esposito-Farèse (DEF) [147, 153]

$$\mathcal{A}_{\rm DEF}(\varphi) = e^{-\beta_0\varphi^2/2}, \tag{2.30}$$

in which induced and dynamical scalarization can occur when β_0 is sufficiently negative. In Fig. 2.3, we plot the ratio C_2/C_1 for compact objects in the various

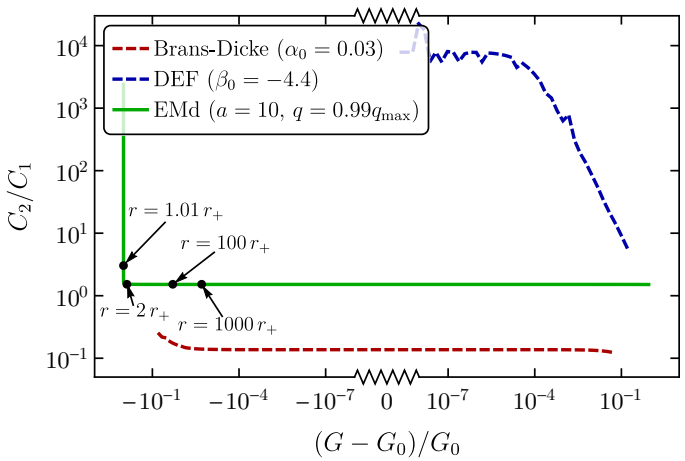

Figure 2.3: Ratio of the coefficients C_2/C_1 defined in Eqs. (2.28b) and (2.28c) as a function of $G_{\rm N}$ for BHs in EMd theory (solid) and neutron stars in various ST theories (dashed). Annotated points depict this ratio at various separations for a test BH with $q = 0.99 q_{\rm max}$ in the background of a BH with $Q = Q_{\rm max}$ in EMd theory (r_+ refers to the outer horizon of the background spacetime).

theories. For the ST theories, we consider neutrons stars with $m = 1.45 M_\odot$ with the piecewise polytropic fit to the SLy equation of state constructed in Ref. [206]. The solid curve depicts this ratio for BHs in EMd theory with coupling $a = 10$. By comparison, this same quantity is shown with red and blue dashed curves for neutron stars in Brans-Dicke gravity with $\alpha_0 = 0.03$ and in the theory of Damour and Esposito-Farèse with $\beta_0 = -4.4$, respectively. Note that by inserting Eq. (2.30) into Eq. (2.26), one sees that this theory is only defined for $G_{\rm N}(\varphi) > G_{\rm N}^0$. For reference, we indicate with black points the separation at which these values are achieved in EMd theory when the test BH in placed in the background of an extremally charged BH; r_+ corresponds to the outer horizon of the background BH. We see that the magnitude of the ratio C_2/C_1 drastically differs between ST theories that manifest

induced and dynamical scalarization (DEF) and EMd theories. This result indicates that a perturbative expansion of the dynamics has a larger regime of validity, and that non-perturbative phenomena are less likely to emerge during the coalescence of binary BHs in EMd theory.

2.3 Post-Newtonian approximation in Einstein-Maxwell-dilaton theory

2.3.1 Two-body dynamics

To go beyond the test-body limit, treating two-body systems with arbitrary mass ratios, we employ the PN approximation, which is valid in the weak-field, slow-motion regime [30]. In Appendix A, we derive results for the conservative dynamics of a binary BH system in EMd theory, at next-to-leading order in the PN expansion, i.e., at 1PN order. We employ the Fokker action method [207] (see also Ref. [208]), which has been used to treat the 4PN dynamics in GR [209], and the 2PN [208] and 3PN [210] dynamics in ST theories. We begin by considering the PN expansions of the EMd action in Eq. (2.2) and the matter action for point particles in Eq. (2.3), using the mass expansion in terms of the α and β parameters from Eq. (2.7). From the initial full action expanded to 1PN order, we obtain field equations for the scalar field, the metric potential, and the electromagnetic 4-potential. The Fokker action is obtained by plugging the (regularized) solutions to the field equations back into the action, eliminating the field degrees of freedom, yielding an action depending only on the matter variables. We work in the harmonic gauge $g^{\mu\nu}\Gamma^{\lambda}_{\mu\nu} = 0$ and the

Lorenz gauge $\partial_\mu A^\mu = 0$ throughout. The final result for the two-body Lagrangian is given by

$$
\begin{aligned}
L = &-m_1 - m_2 + \frac{1}{2}m_1 v_1^2 + \frac{1}{2}m_2 v_2^2 + \left(1 + \alpha_1\alpha_2 - \frac{q_1 q_2}{m_1 m_2}\right)\frac{m_1 m_2}{r} \\
&+ \frac{1}{8}m_1 v_1^4 + \frac{1}{8}m_2 v_2^4 + \frac{q_1 q_2}{2r}\left[\boldsymbol{v_1}\cdot\boldsymbol{v_2} + (\boldsymbol{n}\cdot\boldsymbol{v_1})(\boldsymbol{n}\cdot\boldsymbol{v_2})\right] \\
&+ \frac{m_1 m_2}{2r}\left[(3-\alpha_1\alpha_2)(v_1^2+v_2^2) - (7-\alpha_1\alpha_2)(\boldsymbol{v_1}\cdot\boldsymbol{v_2}) - (1+\alpha_1\alpha_2)(\boldsymbol{n}\cdot\boldsymbol{v_1})(\boldsymbol{n}\cdot\boldsymbol{v_2})\right] \\
&- \frac{m_1 m_2}{2r^2}\left[(1+2\alpha_1\alpha_2)(m_1+m_2) + m_1\alpha_1^2(\alpha_2^2+\beta_2) + m_2\alpha_2^2(\alpha_1^2+\beta_1)\right] \\
&+ \frac{q_1 q_2}{r^2}\left[m_1(1+a\alpha_1) + m_2(1+a\alpha_2)\right] - \frac{1}{2r^2}\left[m_1 q_2^2(1+a\alpha_1) + m_2 q_1^2(1+a\alpha_2)\right] \\
&+ \mathcal{O}\left(\frac{1}{c^4}\right),
\end{aligned}
\tag{2.31}
$$

where $\boldsymbol{r} \equiv \boldsymbol{x}_1 - \boldsymbol{x}_2$ is the separation between the two bodies, and $\boldsymbol{n} \equiv \boldsymbol{r}/r$. This Lagrangian agrees with the one derived by Damour and Esposito-Farèse [147, 208] when the Maxwell fields are zero. The standard 1PN Lagrangian in GR is obtained by setting $q_i = \alpha_i = \beta_i = 0$, while the Lagrangian in EM theory is obtained when $\alpha_i = \beta_i = 0$. Note that, since we use the mass expansion in Eq. (2.7) given in terms of generic parameters α and β, our results are not restricted to BHs in EMd theory, but are applicable to more generic bodies as well.

During the course of this project, the same 1PN Lagrangian for a two-body system in EMd theory was derived independently by Julié in Ref. [202]. While our results agree, our derivation differs from that of Ref. [202] in some notable respects. In Ref. [202], the (unexpanded) field equations were directly obtained from the action (2.2), and then those equations were expanded and solved for the fields. The primary difference with our derivation is in how Ref. [202] constructed the two-body Lagrangian: (i) taking (only) the matter action for one body (without the field part

of the action, and without the matter action for the other body), which would apply if the body were a test body in some given fields, (ii) inserting for those fields the (regularized) solutions to the field equations resulting from the total (two bodies + fields) action, and (iii) taking the resultant Lagrangian and "symmetrizing" it with respect to the two bodies. While this procedure does produce a correct Lagrangian at 1PN order, it is not justified in general, and it is important to see how the result can be obtained from a consistent treatment of the full action for the two bodies and fields. In Ref. [202], it was also found that it is possible to parameterize the 1PN Lagrangian in EMd theory to have the same structure as the 1PN Lagrangian in ST theories, which means that many results in ST theories can be directly extended to EMd theory at 1PN order. We choose not to use that parameterization to make the dependence on the electric charges more apparent, and because many of our results are specific to EMd theory, such as calculating the vector energy flux and developing the EOB Hamiltonians.

The Hamiltonian in the center-of-mass frame can be derived from the Lagrangian using the Legendre transformation [211]

$$H = \boldsymbol{v} \cdot \boldsymbol{p} - L, \tag{2.32}$$

where the relative velocity $\boldsymbol{v} \equiv \boldsymbol{v}_1 - \boldsymbol{v}_2$ and the center-of-mass momentum

$$p_i = \frac{\partial L}{\partial v^i}. \tag{2.33}$$

This leads to the energy

$$
\begin{aligned}
E = M &+ \frac{1}{2}\mu v^2 - \frac{G_{12}M\mu}{r} + \frac{3}{8}(1-3\nu)\mu v^4 \\
&+ \frac{G_{12}M\mu}{2r}\left[\left(\frac{3-\alpha_1\alpha_2}{1+\alpha_1\alpha_2-\frac{q_1q_2}{M\mu}}+\nu\right)v^2+\nu\dot{r}^2\right] \\
&+ \frac{M^2\mu}{2r^2}\Bigg[(1+\alpha_1\alpha_2)^2 + X_2\alpha_2^2\beta_1 + X_1\alpha_1^2\beta_2 + X_1\frac{q_2^2}{M\mu}(1+a\alpha_1) \\
&+ X_2\frac{q_1^2}{M\mu}(1+a\alpha_2) - 2\frac{q_1q_2}{M\mu}\left(1+a\alpha_1X_1+a\alpha_2X_2\right)\Bigg] + \mathcal{O}\left(\frac{1}{c^4}\right), \qquad (2.34)
\end{aligned}
$$

where $\dot{r} = \boldsymbol{n}\cdot\boldsymbol{v}$, and we defined the total mass M, reduced mass μ, symmetric mass ratio ν, and the mass ratios X_i in terms of the constant masses m_1 and m_2 by

$$
\begin{aligned}
M \equiv m_1 + m_2\,, \qquad \mu \equiv \frac{m_1m_2}{M}\,, \qquad \nu \equiv \frac{\mu}{M}\,, \\
X_1 \equiv \frac{m_1}{M}, \qquad X_2 \equiv \frac{m_2}{M}. \qquad (2.35)
\end{aligned}
$$

We also define the coefficient G_{12} by

$$
G_{12} \equiv 1 + \alpha_1\alpha_2 - \frac{q_1q_2}{M\mu}\,, \qquad (2.36)
$$

which reduces to the usual definition in ST theories when the electric charges are zero. The advantage of including the charges in G_{12} is that the Newtonian-order acceleration is simply given by $\boldsymbol{a} = -G_{12}M\boldsymbol{n}/r^2 + \mathcal{O}(1/c^2)$.

Expressing the energy in terms of the center-of-mass momentum $\boldsymbol{p} \equiv \boldsymbol{p_1} = -\boldsymbol{p_2}$, instead of the velocity, we obtain the Hamiltonian

$$
\begin{aligned}
H = M &+ \frac{p^2}{2\mu} - \frac{G_{12}M\mu}{r} - \frac{1}{8}(1-3\nu)\frac{p^4}{\mu^3} - \frac{G_{12}M}{2\mu r}\left[\left(\frac{3-\alpha_1\alpha_2}{1+\alpha_1\alpha_2-\frac{q_1q_2}{M\mu}}+\nu\right)p^2+\nu p_r^2\right] \\
&+ \frac{M^2\mu}{2r^2}\Bigg[(1+\alpha_1\alpha_2)^2 + X_2\alpha_2^2\beta_1 + X_1\alpha_1^2\beta_2 + X_1\frac{q_2^2}{M\mu}(1+a\alpha_1) + X_2\frac{q_1^2}{M\mu}(1+a\alpha_2) \\
&- 2\frac{q_1q_2}{M\mu}\left(1+a\alpha_1X_1+a\alpha_2X_2\right)\Bigg] + \mathcal{O}\left(\frac{1}{c^4}\right), \qquad (2.37)
\end{aligned}
$$

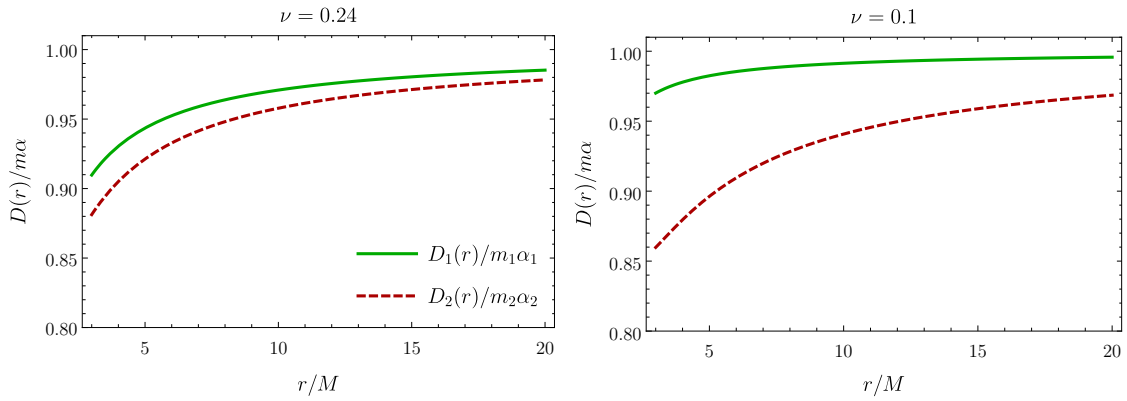

Figure 2.4: Scalar charges scaled by their asymptotic value as a function of the separation r of a binary BH scaled by the total mass. In both plots, the charge-to-mass ratio $q_1/m_1 = q_2/m_2 = 1$ and the dilaton coupling $a = 1$; in the left panel $\nu = 0.24$, while in the right $\nu = 0.1$.

where $p_r = \boldsymbol{n} \cdot \boldsymbol{p}$.

Next, we examine how the scalar charges of the two bodies change with their separation. The dilaton charge is given by

$$D(\varphi) = \frac{d\mathfrak{m}(\varphi)}{d\varphi} = \mathfrak{m}(\varphi)\alpha(\varphi). \tag{2.38}$$

For the two bodies, the dilaton charge as a function of the separation r has the expansion

$$D_1(r) = m_1\Big[\alpha_1 + (\alpha_1^2 + \beta_1)\varphi_1(r) + \frac{1}{2}\big(3\beta_1\alpha_1 + \alpha_1^3 + \beta_1'\big)\varphi_1^2(r) + \mathcal{O}\left(1/c^6\right)\Big], \tag{2.39a}$$

$$D_2(r) = m_2\Big[\alpha_2 + (\alpha_2^2 + \beta_2)\varphi_2(r) + \frac{1}{2}\big(3\beta_2\alpha_2 + \alpha_2^3 + \beta_2'\big)\varphi_2^2(r) + \mathcal{O}\left(1/c^6\right)\Big], \tag{2.39b}$$

where $\beta' \equiv d\beta(\varphi)/d\varphi|_{\varphi_0}$, φ_1 is the scalar field at the location of body 1, and φ_2 is

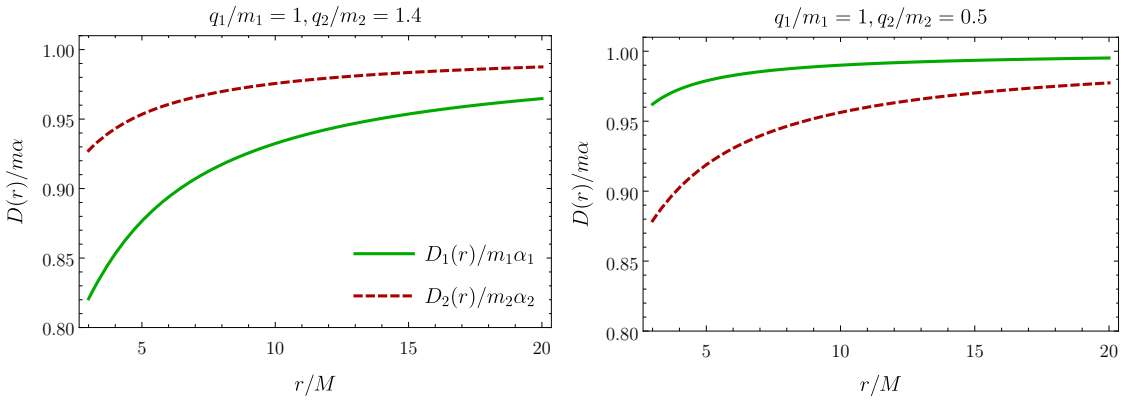

Figure 2.5: Scalar charges of a binary BH as a function of r for equal masses ($\nu = 1/4$), dilaton coupling $a = 1$, and charge-to-mass ratios $q_1/m_1 = 1,\ q_2/m_2 = 1.4$ (left) and $q_1/m_1 = 1,\ q_2/m_2 = 0.5$ (right).

the scalar field at the location of body 2. From the 1PN scalar field in Eq. (A.32),

$$\varphi_1(r) = -\frac{\alpha_2 m_2}{r} + \frac{m_1 m_2}{r^2}\left(\alpha_2 + \alpha_1\alpha_2^2 + \alpha_1\beta_2\right) - \frac{aq_1q_2}{r^2} + \frac{aq_2^2}{2r^2} + \frac{1}{2}\alpha_2 m_2(\boldsymbol{n}\cdot\boldsymbol{a}_2) + \mathcal{O}\left(1/c^6\right), \tag{2.40a}$$

$$\varphi_2(r) = -\frac{\alpha_1 m_1}{r} + \frac{m_1 m_2}{r^2}\left(\alpha_1 + \alpha_2\alpha_1^2 + \alpha_2\beta_1\right) - \frac{aq_1q_2}{r^2} + \frac{aq_1^2}{2r^2} - \frac{1}{2}\alpha_1 m_1(\boldsymbol{n}\cdot\boldsymbol{a}_1) + \mathcal{O}\left(1/c^6\right), \tag{2.40b}$$

where, using $\boldsymbol{a} = -G_{12}M\boldsymbol{n}/r^2 + \mathcal{O}(1/c^2)$ and Eq. (B.19),

$$\boldsymbol{a}_1 = \frac{m_2}{M}\boldsymbol{a} = -\frac{G_{12}m_2}{r^2}\boldsymbol{n} + \mathcal{O}\left(1/c^2\right), \tag{2.41a}$$

$$\boldsymbol{a}_2 = -\frac{m_1}{M}\boldsymbol{a} = \frac{G_{12}m_1}{r^2}\boldsymbol{n} + \mathcal{O}\left(1/c^2\right). \tag{2.41b}$$

In Fig. 2.4, we plot $D_1(r)$ and $D_2(r)$ for charge-to-mass ratios $q_1/m_1 = q_2/m_2 = 1$, dilaton coupling constant $a = 1$, and symmetric mass ratios $\nu = 0.24$ and $\nu = 0.1$. The curves are plotted until $r = 3M$ because the PN expansion becomes inaccurate well before that separation. From the figure, we see that the

scalar charge of both bodies decreases as the separation decreases, with the charge of the lighter body decreasing more quickly. Figure 2.5 shows the scalar charge as a function of the separation for equal masses but with different charge-to-mass ratios. We keep $q_1/m_1 = 1$ while q_2/m_2 takes the values 1.4 and 0.5. The scalar charge of the less-charged body decreases more quickly with decreasing separation. These results are consistent with what was found in the previous section for the scalar charge of a test BH, but here, we do not see a transition or a divergence near the horizon.

2.3.2 Gravitational energy flux

From the 1PN expansion, we computed the next-to-leading order scalar, vector, and tensor energy fluxes for general orbits (see Appendix B for the derivation). In a $1/c$ expansion, the leading terms are the scalar and vector dipole fluxes, which are of order $1/c^3$, while the leading order tensor flux is of order $1/c^5$, which is the same as the next-to-leading order scalar and vector fluxes. We computed the next-to-leading order tensor flux, which is of order $1/c^7$, because that is the maximum level of approximation accessible by use of the 1PN near-field equations. The scalar and vector dipole fluxes depend on the difference between the charges of the two bodies. The scalar flux also includes a monopole term that vanishes for circular orbits.

The total energy flux is the sum of the scalar, vector, and tensor fluxes

$$\mathcal{F} = \mathcal{F}_S + \mathcal{F}_V + \mathcal{F}_T, \tag{2.42}$$

where the expressions for the fluxes through next-to-leading order for general orbits are given in Appendix B. The fluxes for circular orbits are given by

$$\begin{aligned}\mathcal{F}_S =&\frac{\nu^2 x^4}{3G_{12}^2}(\alpha_1-\alpha_2)^2+\frac{\nu^2 x^5}{15G_{12}^2}\left[20f_\gamma(\alpha_1-\alpha_2)^2\right.\\&\left.+5\left(f^S_{v^2}+f^S_{1/r}\right)+16\left(X_1\alpha_2+X_2\alpha_1\right)^2\right]+\mathcal{O}\left(\frac{1}{c^7}\right),\end{aligned}\tag{2.43a}$$

$$\begin{aligned}\mathcal{F}_V =&\frac{2\nu^2 x^4}{3G_{12}^2}\left(\frac{q_1}{m_1}-\frac{q_2}{m_2}\right)^2+\frac{2\nu^2 x^5}{15G_{12}^2}\left[20f_\gamma\left(\frac{q_1}{m_1}-\frac{q_2}{m_2}\right)^2\right.\\&\left.+8\left(X_2\frac{q_1}{m_1}+X_1\frac{q_2}{m_2}\right)^2+5\left(f^V_{v^2}+f^V_{1/r}\right)\right]+\mathcal{O}\left(\frac{1}{c^7}\right),\end{aligned}\tag{2.43b}$$

$$\mathcal{F}_T =\frac{32\nu^2 x^5}{5G_{12}^2}+\frac{2\nu^2 x^6}{105G_{12}^2}\left(f^T_{v^4}+f^T_{v^2/r}+f^T_{1/r^2}+672f_\gamma\right)+\mathcal{O}\left(\frac{1}{c^9}\right),\tag{2.43c}$$

where the coefficients f are given by Eqs. (B.36), (B.56), (B.79), and (B.85). The energy flux is expressed in terms of the parameter x defined by

$$x\equiv\left(G_{12}M\Omega\right)^{2/3},\tag{2.44}$$

where Ω is the orbital frequency, which is "perturbatively gauge-invariant" in the sense that it remains fixed under coordinate transformations to arbitrary PN order.

In Figs. 2.6 and 2.7, we plot the total energy flux in EMd theory with $a=1$ relative to the flux when all charges are zero versus the binary's gauge-invariant velocity $v=(G_{12}M\Omega)^{1/3}$, i.e., we plot $(\mathcal{F}-\mathcal{F}_{q=0})/\mathcal{F}_{q=0}$. For comparison, Fig. 2.6 also includes the energy flux in EM, when scalar charges are zero but not the electric charges. The plots start at $v=(G_{12}M\Omega)^{1/3}=0.15$ which corresponds to a total mass $M=20M_\odot$, and a lower GW frequency in the detector of 10 Hz. In the plots, we used the next-to-leading order scalar and vector fluxes, but only used the leading Newtonian order tensor flux, because the 1PN energy flux in GR is given by

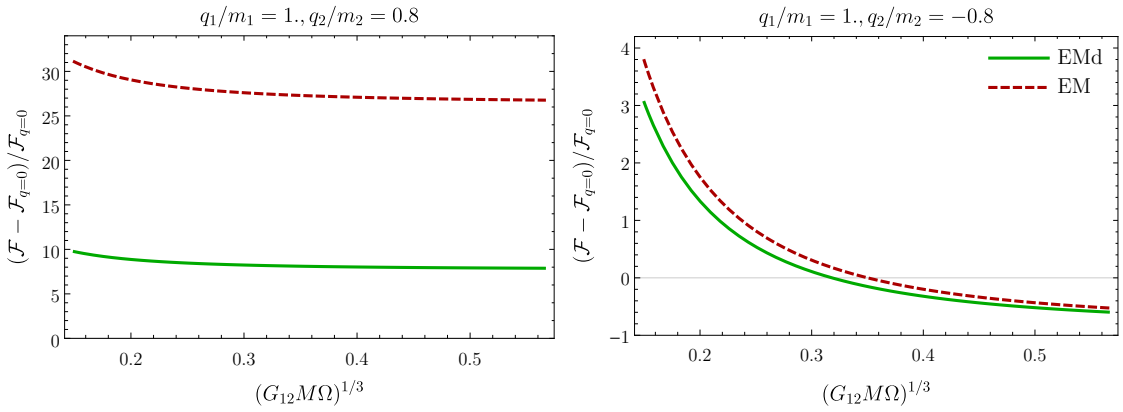

Figure 2.6: Energy flux in EMd theory and EM relative to the uncharged GR flux plotted versus the gauge-invariant velocity for circular orbits $v \equiv (G_{12}M\Omega)^{1/3}$ for coupling constant $a = 1$, for equal masses, and for charge-to-mass ratio $q_1/m_1 = 1, q_2/m_2 = 0.8$ (left) and $q_1/m_1 = 1, q_2/m_2 = -0.8$ (Right).

$\mathcal{F}_{\rm GR} \sim x^5 - \text{const.}\ x^6$; the minus sign of the second term causes the flux to become negative at large frequencies.

From the plots, we see that at small frequencies (large separations), the difference with GR is greater than at larger frequencies because the dipole scalar and vector fluxes dominate ($\mathcal{F}_S \sim x^4$ while $\mathcal{F}_T \sim x^5$). For equal charges, the scalar and vector dipole fluxes are both zero, which means the total energy flux is the tensor flux that is proportional to x^5. Hence, the next-to-leading order flux in EMd theory becomes a constant shift to the GR flux, and the relative flux plotted in the figures becomes a straight line, as can be seen in Fig. 2.7.

In the two panels of Fig. 2.6, we use charge-to-mass ratios $q_1/m_1 = 1,\ q_2/m_2 = 0.8$ (left) and $q_1/m_1 = 1,\ q_2/m_2 = -0.8$ (right). For same-sign charges, at a fixed frequency, there is a greater difference from GR than for opposite-sign charges and

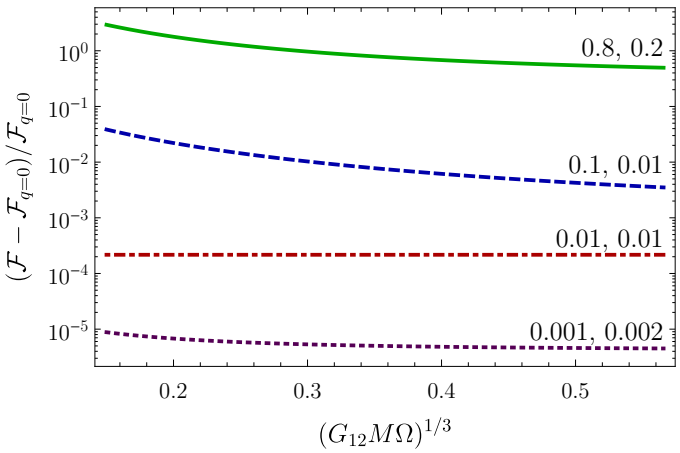

Figure 2.7: Energy flux in EMd theory relative to the uncharged GR flux for coupling constant $a = 1$ plotted versus $v = (G_{12}M\Omega)^{1/3}$, for equal masses, and for various charge-to-mass ratios.

also a greater difference between EMd and EM. This is because the energy flux is inversely proportional to $G_{12}^2 = (1 + \alpha_1\alpha_2 - q_1q_2/m_1m_2)^2$, which is larger when the electric charges have opposite signs than when they have the same sign. In the right panel, the plotted curves become negative when $\mathcal{F} < \mathcal{F}_{q=0}$, which occurs because $G_{12} > 1$ for opposite-sign charges, which makes the EMd flux smaller than the GR flux at some frequency.

In Fig. 2.7, we plot the energy flux for several charge-to-mass ratios. In that figure, we do not plot the flux in EM theory, because it is almost the same as the EMd flux for charges $q_i/m_i \lesssim 0.5$ since $\mathcal{F}_S \propto \alpha_i^2 \propto q_i^4/m_i^4$, which is much smaller than $\mathcal{F}_V \propto q_i^2/m_i^2$ for small charges. The plot shows the flux for same-sign charges in a log plot; for small charges $\lesssim 0.01$, the EMd flux decreases significantly and becomes very close to the GR flux.

The most salient feature that differentiates EMd theory from GR from the

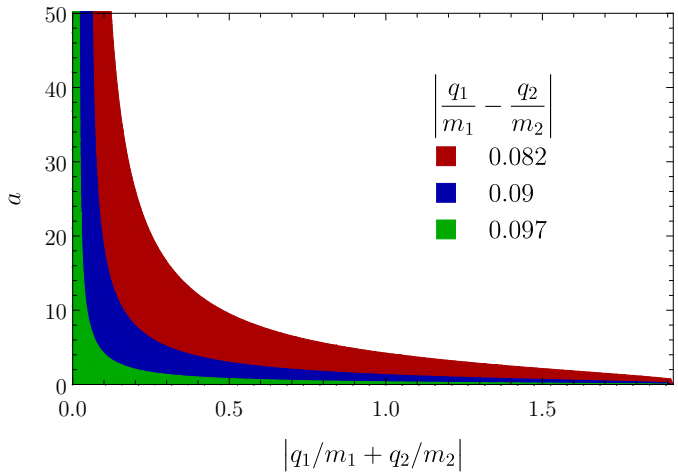

Figure 2.8: Allowed values of EMd coupling a consistent with a dipole flux constraint of $|B| \leq 10^{-3}$ as a function of mass-weighted total electric charge. Colors indicate various possible electric dipoles consistent with the bound on B.

perspective of GW observations is the presence of dipole radiation. At leading order, the energy flux can be written as

$$\mathcal{F} = \mathcal{F}_{\rm GR}\left(1 + Bx^{-1}\right), \tag{2.45}$$

where $\mathcal{F}_{\rm GR}$ is the GR quadrupole flux, and B parameterizes the strength of dipolar emission, which is given by

$$B = \frac{5}{96}\left[(\alpha_1 - \alpha_2)^2 + 2\left(\frac{q_1}{m_1} - \frac{q_2}{m_2}\right)^2\right]. \tag{2.46}$$

The presence of dipole flux has been constrained in several types of binary systems. The best constraints on the B come from radio observations of pulsar–white-dwarf binaries, which lead to the bound $|B| \lesssim 10^{-9}$ [212]. For binaries containing a single BH, the strongest bound comes from low-mass X-ray binaries, in which the companion is a main-sequence star: $|B| \lesssim 2 \times 10^{-3}$ [145]. To date, no

bound has been set from GW observations of binary BHs, but at design sensitivity, LIGO could set a bound of $|B| \lesssim 8 \times 10^{-4}$ for a GW150914-like event, and LISA could lower that bound to 10^{-8} [145].

We wish to understand how well such a bound on dipole radiation in binary BHs can constrain EMd theory. Given the discussion above, we consider a hypothetical binary BH observation that constrains the dipole flux to $|B| \lesssim 10^{-3}$. The coupling a that characterizes EMd theory enters the prediction of B through the dimensionless scalar charges of the two bodies. Equation (2.46) demonstrates that for a given value of B, the scalar and electric dipoles are degenerate, and thus no constraint can be set on a directly with only a bound on the dipole flux. However, if an independent measurement of the total charges could be made — e.g., through measurements of the ringdown spectrum of the final remnant—one can potentially break this degeneracy and constrain EMd theory.

In Fig. 2.8, we show the values of a consistent with $|B| \leq 10^{-3}$ as a function of mass-weighted total charge $|q_1/m_1 + q_2/m_2|$ for various possible values of the electric dipole $|q_1/m_1 - q_2/m_2|$. The maximum allowed electric dipole is achieved in the limit that $a = 0$, wherein the scalar charges of the BHs vanish and our bound on the dipole flux translates directly to the bound on the electric dipole $|q_1/m_1 - q_2/m_2| \lesssim 0.098$. Unsurprisingly, we find that the constraint that can be set on a depends primarily on the magnitude of the electric charges in the binary: for equal-mass systems, the strongest constraints can be set when the BHs have large, nearly-equal charges, and the weakest constraints when the BHs have small, opposite charges. We see that for any realistic constraint on dipole flux, the parameter a is completely unbounded

without an independent measurement of the electric charges.

2.3.3 Gravitational-wave phase in the stationary-phase approximation

Equipped with PN descriptions of the conservative and dissipative sectors of binary dynamics in EMd theory, we compute a key observable for GW detections: the Fourier-domain gravitational waveform. We utilize the stationary-phase approximation to perform this calculation, relying on the fact the GW phase evolves much more rapidly than its amplitude during the adiabatic inspiral along quasi-circular orbits.

We consider a GW detector a distance $R \gg \lambda_{\rm GR} \sim r/v$ from a binary BH. In the vicinity of the detector, the metric takes the form

$$g_{\mu\nu} = \eta_{\mu\nu} + h_{\mu\nu}, \tag{2.47}$$

where $\eta_{\mu\nu}$ is the Minkowski metric and $h_{\mu\nu}$ contains two propagating, transverse-traceless polarizations h_+ and $h_\times$, which comprise the GW produced by the binary.[6] At the fixed distance R, the GW can be decomposed into spin-weighted spherical

[6] A GW detector also responds to the scalar field through the coupling given in Eq. (2.2). These scalar waves represent a transverse breathing polarization of perturbations to the Jordan-Fierz metric. Because standard search techniques are targeted at the transverse-traceless polarizations, we consider only those gravitational modes in this work. Differentiating between the various polarizations of GWs requires a network of detectors; our ability to identify additional GW polarizations will improve as more ground-based detectors come online.

harmonics

$$h_+ - ih_\times = \sum_{\ell \geq 2} \sum_{m=-\ell}^{\ell} {}_{-2}Y_{\ell m}(\Theta, \Phi) h_{\ell m}(t), \tag{2.48}$$

where Φ, Θ are angular coordinates that define the propagation direction from the source to the detector [30]. We further decompose each mode into an amplitude and complex phase

$$h_{\ell m}(t) = A_{\ell m}(t) e^{im\phi(t)}, \tag{2.49}$$

where $\phi(t)$ is the orbital phase of the binary.

We compute the Fourier-transform of the GW using

$$\tilde{h}_{\ell m}(f) = \int_{-\infty}^{\infty} dt\, h_{\ell m}(t) e^{-2i\pi f t}. \tag{2.50}$$

During the adiabatic inspiral, the amplitude and orbital frequency evolve much more slowly than the orbital phase, i.e., $|\dot{A}_{\ell m}/A_{\ell m}| \ll \Omega$ and $|\dot{\Omega}| \ll \Omega^2$ for $m \neq 0$ modes. Thus, the integral in Eq. (2.50) is highly oscillatory and can be approximated by expanding the integrand about the time at which the complex phase is stationary. Using the stationary-phase approximation, the Fourier-domain waveform is then given by

$$\tilde{h}^{\rm SPA}_{\ell m}(f) = \mathcal{A}_{\ell m}(f) e^{-i\psi_{\ell m}(f) - i\pi/4}, \tag{2.51}$$

$$\psi_{\ell m}(f) = 2\pi f t_f^{(m)} - m\phi(t_f^{(m)}), \tag{2.52}$$

$$\mathcal{A}_{\ell m}(f) = A_{\ell m}(t_f^{(m)}) \sqrt{\frac{2\pi}{m\dot{\Omega}(t_f^{(m)})}}, \tag{2.53}$$

where t_f^m is defined implicitly as the time at which $m\Omega(t_f^{(m)}) = 2\pi f$. Following the notation common in the literature, we employ the binary's gauge-invariant velocity

for circular orbits $v \equiv x^{1/2} = (G_{12}M\Omega)^{1/3}$ and introduce a similar notation for the GW frequency f as $v_f \equiv (\pi G_{12} M f)^{1/3}$. Then, by construction, one finds $v(t_f^{(m)}) = (2/m)^{1/3} v_f$ and can rewrite Eq. (2.52) as

$$\psi_{\ell m}(f) = m \left(\frac{1}{G_{12}M} v^3 t(v) - \phi(v) \right) \Big|_{v=(2/m)^{1/3} v_f} . \tag{2.54}$$

From here onwards, we focus only on the dominant $\ell = |m| = 2$ modes and drop the explicit mode numbers for notational simplicity; because we restrict our attention to non-spinning systems, the modes obey the symmetry relation

$$h_{\ell m} = (-1)^{\ell} h^*_{\ell,-m}, \tag{2.55}$$

and thus we can consider only the $m = 2$ mode without loss of generality.

The orbital phase and frequency are computed using the balance equation

$$\frac{dE}{dt} = -\mathcal{F}. \tag{2.56}$$

From this equation, we deduce

$$\phi(v) = \phi_{\rm ref} - \frac{1}{G_{12}M} \int_{v_{\rm ref}}^{v} d\hat{v} \hat{v}^3 \frac{E'(\hat{v})}{\mathcal{F}(\hat{v})}, \tag{2.57}$$

$$t(v) = t_{\rm ref} - \int_{v_{\rm ref}}^{v} d\hat{v} \frac{dE/d\hat{v}}{\mathcal{F}(\hat{v})}, \tag{2.58}$$

where $\phi_{\rm ref}$ and $t_{\rm ref}$ refer to an arbitrary reference point in the evolution of the binary. Inserting these results into Eq. (2.54), the Fourier-domain phase is given by

$$\psi(f) = 2\pi f t_{\rm ref} - \phi_{\rm ref} + \frac{2}{G_{12}M} \int_{v_f}^{v_{\rm ref}} \left(v_f^3 - v^3 \right) \frac{E'(v)}{\mathcal{F}(v)} dv. \tag{2.59}$$

The energy flux in terms of x is given by Eq. (2.43a). The energy E is given by Eq. (2.34), and it can be expressed in terms of x using Eqs. (B.82) and (B.85),

which leads to

$$E = -\frac{\mu}{2} x \left[1 + f_E x + \mathcal{O}\left(1/c^4\right)\right], \tag{2.60}$$

where the coefficient f_E is given by

$$f_E = \frac{-1}{3G_{12}^2}\left[G_{12}^2\left(\frac{1+\nu}{4} + \frac{3-\alpha_1\alpha_2}{1+\alpha_1\alpha_2-\frac{q_1q_2}{M\mu}}\right) - (1+\alpha_1\alpha_2)^2 - X_2\alpha_2^2\beta_1 - X_1\alpha_1^2\beta_2 \right.$$
$$\left. - X_1\frac{q_2^2}{M\mu}(1+a\alpha_1) - X_2\frac{q_1^2}{M\mu}(1+a\alpha_2) + 2\frac{q_1q_2}{M\mu}\left(1 + aX_1\alpha_1 + aX_2\alpha_2\right)\right]. \tag{2.61}$$

To evaluate the integral in Eq. (2.59), we need to distinguish between two regimes, similarly to what was done in Ref. [2]. In one regime, the electric charges are small and the inspiral is driven by the tensor quadrupole flux. In the other regime, the electric charges are large and the inspiral is driven by the dipole flux.

For the quadrupole-driven (QD) case, we approximate the integrand in Eq. (2.59) by

$$\frac{E'(v)}{\mathcal{F}(v)} \simeq \frac{E'(v)}{\mathcal{F}_T(v)}\left[1 - \frac{\mathcal{F}_S(v) + \mathcal{F}_V(v)}{\mathcal{F}_T(v)}\right]. \tag{2.62}$$

Then, we expand the integrand using the next-to-leading order fluxes. Evaluating the integral leads to the phase

$$\psi^{\rm QD}(f) = 2\pi f t_{\rm ref} - \phi_{\rm ref} + \frac{1}{v^5}\left[\rho_0^{\rm QD} + \frac{\rho_{-2}^{\rm QD}}{v^2} + \rho_2^{QD}v^2 + \mathcal{O}\left(v^4\right)\right], \tag{2.63}$$

with the coefficients

$$\rho_0^{\rm QD} = -\frac{G_{12}}{4096\nu}\Bigg\{ -96 + 5\left(f^S_{1/r} + f^S_{v^2}\right) + 10\left(f^V_{1/r} + f^V_{v^2}\right) + 40 f_\gamma \left(\frac{q_1}{m_1} - \frac{q_2}{m_2}\right)^2 + \frac{5}{168}\left(336 f_E - 672 f_\gamma - f^T_{1/r^2} - f^T_{v^2/r} - f^T_{v^4}\right)\left[2\left(\frac{q_1}{m_1} - \frac{q_2}{m_2}\right)^2 + (\alpha_1 - \alpha_2)^2\right] + 16\left(X_2\frac{q_1}{m_1} + X_1\frac{q_2}{m_2}\right)^2 + 20 f_\gamma(\alpha_1 - \alpha_2)^2 + 16\left(X_2\alpha_1 + X_1\alpha_2\right)^2\Bigg\}, \quad (2.64a)$$

$$\rho_{-2}^{\rm QD} = -\frac{5G_{12}}{7168\nu}\left[2\left(\frac{q_1}{m_1} - \frac{q_2}{m_2}\right)^2 + (\alpha_1 - \alpha_2)^2\right], \quad (2.64b)$$

$$\rho_2^{\rm QD} = -\frac{5G_{12}}{1548288\nu}\Bigg\{ -32256 f_E + \left[48 - 20 f_E\left(\frac{q_1}{m_1} - \frac{q_2}{m_2}\right)^2 - 10 f_E\left(\alpha_1 - \alpha_2\right)^2\right] \times \left(672 f_\gamma + f^T_{1/r^2} + f^T_{v^2/r} + f^T_{v^4}\right) - \left(672 f_\gamma + f^T_{1/r^2} + f^T_{v^2/r} + f^T_{v^4} - 336 f_E\right) \times \Bigg[5\left(f^S_{1/r} + f^S_{v^2}\right) + 10\left(f^V_{1/r} + f^V_{v^2}\right) + 20 f_\gamma(\alpha_1 - \alpha_2)^2 + 40 f_\gamma\left(\frac{q_1}{m_1} - \frac{q_2}{m_2}\right)^2 + 16\left(X_2\frac{q_1}{m_1} + X_1\frac{q_2}{m_2}\right)^2 + 16\left(X_2\alpha_1 + X_1\alpha_2\right)^2\Bigg] + \frac{5}{224}\left[2\left(\frac{q_1}{m_1} - \frac{q_2}{m_2}\right)^2 + (\alpha_1 - \alpha_2)^2\right]\left(672 f_\gamma + f^T_{1/r^2} + f^T_{v^2/r} + f^T_{v^4}\right)^2\Bigg\}, \quad (2.64c)$$

where the coefficients f are given by Eqs. (B.36), (B.56), (B.79), and (B.85). When the charges are zero, this phase reduces to the next-to-leading order GR result, i.e., $\rho_0^{\rm QD} \to 3/128\nu$, $\rho_2^{\rm QD} \to 5(743 + 924\nu)/32256\nu$, and $\rho_{-2}^{\rm QD} \to 0$.

For the dipole-driven (DD) case, we take the tensor flux at the same order as the scalar and vector fluxes, i.e., to $\mathcal{O}(x^5)$. Evaluating the integral in (2.59) leads to

$$\psi^{\rm DD}(f) = 2\pi f t_{\rm ref} - \phi_{\rm ref} + \frac{\rho_0^{\rm DD}}{v^3}\left[1 + \rho_2^{\rm DD} v^2 + \mathcal{O}(v^4)\right], \quad (2.65)$$

where the coefficients are given by

$$\rho_0^{\rm DD} = \frac{G_{12}}{\nu}\left[2\left(\frac{q_1}{m_1}-\frac{q_2}{m_2}\right)^2+(\alpha_1-\alpha_2)^2\right]^{-1}, \tag{2.66a}$$

$$\begin{aligned}\rho_2^{\rm DD} = \frac{-9}{10}&\left[2\left(\frac{q_1}{m_1}-\frac{q_2}{m_2}\right)^2+(\alpha_1-\alpha_2)^2\right]^{-1}\left[96+10\left(f^V_{1/r}+f^V_{v^2}\right)+5\left(f^S_{1/r}+f^S_{v^2}\right)\right.\\ &-10(f_E-2f_\gamma)(\alpha_1-\alpha_2)^2+16\left(X_2\alpha_1+X_1\alpha_2\right)^2-20(f_E-2f_\gamma)\left(\frac{q_1}{m_1}+\frac{q_2}{m_2}\right)^2\\ &\left.+80(f_E-2f_\gamma)\frac{q_1q_1}{m_1m_2}+16\left(X_2\frac{q_1}{m_1}+X_1\frac{q_2}{m_2}\right)^2\right].\end{aligned} \tag{2.66b}$$

When we set the electric charges to zero, but keep the scalar charges nonzero, this result agrees with the (ST) result derived in Ref. [2].

We wish to understand how well a GW signal produced in EMd theory [e.g. Eq. (2.63)] can be distinguished observationally from a signal in GR. Answering this question definitively falls beyond the scope of this work. To perform such a study, one would need to perform a Bayesian hypothesis test on injections of EMd signals into detectors with realistic noise, comparing the relative evidence that the signal matches template waveforms in either EMd theory or GR; for examples of such analyses for other modifications to GR, see Refs. [120, 175, 213–215]. Instead of this detailed study, we compute two comparatively simple measures of distinguishability: the difference in total phase, and, in Sec. 2.3.4, the number of "useful" GW cycles.

To compare the phase calculated in EMd theory with that in GR, we need to align the waveforms and then compute dephasing from this alignment point. We choose to do the alignment around the "merger frequency," which for simplicity we choose to be the innermost-stable circular orbit (ISCO) frequency $f_{\rm ISCO} = 6^{-3/2}/\pi M$ for a Schwarzschild BH. Next, we determine $t_{\rm ref}$ and $\phi_{\rm ref}$ such that the waveform

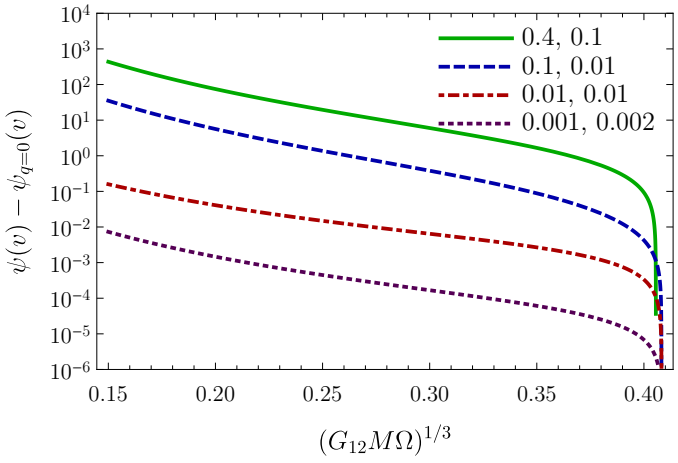

Figure 2.9: Phase difference in radians between EMd theory and GR as a function of v, computed in the quadrupole-driven regime, for various charge-to-mass ratios, and for equal masses ($\nu = 1/4$).

reaches a local maximum at this point and the phase reaches some fixed value, e.g., zero. To satisfy these two conditions, one can choose $t_{\rm ref}$ and $\phi_{\rm ref}$ such that at $f_{\rm ISCO}$, $d\psi(f)/df = 0$ and $\psi(f) = 0$. For the QD case, this leads to

$$\begin{aligned} t_{\rm ref}^{\rm QD} &= 108MG_{12}^{-10/3}\left(10G_{12}^{2/3}\rho_0^{\rm QD} + G_{12}^{4/3}\rho_2^{\rm QD} + 84\rho_{-2}^{\rm QD}\right), \\ \phi_{\rm ref}^{\rm QD} &= 12\sqrt{6}G_{12}^{-7/3}\left(8G_{12}^{2/3}\rho_0^{\rm QD} + G_{12}^{4/3}\rho_2^{\rm QD} + 60\rho_{-2}^{\rm QD}\right). \end{aligned} \tag{2.67}$$

Similarly, for the DD case, we get

$$\begin{aligned} t_{\rm ref}^{\rm DD} &= 6MG_{12}^{-2}\rho_0^{\rm DD}\left(18 + G_{12}^{2/3}\rho_2^{\rm DD}\right), \\ \phi_{\rm ref}^{\rm DD} &= 4\sqrt{\frac{2}{3}}G_{12}^{-1}\rho_0^{\rm DD}\left(9 + G_{12}^{2/3}\rho_2^{\rm DD}\right). \end{aligned} \tag{2.68}$$

In Fig. 2.9, we plot the difference between the phase calculated in EMd theory with $a = 1$ and the phase when all charges are zero, which is the phase in GR up to 1PN order. For the configurations considered here, $v = 0.15$ corresponds to approximately 10 Hz for a $20M_\odot$ system. Because the charges are relatively small,

we compute the phase using Eq. (2.63). For systems whose components' charge-to-mass ratio $q_i/m_i \lesssim 0.01$, the two waveforms differ by less than one radian over the frequency range of a ground-based GW detector. The phase difference does not depend strongly on the value of a; for values of $a \sim 1000$ and charge-to-mass ratios $q_i/m_i \lesssim 10^{-3}$ analogous to those considered in Ref. [199], the phase difference agrees with that shown in Fig. 2.9 within 10%.

2.3.4 Number of useful gravitational-wave cycles

The total number of GW cycles between frequencies $f_{\rm min}$ and $f_{\rm max}$ is given by

$$N_{\rm tot} = \int_{f_{\rm min}}^{f_{\rm max}} \frac{df}{2\pi} \frac{d\phi}{df}, \tag{2.69}$$

where ϕ is the gravitational wave phase. The instantaneous number of cycles spent near some frequency f is defined by multiplying the above integrand by f

$$N(f) \equiv \frac{f}{2\pi} \frac{d\phi}{df}. \tag{2.70}$$

However, GW detectors are not equally sensitive to all parts of the waveform because the noise spectral density of the detector is frequency dependent. A better proxy for how observationally different two waveforms are is to compare the number of "useful" cycles in each. This measure was originally introduced in Ref. [216]. One computes the total phase accumulated in each frequency bin and then weights this estimate by the sensitivity of a detector at that frequency. Because the strain sensitivity of the detector is concentrated in just a window of frequency space, the result would also depend on the mass of the system. The number of useful cycles is

defined by [216]

$$N_{\rm useful}(f) \equiv \left[\int_{f_{\rm min}}^{f_{\rm max}} \frac{df}{f} w(f) N(f)\right] \left[\int_{f_{\rm min}}^{f_{\rm max}} \frac{df}{f} w(f)\right]^{-1}, \tag{2.71}$$

where the weight $w(f) \equiv A^2(f)/fS_n(f)$, while $A(f)$ is the GW amplitude, and $S_n(f)$ is the noise spectral density of the detector. We use the zero-detuned high-power noise spectral density of Advanced LIGO at design sensitivity [217].

Using the balance equation $dE/dt = -\mathcal{F}$, and the relation between the GW phase and orbital frequency $\dot{\phi} = \Omega$, the instantaneous number of cycles in Eq. (2.70) can be reformulated as

$$N(f) = -\frac{v^4}{3\pi M G_{12}} \frac{E'(v)}{\mathcal{F}(v)}, \tag{2.72}$$

which can be computed in the quadrupole-driven regime using Eq. (2.62). For the GW amplitude, we used the Newtonian order approximation for the transverse-traceless polarizations $A(f) \propto v^2$, since the effect from the amplitude on the number of cycles is small compared to the phase. We can then calculate numerically the number of useful cycles using Eq. (2.71).

In Fig. 2.10, we show the relative difference between $N_{\rm useful}$ in EMd theory with $a = 1$ and the same quantity when all charges are zero (GR to 1PN order). The number of cycles in EMd theory is less than in GR except for equal charges, because the leading dipole radiation dominates the Newtonian order corrections to the binding energy. We find that for systems with $q_i/m_i \sim 0.1$, the number of useful cycles in GR and EMd differs by $\mathcal{O}(1)$.

The quantity plotted in Fig. 2.10 provides a rough estimate of the observable size of deviations from GR relative to the overall GW signal strength. We recast

this quantity in terms of the optimal signal-to-noise ratio (SNR) of the waveforms, defined by

$$\mathrm{SNR}^2 = 4\int_{f_{\rm min}}^{f_{\rm max}} df \frac{|\mathcal{A}(f)|^2}{S_n(f)}. \tag{2.73}$$

Using Eq. (2.53), this relation can be rewritten as

$$\mathrm{SNR}^2 = 4\int_{f_{\rm min}}^{f_{\rm max}} \frac{df}{f} w(f) N(f), \tag{2.74}$$

and thus

$$\frac{|N^{q=0}_{\rm useful} - N_{\rm useful}|}{N^{q=0}_{\rm useful}} = \frac{|\left(\mathrm{SNR}^2\right)^{q=0} - \left(\mathrm{SNR}^2\right)|}{\left(\mathrm{SNR}^2\right)^{q=0}} = \frac{2|\Delta\mathrm{SNR}|}{\mathrm{SNR}} + \mathcal{O}\left(\left(\frac{\Delta\mathrm{SNR}}{\mathrm{SNR}}\right)^2\right), \tag{2.75}$$

where, $\Delta\mathrm{SNR} = \left(\mathrm{SNR}^{q=0} - \mathrm{SNR}\right)$ is the difference in SNR between signals in GR and EMd theory. Thus, Fig. 2.10 indicates that corrections arising from the presence of electric and scalar charges in EMd theory can account for only a few percent of the total SNR for systems with electric dipole ~ 0.1.

2.4 Effective-one-body framework

In this section, we construct two EOB Hamiltonians: one based on the GHS metric Eq. (2.8), in which the potential $C(r) \neq 1$, which we call the GHS gauge; the other is based on an approximation to this metric by making a transformation to a gauge were the potential $C(r) = 1$, which we call the Schwarzschild gauge.

The EOB Hamiltonian in the GHS gauge is more physical in the strong-gravity regime since it exactly reproduces the test-body limit of the two-body dynamics.

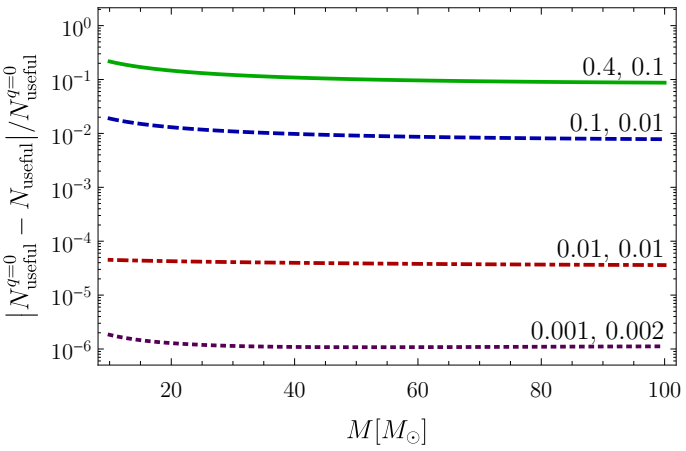

Figure 2.10: Number of useful cycles versus the total mass for various charge-to-mass ratios, and for equal masses ($\nu = 1/4$). The number of cycles in EMd theory is less than in GR except for equal charges.

That is, it belongs to a class of Hamiltonians implementing exact solutions to the field equations for isolated objects/BHs. However, this class of Hamiltonians is very theory specific — for example the analytic ST vacuum metric in Refs. [218, 219] is distinct from the analytic EMd metric when we set the electromagnetic fields to zero. In addition, many BH solutions in alternative theories do not even have an analytic solution that can be used. The advantage of using a Hamiltonian based on the approximate metric in the Schwarzschild gauge, is that it is easier to implement in data-analysis studies of GWs observed by LIGO and Virgo. One would take the existing EOB Hamiltonians in GR as a starting point and add EMd corrections in the same way as, e.g., tidal corrections are added [220]. Within the regime of small deviations from GR, the two EOB Hamiltonians in EMd theory are expected to closely agree.

In Refs. [219, 221], the EOB framework was extended to ST theories. In

Ref. [219], the motion of a binary BH was mapped to the motion of a test body, such that the effective metric is a ν-deformation of the ST metric. This approach is similar to our EOB Hamiltonian in the GHS gauge, but we find a different mapping for the scalar charge. In Ref. [221], the motion of the binary in ST theory was mapped to the motion of a test body around an effective BH in GR, but the effective metric does not reproduce exactly the test-body limit of ST theory. In contrast, whereas our EOB Hamiltonian in the Schwarzschild gauge is also not exact in the test-body limit, it still maps the real problem to an effective one in EMd theory (not in GR).

2.4.1 Effective-one-body Hamiltonian in Garfinkle-Horowitz-Strominger gauge

In the EOB framework, the motion of a binary is mapped to the motion of a test body in the background of an effective metric. In the effective problem in EMd theory, we assume that a test body, with mass μ and electric charge q, is moving in the background of a charged BH with mass M and electric charge Q. To relate the real two-body problem to the effective one, we impose the following conditions: (a) M and μ are the total mass and reduced mass of the real description, i.e., $M = m_1 + m_2$ and $\mu = m_1 m_2/M$; (b) the effective charges Q and q are related to the real charges by $Qq = q_1 q_2$, but we do not assume that Q is the total charge; and (c) the mapping between the real and effective Hamiltonians takes the form

$$\frac{H^{\rm NR}_{\rm eff}(\boldsymbol{R},\boldsymbol{P})}{\mu} = \frac{H^{\rm NR}(\boldsymbol{r},\boldsymbol{p})}{\mu}\left[1+\frac{\nu}{2}\frac{H^{\rm NR}(\boldsymbol{r},\boldsymbol{p})}{\mu}\right], \tag{2.76}$$

where the superscript NR means non-relativistic, i.e., $H^{\rm NR} = H - M$, and the real Hamiltonian H is given by Eq. (2.37). The form (2.76) for the "EOB energy map" [38] has proven useful in GR up to 4PN order [222], in classical electrodynamics to 2PN order [223], and in ST gravity to 2PN order [221, 224]. In the first post-Minkowskian approximation, i.e., to all orders in v/c at linear order in G, it can be shown to exactly resum the dynamics, producing the arbitrary-mass-ratio two-body Hamiltonian from the test-body Hamiltonian [224, 225]. For the coordinates in the effective problem, we use uppercase letters, such as R and P, while for the real problem, we keep using lowercase letters, such as r and p.

The effective action for the test body is given by

$$S_{\rm eff} = \int \left[-\mathfrak{m}(\varphi)\, d\tau_{\rm eff} + qA_\mu dX^\mu\right], \tag{2.77}$$

where $\tau_{\rm eff}$ is the proper time of the BH and the effective test-mass $\mathfrak{m}(\varphi)$ depends on the scalar field φ generated by the BH, and has the expansion in terms of the parameters α and β as

$$\mathfrak{m}(\varphi) = \mu\left[1 + \alpha\varphi + \frac{1}{2}(\alpha^2+\beta)\varphi^2 + \mathcal{O}\left(1/c^6\right)\right]. \tag{2.78}$$

Since we do not know, a priori, how the parameters α and β of the effective test body are related to the real problem, we expand the mass in a $1/R$ expansion

$$\mathfrak{m}(R) = \mu\left[1 + \frac{f_1}{R} + \frac{f_2}{R^2} + \mathcal{O}\left(1/c^6\right)\right] \tag{2.79}$$

and solve for the unknown coefficients f_1 and f_2.

We take the effective metric of the background to be a deformation of the EMd

metric in the GHS gauge

$$ds^2_{\rm eff} = -d\tau^2_{\rm eff} = -A(R)dT^2 + B(R)dR^2 + R^2C(R)d\Omega^2\,, \tag{2.80}$$

with

$$A(R) = \left(1 - \frac{R_+}{R}\right)\left(1 - \frac{R_-}{R}\right)^{\frac{1-a^2}{1+a^2}}\,, \tag{2.81a}$$

$$B(R) = \frac{1}{A(R)}\left(1 + \frac{b_1}{R}\right), \tag{2.81b}$$

$$C(R) = \left(1 - \frac{R_-}{R}\right)^{\frac{2a^2}{1+a^2}}\,, \tag{2.81c}$$

where R_- and R_+ are the radii of the inner and outer horizons of the effective BH, which are given by Eqs. (2.16a) and (2.16b), i.e.,

$$R_- = \frac{1+a^2}{a}D\,, \qquad R_+ = 2M - \frac{1-a^2}{a}D\,. \tag{2.82}$$

We choose to define R_- and R_+ by these relations in terms of D, but not in terms of Q, because the relation between Q and D is deformed by the mapping. We note that in the above metric's ansatz, we have added a deformation to $B(R)$ only because, in EMd theory at 1PN order, the mapping leads to three equations in f_1, f_2, and any deformation to the metric. Thus, we can only determine uniquely one unknown coefficient in the effective metric. So we choose to take that coefficient to be b_1, and assume the possible deformations to $A(R)$ or $C(R)$ to be zero at 1PN order.

The scalar field for a single BH is given by Eq. (2.13); we add a PN deformation g_2/R^2 such that the effective scalar field is given by

$$\varphi(R) = \frac{a}{1+a^2}\ln\left(1 - \frac{R_-}{R} + \frac{1+a^2}{a}\frac{g_2}{R^2}\right). \tag{2.83}$$

The electric potential is given by

$$A_0(R) = -\frac{Q}{R}\,. \tag{2.84}$$

We do not add PN corrections to A_0 because those corrections can be absorbed in the PN corrections to the scalar field or to the relation between D and Q. The coefficient g_2 is not independent of f_1 and f_2, because the mass expansion can also be expanded directly in φ [see Eq. (2.7)]

$$\mathfrak{m}(R) = \mu\left[1 - \frac{D\alpha}{R} + \frac{1}{R^2}\left(g_2\alpha - \frac{D^2\alpha}{2a} - \frac{a}{2}D^2\alpha + \frac{1}{2}D^2\alpha^2 + \frac{1}{2}D^2\beta\right) + \mathcal{O}\left(1/c^6\right)\right]. \tag{2.85}$$

In what follows, we uniquely solve for the coefficients b_1, f_1, and f_2 by matching the real Hamiltonian to the effective one by a canonical transformation. Matching the two mass expansions in Eqs. (2.79) and (2.85) allows us to determine the mapping for the parameters α and β, and for the coefficient g_2. The mapping for α is unique, but the mapping for β and g_2 is not unique at 1PN order.

To find the effective Hamiltonian, we first find the effective Lagrangian, in the equatorial plane $\Theta = \pi/2$,

$$\begin{aligned} L_{\text{eff}} &= qA_0 - \mathfrak{m}(\varphi)\sqrt{-g_{\mu\nu}\frac{dX^\mu}{dT}\frac{dX^\nu}{dT}}, \\ &= qA_0 - \mathfrak{m}(\varphi)\sqrt{A(R) - B(R)\dot{R}^2 - C(R)R^2\dot{\Phi}^2}. \end{aligned} \tag{2.86}$$

Then, applying the Legendre transformation $H_{\text{eff}} = P_R\dot{R} + P_\Phi\dot{\Phi} - L_{\text{eff}}$ yields the effective Hamiltonian

$$H_{\text{eff}} = -qA_0 + \sqrt{A(R)\left[\mathfrak{m}^2(\varphi) + \frac{P_\Phi^2}{C(R)R^2} + \frac{P_R^2}{B(R)}\right]}, \tag{2.87}$$

where $P_\Phi = \partial L_{\rm eff}/\partial\dot{\Phi}$ is the angular momentum, and $P_R = \partial L_{\rm eff}/\partial\dot{R}$ is the radial momentum.

Before matching the Hamiltonians, we need to apply a canonical transformation from the real variables, $\boldsymbol{r}$ and $\boldsymbol{p}$, to the effective ones, $\boldsymbol{R}$ and $\boldsymbol{P}$. At 1PN order, this transformation is given by [38]

$$R^i = r^i + \frac{\partial G_{\rm 1PN}}{\partial p_i}\,, \qquad P_i = p_i - \frac{\partial G_{\rm 1PN}}{\partial r^i}\,, \tag{2.88}$$

with the generating function

$$G_{\rm 1PN}(\boldsymbol{r},\boldsymbol{p}) = (\boldsymbol{r}\cdot\boldsymbol{p})\left(c_1\boldsymbol{p}^2 + \frac{c_2}{r}\right), \tag{2.89}$$

where the coefficients c_1 and c_2 are to be determined by the mapping.

Inserting the expansions of the real and effective Hamiltonians into Eq. (2.76), and applying the canonical transformation, we obtain the five equations:

$$2c_1\mu^2 + \nu = 0\,, \tag{2.90a}$$

$$f_1 + M\alpha_1\alpha_2 = 0\,, \tag{2.90b}$$

$$M - c_2 + \mu + \mu\alpha_1\alpha_2 - \frac{qQ}{M} + aD + c_1 M\mu^2 - \mu c_1 qQ - \mu c_1 f_1\mu = 0\,, \tag{2.90c}$$

$$b_1 + \frac{qQ}{M} + 2M + 2aD + 4c_1\mu qQ + 4c_1\mu^2 f_1 - 2c_2 - \mu - \mu\alpha_1\alpha_2 - 4c_1 M\mu^2 = 0\,, \tag{2.90d}$$

$$\begin{aligned}
&\frac{q^2Q^2}{M^2} + q_2^2 X_1\left(1+a\alpha_1\right) + q_1^2 X_2\left(1+a\alpha_2\right) - 2\mu c_2 + 4\mu f_1 + 2\nu c_2 f_1 - \nu f_1^2 \\
&\quad - 2\nu f_2 + 2M\mu - \frac{2D\mu}{a} + 2aD\mu - \nu D^2 + \nu\frac{D^2}{a^2} + 4M\mu\alpha_1\alpha_2 + 2M\mu\alpha_1^2\alpha_2^2 \\
&\quad + qQ\left(-2 + 2\frac{c_2}{M} - 2\frac{f_1}{M} - 2a\alpha_1 X_1 - 2a\alpha_2 X_2 - 2\alpha_1\alpha_2 - 2\nu - 2\nu\alpha_1\alpha_2\right) \\
&\quad + X_2\nu\beta_1\alpha_2^2 + X_1\nu\beta_2\alpha_1^2 + \mu^2 + 2\mu^2\alpha_1\alpha_2 + \mu^2\alpha_1^2\alpha_2^2 = 0\,.
\end{aligned} \tag{2.90e}$$

Solving these equations respectively for the coefficients c_1, f_1, c_2, b_1, and f_2 yields

$$c_1 = -\frac{\nu}{2\mu^2}\,, \tag{2.91a}$$

$$f_1 = -M\alpha_1\alpha_2\,, \tag{2.91b}$$

$$c_2 = M + \frac{M\nu}{2} + \frac{1}{2}M\nu\alpha_1\alpha_2 - \frac{qQ\nu}{2\mu} + aD\,, \tag{2.91c}$$

$$b_1 = 0\,, \tag{2.91d}$$

$$\begin{aligned} f_2 = {} & \frac{D^2}{2a^2} - \frac{D^2}{2} - \frac{MD}{a} - aMD\alpha_1\alpha_2 + \frac{aqQD}{\mu} + \frac{M}{2}\left[\frac{q_2^2}{m_2}(1+a\alpha_1) + \frac{q_1^2}{m_1}(1+a\alpha_2)\right] \\ & - M^2\left[\alpha_1\alpha_2 - \frac{1}{2}(\alpha_1\alpha_2)^2 - \frac{1}{2}\left(X_2\alpha_2^2\beta_1 + X_1\alpha_1^2\beta_2\right)\right] - aM\frac{q_1q_2}{\mu}\left(X_1\alpha_1 + X_2\alpha_2\right). \end{aligned} \tag{2.91e}$$

To find the mapping of the scalar charge, we identify the mass expansion in Eq. (2.79) with the expansion in Eq. (2.85) to give

$$-D\alpha = f_1\,, \tag{2.92a}$$

$$g_2\alpha - \frac{D^2\alpha}{2a} - \frac{a}{2}D^2\alpha + \frac{1}{2}D^2\alpha^2 + \frac{1}{2}D^2\beta = f_2\,. \tag{2.92b}$$

Inserting the solution for f_1 and f_2 gives a unique mapping for α

$$\alpha = \frac{M}{D}\alpha_1\alpha_2\,, \tag{2.93}$$

and suggests the following mapping for β

$$\beta = \frac{M^2}{D^2}\left(X_2\alpha_2^2\beta_1 + X_1\alpha_1^2\beta_2\right). \tag{2.94}$$

Further, we take the mapping of the dilaton charge D of the effective BH to be the sum of the asymptotic value of the scalar charges of the two bodies, i.e.,

$$D = m_1\alpha_1 + m_2\alpha_2\,. \tag{2.95}$$

The mapping for α and β agrees with what was found in Ref. [219], but the mapping for D is different. The reason we choose this mapping for D is that it leads to a simple deformation to the scalar field

$$g_2 = -\frac{1-a^2}{2a^2}\frac{(\alpha_1-\alpha_2)^2}{\alpha_1\alpha_2}DM\nu\,. \tag{2.96}$$

This deformation vanishes in the test-mass-limit $\nu \to 0$, and also when $a = 1$ or $\alpha_1 = \alpha_2$. Other choices for D lead to complicated expressions for g_2. In obtaining this result for g_2, we use the expression for the electric charge in terms of the scalar charge, which is valid for BHs only,

$$\frac{q_i^2}{m_i^2} = \frac{2}{a}\alpha_i - \frac{1-a^2}{a^2}\alpha_i^2\,. \tag{2.97}$$

This relation follows from Eq. (2.20) after solving for q_i in terms of α_i and setting the scalar field to its asymptotic value.

A convenient mapping for the electric charge is

$$Q^2 = M\left(\frac{q_1^2}{m_1} + \frac{q_2^2}{m_2}\right). \tag{2.98}$$

The reasoning behind this choice is that it is symmetric under the exchange of the two bodies; it has the correct test-body limit, $Q \to q_1$ when $m_2/m_1 \to 0$ with q_2/m_2 held constant; and it appears naturally in EM theory as we show in the next subsection. With that mapping for Q and D, the relation between them is given by

$$Q^2 = \frac{2M}{a}D - \frac{1-a^2}{a^2}D^2 - \frac{1-a^2}{a^2}(\alpha_1-\alpha_2)^2M^2\nu\,. \tag{2.99}$$

One could choose to enforce Eq. (2.17) for generic masses by making a different choice for D or Q, but this seems to lead to very complicated expressions for them.

2.4.2 Effective-one-body Hamiltonian in Schwarzschild gauge

In the EMd metric, the potential $C(r) \neq 1$, but the standard EOB gauge is the Schwarzschild gauge $C(r) = 1$. This is the gauge that was used to derive the original EOB Hamiltonian [38], which was then improved by calibrating it to numerical-relativity simulations [226]. Therefore, to profit from the best available EOB Hamiltonian in GR, we need to construct an EMd-EOB Hamiltonian that is also in the Schwarzschild gauge.

The EMd metric can be transformed to the Schwarzschild gauge by the coordinate transformation $\bar{r}^2 = r^2 C(r)$. However, for arbitrary values of the coupling constant a, the metric cannot be analytically transformed. Instead, we expand the EMd metric (2.8) and transform it to get an approximate EMd metric in the Schwarzschild gauge. We make the coordinate transformation, valid to 1PN order,

$$\begin{aligned} \bar{r}^2 &= r^2 \left[1 - \frac{2a^2 r_-}{(1+a^2)r}\right], \\ \Rightarrow \quad r &= \bar{r} + \frac{a^2}{1+a^2} r_- = \bar{r} + aD\,. \end{aligned} \tag{2.100}$$

With that transformation, and inserting the expressions for r_- and r_+ in terms of M and Q [Eqs. (2.16a) and (2.16b)], we get

$$ds^2 = -\left(1 - \frac{2M}{\bar{r}} + \frac{Q^2}{\bar{r}^2}\right) dt^2 + \left(1 + \frac{2M}{\bar{r}}\right) d\bar{r}^2 + \bar{r}^2 d\Omega^2, \tag{2.101}$$

which is the same as the Reissner–Nordström metric to 1PN order.

As an ansatz for the effective metric, we assume a metric based on the approximate metric (2.101)

$$ds^2_{\rm eff} = -A(R)dt^2 + B(R)dR^2 + R^2 d\Omega^2\,, \tag{2.102}$$

with

$$A(R) = 1 + \frac{a_1}{R} + \frac{a_2}{R^2} + \dots , \tag{2.103a}$$

$$B(R) = 1 + \frac{b_1}{R} + \dots , \tag{2.103b}$$

and we write the mass expansion as

$$\mathfrak{m}(R) = \mu \left[1 + \frac{f_1}{R} + \frac{f_2}{R^2} + \mathcal{O}\left(1/c^6\right) \right], \tag{2.104}$$

where the unknown coefficients a_1, a_2, b_1, f_1, and f_2 are to be determined by the mapping. However, the mapping leads to three equations in those five coefficients, making two of them arbitrary. We choose to take $a_1 = -2M$ and $a_2 = Q^2$ so that the effective metric would agree with the EMd metric in the Schwarzschild gauge to 1PN order. When we solve for b_1, we get $b_1 = 2M$, in agreement with the EMd approximate metric.

For the effective electric potential, we apply the coordinate transformation (2.100) with $\bar{r} = R$ to get

$$A_0(R) = -\frac{Q}{R + aD} \,. \tag{2.105}$$

Applying the same transformation to the scalar field, and adding a PN deformation g_2/R^2, we obtain

$$\varphi(R) = \frac{a}{1+a^2} \ln \left[1 - \frac{1+a^2}{a} \frac{D}{R+aD} + \frac{1+a^2}{a} \frac{g_2}{R^2} \right]. \tag{2.106}$$

The mass expansion in terms of φ, Eq. (2.78), can now be written as an expansion in $1/R$ by

$$\mathfrak{m}(R) = \mu \left[1 - \frac{D\alpha}{R} + \frac{1}{R^2} \left(g_2 \alpha - \frac{D^2 \alpha}{2a} + \frac{a}{2} D^2 \alpha + \frac{1}{2} D^2 \alpha^2 + \frac{1}{2} D^2 \beta \right) + \mathcal{O}\left(1/c^6\right) \right]. \tag{2.107}$$

Following the same method used in the previous subsection, the effective Hamiltonian is given by Eq. (2.87) with the potential $C(R) = 1$. The relation between the real and effective Hamiltonians is given by Eq. (2.76), and the canonical transformation that relates the real and effective variables is given by Eq. (2.88). Matching the real and effective Hamiltonians, we obtain the five equations:

$$2c_1\mu^2 + \nu = 0\,, \tag{2.108a}$$

$$a_1 + 2f_1 + 2M(1 + \alpha_1\alpha_2) = 0\,, \tag{2.108b}$$

$$2c_2 - a_1 - 4M + c_1a_1\mu^2 + 2f_1c_1\mu^2 + 2\frac{qQ}{M} - 2\mu(1 + \alpha_1\alpha_2 - c_1qQ) = 0\,, \tag{2.108c}$$

$$b_1 - 2c_2 + 4c_1\mu qQ + 2a_1c_1\mu^2 + 4c_1f_1\mu^2 - \mu - \mu\alpha_1\alpha_2 + \frac{qQ}{M} = 0\,, \tag{2.108d}$$

$$\begin{aligned} &M^2\alpha_1^2\alpha_2^2 + M^2X_2\alpha_2\beta_1 + M^2X_1\alpha_1^2\beta_2 - a_2 - 2M^2\alpha_1\alpha_2 + \frac{2aqQD}{\mu} \\ &\quad + \frac{m_1q_2^2}{\mu}(1 + a\alpha_1) + \frac{m_2q_1^2}{\mu}(1 + a\alpha_2) - 2a\frac{qQ}{\mu}(m_1\alpha_1 + m_2\alpha_2) - 2f_2 = 0\,. \end{aligned} \tag{2.108e}$$

Solving these equations respectively for the coefficients c_1, f_1, c_2, b_1, and f_2 yields

$$c_1 = -\frac{\nu}{2\mu^2}\,, \tag{2.109a}$$

$$f_1 = -M\alpha_1\alpha_2\,, \tag{2.109b}$$

$$c_2 = M + \frac{M\nu}{2} + \frac{1}{2}M\nu\alpha_1\alpha_2 - \frac{qQ\nu}{2\mu}\,, \tag{2.109c}$$

$$b_1 = 2M\,, \tag{2.109d}$$

$$\begin{aligned} f_2 = &-\frac{a_2}{2} + \frac{aq_1q_2D}{\mu} - a\frac{q_1q_2}{\mu}(m_1\alpha_1 + m_2\alpha_2) + \frac{M}{2}\left[\frac{q_2^2}{m_2}(1 + a\alpha_1) + \frac{q_1^2}{m_1}(1 + a\alpha_2)\right] \\ &- M^2\left[\alpha_1\alpha_2 - \frac{1}{2}(\alpha_1\alpha_2)^2 - \frac{1}{2}\left(X_2\alpha_2^2\beta_1 + X_1\alpha_1^2\beta_2\right)\right]. \end{aligned} \tag{2.109e}$$

Choosing $a_2 = Q^2$, so that the effective metric agrees with the EMd metric to

1PN order, the above solution for f_2 leads to the mapping

$$Q^2 = M\left(\frac{q_1^2}{m_1} + \frac{q_2^2}{m_2}\right). \tag{2.110}$$

This is because, for the case of EM theory, when we take the parameters α and β in the solution for f_2 to be zero, we get $f_2 = -a_2/2 + M(q_1^2/m_1 + q_2^2/m_2)/2$. Hence, requiring that $f_2 = 0$ in EM theory and that $a_2 = Q^2$, naturally leads to the charge map (2.110).

Identifying the mass expansion in Eq. (2.104) with that in Eq. (2.107), leads to the following mapping for α and β

$$\alpha = \frac{M}{D}\alpha_1\alpha_2\,, \tag{2.111}$$

$$\beta = \frac{M^2}{D^2}\left(X_2\alpha_2^2\beta_1 + X_1\alpha_1^2\beta_2\right), \tag{2.112}$$

which is the same mapping that was found in the previous subsection. Further, taking the mapping of the dilaton charge to also be given as in the previous subsection

$$D = m_1\alpha_1 + m_2\alpha_2, \tag{2.113}$$

leads to the astonishingly simple result

$$g_2 = 0. \tag{2.114}$$

With that mapping for D and Q, the relation between them is given by Eq. (2.99).

Interestingly, the above mappings also lead to a ST EOB Hamiltonian in Schwarzschild gauge at 1PN order. A 2PN EOB Hamiltonian based on an exact analytic solution for the metric and scalar field can be found in Ref. [219]. The metric in that work also includes a potential $C(R) \neq 1$, Eq. (II.3) in Ref. [219], and

that metric is unrelated to the EMd metric when the electric charges are zero. The scalar field is given by

$$\varphi_{\rm ST} = \frac{D}{a_*} \log\left[1 - \frac{a_*}{r} + \frac{a_*^2 - 2Ma_*}{2r^2}\right], \tag{2.115}$$

where $a_*^2 = 4(M^2 + D^2)$. The author of Ref. [219] found the same mapping for α and β that we got, but used a different mapping for D (at 2PN order). When we approximately transform the metric and the scalar field to the Schwarzschild gauge, in which the potential $C(R) = 1$, and repeat the same analysis in this section, we get an EOB Hamiltonian with the same mapping for the scalar charge given in Eq. (2.113), and with no deformation to the metric or the scalar field to 1PN order. The point is that the mapping of the scalar charge would be the same in EMd theory and ST theory, which is another hint that Eq. (2.113) is a good choice at 1PN order.

2.4.3 Comparison of two effective-one-body Hamiltonians in Einstein-Maxwell-dilaton theory

In this subsection, we compare the two EMd-EOB Hamiltonians with each other, and also with the EOB Hamiltonian in GR, by calculating the binding energy and the ISCO. The goal is to investigate the range of parameter space where the two EMd-EOB Hamiltonians agree.

The mappings of the electric charge, scalar charge, and the parameters α and

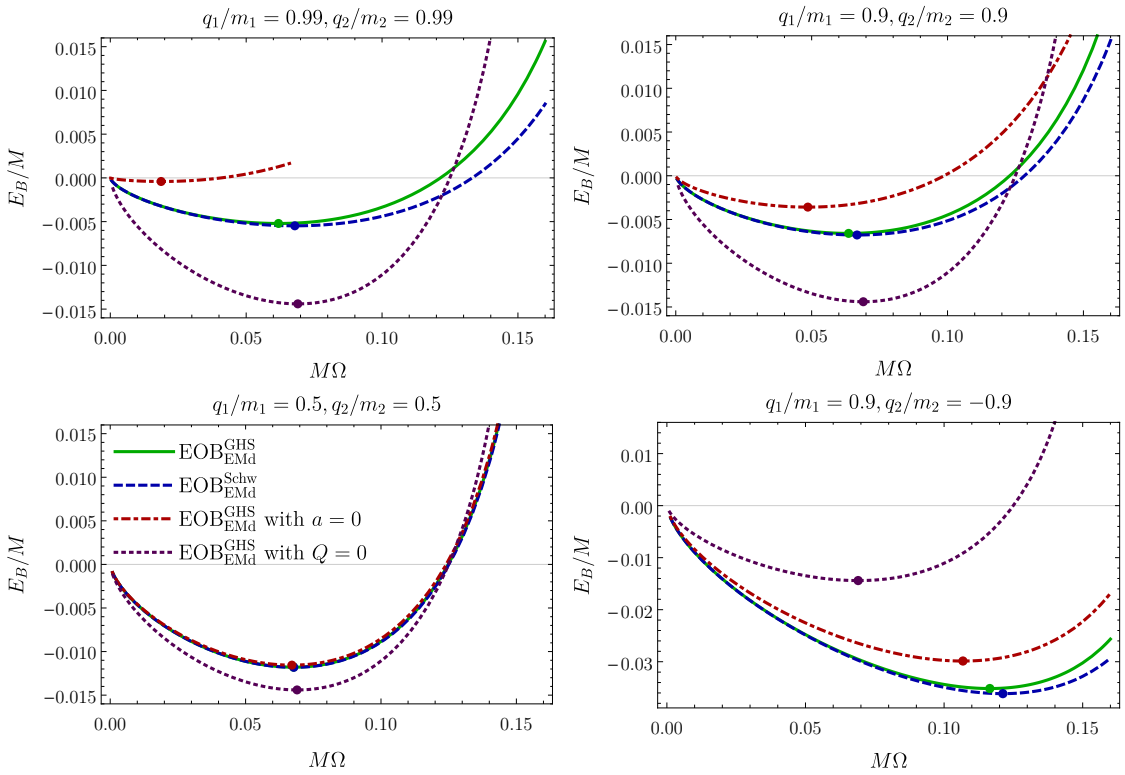

Figure 2.11: Binding energy E_B normalized by the total mass M as a function of $M\Omega$ for equal masses, $\nu = 1/4$, and for charge-to mass-ratios $q_1/m_1 = q_2/m_2 = 0.99,\ 0.9,\ 0.5$, and $q_1/m_1 = -q_2/m_2 = 0.9$. To improve readability, we show the plots only up to the frequency corresponding to $R = 1.05R_{\mathrm{LR}}$ or to energy $E_B/M = 0.015$. The point on each curve indicates the location of the ISCO.

β are the same for the two EMd-EOB Hamiltonians, i.e.,

$$Q^2 = M\left(\frac{q_1^2}{m_1} + \frac{q_2^2}{m_2}\right), \quad D = m_1\alpha_1 + m_2\alpha_2\,,$$
$$\alpha = \frac{M}{D}\alpha_1\alpha_2\,, \quad \beta = \frac{M^2}{D^2}\left(X_2\alpha_2^2\beta_1 + X_1\alpha_1^2\beta_2\right). \tag{2.116}$$

For the EOB Hamiltonian in the GHS gauge, the effective metric is the GHS metric for $\nu = 0$ [Eqs. (2.80)–(2.82) with $b_1 = 0$]. For the EOB Hamiltonian in the Schwarzschild gauge, the effective metric agrees with the Reissner-Nordström metric for $\nu = 0$ [Eq. (2.101)]. Other differences between the two Hamiltonians are in

the parameters of the mass expansion (2.79), the canonical transformation (2.89), and the correction to the scalar field [Eqs. (2.83) and (2.106)]. The parameters in those equations are shown in Table 2.1.

Table 2.1: Difference between the two EOB Hamiltonians in terms of the effective metric and the parameters of the mass expansion, the canonical transformation, and the scalar field.

	EOB in GHS gauge	EOB in Schw gauge
effective metric	Eqs. (2.80)–(2.82)	Eq. (2.101)
c_1	$c_1 = -\nu/2\mu^2$	
c_2	Eq. (2.91c)	Eq. (2.109c)
f_1	$f_1 = -M\alpha_1\alpha_2$	
f_2	Eq. (2.91e)	Eq. (2.109e)
g_2	Eq. (2.96)	$g_2 = 0$

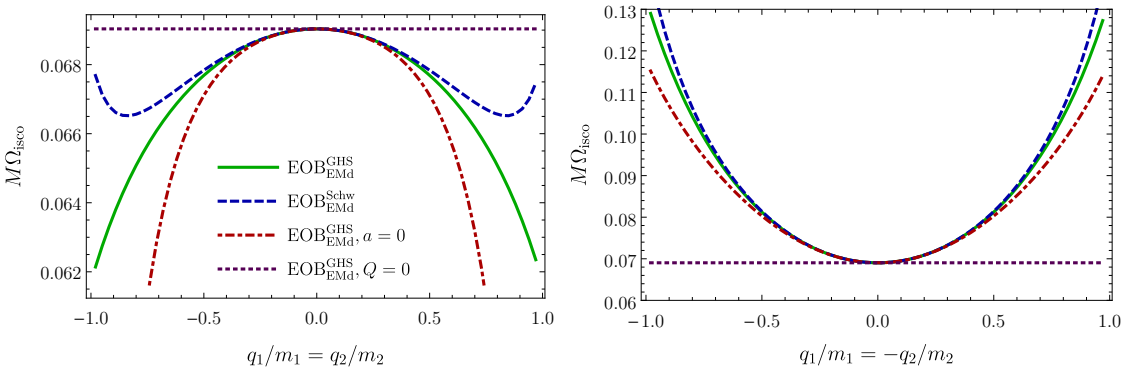

Figure 2.12: Angular frequency at ISCO as a function of the charge-to-mass ratio q_1/m_1 from -0.99 to 0.99. In the left panel, $q_2/m_2 = q_1/m_1$, while in the right, $q_2/m_2 = -q_1/m_1$. An ISCO frequency of 0.062 corresponds to an ISCO radius $\sim 6.4M$, and a frequency of 0.13 corresponds to radius $\sim 3.9M$.

To find the binding energy from the two EOB Hamiltonians, we start with the energy map in Eq. (2.76), which gives the relation between the effective Hamiltonian and the real Hamiltonian. Inverting that relation, we obtain the resummed EOB

Hamiltonian

$$H_{\rm EOB}^{\rm NR} = M\sqrt{1+2\nu\left(\frac{H_{\rm eff}}{\mu}-1\right)} - M\,. \tag{2.117}$$

To obtain the binding energy for circular orbits, we set $P_R = 0$, and solve $\dot{P}_R = -\partial H_{\rm eff}/\partial R = 0$ for the angular momentum P_Φ. However, that equation cannot be solved analytically because of the non-linearity of the Hamiltonian. Hence, we solve the equation numerically for P_Φ at specific values of R. Since we want to plot the binding energy as a function of the orbital frequency Ω, we need to calculate the orbital frequency via

$$\Omega = \frac{\partial H_{\rm EOB}}{\partial P_\Phi} = \frac{\partial H_{\rm EOB}}{\partial H_{\rm eff}}\frac{\partial H_{\rm eff}}{\partial P_\Phi}. \tag{2.118}$$

Then, we calculate the binding energy and orbital frequency as R goes from $100M$ to the radius of the light ring. The light ring (or photon orbit) of a (charged) BH metric in GR is defined as the circular-orbit solution to the geodesic equation of massless particles. This geodesic equation is actually encoded by our effective Hamiltonian if we set $q = 0$ (geodesic motion) and $\mu = 0$ (massless particle). To obtain the light-ring solution in EMd theory, we hence take the effective Hamiltonian for the case $\mu = 0 = q$, and impose the conditions for circular orbits $P_R = 0$ and $\dot{P}_R = 0$. The latter condition means that we look for an extremum of the effective Hamiltonian,

$$0 = \dot{P}_R = -\left.\frac{\partial H_{\rm eff}}{\partial R}\right|_{\mu=q=P_R=0}, \tag{2.119}$$

which is actually a maximum, $\partial^2 H_{\rm eff}/\partial R^2 < 0$, and the light-ring solution is therefore unstable. For the Schwarzschild metric in GR, solving this equation for R gives the

known value $R_{\rm LR} = 3M$. For the EMd metric in the GHS gauge

$$R_{\rm LR} = \frac{3}{2}M + \frac{aD}{2} + \frac{1}{2a}\left[9a^2M^2 - 16aMD + 6a^3MD + 8D^2 - 8a^2D^2 + a^4D^2\right]^{1/2}, \tag{2.120}$$

while for the approximate metric in the Schwarzschild gauge

$$R_{\rm LR} = \frac{1}{2}\left[3M + \sqrt{9M^2 - 8Q^2}\right], \tag{2.121}$$

which is the same as the Reissner-Nordström metric since the potential $A(R)$ is the same in both cases.

In Fig. 2.11, we plot the binding energy scaled by the total mass, E_B/M, versus the orbital frequency $M\Omega$ for equal masses, $\nu = 1/4$, and for charge-to mass-ratios $q_1/m_1 = q_2/m_2 = 0.99,\ 0.9,\ 0.5$ and $q_1/m_1 = -q_2/m_2 = 0.9$. The binding energy diverges at the light ring; to improve readability, we show the plots only up to the frequency corresponding to $R = 1.05R_{\rm LR}$ or to energy $E_B/M = 0.015$. We plot the binding energy for four cases: (a) EMd-EOB Hamiltonian in the GHS gauge; (b) EMd-EOB Hamiltonian in the Schwarzschild gauge; (c) EMd-GHS Hamiltonian with $a = 0$, which is EM theory; and (d) EMd-GHS Hamiltonian in the limit where all charges are zero $Q = 0$, which is the standard uncharged GR case. [The effective Hamiltonian for case (c) is that of a charge moving in the Reissner-Nordström spacetime, and for (d) it is that of a reduced mass in Schwarzschild spacetime.] The difference between the EM case ($a = 0$ curve) and the standard astrophysical scenario of uncharged BHs ($Q = 0$ curve) quantifies the effect of the electric charges, while the difference between the EMd Hamiltonian(s) and the EM case quantifies the effect of the scalar charges.

We see from Fig. 2.11 that the electric charges have a larger effect on the binding energy than the additional scalar charges in EMd theory (except for almost extreme charges). For small electric charges $\lesssim 0.5$ (lower left panel of Fig. 2.11), the difference in binding energy between EMd theory and EM theory at the ISCO is only 9% of the difference between EMd theory and GR with no charges, i.e., the scalar charge has a very small effect. The difference between the two EMd-EOB Hamiltonians increases with increasing electric charge and frequency, but they still agree well. The binding energy of the two Hamiltonians at the ISCO differs by $\sim 6\%$ for charge-to-mass ratio 0.99 and by $\sim 0.1\%$ for charge-to-mass ratio 0.5. For charge-to-mass ratios larger than one, a naked singularity appears in the effective metric in the Schwarzschild gauge; this is an unphysical feature arising from the choice of gauge, and thus the EOB Hamiltonian should not be used for small separations (high frequencies) approaching this singularity. Note that, if one is only interested in the inspiral, then the comparison of the Hamiltonians via the binding energy can be stopped already at the ISCO frequency instead of the LR frequency.

The ISCO marks the end of the inspiral phase of the binary coalescence and the beginning of the plunge. To find the value of the ISCO, we set both the first and second derivatives of the effective Hamiltonian to zero $\partial H_{\rm eff}/\partial R = 0 = \partial^2 H_{\rm eff}/\partial R^2$ and set $P_R = 0$. Then, we solve the two equations numerically for the ISCO radius and angular momentum. The orbital frequency at ISCO can then be calculated from Eq. (2.118).

In Fig. 2.11, the location of the ISCO is indicated by the point on each curve. In Fig. 2.12, we plot the orbital frequency at ISCO, scaled by the mass, i.e., $M\Omega_{\rm ISCO}$,

versus the charge-to-mass ratio q_1/m_1 with $q_2/m_2 = q_1/m_1$ in the left panel, and $q_2/m_2 = -q_1/m_1$ in the right. From the left panel, we see that for high charge-to-mass ratios, the two EOB Hamiltonians do not agree well at this high frequency. For same-sign charges, the ISCO orbital frequency is lower than the uncharged case, which means the ISCO radius is greater than the Schwarzschild value of $6M$. This is because the binding energy of charged BHs is higher (less bound) than the energy of uncharged BHs, as can be seen from the binding energy in Fig. 2.11. For opposite-sign charges, the ISCO orbital frequency is higher than the uncharged case because the binding energy is lower than the energy of uncharged BHs.

2.5 Conclusions

In this work, we analytically modeled the dynamics of binary BHs in EMd theory. In this theory, electrically charged BHs also carry a scalar charge, whereas in GR (and many modified theories of gravity) the scalar charge is zero. Thus, the identification of a BH with scalar charge through GW observations could point to modifications of gravity in the strong-field regime and violations of the strong equivalence principle. Observation of a large electric charge on BHs could be a trace of minicharged dark matter and/or dark photons.

We began by considering the case of a test BH in the background of a more massive companion in EMd theory, wherein the scalar charge of the test BH decreases as it moves radially inwards. Consistent with the results of Ref. [202], we found that the dimensionless charge $\alpha(\varphi)$ exhibits a sharp transition [see Figs. 2.1

and 2.2]. However, we showed that in a binary system, the scalar charge of the test BH will change dramatically only very close to the horizon of the background BH and only if both BHs are nearly-extremally charged. While BHs are not expected to be able to achieve or maintain enough electric charge within the Standard Model of particle physics for these features to be observed, but proposed alternatives like minicharged dark matter and dark photons models may allow such features to become observationally relevant. Our study also showed that binary BHs in EMd theory will not exhibit non-perturbative phenomena akin to induced or dynamical scalarization that are found in certain ST theories [see Fig. 2.3].

We then used the PN approximation in EMd theory to study the dynamics of a two-body system with an arbitrary mass ratio. We derived the two-body 1PN Lagrangian and Hamiltonian, and investigated how the bodies' scalar charges decrease with their separation at next-to-leading PN order. As in the test-BH case, we expect that dramatic changes could occur only for nearly-extremal charged BHs on very compact orbits; this is a regime most easily probed by systems with extreme mass ratios and/or rapidly spinning BHs. We derived the scalar, vector, and tensor energy fluxes at next-to-leading PN order. From the energy flux and binding energy, we calculated the Fourier-domain gravitational waveform for binaries on quasi-circular orbits using the stationary-phase approximation.

Using our PN result, we discussed the possibility of constraining EMd theory with GWs. Given current and projected constraints on dipole radiation, we examined how the degeneracies between electric and scalar charges limit the bounds that can be set on the EMd parameter a — constraining this parameter requires one

to measure the electric charges of each BH independently, and the strength of this bound improves for larger total electric charge [see Fig. 2.8]. We also estimated the observational deviations from GR predicted in EMd theory with two measures: the dephasing between PN waveforms in the stationary-phase approximation [Fig. 2.9], and the difference in the number of useful GW cycles [Fig. 2.10]. For ground-based GW detectors, we found that the presence of electric and scalar charges contributes $\lesssim 1$ radian to the phase provided the black holes have charge-to-mass ratios of $q_i/m_i \lesssim 0.01$ for coupling constant $a = 1$. We showed that the relative difference in useful cycles between EMd theory and GR provides an estimate of the fractional correction to SNR by non-GR corrections; for systems with $q_i/m_i \lesssim 0.1$, the deviations from GR affect the total SNR by a few percent.

Finally, we constructed two EOB Hamiltonians for binary BHs in EMd theory: an EOB Hamiltonian in the GHS gauge, which is based on the exact BH solution, and an EOB Hamiltonian in the Schwarzschild gauge, which is based on an approximation to that solution. The EOB Hamiltonian in the GHS gauge is more physical in the strong-gravity regime, since it exactly reproduces the dynamics of a test body, and hence will be more accurate for systems with a very asymmetric mass ratio. The EOB Hamiltonian in Schwarzschild gauge is easier to implement by taking the existing EOB Hamiltonians in GR as a starting point and adding to it corrections due to EMd theory. We compared the two Hamiltonians by calculating the binding energy and the innermost stable circular orbit, and found that they agree well, except for nearly-extremal charges at high frequencies [see Figs. 2.11 and 2.12]. The binding energy of the two Hamiltonians at the ISCO differs by $\sim 6\%$ for

charge-to-mass ratio 0.99 and by $\sim 0.1\%$ for charge-to-mass ratio 0.5.

An important goal in future continuations of our work would be the construction of a full (inspiral-merger-ringdown) EOB waveform model in EMd theory. For accurate predictions in the late inspiral, one likely needs PN results for the Hamiltonian, fluxes, and modes to the same order as they are available in GR, next to a calibration of the model to NR simulations in EMd theory. Modeling the merger and ringdown requires predictions for the parameters of the final black hole and its quasi-normal modes as a function of the EMd coupling constant a (see, e.g., Refs. [227, 228] for partial results). Since EOB waveform models in existing data-analysis infrastructure are formulated in the Schwarzschild gauge, this gauge is probably the best compromise for the purpose of GW data analysis. This gauge is also better suited for creating a single EOB waveform model covering various alternative theories; for example, we demonstrated that our EOB Hamiltonian in the Schwarzschild gauge can describe both ST and EMd theories. Ultimately, one could aim to construct a generalized EOB framework that uses a physically motivated parameterization to encode a range of possible deviations from GR.

Acknowledgments

M.K. thanks the graduate school and the physics department at the University of Maryland for the International Graduate Research Fellowship. He also thanks the Max Planck Institute for Gravitational Physics for its hospitality and for co-funding his stay during the completion of this work.

Chapter 3: Gravitational waveforms in scalar-tensor gravity at 2PN relative order

Authors: *Noah Sennett, Sylvain Marsat, and Alessandra Buonanno*[1]

Abstract: We compute the gravitational waveform from a binary system in scalar-tensor gravity at 2PN relative order. We restrict our calculation to non-spinning binary systems on quasi-circular orbits and compute the spin-weighted spherical modes of the radiation. The evolution of the phase of the waveform is computed in the time and frequency domains. The emission of dipolar radiation is the lowest-order dissipative process in scalar-tensor gravity. However, stringent constraints set by current astrophysical observations indicate that this effect is sub-dominant to quadrupolar radiation for most prospective gravitational-wave sources. We compute the waveform for systems whose inspiral is driven by: (a) dipolar radiation (e.g., binary pulsars or spontaneously scalarized systems) and (b) quadrupolar radiation (e.g., typical sources for space-based and ground-based detectors). For case (a), we provide compete results at 2PN, whereas for case (b), we must introduce unknown terms in the 2PN flux; these unknown terms are suppressed by constraints on scalar-tensor gravity.

[1]Originally published as Phys. Rev. **D94**, 084003 (2016).

3.1 Introduction

The observation of gravitational-wave (GW) events GW150914 and GW151226 by Advanced LIGO marks the dawn of GW astronomy [182, 184]. We expect to observe several such events per year [73, 213, 229, 230] with the upcoming network of ground-based detectors comprised of Advanced LIGO [231], Advanced VIRGO [232], KAGRA [233], and LIGO-India [234]. These ground-based detectors can observe binary systems containing neutron stars and/or stellar-mass black holes (with a total mass $M \sim 1 - 100 M_{\odot}$); future space-based detectors like the proposed LISA mission [235] will observe binary systems composed of intermediate-mass and/or supermassive black holes ($M \sim 100 - 10^7 M_{\odot}$). Gravitational-wave observations allow us to not only measure the astrophysical properties of these systems but can also be used to test general relativity (GR). Because the coalescence of a compact binary system produces extreme gravitational fields that vary over short time scales, observations of such events allow us to probe the highly-dynamical, strong-field regime of gravity for the first time [73, 122].

The detection and analysis of GWs with ground-based detectors require banks of very accurate template waveforms. The prospects of testing gravity with these detectors hinge on our ability to model waveforms in both GR and alternative theories of gravity. Given a GW detection, one can adopt either a *theory-independent* or *theory-dependent* approach to testing GR. A theory-independent test employs waveforms that deviate from a GR signal in some generic, parameterized manner (for examples, see Refs. [117, 118, 213]). One compares an observed GW signal against

these template waveforms to constrain the deviations from GR. A theory-dependent test instead uses waveforms predicted in a particular alternative theory of gravity, comparing them against the detected GW to estimate the underlying physical parameters of that theory. Each approach has its advantages: theory-independent tests can constrain a wide range of alternative theories while theory-dependent tests can directly constrain the fundamental physics of an alternative theory. Both types of tests were performed for GW150914 and GW151226 by the LIGO and Virgo collaborations in Refs. [73, 122]. For a comprehensive review of proposed theory-independent and theory-dependent tests, see Refs. [79, 88] and references therein.

In this work, we present waveforms in scalar-tensor theories of gravity suitable for theory-dependent tests of GR. In particular, we construct ready-to-use waveforms for the inspiral of non-spinning binary systems accurate up to second post-Newtonian (2PN) order, i.e., $\mathcal{O}\left((v/c)^4\right)$ beyond leading order.[2] We restrict our attention to systems on quasi-circular orbits, as binaries formed in the field are expected to radiate away any initial eccentricity at frequencies too low to be observable by GW detectors.

Scalar-tensor theories are amongst the most natural alternatives to GR. Specifically, we focus on theories where a single massless scalar ϕ non-minimally couples to the metric $g_{\mu\nu}$. Written in the Jordan frame, the action for such theories is given

[2]We describe post-Newtonian (PN) corrections of order $\mathcal{O}(c^{-2n})$ as "nPN," which we also abbreviate with the notation $\mathcal{O}(2n)$.

by

$$S = \int d^4x \frac{\sqrt{-g}}{2\kappa} \left[\phi R - \frac{\omega(\phi)}{\phi} g^{\mu\nu} \nabla_\mu \phi \nabla_\nu \phi \right] + S_m[g_{\mu\nu}, \Xi], \tag{3.1}$$

where $\kappa = 8\pi G_*/c^3$ depends on the bare gravitational coupling constant G_*. The action for the matter in the theory S_m is a function of only the metric and matter degrees of freedom Ξ; the scalar field does not couple to matter directly, only indirectly through its interactions with the metric.

The restricted class of scalar-tensor theories described by Eq. (3.1) has been studied extensively in the literature because it is general enough to manifest many different deviations from GR yet simple enough that its predictions can be worked out completely. At 2PN order, the Fokker Lagrangian for a system of point particles was first computed in Ref. [152] using an effective field-theory approach. The 2PN metric and equations of motion were computed for bodies composed of perfect fluids in Ref. [236]. The post-Minkowskian technique of direct integration of the relaxed Einstein equations (DIRE) was used in a recent series of papers [149–151] to compute the equations of motion for a system of compact objects at 2.5PN order, as well as the gravitational waveform and energy flux at 2PN (relative) order for binaries on generic orbits. For comparison, the entire waveform for non-spinning systems in GR is known at 3PN order [237], and its quadrupolar and octupolar parts are known at 3.5PN order [238, 239] (see Ref. [30] for a review of existing results in GR).

In this work, we specialize the results of Refs. [149–151] to binary systems on quasi-circular orbits and present the waveform in a form that can be easily used to test GR with GWs. This calculation serves as an extension of Ref. [240], in which the

leading-order behavior of the GW signal produced by binary systems was computed in Brans-Dicke theory [178, 179, 241], where the scalar coupling $\omega(\phi) = \omega_{\rm BD}$ is constant. This work extends those earlier findings to higher PN order in a larger class of scalar-tensor theories.

The paper is organized as follows. In Sec. 3.2, we review some preliminary information regarding the production and detection of GWs in scalar-tensor theories. Section 3.3 presents the dynamics for binary systems on quasi-circular orbits. In Sec. 3.4, we compute the hereditary contributions to the gravitational waveform from such systems. We present the binding energy and energy flux in Sec. 3.5 and compute the associated orbital phase evolution. In Sec. 3.6, we decompose the waveform into spin-weighted spherical modes, and in Sec. 3.7, we express these modes in Fourier space using the stationary phase approximation. We provide some concluding remarks in Sec. 3.8. Appendix C details the conversion of our notation to that of Refs. [147, 152], which is commonly found in the literature. Appendix D contains formulae omitted from the main text for the sake of compactness.

All calculations are done both for systems whose inspiral is driven by dipolar radiation and for those driven by quadrupolar radiation; this distinction is discussed in detail in Sec. 3.2.2. Note that the *complete* 2PN (relative) order results are given for only the former case (dipolar-radiation driven systems). The results for the latter case depend on higher-order corrections to the energy flux that have not yet been computed, but we argue in Sec. 3.5.2 that the impact of these missing terms is very small.

Henceforth, we work in units where $G_* = c = 1$.

3.2 Gravitational waves in scalar-tensor gravity

This section contains information concerning the generation of GWs in scalar-tensor gravity that will prove useful throughout the rest of the paper despite not directly contributing to the computation of the waveform. We begin by discussing the behavior of binary systems, tracing new phenomena not found in GR to violations of the strong equivalence principle. We then review the current experimental constraints set on these theories and show that, in most cases, sources for ground- and space-based GW detectors evolve similarly to as in GR. Finally, we discuss the response of a detector to a GW in scalar-tensor gravity and delineate the waveform computed in the subsequent sections.

3.2.1 Binary systems of compact objects

Differences between the dynamics and GW emission of binary systems in scalar-tensor gravity and those in GR ultimately stem from the non-minimal coupling between the metric and scalar field. As a result, the gravitational "constant" experienced by massive bodies depends on the value of the background scalar field in which they are situated. For test bodies, this dependence can be deduced directly from Eq. (3.1): the strength of their gravitational interaction scales as ϕ^{-1}.

The gravitational interaction between compact, self-gravitating bodies is more complex. Because the binding energy of a single self-gravitating body depends on the interactions between all of its constituents, the body's mass $m_A(\phi)$ depends on the local scalar field. This phenomenon is a manifestation of the violation of the

Table 3.1: Parameters that govern gravitational wave production in binary systems. Quantities listed with the subscript 0 are evaluated at the value of the background scalar field ϕ_0.

Parameter	Definition
Weak-field parameters	
G	$G_*\phi_0^{-1}(4+2\omega_0)/(3+2\omega_0)$
ζ	$1/(4+2\omega_0)$
λ_1	$(\mathrm{d}\omega/\mathrm{d}\phi)_0\phi_0\zeta^2/(1-\zeta)$
λ_2	$(\mathrm{d}^2\omega/\mathrm{d}\phi^2)_0\phi_0^2\zeta^3/(1-\zeta)$
Strong-field parameters	
s_A	$[\mathrm{d}\ln m_A(\phi)/\mathrm{d}\ln\phi]_0$
s'_A	$[\mathrm{d}^2\ln m_A(\phi)/\mathrm{d}\ln\phi^2]_0$
s''_A	$[\mathrm{d}^3\ln m_A(\phi)/\mathrm{d}\ln\phi^3]_0$
Binary parameters	
Newtonian	
α	$1-\zeta+\zeta(1-2s_1)(1-2s_2)$
post-Newtonian	
γ	$-2\alpha^{-1}\zeta(1-2s_1)(1-2s_2)$
β_1	$\alpha^{-2}\zeta(1-2s_2)^2\left(\lambda_1(1-2s_1)+2\zeta s'_1\right)$
β_2	$\alpha^{-2}\zeta(1-2s_1)^2\left(\lambda_1(1-2s_2)+2\zeta s'_2\right)$
2nd post-Newtonian	
δ_1	$\alpha^{-2}\zeta(1-\zeta)(1-2s_1)^2$
δ_2	$\alpha^{-2}\zeta(1-\zeta)(1-2s_2)^2$
χ_1	$\alpha^{-3}\zeta(1-2s_2)^3\left[(\lambda_2-4\lambda_1^2+\zeta\lambda_1)(1-2s_1)-6\zeta\lambda_1 s'_1+2\zeta^2 s''_1\right]$
χ_2	$\alpha^{-3}\zeta(1-2s_1)^3\left[(\lambda_2-4\lambda_1^2+\zeta\lambda_1)(1-2s_2)-6\zeta\lambda_1 s'_2+2\zeta^2 s''_2\right]$

strong equivalence principle, as the self-interaction of a massive body is dictated by its composition. As is done in the literature, we adopt an approach proposed by Eardley [242] to handle the interplay between microphysics and gravity that determines the connection between the body's composition and $m_A(\phi)$. We treat compact objects as point particles whose mass is given by $m_A(\phi)$. Rather than solve for this function outright, we parameterize it by its expansion about a background

field ϕ_0

$$m_A(\phi) = m_A^{(0)} \left[1 + s_A \Psi + \frac{1}{2} \left(s_A^2 + s_A' - s_A \right) \Psi^2 + \cdots \right], \tag{3.2}$$

where we've defined

$$m_A^{(0)} \equiv m_A(\phi_0), \tag{3.3}$$

$$s_A \equiv \left(\frac{\mathrm{d} \ln m_A}{\mathrm{d} \ln \phi} \right)_{\phi=\phi_0}, \tag{3.4}$$

$$s_A' \equiv \left(\frac{\mathrm{d}^2 \ln m_A}{\mathrm{d} (\ln \phi)^2} \right)_{\phi=\phi_0}, \tag{3.5}$$

$$\Psi \equiv \frac{\phi - \phi_0}{\phi_0}. \tag{3.6}$$

The parameter s_A is known as the sensitivity of the body. For test bodies, $s_A = 0$, while for stationary black holes, $s_A = 1/2$ [23].[3]

The underlying parameters that govern the orbital dynamics and gravitational emission of binary systems up to 2PN order are given on the left-hand side of Table 3.1. These parameters are classified as either *weak-field* or *strong-field*: the former class influence behavior in all gravitational contexts whereas the latter class only enter in systems with strong gravitational fields, such as those found in self-gravitating compact objects. The weak- and strong-field parameters appear in only a small set of combinations, denoted as the *binary parameters* in Table 3.1. We

[3]The sensitivity of neutron stars is often estimated to be of the order ~ 0.2. While true in Brans-Dicke theory [242, 243] and some slight variations [146], this result does not hold for generic choices of $\omega(\phi)$. One of the most popular classes of scalar-tensor theories, those that allow spontaneous [153] and dynamical scalarization [169, 171], are a striking counterexample. In these theories, neutron-star sensitivities can be large and *negative*; the process of spontaneous scalarization describes stars whose sensitivity diverges, i.e., $s_A \to -\infty$.

have adopted the notation introduced in Refs. [149]; the mapping between these parameters and the notation used in Refs. [147, 152] is given in Appendix C.

Novel behavior in scalar-tensor gravity stems from violations of the strong equivalence principle, and thus, is dictated by the strong-field parameters. For example, dipolar emission, the most prominent new effect not found in GR, is tied to $(s_1 - s_2)^2$. Formally, dipolar radiation is generated at one PN order lower than quadrupolar radiation (the dominant dissipative channel in GR); in keeping with the conventions of Refs. [149–151], we demarcate dipolar emission as a -1PN order effect.

3.2.2 Generic constraints on scalar-tensor gravity

A hundred years of tests have confirmed that gravity closely resembles GR [79]. Restricting our attention to only those theories that satisfy these constraints, we must study the regime in which new scalar-tensor effects are small relative to those also found in GR. In this limit, the structure of the PN expansion is modified; for example, in the frequency band of interest, the dominant dissipative process is the emission of Newtonian order quadrupolar radiation rather than the -1PN dipolar energy flux. We investigate which systems fall within this regime by first mapping the current constraints on scalar-tensor theories to the parameters given in Table 3.1.

The best constraints on weak- and strong-field parameters come from a combination of solar-system experiments and binary-pulsar observations. The weak-field parameters $G, \zeta, \lambda_1, \lambda_2$ are tied to the behavior of the scalar coupling $\omega(\phi)$ near the

background value of the scalar field ϕ_0. These quantities can be expressed in terms of the parametrized post-Newtonian (PPN) parameters $\gamma_{\rm PPN}$ and $\beta_{\rm PPN}$ as well as the 2PN parameter ϵ introduced in Ref. [152]

$$G = \frac{2}{(1+\gamma_{\rm PPN})\phi_0}, \tag{3.7}$$

$$\zeta = \frac{1-\gamma_{\rm PPN}}{2}, \tag{3.8}$$

$$\bar{\lambda}_1 = \frac{2\sqrt{2}(\beta_{\rm PPN}-1)\phi_0}{\sqrt{1+\gamma_{\rm PPN}}}, \tag{3.9}$$

$$\bar{\lambda}_2 = \frac{(\epsilon(\gamma_{\rm PPN}-1)+24(\beta_{\rm PPN}-1)^2)\phi_0^2}{1+\gamma_{\rm PPN}}, \tag{3.10}$$

where we have used the rescaled parameters $\bar{\lambda}_1 \equiv \lambda_1\sqrt{\zeta}$ and $\bar{\lambda}_2 \equiv \lambda_2\zeta$ because λ_1, λ_2 are not well defined in the GR limit.

The current constraints on these parameters are given in Table 3.2. The constant background field ϕ_0 is undetectable with weak-field measurements — at Newtonian order, a redefinition of the field $\phi \to \phi/\phi_0$ can be compensated by the rescaling of the bare gravitational constant $G_* \to G_*/\phi_0$ and the redefinition $\omega \to \phi_0\omega$. For simplicity, we set ϕ_0 to unity in Table 3.2. Note that the constraint on ϵ was estimated in Ref. [152] with only binary-pulsar measurements available at the time; this constraint could be improved by including more recent observations.

The current experimental constraints on the strong-field parameters s_A, s'_A, s''_A are not as restrictive. The best limits on neutron-star sensitivities come from timing measurements of pulsar-white-dwarf binaries [245–248]; white dwarfs are expected to have negligible sensitivity, so the magnitude of dipolar emission is dictated entirely by the sensitivity of the neutron star. Constraints are typically given in terms of

Table 3.2: Constraints on the weak-field parameters in Eqs. (3.7)–(3.10) set by solar-system and binary-pulsar observations. As discussed in the text, we set $\phi_0 = 1$ for simplicity.

Parameter	Constraint	Reference
$\gamma_{\rm PPN} - 1$	2.3×10^{-5}	[180]
$\beta_{\rm PPN} - 1$	7.8×10^{-5}	[79, 244]
ϵ	7×10^{-2}	[152]
$G - 1$	1.2×10^{-5}	
ζ	1.2×10^{-5}	
$\bar{\lambda}_1$	1.6×10^{-4}	
$\bar{\lambda}_2$	8.8×10^{-7}	

the scalar charge α_A, related to the sensitivity by

$$\alpha_A = \frac{1 - 2s_A}{\sqrt{3 + 2\omega_0}}. \tag{3.11}$$

Amongst known pulsar-white-dwarf binaries used to constrain scalar-tensor theories, PSR J0348+0432 hosts the most massive neutron star [248]. The constraints on the scalar dipole reported in Ref. [248] provide an estimate for the maximum scalar charge that this neutron star can have $|\alpha_A| \lesssim 6 \times 10^{-3}$. Extending these data to an absolute bound on the charge of *any* neutron star requires the assumption of a particular choice of $\omega(\phi)$ and equation of state. Working within one of the most popular classes of scalar-tensor theories [153] and selecting certain realistic equations of state, one can produce a global constraint of $|\alpha_A| \lesssim 10^{-2}$ [248, 249]. However, it is conceivable that other theories and/or equations of state allow neutron stars to acquire large scalar charges of $\alpha_A \sim 1$ via the process of spontaneous scalarization [153] while satisfying all current experimental constraints.

Because the weak-field constraints leave $\omega_0 \sim 1/(2\zeta)$ unbounded, no absolute bound can be placed on s_A. To our knowledge, no constraints have been placed

on s'_A and s''_A either; for neutron stars, these higher derivatives can be orders of magnitude larger than s_A (for example, see Fig. 3 of Ref. [3]).

Excluding the possibility of spontaneous scalarization, the constraints on weak-field and strong-field parameters ensure that dipole radiation is suppressed in viable scalar-tensor theories, as can be shown by comparing the relative size of the -1PN and Newtonian order flux, given in Refs. [147, 149] and repeated in Eq. (3.48) below. Despite entering at higher PN order, the next-to-leading order term overpowers the leading-order term when

$$1 \lesssim \left(\frac{24}{5\zeta \mathcal{S}_-^2}\right) (G\alpha M \pi f)^{2/3} , \tag{3.12}$$

where, for simplicity, we have dropped all terms that are not of order $\mathcal{O}(\zeta^{-1})$ and introduced the scalar dipole

$$\mathcal{S}_- \equiv - \alpha^{-1/2} (s_1 - s_2) . \tag{3.13}$$

Given the experimental constraints on ζ and $\mathcal{S}_-$, this threshold is reached at frequencies $f \lesssim 100\mu$Hz in binary neutron star or neutron-star stellar-mass-black-hole systems, and at frequencies $f \lesssim 5\mu$Hz in neutron-star intermediate-mass-black-hole systems. Following this argument, ground- and space-based GW detectors would only observe binary systems whose inspiral is driven by the next-to-leading order flux.[4] On the other hand, the evolution of binary pulsars could be dominated

[4]Unlike the class of scalar-tensor theories considered here, there are alternative theories in which binary black holes can emit dipolar radiation (e.g., dilatonic Einstein-Gauss-Bonnet, dynamical Chern-Simons, etc.). Given the relatively weak constraints on dipolar radiation in vacuum space-times (compared to those from binary pulsars observations), we note that space-based detectors

by dipolar emission. Binary systems that undergo dynamical scalarization may also be exempt from this verdict, as these systems dynamically generate large scalar charges that can substantially enhance dipolar emission [169, 171, 250].

Because non-perturbative scalarization phenomena have not been entirely ruled out, we compute below the gravitational waveform both for systems in which dipolar radiation is dominant and for those in which quadrupolar radiation is dominant. For conciseness, we refer to the former class of systems as *dipole driven* (DD) and the latter class as *quadrupole driven* (QD).

3.2.3 Detector response

We consider the response of a laser interferometer at spatial coordinates $\mathbf{X}$ generated to an incident GW produced by a distant binary system of size d, where $R \equiv |\mathbf{X}| \gg d$. We assume that far from the binary, the metric and scalar field approach the Minkowski metric $\eta^{\mu\nu}$ and a constant background value ϕ_0, respectively, at a rate $\sim R^{-1}$. Let $\hat{\phi} \equiv \phi/\phi_0$ be the normalized scalar field. We introduce the conformally transformed metric

$$\tilde{g}_{\mu\nu} \equiv \hat{\phi} g_{\mu\nu}, \tag{3.14}$$

and the gravitational field[5]

$$h^{\mu\nu} \equiv \eta^{\mu\nu} - \sqrt{-\tilde{g}}\tilde{g}^{\mu\nu}. \tag{3.15}$$

or pulsar timing arrays could, in principle, observe binary black holes driven by dipolar flux. As discussed below, the GW signal from such systems has a distinct structure from that in GR.

[5]Note that in Ref. [30] and the references therein, the metric perturbation is defined with an overall minus sign relative to the definition given here.

The metric at the detector takes the form

$$g_{\mu\nu} = \eta_{\mu\nu} + h_{\mu\nu} - \frac{1}{2} h \eta_{\mu\nu} - \Psi \eta_{\mu\nu} + \mathcal{O}\left(R^{-2}\right), \tag{3.16}$$

where $h \equiv \eta_{\mu\nu} h^{\mu\nu}$ is the trace of $h^{\mu\nu}$ and $h_{\mu\nu} \equiv \eta_{\mu\alpha}\eta_{\nu\beta}h^{\alpha\beta}$ is lowered using the Minkowski metric. Gravitational-wave detectors use laser interferometry to measure the separation between mirrors; we treat these mirrors as test masses. Assuming that the distance between mirrors is smaller than the wavelength of the incident GWs and that the mirrors move slowly, the separation between the mirrors obeys

$$\ddot{\xi}^i = -R_{0i0j}\xi^j, \tag{3.17}$$

where $i, j = 1, 2, 3$ are spatial indices. Working at leading order in $h^{\mu\nu}$ and Ψ, the Riemann tensor is calculated from Eq. (3.16)

$$R_{0i0j} = -\frac{1}{2}\ddot{h}^{ij}_{\rm TT} - \frac{1}{2}\ddot{\Psi}\left(\hat{N}^i\hat{N}^j - \delta^{ij}\right), \tag{3.18}$$

where $\hat{\mathbf{N}} \equiv \mathbf{X}/R$ and $h^{ij}_{\rm TT}$ is the transverse-traceless component of the gravitational field defined as

$$h^{ij}_{\rm TT} = \left(P^{ip}P^{jq} - \frac{1}{2}P^{ij}P^{pq}\right)h^{pq}, \tag{3.19}$$

where $P^{pq} = \delta^{pq} - \hat{N}^p\hat{N}^q$ is the transverse projection operator.

From Eq. (3.18), we see that the GW signal contains a transverse-traceless mode (as in GR) characterized by the field $h^{\mu\nu}$. In scalar-tensor gravity, there is an additional transverse breathing mode produced by Ψ. Extracting this new GW polarization requires a network of detectors; see Ref. [79] and references therein for a discussion of the prospects of detecting GW polarizations absent in GR. We focus exclusively on $h^{\mu\nu}$ for the remainder of this work.

3.3 Dynamics for quasi-circular orbits

In this section, we specialize the results of Ref. [149] for the 2.5PN dynamics of binary systems to the case of quasi-circular orbits. Before proceeding, we establish some notation employed throughout this work. We denote the total mass of the system by $M = m_1 + m_2$ and the symmetric and antisymmetric mass ratio by $\eta = m_1 m_2/M^2$ and $\psi = (m_1 - m_2)/M$, respectively. We signify the symmetric and antisymmetric combinations of parameters given in Table 3.1 by

$$\tau_+ \equiv \frac{1}{2}\left(\tau_1 + \tau_2\right), \tag{3.20a}$$

$$\tau_- \equiv \frac{1}{2}\left(\tau_1 - \tau_2\right), \tag{3.20b}$$

and in addition to $\mathcal{S}_-$ above, we also define

$$\mathcal{S}_+ \equiv \alpha^{-1/2}\left(1 - s_1 - s_2\right). \tag{3.21a}$$

To describe the system's dynamics, we denote the orbital separation by $\mathbf{x} = r\mathbf{n}$, the relative velocity by $\mathbf{v} = \dot{\mathbf{x}}$, and the acceleration by $\mathbf{a} = \dot{\mathbf{v}}$. We construct an orthonormal moving frame $(\mathbf{n}, \boldsymbol{\lambda})$ and define the orbital frequency ω such that $\mathbf{v} = \dot{r}\mathbf{n} + r\omega\boldsymbol{\lambda}$. To avoid confusion, we note that certain variables are used to denote multiple quantities; for example, ω represents both the frequency and scalar coupling, while ϕ, Ψ are used for the phase and scalar field. The usage of each can be inferred from context.

Our analysis of binary systems on quasi-circular orbits begins with the 2.5PN

equation of motion, given in the center-of-mass frame by

$$\begin{aligned}\mathbf{a} =& -\frac{GM\alpha}{r^2}\mathbf{n} + \frac{GM\alpha}{r^2}\left[\mathbf{n}\left(A_{1\mathrm{PN}} + A_{2\mathrm{PN}}\right) + \dot{r}\mathbf{v}\left(B_{1\mathrm{PN}} + B_{2\mathrm{PN}}\right)\right] \\ &+ \frac{8\eta}{5}\frac{(GM\alpha)^2}{r^3}\left[\dot{r}\mathbf{n}\left(A_{1.5\mathrm{PN}} + A_{2.5\mathrm{PN}}\right) - \mathbf{v}\left(B_{1.5\mathrm{PN}} + B_{2.5\mathrm{PN}}\right)\right] . \end{aligned} \tag{3.22}$$

where the expressions for A_i, B_i can be found in Eqs. (1.4)–(1.5) and (6.12)–(6.13) of Ref. [149]. It will prove useful also to write the equations of motion in the generic form

$$\mathbf{a} = (\ddot{r} - r\omega^2)\mathbf{n} + (r\dot{\omega} + 2\dot{r}\omega)\boldsymbol{\lambda} . \tag{3.23}$$

The restriction of the dynamics to quasi-circular orbits follows the same procedure as in GR. For such orbits, the only departure from circular motion is induced by radiation reaction, which enters at 1.5PN order in scalar-tensor theories rather than the usual 2.5PN order in GR. Expressed symbolically, we have $\dot{r}$, $\dot{\omega} = \mathcal{O}(3)$ [instead of $\mathcal{O}(5)$], while $\ddot{r} = \mathcal{O}(6)$ [instead of $\mathcal{O}(10)$].

The first term in Eq. (3.23) determines the conservative sector of the dynamics at 1PN and 2PN order. The scalar product $\mathbf{a}\cdot\mathbf{n} = -r\omega^2 + \mathcal{O}(6)$ produces a relation between the orbital separation and frequency that generalizes Kepler's law. We introduce the PN parameters (recall that we work in units where $c = 1$)

$$\gamma_{\mathrm{PN}} \equiv \frac{GM\alpha}{r}, \tag{3.24a}$$

$$x \equiv (GM\alpha\omega)^{2/3} , \tag{3.24b}$$

which differ from their usual definition in GR by an additional factor α.

At leading order, one obtains $r^3\omega^2 = Gm\alpha + \mathcal{O}(2)$, or $x = \gamma_{\mathrm{PN}}(1 + \mathcal{O}(2))$. From there, solving order by order yields

$$
\begin{aligned}
x =&\gamma_{\rm PN}\left[1+\gamma_{\rm PN}\left(\frac{2\beta_-\psi}{3}-\frac{2\beta_+}{3}-\frac{\gamma}{3}+\frac{\eta}{3}-1\right)\right.\\
&+\gamma_{\rm PN}^2\left(\frac{8\beta_-^2\eta}{\gamma}+\frac{16\beta_-^2\eta}{9}-\frac{4\beta_-^2}{9}+\frac{8\beta_-\beta_+\psi}{9}-\frac{2\beta_-\gamma\psi}{9}+\frac{11\beta_-\psi\eta}{9}-\frac{4\beta_-\psi}{3}\right.\\
&-\frac{8\beta_+^2\eta}{\gamma}-\frac{4\beta_+^2}{9}+\frac{2\beta_+\gamma}{9}+\frac{7\beta_+\eta}{9}+\frac{4\beta_+}{3}-\frac{\gamma^2\eta}{6}+\frac{11\gamma^2}{36}+\frac{17\gamma\eta}{9}+\gamma+\frac{\psi\delta_-}{3}\\
&\left.\left.+\frac{2\psi\chi_-}{3}-\frac{2\delta_+\eta}{3}+\frac{\delta_+}{3}+\frac{2\eta^2}{9}+\frac{4\eta\chi_+}{3}+\frac{49\eta}{12}-\frac{2\chi_+}{3}+1\right)+\mathcal{O}(6)\right], \qquad (3.25a)\\
\gamma_{\rm PN} =&x\left[1+x\left(-\frac{2\beta_-\psi}{3}+\frac{2\beta_+}{3}+\frac{\gamma}{3}-\frac{\eta}{3}+1\right)\right.\\
&+x^2\left(-\frac{8\beta_-^2\eta}{\gamma}-\frac{16\beta_-^2\eta}{3}+\frac{4\beta_-^2}{3}-\frac{8\beta_-\beta_+\psi}{3}-\frac{2\beta_-\gamma\psi}{3}-\frac{\beta_-\psi\eta}{3}-\frac{4\beta_-\psi}{3}\right.\\
&+\frac{8\beta_+^2\eta}{\gamma}+\frac{4\beta_+^2}{3}+\frac{2\beta_+\gamma}{3}-\frac{5\beta_+\eta}{3}+\frac{4\beta_+}{3}+\frac{\gamma^2\eta}{6}-\frac{\gamma^2}{12}-\frac{7\gamma\eta}{3}+\frac{\gamma}{3}-\frac{\psi\delta_-}{3}\\
&\left.\left.-\frac{2\psi\chi_-}{3}+\frac{2\delta_+\eta}{3}-\frac{\delta_+}{3}-\frac{4\eta\chi_+}{3}-\frac{65\eta}{12}+\frac{2\chi_+}{3}+1\right)+\mathcal{O}(6)\right]. \qquad (3.25b)
\end{aligned}
$$

Having derived the reduction to quasi-circular orbits for the conservative dynamics up to 2PN order, we now turn our attention to the dissipative sector. Although only the leading-order radiation-reaction terms are needed to compute the 2PN relative order dynamics, we provide results up to 2.5PN for the sake of completeness. Inserting Eq. (3.25) into the relation $\mathbf{a}\cdot\boldsymbol{\lambda}=r\dot{\omega}+2\dot{r}\omega$ gives the following expressions for $\dot{r}$ and $\dot{\omega}$

$$
\begin{aligned}
\dot{r} =& -\frac{8}{3}\zeta\eta\mathcal{S}_-^2x^2-\frac{8}{3}\eta\delta_{\rm RR}x^3+\mathcal{O}(7)\,, \qquad (3.26a)\\
\dot{\omega} =&\frac{4\zeta\eta\mathcal{S}_-^2x^{9/2}}{G^2M^2\alpha^2}+\frac{4\eta\delta_{\rm RR}x^{11/2}}{G^2M^2\alpha^2}+\mathcal{O}(7)\,, \qquad (3.26b)
\end{aligned}
$$

where we have introduced

$$\delta_{\rm RR} \equiv \frac{24}{5} + 2\gamma - \frac{4\zeta\beta_-\psi\mathcal{S}_-^2}{\gamma} + \frac{8\zeta\beta_-\psi\mathcal{S}_-^2}{3} - \frac{7\zeta\eta\mathcal{S}_-^2}{6} + \frac{4\zeta\beta_+\mathcal{S}_-^2}{\gamma} - \frac{8\zeta\beta_+\mathcal{S}_-^2}{3} + \frac{2\zeta\gamma\mathcal{S}_-^2}{3} - \frac{\zeta\mathcal{S}_-^2}{2} + \frac{4\zeta\beta_-\mathcal{S}_+\mathcal{S}_-}{\gamma} - \frac{4\zeta\beta_+\psi\mathcal{S}_+\mathcal{S}_-}{\gamma}. \tag{3.27}$$

For dipole-driven systems, the second term in Eq. (3.26) is much smaller than the first. Integrating this equation at leading order gives the evolution of the orbital separation and frequency

$$r_{\rm DD}(t) = \left[8\eta\zeta\mathcal{S}_-^2(GM\alpha)^2(t_c - t)\right]^{1/3}(1 + \mathcal{O}(2))\,, \tag{3.28a}$$

$$\omega_{\rm DD}(t) = \left[8\eta\zeta\mathcal{S}_-^2 GM\alpha(t_c - t)\right]^{-1/2}(1 + \mathcal{O}(2))\,, \tag{3.28b}$$

where t_c is the time of coalescence. In the quadrupole-driven regime, the first term in Eq. (3.26) is overpowered by the second. We delay a precise formulation of this limit until Sec. 3.5, but note that the evolution of the inspiraling orbit will take the same form as in GR, given at leading order by

$$r_{\rm GR}(t) = \left[\frac{256(GM)^3\eta}{5}(t_c - t)\right]^{1/4}(1 + \mathcal{O}(2))\,, \tag{3.29a}$$

$$\omega_{\rm GR}(t) = \left[\frac{256(GM)^{5/3}\eta}{5}(t_c - t)\right]^{-3/8}(1 + \mathcal{O}(2))\,. \tag{3.29b}$$

The difference in structure between Eqs. (3.28) and (3.29) stems from radiation reaction entering at a different PN order in the two regimes.

3.4 Radiative coordinates and hereditary contributions

Equipped with the leading-order evolution of the inspiral, we begin our computation of the 2PN order waveform. The waveform was derived for generic orbits in Ref. [150]; schematically, these results are given by

$$h^{ij}_{\rm TT} = \frac{2G(1-\zeta)M\eta}{R}\left[Q^{ij} + P^{1/2}Q^{ij} + PQ^{ij} + P^{3/2}Q^{ij}_{\mathcal{N}} \right.$$
$$\left. + P^{3/2}Q^{ij}_{\mathcal{C}-\mathcal{N}} + P^2 Q^{ij}_{\mathcal{N}} + P^2 Q^{ij}_{\mathcal{C}-\mathcal{N}}\right]_{\rm TT} , \tag{3.30}$$

where TT stands for the transverse-traceless projection given in Eq. (3.19), P denotes the PN order of each term, and $\mathcal{N}$ and $\mathcal{C}-\mathcal{N}$ indicate contributions from the near zone and radiation zone, respectively, as defined in Ref. [150]. The expressions for $P^n Q^{ij}$ are presented in Eq. (7.2) of Ref. [150]. These terms can be categorized as either *instantaneous* or *hereditary*: instantaneous terms depend only on the state of the system at the current retarded time, whereas hereditary terms take the form of integrals extending over the binary's entire history. In Eq. (3.30), $P^{3/2}Q^{ij}_{\mathcal{C}-\mathcal{N}}$ and $P^2 Q^{ij}_{\mathcal{C}-\mathcal{N}}$ are hereditary, while the remaining terms are all instantaneous.

This section details the computation of the hereditary terms for systems on quasi-circular orbits. First, we re-express the waveform in a radiative coordinate system, in which the metric perturbation falls off as $\sim R^{-1}$. We then compute separately the contributions from so-called *tail* and *memory* terms.

3.4.1 Radiative coordinates

We begin by transforming the results of Ref. [150] into radiative coordinates. This reference employed harmonic coordinates $X = (t, \mathbf{X})$, defined by the gauge condition $\partial_\nu h^{\mu\nu} = 0$; however, these coordinates are known to give rise to unwanted logarithms of R in the far-zone expansion. As shown in Ref. [251], it is possible to build another set of coordinates $\bar{X} = (\bar{t}, \bar{\mathbf{X}})$, called radiative coordinates, in which

these logarithms are eliminated and the metric perturbation h^{ij} admits an expansion in powers of $\bar{R}^{-1}$. Here, we will follow the presentation of Ref. [252], in which the construction of this coordinate system is explicitly written at quadratic order in the multipolar post-Minkowskian formalism [253]. Note that our definition $h^{\mu\nu}$ in Eq. (3.14) introduces a sign difference with respect to Ref. [252].

Both hereditary pieces, $P^{3/2}Q^{ij}_{\mathcal{C}-\mathcal{N}}$ and $P^2Q^{ij}_{\mathcal{C}-\mathcal{N}}$, contain integrals with a logarithmic kernel, known as tail terms. The logarithmic terms can be expressed as the second time derivative of the leading-order, linearized metric, as shown by Eq. (2.28) of Ref. [252]. Written in terms of the retarded time $u = t - R/c$, these terms are given by

$$\left(P^{3/2}Q^{ij}_{\mathcal{C}-\mathcal{N}}(u)\right)_{\ln} = 2G(1-\zeta)M\int_0^{+\infty} \mathrm{d}s\, \frac{\mathrm{d}^2}{\mathrm{d}t^2}Q^{ij}(u-s)\ln\left(\frac{s}{2R+s}\right), \tag{3.31a}$$

$$\left(P^{2}Q^{ij}_{\mathcal{C}-\mathcal{N}}(u)\right)_{\ln} = 2G(1-\zeta)M\int_0^{+\infty} \mathrm{d}s\, \frac{\mathrm{d}^2}{\mathrm{d}t^2}P^{1/2}Q^{ij}(u-s)\ln\left(\frac{s}{2R+s}\right). \tag{3.31b}$$

Because we are only interested in the R^{-1} piece of the waveform, we expand the logarithms according to

$$\ln\left(\frac{s}{2R+s}\right) = \ln\left(\frac{s}{2R}\right) + \mathcal{O}\left(\frac{1}{R}\right). \tag{3.32}$$

We define the radiative coordinates as $\bar{X}^\alpha = X^\alpha + \xi^\alpha$, with

$$\xi^\alpha = 2G(1-\zeta)M\delta^\alpha{}_0\ln\left(\frac{R}{r_0}\right), \tag{3.33}$$

where we have introduced an arbitrary constant length scale r_0. The metric perturbation in these new coordinates takes the form

$$\bar{h}^{\alpha\beta} = \left[h^{\alpha\beta} - \partial^\alpha\xi^\beta - \partial^\beta\xi^\alpha + \eta^{\alpha\beta}\partial_\rho\xi^\rho + \xi^\mu\partial_\mu h^{\alpha\beta}\right]_{X=\bar{X}}, \tag{3.34}$$

where we have kept only the relevant terms in Eqs. (2.36) and (2.37) of Ref. [252]. The first three terms describe the usual effect of a first order gauge transformation on the harmonic perturbation; their contribution will be eliminated by the TT projection. The last term combines with the lower boundary term of the integrals in Eq. (3.31) to replace R by the new constant r_0:

$$\left(\overline{P^{3/2}Q^{ij}_{\mathcal{C}-\mathcal{N}}}(\bar{u})\right)_{\ln} = 2G(1-\zeta)M\int_0^{+\infty} \mathrm{d}s\, \frac{\mathrm{d}^2}{\mathrm{d}\bar{t}^2}\overline{Q^{ij}}(\bar{u}-s)\ln\left(\frac{s}{2r_0}\right) + \mathcal{O}\left(\frac{1}{\bar{R}^2}\right), \tag{3.35a}$$

$$\left(\overline{P^{2}Q^{ij}_{\mathcal{C}-\mathcal{N}}}(\bar{u})\right)_{\ln} = 2G(1-\zeta)M\int_0^{+\infty} \mathrm{d}s\, \frac{\mathrm{d}^2}{\mathrm{d}\bar{t}^2}\overline{P^{1/2}Q^{ij}}(\bar{u}-s)\ln\left(\frac{s}{2r_0}\right) + \mathcal{O}\left(\frac{1}{\bar{R}^2}\right). \tag{3.35b}$$

Since the transformation to radiative coordinates affects only the logarithmic terms, from here on, we drop the notation $\bar{X}$, using instead the ordinary notation X to signify these new coordinates.

3.4.2 Tail contributions

The tail terms in the waveform arise from back-scattering of the waves on the curvature of spacetime. In the multipolar post-Minkowskian wave generation formalism of Refs. [252, 253], they appear as interactions between each multipole moment and the mass monopole of the system. In the DIRE formalism [254, 255] used in Refs. [150, 151], tail terms arise from wave-zone contributions to the integrals over the past light-cone of the observer. Recall that these terms take the form of an integral with a logarithmic kernel over the past history of the source.

Since we are only interested in the R^{-1} part of the waveform, we can expand

the logarithms as in Eq. (3.32). Using Eq. (3.25) to replace ω with r, the tail terms then take the generic form

$$I = \int_0^{+\infty} \mathrm{d}s \, \frac{e^{in\varphi(t-s)}}{r^p(t-s)} \ln\left(\frac{s}{2r_0}\right) \tag{3.36}$$

where n, p are integers and φ is the orbital phase of the binary.

To evaluate Eq. (3.36), we make use of the fact that the radiation-reaction timescale is much longer than the orbital period. It was shown in Ref. [256] that ignoring radiation reaction, i.e., approximating the binary orbit as circular (with constant radius and frequency), introduces an error in these integrals of order $\mathcal{O}(\ln c/c^5)$ in GR. The same argument holds in scalar-tensor gravity, with the only difference being that the error is of order $\mathcal{O}(\ln c/c^3)$ for dipole-driven systems due to the different scaling of radiation reaction. Under this assumption that the frequency does not evolve with s, we write $\varphi(t-s) \simeq \varphi(t) - s\omega(t)$. One can then compute the resulting integrals by making use of the formula [256]

$$\int_0^{+\infty} \mathrm{d}y \, e^{i\lambda y} \ln y = -\frac{1}{\lambda}\left[\frac{\pi}{2}\mathrm{sgn}(\lambda) + i\left(\gamma_{\mathrm{E}} + \ln|\lambda|\right)\right], \tag{3.37}$$

where γ_{E} is the Euler-Mascheroni constant.

3.4.3 Memory contributions

Memory terms arise in the waveform as integrals of the product of multipoles without a logarithmic kernel over the history of the source [252, 257]. They can be separated into so-called DC terms, which are non-oscillatory and accumulate over the entire lifetime of the system, and AC, oscillatory terms that, by contrast, depend only on the recent history of the source.

The computation of oscillatory memory terms is identical in GR and in scalar-tensor theories. On quasi-circular orbits, these terms have the structure

$$J = \int_0^{+\infty} \mathrm{d}s \, \frac{e^{in\varphi(t-s)}}{r^p(t-s)}, \tag{3.38}$$

with integers n, p. Thanks to the oscillatory factor $e^{in\varphi}$ in the integrand, it can again be shown (see, e.g., Ref. [258]) that only the recent past contributes in the integral, so that one can approximate $r(t-s) \simeq r(t)$ and $\varphi(t-s) \simeq \varphi(t) - s\omega(t)$ with a negligible relative error of the same PN order as radiation reaction. For dipole-driven inspirals, the result is

$$J_{\mathrm{DD}} = \frac{1}{in} \left(\frac{r(t)^3}{GM\alpha} \right)^{1/2} \frac{e^{in\varphi(t)}}{r^p(t)} + \mathcal{O}(3), \tag{3.39}$$

whereas for quadrupole-driven inspirals, one obtains

$$J_{\mathrm{QD}} = \frac{1}{in} \left(\frac{r(t)^3}{GM\alpha} \right)^{1/2} \frac{e^{in\varphi(t)}}{r^p(t)} + \mathcal{O}(5). \tag{3.40}$$

Note that the only difference between these two cases is the order of the remainders.

The non-oscillatory (DC) memory terms take the form

$$K = \int_0^{+\infty} \mathrm{d}s \, \frac{1}{r^p(t-s)}. \tag{3.41}$$

Their computations in GR and scalar-tensor theory differ. Non-oscillatory terms are enhanced by the accumulation of the integrand over the long radiation-reaction timescale, an effect which formally *decreases* their PN order. The result depends here on the rate of evolution of the quasi-circular inspiral under radiation reaction. For dipole-driven systems, these DC memory terms formally appear at the 1.5PN order in the expression of the multipole moments, but the integration over the

radiation-reaction timescale (formally of -1.5PN order) pushes this contribution back to Newtonian order. Using the leading-order evolution of the quasi-circular inspiral given by Eq. (3.28), one obtains

$$K_{\rm DD} = \frac{3r^{3-p}(t)}{8(p-3)\zeta\eta\mathcal{S}_-^2(GM\alpha)^2} + \mathcal{O}(-1), \tag{3.42}$$

for $p > 3$.

The contribution from non-oscillatory memory terms in quadrupole-driven systems is more difficult to compute. Following Eq. (3.12), any system with non-zero scalar dipole will have been dominated by dipolar radiation at some point during its lifetime. The transition between the dipole-driven and quadrupole-driven regimes needs to be accommodated in the integral in Eq. (3.41). Such a calculation goes beyond the scope of this work.

3.5 Balance equation and phase evolution

Having computed all of the hereditary terms for quasi-circular orbits, one can use Eqs. (3.25) to express the waveform entirely in terms of the instantaneous orbital phase φ and frequency ω of the binary. We now need the evolution of these quantities at 2PN order to finish our calculation of the waveform. This level of accuracy cannot be achieved using only the dynamics of the binary presented in Sec. 3.3. In place of the higher-order radiation-reaction force, we use the total energy flux $\mathcal{F}$ and the balance equation

$$\frac{\mathrm{d}E}{\mathrm{d}t} = -\mathcal{F}, \tag{3.43}$$

which can be reformulated using $\dot{\varphi} = \omega$ as

$$\frac{\mathrm{d}\varphi}{\mathrm{d}x} = -\frac{1}{GM\alpha} x^{3/2} \frac{\mathrm{d}E/\mathrm{d}x}{\mathcal{F}(x)}. \tag{3.44}$$

We calculate the energy for systems restricted to quasi-circular orbits by applying the results of Sec. 3.3 to those of Ref. [149]. The energy measured in an arbitrary frame is given by Eq. (6.4) of Ref. [149]. After shifting to the center-of-mass frame with Eqs. (6.9) and (6.10) of Ref. [149], we reduce this expression to the case of quasi-circular orbits using Eqs. (3.25) and (3.26) and obtain

$$\begin{aligned} E_{\mathrm{circ}} = -\frac{1}{2} M\eta x \Bigg[1 + x \left(-\frac{2\beta_- \psi}{3} + \frac{2\beta_+}{3} - \frac{2\gamma}{3} - \frac{\eta}{12} - \frac{3}{4} \right) \\ + x^2 \left(-\frac{16\beta_-^2 \eta}{\gamma} - \frac{16\beta_-^2 \eta}{3} + \frac{4\beta_-^2}{3} - \frac{8\beta_- \beta_+ \psi}{3} - \frac{4\beta_- \gamma \psi}{3} + \frac{\beta_- \psi \eta}{3} - \beta_- \psi \right. \\ + \frac{16\beta_+^2 \eta}{\gamma} + \frac{4\beta_+^2}{3} + \frac{4\beta_+ \gamma}{3} - \frac{19\beta_+ \eta}{3} + \beta_+ + \frac{\gamma^2 \eta}{3} - \frac{19\gamma^2}{12} + \frac{11\gamma\eta}{3} - \frac{14\gamma}{3} \\ \left. + \frac{\psi \delta_-}{3} - \frac{4\psi \chi_-}{3} + \frac{4\delta_+ \eta}{3} + \frac{\delta_+}{3} - \frac{\eta^2}{24} - \frac{8\eta\chi_+}{3} + \frac{19\eta}{8} + \frac{4\chi_+}{3} - \frac{27}{8} \right) \Bigg] . \end{aligned} \tag{3.45}$$

The total emitted energy flux, including both tensor and scalar contributions, was given for generic orbits in Ref. [151] with the structure

$$\mathcal{F} = \mathcal{F}_{-1} + \mathcal{F}_0 + \mathcal{F}_{0.5,\mathcal{C}} + \mathcal{F}_{0.5,\mathcal{C}-\mathcal{N}} + \mathcal{F}_1 + \mathcal{O}(3), \tag{3.46}$$

where the number in the index indicates the PN order of each term. The -1PN term comes from dipolar, scalar radiation and is responsible for the appearance of radiation-reaction effects at 1.5PN order. Note that while the flux we consider is given at 1PN (using the order-counting scheme from GR), it corresponds to 2PN relative order.

The individual terms in Eq. (3.46) are given in the center-of-mass frame in Eq. (6.8) of Ref. [151]. The term $\mathcal{F}_{0.5,\mathcal{C}-\mathcal{N}}$ includes a logarithmic hereditary term

coming from the product of the leading-order term and a tail term (at 1.5PN relative order) in the scalar waveform. We calculate this tail contribution using the method detailed in Sec. 3.4.2. Then, as before, we use the results of Sec. 3.3 to compute the total energy flux for quasi-circular orbits $\mathcal{F}(x)$ that will be given in Eqs. (3.48) and (3.55) below.

Equipped with expressions for the binding energy $E(x)$ and the total energy flux $\mathcal{F}(x)$ both at the 2PN relative order, we proceed to evaluate the orbital phasing of the binary using Eq. (3.44). Different approaches have been proposed in the literature to integrate the balance equation, differing by the choice of integration variables (time or frequency) and by the choice of either numerical integration or analytical integration of a re-expansion of Eq. (3.44) (see, e.g., Ref. [259] for a definition and comparison of these so-called Taylor approximants). Our purpose here is not to compare these different approaches, but to examine the new contributions in the phasing that arise in scalar-tensor theories. We adopt a method (corresponding to the TaylorT2 approximant) that provides a result in analytic form: the ratio $-(\mathrm{d}E/\mathrm{d}x)/\mathcal{F}(x)$ is re-expanded in x, truncated at relative 2PN order, and then integrated term by term. For this purpose, it will be convenient to introduce the notation

$$\rho(x) \equiv -\frac{1}{GM\alpha}\frac{1}{\mathcal{F}(x)}\frac{\mathrm{d}E}{\mathrm{d}x}. \tag{3.47}$$

Care must be taken before re-expanding this ratio in the PN parameter x: we distinguish between the dipole-driven case in which the dipolar term $\mathcal{F}_{-1}$ [defined in Eq. (3.46)] dominates the denominator and the quadrupole-driven case wherein

$\mathcal{F}_0$ dominates due to the smallness of scalar-tensor parameters.

3.5.1 The dipole-driven regime

We first consider systems whose inspiral is driven by dipolar radiation. As discussed in Sec. 3.2.2, this regime is reached by binaries with large separations (binary pulsars) or large scalar dipoles (spontaneously scalarized systems). Dynamically scalarized systems begin in the quadrupole-driven regime but then abruptly become dipole-driven at some point during their evolution; in principle, one must account for both stages when modeling their inspiral, but we will not pursue such a treatment here.[6] Factoring out the leading order dipolar flux in Eq. (3.46), we obtain

$$\mathcal{F}^{\rm DD}(x) = \frac{4\mathcal{S}_-^2\zeta\eta^2 x^4}{3G\alpha}\left[1 + f_2^{\rm DD}x + f_3^{\rm DD}x^{3/2} + f_4^{\rm DD}x^2 + \mathcal{O}(5)\right], \tag{3.48}$$

where explicit expressions for the coefficients $f_n^{\rm DD}$ are given in Eq. (D.2). The leading order of the flux carries a factor $\mathcal{S}_-^2$ characteristic of dipolar radiation.

In this case, we simply re-expand the ratio $\rho(x)$ in x at 2PN relative order and obtain

$$\rho^{\rm DD}(x) = \frac{3}{8\mathcal{S}_-^2\zeta\eta x^4}\left[1 + \rho_2^{\rm DD}x + \rho_3^{\rm DD}x^{3/2} + \rho_4^{\rm DD}x^2 + \mathcal{O}(5)\right], \tag{3.49}$$

where the coefficients $\rho_n^{\rm DD}$ are given explicitly in Eq. (D.6). By integrating Eq. (3.44)

[6] Reference [3] (reproduced in Chapter 4) argues that the PN approximation breaks down as dynamical scalarization occurs, but that a straightforward resummation of PN results can provide an accurate waveform model valid in this regime.

term-by-term, the phasing is then given by

$$\varphi(x) = -\frac{1}{4\mathcal{S}_-^2\zeta\eta x^{3/2}}\left[1 + 3x\rho_2^{\rm DD} - \frac{3}{2}x^{3/2}\ln x\rho_3^{\rm DD} - 3x^2\rho_4^{\rm DD} + \mathcal{O}(5)\right], \tag{3.50}$$

where we have dropped an arbitrary additive constant that can be fixed by specifying the value of the phase at a given frequency.

3.5.2 The quadrupole-driven regime

For quadrupole-driven systems, the flux should be expanded about the Newtonian-order term $\mathcal{F}_0$ in Eq. (3.46) rather than the leading-order -1PN term. To accomplish this reordering of the PN approximation, we expand the flux in the PN parameter x and an additional parameter that describes the smallness of non-GR effects. There exists some flexibility in the choice of this second small parameter; the weak-field parameters listed in Table 3.1 describe the smallness of scalar-tensor corrections in complementary ways, and these quantities appear in the waveform in several combinations (e.g., the binary parameters).

We adopt a prescription that generalizes the approach of Ref. [240] to more generic scalar-tensor theories and to higher PN order. In the present quadrupole-driven case, we split the flux into pieces independent and dependent on the scalar dipole

$$\mathcal{F}^{\rm QD} = \mathcal{F}_{\text{non-dip}} + \mathcal{F}_{\rm dip}, \tag{3.51}$$

where we have defined

$$\mathcal{F}_{\text{non-dip}} \equiv \lim_{\mathcal{S}_- \to 0} \mathcal{F}, \tag{3.52}$$

$$\mathcal{F}_{\text{dip}} \equiv \mathcal{F} - \mathcal{F}_{\text{non-dip}}. \tag{3.53}$$

We refer to $\mathcal{F}_{\text{dip}}$ and $\mathcal{F}_{\text{non-dip}}$ as the "dipolar part" and "non-dipolar part" of the flux, respectively. Note that these labels do not correspond precisely to the multipolar structure of the source; for example, $\mathcal{F}_{\text{dip}}$ contains contributions from time derivatives of the scalar monopole and quadrupole. Instead, $\mathcal{F}_{\text{dip}}$ represents the part of the flux that vanishes when $s_1 = s_2$

We compute the phasing at first order in the small quantity $\mathcal{F}_{\text{dip}}/\mathcal{F}_{\text{non-dip}}$, employing the approximation

$$-\frac{\mathrm{d}E/\mathrm{d}x}{\mathcal{F}(x)} \simeq -\frac{\mathrm{d}E/\mathrm{d}x}{\mathcal{F}_{\text{non-dip}}(x)}\left(1 - \frac{\mathcal{F}_{\text{dip}}(x)}{\mathcal{F}_{\text{non-dip}}(x)}\right) \tag{3.54}$$

in Eq. (3.47). Evaluating the right-hand side of this equation requires knowledge of $\mathcal{F}_{\text{dip}}$ and $\mathcal{F}_{\text{non-dip}}$ each at 2PN relative order.

We obtain for the dipolar and non-dipolar parts

$$\mathcal{F}_{\text{non-dip}}(x) = \frac{32\eta^2\xi x^5}{5G\alpha}\left[1 + f_2^{\text{nd}}x + \mathcal{O}(3)\right], \tag{3.55a}$$

$$\mathcal{F}_{\text{dip}}(x) = \frac{4\mathcal{S}_-^2\zeta\eta^2 x^4}{3G\alpha}\left[1 + f_2^{\text{d}}x + f_3^{\text{d}}x^{3/2} + f_4^{\text{d}}x^2 + \mathcal{O}(5)\right], \tag{3.55b}$$

where the coefficients f_n^{nd} and f_n^{d} can be found in Eqs. (D.10) and (D.14) of Appendix D. The leading order dipolar part of the flux (3.55b) is the same as in Eq. (3.48). The leading order non-dipolar part (3.55a) is simply the quadrupolar flux in GR with an additional factor of ξ/α, where we have defined $\xi \equiv 1 + \gamma/2 + \zeta\mathcal{S}_+^2/6$.

Note that because it enters at Newtonian order (rather than -1PN), the non-dipolar part of the flux is only known to 1PN relative order. A complete calculation of the phasing at 2PN relative order requires the 1.5PN and 2PN corrections to the non-dipolar flux. In place of these unknown terms, we use

$$\mathcal{F}_{\text{non-dip}} = \mathcal{F}_{\text{2PN}}^{(\text{GR})} + \mathcal{F}_{\text{non-dip}}^{(\text{ST})}, \tag{3.56}$$

with

$$\mathcal{F}_{\text{non-dip}}^{(\text{ST})} = \mathcal{F}_{\text{non-dip}}^{(\text{ST})\text{1PN}} + \frac{32\eta^2 x^5}{5G\alpha}\xi\left[f_3^{\text{ST}} x^{3/2} + f_4^{\text{ST}} x^2 + \mathcal{O}(5)\right]. \tag{3.57}$$

In the above, $\mathcal{F}_{\text{2PN}}^{(\text{GR})}$ is the PN expanded flux in GR up to 2PN order, with the natural replacement $G_* \to G\alpha$. The first term in Eq. (3.57) denotes the known contributions to the non-dipolar flux that only arise in scalar-tensor theories, which can be obtained by subtracting the GR terms from (3.55a). We introduce the unknown coefficients f_3^{ST} and f_4^{ST} to represent our ignorance of the new scalar-tensor contributions at 1.5PN and 2PN order. In the quadrupole-driven context, experimental constraints on the weak-field parameters imply that these contributions should be much smaller than the 2PN GR terms. Moreover, these terms are doubly suppressed in the second term of Eq. (3.54) because $\mathcal{F}_{\text{dip}}$ is already of the first order in the small scalar-tensor coefficients. We will keep these unknown coefficients throughout our calculation for completeness.

We repeat the computation of the phasing from Sec. 3.5.1 but using the approximation (3.54). We write $\rho(x) = \rho_{\text{non-dip}}(x) + \rho_{\text{dip}}(x)$, where we have defined

$$\rho_{\text{non-dip}}(x) \equiv -\frac{1}{GM\alpha}\frac{1}{\mathcal{F}_{\text{non-dip}}(x)}\frac{\mathrm{d}E}{\mathrm{d}x}, \tag{3.58a}$$

$$\rho_{\text{dip}}(x) \equiv \frac{1}{GM\alpha}\frac{\mathcal{F}_{\text{dip}}(x)}{\mathcal{F}_{\text{non-dip}}(x)^2}\frac{\mathrm{d}E}{\mathrm{d}x}, \tag{3.58b}$$

which can be expanded in the form

$$\rho_{\text{non-dip}}(x) = \frac{5}{64x^5\eta\xi}\left[1 + \rho_2^{\text{nd}}x + \rho_3^{\text{nd}}x^{3/2} + \rho_4^{\text{nd}}x^2 + \mathcal{O}(5)\right], \tag{3.59a}$$

$$\rho_{\text{dip}}(x) = -\frac{25\mathcal{S}_-^2\zeta}{1536x^6\eta\xi^2}\left[1 + \rho_2^{\text{d}}x + \rho_3^{\text{d}}x^{3/2} + \rho_4^{\text{d}}x^2 + \mathcal{O}(5)\right]. \tag{3.59b}$$

The expressions for the coefficients ρ_n^{nd}, ρ_n^{d} are given in Eqs. (D.16) and (D.20) in Appendix D. Using the decomposition in Eq. (3.58), we integrate Eq. (3.44) and obtain the phase evolution

$$\varphi(x) = \varphi_{\text{non-dip}}(x) + \varphi_{\text{dip}}(x), \tag{3.60}$$

with

$$\varphi_{\text{non-dip}}(x) = -\frac{1}{32x^{5/2}\eta\xi}\left[1 + \frac{5}{3}\rho_2^{\text{nd}}x + \frac{5}{2}\rho_3^{\text{nd}}x^{3/2} + 5\rho_4^{\text{nd}}x^2 + \mathcal{O}(5)\right], \tag{3.61a}$$

$$\varphi_{\text{dip}}(x) = \frac{25\mathcal{S}_-^2\zeta}{5376x^{7/2}\eta\xi^2}\left[1 + \frac{7}{5}\rho_2^{\text{d}}x + \frac{7}{4}\rho_3^{\text{d}}x^{3/2} + \frac{7}{3}\rho_4^{\text{d}}x^2 + \mathcal{O}(5)\right], \tag{3.61b}$$

where we have ignored an arbitrary additive constant phase.

3.6 Spin-weighted spherical modes of the waveform

Combining the results of the previous sections, we present the gravitational waveform in a convenient form for use with GW detectors. First, we decompose the waveform h_{ij}^{TT} as given in Eq. (3.30) into its plus and cross polarizations. We

introduce the spherical coordinates (R, Θ, Φ) in the center-of-mass frame and define the usual orthonormal triad $\{\hat{\mathbf{N}}, \hat{\mathbf{P}}, \hat{\mathbf{Q}}\}$ where $\hat{\mathbf{N}} = \mathbf{e}_R$, and $\hat{\mathbf{P}}$ and $\hat{\mathbf{Q}}$ lie along the major and minor axes, respectively, of the projection of the orbital plane onto the plane of the sky. The plus and cross polarizations of the waveform are defined as the projections

$$h_+ = \frac{1}{2}\left(\hat{P}_i\hat{P}_j - \hat{Q}_i\hat{Q}_j\right) h_{ij}^{\mathrm{TT}}, \tag{3.62a}$$

$$h_\times = \frac{1}{2}\left(\hat{P}_i\hat{Q}_j + \hat{Q}_i\hat{P}_j\right) h_{ij}^{\mathrm{TT}}. \tag{3.62b}$$

We then decompose the waveform into spin-weighted spherical harmonics according to [260]

$$h_+ - ih_\times = \sum_{\ell\geq 2}\sum_{m=-\ell}^{\ell} {}_{-2}Y_{\ell m}(\Theta,\Phi) h_{\ell m}, \tag{3.63}$$

where the coefficients $h_{\ell m}$ are the spin-weighted spherical modes that we wish to compute.

We introduce, as in GR, a convenient new orbital phase variable that allows us to formally absorb the logarithms appearing in the polarizations $h_+, h_\times$:

$$\phi \equiv \varphi - \frac{2(1-\zeta)}{\alpha} x^{3/2}\left[\ln\left(4r_0\omega\right) + \gamma_{\mathrm{E}} - \frac{11}{12}\right], \tag{3.64}$$

where r_0 is the length scale associated with the transformation to radiative coordinates introduced in Sec. 3.4.1. This definition differs from its GR counterpart[7] [261] by only a factor of $(1-\zeta)/\alpha$. Note that the difference between ϕ and φ is of at least 3PN relative order because the leading-order term in the phase is formally $\mathcal{O}(-3)$

[7]Note that in the notation of Ref. [30] and references therein, this redefined phase is denoted by ψ. We instead use ϕ to avoid confusion with our $\psi = (m_1 - m_2)/M$.

in dipole-driven systems and $\mathcal{O}(-5)$ in quadrupole-driven systems. Given that we control the phasing of the binary only at 2PN relative order, we can ignore this correction.

For the mode amplitudes, we adopt the notation

$$h_{\ell m} \equiv \frac{2GM(1-\zeta)\eta x}{R}\sqrt{\frac{16\pi}{5}}\hat{H}_{\ell m}e^{-im\phi}, \tag{3.65}$$

where the appropriate phase factor is scaled out for each mode as well as the leading order amplitude of the 22 mode, which differs from its value in GR by only a factor of $1-\zeta$.

Because we consider only non-spinning binaries, and consequently, those on planar orbits, the modes obey the symmetry relation

$$h_{\ell m} = (-1)^{\ell} h^{*}_{\ell,-m}\,. \tag{3.66}$$

Thus, one needs only the modes with $m \geq 0$ to specify the waveform. Combining the results of the previous sections, we obtain at 2PN order for the quantities $\hat{H}_{\ell m}$[8]:

$$\begin{aligned}
\hat{H}_{2,2} =& 1 + x\left(\frac{4\beta_-\psi}{3} - \frac{4\beta_+}{3} - \frac{2\gamma}{3} + \frac{55\eta}{42} - \frac{107}{42}\right) \\
&+ x^{3/2}\left(-\frac{2\pi\zeta}{\alpha} + \frac{2\pi}{\alpha} - \frac{3}{2}i\zeta\eta\mathcal{S}_-^2 - \frac{1}{3}i\zeta\mathcal{S}_-^2 + \frac{1}{3}i\zeta\mathcal{S}_+^2\right) \\
&+ x^2\left(\frac{16\beta_-^2\eta}{\gamma} + \frac{16\beta_-^2\eta}{3} - \frac{4\beta_-^2}{3} + \frac{8\beta_-\beta_+\psi}{3} + \frac{19\beta_-\psi\eta}{7} - \frac{113\beta_-\psi}{63} - \frac{16\beta_+^2\eta}{\gamma}\right. \\
&\left. - \frac{16\beta_+^2\eta}{\gamma} - \frac{4\beta_+^2}{3} + \frac{23\beta_+\eta}{7} + \frac{113\beta_+}{63} - \frac{\gamma^2\eta}{3} + \frac{5\gamma^2}{12} - \frac{74\gamma\eta}{21} - \frac{\gamma}{21} + \frac{\psi\delta_-}{3}\right)
\end{aligned}$$

[8]Recall that our definition for $h^{\mu\nu}$ (3.14) introduces a sign difference relative to the results summarized in Ref. [30].

$$+\frac{4\psi\chi_-}{3}-\frac{4\delta_+\eta}{3}+\frac{\delta_+}{3}+\frac{2047\eta^2}{1512}+\frac{8\eta\chi_+}{3}-\frac{1069\eta}{216}-\frac{4\chi_+}{3}-\frac{2173}{1512}\Bigg) \tag{3.67a}$$

$$\begin{aligned}\hat{H}_{2,1}=&\frac{1}{3}i\psi\sqrt{x}\left[1+x\left(2\beta_-\psi-2\beta_++\frac{\gamma}{2}+\frac{5\eta}{7}-\frac{17}{28}\right)\right.\\&\left.+x^{3/2}\left(-\frac{\pi\zeta}{\alpha}+\frac{i\zeta}{2\alpha}+\frac{i\zeta\ln(16)}{2\alpha}+\frac{\pi}{\alpha}-\frac{i}{2\alpha}-\frac{i\ln(16)}{2\alpha}-\frac{4}{3}i\zeta\eta\mathcal{S}_-^2-\frac{4i\zeta\eta\mathcal{S}_-\mathcal{S}_+}{3\psi}\right)\right]\end{aligned} \tag{3.67b}$$

$$\begin{aligned}\hat{H}_{3,3}=&-\frac{3}{4}i\sqrt{\frac{15}{14}}\psi\sqrt{x}\left[1+x\left(2\beta_-\psi-2\beta_+-\gamma+2\eta-4\right)\right.\\&+x^{3/2}\left(-\frac{3\pi\zeta}{\alpha}+\frac{21i\zeta}{5\alpha}-\frac{6i\zeta\ln\left(\frac{3}{2}\right)}{\alpha}+\frac{3\pi}{\alpha}-\frac{21i}{5\alpha}+\frac{6i\ln\left(\frac{3}{2}\right)}{\alpha}-\frac{8}{9}i\zeta\eta\mathcal{S}_-^2\right.\\&\left.\left.-\frac{3}{10}i\zeta\mathcal{S}_-^2+\frac{8i\zeta\eta\mathcal{S}_-\mathcal{S}_+}{9\psi}+\frac{3}{10}i\zeta\mathcal{S}_+^2\right)\right]\end{aligned} \tag{3.67c}$$

$$\begin{aligned}\hat{H}_{3,2}=&\frac{x}{54\sqrt{35}}\left[90-270\eta+x\left(-720\beta_-\psi\eta+240\beta_-\psi+720\beta_+\eta-240\beta_+\right.\right.\\&\left.\left.-365\eta^2+725\eta-193\right)\right]\end{aligned} \tag{3.67d}$$

$$\begin{aligned}\hat{H}_{3,1}=&\frac{i\psi\sqrt{x}}{12\sqrt{14}}\left[1+x\left(2\beta_-\psi-2\beta_+-\gamma-\frac{2\eta}{3}-\frac{8}{3}\right)\right.\\&+x^{3/2}\left(-\frac{\pi\zeta}{\alpha}+\frac{7i\zeta}{5\alpha}+\frac{2i\zeta\ln(2)}{\alpha}+\frac{\pi}{\alpha}-\frac{7i}{5\alpha}-\frac{2i\ln(2)}{\alpha}-\frac{40}{3}i\zeta\eta\mathcal{S}_-^2\right.\\&\left.\left.-\frac{1}{10}i\zeta\mathcal{S}_-^2+\frac{8i\zeta\eta\mathcal{S}_-\mathcal{S}_+}{3\psi}+\frac{1}{10}i\zeta\mathcal{S}_+^2\right)\right]\end{aligned} \tag{3.67e}$$

$$\begin{aligned}\hat{H}_{4,4}=&\frac{4x}{297\sqrt{35}}\left[990\eta-330+x\left(2640\beta_-\psi\eta-880\beta_-\psi-2640\beta_+\eta+880\beta_+\right.\right.\\&\left.\left.-1320\gamma\eta+440\gamma+2625\eta^2-6365\eta+1779\right)\right]\end{aligned} \tag{3.67f}$$

$$\hat{H}_{4,3}=\frac{9i\psi(2\eta-1)x^{3/2}}{4\sqrt{70}} \tag{3.67g}$$

$$\begin{aligned}\hat{H}_{4,2}=&-\frac{1}{63}\sqrt{5}x\left[3\eta-1+x\left(8\beta_-\psi\eta-\frac{8\beta_-\psi}{3}-8\beta_+\eta+\frac{8\beta_+}{3}-4\gamma\eta+\frac{4\gamma}{3}\right.\right.\\&\left.\left.+\frac{19\eta^2}{22}-\frac{805\eta}{66}+\frac{437}{110}\right)\right]\end{aligned} \tag{3.67h}$$

$$\hat{H}_{4,1}=-\frac{i\psi(2\eta-1)x^{3/2}}{84\sqrt{10}} \tag{3.67i}$$

$$\hat{H}_{5,5} = -\frac{625i\psi(2\eta-1)x^{3/2}}{96\sqrt{66}} \tag{3.67j}$$

$$\hat{H}_{5,4} = -\frac{32\left(5\eta^2-5\eta+1\right)x^2}{9\sqrt{165}} \tag{3.67k}$$

$$\hat{H}_{5,3} = \frac{9}{32}i\sqrt{\frac{3}{110}}\psi(2\eta-1)x^{3/2} \tag{3.67l}$$

$$\hat{H}_{5,2} = \frac{2\left(5\eta^2-5\eta+1\right)x^2}{27\sqrt{55}} \tag{3.67m}$$

$$\hat{H}_{5,1} = -\frac{i\psi(2\eta-1)x^{3/2}}{288\sqrt{385}} \tag{3.67n}$$

$$\hat{H}_{6,6} = \frac{54\left(5\eta^2-5\eta+1\right)x^2}{5\sqrt{143}} \tag{3.67o}$$

$$\hat{H}_{6,5} = 0 \tag{3.67p}$$

$$\hat{H}_{6,4} = -\frac{128}{495}\sqrt{\frac{2}{39}}\left(5\eta^2-5\eta+1\right)x^2 \tag{3.67q}$$

$$\hat{H}_{6,3} = 0 \tag{3.67r}$$

$$\hat{H}_{6,2} = \frac{2\left(5\eta^2-5\eta+1\right)x^2}{297\sqrt{65}} \tag{3.67s}$$

$$\hat{H}_{6,1} = 0, \tag{3.67t}$$

where we omit the common remainder $\mathcal{O}(5)$ for all modes.

The $h_{\ell m}$ modes with $m = 0$ correspond to non-oscillatory memory terms. As discussed in Sec. 3.4.3, even systems presently driven by quadrupolar radiation will have undergone a dipole-driven phase in the distant past, which complicates the calculation of these DC memory terms. Hence, we limit ourselves to the dipole-driven case and use Eq. (3.42). Working at Newtonian order, the only non-zero mode is h_{20}, which reads

$$\hat{H}^{\rm DD}_{2,0} = \frac{1}{4\sqrt{6}} + \mathcal{O}(2). \tag{3.68}$$

3.7 Stationary phase approximation

In this section, we compute the Fourier transform of the gravitational waveform using the stationary phase approximation (SPA). This technique is only applicable to oscillatory modes; we do not consider the $m = 0$ modes here.

We adopt the following convention for the Fourier transform of a function g:

$$\tilde{g}(f) \equiv \int_{-\infty}^{+\infty} \mathrm{d}t\, e^{+2i\pi ft} g(t). \tag{3.69}$$

Note that this convention differs from the standard one, in which the argument of the exponential has a minus sign. Our convention ensures that modes proportional to $e^{-im\varphi}$ with positive mode number m and increasing orbital phase φ have power in positive frequencies in the Fourier domain. Our results can be converted to the more common convention by taking $f \to -f$.

Combining the terms in Eq. (3.65), the $h_{\ell m}$ modes can be written as

$$h_{\ell m}(t) = A_{\ell m}(t) e^{-im\varphi(t)}, \tag{3.70}$$

where $A_{\ell m}$ is the (complex) amplitude. Note that we use φ to describe the phase rather than ϕ defined in Eq. (3.64) — we ignore the 3PN correction $\phi - \varphi$, which can be thought of as a small phase correction to the amplitude at higher order than we work.

The $h_{\ell m}$ modes for $m \neq 0$ are rapidly oscillatory, slowly chirping signals. Put more precisely, during the inspiral, the modes satisfy $|\dot{A}_{\ell m}/A_{\ell m}| \ll \omega$ and $|\dot{\omega}| \ll \omega^2$, which indicates that the SPA is applicable to the waveform [262]. Applying the

Fourier transform (3.69) to Eq. (3.70) gives

$$h^{\rm SPA}_{\ell m}(f) = \mathcal{A}_{\ell m}(f) e^{-i\Psi_{\ell m}(f) - i\pi/4}\,, \tag{3.71a}$$

$$\Psi_{\ell m}(f) = m\varphi(t^{(m)}_f) - 2\pi f t^{(m)}_f\,, \tag{3.71b}$$

$$\mathcal{A}_{\ell m}(f) = A_{\ell m}(t^{(m)}_f)\sqrt{\frac{2\pi}{m\dot{\omega}(t^{(m)}_f)}}, \tag{3.71c}$$

where $\omega = \dot{\varphi}$ and $t^{(m)}_f$ is defined implicitly as the time at which $m\omega(t^{(m)}_f) = 2\pi f$. Note the m-dependence of this time-to-frequency correspondence; at a given time, the different harmonics in the signal correspond to gravitational wave emission at different frequencies.

In keeping with the notation common in the literature, we introduce the new PN tracking parameter $v = x^{1/2} = (GM\alpha\omega)^{1/3}$, tied to the orbital frequency ω. It is customary to introduce a similar notation for the frequency f as $v_f = (\pi GM\alpha f)^{1/3}$. Since $v(t^{(m)}_f) = (2/m)^{1/3} v_f$, Eq. (3.71b) can be rewritten as

$$\Psi_{\ell m}(f) = m\left(\varphi(v) - \frac{1}{GM\alpha} v^3 t(v)\right)\Big|_{v=(2/m)^{1/3}v_f}. \tag{3.72}$$

We compute the functions $\varphi(v)$ and $t(v)$ using a similar method to the phasing as in Eq. (3.44). From the balance equation (3.44) we deduce

$$\varphi(v) = \varphi(v_0) - \frac{1}{GM\alpha}\int_{v_0}^{v} \mathrm{d}v\, v^3 \frac{\mathrm{d}E/\mathrm{d}v}{\mathcal{F}(v)}, \tag{3.73a}$$

$$t(v) = t(v_0) - \int_{v_0}^{v} \mathrm{d}v\, \frac{\mathrm{d}E/\mathrm{d}v}{\mathcal{F}(v)}, \tag{3.73b}$$

where v_0 is related to the orbital frequency at some reference point in the evolution. Likewise, the factor entering the Fourier-domain amplitude (3.71c) is computed using

$$\frac{1}{\dot{\omega}} = -\frac{GM\alpha}{3v^2}\frac{1}{\mathcal{F}(v)}\frac{\mathrm{d}E}{\mathrm{d}v}. \tag{3.74}$$

We evaluate Eqs. (3.73) and (3.74) using a prescription akin to that in Sec. 3.5 (corresponding now to the TaylorF2 approximant [259]): the expressions are re-expanded in v, truncated at relative 2PN order, and then integrated term by term. For the sake of compactness, we write $\varphi(v)$, $t(v)$, and $1/\dot{\omega}$ in terms of the expansion of the dimensionless ratio $\rho(x)$ introduced in Eq. (3.47), using

$$-\frac{1}{GM\alpha}\frac{1}{\mathcal{F}(v)}\frac{\mathrm{d}E}{\mathrm{d}v} = 2v\rho(v^2). \tag{3.75}$$

3.7.1 The dipole-driven regime

For the dipole-driven regime, we insert Eq. (3.75) into Eq. (3.73) using the expansion (3.49) and integrate, yielding

$$\varphi^{\mathrm{DD}}(v) = \frac{-1}{4\mathcal{S}_-^2\zeta\eta v^3}\left[1 + 3\rho_2^{\mathrm{DD}}v^2 - 3\rho_3^{\mathrm{DD}}v^3\ln v - 3\rho_4^{\mathrm{DD}}v^4\right], \tag{3.76a}$$

$$\frac{t^{\mathrm{DD}}(v)}{GM\alpha} = \frac{-1}{8\mathcal{S}_-^2\zeta\eta v^6}\left[1 + \frac{3}{2}\rho_2^{\mathrm{DD}}v^2 + 2\rho_3^{\mathrm{DD}}v^3 + 3\rho_4^{\mathrm{DD}}v^4\right], \tag{3.76b}$$

where we have dropped the integration constants for now.

Combining these two expressions gives the SPA phase (3.72)

$$\Psi_{\ell m}^{\mathrm{DD}}(f) = -\frac{m}{8\mathcal{S}_-^2\zeta\eta v^3}\left[1 + \frac{9}{2}\rho_2^{\mathrm{DD}}v^2 - 2\rho_3^{\mathrm{DD}}v^3(1+3\ln v) - 9\rho_4^{\mathrm{DD}}v^4\right] + m\varphi_0 - 2\pi f t_0\,, \tag{3.77}$$

where v is evaluated at $v = (2/m)^{1/3}v_f$, and where we restored constants t_0 and φ_0 which are the sums of $\varphi(v_0)$, $t(v_0)$ with the terms from the lower boundary of the integrals. The coefficients ρ_n^{DD} are given in Eq. (D.6).

Similarly, the complex amplitude is given by

$$\mathcal{A}^{\rm DD}_{\ell m}(f) = \frac{2G^2(1-\zeta)M^2\alpha\pi\eta^{1/2}}{R\zeta^{1/2}|\mathcal{S}_-|}\sqrt{\frac{4}{5}}\sqrt{\frac{2}{m}}\frac{\hat{H}_{\ell m}(v)}{v^{5/2}}\left[1+\frac{1}{2}v^2\rho^{\rm DD}_2+\frac{1}{2}v^3\rho^{\rm DD}_3 + \frac{1}{2}v^4\left(\rho^{\rm DD}_4-\frac{1}{4}(\rho^{\rm DD}_2)^2\right)\right], \tag{3.78}$$

where $\hat{H}_{\ell m}(v)$ is given by Eq. (3.67) with the replacement $x = v^2$ and, as before, v is evaluated at $v = (2/m)^{1/3}v_f$.

Note that because $\hat{H}_{\ell m}$ are complex they can affect the phase of the waveform. In particular, they can carry an overall minus sign or factor $\pm i$, which should be included in the phase of the mode. In addition, higher-order terms can have a factor $\pm i$ differing from the one entering at leading order, which induce corrective phases. However, those phases turn out to be negligible, entering at higher PN order than the 2PN relative order we consider.

3.7.2 The quadrupole-driven regime

We follow the same treatment for the quadrupole-driven systems as laid out in Sec. 3.5.2: we split the flux into dipolar and non-dipolar parts, and expand $\rho(v)$ to first order in the ratio $\mathcal{F}_{\rm dip}/\mathcal{F}_{\text{non-dip}}$ according to Eq. (3.54). The first and second terms in Eq. (3.54) produce a non-dipolar and dipolar contribution, respectively, to the phase and amplitude of the SPA waveform.

The non-dipolar contribution to the phasing is constructed by inserting Eq. (3.75) into the integrals in Eq. (3.73) and using the expansion (3.59a). Ignoring

the integration constants for now, we find

$$\varphi^{\text{non-dip}}(v) = -\frac{1}{32v^5\eta\xi}\left[1+\frac{5}{3}\rho_2^{\text{nd}}v^2+\frac{5}{2}\rho_3^{\text{nd}}v^3+5\rho_4^{\text{nd}}v^4+\mathcal{O}(5)\right], \tag{3.79a}$$

$$\frac{t^{\text{non-dip}}(v)}{GM\alpha} = -\frac{5}{256v^8\eta\xi}\left[1+\frac{4}{3}\rho_2^{\text{nd}}v^2+\frac{8}{5}\rho_3^{\text{nd}}v^3+2\rho_4^{\text{nd}}v^4+\mathcal{O}(5)\right], \tag{3.79b}$$

and thus, the corresponding contribution to the Fourier-domain phase for the $h_{\ell m}$ mode is given by

$$\Psi_{\ell m}^{\text{non-dip}}(f) = m\left[-\frac{3}{256v^5\eta\xi}\left(1+\frac{20}{9}\rho_2^{\text{nd}}v^2+4\rho_3^{\text{nd}}v^3+10\rho_4^{\text{nd}}v^4\right)\right]\Big|_{v=(2/m)^{1/3}v_f}. \tag{3.80}$$

Similarly, we use Eq. (3.59b) to compute the contribution to the phasing from the dipolar energy flux

$$\varphi^{\text{dip}}(v) = \frac{25\mathcal{S}_-^2\zeta}{5376v^7\eta\xi^2}\left[1+\frac{7}{5}\rho_2^{\text{d}}v^2+\frac{7}{4}\rho_3^{\text{d}}v^3+\frac{7}{3}\rho_4^{\text{d}}v^4+\mathcal{O}(5)\right], \tag{3.81a}$$

$$\frac{t^{\text{dip}}(v)}{GM\alpha} = \frac{5\mathcal{S}_-^2\zeta}{1536v^{10}\eta\xi^2}\left[1+\frac{5}{4}\rho_2^{\text{d}}v^2+\frac{10}{7}\rho_3^{\text{d}}v^3+\frac{5}{3}\rho_4^{\text{d}}v^4+\mathcal{O}(5)\right], \tag{3.81b}$$

$$\Psi_{\ell m}^{\text{dip}}(f) = m\left[\frac{5\mathcal{S}_-^2\zeta}{3584v^7\eta\xi^2}\left(1+\frac{7}{4}\rho_2^{\text{d}}v^2+\frac{5}{2}\rho_3^{\text{d}}v^3+\frac{35}{9}\rho_4^{\text{d}}v^4\right)\right]\Big|_{v=(2/m)^{1/3}v_f}. \tag{3.81c}$$

Combining these two pieces and restoring the constants φ_0 and t_0, the Fourier-domain phase is then simply

$$\Psi_{\ell m}^{\text{QD}}(f) = \Psi_{\ell m}^{\text{non-dip}}(f) + \Psi_{\ell m}^{\text{dip}}(f) + m\varphi_0 - 2\pi f t_0. \tag{3.82}$$

The coefficients ρ_n^{nd} and ρ_n^{d} are given in Eqs. (D.16) and (D.20). When restricted to Brans-Dicke theory, Eq. (3.82) reproduces the leading order deviation in the phase from GR derived in Ref. [240] at order $\mathcal{O}(1/\omega_{\text{BD}})$, which is equivalent to first order in $\mathcal{F}_{\text{dip}}/\mathcal{F}_{\text{non-dip}}$. For systems containing a very massive black hole, i.e.,

$s_1 = 1/2$, $s_1' = s_1'' = 0$ and $m_1 \gg m_2$, we recover the phase up to 2PN relative order derived in Ref. [263].

The computation of the Fourier-domain amplitude closely follows that of the dipole-driven regime. In place of $\sqrt{\rho(v)}$, one instead uses

$$\sqrt{\rho(v)} \simeq \sqrt{\rho^{\text{non-dip}}(v)} \left[1 + \frac{1}{2} \frac{\rho^{\text{dip}}(v)}{\rho^{\text{non-dip}}(v)}\right]. \tag{3.83}$$

Finally, one re-expands this expression using Eqs. (3.59a) and (3.59b) and inserts the result in to Eq. (3.71c).

3.8 Conclusions

We have computed the gravitational waveform at 2PN relative order for a compact binary system on quasi-circular orbits in scalar-tensor theories with a single massless scalar. The phase and amplitude are presented in ready-to-use form for all h_{lm} modes. We used the stationary phase approximation to express the waveform in Fourier space. We performed these calculations for systems whose inspiral is driven by the emission of dipolar radiation and those driven by quadrupolar flux. Because of the tight constraints on scalar-tensor gravity, only very low-frequency systems (e.g., binary pulsars) or those that host non-perturbative scalarization phenomena (e.g., spontaneous or dynamical scalarization) fall within this first regime — most prospective GW sources will be quadrupolar-driven.

We conclude with a brief discussion of the potential utility of our results for testing GR with GWs. The early inspiral offers the best prospects for detecting the emission of dipolar radiation by compact binary systems, as radiation reac-

tion enters at lower PN order in scalar-tensor theories than in GR. Thus, the best constraints would come from observation of neutron star-black hole binaries with space-based detectors.[9] Current estimates on the detectability of scalar-tensor effects have predominantly been made using the leading-order correction to the GW phase [240, 264–267] (although Ref. [263] used 3.5PN scalar-tensor waveforms in studying extreme mass ratio inspirals).

Using Eq. (3.82), we estimate the upper bound on the contribution of each PN correction to the phase. We consider the phase accumulated by a $100 - 1.4M_\odot$ system during an observation period of one year, spanning the frequency range $f \in (0.065\text{Hz}, 1\text{Hz})$, subject to the experimental constraints discussed in Sec. 3.2.2. Relative to the 7.7×10^6 cycles produced by the Newtonian-order GR term, the leading-order scalar-tensor correction decreases the phase by up to ~ 600 GW cycles.[10] The 1PN relative order correction increases the total phase by another ~ 2 cycles, although this piece would be difficult to detect, as it takes the same form as the leading-order GR term. The 1.5PN relative order correction adds ~ 3 GW cycles to the inspiral, and the 2PN order effect is below the limit of eLISA detectability, only contributing ~ 0.1 cycles over the year. We emphasize that these values are only an order-of-magnitude estimate of the possible impact of higher-order scalar-tensor corrections; a more extensive parameter estimation study is needed to truly

[9] Up to 2PN order, the signal produced by binary black holes is known to be identical to that in GR up to an undetectable rescaling of the gravitational constant G. [150]

[10] Note that this bound comes from assuming a neutron-star scalar charge of $\alpha_A \sim 6 \times 10^{-3}$, whereas Refs. [240, 264–267] considered the maximum charge found in Brans-Dicke gravity $\alpha_A \sim 2 \times 10^{-3}$.

determine the detectability of these effects.

3.9 Acknowledgements

We are grateful to Ryan Lang for providing a *Mathematica* notebook containing the results of Ref. [151] and to Lijing Shao for useful discussions concerning current binary pulsar constraints. N.S. acknowledges support from NSF Grant No. PHY-1208881. S.M. acknowledges support from NASA grant 11-ATP-046 and NASA grant NNX12AN10G at the University of Maryland, College Park. N.S. thanks the Max Planck Institute for Gravitational Physics for its hospitality during the completion of this work.

Chapter 4: Modeling dynamical scalarization with a resummed post-Newtonian expansion

Authors: *Noah Sennett and Alessandra Buonanno*[1]

Abstract: Despite stringent constraints set by astrophysical observations, there remain viable scalar-tensor theories that could be distinguished from general relativity with gravitational-wave detectors. A promising signal predicted in these alternative theories is dynamical scalarization, which can dramatically affect the evolution of neutron-star binaries near merger. Motivated by the successful treatment of spontaneous scalarization, we develop a formalism that partially resums the post-Newtonian expansion to capture dynamical scalarization in a mathematically consistent manner. We calculate the post-Newtonian order corrections to the equations of motion and scalar mass of a binary system. Through comparison with quasi-equilibrium configuration calculations, we verify that this new approximation scheme can accurately predict the onset and magnitude of dynamical scalarization.

[1]Originally published as Phys. Rev. **D93**, 124004 (2016).

4.1 Introduction

The detection of gravitational-wave (GW) event GW150914 by Advanced LIGO heralds a new era of experimental relativity [184]. Every test of the past hundred years has indicated that gravity behaves as predicted by general relativity (GR). Until now, the best constraints have come from solar-system experiments [79] and binary-pulsar observations [89, 249]. These measurements probe the mildly-relativistic, strong-field regime of gravity generated by objects with velocities $v/c \lesssim 10^{-3}$ and gravitational fields $\Phi_{\rm Newt}/c^2 \lesssim 10^{-1}$ (see Table 4 of Ref. [79] for a summary of model-independent constraints).

For the first time, these constraints can be extended through the direct observation of strong, dynamical gravitational fields. In particular, GW detectors can track the coalescence of compact objects in binary systems, a process in which the objects are highly-relativistic and strongly self-gravitating, with $v/c \sim 0.5$ and $\Phi_{\rm Newt}/c^2 \sim 0.5$. We expect to observe several GWs per year [229, 231] with the upcoming global network of detectors comprised of Advanced LIGO [230], advanced Virgo [64], and KAGRA [233].

These ground-based GW detectors will be able to observe binaries of solar-mass objects for thousands of orbital cycles before merger. Significant effort has gone into the development of techniques to test GR with these measurements; see Refs. [88, 268] and references therein. During the first stage of a binary's coalescence (the early inspiral), the waveform measured by the detector is well described within the stationary-phase approximation. The waveform generated in GR for the early

inspiral can be approximated by

$$h_{\rm GR}(\boldsymbol{\theta}; f) = \frac{\mathcal{A}(\boldsymbol{\theta})}{D} f^{-7/6} e^{i\psi(\boldsymbol{\theta}; f)}, \tag{4.1}$$

where f is the observed frequency, D is the distance to the binary, and $\mathcal{A}$ and ψ are the amplitude and phase of the GW, respectively, dependent on the intrinsic (e.g. chirp mass, component spins, etc.) and extrinsic (e.g. sky position, time of coalescence, etc.) parameters of the binary, represented collectively by $\boldsymbol{\theta}$.

Using this signal as a baseline, one can parameterize any non-GR waveform in the early inspiral as

$$h(\boldsymbol{\theta}; f) = h_{\rm GR}(\boldsymbol{\theta}; f)\,(1 + \delta\mathcal{A}(\boldsymbol{\theta}, \boldsymbol{\zeta}; f))\, e^{i\delta\psi(\boldsymbol{\theta}, \boldsymbol{\zeta}; f)} \tag{4.2}$$

where $\boldsymbol{\zeta}$ represents the parameters that characterize the alternative theory [117, 118]. Then, given a GW detection, Bayesian inference can be used to estimate $\delta\mathcal{A}$ and $\delta\psi$ [120, 213, 214, 269–271]. Typically one expands these functions in powers of the frequency f (and its logarithm $\log f$), then performs a hypothesis test to constrain the corresponding expansion coefficients. This approach can be used either to search for generic deviations from GR by treating these coefficients independently or to test a specific alternative theory against GR by relating the coefficients to the underlying physical parameters $\boldsymbol{\zeta}$. Using a parameterized waveform that also included the merger and ringdown signal, both types of tests were done for GW150914 in Ref. [122]: with the former, the authors constrained the higher-order expansion coefficients in $\delta\psi$, and with the latter, they placed a lower bound on the Compton wavelength λ_g of the graviton in a hypothetical massive gravity theory [111] (λ_g is signified by $\boldsymbol{\zeta}$ in our notation).

However, this type of analysis rests on the assumption that $\delta\mathcal{A}$ and $\delta\psi$ admit expansions in powers of f. There exist certain alternative theories of gravity where this assumption of analyticity breaks down due to phase transitions or resonant effects [271]. Fortunately, several complementary tests were performed in Ref. [122] to verify that GW150914 is indeed consistent with GR. Still, our ability to model non-analytic features in waveforms is essential in case future events do not match the predictions of GR as closely.

The task of modeling a non-analytic deviation $\delta\psi$ in a generic, theory-independent way is intractable. Instead, previous work has focused on modeling specific non-GR phenomena predicted in particular alternative theories of gravity. We continue this effort here, focusing on dynamical scalarization (DS), an effect that can arise in neutron-star binaries in certain scalar-tensor (ST) theories of gravity [169, 171]. Previous efforts to model this effect have simply grafted models of DS onto independently developed analytic approximations of the inspiral [170, 175, 271]. In this work, we propose a new perturbative formalism that incorporates DS from first principles. Our aim is to lay the groundwork for a model whose accuracy can be improved iteratively in a way that is more straightforward and self-consistent than previous methods.

The paper is organized as follows. In Sec. 4.2, we examine the relationship between DS and the better understood phenomenon of spontaneous scalarization. From this discussion, we motivate a resummation of the post-Newtonian formalism to incorporate DS, which is then developed in Sec. 4.3. We derive the equations of motion for a neutron-star binary up to next-to-leading order in Secs. 4.4 and

4.5. In Secs. 4.6 and 4.7, we calculate its scalar mass (a measure of the system's scalarization) at the same order. As a test of its validity, in Sec. 4.8, we compare our model with numerical quasi-equilibrium configurations of neutron stars [172] and previous analytical models [170]. We provide a summary in Sec. 4.9 and outline the future work needed to produce waveforms with our model.

4.2 Non-perturbative phenomena in scalar-tensor gravity

Scalar-tensor theories of gravity are amongst the most natural and well-motivated alternatives to GR. We consider the class of theories detailed in Ref. [147], in which a massless scalar field couples non-minimally to the metric, effectively allowing a spin-0 polarization of the graviton. These theories are described by the action

$$S = \int d^4x \frac{c^3\sqrt{-g}}{16\pi G}\left[\phi R - \frac{\omega(\phi)}{\phi} g^{\mu\nu}\nabla_\mu\phi\nabla_\nu\phi\right] + S_m[g_{\mu\nu}, \Xi], \tag{4.3}$$

where Ξ represents all of the matter degrees of freedom in the theory. Note that in the limit that $\omega \to \infty$, the scalar field relaxes to a constant value, and the theory reduces to GR with the modified gravitational constant $G_{\rm eff} = G/\phi$; we refer to this extreme as the GR limit.

The form of the action in Eq. (4.3) is known as the "Jordan frame" action. Alternatively, the action can be cast into the "Einstein frame" by performing a conformal transformation $\tilde{g}_{\mu\nu} \equiv \phi g_{\mu\nu}$ as

$$S = \int d^4x \frac{c^3\sqrt{-\tilde{g}}}{16\pi G}\left[\tilde{R} - 2\tilde{g}^{\mu\nu}\nabla_\mu\tilde{\varphi}\nabla_\nu\tilde{\varphi}\right] + S_m\left[e^{-\int 2d\tilde{\varphi}/\sqrt{3+2\omega(\tilde{\varphi})}}\tilde{g}_{\mu\nu}, \Xi\right], \tag{4.4}$$

where we have introduced the scalar field

$$\tilde{\varphi} \equiv \int d\phi \frac{\sqrt{3+2\omega(\phi)}}{2\phi}. \tag{4.5}$$

From Eq. (4.4), we see that the coupling of the scalar field to matter (through the metric $\tilde{g}_{\mu\nu}$) is characterized by

$$a = (3+2\omega)^{-1/2}. \tag{4.6}$$

Measurable phenomena absent in GR arise in theories whose coupling is linear in $\tilde{\varphi}$

$$a = \frac{B\tilde{\varphi}}{2}. \tag{4.7}$$

This coupling can be expressed in terms of Jordan frame variables as

$$\frac{1}{\omega(\phi)+3/2} = B\log\phi, \tag{4.8}$$

and imposes the relation between ϕ and $\tilde{\varphi}$

$$\phi = \exp(B\tilde{\varphi}^2/2). \tag{4.9}$$

Damour and Esposito-Farèse discovered an instability in the scalar field triggered by the presence of relativistic matter in theories with $B > 0$ [153].[2] For

[2]Based off the work of Refs. [152, 272, 273], the authors of Ref. [175] recently discussed a related instability in this theory that would cause the scalar field to grow rapidly over cosmological timescales throughout the Universe. Consequently, the scalar field today would be so large that its presence would have already been detected by solar-system experiments. The addition of a potential $V(\phi)$ or slight modification of $\omega(\phi)$ could ameliorate this issue while preserving the neutron star phenomena discussed in this work (for example, see Ref. [161]). As is done in the literature, we ignore here this cosmological problem.

sufficiently large B, compact neutron stars were found to undergo a phase transition now known as spontaneous scalarization. Spontaneously scalarized stars are expected to behave differently than their (un-scalarized) GR counterparts (see Refs. [274–278] for examples of such deviations).

Observation of a scalarized star would be a smoking gun for modifying gravity; in turn, our lack of evidence for such stars places constraints on this class of ST theories [247]. Because scalarization arises from the non-linear interaction between strong gravitational fields and matter, it is unconstrained by weak-field experiments and GW150914. However, pulsar timing measurements have ruled out nearly all theories that can sustain spontaneous scalarization [247].

Dynamical scalarization is a similar phenomenon revealed by recent numerical-relativity simulations that is not ruled out by binary-pulsar observations [169, 171]. In a binary system, neutron stars too diffuse to spontaneously scalarize in isolation were found to scalarize collectively. Despite the name, DS has also been found in recent quasi-equilibrium calculations [172]; the phenomenon is caused by the proximity of the neutron stars rather than their dynamical evolution. The onset of DS produces an abrupt change in the stars' motion, generating sharp features in the GW signal produced by the binary.

Gravitational-wave detectors may be able to extend the current constraints on ST theories by searching for DS [175]. This endeavor hinges on our ability to accurately and efficiently model GWs from binaries that undergo DS. Such effects have been modeled by using a Heaviside function for $\delta\psi$ in Eq. (4.2) [175, 271] or augmenting the post-Newtonian (PN) evolution of the binary with a semi-analytic

feedback model [170]. This work follows a general strategy similar to that of Ref. [170]. However, we adopt a top-down approach to incorporate DS into the PN formalism in hopes of creating a model that is more consistent and streamlined conceptually (see Appendix G for a detailed analysis of the results of Ref. [170]).

The PN expansion is an effective tool for analytically approximating the evolution of binary systems of interest to ground-based GW detectors. In this approach, one expands solutions to the Einstein equations about flat space in the small parameter $\epsilon \sim GM/rc^2 \sim (v/c)^2 < 1$, where M, r, v represent the characteristic mass, distance, and velocity scales in the problem, respectively. In ST theories, this expansion is done about the Minkowski metric $\eta_{\mu\nu}$ and background field ϕ_0 (assumed to be constant and homogeneous over the time and distance scales of the evolution of a binary system). We refer to the ϵ^{n+1} corrections to these quantities as the "nPN" fields. We define *non-perturbative phenomena* as behavior found in the full gravitational theory that cannot be recovered at any finite PN order.

In the remainder of this section, we argue that DS is a non-perturbative phenomenon. First, we review the analytic treatment of spontaneous scalarization, describing the way in which the phenomenon has been identified as non-perturbative and then incorporated into the PN expansion in a rigorous manner. We then perform a similar analysis for DS and present a quantitative argument that the phenomenon is non-perturbative. Finally, we describe how the analytic treatment of spontaneous scalarization could be adapted to incorporate DS into the PN formalism.

4.2.1 Spontaneous scalarization: single neutron star

In ST theories, static, spherically symmetric spacetimes are characterized by three parameters: the asymptotic field ϕ_0, the Arnowitt-Deser-Misner (ADM) mass m, and the scalar charge α [147, 279]. These parameters can be extracted from the asymptotic behavior of the metric and scalar field

$$\lim_{|\mathbf{x}|\to\infty} g_{ij} = \left(1 + \frac{2Gm}{|\mathbf{x}|c^2}\right)\delta_{ij} + \mathcal{O}\left(|\mathbf{x}|^{-2}\right), \tag{4.10}$$

$$\lim_{|\mathbf{x}|\to\infty} \phi = \phi_0 + \frac{2G\mu_0 m\alpha}{|\mathbf{x}|c^2} + \mathcal{O}\left(|\mathbf{x}|^{-2}\right), \tag{4.11}$$

where we have defined

$$\mu_0 \equiv \frac{1}{\sqrt{3+2\omega(\phi_0)}} = \sqrt{\frac{B\log\phi_0}{2}}. \tag{4.12}$$

It was shown in Ref. [147] that the scalar charge of an isolated star can be written in the PN expansion as

$$\alpha = \mu_0\left[1 + A_1\left(\frac{Gm}{Rc^2}\right) + A_2\left(\frac{Gm}{Rc^2}\right)^2 + \cdots\right], \tag{4.13}$$

where R is the radius of the body, and the coefficients A_i are of order unity. Because μ_0 vanishes in the GR limit, one finds that the right hand side of Eq. (4.13), truncated at any finite order, must vanish as well. However, as first discovered in Ref. [153], exactly solving the geometry numerically shows that a sufficiently compact body can sustain an appreciable scalar charge even when $\mu_0 = 0$ (corresponding to the GR limit $\phi_0 = 1$).[3] Thus, we would describe this scalarization as non-perturbative (in the sense defined above). Figure 4.1 depicts the sharp growth in

[3]Because of the additional prefactor of μ_0, the $|\mathbf{x}|^{-1}$ term in Eq. (4.11) vanishes even for

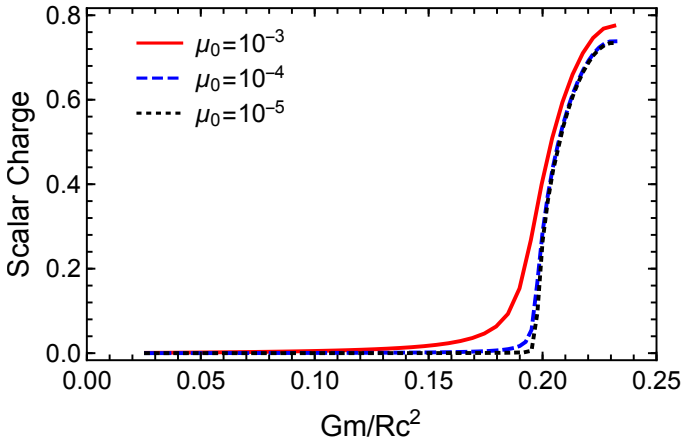

Figure 4.1: The scalar charge of an isolated non-spinning neutron star as a function of its compactness in the limit that μ_0 approaches zero (the GR limit). We use the theory parameter $B = 9$ with a piecewise polytropic fit to the APR4 equation of state detailed in Ref. [206].

scalar charge in the limit $\mu_0 \to 0$ as one increases the compactness of a neutron star. For this figure and all that follow, we use a piecewise polytropic fit [206] to the APR4 equation of state given in Ref. [280].

The tension between the analytic and numerical results suggests that the PN expansion must break down beyond some compactness Gm/Rc^2 for this class of ST theories. The scalar charge is non-analytic at this critical compactness, at which point the isolated body undergoes a phase transition. Analogous to ferromagnetism, the derivative of the charge diverges when μ_0 approaches zero, indicating that this transition is of second order. Beyond the critical point, the vanishing of μ_0 in the GR limit is compensated by the divergence of the bracketed sum in Eq. (4.13). The only

spontaneously scalarized stars in the GR limit. The dramatic effect of spontaneous scalarization is more easily seen through $\tilde{\varphi}$ [given in Eq. (4.9)], which can be approximated as $\tilde{\varphi} = \tilde{\varphi}_0 + \frac{Gm\alpha}{|\mathbf{x}|c^2} + \mathcal{O}\left(|\mathbf{x}|^{-2}\right)$, where $\phi_0 = \phi(\tilde{\varphi}_0)$.

astrophysical objects that could reach this critical compactness are neutron stars and black holes. However, no-hair theorems protect isolated black holes from developing a scalar charge [23]. We focus exclusively on neutron stars for the remainder of this work.

In anticipation of our discussion of dynamical scalarization, we briefly review how spontaneous scalarization is incorporated into analytic models of binary pulsars. A binary system of non-spinning stars is characterized by two length scales: the characteristic size of the bodies R and their separation r. As in the case of an isolated body, the individual stars can spontaneously scalarize if they exceed some critical compactness, at which point the PN expansion no longer accurately predicts the evolution of the binary. Damour and Esposito-Farèse developed the "post-Keplerian" (PK) expansion to accommodate such systems [147, 208] (not to be confused with the "parameterized post-Keplerian" formalism for modeling binary pulsars in generic alternative theories [281]). In the PK approach, one expands only in Gm/rc^2, leaving quantities dependent on R unexpanded (e.g the scalar charge α). Equivalently, one can recombine the sum in powers of Gm/Rc^2 in the PN expansion to produce the PK expansion. The relationship between the PN and PK expansions is summarized in the bottom two panels of Fig. 4.2 (the remaining panels are discussed in Sec. 4.2.2). Spontaneous scalarization is captured by explicitly including all of the terms in Eq. (4.13) at each order in the PK expansion.

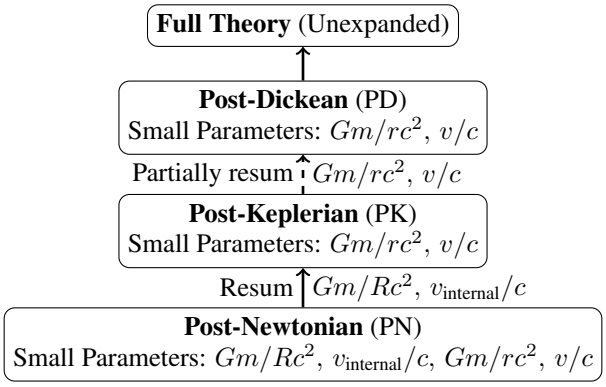

Figure 4.2: Analytic approximations of ST theories. Starting from the PN expansion about the Minkowski metric $\eta_{\mu\nu}$ and the background field ϕ_0, one resums all expansions in the compactness Gm/Rc^2 and associated internal velocity $v_{\rm Internal}/c$ to capture spontaneous scalarization. Recombining these expansions produces the PK approximation. To capture dynamical scalarization, one resums the PK expansion in Gm/rc^2 and v/c. Fully recombining these expansions reproduces the original (unexpanded) theory. Instead, one partially resums the PK expansions to generate the PD approximation.

4.2.2 Dynamical scalarization: neutron-star binaries

Despite its successful application to binary pulsars, the PK approximation does not predict dynamical scalarization. The asymptotic scalar field for a binary system has been computed recently to 1.5PK order in Ref. [151].[4] For a system

[4]In the literature, the distinction between the PN and PK expansions is often overlooked; the PK expansion (i.e., the approximation in which power series in Gm/Rc^2 have been resummed) is often referred to as the "PN expansion," (for example Refs. [79, 149, 151]). To avoid confusion, we have taken care to distinguish the two in Sec. 4.2 when discussing spontaneous scalarization. Because both the PN and PK expansions fail to capture dynamical scalarization, starting from Sec. 4.3, we continue the popular conflation of these two approximation schemes, referring to the expansions collectively as "PN."

containing neutron stars too diffuse to spontaneously scalarize individually, the PK prediction of the total scalar charge remains small as the binary coalesces. However, numerical-relativity calculations indicate that the scalar charge can greatly increase beyond this estimate as the two neutron stars draw close [169, 171, 172]. We postpone a quantitative comparison between these analytic and numerical predictions until Sec. 4.8 (see Fig. 4.6); we must first formulate a precise measure of the scalarization of a binary system. Akin to spontaneous scalarization, we suspect that the mismatch between analytic and numerical results stems from a breakdown of the PK expansion. We posit that DS is a non-perturbative phenomenon, and hence the PK expansion needs to be suitably modified to capture it.

To support this intuition, we carefully examine how the mass and scalar charge of a star depend on the nearby scalar field. For an isolated body, these are the relations $m(\phi_0)$ and $\alpha(\phi_0)$ where ϕ_0, m, and α are defined in Eqs. (4.10) and (4.11). As shown in Appendix A of Ref. [147], the scalar charge is related to the mass by

$$\alpha_A(\phi_0) = \mu_0 \left(1 - 2\frac{d\log m_A}{d\log \phi_0}\right). \tag{4.14}$$

The dependence of the mass on ϕ_0 can only be found by numerically solving the Tolman-Oppenheimer-Volkoff (TOV) equations modified for ST gravity with a given equation of state [153].

The mass and scalar charge of each neutron star in a binary system can be similarly determined provided that the system is well-separated ($R/r \ll 1$). Working at leading order in R/r, each star can be treated as an isolated body immersed in the scalar field produced by its partner [147]. At a distance $|\mathbf{x}| = d \sim \sqrt{Rr}$ from

each star ("far" from the star relative to R), the metric and scalar field will behave as in Eqs. (4.10) and (4.11) with ϕ_0 replaced by the background field produced by the other star. As above, we numerically solve the modified TOV equations to relate the mass m and scalar charge α to this background scalar field. Because we work in the limit $d/r = \sqrt{R/r} \to 0$, this matching occurs effectively at each star relative to r, the smallest distance scale relevant to GW generation.[5] In this limit, the TOV equations provide us with the dependence on the mass and charge on the *local* scalar field for each body in a binary system, i.e. the functions $m(\phi)$ and $\alpha(\phi)$ where ϕ is evaluated *at* the star.

To analytically model these relations using the PK approximation, one must expand m and α about the background field ϕ_0, where now ϕ_0 is the value taken very far from the binary system at $|\mathbf{x}| \gg r$. Because the analytic form of the function $m(\phi)$ is unknown, Eardley [242] proposed the agnostic expansion

$$m_A(\phi) = m_A^{(0)} \left[1 + s_A \Psi + \frac{1}{2} \left(s_A^2 - s_A + s'_A \right) \Psi^2 + \cdots \right], \tag{4.15}$$

where

$$m_A^{(0)} \equiv m_A(\phi_0), \tag{4.16}$$

$$s_A \equiv \left(\frac{d \log m_A}{d \log \phi} \right)_{\phi=\phi_0}, \tag{4.17}$$

$$s'_A \equiv \left(\frac{d^2 \log m_A}{d(\log \phi)^2} \right)_{\phi=\phi_0}, \tag{4.18}$$

$$\Psi \equiv \frac{\phi - \phi_0}{\phi_0} \propto \frac{Gm}{rc^2}. \tag{4.19}$$

[5] In this work, we ignore all effects that arise from the finite size of the neutron stars. Such effects could influence the dynamics of a binary system of scalarized stars at 1PK order [282].

We plot the magnitude of the coefficients in Eq. (4.15) in Fig. 4.3 across a range of scalar field values reached during the coalescence of a binary neutron star system [169, 171]. Using the model of Ref. [170], we estimate that DS occurs when the field at each body reaches a value of

$$\Psi \sim 10^{-4}, \tag{4.20}$$

depicted as the pink region in the figure.

For neutron stars with realistic, piecewise polytropic equations of states (e.g. fits to APR4 and H4 defined in Ref. [206]), we find that for Ψ near this maximal value,

$$\left|\frac{C_{n+1}}{C_n}\right| \sim 10^3 - 10^5, \tag{4.21}$$

for $n = 1, 2$, where C_i is the coefficient of the i-th PN correction in Eq. (4.15).

Comparing Eqs. (4.20) and (4.21), we see that the rapid growth of the expansion coefficients in Eq. (4.15) can overpower the "smallness" of our expansion parameter Ψ. In particular, the relative contribution of each term on the right hand side of Eq. (4.15) does not diminish as one moves to increasingly higher order. These symptoms indicate that $m(\phi)$ may not be analytic in this regime, and thus, the PK expansion would break down at this point in the binary's evolution. Inspired by the treatment of spontaneous scalarization, we posit that the best way to work around this restriction is to resum the expansion in Eq. (4.15). The hierarchy of these expansions is outlined in Fig. 4.2.

Unfortunately, such a prescription is not as straightforward as the case for spontaneous scalarization. To capture spontaneous scalarization, one simply "un-

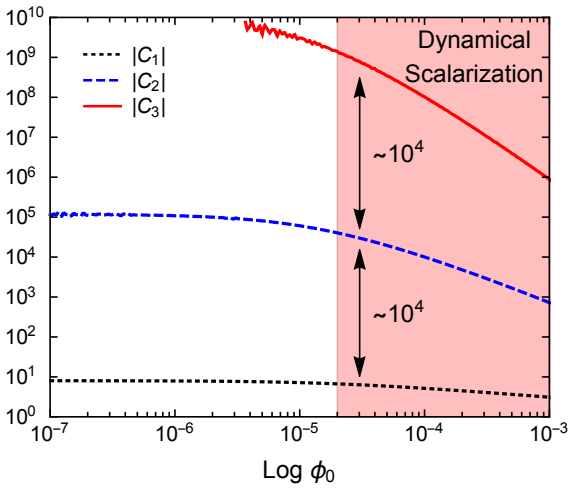

Figure 4.3: Magnitude of the coefficients of the expansion $m(\phi) = m^{(0)}\left(1 + C_1\Psi + C_2\Psi^2 + \cdots\right)$ across the typical scalar field values achieved during the evolution of a compact binary. Values shown here are for an isolated body with $m(\phi_0) = 1.35M_\odot$ and APR4 equation of state with $B = 9$. Interpolation errors dominate the computation of C_3 for small values of $\log\phi_0$; we omit these regions of the curve.

expands" all expansions in Gm/Rc^2 in the PN approximation [i.e. those of the form as in Eq. (4.13)], leaving only expansions in Gm/rc^2 and the corresponding orbital velocity v/c. Completely resumming *these* expansions would reproduce the full ST theory. Instead, we need to choose certain quantities dependent on Gm/rc^2 to resum, and leave the rest expanded. Based on the discussion above, we suspect that the best quantities to keep unexpanded are the mass $m(\phi)$ and its derivatives (including the scalar charge $\alpha(\phi)$). However, *a priori*, there is no clear indication of precisely "what to resum." We need to incorporate the flexibility of this choice into our model.

4.3 The post-Dickean expansion

4.3.1 Action and field equations

We refer to our method of resumming the PN expansion as the "post-Dickean" (PD) approach — named after Robert Dicke, one of several pioneers of ST gravity [177–179, 283, 284] who made many important contributions to experimental relativity throughout his career. For notational convenience, we introduce an auxiliary field ξ that is related to ϕ in a small neighborhood of each particle's worldline.[6] This new field is used to demarcate the resummed variables (m and its derivatives). We explicitly constrain ξ in the matter action via the Lagrange multipliers λ_A

$$S_m \equiv c^2 \sum_A \int d^4x \int d\tau_A \delta^{(4)} \left(x - \gamma_A(\tau_A)\right) \times \left(m_A(\phi, \xi) + \lambda_A(\tau_A) \left(F(\phi) - \xi\right)\right), \tag{4.22}$$

where the arbitrary functions $m(\phi, \xi)$ and $F(\phi)$ encode our choice of how to resum the mass and scalar charge, respectively.

[6] Formally, the matching of ξ and ϕ is done at the boundary of the *body zone*, defined at a distance $d \sim \sqrt{Rr}$ from each body. As justified in Appendix A of Ref. [147], in the limit that $d/r \to 0$, we can represent each body as a point particle; in this limit, the matching of the two field variables is done exactly on each body's worldline.

With this expression, the action in Eq. (4.3) gives rise to the field equations

$$F\left(\phi(\gamma_A(\tau_A))\right) = \xi(\gamma_A(\tau_A)), \tag{4.23}$$

$$u_A^\sigma \nabla_\sigma \left(m(\phi,\xi) u_A^\alpha\right) = -\frac{Dm}{D\phi}\partial^\alpha \phi \tag{4.24}$$

$$\begin{aligned} R_{\mu\nu} - \frac{1}{2}R g_{\mu\nu} =& \frac{\omega(\phi)}{\phi^2}\left(\nabla_\mu\phi\nabla_\nu\phi - \frac{1}{2}g_{\mu\nu}g^{\alpha\beta}\nabla_\alpha\phi\nabla_\beta\phi\right) \\ &+ \frac{1}{\phi}\left(\nabla_\mu\nabla_\nu\phi - g_{\mu\nu}\Box\phi\right) + \frac{8\pi G}{\phi c^4}T_{\mu\nu}, \end{aligned} \tag{4.25}$$

$$\Box\phi = \frac{1}{3+2\omega(\phi)}\left(\frac{8\pi G}{c^4}T - \frac{16\pi G}{c^4}\phi\frac{DT}{D\phi} - \frac{d\omega}{d\phi}g^{\alpha\beta}\nabla_\alpha\phi\nabla_\beta\phi\right), \tag{4.26}$$

where we have defined

$$\frac{D}{D\phi} \equiv \frac{\partial}{\partial\phi} + \frac{dF}{d\phi}\frac{\partial}{\partial\xi}, \tag{4.27}$$

$$\begin{aligned} T^{\mu\nu} \equiv& \frac{2c}{\sqrt{-g}}\frac{\delta S_m}{\delta g_{\mu\nu}} \\ =& c^3\sqrt{-g}\sum_A \int d\tau_A m_A(\phi,\xi) u_A^\mu u_A^\nu \delta^{(4)}(x - \gamma_A(\tau_A)), \end{aligned} \tag{4.28}$$

where γ_A, τ_A, and $u_A^\mu = \frac{d\gamma_A^\mu}{d\tau_A}$ are the worldline, proper time, and four velocity of particle A, respectively.

In this work, we focus on only a few, natural choices for m and F, given in Table 4.1. Physically, the choice of $m^{(\mathrm{RJ})}$ corresponds to resumming the mass measured in the Jordan frame, while the choice and $m^{(\mathrm{RE})}$ corresponds to resumming the Einstein-frame mass

$$m^{(E)}(\phi) = \frac{m(\phi)}{\sqrt{\phi}}. \tag{4.29}$$

The choices of $F^{(\phi)}$ and $F^{(\tilde{\varphi})}$ respectively equate the auxiliary field ξ to ϕ and $\tilde{\varphi}$, defined in Eq. (4.9). We refer to the joint selection of m and F as the *resummation scheme*. The PD parameterization also encompasses the (non-resummed) PN

Table 4.1: Resummation schemes discussed in this work. We abbreviate $m(\phi, \xi)$ with m and $F(\phi)$ with F.

	$F^{(\phi)}$	$F^{(\tilde{\varphi})}$
$m^{(\mathrm{RJ})}$	$m = m(\xi)$ $F = \phi$	$m = m(\xi)$ $F = \sqrt{2 \log \phi / B}$
$m^{(\mathrm{RE})}$	$m = (\phi/\xi)^{1/2} m(\xi)$ $F = \phi$	$m = \phi^{1/2} e^{-B\xi^2/4} m(\xi)$ $F = \sqrt{2 \log \phi / B}$
$m^{(\mathrm{PN})}$	$m = m(\phi)$	

expansion; this limit is reached with the choice of $m^{(\mathrm{PN})}$ given in the table (recall that here "PN" is used to refer collectively to the post-Newtonian and -Keplerian approximations).

4.3.2 Relaxed field equations

To solve Eqs. (4.25) and (4.26), we employ a technique known as direction integration of the relaxed Einstein equations, originally developed in GR in Refs. [285–289] and then extended to ST gravity in Refs. [149–151]. The remainder of this section closely follows the framework presented in Sec. II.B of Ref. [149]. We define

$$\mathfrak{g}^{\mu\nu} \equiv \sqrt{-g} g^{\mu\nu}, \tag{4.30}$$

$$H^{\mu\alpha\nu\beta} \equiv \mathfrak{g}^{\mu\nu}\mathfrak{g}^{\alpha\beta} - \mathfrak{g}^{\alpha\nu}\mathfrak{g}^{\mu\beta}. \tag{4.31}$$

As in general relativity, the following identity holds:

$$H^{\mu\alpha\nu\beta}{}_{,\alpha\beta} = (-g)(2R_{\mu\nu} - R g_{\mu\nu} + \frac{16\pi G}{c^4} t^{\mu\nu}_{\mathrm{LL}}), \tag{4.32}$$

where $t_{\rm LL}^{\mu\nu}$ is the Landau-Lifshitz pseudotensor.

We assume that far from any sources, the metric reduces to the Minkowski metric $\eta_{\mu\nu}$ and that the scalar field approaches a constant value ϕ_0. Let $\varphi \equiv \phi/\phi_0$ be the normalized scalar field. We introduce the conformally transformed metric

$$\tilde{g}_{\mu\nu} \equiv \varphi g_{\mu\nu}, \tag{4.33}$$

the gravitational field

$$\tilde{h}^{\mu\nu} \equiv \eta^{\mu\nu} - \sqrt{-\tilde{g}}\tilde{g}^{\mu\nu}, \tag{4.34}$$

and the "conformal gothic metric"

$$\tilde{\mathfrak{g}}^{\mu\nu} \equiv \sqrt{-\tilde{g}}\tilde{g}^{\mu\nu}. \tag{4.35}$$

We impose the Lorentz gauge condition

$$\partial_\nu \tilde{h}^{\mu\nu} = 0. \tag{4.36}$$

Substituting Eqs. (4.30)–(4.34) into the gauge condition (4.36), the field equation (4.25) is rewritten as

$$\Box_\eta \tilde{h}^{\mu\nu} = -\frac{16\pi G}{c^2}\tau^{\mu\nu}, \tag{4.37}$$

where $\Box_\eta$ is the Minkowski space d'Alembertian and

$$\tau^{\mu\nu} \equiv (-g)\frac{\varphi}{\phi_0 c^2}T^{\mu\nu} + \frac{c^2}{16\pi G}\left(\Lambda^{\mu\nu} + \Lambda_S^{\mu\nu}\right), \tag{4.38}$$

$$\Lambda^{\mu\nu} \equiv \frac{16\pi G}{c^4}\left[(-g)t_{\rm LL}^{\mu\nu}\right](\tilde{\mathfrak{g}}^{\mu\nu}) + \partial_\beta\tilde{h}^{\mu\alpha}\partial_\alpha\tilde{h}^{\nu\beta} - \tilde{h}^{\alpha\beta}\partial_\alpha\partial_\beta\tilde{h}^{\mu\nu}, \tag{4.39}$$

$$\Lambda_S^{\mu\nu} \equiv \frac{3+2\omega}{\varphi^2}\partial_\alpha\varphi\partial_\beta\varphi\left(\tilde{\mathfrak{g}}^{\mu\alpha}\tilde{\mathfrak{g}}^{\nu\beta} - \frac{1}{2}\tilde{\mathfrak{g}}^{\mu\nu}\tilde{\mathfrak{g}}^{\alpha\beta}\right), \tag{4.40}$$

where the notation $[(-g)t^{\mu\nu}_{\rm LL}](\tilde{\mathfrak{g}}^{\mu\nu})$ indicates that the Landau-Lifshitz pseudotensor should be calculated using $\tilde{\mathfrak{g}}$ rather than the physical metric g. Similarly, the scalar field equation (4.26) can be recast into the form

$$\Box_\eta \varphi = -\frac{8\pi G}{c^2}\tau_s, \tag{4.41}$$

with

$$\begin{aligned}\tau_s \equiv &-\frac{1}{3+2\omega}\sqrt{-g}\frac{\varphi}{\phi_0 c^2}\left(T - 2\phi\frac{DT}{D\phi}\right) - \frac{c^2}{8\pi G}\tilde{h}^{\alpha\beta}\partial_\alpha\partial_\beta\varphi \\ &+ \frac{c^2}{16\pi G}\frac{d}{d\varphi}\left[\log\left(\frac{3+2\omega}{\varphi^2}\right)\right]\partial_\alpha\varphi\partial_\beta\varphi\tilde{\mathfrak{g}}^{\alpha\beta}.\end{aligned} \tag{4.42}$$

The differential equations (4.37) and (4.41) can be solved formally using the standard flat-space Green's function; we only consider retarded solutions, i.e. those with no incoming radiation

$$\tilde{h}^{\mu\nu}(t,\mathbf{x}) = \frac{4G}{c^2}\int d^3x' \frac{\tau^{\mu\nu}(t-|\mathbf{x}-\mathbf{x}'|,\mathbf{x}')}{|\mathbf{x}-\mathbf{x}'|}, \tag{4.43}$$

$$\varphi(t,\mathbf{x}) = 1 + \frac{2G}{c^2}\int d^3x' \frac{\tau_s(t-|\mathbf{x}-\mathbf{x}'|,\mathbf{x}')}{|\mathbf{x}-\mathbf{x}'|}, \tag{4.44}$$

where the integration constant is explicitly added to enforce the asymptotic boundary condition on the scalar field. By construction, the constraint equation Eq. (4.23) acts as an additional boundary condition on the scalar field along the worldline of each body; this constraint distinguishes our work from the PN solutions found in Refs. [149–151].

We approximate the formal solutions given in Eqs. (4.43) and (4.44) with an expansion in terms of $\epsilon \sim (v/c)^2 \sim Gm/rc^2$. However, to capture the strong-field effects behind dynamical scalarization, *we expand only the metric $g_{\mu\nu}$ and scalar field ϕ, leaving ξ unexpanded.* Note that ξ appears only in the function $m_A(\phi,\xi)$ in

Eqs. (4.37) and (4.41). Thus, by not expanding ξ, we effectively resum the variable mass found in the PN treatment. This treatment also resums the scalar charge, which is governed by the derivative of m [see Eq. (4.14) or (4.76)]. The constraint equation Eq. (4.23) is used to solve ξ exactly on each worldline at a given order in ϵ.

4.4 Structure of the near-zone fields

The resummation detailed above only enters through the sources, i.e. the stress-energy tensor $T^{\mu\nu}$ and its derivatives. As such, we adopt the same techniques used for the PN calculation of the metric and scalar field in Refs. [149–151]. We summarize this approach below, leaving our results in terms of $T^{\mu\nu}$ and its derivatives. For more detail, see Secs. III and IV of Ref. [149].

The integration in Eqs. (4.43) and (4.44) is done over the flat space past null cone $\mathcal{C}$ emanating from the point $(t, \mathbf{x})$. We divide this three-dimensional hypersurface into two regions. For matter sources of characteristic size $\mathcal{S}$, we define the *near zone* as the worldtube with $|\mathbf{x}| < \mathcal{R}$ where $\mathcal{R} \sim \mathcal{S}/v$ is the characteristic wavelength of the emitted gravitational radiation. The *radiation zone* is the region outside of the near zone, that is, $|\mathbf{x}| > \mathcal{R}$. We demarcate the intersection of $\mathcal{C}$ with the near zone as $\mathcal{N}$ and the intersection of $\mathcal{C}$ with the radiation zone as $\mathcal{C} - \mathcal{N}$.

We focus first on finding the metric and scalar field in the near zone, as these determine the equations of motion of the binary system through Eq. (4.24). Fol-

lowing Refs. [149, 288], we establish the following notation

$$\begin{aligned} N &\equiv \tilde{h}^{00}, \qquad K^i \equiv \tilde{h}^{0i}, \\ B^{ij} &\equiv \tilde{h}^{ij}, \qquad B \equiv \tilde{h}^{ii}. \end{aligned} \tag{4.45}$$

To post-Newtonian order, we express the metric in terms of these fields using Eqs. (4.33) and (4.34)

$$g_{00} = -1 + \left(\frac{1}{2}N + \Psi\right) + \left(\frac{1}{2}B - \frac{3}{8}N^2 - \frac{1}{2}N\Psi - \Psi^2\right) + \mathcal{O}\left(\frac{1}{c^6}\right), \tag{4.46}$$

$$g_{0i} = -K^i + \mathcal{O}\left(\frac{1}{c^5}\right), \tag{4.47}$$

$$g_{ij} = \delta_{ij}\left[1 + \left(\frac{1}{2}N - \Psi\right)\right] + \mathcal{O}\left(\frac{1}{c^4}\right), \tag{4.48}$$

where Ψ was defined in Eq. (4.19).

At the point $(t, \mathbf{x})$ in the near zone, the near-zone contribution to the integrals in Eqs. (4.43) and (4.44) can be expanded in powers of $|\mathbf{x} - \mathbf{x}'|$

$$N_{\mathcal{N}}(t, \mathbf{x}) = \frac{4G}{c^2}\int_{\mathcal{M}} \frac{\tau^{00}(t, \mathbf{x}')}{|\mathbf{x} - \mathbf{x}'|} d^3x' + \frac{2G}{c^4}\partial_t^2 \int_{\mathcal{M}} \tau^{00}(t, \mathbf{x}')|\mathbf{x} - \mathbf{x}'| d^3x' + N_{\partial\mathcal{M}} + \mathcal{O}\left(\frac{1}{c^6}\right), \tag{4.49}$$

$$K^i_{\mathcal{N}}(t, \mathbf{x}) = \frac{4G}{c^2}\int_{\mathcal{M}} \frac{\tau^{0i}(t, \mathbf{x}')}{|\mathbf{x} - \mathbf{x}'|} d^3x' + K^i_{\partial\mathcal{M}} + \mathcal{O}\left(\frac{1}{c^5}\right), \tag{4.50}$$

$$B^{ij}_{\mathcal{N}}(t, \mathbf{x}) = \frac{4G}{c^2}\int_{\mathcal{M}} \frac{\tau^{ij}(t, \mathbf{x}')}{|\mathbf{x} - \mathbf{x}'|} d^3x' + B^{ij}_{\partial\mathcal{M}} + \mathcal{O}\left(\frac{1}{c^4}\right), \tag{4.51}$$

$$\begin{aligned} \Psi_{\mathcal{N}}(t, \mathbf{x}) = &\frac{2G}{c^2}\int_{\mathcal{M}} \frac{\tau_s(t, \mathbf{x}')}{|\mathbf{x} - \mathbf{x}'|} d^3x' - \frac{2G}{c^3}\partial_t \int_{\mathcal{M}} \tau_s(t, \mathbf{x}') d^3x' \\ &+ \frac{G}{c^4}\partial_t^2 \int_{\mathcal{M}} \tau_s(t, \mathbf{x}')|\mathbf{x} - \mathbf{x}'| d^3x' + \mathcal{O}\left(\frac{1}{c^6}\right), \end{aligned} \tag{4.52}$$

where $\mathcal{M}$ is a constant-time hypersurface which covers the near zone and we have used Eq. (4.36) to eliminate the first order correction in Eq. (4.49). There will

also be a contribution to the fields at $(t, \mathbf{x})$ from the radiation zone, but these only enter at higher order [149]. The boundary terms $N_{\partial\mathcal{M}}, K^i_{\partial\mathcal{M}}, B^{ij}_{\partial\mathcal{M}}$ depend on the value of $\mathcal{R}$. Because the left hand side of Eqs. (4.49)–(4.52) should not depend on the arbitrarily chosen boundary between the near and radiation zones, we argue (as in Ref. [149]) that these terms are exactly cancelled by the contributions from the radiation zone. This cancellation was shown explicitly in GR in Refs. [287, 288].

All that remains is to expand the sources $\tau^{\mu\nu}$ and τ_s. We first define the densities

$$\sigma \equiv (T^{00} + T^{ii})c^{-2}, \tag{4.53}$$

$$\sigma^i \equiv T^{0i}c^{-2}, \tag{4.54}$$

$$\sigma^{ij} \equiv T^{ij}c^{-2}, \tag{4.55}$$

$$\sigma_s \equiv -\frac{T}{c^2} + \frac{2\phi}{c^2}\frac{DT}{D\phi}. \tag{4.56}$$

We expand Eqs. (4.38) and (4.42) to post-Newtonian order

$$\tau^{00} = \frac{1}{\phi_0}\left[\sigma - \sigma^{ii} + \frac{G}{\phi_0 c^2}\left(4\sigma U - \frac{7}{8\pi}(\nabla U)^2\right) - \frac{G{\mu_0}^2}{\phi_0 c^2}\left(6\sigma U_s - \frac{1}{8\pi}(\nabla U_s)^2\right)\right], \tag{4.57}$$

$$\tau^{0i} = \frac{\sigma^i}{\phi_0}, \tag{4.58}$$

$$\tau^{ii} = \frac{1}{\phi_0}\left[\sigma^{ii} - \frac{1}{8\pi}\frac{G}{\phi_0 c^2}(\nabla U)^2 - \frac{1}{8\pi}\frac{G{\mu_0}^2}{\phi_0 c^2}(\nabla U_s)^2\right] \tag{4.59}$$

$$\tau_s = \frac{{\mu_0}^2}{\phi_0}\left[\sigma_s + 2\frac{G}{\phi_0 c^2}\sigma_s U + \frac{G(B - 2{\mu_0}^2)}{\phi_0 c^2}\sigma_s U_s - \frac{1}{8\pi}\frac{G(B + 4{\mu_0}^2)}{\phi_0 c^2}(\nabla U_s)^2\right], \tag{4.60}$$

where we have introduced the potentials

$$U \equiv \int_{\mathcal{M}} \frac{\sigma(t,\mathbf{x}')}{|\mathbf{x}-\mathbf{x}'|} d^3x', \tag{4.61}$$

$$U_s \equiv \int_{\mathcal{M}} \frac{\sigma_s(t,\mathbf{x}')}{|\mathbf{x}-\mathbf{x}'|} d^3x'. \tag{4.62}$$

Plugging these expressions back into Eqs. (4.46)–(4.52), the 1PD metric and scalar field are given by

$$\begin{aligned} g_{00} =& -1 + \frac{2G}{\phi_0 c^2} U + \frac{2G\mu_0}{\phi_0 c^2} U_s - \frac{2G}{c^3}\dot{M}_s - \frac{2G^2}{\phi_0^2 c^4} U^2 + \frac{G^2\mu_0(B-4\mu_0)}{2\phi_0^2 c^4} U_s^2 - \frac{G^2\mu_0}{\phi_0^2 c^4} U U_s \\ &+ \frac{4G^2\mu_0}{\phi_0^2 c^4}\Phi_2^s - \frac{12G^2\mu_0}{\phi_0^2 c^4}\Phi_{2s} + \frac{G^2\mu_0(B-8\mu_0)}{\phi_0^2 c^4}\Phi_{2s}^s + \frac{G}{\phi_0 c^4}\ddot{X} + \frac{G\mu_0}{\phi_0 c^4}\ddot{X}_s + \mathcal{O}\left(\frac{1}{c^6}\right), \end{aligned} \tag{4.63}$$

$$g_{0i} = -\frac{4G}{\phi_0 c^2} V^i + \mathcal{O}\left(\frac{1}{c^5}\right), \tag{4.64}$$

$$g_{ij} = \delta_{ij}\left[1 + \frac{2G}{\phi_0 c^2} U - \frac{2G\mu_0}{\phi_0 c^2} U_s\right] + \mathcal{O}\left(\frac{1}{c^4}\right), \tag{4.65}$$

$$\begin{aligned} \phi =& \phi_0 + \frac{2G\mu_0 U_s}{c^2} - \frac{2G}{c^3}\dot{M}_s \\ &+ \frac{G\mu_0}{c^2}\left[\frac{G(B+4\mu_0)}{2\phi_0 c^2} U_s^2 + 4\frac{G}{\phi_0 c^2}\Phi_2^s + \frac{G(B-8\mu_0)}{\phi_0 c^2}\Phi_{2s}^s + \ddot{X}_s\right] + \mathcal{O}\left(\frac{1}{c^6}\right), \end{aligned} \tag{4.66}$$

with the additional potentials

$$M_s \equiv \int \sigma_s(t, \mathbf{x}') d^3x', \tag{4.67}$$

$$V^i \equiv \int \frac{\sigma^i(t, \mathbf{x}')}{|\mathbf{x} - \mathbf{x}'|} d^3x', \tag{4.68}$$

$$\Phi_2^s \equiv \int \frac{\sigma_s(t, \mathbf{x}') U(t, \mathbf{x}')}{|\mathbf{x} - \mathbf{x}'|} d^3x', \tag{4.69}$$

$$\Phi_{2s} \equiv \int \frac{\sigma(t, \mathbf{x}') U_s(t, \mathbf{x}')}{|\mathbf{x} - \mathbf{x}'|} d^3x', \tag{4.70}$$

$$\Phi_{2s}^s \equiv \int \frac{\sigma_s(t, \mathbf{x}') U_s(t, \mathbf{x}')}{|\mathbf{x} - \mathbf{x}'|} d^3x', \tag{4.71}$$

$$X \equiv \int \sigma(t, \mathbf{x}') |\mathbf{x} - \mathbf{x}'| d^3x', \tag{4.72}$$

$$X_s \equiv \int \sigma_s(t, \mathbf{x}') |\mathbf{x} - \mathbf{x}'| d^3x', \tag{4.73}$$

4.5 Two-body Equations of motion

4.5.1 Newtonian order

We now apply these calculations to a binary system whose stress-energy tensor is given by Eq. (4.28). To highlight the novel aspects of the PD approach, we explicitly work out the leading-order equations of motion here before calculating their higher-order corrections in the following section. In keeping with PN conventions, we describe the leading order as Newtonian and the next-to-leading order as post-Dickean or "1PD."

At Newtonian order, the densities defined in Eqs. (4.53) and (4.54) are given

by

$$\sigma = \sum_A m_A(\phi,\xi)\delta^{(3)}(x-x_A) + \mathcal{O}\left(\frac{1}{c^2}\right), \tag{4.74}$$

$$\sigma_s = \sum_A m_A(\phi,\xi)\frac{\alpha_A(\phi,\xi)}{\mu_0}\delta^{(3)}(x-x_A) + \mathcal{O}\left(\frac{1}{c^2}\right). \tag{4.75}$$

where we have introduced the scalar charge of each body

$$\alpha_A(\phi,\xi) \equiv \left(\frac{B\log\phi}{2}\right)^{1/2}\left(1 - 2\phi\frac{D\log m_A}{D\phi}\right). \tag{4.76}$$

Our definition of the scalar charge is the natural generalization of the expression used in Ref. [147]; with no resummation, i.e. $m(\phi,\xi) = m(\phi)$, one recovers the definition

$$\alpha_A = -\frac{d\log m_A^{(E)}}{d\tilde{\varphi}}, \tag{4.77}$$

where $\tilde{\varphi}$ is defined in Eq. (4.9).

Evaluating Eq. (4.66) at Newtonian order, the scalar field for a 2-body system is given by

$$\begin{aligned}\phi =& \phi_0 + 2\frac{G{\mu_0}^2 U_s}{c^2},\\ =& \phi_0 + \frac{2Gm_1\mu_0\alpha_1}{c^2 r_1} + \mathcal{O}\left(\frac{1}{c^3}\right) + (1 \rightleftharpoons 2),\end{aligned} \tag{4.78}$$

where we have adopted the shorthand

$$\begin{aligned} m_A \equiv& m_A(\phi(x_A),\xi(x_A)), \qquad \alpha_A \equiv \alpha_A(\phi(x_A),\xi(x_A)),\\ & r_A \equiv |\mathbf{x}-\mathbf{x}_A|, \qquad \mathbf{n}_A \equiv (\mathbf{x}-\mathbf{x}_A)/r_A.\end{aligned} \tag{4.79}$$

Because m_A and α_A depend on ϕ, these quantities must be expanded around the background field ϕ_0. We suppress these expansions (given in Appendix E) throughout the remainder of this work for notational convenience, denoting with the short-

hand in Eq. (4.79) that the mass and charge should be expanded and truncated at the appropriate PD order.

On each worldline, we *exactly* solve (i.e. not perturbatively) Eq. (4.23), ignoring the divergent terms that arise from self-interactions of each body

$$\xi(x_1) = \begin{cases} \phi_0 + \frac{2Gm_2\mu_0\alpha_2}{c^2 r}, & \text{if } F(\phi) = \phi \\ \tilde{\varphi}_0 + \frac{Gm_2\alpha_2}{c^2 r}, & \text{if } F(\phi) = \sqrt{\frac{2\log\phi}{B}} \end{cases} \tag{4.80}$$

$$\xi(x_2) = (1 \leftrightharpoons 2)\,, \tag{4.81}$$

where $r \equiv |\mathbf{x}_1 - \mathbf{x}_2|$ is the orbital separation of the binary and

$$\tilde{\varphi}_0 \equiv \frac{2\mu_0}{B} = \sqrt{\frac{2\log\phi_0}{B}}. \tag{4.82}$$

Note that this system of equations cannot be solved analytically, as m_A and α_A depend on ξ along each worldline. This final step is analogous to the feedback model proposed in Ref. [170]; with the choice of $F^{(\tilde{\varphi})}$ given in Table 4.1, we exactly reproduce this model.

Plugging in the expressions for the metric and scalar field into Eq. (4.24), we find the Newtonian equations of motion

$$a_1^i = -\frac{Gm_2\,(1+\alpha_1\alpha_2)}{\phi_0 r^2} n^i, \tag{4.83}$$

$$a_2^i = (1 \leftrightharpoons 2)\,, \tag{4.84}$$

where $\mathbf{n} \equiv (\mathbf{x}_1 - \mathbf{x}_2)/r$. The mass m_A and scalar charge α_A depend on the choice of resummation scheme; their leading order piece is given in Appendix E.

4.5.2 Post-Dickean order

To find the equations of motion of the binary to next order in c^{-2}, we expand the stress-energy tensor and evaluate the potentials introduced in Sec. 4.4 (see Appendix F).

On each worldline, we plug the above potentials into Eq. (4.66) and numerically solve Eq. (4.23)

$$\xi(x_1) = \begin{cases} \phi_0 + \dfrac{2G\mu_0 m_2\alpha_2}{\phi_0 r c^2} + \dfrac{Gm_2\alpha_2}{\phi_0 r c^4}\Big[-\mu_0(\mathbf{v}_2\cdot\mathbf{n})^2 & \\ \quad +\alpha_2\left(\dfrac{B}{2}+2{\mu_0}^2\right)\dfrac{Gm_2}{\phi_0 r} & \text{if } F(\phi)=\phi \\ \quad -\left(2{\mu_0}^2\alpha_1+\mu_0\left(3+\alpha_1\alpha_2\right)\right)\dfrac{Gm_1}{\phi_0 r}\Big], & \\ \tilde{\varphi}_0 + \dfrac{Gm_2\alpha_2}{\phi_0 r c^2} + \dfrac{Gm_2\alpha_2}{\phi_0 r c^4}\left[-\dfrac{1}{2}(\mathbf{v}_2\cdot\mathbf{n})^2\right. & \\ \quad \left.-\left(\dfrac{3}{2}+\mu_0\alpha_1+\dfrac{1}{2}\alpha_1\alpha_2\right)\dfrac{Gm_1}{\phi_0 r}\right], & \text{if } F(\phi)=\sqrt{\frac{2\log\phi}{B}} \end{cases} \tag{4.85}$$

$$\xi(x_2) = (1 \rightleftharpoons 2)\,. \tag{4.86}$$

Substituting Eqs. (4.63)-(4.66) into Eq. (4.24), we find the following equation of motions for each particle

$$\begin{aligned} a^i_{(1)} = &-\frac{Gm_2\left(1+\alpha_1\alpha_2\right)}{\phi_0 r^2}n^i + \frac{Gm_2}{\phi_0 r^2 c^2}n^i\Big[-\left(1-\alpha_1\alpha_2\right)v_1^2 - 2(v_2^2 - 2\mathbf{v_1}\cdot\mathbf{v_2}) \\ &+\frac{3}{2}\left(1+\alpha_1\alpha_2\right)\left(\mathbf{v}_2\cdot\mathbf{n}\right)^2 + \left(5+\mu_0\alpha_1\right)\left(1+\alpha_1\alpha_2\right)\frac{Gm_1}{\phi_0 r} \\ &+4\left(1+\alpha_1\alpha_2\right)\frac{Gm_2}{\phi_0 r}\Big] + \frac{Gm_2}{\phi_0 r^2 c^2}(v_1-v_2)^i\left[4\left(\mathbf{v}_1\cdot\mathbf{n}\right)-\left(3-\alpha_1\alpha_2\right)\left(\mathbf{v}_2\cdot\mathbf{n}\right)\right], \end{aligned} \tag{4.87}$$

$$a^i_{(2)} = (1 \rightleftharpoons 2)\,, \tag{4.88}$$

where m and α themselves receive post-Dickean corrections dependent on the resummation scheme used (see Appendix E).

For reference later, the 1PN equations of motion (with no resummation of the mass) are recovered with the choice $m^{(\mathrm{PN})}$

$$\begin{aligned} a^i_{1\,(\mathrm{PN})} = &-\frac{G\bar{m}_2\left(1+\bar{\alpha}_1\bar{\alpha}_2\right)}{\phi_0 r^2}n^i + \frac{G\bar{m}_2}{\phi_0 r^2 c^2}n^i\Bigg[-\left(1-\bar{\alpha}_1\bar{\alpha}_2\right)v_1^2 - 2\left(v_2^2 - 2\mathbf{v}_1\cdot\mathbf{v}_2\right) \\ &+\frac{3}{2}\left(1+\bar{\alpha}_1\bar{\alpha}_2\right)\left(\mathbf{v}_2\cdot\mathbf{n}\right)^2 + \left(4+4\bar{\alpha}_1\bar{\alpha}_2-\bar{\alpha}_1'\bar{\alpha}_2^2\right)\frac{G\bar{m}_2}{\phi_0 r} \\ &+\left(\left(5+\bar{\alpha}_1\bar{\alpha}_2\right)\left(1+\bar{\alpha}_1\bar{\alpha}_2\right)-\bar{\alpha}_2'\bar{\alpha}_1^2\right)\frac{G\bar{m}_1}{\phi_0 r}\Bigg] \\ &+\frac{G\bar{m}_2}{\phi_0 r^2 c^2}(v_1-v_2)^i\left[4\left(\mathbf{v}_1\cdot\mathbf{n}\right)-\left(3-\bar{\alpha}_1\bar{\alpha}_2\right)\left(\mathbf{v}_2\cdot\mathbf{n}\right)\right], \end{aligned} \tag{4.89}$$

$$a^i_{2\,(\mathrm{PN})} = (1 \rightleftharpoons 2)\,, \tag{4.90}$$

where we have introduced the shorthand

$$\bar{m}_i \equiv m_i(\phi_0), \tag{4.91}$$

$$\bar{\alpha}_i \equiv \mu_0\left(1-2\frac{d\log m_i}{d\log\phi}\right)_{\phi=\phi_0}, \tag{4.92}$$

$$\bar{\alpha}_i' \equiv \frac{B\bar{\alpha}_i}{2\mu_0} - 4\mu_0^2\left(\frac{d^2\log m_i}{d(\log\phi)^2}\right)_{\phi=\phi_0}. \tag{4.93}$$

The apparent differences between Eqs. (4.87)–(4.88) and Eqs. (4.89)–(4.90) are simply artifacts of the different notations. The disparities stem from the presence in Eq. (4.89) of higher-order terms from expansions like Eq. (4.15). These terms are absorbed into the definitions of m_A and α_A in the PD expansion [see Eq. (4.79)]. We emphasize the differences between these two notations because the analytic model proposed in Ref. [170] directly adapted the equations of motion written as in Eqs.

(4.89) and (4.90). Beyond post-Newtonian order, we expect a greater proportion of the corresponding terms in each notation to differ.

For a generic resummation scheme, the 1PD Eqs. (4.87) and (4.88) are not solutions to the Euler-Lagrange equations for any Fokker Lagrangian (a Lagrangian dependent solely on the the positions and velocities of the two bodies). A simple calculation reveals that the equations of motion can be integrated back to such a Lagrangian only when no resummation is performed, i.e. when $m^{(\mathrm{PN})}$ is used.[7] The absence of a PD Fokker Lagrangian suggests that our model of DS requires the two-body phase space to be augmented with additional degrees of freedom besides the bodies' positions and velocities, such as the scalar field ξ. We conjecture that any other extension to the PN formalism to incorporate DS will also require new, dynamical degrees of freedom.

4.6 Structure of the far-zone fields

Having solved the dynamics of the binary, we now shift our attention to observables that can be extracted from the asymptotic geometry of the system. Our interest in this type of quantity is twofold. First, such objects encode all information needed to estimate GW signals (e.g. the waveform and its phase evolution estimated from the Bondi mass and flux). Second, there are several gauge-invariant quantities defined asymptotically that are easily computed in numerical relativity (e.g. the ADM mass and angular momentum) and thus can be used to directly check the

[7] This result contradicts the assertion of Ref. [170] that such a Lagrangian can be constructed by resumming (or not expanding) the scalar charge α in the PK Lagrangian of Ref. [208].

validity of our model. For simplicity, in this work we restrict our attention to the scalar mass, a coordinate independent measure of a spacetime's scalarization. We define the scalar mass at retarded time τ as

$$M_S(\tau) \equiv -\frac{c^2}{8\pi G} \oint_{\substack{|\mathbf{x}|\to\infty \\ t-|\mathbf{x}|=\tau}} \delta^{ij}\partial_i\phi \, dS_j, \tag{4.94}$$

$$= -\frac{\phi_0 c^2}{8\pi G} \oint_{\substack{|\mathbf{x}|\to\infty \\ t-|\mathbf{x}|=\tau}} \delta^{ij}\partial_i\Psi \, dS_j, \tag{4.95}$$

where S_j is the surface-area element in flat space. We leave the other useful quantities described above for future work.

Calculating the scalar mass requires knowledge of the scalar field at a distance $|\mathbf{x}| = R \gg \mathcal{R}$ (recall that $\mathcal{R}$ is the boundary of the near zone). As in the near zone, we will recycle the tools used to determine the scalar field in the radiation zone from previous PN calculations. We summarize this calculation for a generic stress-energy tensor below; for more detail, see Refs. [150, 151]

At the order at which we work, the scalar field at null infinity receives contributions from both the near and radiation zones, which we denote as $\Psi_{\mathcal{N}}$ and $\Psi_{\mathcal{C}-\mathcal{N}}$, respectively. We compute each piece separately, dropping any terms dependent on $\mathcal{R}$, which we assume will cancel when the pieces are combined (as was done in Sec. 4.4).

4.6.1 Near-zone contribution to the scalar field

The contribution to the scalar field at the point $(t, \mathbf{x})$ in the radiation zone from points $(t', \mathbf{x}')$ in the near zone is found by expanding the integral expression

given in Eq. (4.44) in powers of $|\mathbf{x}'|/R$

$$\Psi_{\mathcal{N}} = \sum_{m=0}^{\infty} \frac{2G}{c^{2+m}} \frac{1}{m!} \frac{\partial^m}{\partial t^m} \int_{\mathcal{M}'} \tau_s(\tau, \mathbf{x}') \frac{(\hat{\mathbf{N}} \cdot \mathbf{x}')}{R} d^3x', \tag{4.96}$$

$$= \frac{2G}{c^2} \sum_{m=0}^{\infty} \frac{(-1)^m}{m!} \partial_{k_1} \cdots \partial_{k_m} \left(\frac{1}{R} \mathcal{I}_s^{k_1 \cdots k_m}(\tau) \right), \tag{4.97}$$

where $\hat{\mathbf{N}} \equiv \mathbf{x}/R$, $\mathcal{M}'$ is the intersection of the near zone with a hypersurface of constant retarded time $\tau = t - R$, and we have introduced the scalar multipole moments

$$\mathcal{I}_s^{k_1 \cdots k_m}(\tau) \equiv \int_{\mathcal{M}'} \tau_s(\tau, \mathbf{x}) x^{k_1} \cdots x^{k_m} d^3x. \tag{4.98}$$

We note that the terms that fall off faster that R^{-1} in Eq. (4.97) will not contribute to the scalar mass; dropping these terms, the remaining piece of the scalar field is given by

$$\Psi_{\mathcal{N}} = \sum_{m=0}^{\infty} \frac{2G}{Rc^{2+m}} \frac{1}{m!} \hat{N}^{k_1} \cdots \hat{N}^{k_m} \frac{d^m}{dt^m} \mathcal{I}_s^{k_1 \cdots k_m}(\tau), \tag{4.99}$$

We also note that only terms with even parity (with respect to inversions of $\mathbf{x}$) will contribute to the scalar mass. These are the terms in Eq. (4.99) with even m.

The source τ_s in the near zone is needed at higher order than what was given

in Eq. (4.60) to calculate the 1PD scalar mass

$$\begin{aligned}\tau_s =&\frac{{\mu_0}^2}{\phi_0}\left[\sigma_s + 2\frac{G}{\phi_0 c^2}\sigma_s U + \frac{G(B-2{\mu_0}^2)}{\phi_0 c^2}\sigma_s U_s - \frac{1}{8\pi}\frac{G(B+4{\mu_0}^2)}{\phi_0 c^2}(\nabla U_s)^2\right]\\ &+\frac{G\mu_0^2(1+\mu_0^2)}{\phi_0^2 c^4}\sigma_s\left\{\frac{G}{\phi_0}\left[2U^2-(2B-4\mu_0^2)(UU_s+\Phi_2^s)-12\mu_0^2\Phi_{2s}\right]-(4\Phi_1-\ddot{X})\right.\\ &\left.+\frac{G(B^2-10B\mu_0^2+8\mu_0^2)}{4\phi_0}U_s^2+\frac{G(B-8\mu_0^2)(B-2\mu_0^2)}{2\phi_0}\Phi_{2s}^s+\frac{B-2\mu_0^2}{2}\ddot{X}_s\right\}\\ &-\frac{G\mu_0^2}{8\pi\phi_0^2 c^4}\left\{8U\ddot{U}_s+16V^j\partial_j\dot{U}_s+8\Phi_1^{ij}\partial_i\partial_j U_s-(B+4\mu_0^2)(\dot{U}_s^2-\boldsymbol{\nabla}U_s\cdot\boldsymbol{\nabla}\ddot{X}_s)\right.\\ &+\frac{G\mu_0^2(6B+8\mu_0^2)}{\phi_0}U_s\left(\boldsymbol{\nabla}U_s\right)^2+\frac{G(B-8\mu_0^2)(B+4\mu_0^2)}{\phi_0}\boldsymbol{\nabla}U_s\cdot\boldsymbol{\nabla}\Phi_{2s}^s\\ &\left.-\frac{G}{\phi_0}\left[-4(B+4\mu_0^2)\boldsymbol{\nabla}U_s\cdot\boldsymbol{\nabla}\Phi_2^s-8P_2^{ij}\partial_i\partial_j U_s-8\mu_0^2P_{2s}^{ij}\partial_i\partial_j U_s\right]\right\},\end{aligned} \tag{4.100}$$

where, in addition to the potentials introduced in Sec. 4.4, we define

$$\Phi_1 \equiv \int\frac{\sigma^{ii}(t,\mathbf{x}')}{|\mathbf{x}-\mathbf{x}'|}d^3x', \tag{4.101}$$

$$\Phi_1^{ij} \equiv \int\frac{\sigma^{ij}(t,\mathbf{x}')}{|\mathbf{x}-\mathbf{x}'|}d^3x', \tag{4.102}$$

$$P_2^{ij} \equiv \frac{1}{4\pi}\int\frac{\partial_i U(t,\mathbf{x}')\partial_j U(t,\mathbf{x}')}{|\mathbf{x}-\mathbf{x}'|}d^3x', \tag{4.103}$$

$$P_{2s}^{ij} \equiv \frac{1}{4\pi}\int\frac{\partial_i U_s(t,x')\partial_j U_s(t,x')}{|\mathbf{x}-\mathbf{x}'|}d^3x'. \tag{4.104}$$

4.6.2 Radiation-zone contribution to the scalar field

We rewrite the integral in Eq. (4.44) in a more useful way when working far from the system

$$\Psi = \frac{2G}{c^2}\int\frac{\tau_s(R'+\tau',\mathbf{x}')\delta(t'-t+|\mathbf{x}-\mathbf{x}'|-R')}{|\mathbf{x}-\mathbf{x}'|}d^4x', \tag{4.105}$$

where $R' = |\mathbf{x}'|$ and $\tau' = t' - R'$. Thus, the contribution to the scalar field from the radiation zone (i.e. $R' > \mathcal{R}$) is given by

$$\begin{aligned}\Psi_{\mathcal{C}-\mathcal{N}} =& \frac{2G}{c^2}\int_{\tau-2\mathcal{R}}^{\tau} d\tau' \int_0^{2\pi} d\phi \int_{1-\upsilon}^{1} \frac{\tau_s(\tau'+R',\mathbf{x}')}{t-\tau'-\hat{\mathbf{N}}'\cdot\mathbf{x}}(R')^2 d(\cos\theta') \\ &+ \frac{2G}{c^2}\int_{-\infty}^{\tau-2\mathcal{R}} \oint \frac{\tau_s(\tau'+R',\mathbf{x}')}{t-\tau'-\hat{\mathbf{N}}'\cdot\mathbf{x}}(R')^2 d^2\Omega'\end{aligned} \tag{4.106}$$

where $\upsilon = (\tau-\tau')(2R-2\mathcal{R}+\tau-\tau')/(2R\mathcal{R})$ and $\hat{\mathbf{N}}' = \mathbf{x}'/R'$. The source τ_s takes a different form in the radiation zone than in Eq. (4.100). To the order at which we work, the source in the radiation zone is given by

$$\tau_s = -\frac{B+4\mu_0^2}{32\pi G\mu_0^2}\left[c^2(\boldsymbol{\nabla}\Psi)^2 - \dot{\Psi}^2\right] - \frac{1}{8\pi G}N\ddot{\Psi}. \tag{4.107}$$

The stress-energy tensor does not appear in this expression (under the guise of σ or σ_s) because the radiation zone does not contain any matter. In computing the source τ_s, we can ignore the radiation-zone contribution to the scalar field, as the corresponding contributions to the source will enter at beyond the order that we work. Thus, we use the scalar field as given in Eq. (4.97); the metric field N can be expanded in a similar way. At this order, only the monopole and dipole pieces of these fields appear in τ_s.

$$N = \frac{4G}{c^2}\frac{\mathcal{I}}{R} + \cdots, \tag{4.108}$$

$$\Psi = \frac{2G}{c^2}\frac{\mathcal{I}_s}{R} - \frac{2G}{c^2}\partial_i\left(\frac{\mathcal{I}_s^i}{R}\right) + \cdots, \tag{4.109}$$

where the mass monopole moment $\mathcal{I}$ is defined as in Eq. (4.98) with τ^{00}. Plugging these expressions into Eq. (4.107), we find

$$\begin{aligned}\tau_s =& -\frac{G(B+4\mu_0^2)}{2\pi\mu_0^2c^2}\left(\frac{\mathcal{I}_s\dot{\mathcal{I}}_s}{R^3c} + \frac{(\mathcal{I}_s)^2}{R^4}\right) - \frac{G}{\pi c^4}\frac{\mathcal{I}\ddot{\mathcal{I}}_s}{R^2} - \frac{G}{\pi c^4}\left(\frac{\mathcal{I}\dddot{\mathcal{I}}_s^j}{R^2c} + \frac{\mathcal{I}\ddot{\mathcal{I}}_s^j}{R^3}\right)\hat{N}^j \\ &- \frac{G(B+4\mu_0^2)}{\pi c^2}\left(\frac{\mathcal{I}_s\ddot{\mathcal{I}}_s^j}{R^3c^2} + \frac{2\mathcal{I}_s\dot{\mathcal{I}}_s^j}{R^4c} + \frac{2\mathcal{I}_s\mathcal{I}_s^j}{R^5} + \frac{\dot{\mathcal{I}}_s\dot{\mathcal{I}}_s^j}{R^3c^2} + \frac{\dot{\mathcal{I}}_s\mathcal{I}_s^j}{R^4c}\right)\hat{N}^j.\end{aligned} \tag{4.110}$$

where we've used the fact that the moments are functions of retarded time, so that $\partial_j \mathcal{I}_s^j = -\dot{\mathcal{I}}_s^j \hat{N}^j/c$. The first line of Eq. (4.110) contains the lowest order terms, which enter at c^{-3} order relative to the leading contribution to $\Psi_{\mathcal{N}}$ from the near zone, while the second line contains terms that are suppressed by one additional factor of c.

We note that all of the terms in τ_s in the radiation zone take the form

$$\tau_s(l,n) = \frac{1}{4\pi}\frac{f(\tau)}{R^n}\hat{N}^{k_1}\cdots\hat{N}^{k_l}. \tag{4.111}$$

With this information, each corresponding term in Eq. (4.106) can be rewritten as

$$\Psi_{\mathcal{C}-\mathcal{N}}(l,n) = \frac{2G}{Rc^2}\hat{N}^{k_1}\cdots\hat{N}^{k_l}\left[\int_0^{\mathcal{R}} f(\tau-2s)A(s,R)ds + \int_{\mathcal{R}}^{\infty} f(\tau-2s)B(s,R)ds\right], \tag{4.112}$$

with

$$A(s,R) \equiv \int_{\mathcal{R}}^{R+s} \frac{P_l(\Lambda)}{p^{n-1}}dp, \tag{4.113}$$

$$B(s,R) \equiv \int_{s}^{R+s} \frac{P_l(\Lambda)}{p^{n-1}}dp, \tag{4.114}$$

$$\Lambda \equiv \frac{R+2s}{R} - \frac{2s(R+s)}{Rp}, \tag{4.115}$$

and where $P_l(\Lambda)$ are Legendre polynomials.

Given Eq. (4.110), we see that $l = 0, 1$ and $n = 2-5$ integrals contribute to the scalar field at this order. However, by inspection, the $l = 1$ terms have odd parity, and thus will not contribute to the scalar mass. The $l = 0$ contributions [in

the notation of Eq. (4.112)] are given by

$$\begin{aligned}\Psi_{\mathcal{C}-\mathcal{N}}(0,2) =& -\frac{4G^2}{Rc^6}\int_{-\infty}^{\tau} du \left(\log\left(R+\frac{\tau}{2}-\frac{u}{2}\right)\left[\mathcal{I}\ddot{\mathcal{I}}_s\right]_u \right.\\ &\left. -\log\left(\mathcal{R}+\frac{\tau}{2}-\frac{u}{2}\right)\left[\mathcal{I}\ddot{\mathcal{I}}_s\right]_{u-2\mathcal{R}}\right) - \log\mathcal{R}\int_{\tau-2\mathcal{R}}^{\tau} du\left[\mathcal{I}\ddot{\mathcal{I}}_s\right]_u ,\end{aligned} \tag{4.116}$$

$$\begin{aligned}\Psi_{\mathcal{C}-\mathcal{N}}(0,3) =& \frac{2G^2}{Rc^5}\frac{B+4\mu_0^2}{\mu_0^2}\left(\frac{\mathcal{I}_s^2(\tau)}{2R}-\frac{\mathcal{I}_s^2(\tau)}{2\mathcal{R}}\right.\\ &\left. -\int_{-\infty}^{\tau} du\left(\frac{[\mathcal{I}_s^2]_u}{(2R+\tau-u)^2}-\frac{[\mathcal{I}_s^2]_{u-2\mathcal{R}}}{(2\mathcal{R}+\tau-u)^2}\right)\right),\end{aligned} \tag{4.117}$$

$$\begin{aligned}\Psi_{\mathcal{C}-\mathcal{N}}(0,4) =& \frac{4G^2}{Rc^4}\frac{B+4\mu_0^2}{\mu_0^2}\left(\int_{-\infty}^{\tau} du\left(\frac{[\mathcal{I}_s^2]_u}{(2R+\tau-u)^2}-\frac{[\mathcal{I}_s^2]_{u-2\mathcal{R}}}{(2\mathcal{R}+\tau-u)^2}\right)\right.\\ &\left. -\frac{1}{(2\mathcal{R})^2}\int_{\tau-2\mathcal{R}}^{\tau} du\left[\mathcal{I}_s^2\right]_u\right),\end{aligned} \tag{4.118}$$

where we have used the shorthand $[fg]_x = f(x)g(x)$. Nearly all of these terms are hereditary, i.e. depend on the full history of the system up to the retarded time τ. The one exception is the first term in Eq. (4.117), but this term falls off too quickly with R to contribute to the scalar mass.

4.7 Two-body Scalar mass

Having expressed the scalar field in the radiation zone entirely in terms of the (even) scalar multipole moments, we now specialize to an inspiraling binary system. Plugging the potentials for a two-body system (Appendix F) into Eq. (4.100), we integrate to find the scalar moments. Integrals containing σ_s can be evaluated directly as they contain delta functions at the worldlines of the bodies. The remaining terms are integrated by parts, using techniques analogous to those outlined in Sec. III of Ref. [150]. The multipoles needed to compute the scalar mass

at 1PD order are given by

$$\begin{aligned}\mathcal{I}_s =&\frac{\mu_0 m_1 \alpha_1}{\phi_0}\left\{1-\frac{v_1^2}{2c^2}-\frac{Gm_2}{\phi_0 r c^2}\left(1+\mu_0\alpha_2\right)-\frac{v_1^4}{8c^4}+\frac{Gm_2}{\phi_0 r c^2}\left[-\frac{3}{2}\frac{\left(\mathbf{v}_2\cdot\mathbf{n}\right)^2}{c^2}\right.\right.\\&+\left(\frac{2\mu_0(1-\alpha_2\mu_0)-B\alpha_2}{4\mu_0}\right)\frac{v_1^2}{c^2}+\left(\frac{B\alpha_2-8\mu_0+6\alpha_2\mu_0^2}{4\mu_0}\right)\frac{\left(\mathbf{v}_1\cdot\mathbf{n}\right)^2}{c^2}\\&\left.+\left(\frac{\alpha_2(B+4\mu_0^2)}{4\mu_0}\right)\frac{\left(\mathbf{v}_1\cdot\mathbf{v}_2\right)}{c^2}-\left(\frac{B\alpha_2-16\mu_0+4\alpha_2\mu_0^2}{4\mu_0}\right)\frac{\left(\mathbf{v}_1\cdot\mathbf{n}\right)\left(\mathbf{v}_2\cdot\mathbf{n}\right)}{c^2}\right]\\&+\frac{G^2m_1m_2}{\phi_0^2r^2c^4}\left[-\frac{1}{2}+\mu_0\alpha_1-\frac{(B-6\mu_0^2)\alpha_2}{4\mu_0}-\frac{(B+6-6\mu_0^2)\alpha_1\alpha_2}{4}\right.\\&\left.-\frac{(B+2\mu_0^2)\alpha_1\alpha_2^2}{4\mu_0}\right]+\frac{G^2m_2^2}{2\phi_0^2r^2c^4}-\frac{Gm_2}{\phi_0c^4}\left[\frac{B\alpha_2-4\mu_0(1-\alpha_2\mu_0)}{2\mu_0}\right]\left(\mathbf{a}_1\cdot\mathbf{n}\right)\Bigg\}\\&+\left(1\rightleftharpoons 2\right),\end{aligned} \tag{4.119}$$

$$\begin{aligned}\mathcal{I}_s^{ij} =&\frac{\mu_0 m_1\alpha_1 x_1^i x_1^j}{\phi_0}\left[1-\frac{v_1^2}{2c^2}-\frac{Gm_2}{\phi_0 r c^2}\left(1+\mu_0\alpha_2\right)\right]+\frac{Gm_1m_2\alpha_1\alpha_2(B+4\mu_0^2)r}{4\phi_0^2\mu_0c^2}\delta^{ij}\\&+\left(1\rightleftharpoons 2\right),\end{aligned} \tag{4.120}$$

$$\mathcal{I}_s^{ijkl} =\frac{\mu_0 m_1\alpha_1 x_1^i x_1^j x_1^k x_1^l}{\phi_0}+\left(1\rightleftharpoons 2\right). \tag{4.121}$$

We evaluate Eq. (4.99) with these moments to compute the near zone contribution to the scalar field. Before proceeding, we briefly detail how time derivatives of the masses m_i and scalar charges α_i are handled. Recall that the dependence of each body's mass (and scalar charge) on the local scalar field is decomposed into a resummed and expanded piece, represented by its dependence on ξ and ϕ, respectively. Thus, the derivative of the mass would be given by

$$\frac{dm_A}{dt}=\frac{\partial m_A}{\partial\phi}v_A^\mu\partial_\mu\phi+\frac{\partial m_A}{\partial\xi}v_A^\mu\partial_\mu\xi, \tag{4.122}$$

where $v_A^\mu = u_A^\mu/u_A^0$. To reinforce that the fields ϕ and ξ really represent the same physical scalar, we relate the two through Eq. (4.23). Thus (assuming differentiability), their gradients along each worldline are related as

$$u_A^\mu \partial_\mu \xi = \frac{dF}{d\phi} u_A^\mu \partial_\mu \phi. \tag{4.123}$$

In truth, because we expand only ϕ and not ξ, Eqs. (4.23) and (4.123) only hold in an approximate sense [e.g. up to 1PD order when using Eq. (4.85)]. Nevertheless, one finds that

$$\frac{dm_A}{dt} = \frac{Dm_A}{D\phi} v^\mu \partial_\mu \phi + \mathcal{O}\left(\frac{1}{c^4}\right). \tag{4.124}$$

Because the time dependence of the mass enters only through the scalar field (whose leading order term is constant), its derivative is suppressed by an additional factor of c^{-2} more than dimensional analysis would suggest, i.e. $\dot{m}/m \sim c^{-2}$. This suppression greatly simplifies our calculation of the scalar field.

Equipped with the scalar moments and a prescription for differentiating with respect to time, we calculate the near-zone contribution to the scalar field of a binary system

$$\Psi_{\mathcal{N}} = \Psi_{\mathcal{N}}^{(-1)} + \Psi_{\mathcal{N}}^{(0)} + \Psi_{\mathcal{N}}^{(1)}, \tag{4.125}$$

with

$$\Psi_{\mathcal{N}}^{(-1)} = \frac{2G\mu_0 m_1 \alpha_1}{\phi_0 R c^2} + (1 \rightleftharpoons 2) \tag{4.126}$$

$$\begin{aligned}\Psi_{\mathcal{N}}^{(0)} = &\frac{2G\mu_0 m_1 \alpha_1}{\phi_0 R c^2} \left\{ -\frac{v_1^2}{2c^2} + \frac{(\hat{\mathbf{N}}\cdot\mathbf{v}_1)^2}{c^2} - \frac{Gm_2}{\phi_0 r c^2}(1 + \mu_0\alpha_2 \right. \\ &\left. + (1+\alpha_1\alpha_2)\frac{(\hat{\mathbf{N}}\cdot\mathbf{x}_1)^2 - (\hat{\mathbf{N}}\cdot\mathbf{x}_1)(\hat{\mathbf{N}}\cdot\mathbf{x}_2)}{r^2} \right) \right\} + (1 \rightleftharpoons 2)\end{aligned} \tag{4.127}$$

$$
\begin{aligned}
\Psi^{(1)}_{\mathcal{N}} =& \frac{2G\mu_0 m_1\alpha_1}{\phi_0 Rc^2}\left\{-\frac{v_1^4}{8c^4}+\frac{Gm_2}{\phi_0 rc^2}\left[\left(\frac{1+\mu_0\alpha_2}{2}\right)\frac{v_1^2}{c^2}-\left(\frac{4-\mu_0\alpha_2}{2}\right)\frac{(\mathbf{v}_1\cdot\mathbf{n})^2}{c^2}\right.\right.\\
&\left.-\frac{3(\mathbf{v}_2\cdot\mathbf{n})^2}{2c^2}+\frac{4(\mathbf{v}_1\cdot\mathbf{n})(\mathbf{v}_2\cdot\mathbf{n})}{c^2}\right]-\frac{G^2m_1m_2}{\phi_0 r^2c^4}\left[\frac{1}{2}-\mu_0\alpha_1-\frac{5\mu_0\alpha_2}{2}\right.\\
&\left.+\frac{(6+B-6\mu_0^2)\alpha_1\alpha_2}{4}+2\alpha_2^2-\frac{\mu_0\alpha_1\alpha_2^2}{2}\right]-\frac{3G^2m_2^2}{2\phi_0^2r^2c^4}\\
&-\left(\frac{v_1^2}{2c^2}+\frac{Gm_2(1+\mu_0\alpha_2)}{\phi_0 rc^2}\right)\frac{(\mathbf{v}_1\cdot\hat{\mathbf{N}})^2}{c^2}\\
&+\frac{Gm_2}{\phi_0 rc^2}\left(-4(\mathbf{v}_1\cdot\mathbf{n})+(3-\alpha_1\alpha_2)(\mathbf{v}_2\cdot\mathbf{n})\right)\frac{(\mathbf{x}_1\cdot\hat{\mathbf{N}})(\mathbf{v}_2\cdot\hat{\mathbf{N}})}{rc}\\
&+\frac{Gm_2}{\phi_0 rc^2}\left[\left(8-\left(2\mu_0+\frac{B}{\mu_0}+4\mu_0\phi_0\frac{D(\log m_1\alpha_1)}{D\phi}\right)\alpha_2+2\alpha_1\alpha_2\right)\frac{(\mathbf{v}_1\cdot\mathbf{n})}{c}\right.\\
&\qquad\left.-\left(5-\left(2\mu_0+\frac{B}{\mu_0}+4\mu_0\phi_0\frac{D(\log m_1\alpha_1)}{D\phi}\right)\alpha_2-\alpha_1\alpha_2\right)\frac{(\mathbf{v}_2\cdot\mathbf{n})}{c}\right]\frac{(\mathbf{x}_1\cdot\hat{\mathbf{N}})(\mathbf{v}_1\cdot\hat{\mathbf{N}})}{rc}\\
&+\frac{Gm_2}{\phi_0 rc^2}\left[\frac{4\mu_0^2(\mathbf{v}_1\cdot\mathbf{n})}{c}-\frac{4\mu_0^2(\mathbf{v}_2\cdot\mathbf{n})}{c}\right]\frac{(\mathbf{x}_2\cdot\hat{\mathbf{N}})(\mathbf{v}_2\cdot\hat{\mathbf{N}})}{rc}\\
&+\frac{Gm_2}{\phi_0 rc^2}\left[-\frac{(1-3\alpha_1\alpha_2)v_1^2}{2c^2}-\frac{2v_2^2}{c^2}+\frac{4(\mathbf{v}_1\cdot\mathbf{v}_2)}{c^2}+\frac{3(1+\alpha_1\alpha_2)(\mathbf{v}_2\cdot\mathbf{n})^2}{2c^2}\right.\\
&\qquad\left.+\frac{Gm_1(1+\alpha_1\alpha_2)(5+\mu_0\alpha_1)}{\phi_0 rc^2}+\frac{Gm_2(1+\alpha_1\alpha_2)(5+\mu_0\alpha_2)}{\phi_0 rc^2}\right]\frac{(\mathbf{x}_1\cdot\hat{\mathbf{N}})(\mathbf{n}\cdot\hat{\mathbf{N}})}{r}\\
&+\frac{Gm_2}{\phi_0 rc^2}\left[\frac{1}{2}\left(2-\left(\mu_0+\frac{B}{2\mu_0}+2\phi_0\mu_0\frac{D(\log m_1\alpha_1)}{D\phi}\right)\alpha_2+\alpha_1\alpha_2\right)\frac{v_1^2}{c^2}\right.\\
&\qquad+\frac{1}{2}\left(1-\left(\mu_0+\frac{B}{2\mu_0}+2\phi_0\mu_0\frac{D(\log m_1\alpha_1)}{D\phi}\right)\alpha_2\right)\frac{v_2^2}{c^2}\\
&\qquad-\frac{1}{2}\left(3-\left(2\mu_0+\frac{B}{\mu_0}+4\phi_0\mu_0\frac{D(\log m_1\alpha_1)}{D\phi}\right)\alpha_2+\alpha_1\alpha_2\right)\frac{(\mathbf{v}_1\cdot\mathbf{v}_2)}{c^2}\\
&\qquad-\frac{3}{2}\left(2-\left(\mu_0+\frac{B}{2\mu_0}+2\phi_0\mu_0\frac{D(\log m_1\alpha_1)}{D\phi}\right)\alpha_2+\alpha_1\alpha_2\right)\frac{(\mathbf{v}_1\cdot\mathbf{n})^2}{c^2}\\
&\qquad-\frac{3}{2}\left(1-\left(\mu_0+\frac{B}{2\mu_0}+2\phi_0\mu_0\frac{D(\log m_1\alpha_1)}{D\phi}\right)\alpha_2\right)\frac{(\mathbf{v}_2\cdot\mathbf{n})^2}{c^2}\\
&\qquad+\frac{3}{2}\left(3-\left(2\mu_0+\frac{B}{\mu_0}+4\phi_0\mu_0\frac{D(\log m_1\alpha_1)}{D\phi}\right)\alpha_2+\alpha_1\alpha_2\right)\frac{(\mathbf{v}_1\cdot\mathbf{n})(\mathbf{v}_2\cdot\mathbf{n})}{c^2}\\
&\qquad-\frac{1}{2}\left(2+3\alpha_1\alpha_2+2\mu_0^2\alpha_2^2+\alpha_1^2\alpha_2^2\right.\\
&\qquad\qquad\left.\left.-\left(\mu_0+\frac{B}{2\mu_0}+2\phi_0\mu_0\frac{D(\log m_1\alpha_1)}{D\phi}\right)(1+\alpha_1\alpha_2)\alpha_2\right)\frac{Gm_2}{\phi_0 rc^2}\right.
\end{aligned}
$$

$$
\begin{aligned}
&-\frac{1}{2}\Bigg(1+\alpha_1\alpha_2+2\mu_0^2\alpha_2^2 \\
&\qquad -\left(\mu_0+\frac{B}{2\mu_0}+2\phi_0\mu_0\frac{D(\log m_1\alpha_1)}{D\phi}\right)(1+\alpha_1\alpha_2)\alpha_2\Bigg)\frac{Gm_1}{\phi_0 rc^2}\Bigg]\frac{(\mathbf{x}_1\cdot\hat{\mathbf{N}})^2}{r^2} \\
&+\frac{Gm_2}{\phi_0 rc^2}\left[\frac{\mu_0^2v_1^2}{c^2}+\frac{\mu_0^2v_2^2}{c^2}-\frac{2\mu_0^2(\mathbf{v}_1\cdot\mathbf{v}_2)}{c^2}-\frac{3\mu_0^2(\mathbf{v}_1\cdot\mathbf{n})^2}{c^2}-\frac{3\mu_0^2(\mathbf{v}_2\cdot\mathbf{n})^2}{c^2}\right. \\
&\qquad \left.+\frac{6\mu_0^2(\mathbf{v}_1\cdot\mathbf{n})(\mathbf{v}_2\cdot\mathbf{n}))}{c^2}-\frac{G\mu_0^2m_2}{\phi_0 rc^2}-\frac{G\mu_0^2m_1}{\phi_0 rc^2}\right]\frac{(\mathbf{x}_2\cdot\hat{\mathbf{N}})^2}{r^2}+\frac{(\mathbf{v}_1\cdot\hat{\mathbf{N}})^4}{c^4} \\
&-\frac{2Gm_2(1+\alpha_1\alpha_2)}{\phi_0 rc^2}\frac{(\mathbf{x}_1\cdot\hat{\mathbf{N}})^2(\mathbf{v}_1\cdot\hat{\mathbf{N}})^2}{r^2c^2}-\frac{6Gm_2(1+\alpha_1\alpha_2)}{\phi_0 rc^2}\frac{(\mathbf{x}_1\cdot\hat{\mathbf{N}})(\mathbf{v}_1\cdot\hat{\mathbf{N}})^2(\mathbf{n}\cdot\hat{\mathbf{N}})}{rc^2} \\
&+\frac{2Gm_2(1+\alpha_1\alpha_2)}{\phi_0 rc^2}\frac{(\mathbf{x}_1\cdot\hat{\mathbf{N}})^2(\mathbf{v}_1\cdot\hat{\mathbf{N}})(\mathbf{v}_2\cdot\hat{\mathbf{N}})}{r^2c^2} \\
&+\frac{6Gm_2(1+\alpha_1\alpha_2)}{\phi_0 rc^2}\left[\frac{(\mathbf{v}_1\cdot\mathbf{n})}{c}-\frac{(\mathbf{v}_2\cdot\mathbf{n})}{c}\right]\frac{(\mathbf{x}_1\cdot\hat{\mathbf{N}})^2(\mathbf{v}_1\cdot\hat{\mathbf{N}})(\mathbf{n}\cdot\hat{\mathbf{N}})}{r^2c} \\
&+\frac{Gm_2(1+\alpha_1\alpha_2)}{\phi_0 rc^2}\left[\frac{(\mathbf{v}_1\cdot\mathbf{n})}{c}-\frac{(\mathbf{v}_2\cdot\mathbf{n})}{c}\right]\frac{(\mathbf{x}_1\cdot\hat{\mathbf{N}})^3(\mathbf{v}_1\cdot\hat{\mathbf{N}})}{r^3c} \\
&-\frac{Gm_2(1+\alpha_1\alpha_2)}{\phi_0 rc^2}\left[\frac{(\mathbf{v}_1\cdot\mathbf{n})}{c}-\frac{(\mathbf{v}_2\cdot\mathbf{n})}{c}\right]\frac{(\mathbf{x}_1\cdot\hat{\mathbf{N}})^3(\mathbf{v}_2\cdot\hat{\mathbf{N}})}{r^3c} \\
&+\frac{3G^2m_2^2(1+\alpha_1\alpha_2)^2}{2\phi_0^2r^2c^4}\frac{(\mathbf{x}_1\cdot\hat{\mathbf{N}})^2(\mathbf{n}\cdot\hat{\mathbf{N}})^2}{r^2} \\
&+\frac{Gm_2(1+\alpha_1\alpha_2)}{\phi_0 rc^2}\left[\frac{v_1^2}{2c^2}+\frac{v_2^2}{2c^2}-\frac{(\mathbf{v}_1\cdot\mathbf{v}_2)}{c^2}-\frac{5(\mathbf{v}_1\cdot\mathbf{n})^2}{2c^2}+\frac{5(\mathbf{v}_1\cdot\mathbf{n})(\mathbf{v}_2\cdot\mathbf{n})}{c^2}\right. \\
&\qquad \left.-\frac{5(\mathbf{v}_2\cdot\mathbf{n})^2}{2c^2}-\frac{Gm_1(1+\alpha_1\alpha_2)}{3\phi_0 rc^2}-\frac{Gm_2(1+\alpha_1\alpha_2)}{3\phi_0 rc^2}\right]\frac{(\mathbf{x}_1\cdot\hat{\mathbf{N}})^3(\mathbf{n}\cdot\hat{\mathbf{N}})}{r^3}\Bigg\} \\
&+(1\rightleftharpoons 2)\,, \qquad (4.128)
\end{aligned}
$$

where we have dropped the pieces that do not contribute to the scalar mass and have used Eqs. (4.83) and (4.84) to eliminate the bodies' accelerations.

To the order at which we work, the radiation-zone contribution to scalar mass is zero. The scalar monopole $\mathcal{I}_s$ is the only multipole that enters in Eqs. (4.116)–(4.118); as discussed above, at leading order, the monopole is constant in time. This insight allows one to trivially evaluate these hereditary integrals. The non-zero

terms either depend on the arbitrarily chosen boundary $\mathcal{R}$ (and thus are canceled by near-zone contributions to the scalar field) or fall off too quickly with R to contribute to the scalar mass.

Computing the scalar mass from the scalar field given in Eqs. (4.125)–(4.128) is most easily done in the center of mass frame. However, we cannot compute the exact transformation to this frame in the PD formalism without first calculating the total momentum of the system.[8] Instead, we consider frames in which the two bodies' positions are related by $\mathbf{x}_1 \propto -\mathbf{x}_2$. Without dissipative effects, we expect the center of mass frame to satisfy this criterion.

Furthermore, we restrict our attention to binary systems undergoing circular motion. Neutron-star binaries are expected to radiate away any eccentricity relatively early in their evolution, long before they would be detectable by ground-based experiments like LIGO, thereby justifying this approximation.

We plug the expression for the scalar field in Eq. (4.125) into Eq. (4.95) to obtain the scalar mass. This surface integral can be computed easily using the standard angular coordinates (θ, ϕ) on the coordinate sphere of radius R. The scalar mass takes the exact same form as the scalar field with the $\hat{\mathbf{N}}$-dependent

[8] In the PN formalism, the transformation to the center of mass frame is derived by forcing the total momentum of the binary system to vanish. The momentum is difficult to calculate within the PD approach because the equations of motion cannot be derived from a Lagrangian dependent solely on the particles' positions and velocities. Thus, the exact transformation to the center of mass frame remains unknown.

terms replaced by the geometric quantities derived below

$$-\oint_{R\to\infty}\partial_i\left(\frac{f(\theta,\phi)}{R}\right)dS_i=\int f(\theta,\phi)d(\cos\theta)d\phi, \tag{4.129}$$

and

$$\int(\hat{\mathbf{N}}\cdot\mathbf{x}_A)(\hat{\mathbf{N}}\cdot\mathbf{x}_B)d(\cos\theta)d\phi=\frac{4\pi}{3}\tilde{\gamma}_{AB}x_Ax_B, \tag{4.130}$$

$$\int(\hat{\mathbf{N}}\cdot\mathbf{v}_A)(\hat{\mathbf{N}}\cdot\mathbf{v}_B)d(\cos\theta)d\phi=\frac{4\pi}{3}\tilde{\gamma}_{AB}v_Av_B, \tag{4.131}$$

$$\int(\hat{\mathbf{N}}\cdot\mathbf{x}_A)(\hat{\mathbf{N}}\cdot\mathbf{x}_B)(\hat{\mathbf{N}}\cdot\mathbf{x}_C)(\hat{\mathbf{N}}\cdot\mathbf{x}_D)d(\cos\theta)d\phi=\frac{4\pi}{5}\tilde{\gamma}_{AB}\tilde{\gamma}_{CD}x_Ax_Bx_Cx_D, \tag{4.132}$$

$$\int(\hat{\mathbf{N}}\cdot\mathbf{v}_A)(\hat{\mathbf{N}}\cdot\mathbf{v}_B)(\hat{\mathbf{N}}\cdot\mathbf{v}_C)(\hat{\mathbf{N}}\cdot\mathbf{v}_D)d(\cos\theta)d\phi=\frac{4\pi}{5}\tilde{\gamma}_{AB}\tilde{\gamma}_{CD}v_Av_Bv_Cv_D, \tag{4.133}$$

$$\int(\hat{\mathbf{N}}\cdot\mathbf{x}_A)(\hat{\mathbf{N}}\cdot\mathbf{x}_B)(\hat{\mathbf{N}}\cdot\mathbf{v}_C)(\hat{\mathbf{N}}\cdot\mathbf{v}_D)d(\cos\theta)d\phi=\frac{4\pi}{15}\tilde{\gamma}_{AB}\tilde{\gamma}_{CD}x_Ax_Bv_Cv_D, \tag{4.134}$$

where we have defined

$$\tilde{\gamma}_{AB}\equiv\begin{cases}1, & \text{if } A=B\\ \\ -1, & \text{if } A\neq B\end{cases}. \tag{4.135}$$

The scalar mass is given by

$$\begin{aligned}M_S=&\frac{m_1\alpha_1\mu_0}{\phi_0}\left[1-\frac{v_1^2}{6c^2}-\frac{Gm_2}{\phi_0rc^2}\left(1+\mu_0\alpha_2+\left(\frac{1+\alpha_1\alpha_2}{3}\right)\frac{r_1}{r}\right)\right]\\&+\Big[\text{1PD}\Big]+(1\rightleftharpoons 2)\,,\end{aligned} \tag{4.136}$$

where the 1PD terms are represented only schematically for the sake of compactness.

4.8 Validity of the Post-Dickean expansion

The PD expansion was motivated through analogy: spontaneous and dynamical scalarization are suspected to arise from similar mechanisms, and so the analytic

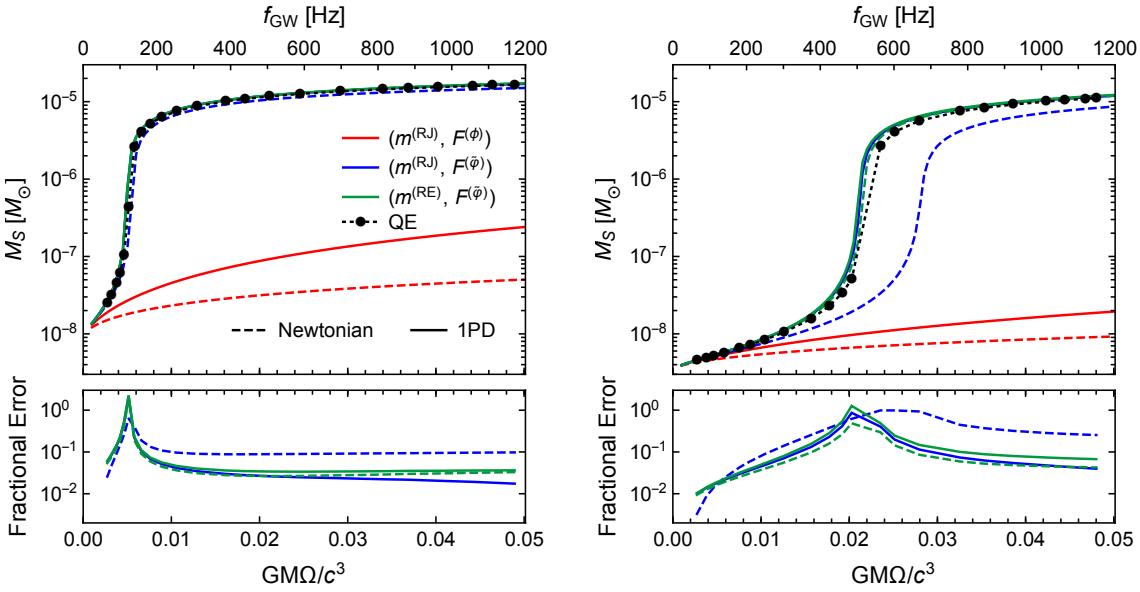

Figure 4.4: Scalar mass of a $(1.35+1.35)M_\odot$ neutron-star binary system on a circular orbit as a function of the orbital angular frequency and gravitational wave frequency ($f_{\rm GW} = \Omega/\pi$). The scalar mass is computed at Newtonian (dashed) and 1PD (solid) order for resummation schemes listed in Table 4.1. We also plot the quasi-equilibrium configuration calculations (QE) reported in Ref. [172] (dotted). The bottom panels depict the magnitude of the fractional error between the PD and quasi-equilibrium results. We use the APR4 equation of state with (left) $B = 9$, $\tilde{\varphi}_0 = 3.33 \times 10^{-11}$ and (right) $B = 8.4$, $\tilde{\varphi}_0 = 3.45 \times 10^{-11}$.

techniques applied to the former (resummation of expansions in Gm/Rc^2) should also be used with latter (partial resummation of expansions in Gm/rc^2). While such reasoning seems plausible, ultimately, the validity of our model can only be checked via comparison with high-precision numerical calculations. In absence of long numerical-relativity simulations of DS, we compare the PD approximation to recent quasi-equilibrium configuration calculations. We also closely examine the differences between the PD approximation and the analytic model proposed in Ref. [170] for completeness

4.8.1 Quasi-equilibrium configurations

The scalar mass of an equal-mass binary system was calculated along sequences of quasi-equilibrium configurations in Ref. [172]. Inherent to these calculations is the assumption of a conformally flat and stationary spacetime; physically, each configuration represents a binary system following a circular orbit. Despite neglecting the loss of energy and angular momentum through the emission of gravitational radiation, this setup is believed to closely resemble the adiabatic inspiral of a neutron-star binary system. Systematic errors enter these quasi-equilibrium calculations through the physical assumptions made above and imperfect numerical convergence, particularly at higher frequencies. At present, the magnitude of these errors is not well-understood.

We compare the PD predictions of the scalar mass with these numerical results to validate the accuracy of the model. Figure 4.4 depicts the scalar mass as a

function of orbital frequency Ω for a (1.35+1.35) $M_\odot$ binary system, where the PD corrections to Kepler's third law for an equal mass system (derived from the equations of motion)

$$\Omega^2 = \frac{GM(1+\alpha^2)}{r^3\phi_0} - \frac{G^2M^2(1+\alpha^2)(11+2\mu_0\alpha+\alpha^2)}{4r^4\phi_0^2c^2}, \tag{4.137}$$

are used to replace the r-dependence in Eq. (4.136), and where $M = m_1 + m_2$ and $\alpha = \alpha_1 = \alpha_2$. The scalar mass is computed at Newtonian (dashed) and 1PD (solid) order; note that the former calculation is done consistently at Newtonian order [e.g. only the first term in Eq. (4.137) is used]. We employ the APR4 equation of state, for which the allowed range of theory parameters in which DS can occur is spanned by $B \in [8, 9]$ (see Ref. [171] for more detail). From this range, we focus on the cases $B = 9$ and $B = 8.4$, corresponding to the choices $\tilde{\varphi}_0 = 3.33 \times 10^{-11}$ and $\tilde{\varphi}_0 = 3.45 \times 10^{-11}$ considered in Ref. [172]. For all PD calculations, we use a Newton-Raphson method to numerically solve Eqs. (4.85) and (4.86) to within a fractional error of 10^{-7}.

Recall that the PD expansion encodes a flexibility in "what to resum" in the choice of $m(\phi, \xi)$ and $F(\phi)$. We compare each combination of the choices in Table 4.1 in Fig. 4.4, denoting each resummation scheme by the pair (m, F). The scalar mass estimated with the $(m^{(\mathrm{RJ})}, F^{(\phi)})$ and $(m^{(\mathrm{RE})}, F^{(\phi)})$ resummation schemes differ by only $\sim 0.01\%$; to improve legibility, we only plot the former (in red).

The two most important features depicted in Fig. 4.4 that we hope to recover with our model are the frequency at which DS occurs Ω_{DS} and the magnitude of the scalar mass after scalarization. We extract the onset of DS from the figure using

the fitting procedure detailed in Ref. [172]; these values are given in Table 4.2. One finds that the scalar mass M_S can be well approximated by

$$\left(1+\left(\frac{M_S}{M\mu_0}\right)^2\right)^{10/3} = \begin{cases} 1, & \text{if } \Omega < \Omega_{\rm DS} \\ a_0 + a_1 x, & \text{if } \Omega > \Omega_{\rm DS} \end{cases} \tag{4.138}$$

where $x \equiv (GM\Omega/c^3)^{2/3}$. We determine the coefficients a_0 and a_1 by fitting the high frequency part of the curves in Fig. 4.4 and then find $\Omega_{\rm DS}$ from the intersection of this linear function with 1.

The 1PD predictions for both the location and magnitude of scalarization match the results of Ref. [172] at the $\lesssim 10\%$ level for the choice $F^{(\tilde{\varphi})}$. (Note that the peaks in the relative error seen in the bottom panels of Fig. 4.4 stem from the slight misalignment of the scalar mass predictions at the sharp onset of DS.) Interestingly, for systems that scalarize later in the inspiral (i.e. smaller values of B), the Newtonian order prediction in the $(m^{(\rm RE)}, F^{(\tilde{\varphi})})$ scheme agrees more closely with the numerical results. Without a more comprehensive study of various resummation schemes or the PD expansion at higher order, it is difficult to say whether this agreement is coincidental.

The choice of $m(\phi, \xi)$ seems to have little effect on the scalar mass predictions of the PD model. The two resummation schemes with $F^{(\phi)}$ are essentially indistinguishable, while the schemes with $F^{(\tilde{\varphi})}$ appear to converge to within a few percent at 1PD order.

On the other hand, the choice of $F(\phi)$ drastically alters the growth of the scalar mass. Of the two options presented in Table 4.1, only $F^{(\tilde{\varphi})}$ reproduces the sharp

Table 4.2: Orbital angular frequency and gravitational wave frequency at which dynamical scalarization occurs ($f^{\rm GW} = \Omega/\pi$) for the systems considered in Fig. 4.4. Only resummation schemes with the choice $F^{(\tilde{\varphi})}$ produce DS. For comparison, we list the results of the quasi-equilibrium configuration calculations (QE) of Ref. [172].

B	Model	Order	$GM\Omega_{\rm DS}/c^3$	$f^{\rm GW}_{\rm DS}$ [Hz]
9.0	$(m^{(\rm RJ)}, F^{(\tilde{\varphi})})$	Newtonian	0.0044	106
9.0	$(m^{(\rm RJ)}, F^{(\tilde{\varphi})})$	1PD	0.0047	112
9.0	$(m^{(\rm RE)}, F^{(\tilde{\varphi})})$	Newtonian	0.0052	124
9.0	$(m^{(\rm RE)}, F^{(\tilde{\varphi})})$	1PD	0.0051	122
9.0	QE	——	0.0051	123
8.4	$(m^{(\rm RJ)}, F^{(\tilde{\varphi})})$	Newtonian	0.0282	674
8.4	$(m^{(\rm RJ)}, F^{(\tilde{\varphi})})$	1PD	0.0212	508
8.4	$(m^{(\rm RE)}, F^{(\tilde{\varphi})})$	Newtonian	0.0217	520
8.4	$(m^{(\rm RE)}, F^{(\tilde{\varphi})})$	1PD	0.0212	508
8.4	QE	——	0.0223	534

transition consistent with dynamical scalarization. The significance of the choice of F can be seen by studying the behavior of the scalar charge $\alpha(\phi, \xi)$. Because the definition of ξ relies on the choice of resummation scheme [see Eq. (4.23)], we invert this definition and instead consider the dependence of the charge on an auxiliary field χ that is the same in all resummation schemes, defined as

$$\chi \equiv \sqrt{\frac{2\log(F^{-1}(\xi))}{B}} = \begin{cases} \sqrt{\frac{2\log\xi}{B}}, & \text{if } F(\phi) = \phi \\ \xi, & \text{if } F(\phi) = \sqrt{\frac{2\log\phi}{B}} \end{cases} \tag{4.139}$$

Figure 4.5 shows the leading order piece of the scalar charge α in the $(m^{(\rm RJ)}, F^{(\phi)})$ and $(m^{(\rm RE)}, F^{(\tilde{\varphi})})$ resummation schemes given in Eqs. (E.2) and (E.4). The resummed scalar charges in each scheme agree at $\chi = \tilde{\varphi}_0$, but they scale as

$$\alpha^{(\rm RJ,\phi)} \sim \frac{d\log m}{d\xi} \sim \frac{d\log m}{d\chi}\frac{1}{B\chi}e^{-B\chi^2/2} \sim \frac{d\log m}{d\chi}\frac{1}{\chi}, \tag{4.140}$$

$$\alpha^{(\rm RE,\tilde{\varphi})} \sim \frac{d\log m^{(E)}}{d\xi} \sim \frac{d\log m}{d\chi} - \frac{B\chi}{2} \sim \frac{d\log m}{d\chi}, \tag{4.141}$$

where we have used the fact that $\chi \ll 1$.

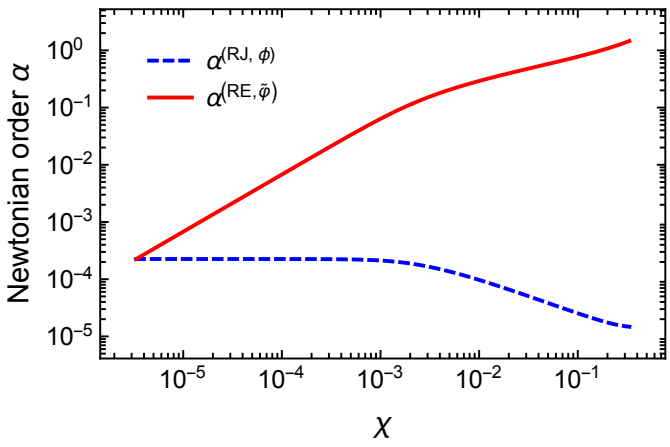

Figure 4.5: Newtonian order contribution to the scalar charge α of each neutron star in a $(1.35+1.35)M_\odot$ binary system as a function of the auxiliary field χ in the $(m^{(\mathrm{RJ})}, F^{(\phi)})$ and $(m^{(\mathrm{RE})}, F^{(\tilde{\varphi})})$ resummation schemes. We use the APR4 equation of state with $B = 9$, $\tilde{\varphi}_0 = 3.33 \times 10^{-11}$.

Without the additional factor of χ^{-1}, the scalar charge in the $(m^{(\mathrm{RE})}, F^{(\tilde{\varphi})})$ scheme grows with the local scalar field (the red curve in Fig. 4.5). This trend enables a positive feedback loop that ultimately emulates DS [170]. Intuitively, an increase in the field χ at one body increases its charge α, which, in turn, increases the field χ at the other body (and so on). No such feedback is possible within the $(m^{(\mathrm{RJ})}, F^{(\phi)})$ resummation scheme because α does not increase with greater ξ.

4.8.2 Earlier analytic models

The first analytic model of DS was proposed in Ref. [170]. This model used the 2.5PN equations of motion computed in Ref. [149], but altered the coefficients using a feedback mechanism designed to mimic DS. To 1PN order, these modified equations of motion are given in Eqs. (4.89)–(4.92) but with the important difference that $\bar{m}_i$ and $\bar{\alpha}_i$ are evaluated at an enhanced field value φ_B instead of at ϕ_0. To

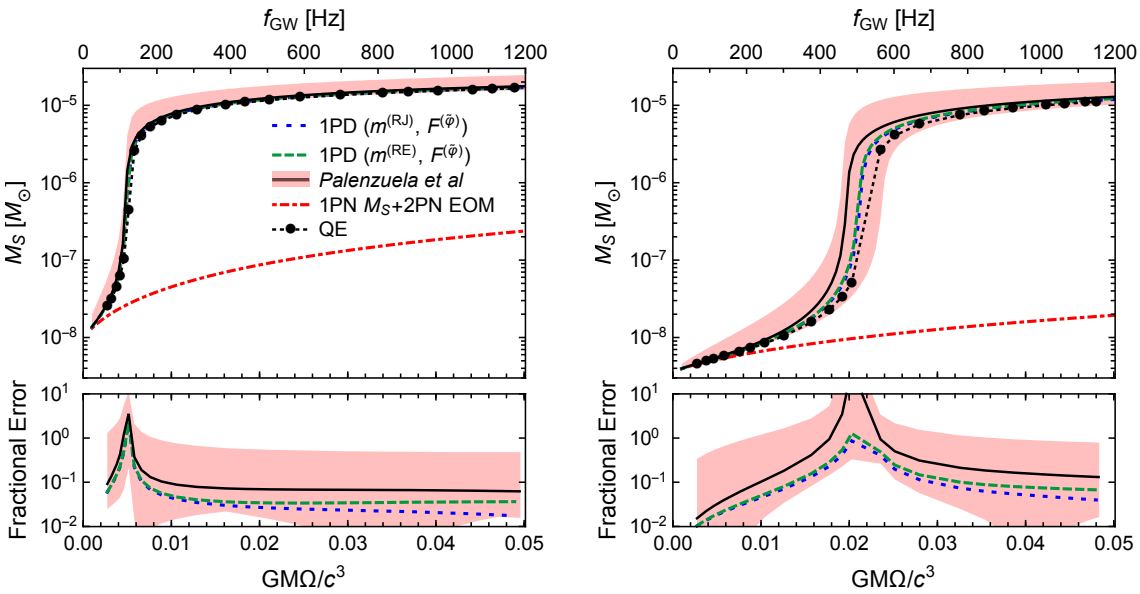

Figure 4.6: Scalar mass as a function of orbital frequency Ω and gravitational wave frequency $f_{\rm GW}$ of the binary system depicted in Fig. 4.4. The post-Dickean curves are calculated at 1PD order with the resummation schemes using $F^{(\tilde{\varphi})}$. The model proposed in Ref. [170] is plotted in black alongside the variations that we develop in Appendix G, which are collectively depicted by the pink region. For comparison, we plot the 1PN scalar mass (red) computed using the results of Ref. [151] (we use the 2PN equations of motion of Ref. [149] to restrict to circular orbits). The bottom panels depict the magnitude of the fractional error between the models and the quasi-equilibrium configurations (QE) of Ref. [172].

determine φ_B the authors numerically solved the Newtonian order relations

$$\varphi_B^{(1)} = \tilde{\varphi}_0 + \frac{G\bar{m}_2(\varphi_B^{(2)})\bar{\alpha}_2(\varphi_B^{(2)})}{\phi_0 r c^2}, \tag{4.142}$$

$$\varphi_B^{(2)} = (1 \rightleftharpoons 2)\,. \tag{4.143}$$

Additionally, the authors explicitly set the derivatives of the scalar charge $\bar{\alpha}'$, $\bar{\alpha}''$ to zero.

As reported in Ref. [170], this model captures dynamical scalarization and produces results (qualitatively) consistent with numerical-relativity simulations. The

model is easily implemented because it directly augments the PN results of Ref. [149] with Eqs. (4.142) and (4.143). However, mixing the Newtonian order feedback mechanism with higher-order equations of motion produces technical ambiguities in the model; we address these uncertainties in greater detail in Appendix G.

Comparing Eq. (4.80) with Eq. (4.142), we immediately see that our PD approach recovers the feedback mechanism of Ref. [170] at Newtonian order with the resummation schemes that use $F^{(\bar{\varphi})}$. Similarly, comparing Eq. (4.83) with Eq. (4.89), we see that the equations of motion for the binary system agree at Newtonian order with those of Ref. [170] provided we also use $m^{(\mathrm{RJ})}$.

Disparities arise between the two formalisms beyond Newtonian order. For the same resummation scheme adopted above, the auxiliary field given in Eq. (4.85) is the natural extension of the feedback model of Ref. [170] to higher order. Beyond the difference between ξ and φ_B, the equations of motion of each approach [Eq. (4.87) and Eq. (4.89)] differ only in the terms proportional to r^{-2} (recall that m_i and α_i receive PD corrections as discussed in Appendix E). However, as discussed at the end of Sec. 4.5, we expect a greater proportion of terms in the model of Ref. [170] to disagree with the PD equations of motion beyond post-Newtonian order.

To provide some context of the PD expansion's place relative to previous models, the scalar mass predicted by each of the analytic approximations discussed above is plotted in Fig. 4.6. As discussed in Sec 4.2.2, the unaltered PN approximation (denoted in red) does not reproduce DS, giving a scalar mass orders of magnitude smaller than numerical predictions. In contrast, the PD approximation (blue and green) agrees with the quasi-equilibrium calculations (dotted black) reported in Ref.

[172] at the level of $\lesssim 10\%$ when equipped with the proper resummation scheme. This level of accuracy is comparable to that achieved by the analytic model proposed in Ref. [170] (solid black). In addition, the technical ambiguities found in this earlier model (see Appendix G) generate some systematic uncertainty in its predictions. As a rough estimate of this uncertainty, we denote with the pink region the range of values spanned by all of the alternatives considered in Figs. G.1 and G.2. The PD formalism alleviates this issue by resumming the PN approximation in a mathematically consistent way, albeit with a freedom in the exact choice of quantities to resum.

4.9 Conclusions

In this work, we proposed the post-Dickean expansion, a new model of dynamical scalarization constructed by resumming the post-Newtonian expansion. The motivation for this approach stems from the success of previous analytic treatments of spontaneous scalarization, a phenomenon suspected to be closely related to DS. By appropriating tools from recent PN calculations [149–151], we derived the equations of motion and the scalar mass (a measure of scalarization) of a binary system at post-Newtonian order. Comparisons with recent numerical results [172] indicate that our new formalism captures DS accurately. The PD model exactly coincides with the analytic model introduced in Ref. [170] at leading order, but the ambiguities that arise at higher order in that earlier work are avoided with the PD approach because of its more rigorous and self-consistent formulation.

While this work establishes a framework for modeling DS, several further steps remain before it can be used to generate waveforms needed to test GR with GW detectors. Fortunately, most of these remaining calculations are straightforward, albeit lengthy. The waveform was recently computed to 2PN order in Ref. [2, 150].[9] Similarly to what was done in Secs. 4.4 and 4.6, the PD waveform can be calculated in precisely the same way as the PN result with a slightly modified stress-energy tensor. To reach the 2PD accuracy, one would also need to derive the equations of motion at that order. Again, all of the necessary steps have been completed for the PN calculation [149], so one can simply recycle that work with a new stress-energy tensor to produce the corresponding PD result.

The evolution of a binary system directly impacts the GW signal it produces. Thus, in conjunction with the waveform calculation sketched above, one would need to estimate the phase evolution of a binary in the PD formalism. One approach, analogous to what was done in Refs. [170, 175], would be to directly integrate the equations of motion. However, earlier surveys of PN models in GR indicate that such a procedure can produce unreliable waveforms [290]. Instead, a better approximation can be found by balancing the change in the (conservative) binding energy and the radiated flux far from the system. The flux was computed to 1PN order in Ref. [151]; this calculation could be redone in the PD expansion with a

[9] Advanced LIGO is most sensitive to a GW's transverse-traceless polarizations, for which the 2PN calculation was done. An additional transverse "breathing" mode would accompany the signal; this third polarization is determined by Ψ and has only been computed to 1.5PN order [151].

modified stress-energy tensor.

Unfortunately, the PD binding energy cannot be easily recomputed with existing PN work. To date, this energy has been calculated in the PN approach by integrating the (conservative) equations of motion to produce a Lagrangian and performing a Legendre transformation. However, as discussed at the end of Sec. 4.5, no such Lagrangian exists for the PD equations of motion because of the presence of the auxiliary field ξ. Without this shortcut, one would need to instead calculate the ADM energy at spatial infinity. To our knowledge, the full asymptotic metric has not been computed at spatial infinity to any PN order for the class of ST theories we consider. In principle, the 1PD energy could be estimated at null infinity because the system is fully conservative up to that order, but the results of Ref. [150] would have to be considerably extended, as the author computed only the traceless piece of the asymptotic metric. A more systematic approach should mimic the PN calculation of the ADM Hamiltonian in GR [291], in which all of the gravitational degrees are integrated out, leaving an energy dependent only on each body's position, momentum, and local scalar field ξ.

Besides the litany of PN results that need to be recomputed in the PD formalism to produce waveforms, the model could offer a better physical understanding of DS. Surprisingly, we found that the PD predictions were largely independent of the choice $m(\phi, \xi)$ in the resummation scheme. While this result needs to be confirmed with a more comprehensive survey of possible schemes, the dependence of our formalism on the sole function $F(\phi)$ suggests that DS could be modeled with a single effective potential for the scalar charge at the level of the action. An analogous

method was employed in Ref. [292], in which the quadrupole modes of a neutron star were promoted to dynamical field variables governed by an effective potential to model their response to the tidal fields produced by a companion black hole. This procedure could be adopted for dynamical scalarization, where each body's scalar monopole (i.e. scalar charge) dynamically responds to the monopolar scalar field sourced by the companion star [293]. This investigation could offer a more intuitive view of DS as a non-linear phenomenon.

4.10 Acknowledgements

We are grateful to Gilles Esposito-Farèse, Jan Steinhoff, Enrico Barausse, and Nicolàs Yunes for useful discussions and comments. N.S. and partially A.B. acknowledge support from NSF Grant No. PHY-1208881. A.B. also acknowledges partial support from NASA Grant NNX12AN10G. N.S. thanks the Max Planck Institute for Gravitational Physics for its hospitality during the completion of this work.

Chapter 5: Effective action model of dynamically scalarizing binary neutron stars

Authors: *Noah Sennett, Lijing Shao, and Jan Steinhoff*[1]

Abstract: Gravitational waves can be used to test general relativity (GR) in the highly dynamical strong-field regime. Scalar-tensor theories of gravity are natural alternatives to GR that can manifest nonperturbative phenomena in neutron stars (NSs). One such phenomenon, known as dynamical scalarization, occurs in coalescing binary NS systems. Ground-based gravitational-wave detectors may be sensitive to this effect, and thus could potentially further constrain scalar-tensor theories. This type of analysis requires waveform models of dynamically scalarizing systems; in this work we devise an analytic model of dynamical scalarization using an effective action approach. For the first time, we compute the Newtonian-order Hamiltonian describing the dynamics of a dynamically scalarizing binary in a self-consistent manner. Despite only working to leading order, the model accurately predicts the frequency at which dynamical scalarization occurs. In conjunction with Landau theory, our model allows one to definitively establish dynamical scalarization as a second-order phase transition. We also connect dynamical scalarization to the

[1]Originally published as Phys. Rev. **D96**, 084019 (2017).

related phenomena of spontaneous scalarization and induced scalarization; these phenomena are naturally encompassed into our effective action approach.

5.1 Introduction

Over a century of experiments have shown that general relativity (GR) very accurately describes the behavior of gravity. The bulk of these tests have come from measurements of gravitationally bound systems, either with electromagnetic observations of our Solar System [79] and binary pulsars [249, 294] or with gravitational-wave (GW) observations of coalescing binary black holes [73, 122, 123, 184]. Combined, these systems probe GR over a large phase space, with gravitational fields whose relative strength and dynamism span many orders of magnitude [89, 187, 295, 296]. However, one corner of parameter space that has not yet been directly tested is the highly-dynamical, strong-field regime of gravity coupled to matter, which would be reached in the merger of a neutron star (NS) binary system.

GWs from coalescing binary neutron stars (BNSs) are expected to be detected by Advanced LIGO in the near future [297]. Tests of GR are done using Bayesian inference [122], comparing the relative probability that the measured data are consistent with a GR waveform over a non-GR waveform to search for possible deviations from GR. Waveforms in alternative theories of gravity can be written schematically in the Fourier domain as

$$h(\boldsymbol{\theta}; f) = h_{\rm GR}(\boldsymbol{\theta}; f)\,[1 + \delta\mathcal{A}(\boldsymbol{\theta}; f)]\,e^{i\delta\psi(\boldsymbol{\theta};f)}, \tag{5.1}$$

where f is the observed GW frequency, $\boldsymbol{\theta}$ represents the intrinsic (e.g., component

masses, spins, etc.) and extrinsic (e.g., distance, sky position, etc.) parameters of the binary. We have used $h_{\rm GR}(\boldsymbol{\theta}; f)$ to represent the expected waveform in GR while $\delta\mathcal{A}$ and $\delta\psi$ are the deviations in the amplitude and phase, respectively, from GR [117, 118, 120, 176]. One makes an ansatz for δA as parameterized by a set of coefficients $\{\alpha_i\}$ and for $\delta\psi$ as parameterized by another set of coefficients $\{\beta_j\}$. A common choice—the so-called restricted waveforms—is for δA to be identically zero while, for frequencies corresponding to the inspiral, $\delta\psi$ is expanded in powers of the frequency f and its logarithm $\log f$ [118, 120, 176]. For this choice, the parameters $\{\beta_j\}$ are simply the coefficients of the power series in f and $\log f$—they measure the deviations from GR that appear at each order in a post-Newtonian (PN) expansion of the phase. Because this approach makes no reference to a particular alternative theory of gravity, constraining the parameters $\{\beta_j\}$ can simultaneously constrain many alternative theories using appropriate mappings.

However, this theory-agnostic approach does not capture all possible deviations from GR because it relies on the assumption that $\delta\psi(\boldsymbol{\theta}; f)$ admits a series expansion in f and $\log f$ during the early inspiral. In this paper, we study a particular class of scalar-tensor theories of gravity in which BNSs can undergo a phase transition known as *dynamical scalarization* [169]; the GW signals from such systems cannot be expanded in a simple power series. Through this phenomenon, BNSs abruptly transition from a configuration that closely resembles a BNS in GR to a drastically different state. Previous efforts to model dynamically scalarizing systems have relied on phenomonological waveform models or analytic approximations of the equations of motion [3, 170, 175, 271]. We continue these efforts in this

work by reformulating the PN dynamics of BNSs with dynamical scalar charges in a manner analogous to the treatment of dynamical tides in GR [298, 299]. Using this approach, we explicitly construct a two-body Hamiltonian that incorporates dynamical scalarization; in contrast, in Refs. [3, 170], only the PN equations of motion were calculated. Our results comprise an important step towards fully-consistent waveform models of dynamical scalarization and offer a clear interpretation of the phenomenon as a phase transition.

The paper is organized as follows. In Sec. 5.2, we provide an overview to scalar-tensor theories and certain nonperturbative phenomena for NSs. In Sec. 5.3 we construct an effective action to model the dynamical scalarization of BNSs. In Sec. 5.4 we compare results obtained from our model to previous analytic approaches and numerical quasi-equilibrium (QE) configuration calculations. In Sec. 5.5, we use our model to solidify the interpretation of dynamical scalarization as a phase transition and then discuss possible extensions to the model. Finally, we present some concluding remarks in Sec. 5.6.

Throughout the paper we use the conventions of Misner, Thorne, and Wheeler [15] for the metric signature and Riemann tensor. We work in units in which the speed of light and the bare gravitational constant in the Einstein frame are unity.

5.2 Nonperturbative phenomena in scalar-tensor gravity

Scalar-tensor theories of gravity are amongst the most natural and well-motivated alternatives to GR [79, 89]. We consider the class of theories detailed in

Ref. [147], in which a massless scalar field couples nonminimally to the metric. These theories are described in the Jordan frame by the action,

$$S = \int d^4x \frac{\sqrt{-\tilde{g}}}{16\pi\tilde{G}} \left[\phi\tilde{R} - \frac{\omega(\phi)}{\phi} \tilde{g}^{\mu\nu} \nabla_\mu \phi \nabla_\nu \phi \right] + S_m[\tilde{g}_{\mu\nu}, \chi], \tag{5.2}$$

where χ represents all of the matter degrees of freedom in the theory and $\tilde{G}$ is the bare gravitational coupling constant in the Jordan frame. Alternatively, the action can be written in the Einstein frame by performing a conformal transformation, $g_{\mu\nu} \equiv \phi\tilde{g}_{\mu\nu}$, as

$$S = \int d^4x \frac{\sqrt{-g}}{16\pi} \left[R - 2g^{\mu\nu} \nabla_\mu \varphi \nabla_\nu \varphi \right] + S_m \left[A^2(\varphi) g_{\mu\nu}, \chi \right], \tag{5.3}$$

where we have introduced the scalar field,

$$\varphi \equiv \int d\phi \frac{\sqrt{3 + 2\omega(\phi)}}{2\phi}, \tag{5.4}$$

and defined

$$A(\varphi) \equiv \exp\left(- \int \frac{d\varphi}{\sqrt{3 + 2\omega(\varphi)}} \right). \tag{5.5}$$

Varying the Einstein-frame action yields the field equations

$$R_{\mu\nu} - \frac{1}{2} R g_{\mu\nu} = 8\pi T_{\mu\nu} + 2\nabla_\mu \varphi \nabla_\nu \varphi - g_{\mu\nu} g^{\rho\sigma} \nabla_\rho \varphi \nabla_\sigma \varphi, \tag{5.6}$$

$$\Box\varphi = 4\pi\alpha(\varphi) T, \tag{5.7}$$

where $T^{\mu\nu} \equiv 2(-g)^{-1/2} \delta S_m / \delta g_{\mu\nu}$ is the stress-energy tensor of matter, $T \equiv g_{\mu\nu} T^{\mu\nu}$ is its trace, and we have introduced the coupling,

$$\alpha(\varphi) \equiv - \frac{d \log A}{d\varphi} = (3 + 2\omega)^{-1/2}. \tag{5.8}$$

Much of the seminal research in scalar-tensor alternatives to GR considered the simple choice of a constant coupling α, corresponding to Jordan-Fierz-Brans-Dicke theory [178, 179, 300]. This theory is currently well-constrained by measurements from the Cassini probe [180] and of binary pulsars [249, 294]; future observations by Advanced LIGO are not expected to improve these constraints [301]. Instead, in this work we consider theories whose coupling is linear in φ,

$$\alpha(\varphi) = -\beta\varphi. \tag{5.9}$$

Such theories can give rise to phenomena that are potentially detectable by Advanced LIGO while evading the bounds set by the Cassini probe [153, 169].[2] In

[2]Cosmological considerations can further constrain the class of theories with the coupling given by Eq. (5.9). In particular, when β is negative, the theory evolves rapidly away from GR over cosmological timescales [152, 175, 273]; this evolution cannot be reconciled with current Solar System observations without fine-tuning the theory at some point in the distant past. One can solve this cosmological issue by generalizing the coupling (5.9) to a higher-order polynomial in φ, which causes the scalar field to evolve to a local minimum of $A(\varphi)$ rather than diverge [302]. However, when expanded around this local minimum, the leading order term of the modified coupling $\alpha(\varphi)$ will have the opposite sign as in Eq. (5.9), and thus such theories no longer manifest the nonperturbative scalarization phenomena that we study here [302]. Alternatively, one can add a mass term for the scalar field to Eq. (5.3) to evade the cosmological constraints on these theories [152, 303]. Neutron stars can undergo nonperturbative phenomena analogous to those we consider here when immersed in a constant background massive scalar field [95, 161]. However, recent work has revealed that this background field should in fact oscillate over relatively short timescales in massive scalar-tensor theories [303]. It remains to be seen whether NSs embedded in an oscillatory background scalar field can also exhibit nonperturbative phenomena. As is commonly done in the literature [3, 147, 152, 153, 169–172, 175], we ignore these cosmological concerns here.

particular, for sufficiently negative β, such theories can manifest *spontaneous scalarization*, *dynamical scalarization*, and *induced scalarization*.[3]

Before discussing these phenomena in detail, we briefly examine the structure of NS solutions to Eqs. (5.6) and (5.7) to establish some useful notation. For simplicity, we consider a static matter source. Working far from all matter, one can expand the metric about a Minkowskian background in powers of $\epsilon \sim m_E/r \ll 1$ where m_E is the total mass (measured in the Einstein frame) using the post-Minkowskian formalism (see Ref. [30] and references within). To leading order in ϵ, Eq. (5.7) reduces to the Poisson equation on a flat background, whose solution in this region takes the generic form,

$$\varphi(r) = \varphi_0 + \frac{Q}{r} + \mathcal{O}\left(\frac{1}{r^2}\right), \tag{5.10}$$

where we have introduced a constant background field φ_0 and defined the *scalar charge* Q as the scalar monopole moment of the source.

5.2.1 Spontaneous scalarization

Damour and Esposito-Farèse discovered that the presence of relativistic matter in theories with negative β can trigger an instability in the scalar field [153]. In such theories, a sufficiently compact NS can undergo a phase transition known as *spontaneous scalarization* corresponding to the spontaneous breaking of the symmetry $\varphi \to -\varphi$ in Eq. (5.3). Given current constraints from binary pulsars (see below) [6, 248, 249, 294, 305], numerical solutions to Eqs. (5.6) and (5.7) reveal that

[3] See Refs. [156, 157, 304] for a discussion of similar phenomena in theories with positive β.

an isolated NS can develop a scalar charge of order

$$\frac{Q}{m_E} \lesssim 10^{-1}, \tag{5.11}$$

through spontaneous scalarization. This figure should be contrasted with a PN prediction for this quantity,

$$\begin{aligned} \frac{Q}{m_E} &= -\beta\varphi_0 \left(1 + a_1 C + a_2 C^2 + \cdots\right) \\ &\lesssim 10^{-5} \left(1 + a_1 C + a_2 C^2 + \cdots\right), \end{aligned} \tag{5.12}$$

where the coefficients a_i are of order unity and $C \equiv m_E/R$ is the compactness of the NS [147]. The drastic difference in magnitude between Eqs. (5.11) and (5.12) indicates that the PN expansion does not predict spontaneous scalarization. In this sense, we describe spontaneous scalarization as *nonperturbative*; loosely speaking, one must include every term in the infinite sum in Eq. (5.12) to recover the phenomenon.

The best constraints on spontaneous scalarization come from timing measurements of white dwarf-NS binaries (see, e.g., Refs. [6, 152, 247–249, 305]). Unlike NSs, white dwarfs (WDs) are too diffuse to develop any significant scalar charge through spontaneous scalarization. Consequently, WD-NS binaries can emit substantial scalar dipole flux $\mathcal{F}_{\rm dip}$, which scales as

$$\mathcal{F}_{\rm dip} \propto \left(\frac{Q_{\rm NS}}{m^E_{\rm NS}} - \frac{Q_{\rm WD}}{m^E_{\rm WD}}\right)^2 \approx \left(\frac{Q_{\rm NS}}{m^E_{\rm NS}}\right)^2, \tag{5.13}$$

where $m^E_{\rm WD}$ and $m^E_{\rm NS}$ are the masses, and $Q_{\rm WD}$ and $Q_{\rm NS}$ are the scalar charges of the WD and NS, respectively. Pulsar timing experiments are sensitive to any anomalous decrease in the orbital period of the binary, and thus can constrain $\mathcal{F}_{\rm dip}$

and consequently $Q_{\rm NS}/m^E_{\rm NS}$; we refer readers to Ref. [6] for the current best limits on spontaneous scalarization from pulsar timing.

5.2.2 Dynamical and induced scalarization

More recently, a similar phenomenon, known as *dynamical scalarization*, was uncovered in numerical-relativity (NR) simulations of BNSs in the same class of scalar-tensor theories with negative β [169, 171, 172]. These simulations considered binary systems composed of NSs too diffuse to undergo spontaneous scalarization in isolation. As the binaries coalesced, it was found that the presence of a companion allowed the NSs to scalarize abruptly, developing scalar charges of the same order of magnitude as might occur through spontaneous scalarization. A related phenomenon, known as *induced scalarization*, was also discovered [169], in which a spontaneously scalarized star generates a scalar charge on a companion too diffuse to scalarize in isolation. For simplicity, we primarily focus on dynamical scalarization in this work; however, the model we develop can be applied to systems that undergo induced scalarization as well.

Numerical relativity simulations show that dynamical and induced scalarization hasten the plunge and merger of BNSs relative to the same systems in GR [169, 171]. Two factors dictate the difference in merger time for scalarized versus unscalarized systems: (i) an enhancement in energy flux, and (ii) a modification to the binding energy. A scalarized BNS system will emit energy more rapidly than an unscalarized system; the dissipative channels available in GR (e.g., tensor

quadrupole radiation) are enhanced for bodies with scalar charge and new channels become available (e.g., scalar dipole radiation). Modifications to the binding energy of scalarized systems are not well understood. In Ref. [172], the binding energy was argued to decrease (in magnitude) in scalarized systems, prompting an earlier merger, whereas in this paper, we argue that it should instead increase (see Sec. 5.4.2 for more detail).

Advanced LIGO will be able to distinguish between the coalescence of scalarized and unscalarized NSs provided that their scalar charges: (i) are sufficiently large and (ii) develop early enough in the inspiral (in the case of dynamical scalarization) [6, 175, 271]. Observation of such scalarization would provide direct evidence for modifications of GR in the strong-field regime; conversely, lack of evidence of scalarization can further constrain the space of viable scalar-tensor theories. Depending on the NS masses and equation of state (EOS) observed in coalescing BNS systems, Advanced LIGO could provide constraints competitive with current binary-pulsar limits [6].

Searches for deviations from GR with GWs rely on accurate and faithful waveform models in modified gravity. Several models of dynamical scalarization have been proposed in the literature, but none at the level of sophistication of waveforms in GR. The simplest of these approaches phenomenologically model $\delta\psi(\boldsymbol{\theta}; f)$ to reproduce features expected to arise in dynamically scalarized systems. For example, one can model $\delta\psi(\boldsymbol{\theta}; f)$ by a polynomial in f to capture effects such as scalar dipole radiation and/or use a Heaviside step function to mimic the abrupt growth of scalar charge and hastened merger triggered by dynamical scalarization. Detectability

studies reveal that such models may be sufficient to identify dynamical scalarization with Advanced LIGO [175, 271]. However, the accuracy of phenomenological waveform models cannot be established *a priori*. Ultimately, one must validate and/or calibrate these models using independent waveforms. In GR, this comparison is made with both analytic and NR waveforms (e.g., the IMRPhenom waveform family [306]). Because very few NR simulations of dynamical scalarization have been produced to date, one must rely solely on more sophisticated analytic models of this phenomenon to verify the accuracy of phenomenological models.

A more sophisticated approach towards waveform modeling, and one we shall pursue in the present work, is to solve the field equations (5.6) and (5.7) in some perturbative fashion (see Sec. 5.3). The PN approximation is an example of such an approach; PN waveforms are useful inspiral models in their own right and also serve as the foundation for more refined waveform models, such as the effective-one-body (EOB) formalism [38, 39]. Dynamical scalarization can be modeled by augmenting [170] or resumming [3] the PN dynamics in scalar-tensor gravity; such modifications are necessary because dynamical scalarization is a nonperturbative phenomenon in the same sense as spontaneous scalarization [3]. Both of these analytic approaches suffer from two shortcomings. First, simulating the dynamics with these models requires one to solve a system of algebraic equations at each moment in time involving the function $m_E(\varphi)$, which measures the complete (nonperturbative) dependence of the NS mass on the scalar field in which it is immersed. Second, these approaches only model the dynamics at the level of the equations of motion; no rigorous formulation of the two-body Hamiltonian has been constructed.

In the next section, we develop a new analytic model of dynamical scalarization that addresses these shortcomings using an effective-action approach. First, the scalar charges Q are given by roots of a system of polynomial equations; for systems with no background scalar field φ_0, the algebraic system reduces to a pair of cubic equations that have a closed-form solution. These algebraic equations depend on only two new parameters per NS [as opposed to the complete functions $m_E(\varphi)$] that can be directly interpreted as the separation at which dynamical scalarization begins and the magnitude of scalar charge that develops. Second, the new model allows one to construct a simple two-body Hamiltonian and thus also compute the binding energy of a binary system. The Hamiltonian is a fundamental building block in the construction of perturbative waveform models. For example, the binding energy, in conjunction with the energy flux, allows one to compute the phase evolution through the balance equation [30], and the Hamiltonian is the natural starting point in constructing an EOB description of the dynamics. Additionally, our new formulation allows for a more nuanced interpretation of dynamical scalarization as a phase transition than exists in the literature and more intimately connects dynamical and spontaneous scalarization.

5.3 Effective action with a dynamical scalar charge

We construct a model for dynamical scalarization by explicitly re-parameterizing the standard point-particle action for a BNS in terms of the scalar charges of its components. This approach closely resembles the treatment of extended bodies in

GR in terms of their multipolar structure; in fact, as can be seen from Eq. (5.10), the scalar charge is simply the scalar monopole moment of an extended body. The gravitational fields (tensor and scalar) produced by a system of compact bodies can be represented completely in terms of the bodies' multipoles through matched asymptotic expansions [30, 147]. In turn, these external fields affect the multipolar structure of the compact bodies. This response must be included into the point-particle model in some way. For example, a constant external tidal field $\mathcal{G}_{i_1\ldots i_\ell}$ will induce a multipole $\mathcal{Q}_{i_1\ldots i_\ell}$ as determined by the tidal deformability λ_ℓ

$$\mathcal{Q}_{i_1\ldots i_\ell} = -\lambda_\ell \mathcal{G}_{i_1\ldots i_\ell}. \tag{5.14}$$

(See Ref. [307] for more detail.) A more sophisticated model is needed to capture dynamical tides, i.e., tidal fields that vary on periods comparable to the relaxation timescale of the compact body (see Refs. [292, 299, 308, 309] and references therein).

As can be seen from the arguments of the matter action S_m in Eq. (5.3), compact objects in scalar-tensor gravity interact with the scalar field in conjunction with the Einstein frame metric. For non-self-gravitating objects (i.e., test particles), this interaction is characterized simply by $A(\varphi)$. However, the internal gravitational interactions in self-gravitating objects can dramatically change the couplings to the metric and scalar field; these differences represent violations of the strong equivalence principle. As first proposed by Eardley [310], the response of a body's mass monopole m_E to an external scalar field can be encoded into a generic function $m_E(\varphi)$. As shown in Appendix A of Ref. [147], the scalar monopole Q induced by

an external scalar field is given by

$$Q = -\frac{dm_E}{d\varphi}. \tag{5.15}$$

For bodies immersed in weak scalar fields, Eq. (5.15) reduces to a linear relation analogous to Eq. (5.14). However dynamical scalarization occurs outside of this linear regime: the complete expression $m_E(\varphi)$ is needed to accurately model this phenomenon.

In this section, we develop a model inspired by the treatment of non-adiabatic tides in GR [292, 299, 308, 309]. We rewrite the point-particle action using Q in place of φ and promote the scalar charge Q to a dynamical degree of freedom. We find that this action can be expressed as a simple effective action for a dynamical scalar charge linearly coupled to an external scalar field. The complete function $m_E(\varphi)$ is condensed into the coupling coefficients (or "form factors") in the effective action. Thus, the predictions of the model are parameterized by a small set of coefficients and are easy to study without reference to any particular BNS system; in contrast previous analytic models [3, 170] required the full form of $m(\varphi)$ to be predictive.

In Sec. 5.3.1, we develop the framework for our new effective point-particle action for a single NS and discuss possible extensions for future work. Using this approach, we compute the dynamics for a binary system of two point particles in Sec. 5.3.2.

5.3.1 The effective point-particle action

We begin with the standard model of the orbital dynamics of compact objects in scalar-tensor gravity. If the orbital separation is much larger than the size of the bodies, one can represent each star as a point particle governed by an action of the form [147, 208, 276],

$$S_m = -\int d\sigma \sqrt{-u^\mu u_\mu} m_E(\varphi), \tag{5.16}$$

where $z^\mu(\sigma)$ is the object's worldline parametrized by a generic parameter σ, $u^\mu \equiv dz^\mu/d\sigma$ is its four-velocity, and $m_E(\varphi)$ is its Einstein-frame mass as a function of the scalar field along the worldline $\varphi(z^\mu)$. Inserting the source (5.16) into Eq. (5.7), one finds that the compact object generates a scalar field given by

$$\Box\varphi = 4\pi \int d\sigma \frac{\sqrt{-u^\nu u_\nu}}{\sqrt{-g}} \frac{dm_E}{d\varphi} \delta^{(4)}(x^\mu - z^\mu), \tag{5.17}$$

where the derivative of the mass is evaluated at $\varphi(z^\mu)$. Similarly, the influence of the object on the metric can be found by inserting Eq. (5.16) into Eq. (5.6).

Next, we convert the action (5.16) from a function of the external field φ imposed on the body to one of the scalar charge Q. These two quantities offer complementary descriptions of the local geometry of the compact body; one can convert between the two using Eq. (5.15). To rewrite the action as a function of Q, we adopt a method first introduced in Ref. [152]; we define a new potential $m(Q)$ given by the Legendre transformation of the mass $m_E(\varphi)$,

$$m(Q) \equiv m_E(\varphi) + Q\varphi. \tag{5.18}$$

Inserting this definition into Eq. (5.16), the action reads

$$S_m = -\int d\sigma \sqrt{-u^\mu u_\mu}\,[m(Q) - Q\varphi]\,. \tag{5.19}$$

Now we promote Q to an independent degree of freedom in the model; variation of the action with respect to this variable gives an additional equation of motion in the dynamics.

The notation in Eq. (5.18) is intentionally suggestive; as we will show in Sec. 5.3.2, $m(Q)$ assumes the role of the particle's mass in the orbital dynamics rather than $m_E(\varphi)$. A natural analogy can be drawn to thermodynamics: consider, for example, an ideal gas composed of a fixed number of particles held at a constant temperature. The state of the system can be described by either its pressure—an intrinsic quantity, analogous to φ—or its volume—an extrinsic quantity, analogous to Q. While the internal energy—analogous to $m_E(\varphi)$—has a natural interpretation as the thermal energy of the gas, it is often more convenient to use the free energy—analogous to $m(Q)$—to describe certain physical processes. As was discussed in Ref. [152] (and will be revisited in Sec. 5.5), the equilibrium state for an isolated NS will minimize the function $m(Q)$; again, this quantity plays the role of an effective free energy of each NS in a binary system.

We expand the potential $m(Q)$ in a power series to quartic order,

$$m(Q) = c^{(0)} + c^{(1)}Q + \frac{c^{(2)}}{2!}Q^2 + \frac{c^{(3)}}{3!}Q^3 + \frac{c^{(4)}}{4!}Q^4 + \mathcal{O}\left(Q^5\right). \tag{5.20}$$

Recall that the action (5.3) equipped with the coupling (5.9) is invariant under the symmetry $\varphi \to -\varphi$. Thus, we expect the mass of an isolated NS $m_E(\varphi)$ to also respect this symmetry, even in the presence of spontaneous scalarization. From

Eq. (5.15), we see that this parity transformation will also send $Q \to -Q$. Performing both of these transformations leaves the right hand side of Eq. (5.18) unchanged, and thus we can conclude that $m(Q)$ must be an even function of Q.

Some of the coefficients $c^{(n)}$ have an immediate interpretation. The leading $c^{(0)}$ describes the body's mass in absence of any scalar charge, i.e., the ADM mass in GR, and so we also denote it as $c^{(0)} = m^{(0)}$. Furthermore, a background scalar field φ_0 can be handled by working instead with the field,

$$\hat{\varphi} \equiv \varphi - \varphi_0, \tag{5.21}$$

leading to an additional coupling $-Q\varphi_0$ in the Lagrangian. This term can be absorbed into $m(Q)$ by setting $c^{(1)} = -\varphi_0$, and thus we can interpret $c^{(1)}$ as a cosmologically imposed background scalar field. Note that the addition of a nonzero scalar background weakly breaks the symmetry $\varphi \to -\varphi$ in the point-particle action, prompting us to relax the conclusion that $m(Q)$ is a strictly even function. However, all other odd powers of Q will still vanish, i.e., $c^{(3)} = 0$.

Given the discussion above, our model for $m(Q)$ reduces to

$$m(Q) = m^{(0)} - \varphi_0 Q + \frac{c^{(2)}}{2} Q^2 + \frac{c^{(4)}}{24} Q^4 + \mathcal{O}(Q^6). \tag{5.22}$$

Potentials of this form are widely used to describe systems that exhibit spontaneous symmetry breaking (see also Sec. 5.5); the Higgs mechanism is one notable example [311]. Reference [152] employed a similar potential to model isolated NSs near the critical point for spontaneous scalarization. In the present work, we show that the ansatz (5.22) remains valid for NSs far from this critical point; we describe the

procedure by which we numerically compute the various coefficients for a particular NS in Sec. 5.4.1.

One ingredient conspicuously absent from our effective action (5.19) is the *dynamical* response of the scalar charges to changes in the scalar field. In truth, our model is only valid in the adiabatic limit, wherein the external fields evolve over timescales much longer than the relaxation time of NSs. Given the abrupt nature of dynamical scalarization, the validity of our assumption of adiabaticity should be studied in greater detail; we reserve this analysis for future work. If one rapidly changes the external scalar field, the NS's scalar charge cannot respond instantaneously. In general, physical systems undergo (harmonic) oscillations around equilibrium configurations under small perturbations. Thus, one expects the scalar charge to behave approximately like a harmonic oscillator driven by the external fields, characterized by an action of the form (5.19) with

$$m(Q,\dot{Q}) = m^{(0)} - \varphi_0 Q + \frac{c^{(2)}}{2}\left(\frac{\dot{Q}^2}{\omega_0^2 u^\mu u_\mu} + Q^2\right), \tag{5.23}$$

where $\dot{Q} = dQ/d\sigma$ and ω_0 is the resonant frequency of this scalar mode. This action is analogous to the dynamical tidal model in Ref. [299]: Q corresponds to the dynamical quadrupole, φ to the tidal field, $1/c^{(2)}$ to the tidal deformability, and ω_0 to the oscillation mode frequency. In general, one should add separate dynamical degrees of freedom for every oscillation mode of the NS. Identifying all dynamical degrees of freedom relevant for the scale of interest is very important in constructing an effective action (see, e.g., Ref. [312]). Note that when the dynamics of the system occur much more slowly than the resonant frequency, i.e. $\dot{Q} \ll \omega_0$, and we restore the

Q^4 interaction, Eq. (5.23) reduces to the adiabatic model (5.22) considered earlier.

Viewed from an effective field theory perspective, our effective action model of dynamical scalarization may appear too simplistic. In general, one should add to the action all possible combinations of Q, u^μ, the scalar field φ, and the curvature (and derivatives of these variables) allowed by the symmetries of the theory, up to terms negligible for the desired accuracy of the model. Not all of these interactions are independent, since some might be related by redefinitions of the other dynamical variables; the redundant terms should be dropped. In the present model, we consider only couplings of the scalar charge to itself, as well as a linear coupling of the charge to the scalar field. A broader class of interactions would allow our model to reproduce other interesting phenomena. For example, the induction of scalar charges on black holes from time-varying external fields can be modeled with an effective action [313, 314]. We delay such an investigation for future work; for the present work, the effective action model given by Eqs. (5.19) and (5.22) is sufficient to reproduce dynamical scalarization.

5.3.2 Dynamics of a binary system

We now turn to the task of translating the action [which will contain a copy of Eq. (5.19) for each NS] into a Hamiltonian describing the orbital dynamics of a BNS. Using the PN approximation, we expand the metric and scalar field in powers of v/c and solve the field equations (5.6) and (5.7) at each order. An efficient method for solving the two-body dynamics is through a Fokker action[4] together with

[4]This means to insert the perturbative solution to the field equations into the full action.

a diagrammatic method to represent the perturbative expansion [208]. Similarly, one can integrate out the fields perturbatively using techniques from quantum field theory [315], i.e., Feynman integrals and diagrams.

We consider only the leading-order (Newtonian) approximation of the orbital dynamics in the present work. Thus, the accuracy of our model will degrade towards the end of the inspiral. However, because Advanced LIGO is only sensitive to dynamical scalarization that occurs in the very early inspiral [175, 271], our model can still be applied to the systems of scientific interest; we pursue extensions of our model to higher PN order in future work.

The PN expansions of the metric $g_{\mu\nu}$ and the scalar field $\hat{\varphi}$ are given by

$$g_{\mu\nu} = \eta_{\mu\nu} + h_{\mu\nu} + \mathcal{O}\left(c^{-4}\right), \tag{5.24}$$

$$\hat{\varphi} = \psi + \mathcal{O}\left(c^{-4}\right), \tag{5.25}$$

where $\eta_{\mu\nu}$ is the Minkowski metric and $\hat{\varphi}$ vanishes at infinity by construction. The leading-order PN corrections enter with the following powers of c:

$$\begin{aligned} h_{00} &\sim \mathcal{O}\left(c^{-2}\right), & h_{0i} &\sim \mathcal{O}\left(c^{-3}\right), \\ h_{ij} &\sim \mathcal{O}\left(c^{-4}\right), & \psi &\sim \mathcal{O}\left(c^{-2}\right). \end{aligned} \tag{5.26}$$

Inserting the expansions (5.24) and (5.25) into the field equations (5.6) and (5.7) with the source (5.19), one finds the Newtonian-order solution to the metric and

scalar field,

$$h_{00}(\mathbf{x},t) = \frac{m_A(Q_A)}{|\mathbf{x}-\mathbf{z_A}(t)|} + \frac{m_B(Q_B)}{|\mathbf{x}-\mathbf{z_B}(t)|} + \mathcal{O}\left(c^{-4}\right), \tag{5.27a}$$

$$\psi(\mathbf{x},t) = \frac{Q_A}{|\mathbf{x}-\mathbf{z_A}(t)|} + \frac{Q_B}{|\mathbf{x}-\mathbf{z_B}(t)|} + \mathcal{O}\left(c^{-4}\right), \tag{5.27b}$$

$$h_{0i}(\mathbf{x},t) \sim \mathcal{O}\left(c^{-3}\right), \tag{5.27c}$$

$$h_{ij}(\mathbf{x},t) \sim \mathcal{O}\left(c^{-4}\right), \tag{5.27d}$$

where the labels A and B distinguish the two NSs. Henceforth, we suppress the explicit dependence of each body's mass m on its corresponding scalar charge for notational convenience.

Inserting these solutions into the action and dropping singular self-interactions, we find the leading-order two-body action,

$$S \approx \int dt \bigg[- m_A - m_B + \frac{m_A}{2}\mathbf{v}_A^2 + \frac{m_B}{2}\mathbf{v}_B^2 + \frac{m_A m_B}{r} + \frac{Q_A Q_B}{r} \bigg], \tag{5.28}$$

where $v^i \equiv dz^i/dt$ is the Newtonian velocity and $r \equiv |\mathbf{z}_A - \mathbf{z}_B|$ and we have corrected for any double counting. Legendre transforming the Lagrangian yields the Hamiltonian,

$$H = m_A + m_B + \frac{\mathbf{p}_A^2}{2m_A} + \frac{\mathbf{p}_B^2}{2m_B} - \frac{m_A m_B}{r} - \frac{Q_A Q_B}{r}, \tag{5.29}$$

where the canonical momenta are $\mathbf{p}_{A,B} = m_{A,B}\mathbf{v}_{A,B}$. The equation of motion for Q_A reads

$$0 = \frac{\partial H}{\partial Q_A} = z_A \left(-\varphi_0 + c_A^{(2)} Q_A + \frac{c_A^{(4)}}{6} Q_A^3 \right) - \frac{Q_B}{r}, \tag{5.30}$$

with the redshift given by

$$z_A = \frac{\partial H}{\partial m_A} = 1 - \frac{\mathbf{p}_A^2}{2m_A^2} - \frac{m_B}{r}, \tag{5.31}$$

and the equation of motion for Q_B takes the same form but with the body labels exchanged $A \leftrightarrow B$. The scalar charges are given by the roots of these two cubic equations.[5] Closed form solutions can be found using computer algebra for $\varphi_0 \neq 0$, but the result is rather lengthy and not very illuminating; we do not provide them here for space considerations.

While Eq. (5.30) may seem daunting, simple analytic solutions for the scalar charge can be easily found in special, but very relevant cases. We restrict our attention to the theories that exactly preserve the symmetry $\varphi \to -\varphi$, i.e., we set the background scalar field $\varphi_0 = 0$. Next, for simplicity, we will neglect the $\mathcal{O}(c^{-2})$ corrections to the redshift z_A in Eq. (5.30); including these terms does not change the qualitative behavior of the solutions discussed below. Finally, we specialize to the case of equal-mass binaries and assume that the NSs have identical properties, i.e. $m_A^{(0)} = m_B^{(0)}$ and $c_A^{(i)} = c_B^{(i)}$. Under these assumptions, Eq. (5.30) reduces to

$$0 = \frac{\partial H}{\partial Q} = -2Q \left[\frac{1}{r} - c^{(2)} - \frac{c^{(4)}}{6} Q^2 \right], \tag{5.32}$$

where we have dropped the body labels. As expected, the trivial solution $Q = 0$ satisfies this equation. However, this is not necessarily the only solution; if the trivial solution is unstable, the BNS system will transition to a state with nonzero scalar charge. The requirement for stability,

$$0 \leq \frac{\partial^2 H}{\partial Q^2} = 2c^{(2)} - \frac{2}{r} + c^{(4)} Q^2, \tag{5.33}$$

[5] For consistency, we truncate Eq. (5.30) at cubic order in the scalar charges, e.g. dropping the term proportional to $Q_A^3 Q_B$ that would arise from the product of m_B and Q_A^3.

is violated for $Q = 0$ when $1/r > c^{(2)}$. The stable solutions therefore read,

$$Q = \begin{cases} 0 & \text{for} \quad 1/r \leq c^{(2)} \\ \pm\sqrt{\dfrac{6}{c^{(4)}}}\sqrt{\dfrac{1}{r} - c^{(2)}} & \text{for} \quad 1/r \geq c^{(2)} \end{cases}, \tag{5.34}$$

which contains a phase transition at $r_{\rm DS} = 1/c^{(2)}$.

Equation (5.34) provides some intuition into the physical interpretation of the coefficients $c^{(2)}$ and $c^{(4)}$. The parameter $c^{(2)}$ determines the orbital scale of the phase transition to the scalarized regime, where the scalar-parity symmetry is broken and the solution bifurcates. The parameter $c^{(4)}$ determines the size of the scalar charge in this regime. Notice that for negative $c^{(2)}$ the NS is scalarized for all r. In fact, this situation corresponds to spontaneous scalarization; we discuss the connection between spontaneous and dynamical scalarization in greater detail in Sec. 5.5.

Finally, we compute the Newtonian-order equations of motion for each NS. Working from the Hamiltonian (5.29), the equations of motion are given by,

$$\ddot{\mathbf{z}}_A = -\frac{m_B\left(1 + \alpha_A\alpha_B\right)}{r^2}\mathbf{n}, \tag{5.35}$$

where $\alpha_{A,B} \equiv Q_{A,B}/m_{A,B}$ and $\mathbf{n} \equiv (\mathbf{z}_A - \mathbf{z}_B)/r$. Note that α_A differs from the quantity found in Eqs. (5.11)– (5.13) because it uses $m(Q)$ in place of $m_E(\varphi)$. We also derive Kepler's third law for circular orbits

$$\Omega^2 = \frac{\left(m_A + m_B\right)\left(1 + \alpha_A\alpha_B\right)}{r^3}, \tag{5.36}$$

where Ω is the orbital frequency.

5.4 Results

The previous sections aimed to motivate and develop a novel analytic model of dynamical scalarization; in this section, we test the accuracy of this approach by comparing against previous models [3] and numerical QE configuration calculations [172]. The dynamics are determined entirely by the coefficients $c^{(i)}$, as can be seen by inserting Eq. (5.22) and the solution of the cubic equations (5.30) for $Q_{A,B}$ into the Hamiltonian (5.29). These coefficients characterize the behavior of each compact body *in isolation*, and thus can be computed straightforwardly.

To facilitate comparison with previous work, we restrict our attention to the binary systems considered in Refs. [3, 172]. We consider $(1.35 + 1.35)\,M_\odot$ nonspinning BNS systems with a piecewise polytropic fit to the APR4 EOS; see Ref. [206] for more details on this EOS and its polytropic fit. We examine configurations with $\beta = -4.2$ and $\beta = -4.5$, where β characterizes the strength of the scalar coupling (5.9). Finally, we add the background scalar field $\varphi_0 = 10^{-5}/\sqrt{-2\beta}$, which satisfies binary-pulsar constraints for this EOS [171].

5.4.1 Computing $c^{(i)}$

The coefficients $c^{(i)}$ describe how the energy of an isolated NS varies with its scalar charge Q. Thus, to extract these coefficients, we study the behavior of the NS under infinitesimal changes in Q. In practice, we compute sequences of NS solutions with equal baryonic mass with incremental changes to the mass m_E, scalar charge Q, and asymptotic field φ. Spherically symmetric solutions for perfect fluid stars are

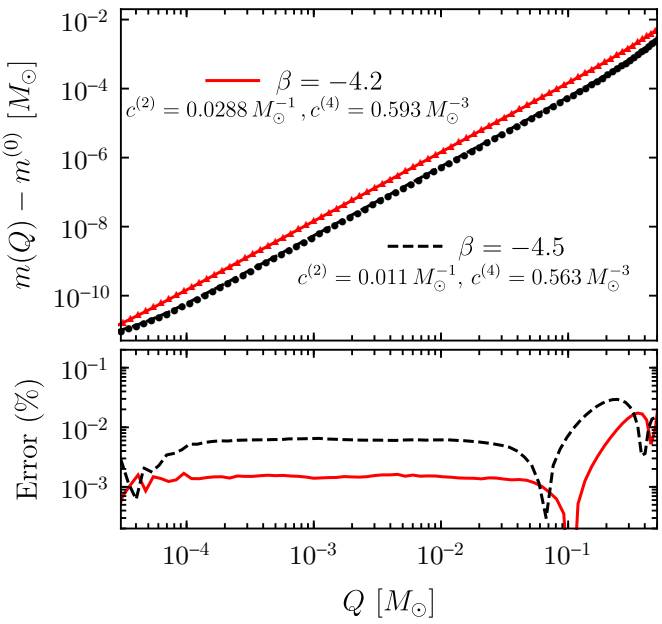

Figure 5.1: Potential m as a function of scalar charge Q for a $1.35\,M_\odot$ NS with the APR4 EOS. *Top:* The numerical values and polynomial fit are plotted with points and lines, respectively, for $\beta = -4.2$ (red) and $\beta = -4.5$ (dashed black). We have subtracted the leading-order term $m^{(0)} = 1.35\,M_\odot$ from m to improve readability. *Bottom:* We plot the fractional error in $m(Q) - m^{(0)}$ between the numerical data and polynomial fits.

found by solving the Tolman-Oppenheimer-Volkoff (TOV) equations; the extensions of these equations to scalar-tensor gravity were derived in Refs. [152, 153]. We solve these equations using fourth order Runge-Kutta methods and use standard shooting techniques to construct solutions with the same baryonic mass. The quantities m_E, Q, φ parameterize the asymptotic behavior of each numerical solution; we extract m_E, Q, φ using the relations detailed in Refs. [152, 153]. Equipped with these quantities, we then compute $m(Q)$ using Eq. (5.18).

We compute the coefficients $c^{(i)}$ by fitting the numerically computed $m(Q)$ with a polynomial of the form (5.22). The numerical values and polynomial fit

of $m(Q)$ are plotted with dots and solid lines, respectively, in the top panel of Fig. 5.1 for the NS parameters discussed above. To improve readability, we have subtracted the leading-order coefficient $m^{(0)} = 1.35 M_\odot$ from m. The values for $c^{(i)}$ computed through the polynomial fit are also given in Fig. 5.1; the i-th coefficient has dimension of $[\text{mass}]^{i-1}$. The bottom panel of the figure shows the fractional error between numerical values and polynomial fits of $m - m^{(0)}$. We see that deviations are generally of the order $\lesssim 0.01\%$, slightly worsening as the charge increases. The range in Q plotted here covers the typical range achievable by this NS over an entire inspiral in which dynamical scalarization occurs. As a check of our initial ansatz (5.22), we also fit the data to polynomials including Q^3, Q^5 and Q^6 terms; we find that these additional powers of Q shift our estimates for $c^{(i)}$ by less than $\sim 0.1\%$ and only marginally improve the overall agreement to data.

5.4.2 Comparison against previous models

As a first test of our model, we compute the scalar charge Q as a function of frequency. Because we only consider equal-mass systems, this relation can be found by solving the cubic equation (5.30) for $Q = Q_A = Q_B$ as a function of separation r. Then, by inserting this result into Eq. (5.36), we determine an exact relation between r and the orbital frequency Ω. Finally, we invert this relation and insert it into the solution to Eq. (5.32) to find an implicit expression for $Q(\Omega)$. We plot $Q(\Omega)$ in Fig. 5.2 computed with our model in red. The lower axis gives the dimensionless

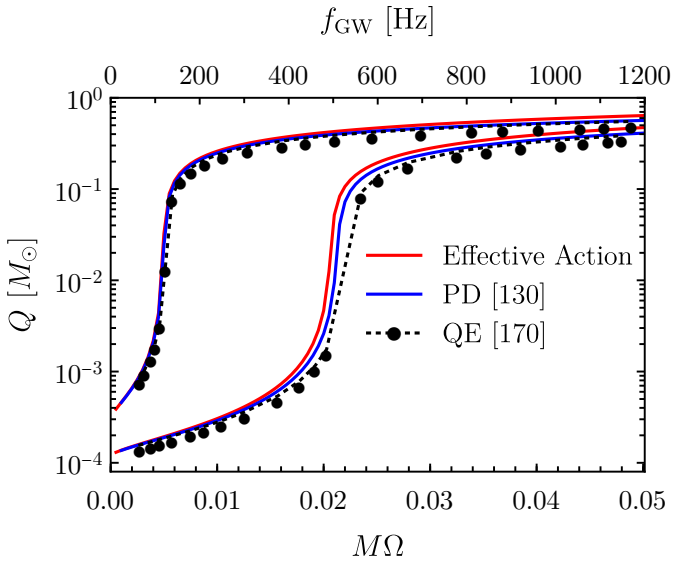

Figure 5.2: Scalar charge of each star as a function of frequency for a $(1.35 + 1.35)\, M_\odot$ BNS with the APR4 EOS. The lower axis indicates the orbital frequency Ω; the upper axis shows the dominant GW frequency $f_{\rm GW} = \Omega/\pi$. The model developed here using an effective action is shown in red. The analytic post-Dickean (PD) model of Ref. [3] is shown in blue. The numerical calculations of quasi-equilibrium (QE) configurations performed in Ref. [172] are shown in black. The curves depicting earlier scalarization were computed with $\beta = -4.5$; the other set of curves correspond to $\beta = -4.2$.

orbital frequency, normalized by the total rest mass M, which we define as,

$$M \equiv m_A^{(0)} + m_B^{(0)}, \tag{5.37}$$

i.e. the sum of the component ADM masses in GR. The upper axis gives the dominant frequency $f_{\rm GW} = \Omega/\pi$ of the GWs produced by the binary in hertz.

We plot in blue the predictions of the *post-Dickean* (PD) model constructed in Ref. [3]. The PD approach resums the PN dynamics to reproduce dynamical scalarization. To accomplish this resummation, one promotes the mass m_E and its derivatives to functions of two scalar fields $m_E(\varphi, \xi)$, Then, one field (φ) is integrated

out of the point-particle action (5.16) through a standard PN expansion, while the other (ξ) is treated as a new dynamical degree of freedom in the theory. In this way, the PD approximation resembles the model presented here. Both methods introduce new degrees of freedom at the level of the action, and extremizing the action with respect to these quantities yields algebraic equations that relate the quantities to the bodies' positions and momenta. However, in the PD approach, these equations involve the potentially complicated function $m_E(\varphi, \xi)$ and its derivatives, whereas in the formalism presented here, one needs only the coefficients $c^{(i)}$. In the notation of Ref. [3], we define the natural analog of the scalar charge as $Q \equiv m^{(\mathrm{RE},\varphi)}\alpha^{(\mathrm{RE},\varphi)}/\sqrt{\phi_0}$ and plot this quantity in the figure; see Eqs. (A3) and (A4) in Ref. [3] for the explicit definitions of these quantities. The blue curve shown in Fig. 5.2 corresponds to the next-to-leading-order dynamics in an expansion in c^{-2}.

Finally, we plot the results of the numerical QE configuration calculations performed in Ref. [172] with black dots. These calculations were made under the assumption of conformal flatness and stationarity; physically, each configuration represents a binary on an exactly circular orbit emitting no GWs. This setup is used to approximate a BNS during its adiabatic inspiral. The scalar mass M_{S} of the total system, defined in the Jordan frame, was computed in Ref. [172]. To convert this quantity to the scalar charge of the full system, we use $Q_{\mathrm{tot}} = M_{\mathrm{S}}/(-\beta\varphi_0)$; this conversion is discussed in detail in footnote 2 of Ref. [172]. For simplicity, we assume that the component scalar charges are simply half of the total scalar charge, $Q = Q_{\mathrm{tot}}/2$.

As evidenced by Fig. 5.2, we find very close agreement to previous predictions

of the evolution of the scalar charge with our effective-action model. A key feature is the frequency $\Omega_{\rm DS}$ at which dynamical scalarization occurs. As discussed above, our model predicts the onset of dynamical scalarization when the binary separation $r = 1/c^{(2)}$. Converting the separation into an orbital frequency using Eq. (5.36), we find agreement to within $\lesssim 10\%$ compared to the values presented in Table II of Ref. [3] for both the PD model and the QE configuration calculations.[6] We emphasize that our effective action model is in no way calibrated to fit the QE results; the only numerical input to the model comes from isolated NS solutions of the TOV equations.

Having computed $Q(\Omega)$, we now compute the energy of the binary system as a function of frequency. We define the binding energy E_B of the binary as,

$$E_B \equiv H - M, \tag{5.38}$$

and use Eq. (5.29) to evaluate the Hamiltonian. Using Eq. (5.36) to convert r to Ω we plot the binding energy (normalized by the total mass M) as a function of orbital frequency in Fig. 5.3. We also plot the binding energy computed from QE configurations in Ref. [172] as dashed lines and the 4PN prediction for nonspinning point particles in GR [316] as a green dashed-dotted line.[7] To improve comparison, we have added to the predictions of our effective-action model (computed at New-

[6] The agreement can be slightly improved by neglecting the $\mathcal{O}\left(c^{-2}\right)$ contributions to the redshift variables (5.31) that enter into Eq. (5.30)

[7] We use the 4PN binding energy in GR as our benchmark rather than more sophisticated estimates for simplicity. For the frequency range we consider, the 4PN energy is visually indistinguishable from the predictions of the EOB formalism [45].

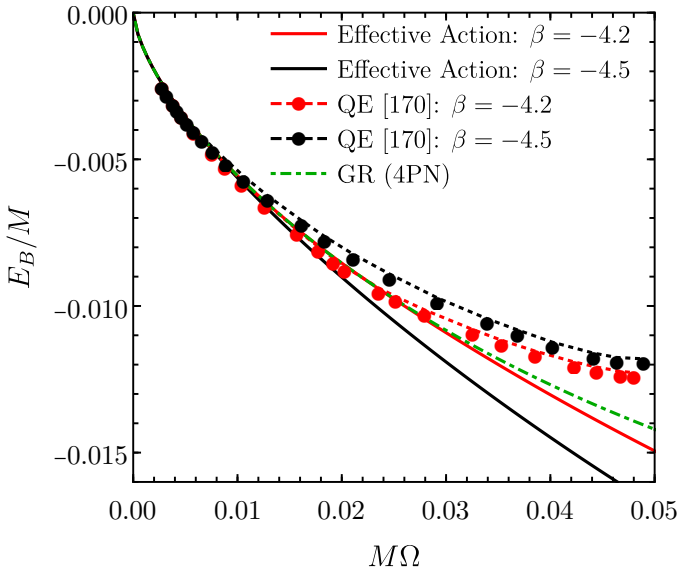

Figure 5.3: Binding energy E_B normalized by the total mass $M = 2.7M_\odot$ as a function of orbital frequency for the same BNS system as in Fig. 5.2. The predictions of the effective action model introduced here are shown in solid lines; we add to our Newtonian-order result the 1PN, 2PN, 3PN, and 4PN contributions found in GR. The QE configuration calculations performed in Ref. [172] are shown with dashed lines. Red (black) curves correspond to $\beta = -4.2$ ($\beta = -4.5$). For comparison, we have also plotted in green the 4PN prediction for the point-particle binding energy in GR.

tonian order), the 1PN, 2PN, 3PN, and 4PN corrections to the binding energy in GR. These corrections raise the binding energy closer to the other curves in Fig. 5.3, but do not influence the ordering of the various curves, and thus do not affect our conclusions.

As expected, prior to the onset of dynamical scalarization, the binding energy closely resembles that of the corresponding system in GR. After dynamical scalarization occurs, we find significant differences between our analytic model and the QE results of Ref. [172]: the present model predicts an increase in the magnitude of the binding energy $|E_B|$ relative to GR whereas the QE computations indicate that the magnitude should decrease. Given the interpretation of dynamical scalarization as a phase transition detailed in Sec. 5.5, one expects the scalarized binary to be more tightly bound than the corresponding unscalarized binary, i.e., the GR prediction. If this were not the case, dynamical scalarization would be an endothermic process (requiring energy input) and the $\varphi \to -\varphi$ symmetry would not spontaneously break. Based on this intuition, the predictions of our model in Fig. 5.3 appear qualitatively correct. The cause of the disagreement between our model and Ref. [172] remains unclear. The discrepancy could stem from the assumption of conformal flatness and/or the presence of tidal interactions absent in our point-particle model of the dynamics. However, to explain the disagreement in Fig. 5.3, these factors would need to play a more significant role in the presence of scalar charges; analogous calculations done in GR agree with analytic point-particle predictions of the binding energy much more closely than the deviations shown in Fig. 5.3 (see, e.g., Ref. [317]).

5.5 Dynamical scalarization as a phase transition

Having validated its accuracy in Sec. 5.4, in this section we explore an important conceptual implication of our effective action model: we definitively establish dynamical scalarization as a second-order phase transition. Using the Landau theory of phase transitions [318], we discuss the scalarization of an isolated NS (spontaneous scalarization), an equal-mass BNS (dynamical scalarization), and an unequal-mass BNS (spontaneous, induced, and dynamical scalarization).

The approach by Landau [318] allows one to relate certain types of phase transitions to broken symmetries. We begin with a schematic review, closely following Ref. [318]. Consider a system described by a set of state variables $\boldsymbol{\zeta}$ and thermodynamic potential $\Xi(\boldsymbol{\zeta})$ that undergoes a second-order transition between two phases at some critical point $\boldsymbol{\zeta}^*$. The degree of symmetry in each phase can be described by an order parameter η. We choose the order parameter such that it vanishes for the phase with greater symmetry, but in the other phase, the breaking of some of these symmetries causes η to be nonzero. To exhibit a second-order phase transition, the thermodynamic potential must admit an expansion near the critical point of the form

$$\Xi(\boldsymbol{\zeta}, \eta) = \Xi_0(\boldsymbol{\zeta}) + \Xi_2(\boldsymbol{\zeta})\eta^2 + \Xi_4(\boldsymbol{\zeta})\eta^4 + \mathcal{O}\left(\eta^6\right), \tag{5.39}$$

where the coefficients obey the following conditions:

$$\Xi_4(\boldsymbol{\zeta}) > 0, \tag{5.40}$$

$$\Xi_2(\boldsymbol{\zeta}^*) = 0. \tag{5.41}$$

The first condition guarantees that the system has an equilibrium solution (found at the minimum of Ξ). We discuss the second condition below.

For states "above" $\boldsymbol{\zeta}^*$, i.e., those for which $\Xi_2(\boldsymbol{\zeta}) > 0$, the potential (5.39) is positive definite, and so the system reaches equilibrium in the more symmetric state (the one in which η vanishes). However, as one passes through the point $\boldsymbol{\zeta}^*$, the coefficient $\Xi_2(\boldsymbol{\zeta})$ changes sign; now the potential (5.39) is minimized for configurations with nonzero values of η.

In anticipation of later discussion, we generalize the treatment above to systems described by a vector order parameter $\boldsymbol{\eta} \in \mathbb{R}^n$, where Euclidean coordinates are denoted with unitalicized Latin indices. In this generalization, the functions $\Xi_m(\boldsymbol{\zeta})$ become rank-m tensors of dimension n such that Eq. (5.39) becomes

$$\Xi(\boldsymbol{\zeta}, \boldsymbol{\eta}) = \Xi_0(\boldsymbol{\zeta}) + [\Xi_2(\boldsymbol{\zeta})]_{\mathrm{ab}}\, \eta^{\mathrm{a}}\eta^{\mathrm{b}} + [\Xi_4(\boldsymbol{\zeta})]_{\mathrm{abcd}}\, \eta^{\mathrm{a}}\eta^{\mathrm{b}}\eta^{\mathrm{c}}\eta^{\mathrm{d}} + \mathcal{O}\left(\boldsymbol{\eta}^6\right). \tag{5.42}$$

The conditions (5.40) and (5.41) must be appropriately extended, as well. To ensure that the system has an equilibrium solution, we require that Ξ_4 be positive definite, in the sense that

$$[\Xi_4(\boldsymbol{\zeta})]_{\mathrm{abcd}}\, \eta^{\mathrm{a}}\eta^{\mathrm{b}}\eta^{\mathrm{c}}\eta^{\mathrm{d}} > 0, \qquad \forall\, \boldsymbol{\eta} \in \mathbb{R}^n. \tag{5.43}$$

The n-dimensional generalization of Eq. (5.41) is

$$\det\left([\Xi_2(\boldsymbol{\zeta}^*)]_{\mathrm{ab}}\right) = 0. \tag{5.44}$$

Note that in the phase with greater symmetry, our assumption that Ξ is minimized when $\boldsymbol{\eta}$ vanishes ensures that all eigenvalues of the matrix $[\Xi_2(\boldsymbol{\zeta}^*)]_{\mathrm{ab}}$ must be positive. In the less symmetric phase, at least one of the eigenvalues must be negative;

however, the determinant of the matrix remains positive if an even number of eigenvectors have negative eigenvalues.

5.5.1 Spontaneous scalarization of an isolated body

The classical illustration of a second-order phase transition is spontaneous magnetization in a ferromagnet at the Curie temperature T_C. In this example, Ξ is the energy E of the system and $\boldsymbol{\zeta}$ represents the temperature and external magnetic field $\boldsymbol{B}$. The order parameter η is the total magnetization $\boldsymbol{M} \equiv -\partial E/\partial \boldsymbol{B}$, which is thermodynamically conjugate to $\boldsymbol{B}$. Inspired by this example, Damour and Esposito-Farése [152] considered a phenomenological model of spontaneous scalarization following the Landau ansatz (5.39). Starting from the total energy of an isolated NS $m_E(\varphi)$, the authors selected the potential $m(Q)$, defined as in Eq. (5.18), to play the role of Ξ. The bulk properties of the NS are its baryonic mass $\bar{m}$ and external scalar field φ. Analogous to spontaneous magnetization, the authors identified the order parameter Q as the conjugate variable to the scalar field [c.f. Eq. (5.15)].[8] The behavior of the potential m around the critical baryonic mass $\bar{m}_{\rm cr}$ was modeled by [152]

$$m(Q) = \frac{1}{2} a \left(\bar{m}_{\rm cr} - \bar{m}\right) Q^2 + \frac{1}{4} b Q^4, \tag{5.45}$$

where a and b are constant (positive) coefficients. Above the critical baryonic mass, NSs equilibrate in configurations with nonzero scalar charge.

[8] The notation of Ref. [152] differs from that used here. The original notation can be recovered with the following substitutions: $\varphi \to \varphi_0$, $Q \to \omega_A$, $m_E(\varphi) \to m_A(\omega_A, \varphi_0)$, $m(Q) \to \mu(\omega_A)$.

By design, our point-particle model (5.22) takes the same form as Eq. (5.45), and thus can model spontaneous scalarization as well. Unlike Eq. (5.45), we do not factor out any mass-dependence of the coefficients $c^{(i)}$. As demonstrated in Section 5.4.1, our model remains valid for stars with $\bar{m} \not\approx \bar{m}_{\rm cr}$—these stars were not considered in Ref. [152]. The coefficient $c^{(2)}$ plays the role of Ξ_2 in the Landau ansatz (5.39); note that this coefficient depends on the properties of the NS (e.g., the mass and EOS) and on the scalar-tensor coupling (characterized by β). The critical point at which a NS transitions from an unscalarized state ($Q = 0$) to a spontaneously scalarized state ($Q \neq 0$) occurs when $c^{(2)}$ is zero. Neutron stars with negative values of $c^{(2)}$ must spontaneously scalarize; the unscalarized state is unstable.

5.5.2 Dynamical scalarization of equal-mass binaries

With our effective action model, we can now apply this analysis to a binary system of NSs. For simplicity, we begin by studying equal-mass systems with zero background scalar field φ_0. We assume that NSs have the same properties as well, i.e., $c_A^{(i)} = c_B^{(i)}$. For illustrative purposes, we drop the $\mathbf{p}^2$ and m/r terms in the Hamiltonian (5.29); restoring these terms does not affect the qualitative behavior we describe below.

Under these assumptions, the Hamiltonian is given by

$$H = 2m^{(0)} + \left(c^{(2)} - \frac{1}{r}\right) Q^2 + \frac{c^{(4)}}{12} Q^4, \tag{5.46}$$

where we have dropped the body labels. This expression takes the same form

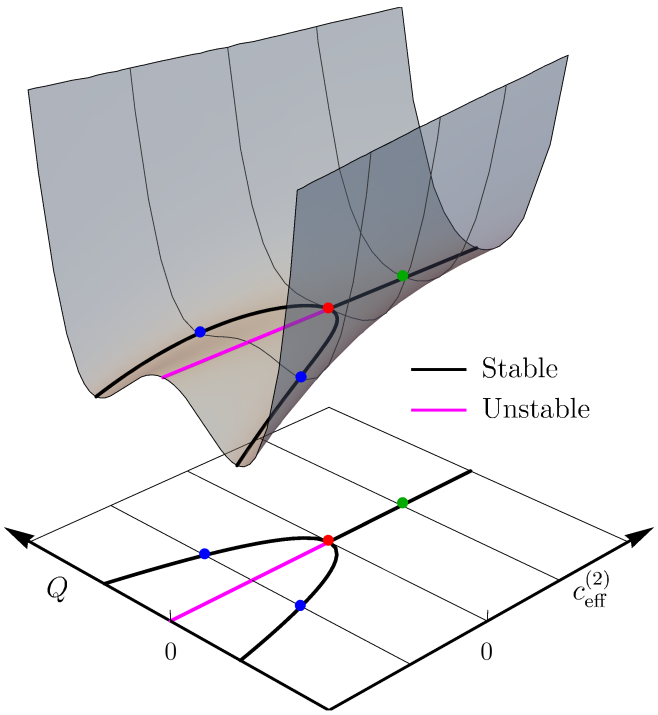

Figure 5.4: Illustration of the Hamiltonian of an equal-mass BNS as function of scalar charge and effective coefficient $c^{(2)}_{\rm eff} = c^{(2)} - 1/r$. Solutions to the equations of motion are highlighted with solid lines. When $c^{(2)}_{\rm eff}$ becomes negative, the trivial solutions $Q = 0$ become unstable. The bottom lower plane shows the projection of the solutions.

as Eq. (5.39). Using the same analysis as in the previous subsection, we show that dynamical scalarization is a second-order phase transition that occurs at a separation $r_{\rm DS} = 1/c^{(2)}$; this conclusion agrees with our prediction in Eq. (5.34). By comparing Eqs. (5.22) and (5.46) we see that an equal-mass dynamically scalarizing system behaves like an isolated NS with an effective coefficient $c^{(2)}_{\rm eff} \equiv c^{(2)} - 1/r$ that decreases as the binary coalesces.

In Fig. 5.4, we plot the simplified Hamiltonian (5.46) as a function of charge and effective coefficient $c^{(2)} - 1/r$. For positive values of this effective coefficient, the energy is minimized in the trivial configuration $Q = 0$. Below the critical

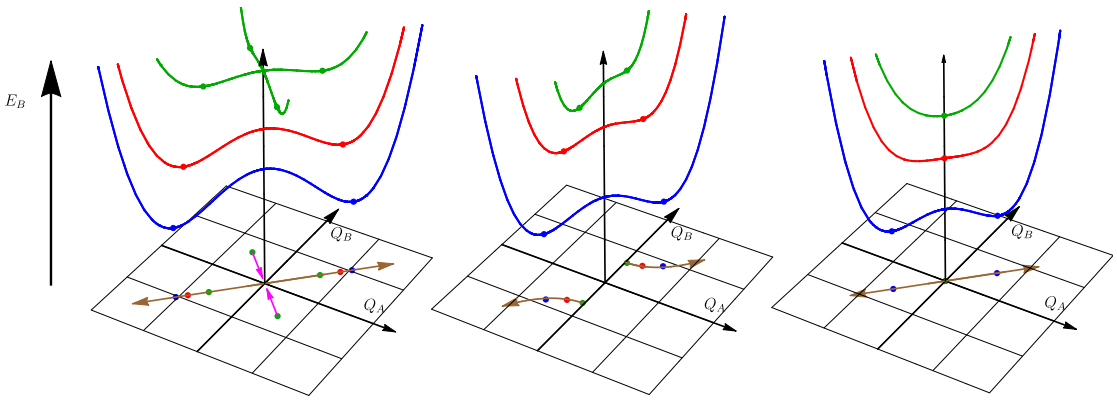

Figure 5.5: Illustration of the binding energy as a function of scalar charge for BNSs that undergo: (left) spontaneous scalarization, (middle) induced scalarization, and (right) dynamical scalarization. Equilibrium solutions are highlighted with dots. The solutions are projected onto the (Q_A, Q_B) plane below; colored arrows indicate the flow of these solutions as the binary coalesces.

point $c_{\rm eff}^{(2)} = 0$, the unscalarized state becomes unstable; instead, the binary system transitions into a scalarized state. The bottom plane shows the projection of the equilibrium solutions in black. As predicted by Eq. (5.34), the stable solutions bifurcate at the critical point, spontaneously breaking the scalar-parity symmetry of the theory. Note that this entire discussion can be applied directly to isolated NSs that undergo spontaneous scalarization by taking $r \to \infty$.

5.5.3 Scalarization of unequal-mass binaries

Finally, we turn our attention to the critical phenomena that can occur in unequal-mass binaries. The (vector) order parameter $\boldsymbol{\eta} \in \mathbb{R}^2$ is given by

$$(\eta^1, \eta^2) = (Q_A, Q_B)\,. \tag{5.47}$$

Again, we assume that the background scalar field φ_0 vanishes and drop the $\mathbf{p}^2$ and m/r terms in the Hamiltonian (5.29); these simplifications do not affect the qualitative behavior described below. Under these assumptions, the Hamiltonian takes the same form as Eq. (5.42) with

$$\Xi_0 = m_A^{(0)} + m_B^{(0)}, \tag{5.48}$$

$$[\Xi_2]_{\rm ab} = \frac{1}{2}\begin{pmatrix} c_A^{(2)} & -r^{-1} \\ -r^{-1} & c_B^{(2)} \end{pmatrix}, \tag{5.49}$$

$$[\Xi_4]_{\rm abcd} = \frac{1}{24}\left(c_A^{(4)}\delta^1_{\rm a}\delta^1_{\rm b}\delta^1_{\rm c}\delta^1_{\rm d} + c_B^{(4)}\delta^2_{\rm a}\delta^2_{\rm b}\delta^2_{\rm c}\delta^2_{\rm d}\right). \tag{5.50}$$

We examine the Hamiltonian (5.29) for systems that undergo:

1. *Spontaneous scalarization*: Both stars are initially scalarized ($c_A^{(2)} < 0$, $c_B^{(2)} < 0$),

2. *Induced scalarization*: Only one star is initially scalarized ($c_A^{(2)} > 0$, $c_B^{(2)} < 0$),

3. *Dynamical scalarization*: Neither star is initially scalarized ($c_A^{(2)} > 0$, $c_B^{(2)} > 0$).

For all three cases, we restrict our attention to binaries following circular orbits. The binding energy is shown in Fig. 5.5 as a function of the NS charges. We show only the slices of the full graph $H(Q_A, Q_B)$ that pass through equilibrium solutions; for comparison, these curves correspond to the thin black lines on the surface in Fig. 5.4. Moving from left to right, the plots correspond to spontaneous, induced, and dynamical scalarization, respectively. Moving downwards in each plot, the green, red, and blue curves depict the binding energy at progressively smaller separations. The equilibrium solutions are denoted with dots on the curves and are projected onto the

(Q_A, Q_B)-plane in the color corresponding to their separation. The colored arrows depict the flow of equilibrium solutions as the separation decreases.

At large separations (green), there exist four stable configurations for spontaneously scalarized binaries (left panel): each NS can exhibit a positive or negative scalar charge, and the choices for each are uncorrelated. However, as the separation decreases (red and blue), configurations in which the two stars have opposite-parity charges become energetically unfavorable. As indicated by the pink arrows, these solutions flow towards the origin and transform into a saddle point, i.e., this branch of solutions becomes unstable. Thus, at this critical separation (red) there exists a new phase transition distinct from those discussed above. From Eqs. (5.44) and (5.49), we find that this critical point occurs at a separation of $r^* = (c_A^{(2)} c_B^{(2)})^{-1/2}$. Unlike with dynamical scalarization, the more symmetric state phase occurs at separations smaller than r^*. The equilibrium solutions with charges of the same sign flow away from the origin as the binary coalesces. The charge of each spontaneously scalarized star will continue to grow during the inspiral due to feedback from its companion.

Binaries that undergo induced scalarization (middle panel) begin with an unscalarized star $Q_A = 0$ and a scalarized star $Q_B \neq 0$ (green). As the stars are brought closer together (red), the unscalarized star rapidly develops scalar charge, whereas the initially scalarized star remains (approximately) unchanged. However, as the separation decreases further (blue), the two charges become of the same order of magnitude and continue to increase at roughly the same rate through the remainder of the coalescence. Unlike for spontaneous and dynamical scalarization, the branches of equilibrium solutions are disjoint throughout the entire coalescence,

i.e. the colored arrows in Fig. 5.5 never meet. Because $c_A^{(2)}$ and $c_B^{(2)}$ have opposite signs, the determinant of $[\Xi_2]_{\rm ab}$ [given in Eq. (5.49)] is negative for all separations. Induced scalarization fails to meet condition (5.44) and therefore cannot be classified as a phase transition.

Finally, initially unscalarized unequal-mass binaries (right panel) evolve similarly as in Fig. 5.4. As seen in Fig. 5.5, the binary system begins in an unscalarized state (green). At the critical transition point (red), the effective $c^{(2)}$ coefficient vanishes; beyond that point (blue), scalarization becomes energetically favorable. Again, Eqs. (5.44) and (5.49) reveal that dynamical scalarization occurs at a separation of $r_{\rm DS} = (c_A^{(2)} c_B^{(2)})^{-1/2}$, which reduces to the result in Sec. 5.5.2 when $c_A^{(2)} = c_B^{(2)}$. As before, the scalar charges continue to grow after the onset of dynamical scalarization.

5.6 Conclusions

In the present paper, we developed a new point-particle model for NSs in scalar-tensor gravity that can reproduce spontaneous, induced, and dynamical scalarization. The model parametrizes the various scalarization phenomena by just two coefficients $c^{(2)}$, $c^{(4)}$ for each NS. This approach should be contrasted with previous analytic models of dynamical scalarization [3, 170], which relied upon numerically solving equations containing the generic function $m_E(\varphi)$. For the first time, we have computed a two-body Hamiltonian that incorporates dynamical scalarization in a self-consistent manner (see Ref. [3] for a discussion of previous attempts). Observ-

ables derived from the model at leading order in the PN expansion were shown to be in good agreement with earlier analytic models and numerical QE calculations. The identification of the relevant dynamical variables in the effective action is crucial to our model.

Analogous to the analysis done in Ref. [152] concerning spontaneous scalarization, our model rigorously establishes dynamical scalarization as a phase transition as per Landau theory [318]. Additionally, it demonstrates the intimate connection between spontaneous and dynamical scalarization. The mapping between an equal-mass BNS undergoing dynamical scalarization and an effective spontaneously scalarized NS is detailed in Sec. 5.5.2.

Our effective action stands as an important first step towards accurate analytic waveforms of dynamically scalarizing BNSs. The model benefits from its close analogy to the effective action model of dynamical tides detailed in Refs. [292, 299]—the dynamical scalar monopole Q here corresponds to the dynamical gravitational quadrupole therein. References [292, 299] derived an accurate EOB [38, 39] waveform model incorporating dynamical tidal interactions. Using this model as a template, one could construct an analogous model for dynamical scalar-tensor effects. This construction will require calculations of dissipative effects and higher PN order results for the conservative dynamics.

Another avenue for future work is the addition of kinetic-energy terms to the effective action as in Eq. (5.23). Resonant effects play an important role in the dynamical tides model of Refs. [292, 299]; it remains to be seen whether analogous effects could be important with dynamical scalar charges. Formulating the effective

action in this manner offers a conceptual advantage over the current model, as it guarantees that all of the equations of motion are ordinary differential equations (rather than a mix of nonlinear algebraic and differential equations).

Finally, an intriguing extension of this work is to theories with a massive scalar field. Pulsar timing cannot constrain sufficiently short-range scalar fields, so a much wider range of parameter space of massive scalar-tensor theories remains to be constrained by GW observations than that of theories with a massless scalar [161]. The PN dynamics of a simple massive scalar-tensor theory were investigated in Ref. [94], and spontaneous scalarization of isolated NSs was studied in Refs. [95, 161]; the framework we have presented above could synthesize these results with appropriate modifications to the field equations (5.6) and (5.7).

5.7 Acknowledgments

We are grateful to Andrea Taracchini for discussions and Alessandra Buonanno for helpful comments.

Chapter 6: Theory-agnostic modeling of dynamical scalarization in compact binaries

Authors: *Mohammed Khalil, Noah Sennett, Jan Steinhoff, and Alessandra Buonanno*[1]

Abstract: Gravitational wave observations can provide unprecedented insight into the fundamental nature of gravity and allow for novel tests of modifications to General Relativity. One proposed modification suggests that gravity may undergo a phase transition in the strong-field regime; the detection of such a new phase would comprise a smoking-gun for corrections to General Relativity at the classical level. Several classes of modified gravity predict the existence of such a transition—known as *spontaneous scalarization*—associated with the spontaneous symmetry breaking of a scalar field near a compact object. Using a strong-field-agnostic effective-field-theory approach, we show that all theories that exhibit spontaneous scalarization can also manifest *dynamical scalarization*, a phase transition associated with symmetry breaking in a binary system. We derive an effective point-particle action that provides a simple parametrization describing both phenomena, which establishes a foundation for theory-agnostic searches for scalarization in gravitational-wave obser-

[1]Originally published as Phys. Rev. **D100**, 124013 (2019).

vations. This parametrization can be mapped onto any theory in which scalarization occurs; we demonstrate this point explicitly for binary black holes with a toy model of modified electrodynamics.

6.1 Introduction

Classical gravity described by General Relativity (GR) has passed many experimental tests, from the scale of the Solar System [79] and binary pulsars [249, 294] to the coalescence of binary black holes (BHs) [10, 73, 122, 123, 184] and neutron stars (NSs) [9]. Despite its observational success, certain theoretical aspects of GR (e.g., its nonrenormalizability and its prediction of singularities [319]) impede progress toward a complete theory of quantum gravity; yet, strong-field modifications of the theory may alleviate these issues [83].

Gravitational wave (GW) observations probe the nonlinear, strong-field behavior of gravity and thus can be used to search for (or constrain) deviations from GR in this regime. Because detectors are typically dominated by experimental noise, sophisticated methods are required to extract GW signals. The most sensitive of these techniques rely on modeled predictions of signals (gravitational waveforms), which are matched against the data. This same approach can be adopted to test gravity with GWs; to do so requires accurate signal models that faithfully incorporate the effects from the strong-field deviations one hopes to constrain [79]. Ideally, these models would be agnostic about details of the strong-field modifications to GR, so that a single test could constrain a variety of alternative theories of gravity.

This work establishes a framework for such tests given the hypothetical scenario in which the gravitational sector manifests phase transitions, with only one phase corresponding to classical GR. This proposal comprises an attractive target for binary pulsar and GW tests of gravity; if the transition between phases arises only in the strong-gravity regime (e.g., in the presence of large curvature, relativistic matter, etc.), then such a theory could generate deviations from GR in compact binary systems while simultaneously evading stringent constraints set by weak-gravity tests. We consider the case wherein the "new" phases arise via spontaneous symmetry breaking in the gravitational sector. Similar phase transitions occur in many areas of contemporary physics—perhaps the most famous example is the electroweak symmetry breaking through the Higgs field [320–322]—so it is sensible to consider their appearance in gravity as well. As a first step, we focus on a simple set of such gravitational theories, in which the transition from GR to a new phase most closely resembles the spontaneous magnetization of a ferromagnet; however, these theories can also be extended to instead replicate the standard Higgs mechanism in the gravitational sector [323, 324].

Specifically, we investigate the nonlinear *scalarization* of nonrotating compact objects (BHs and NSs), which arises from spontaneous symmetry breaking of an additional scalar component of gravity [4, 152]. *Spontaneous scalarization*—the scalarization of a single, isolated object—has been found in several scalar extensions of GR, including massless [153–159] and massive [160–162] scalar-tensor (ST) theories and extended scalar-tensor-Gauss-Bonnet (ESTGB) theories [163–168]. Similar phenomena can also occur for vector [325, 326], gauge [324], and spinor [327] fields.

In contrast, *dynamical scalarization*—scalarization that occurs during the coalescence of a binary system—has been demonstrated and modeled only for NS binaries in ST theories [3, 4, 169–172, 175, 328].

A scalarized compact object emits scalar radiation when accelerated, analogous to an accelerated electric charge. In a binary system, the emission of scalar waves augments the energy dissipation through the (tensor) GWs found in GR, hastening the orbital decay. Radio observations of binary pulsars [6, 249, 294, 329] and GW observations of coalescing BHs and NSs [9, 10] are sensitive to anomalous energy fluxes, and thus can be used to constrain the presence of scalarization in such binaries. In addition to the tensor radiation mentioned above, binaries containing spontaneously scalarized components also emit scalar radiation throughout their entire evolution. In contrast, dynamically scalarizing binaries transition from an unscalarized (GR) state to a scalarized (non-GR) state at some critical orbital separation, emitting scalar waves only after this point. Because this is a second-order phase transition [4], the emitted GWs contain a sharp feature corresponding to the onset of dynamical scalarization. This feature cannot be replicated within typical theory-agnostic frameworks used to test gravity [117, 118, 120, 176], as these only consider smooth deviations from GR predictions, e.g., modifications to the coefficients of a power-series expansion of the phase evolution.

While one could attempt to model dynamical scalarization phenomenologically by adding nonanalytic functions to such frameworks [175, 271], in this work, we propose a complementary theory-agnostic approach. We focus on a specific non-GR effect, here scalarization, but remain agnostic toward the particular alternative

theory of gravity in which it occurs. The basis for our framework is effective field theory. Scalarization arises from strong-field, nonlinear scalar interactions in the vicinity of compact objects; the details of this short-distance physics depends on the specific alternative to GR that one considers. By integrating out these short-distance scales, we construct an effective point-particle action for scalarizing bodies in which the relevant details of the modification to GR are encapsulated in a small set of form factors. The coefficients of these couplings offer a concise parametrization ideal for searches for scalarization with GWs. The essential step in constructing this effective theory is identifying the fields and symmetries relevant to this phenomenon. Starting from the perspective that scalarization coincides with the appearance of a tachyonic scalar mode of the compact object, we derive the unique leading-order effective action valid near the critical point of the phase transition. Though this effective action matches that of Ref. [4]—which describes the scalarization of NSs in ST theories[2]—the approach described here is valid for a broader range of non-GR theories.

Our proposed parametrization of scalarization is directly analogous to the standard treatment of tidal interactions in compact binary systems. Tidal effects enter GW observables through a set of parameters that characterize the response of each compact object to external tidal fields [308]. These parameters are determined by the structure of the compact bodies—for example, the short-distance nuclear interactions occurring in the interior of a NS. This description of tidal effects is applicable to a broad range of nuclear models (i.e., NS equations of state) and offers

[2]Dynamical scalarization was also modeled at the level of equations of motion in Refs. [3, 170].

a more convenient parametrization of unknown nuclear physics for GW measurements [186, 330] than directly incorporating nuclear physics into GW models. From the perspective of modeling compact binaries, the primary difference between tidal effects and scalarization is that the latter is an inherently nonlinear phenomenon, necessitating higher-order interactions in an effective action.

Beyond offering a convenient parametrization for GW tests of gravity, our effective action also elucidates certain generic properties of scalarization phenomena. Using a simple analysis of energetics based on the effective theory, we argue that *any theory that admits spontaneous scalarization must also admit dynamical scalarization*. Additionally, this type of analysis can provide further insights regarding the (nonperturbative) stability of scalarized configurations and the critical phenomena close to the scalarization phase transition. We illustrate these points by applying our energetics analysis to a simple Einstein-Maxwell-scalar (EMS) theory in which electrically charged BHs can spontaneously scalarize, complementing previous results for NSs in ST theories [4].

The paper is organized as follows. In Sec. 6.2, we first review the mechanism of scalarization as the spontaneous breaking of the $\mathbb{Z}_2$ symmetry of a scalar field driven by a linear scalar-mode instability. Then, we construct an effective worldline action for a compact object interacting with a scalar field valid near the onset of scalarization. In Sec. 6.3, we discuss how the relevant coefficients in the action can be matched to the energetics of an isolated static compact object in an external scalar field, demonstrating the procedure explicitly with BHs in the EMS theory of Ref. [158]. In Sec. 6.4, we employ the effective action to further investigate scalar-

ization in this EMS theory: we examine the stability of scalarized configurations, compute the critical exponents of the scalarization phase transition, and predict the frequency at which dynamical scalarization occurs for binary BHs. We also argue that dynamical scalarization is as ubiquitous as spontaneous scalarization in modified theories of gravity. Finally, in Sec. 6.5, we summarize the main implications of our findings, and discuss future applications of our framework. The appendixes provide a derivation of a more general effective action and details on the construction of numerical solutions for isolated BHs in EMS theory.[3]

6.2 Linear mode instability and effective action close to critical point

In this section, we review the connection between the appearance of an unstable scalar mode in an unscalarized compact object and the existence of a scalarized state for the same body. We then derive an effective action close to this critical point at which this mode becomes unstable.

As an illustrative toy model for this discussion, we consider the modified theory of electrodynamics introduced in Ref. [158] (hereafter referred to as EMS theory for brevity), whose action is given by

$$S_{\rm field} = \int d^4x \, \frac{\sqrt{-g}}{16\pi} \left[R - 2\partial_\mu \phi \partial^\mu \phi - f(\phi) F^{\mu\nu} F_{\mu\nu} \right] , \tag{6.1}$$

where R is the Ricci scalar, g is the determinant of the metric $g_{\mu\nu}$, and $F_{\mu\nu} =$

[3]Throughout this work, we use the conventions of Misner, Thorne, and Wheeler [15] for the metric signature and Riemann tensor and work in units in which the speed of light and bare gravitational constant are unity.

$\partial_\mu A_\nu - \partial_\nu A_\mu$ is the electromagnetic field tensor. In this work, we consider two choices of scalar couplings:

$$f_1(\phi) = e^{-\alpha\phi^2}, \tag{6.2}$$

$$f_2(\phi) = \left(1 + \alpha\phi^2 - \frac{1}{2}\alpha^2\phi^4\right)^{-1}, \tag{6.3}$$

where α is a dimensionless coupling constant. While the two couplings have the same behavior near $\phi = 0$, their behavior for large field value differs drastically. The former choice was used in Ref. [158] to construct stable scalarized BH solutions, whereas we introduce the latter in this work to demonstrate a theory in which no stable scalarized BH configurations exist (see Sec. 6.4).

The absence of any linear coupling of ϕ to the Maxwell term implies that any solution in Einstein-Maxwell (EM) theory, i.e., with $\phi = 0$, also solves the field equations of Eq. (6.1); however, stable solutions in EM theory may be unstable in EMS theory. To see this, we write the scalar-field equation schematically as

$$\Box\phi = m_{\rm eff}^2\,\phi, \qquad m_{\rm eff}^2 = \frac{f'(\phi)}{4\phi} F^{\mu\nu}F_{\mu\nu}. \tag{6.4}$$

We consider an electrically charged BH, for which $F^{\mu\nu}F_{\mu\nu} < 0$ and thus the effective-mass squared $m_{\rm eff}^2$ is negative for $\alpha < 0$. One can decompose ϕ into Fourier modes with frequency ω and wave vector $\boldsymbol{k}$, which satisfy the dispersion relation $\omega^2 \approx \boldsymbol{k}^2 + m_{\rm eff}^2(\boldsymbol{k})$, where curvature corrections have been dropped for simplicity. We see that if $m_{\rm eff}^2(\boldsymbol{k})$ is sufficiently negative, then ω^2 is also negative, leading to a tachyonic instability. The critical point at which this tachyonic instability first appears can be determined by identifying linearly unstable quasinormal scalar modes of the EM

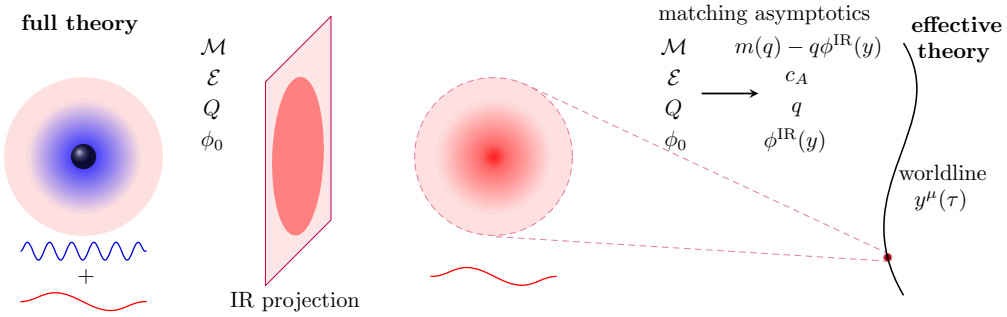

Figure 6.1: An illustration of the approach used in this work (read from left to right). (*Left*) The fields describing an isolated compact object in equilibrium are decomposed into short- (UV) and long- (IR) wavelength modes, depicted in blue and red, respectively. (*Center*) We integrate out the UV modes via an IR projection. (*Right*) By matching asymptotics, we identify the coarse-grained compact object with an effective point-particle model that describes the IR sector of the full theory. Section 6.3 contains a detailed description of this procedure and the definitions of all quantities shown above.

solution [164, 331] or by constructing sequences of fully nonlinear, static scalarized solutions (as we do here) [158, 331].

The tachyonic instability drives the body away from the unscalarized solution, thereby breaking the symmetry $\phi \to -\phi$ in Eq. (6.1). For a stable scalarized equilibrium configuration to exist, this instability must saturate in the nonlinear regime [332]. These two conditions—the existence of a tachyonic instability and its eventual saturation—are satisfied in all of the theories discussed previously [153–168, 324–327]. The only difference between these theories is the form of $m^2_{\rm eff}$; for example, in ST theories $m^2_{\rm eff}$ depends on the stress-energy tensor, while in ESTGB it depends on the Gauss-Bonnet invariant. Indeed, theories which meet these two criteria can be straightforwardly constructed, which is the reason why scalarization is such a ubiquitous phenomenon.

An even simpler perspective on scalarization arises from a coarse-grained, or effective, theory. Let us derive it explicitly. We start by splitting the fields into the short- (or ultraviolet, UV) and long- (or infrared, IR) wavelength regimes separated by the object's size $\sim R$, i.e., $\phi = \phi^{\rm IR} + \phi^{\rm UV}$, and spatially average over (integrate out) the UV parts. This effectively shrinks the compact object to a point and its effective action is given by an integral over a worldline $y^\mu(\tau)$, where τ is the proper time (see Fig. 6.1 for a schematic illustration). Dynamical short-length-scale processes like oscillations of the object are represented by dynamical variables on the worldline. For simplicity, we assume that we can also average over fast oscillation modes and only retain the monopolar mode associated to a linear tachyonic instability, denoted by $q(\tau)$. This mode $q(\tau)$ can indeed be excited by IR fields, since its frequency (or effective mass) vanishes at the critical point.

Effective actions are usually constructed by making an ansatz respecting certain symmetries and including only terms up to a given power in the cutoff between IR and UV scales. The relevant symmetries here are diffeomorphism, $U(1)$-gauge, worldline-reparametrization, time-reversal[4], and scalar-inversion invariance. The last reads $\phi \to -\phi$ in the full theory, so in the effective action it decomposes into simultaneous IR $\phi^{\rm IR} \to -\phi^{\rm IR}$ and UV $q \to -q$ transformations. The IR fields are of order $\phi^{\rm IR} \sim \mathcal{O}(R/r)$ on the worldline, where r is the typical IR scale (e.g., the separation of a binary). Now, the oscillator equation for the mode $q(\tau)$ driven by

[4]Time reversal is an approximate symmetry of compact objects in an adiabatic setup, like the inspiral of a binary system. In this case, a compact object's entropy remains approximately constant.

the IR field $\phi^{\rm IR}$ can be schematically written as

$$c_{\dot{q}^2}\ddot{q} + V'(q) = \phi^{\rm IR}(y), \quad V(q) = \frac{c_{(2)}}{2}q^2 + \frac{c_{(4)}}{4!}q^4 + \ldots, \tag{6.5}$$

where $\dot{} = d/d\tau$ and the $c_{\ldots}$ are constant coefficients determined by the UV physics. (The singular self-field contribution to $\phi^{\rm IR}(y)$ must be removed using some regularization prescription.) The normalization of q is chosen to fix the coefficient of $\phi^{\rm IR}(y)$; for all that follows, we simply assume that $c_{\dot{q}^2} > 0$. Close to the critical point, the quadratic term in V is negligible, and thus from Eq. (6.5), one finds that for equilibrium configurations ($\dot{q} = 0$), q scales as $q^3 \sim \phi^{\rm IR}$. More generally, the mode q oscillates around this equilibrium point provided that the IR field evolves slowly relative to the frequency of the mode, i.e., $\dot{\phi}^{\rm IR} = \dot{y}^\mu \partial_\mu \phi^{\rm IR} \ll \dot{q}/q$; this condition is satisfied for binary systems on quasicircular orbits (which we restrict our attention to in this work), but could be violated for highly eccentric orbits. For small perturbations around equilibrium, one finds that $\dot{q} \sim \delta\sqrt{\phi^{\rm IR}}$ and $\ddot{q} \sim \delta\phi^{\rm IR}$ where $\delta \equiv (q - q_0)/q_0 \ll 1$ is the fractional deviation from the equilibrium point q_0.

Using the scaling relations derived above, we construct the most generic effective action for a nonrotating compact object with a dynamical mode $q(\tau)$ described by Eq. (6.5) close to the critical point, up to order $\mathcal{O}(R^2/r^2)$

$$\begin{aligned} S_{\rm CO}^{\rm crit} &= \int d\tau \left[\frac{c_{\dot{q}^2}}{2}\dot{q}^2 + \phi^{\rm IR}(y)q - c_{(0)} - \frac{c_{(2)}}{2}q^2 - \frac{c_{(4)}}{4!}q^4 \right. \\ &\qquad \left. + c_A A_\mu^{\rm IR}(y)\dot{y}^\mu + \mathcal{O}\left(\frac{R^2}{r^2}\right) \right], \end{aligned} \tag{6.6}$$

$$\begin{aligned} &= \int d\tau \left[\frac{c_{\dot{q}^2}}{2}\dot{q}^2 + \phi^{\rm IR}(y)q - m(q) \right. \\ &\qquad \left. + c_A A_\mu^{\rm IR}(y)\dot{y}^\mu + \mathcal{O}\left(\frac{R^2}{r^2}\right) \right], \end{aligned} \tag{6.7}$$

where CO stands for compact object and for later convenience we define

$$m(q) \equiv c_{(0)} + V(q). \tag{6.8}$$

Terms containing time derivatives of $\phi^{\rm IR}$ all enter at higher order in R/r than we work, e.g., $\ddot{\phi}^{\rm IR} q \sim \dot{\phi}^{\rm IR}\dot{q} \sim \phi^{\rm IR}\ddot{q} \sim \mathcal{O}(R^2/r^2)$, and thus are absent in Eq. (6.7). A reparametrization-invariant action is obtained by replacing $d\tau$ with

$$d\tau = d\sigma \sqrt{-g^{\rm IR}_{\mu\nu}(y) \frac{dy^\mu}{d\sigma}\frac{dy^\nu}{d\sigma}}, \tag{6.9}$$

where σ is an arbitrary affine parameter, and replacing derivatives $d/d\tau$ accordingly. The complete effective action reads

$$S_{\rm eff} = S^{\rm IR}_{\rm field} + S^{\rm crit}_{\rm CO}, \tag{6.10}$$

where more copies of $S^{\rm crit}_{\rm CO}$ can be added depending on the number of objects in the system and $S^{\rm IR}_{\rm field}$ is given by Eq. (6.1) with IR labels on the fields. The equations of motion and field equations are obtained by independent variations of $y^\mu(\sigma)$, $q(\sigma)$, and $\phi^{\rm IR}(x)$, $g^{\rm IR}_{\mu\nu}(x)$, $A^{\rm IR}_\mu(x)$.

The simplicity of $S^{\rm crit}_{\rm CO}$ is striking, but we recall that it is only valid close to the critical point of a monopolar, tachyonic, linear instability of a scalar mode. (A more generic effective action valid away from the critical point is discussed in Appendix H.) Despite its simplicity, the effective action (6.10) is theory agnostic, in the sense that it is constructed assuming only the scalar-inversion symmetry and that the nonrotating compact object hosts such a mode; in particular, it should hold for the cases studied in Refs. [153–168, 324–327] and similar work to come. We emphasize that strong-field UV physics at the body scale is parametrized through the numerical

coefficients $c_{...}$, which can be matched to a specific theory and compact object, or be constrained directly from observations (analogous to tidal parameters [9, 330]).

6.3 Matching strong-field physics into black-hole solutions

As an illustrative example of the effective-action framework derived above, we now compute the sought-after coefficients $c_{...}$ for BHs in EMS theory.

For this purpose, we match a BH solution in the full theory (6.1) to a generic solution of the coarse-grained effective theory (6.10) for an isolated body. Schematically, the former represents the full solution at all scales, while the latter only represents its projection onto IR scales. We focus first on BH solutions of the full theory (6.1), restricting our attention to equilibrium/static, electrically charged, spherically symmetric solutions.

In EMS theory, this family of solutions is characterized by three independent parameters, which we take to be the electric charge $\mathcal{E}$, the BH entropy $\mathcal{S}$, and the asymptotic scalar field ϕ_0, assuming a vanishing asymptotic electromagnetic field and an asymptotically flat metric. The electric charge is globally conserved by the $U(1)$ symmetry of the theory and the entropy remains constant under reversible processes, which we have implicitly restricted ourselves to by assuming time-reversal symmetry in the effective action. Thus, we use a sequence of solutions with fixed $\mathcal{E}$ and $\mathcal{S}$ to represent the response of a BH to a varying scalar background ϕ_0. Since EMS theory modifies electrodynamics, but not gravity or the coupling to gravity, the entropy of a charged BH is the same as in GR, i.e., it is proportional to the

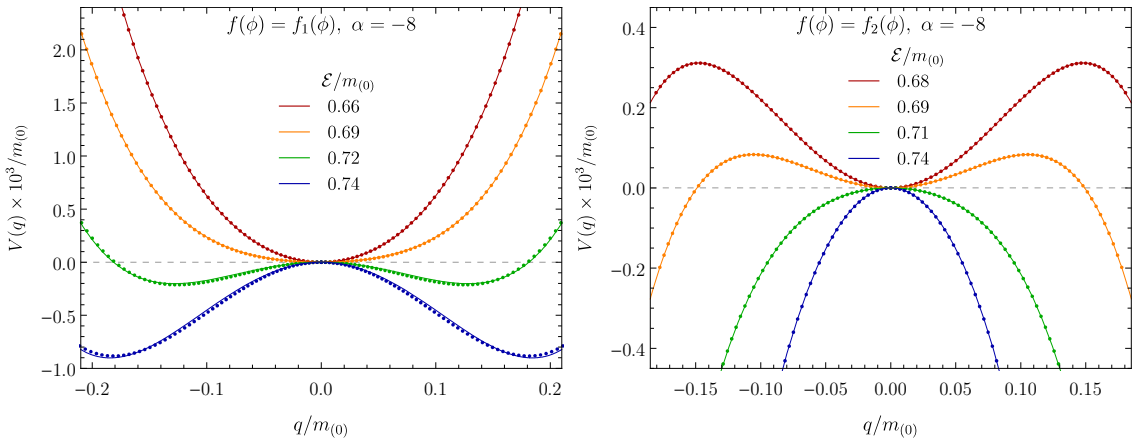

Figure 6.2: The potential $V(q)$ for $\alpha = -8$ and different electric charges $\mathcal{E}$. The left and right panels correspond to BHs in EMS theory with coupling $f_1(\phi)$ [Eq. (6.2)] and $f_2(\phi)$ [Eq. (6.3)], respectively. The numerical solutions and polynomial fits are indicated with points and lines, respectively.

horizon area. See also Ref. [158] for the first law of BH thermodynamics in EMS theory.

The asymptotic behavior of the fields take the form

$$\begin{pmatrix} \phi \\ A_0 \\ g_{00} \end{pmatrix} = \begin{pmatrix} \phi_0 \\ 0 \\ -1 \end{pmatrix} + \begin{pmatrix} Q(\phi_0) \\ -\mathcal{E}e^{\alpha\phi_0^2} \\ 2\mathcal{M}(\phi_0) \end{pmatrix} \frac{1}{|\boldsymbol{X}|} + \mathcal{O}(|\boldsymbol{X}|^{-2}), \tag{6.11}$$

where $Q(\phi_0)$ is the scalar charge of the BH and $\mathcal{M}(\phi_0)$ is its gravitational mass.[5] We construct these solutions numerically (see Appendix I for details), and then compute $\phi_0, \mathcal{M}$, and Q directly from their asymptotic behavior.

Next, we turn our attention to the description of these BH solutions in the

[5]The quantities $Q(\phi_0)$ and $\mathcal{M}(\phi_0)$ describing the asymptotic behavior of the solution also depend on the parameters $\mathcal{E}$ and $\mathcal{S}$, but we suppress the dependence in our notation for brevity. Derivatives of Q and $\mathcal{M}$ are taken holding $\mathcal{E}$ and $\mathcal{S}$ constant.

effective theory (6.10). We set up the solution under the same boundary conditions as the numerical sequence described above; in particular, we look at isolated equilibrium configurations, $y^\alpha \partial_\alpha g^{\rm IR}_{\mu\nu} \approx y^\alpha \partial_\alpha A^{\rm IR}_0 \approx y^\alpha \partial_\alpha \phi^{\rm IR} \approx \dot{q} \approx 0$. We construct a coordinate system $\boldsymbol{x}$ in which the worldline has spatial components $\boldsymbol{y} = \boldsymbol{0}$, so that all fields are independent of time. Furthermore, relying on the fact that both solutions are asymptotically flat, we choose the coordinates $\boldsymbol{x}$ such that they match the numerical coordinates $\boldsymbol{X}$ in the asymptotic region, i.e., $\boldsymbol{x} = \boldsymbol{X} + \mathcal{O}(|\boldsymbol{X}|^{-1})$. Then working to linear order in the fields, we find

$$\begin{pmatrix} \phi^{\rm IR} \\ A^{\rm IR}_0 \\ g^{\rm IR}_{00} \end{pmatrix} = \begin{pmatrix} \phi_0 \\ 0 \\ -1 \end{pmatrix} + \begin{pmatrix} q \\ -c_A e^{\alpha[\phi^{\rm IR}(y)]^2} \\ 2[m(q) - \phi^{\rm IR}(y) q] \end{pmatrix} \frac{1}{|\boldsymbol{x}|} + \dots . \tag{6.12}$$

These fields are singular when evaluated on the worldline, $\boldsymbol{x} = \boldsymbol{y} = \boldsymbol{0}$. This can be cured by appropriately regularizing the solution; here, we simply keep the finite part and drop the singular self-field part, e.g., $\phi^{\rm IR}(y) = \phi_0$. The situation is analogous to the singular fields that arise in electrostatics when an extended source is approximated by a point charge.

In addition to a solution for the fields, a variation of q in the effective action leads to

$$\phi_0 = \frac{dm}{dq} = \frac{dV}{dq} = c_{(2)} q + \frac{c_{(4)} q^3}{3!} + \mathcal{O}\left(\frac{R^2}{r^2}\right). \tag{6.13}$$

The matching now consists of identifying the IR-scale fields in the solution of the full theory (6.11) with the fields predicted in the IR effective theory (6.12). We extract the IR-scale fields from the former solution using an appropriate IR projector $P^{\rm IR}[\cdot]$, such that the matching conditions are given explicitly as $P^{\rm IR}[\phi] = \phi^{\rm IR}$ (and

likewise for the other fields). Such a projector is most easily formulated in the Fourier domain, so we first compute the (spatial) Fourier transform of the fields (6.11), denoted by a tilde

$$\tilde{\phi}(\boldsymbol{K}) = \phi_0 \delta(\boldsymbol{K}) + \frac{4\pi Q(\phi_0)}{\boldsymbol{K}^2} + \mathcal{O}(|\boldsymbol{K}|^{-1}). \tag{6.14}$$

We employ the simple projector $P^{\rm IR}[\tilde{\phi}] \equiv \tilde{\phi}(\boldsymbol{K})\Theta(K^{\rm IR} - |\boldsymbol{K}|)$, where Θ is the Heaviside function and $K^{\rm IR}$ is the cutoff scale. Applying this projection to Eq. (6.14) and taking the inverse Fourier transform, one finds that $P^{\rm IR}[\phi]$ takes the same form as Eq. (6.11) on scales longer than the cutoff, i.e., for $|\boldsymbol{X}| \gg 1/K^{\rm IR}$. Then, our matching conditions $P^{\rm IR}[\phi] = \phi^{\rm IR}, P^{\rm IR}[A_0] = A_0^{\rm IR}, P^{\rm IR}[g_{00}] = g_{00}^{\rm IR}$ reduce to

$$Q(\phi_0) = q, \quad \mathcal{E} = c_A, \quad \mathcal{M}(\phi_0) = m(q) - \phi_0 q, \tag{6.15}$$

where we have used $\phi^{\rm IR}(y) = \phi_0$ as discussed above. Note that the last equation and $m'(q) = \phi_0$ (6.13) reveal that the two measures of energy $\mathcal{M}$ and m are related by a Legendre transformation of the conjugate variables (q, ϕ_0). Hence, we find that $Q = q = -\mathcal{M}'(\phi_0)$, in agreement with the first law of BH thermodynamics [333, 334].

While $\mathcal{M}(\phi_0)$ is the gravitational mass of the system, $m(q)$ represents the "gravitational free energy" of the body (see also Sec. III.A of Ref. [4]). That is, m is the mass/energy with the potential energy $-\phi_0 q$ (due to the external scalar field) subtracted from $\mathcal{M}$. We find below that m—not $\mathcal{M}$—serves as better representation of "point-particle mass" found in the Lagrangian or Hamiltonian description of a binary system; of course, both quantities reduce to the standard ADM mass in GR in the absence of scalarization. Furthermore, away from the critical point, it is not

necessary to treat the mode q as a dynamical variable. This means that we can set $\dot{q} = 0$ and remove q from the action (6.7). The latter is achieved by virtue of the Legendre transformation between $m(q)$ in Eq. (6.7) and $\mathcal{M}(\phi^{\rm IR}(y))$,

$$S_{\rm CO} = \int d\tau \Big[- \mathcal{M}(\phi^{\rm IR}(y)) + \mathcal{E} A^{\rm IR}_{\mu}(y) \dot{y}^{\mu} + \dots \Big]. \tag{6.16}$$

We see that $\mathcal{M}$ plays the role of the Eardley mass [204] in the action now. We note that since the Eardley mass and $m(q)$ are related by a Legendre transformation, they contain the same information.

To compute the values of the various $c_{\dots}$, we numerically construct a sequence of BH solutions as described above and extract the functions $\mathcal{M}(\phi_0)$ and $Q(\phi_0)$. From there we obtain $m(q)$ and $V(q)$ numerically from Eq. (6.15), as illustrated in Fig. 6.2. Each curve indicates a BH sequence with a different electric charge-to-mass ratio $\mathcal{E}/m^{(0)}$, where $m^{(0)} \equiv c_{(0)}$ is the mass of the isolated BH with no scalar charge. The points indicate the numerically computed solutions, which are calculated by solving the field equations with different boundary conditions for the scalar field (see Appendix I). The solid lines are polynomial fits of the form (6.5), from which we extract the values of the coefficients $c_{(2)}$ and $c_{(4)}$.

It is remarkable that from equilibrium solutions one can fix the potential of a dynamical (nonequilibrium) mode to order q^4. This connection is nontrivial, and it breaks down when one relaxes the assumption of being close to the critical point. For instance, if terms like $(\phi^{\rm IR})^2$ are included in Eq. (6.7), then $Q \neq q$; or consider the case of a minimally coupled scalar field ($\alpha = 0$), wherein no-hair theorems [23, 148] guarantee that $\mathcal{M}(\phi_0) = $ const—the energy of an equilibrium BH obviously does

not encode any information about dynamical modes.

Having described how to compute the coefficients $c_{...}$ in the effective action (6.7), the following section illustrates how this action can be used to study spontaneous and dynamical scalarization.

6.4 Modeling strong-gravity effects within the theory-agnostic framework

In this section, we show how spontaneous and dynamical scalarization can be understood from the effective theory (6.7), based on a simple analysis of energetics. We use this effective action to investigate the properties of these critical phenomena, namely their critical exponents. Though we use EMS theory to make quantitative predictions throughout this section, we emphasize again that the qualitative behavior we find should hold generically for all theories in which spontaneous scalarization occurs. More specifically, theories in which scalarized configurations are stable are analogous to EMS theory with scalar coupling $f_1(\phi)$, whereas those where such configurations are unstable correspond to the coupling $f_2(\phi)$ (see the following subsection for details). Extending the predictions made below to other theories only requires computation of the effective mode potential $V(q)$, as described in the previous section, and the inclusion of any new long-range fields not present in EMS theory that impact the motion of binary systems.

6.4.1 Spontaneous scalarization

Recall that a spontaneously scalarized object is one that hosts a nonzero scalar charge even in the absence of an external scalar field $\phi_0 = 0$. From Eq. (6.13) we see that $\phi_0 = 0$ corresponds to extrema of $V(q)$ for equilibrium configurations. Furthermore, since $V(q)$ is the oscillation-mode potential, q dynamically evolves into a minimum of $V(q)$ [see Eq. (6.5)]. Thus, the existence of spontaneously scalarized configurations is indicated by nontrivial extrema of $V(q)$, and the stability of these configurations depends on whether such points are local minima (stable) or maxima (unstable). For example, the left panel Fig. 6.2 depicts the appearance of spontaneously scalarized BH solutions as one increases the charge-to-mass ratio in EMS theory with coupling $f_1(\phi)$. Without enough electric charge (e.g., the red and orange curves, with $c_{(2)} > 0$), the EM (unscalarized) solutions are the only stable BH solutions, but by increasing the charge beyond a critical value (e.g., the green and blue curves, with $c_{(2)} < 0$), the EM solution becomes unstable and the stable solutions instead occur at nonvanishing values of q.

Our approach allows one to determine the values of the coupling α and the electric charge $\mathcal{E}$ at which spontaneous scalarization first occurs ($c_{(2)} = 0$) using only sequences of equilibrium BH solutions. A more direct approach employed in the past was to search for instabilities of linear, dynamical scalar perturbations on a (GR) Reissner-Nordström background [331]. We find that the two methods provide the same predictions. For the choice of coupling $f_1(\phi)$, we compute the critical coupling as a function of the electric charge $\alpha_{\rm crit}(\mathcal{E})$ where $c_{(2)} = 0$ and find that our

results agree with the predictions of Ref. [331] at the onset of the linear instability of the $\ell = 0$ scalar mode to within 1%. For theories in which scalarized solutions are easy to construct, like the EMS theory considered here, our approach can more efficiently compute this critical point than a perturbative stability analysis. We see that the effective potential $V(q)$ provides strong indications for a linear scalar-mode instability and its nonlinear saturation.

The same energetics argument reveals drastically different behavior in the EMS theory with coupling $f_2(\phi)$, depicted in the right panel of Fig. 6.2. Recall that $f_1(\phi) \approx f_2(\phi)$ for small field values, but the two choices differ in the nonlinear regime, which will dramatically impact the stability of scalarized solutions. This distinction is reflected in our effective action by the sign of $c_{(4)}$; this coefficient is positive for the choice of coupling $f_1(\phi)$ and negative for $f_2(\phi)$. Our simple energetics arguments reveal that above some critical electric charge (e.g., the green and blue curves with $c_{(2)} < 0$), no spontaneously scalarized solutions exist, whereas below this value (e.g., the red and orange curves with $c_{(2)} > 0$) spontaneously scalarized solutions may exist, but are unstable to scalar perturbations. In the former case (the green and blue curves), there is no sign of a nonlinear saturation of the tachyonic instability of the EM solution; no stable equilibrium solutions seem to exist. However, it is impossible to infer how the unstable EM solutions would evolve using our effective theory, since the assumption of time-reversal symmetry (or constant BH entropy) will likely break down. Numerical-relativity simulations are needed to answer this question (or the construction of a more generic effective theory).

The importance of nonlinear interactions in stabilizing spontaneously scalar-

ized solutions has been studied extensively in the context of ESTGB theories [335–337]. For those theories, exponential couplings (equivalent to our f_1) or quartic couplings ($f \sim -\phi^2 + \phi^4$) provide stable scalarized solutions, whereas with quadratic couplings ($f \sim -\phi^2$), all scalarized solutions are unstable. Interestingly, quadratic couplings predict stable scalarized solutions in EMS theories [338], but our analysis suggests that stability is not guaranteed for generic couplings. The stability analyses in these references involve studying linearized perturbations on scalarized backgrounds. Though technically only valid near the critical point of the spontaneous scalarization phase transition and for small q, our approach offers a much easier alternative for estimating stability. We find that our approach correctly reproduces the findings of these stability analyses for scalarized BHs in EMS theories [338, 339].

6.4.2 Critical exponents of phase transition in gravity

The point-particle action (6.7) also offers some insight into the critical behavior that arises near the onset of spontaneous scalarization. For this discussion, we restrict our attention to the scalar coupling $f_1(\phi)$, for which spontaneously scalarized configurations are stable. Considering the various coefficients $c_{...}$ as functions of the electric charge $\mathcal{E}$ and entropy $\mathcal{S}$ of a BH and the overall coupling constant α, the effective potential $V(q)$ corresponds precisely to the standard Landau model of second-order phase transitions [318, 340]. Compared to the archetypal example of ferromagnetism, the role of temperature T is played by either $\mathcal{E}$ or α. This connection reveals that (i) spontaneous scalarization is a second-order phase transition and

(ii) the critical exponents characterizing this phase transition match the universal values predicted by the Landau model. Point (i) was already demonstrated for NSs in ST theories in Ref. [4], but point (ii) is new to this work; we elaborate on (ii) below.

Critical exponents dictate how a system behaves close to a critical point (e.g., the location of a second-order phase transition). Such phenomena have first been discovered in GR in the context of critical collapse [341–344], but also appear in perturbations of extremal BHs [345, 346]. Applied to the current example of spontaneous scalarization, we study how the structure of the BH solutions varies as we approach the critical point at which spontaneous scalarization first occurs, parametrized by $\xi \to 0$ where ξ could be either $\xi = (\alpha - \alpha_c)/\alpha_c$ at fixed $\mathcal{E}$ (identifying temperature as $T \sim -1/\alpha$) or $\xi = (\mathcal{E} - \mathcal{E}_c)/\mathcal{E}_c$ at fixed α (identifying $T \sim 1/\mathcal{E}$). For example, the critical exponent β of a Landau model is given by the scaling of the order parameter $q \propto \xi^\beta$ as $\xi \to 0^+$.

The effective potential $V(q)$ in Eq. (6.5) depends on the properties of the BH solution; this dependence is suppressed in the notation used in the previous section, but here we explicitly restore it. In particular, close to the critical point, the potential takes the form

$$V(q;\xi) = \frac{c_{(2)}(\xi)}{2} q^2 + \frac{c_{(4)}(\xi)}{4!} q^4 . \tag{6.17}$$

If $c_{(2)}(\xi)$ and $c_{(4)}(\xi)$ are analytic functions, they must take the following form near $\xi = 0$,

$$c_{(2)}(\xi) = a\,\xi + \mathcal{O}\left(\xi^2\right), \qquad c_{(4)}(\xi) = b + \mathcal{O}\left(\xi\right), \tag{6.18}$$

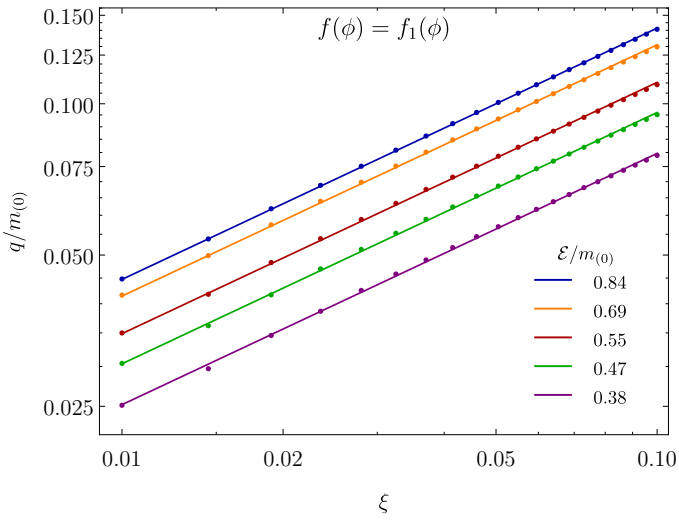

Figure 6.3: Scalar charge q as a function of $\xi \equiv (\alpha - \alpha_c)/\alpha_c$ for different electric charges with coupling $f_1(\phi)$ [Eq. (6.2)]. The numerical solutions are indicated with points, while the solid lines are best fits with slope 1/2. We see that the solutions agree well with the expected scaling $q \propto \xi^{1/2}$.

where a and b are positive constants. Then, the minima of $V(q;\xi)$ occur at

$$q = \pm\sqrt{\frac{-6c_{(2)}}{c_{(4)}}} = \pm\sqrt{\frac{-6a}{b}}\,\xi^{1/2}, \tag{6.19}$$

thus, $q \propto \xi^{1/2}$ as $\xi \to 0^+$. For this system, q represents an order parameter, and thus the critical exponent β is 1/2.

We numerically confirm this claim by computing the scalar charge q of electrically charged BHs as a function of ξ near the critical point. Fixing the electric charge $\mathcal{E}$, we first determine the critical coupling $\alpha_{\rm crit}$ at which $c_{(2)}$ vanishes. We then compute q for couplings just below this value, i.e., for $\xi = (\alpha - \alpha_{\rm crit})/\alpha_{\rm crit} \gtrsim 0$. The dependence of q on ξ is depicted in Fig. 6.3; we find that $q \propto \xi^{1/2}$ agrees well with our numerical results.

Similarly, we compute the other standard critical exponents describing the

phase transition. In particular, both the analytic model (6.17) and our numerical solutions indicate that $\gamma = 1$ where $\chi = dq/d\phi_0 \propto |\xi|^{-\gamma}$ for $\xi \to 0^{\pm}$, and $\delta = 3$ where $q \propto \phi_0^{1/\delta}$ at $\xi = 0$. These findings are consistent with the Landau model for phase transitions. It would be interesting to find a correspondence to a correlation length in the future, so that all standard critical exponents can be studied. The introduction of a correlation length (becoming infinite as $c_{(2)} \to 0$) as another scale next to the size of the compact object could also allow for a more formalized power counting for the construction of the effective action close to the critical point.

6.4.3 Dynamical scalarization

We now employ our effective action to study the dynamical scalarization of binary systems in EMS theory, only considering the scalar coupling $f_1(\phi)$ except where noted. For this purpose, we integrate out the remaining IR fields from the complete action (i.e., the field part, suitable gauge-fixing parts, and a copy of $S_{\rm CO}^{\rm crit}$ for each body).[6] We employ a weak-field and slow-motion (i.e., post-Newtonian, PN) approximation. These approximations are not independent here, since a wide separation of the binary (weak field) implies slow motion due to the third Kepler law for bound binaries. The leading order in this approximation is just the Newtonian limit of the relativistic theory we are considering. Therefore, the Lagrangian of the

[6]Strictly speaking, the IR fields are split again into body-scale and radiation-scale parts, and we integrate out the body-scale fields [315]. This would be necessary for a treatment of radiation from the binary using effective-field-theory methods [347].

binary to leading order (LO) reads[7]

$$\begin{aligned} L^{\rm LO} = &-m_A\left[1-\frac{\dot{\boldsymbol{y}}_A^2}{2}\right]-m_B\left[1-\frac{\dot{\boldsymbol{y}}_B^2}{2}\right]+\frac{c_{\dot{q}^2,A}}{2}\dot{q}_A^2 \\ &+\frac{c_{\dot{q}^2,B}}{2}\dot{q}_B^2+\frac{m_A m_B}{r}+\frac{\mathcal{E}_A\mathcal{E}_B}{r}+\frac{q_A q_B}{r}, \end{aligned} \tag{6.20}$$

where A and B label the bodies, $r=|\boldsymbol{y}_A-\boldsymbol{y}_B|$ is their separation, and in this section the dot $\dot{}$ indicates a derivative with respect to coordinate time. We have suppressed the dependence of m_A on q_A for brevity, but recall that the "free energy" of each body takes the form

$$\begin{aligned} m_A(q_A) &= m_{(0),A}+V(q_A) \\ &= c_{(0),A}+\frac{c_{(2),A}}{2}q_A^2+\frac{c_{(4),A}}{4!}q_A^4. \end{aligned} \tag{6.21}$$

Notice that $m_A(q_A)$ plays the role of the body's mass in the binary Lagrangian because (i) it couples to gravity like a mass, see Eq. (6.7), and (ii) it is independent of the fields, so that for the purpose of integrating out the fields it can be treated as a constant. The Hamiltonian for the binary can be obtained via a Legendre transformation

$$\begin{aligned} H^{\rm LO} = &\, m_A+m_B+\frac{\boldsymbol{p}_A^2}{2m_A}+\frac{\boldsymbol{p}_B^2}{2m_B}+\frac{p_{q,A}^2}{2c_{\dot{q}^2,A}}+\frac{p_{q,B}^2}{2c_{\dot{q}^2,B}} \\ &-\frac{m_A m_B}{r}+\frac{\mathcal{E}_A\mathcal{E}_B}{r}-\frac{q_A q_B}{r}, \end{aligned} \tag{6.22}$$

with the pairs of canonical variables $(\boldsymbol{y}_{A/B},\boldsymbol{p}_{A/B})$ and $(q_{A/B},p_{q,A/B})$.

Following Ref. [4], let us now consider a special case that allows simple analytic solutions for the scalar charges of the bodies. We henceforth assume that the scalar charges evolve adiabatically $p_{q,A/B}\approx 0$ and that the two bodies are identical, i.e.,

[7] We have also gauge-fixed the worldline parameters to the coordinate time $\sigma=t$ as usual in the PN approximation.

$q \equiv q_A = q_B$, $c_{(2)} \equiv c_{(2),A} = c_{(2),B}$, etc. The Hamiltonian in the center-of-mass system $\boldsymbol{p} \equiv \boldsymbol{p}_A = -\boldsymbol{p}_B$ now reads

$$H^{\rm LO,adiab.} = 2m + \frac{\boldsymbol{p}^2}{m} - \frac{m^2}{r} + \frac{\mathcal{E}^2}{r} - \frac{q^2}{r}. \tag{6.23}$$

Under these assumptions and recalling again that $m = m(q)$, the equation of motion for the scalar charge q is given by

$$0 \approx \dot{p}_q = \frac{\partial H^{\rm LO,adiab.}}{\partial q} = 2z\left(c_{(2)}q + \frac{c_{(4)}}{6}q^3\right) - \frac{2q}{r}, \tag{6.24}$$

with the redshift

$$z \equiv 1 - \frac{\mathbf{p}^2}{2m^2} - \frac{m}{r}. \tag{6.25}$$

For simplicity, we neglect relativistic corrections to the redshift from here onward, i.e., $z \approx 1$; restoring these corrections does not affect the qualitative behavior that we describe. Equation (6.24) has three solutions: an unscalarized solution with $q = 0$ and a two scalarized solutions with nonzero q of opposite signs. The condition for stability of these solutions is that they are located at a minimum of the energy of the binary,

$$0 \leq \frac{\partial^2 H^{\rm LO,adiab.}}{\partial q^2} \approx 2c_{(2)} - \frac{2}{r} + c_{(4)}q^2, \tag{6.26}$$

which is violated for $q = 0$ when $1/r > c_{(2)}$. Hence, the stable solutions are given by

$$q = \begin{cases} 0 & \text{for} \quad 1/r \leq c_{(2)} \\ \pm\sqrt{\dfrac{6}{c_{(4)}}}\sqrt{\dfrac{1}{r} - c_{(2)}} & \text{for} \quad 1/r \geq c_{(2)} \end{cases}, \tag{6.27}$$

which contain a phase transition at $r = 1/c_{(2)}$ corresponding to the spontaneous breaking of the $q \to -q$ symmetry of the effective action. Recall that $c_{(2)} < 0$

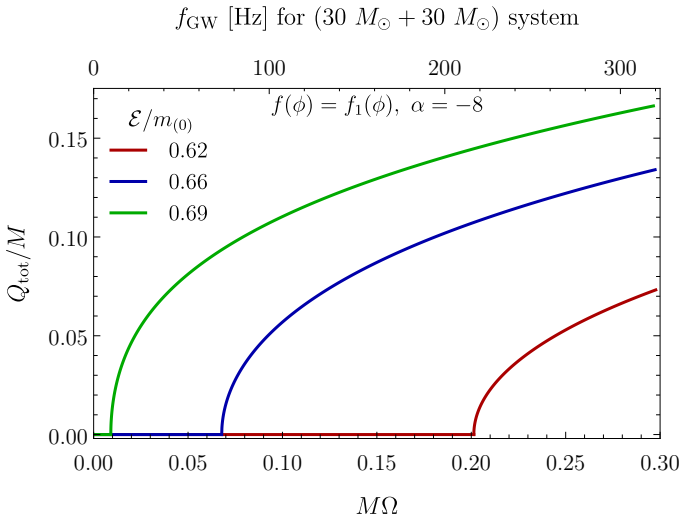

Figure 6.4: Scalar charge $Q_{\rm tot}$ of an equal mass binary as a function of orbital frequency Ω or GW frequency $f_{\rm GW} = \Omega/\pi$ for coupling $f_1(\phi)$ [Eq. (6.2)] with $\alpha = -8$.

corresponds to the case where each object is spontaneously scalarized, for which the bottom condition in Eq. (6.27) always holds, and thus $q \neq 0$ over all separations.

Restricting our attention to circular orbits, we plot in Fig. 6.4 the total scalar charge of the binary $Q_{\rm tot} \equiv q_A + q_B$ as a function of orbital frequency, given by Kepler's law as

$$\Omega^2 = \frac{1}{r^3}\left(m_A + m_B\right)\left(1 + \frac{q_A q_B}{m_A m_B} - \frac{\mathcal{E}_A \mathcal{E}_B}{m_A m_B}\right). \tag{6.28}$$

For simplicity, we only show the positive scalar charge branch of solutions. The frequency is shown both as the dimensionless combination $M\Omega$ with $M \equiv m_A^{(0)} + m_B^{(0)}$ and as the equivalent GW frequency $f_{\rm GW} = \Omega/\pi$ for a $(30M_\odot + 30M_\odot)$ binary system. The plotted curves correspond to solutions with coupling constant $\alpha = -8$, and the colors correspond to different values of the electric charge. The scalar charge vanishes below the onset of dynamical scalarization; the scalar charge grows abruptly

at some critical frequency $\Omega_{\rm scal}$ (as evidenced by kinks in the plotted curves) because dynamical scalarization is a second-order phase transition—see Ref. [4] for a more detailed argument that dynamical scalarization is a phase transition.

In Fig. 6.5, we depict the scalarization of binary systems for various charge-to-mass ratios and couplings α. The solid lines indicate the critical frequency $\Omega_{\rm scal}$ at which dynamical scalarization begins; the heavily shaded regions above these lines correspond to dynamically scalarized binaries after the onset of this transition. The critical point $c_{(2)} = 0$, corresponding to $\Omega_{\rm scal} \to 0$, represents the division between binaries that dynamically scalarize and those whose component BHs (individually) spontaneously scalarize; we depict all spontaneously scalarized configurations with a lighter shading. Thus, we see that our effective action, which was matched to isolated objects and models spontaneous scalarization, predicts dynamical scalarization as well. Refined predictions can be obtained by perturbatively calculating the binary Lagrangian to higher PN orders and also the emitted radiation; both are possible using effective-field-theory techniques [315, 347, 348] or more traditional methods where extended bodies are represented by point particles, e.g., Refs. [30, 210].

The same calculation can be repeated for binary systems with the choice $f(\phi) = f_2(\phi)$. As before, the unscalarized $q = 0$ solution is stable for above $r = 1/c_{(2)}$. However, because $c_{(4)} < 0$, no stable dynamically scalarized branch exists below that separation; instead, the system becomes "dynamically" unstable after this critical point. The phase diagram for this choice of coupling takes the same form as Fig. 6.5, but here the shaded regions correspond to scenarios in which no stable configuration exists. At the onset of instability, the scalar radiation will

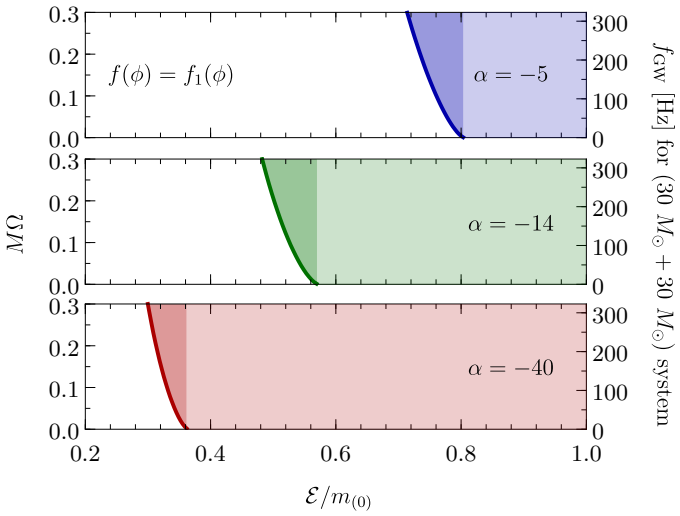

Figure 6.5: Scalarization of binary systems with various electric charges for scalar coupling $f_1(\phi)$ [Eq. (6.2)] with different coupling strengths α. Lightly and heavily shaded regions indicate spontaneously and dynamically scalarized configurations, respectively. The solid lines depict the onset of dynamical scalarization $\Omega_{\rm scal}$ as a function of electric charge.

likely grow rapidly and the GW frequency will decrease more rapidly compared to the EM case. However, long-term predictions are not possible with our effective theory since the assumption of time-reversal symmetry likely breaks down, as for the unstable isolated BHs.

6.5 Conclusions

In this work, we developed a simple energetic analysis of spontaneous and dynamical scalarization, based on a strong-field-agnostic effective-field-theory approach (extendable beyond the scalar-field case [324, 325, 327] in the future). We demonstrated our analysis for BHs with modified electrodynamics here, complementing the study of NS in ST gravity from Ref. [4]. The theory-agnostic nature

of our approach allowed us to draw general conclusions about scalarization As an example, we found that dynamical scalarization generically occurs in theories that admit spontaneous scalarization. Specific examples of theories for which our findings apply include those discussed in Refs. [154, 155, 161, 163–167, 324–327].

The recent discovery of spontaneous scalarization in ESTGB theories [163–167] has sparked significant interest in this topic. Our work predicts that dynamical scalarization can occur in binary systems in these theories and allows one to straightforwardly estimate the orbital frequency at which it occurs using only information derivable from isolated BH solutions. Such information is valuable for guiding numerical-relativity simulations in these theories, for which there has been recent progress [349]. Eventually higher PN orders in specific theories could be added to our model to derive more accurate predictions, and the framework could be extended to massive scalars or other types of new fields.

We demonstrated how scalarization, as an exemplary strong-gravity modification of GR, is parametrized by just a few constants in the effective action (which vanish in GR). Hence, our effective action provides an ideal foundation for a strong-field-agnostic framework for testing dynamical scalarization. Ultimately, one needs to incorporate self-consistently such effects into gravitational waveform models. This undertaking will require the computation of dissipative effects (analogous to the standard PN treatment in GR) and the mode dynamics during scalarization, characterized (in part) by $c_{\hat{q}^2}$. The effective action can also, in principle, be extended to include other strong-field effects influencing the inspiral of a binary, e.g., phenomena like floating orbits [350, 351] or induced hair growth [314, 352].

Independent of GW tests of GR, further study of dynamical scalarization could offer some insight into the nonlinear behavior of merging binary NSs in GR. As discussed in the Introduction, scalarization and tidal interactions enter models of the inspiral dynamics in a similar manner; in fact, the effective action treatment of dynamical tides (in GR) [299] is completely analogous to the approach adopted here for scalarization. Unlike the case with tides, our model of scalarization includes nonlinear interactions via the q^4 term. Nonlinear tidal effects could be relevant for GW observations of binary NSs [353, 354], but are difficult to handle in GR. Furthermore, mode instabilities also occur for NSs in GR [355, 356]. Dynamical scalarization can be used as a toy model for these types of effects, and further exploration of this non-GR phenomenon could improve gravitational waveform modeling in GR.

Our effective action approach allowed us to study the critical phenomena at the onset of scalarization; further study could also provide insight into critical phenomena in GR. The critical exponents we obtained numerically agree with the analytic predictions from Landau's mean-field treatment of ferromagnetism [318, 340]. Only missing here is a proper definition of correlation length, which we leave for future work. In GR, the BH limit of compact objects has been suggested to play the role of a critical point and lead to the quasiuniversal relations for NS properties [357, 358]. These quasiuniversal relations are invaluable for GW science because they reduce the number of independent parameters needed to describe binary NSs, improving the statistical uncertainty of measurements. In the BH limit (for nonrotating configurations), the leading tidal parameter vanishes [307, 359, 360], like $c_{(2)}$ at the critical point here. Better theoretical understanding of the origin of these universal

relations could help improve their accuracy; utilizing information from the critical phenomena at the BH limit is a compelling idea, and scalarization could serve as a toy model in that regard.

6.6 Acknowledgements

We thank Emanuele Berti, Caio Macedo, Néstor Ortiz, and Fethi Ramazanoğlu for useful discussions.

Chapter 7: Constraining nonperturbative strong-field effects in scalar-tensor gravity by combining pulsar timing and laser-interferometer gravitational-wave detectors

Authors: *Lijing Shao, Noah Sennett, Alessandra Buonanno, Michael Kramer, and Norbert Wex*[1]

Abstract: Pulsar timing and laser-interferometer gravitational-wave (GW) detectors are superb laboratories to study gravity theories in the strong-field regime. Here we combine those tools to test the mono-scalar-tensor theory of Damour and Esposito-Farèse (DEF), which predicts nonperturbative scalarization phenomena for neutron stars (NSs). First, applying Markov-chain Monte Carlo techniques, we use the absence of dipolar radiation in the pulsar-timing observations of five binary systems composed of a NS and a white dwarf, and eleven equations of state (EOSs) for NSs, to derive the most stringent constraints on the two free parameters of the DEF scalar-tensor theory. Since the binary-pulsar bounds depend on the NS mass and the EOS, we find that current pulsar-timing observations leave *scalarization windows*, i.e., regions of parameter space where scalarization can still be prominent. Then, we investigate if these scalarization windows could be closed and if pulsar-

[1]Originally published as Phys. Rev. **X7**, 041025 (2017).

timing constraints could be improved by laser-interferometer GW detectors, when spontaneous (or dynamical) scalarization sets in during the early (or late) stages of a binary NS (BNS) evolution. For the early inspiral of a BNS carrying constant scalar charge, we employ a Fisher matrix analysis to show that Advanced LIGO can improve pulsar-timing constraints for some EOSs, and next-generation detectors, such as the Cosmic Explorer and Einstein Telescope, will be able to improve those bounds for all eleven EOSs. Using the late inspiral of a BNS, we estimate that for some of the EOSs under consideration the onset of dynamical scalarization can happen early enough to improve the constraints on the DEF parameters obtained by combining the five binary pulsars. Thus, in the near future the complementarity of pulsar timing and direct observations of GWs on the ground will be extremely valuable in probing gravity theories in the strong-field regime.

7.1 Introduction

In general relativity (GR), gravity is mediated solely by a rank-2 tensor, namely the spacetime metric $g_{\mu\nu}$. Scalar-tensor theories of gravity, which add a scalar component to the gravitational interaction, are popular alternatives to GR. Though first proposed in 1921 [361], contemporary interest in these theories has been spurred by their potential connection to inflation and dark energy, as well as possible unified theories of quantum gravity [87]. A modern framework for the class of scalar-tensor theories we consider was developed in Refs. [97, 147, 178, 179, 300, 362] (see also more generic Horndeski scalar-tensor theories in Ref. [90]).

Ultimately, the existence (or absence) of scalar degrees of freedom in gravity will be decided by experiments. Most scalar-tensor theories are designed to be *metric theories of gravity*, that is, they respect the Einstein equivalence principle [79, 97]. Therefore, precision tests of the weak-equivalence principle, the local Lorentz invariance, and the local position invariance in flat spacetime are unable to constrain them [79, 89, 97, 305]. However, such theories generally violate the strong-equivalence principle. Tests of the strong-equivalence principle with self-gravitating bodies provide an ideal window to experimentally search for (or rule out) the scalar sector of gravity [79, 97, 363].

Particularly prominent violations of the strong-equivalence principle are known to arise in the class of massless mono-scalar-tensor theories, studied by Damour and Esposito-Farèse in the form of *nonperturbative strong-field effects* in neutron stars (NSs) [152, 153, 276]. In this work, we investigate the extent to which pulsar timing and ground-based gravitational-wave (GW) observations can constrain these phenomena (space-based GW experiments [266, 364, 365] are beyond the scope of this work). Our results demonstrate that, depending on the parameters of binary systems and NS equations of state (EOSs), these two types of experiments can provide complementary bounds on scalar-tensor theories [79, 89, 171, 187, 305]. These results are especially timely as new instruments come online in the upcoming years in both fields [366, 367].

The paper is organized as follows. In the next section, we briefly review two nonperturbative phenomena, notably spontaneous scalarization [152, 153] and dynamical scalarization [3, 169–172], that arise in certain scalar-tensor theories of

gravity. Then, in Sec. 7.3, we derive stringent constraints on these theories by combining state-of-the-art pulsar observations of five NS-white dwarf (WD) systems. In Sec. 7.4, we employ these constraints and investigate the potential detectability of nonperturbative effects in binary NS (BNS) systems using the Advanced Laser Interferometer Gravitational-wave Observatory (LIGO) [63] and next-generation ground-based detectors. Finally, in Sec. 7.5, we discuss the main results and implications of our finding, and give perspectives for future observations.

7.2 Nonperturbative strong-field phenomena in scalar-tensor gravity

In this work, we focus on the class of mono-scalar-tensor theories that are defined by the following action in the Einstein-frame [152, 153, 178, 362],

$$S = \frac{c^4}{16\pi G_*}\int \frac{\mathrm{d}^4x}{c}\sqrt{-g_*}\left[R_* - 2g_*^{\mu\nu}\partial_\mu\varphi\partial_\nu\varphi - V(\varphi)\right] + S_m\left[\psi_m; A^2(\varphi)g^*_{\mu\nu}\right], \quad (7.1)$$

where G_* is the bare gravitational coupling constant, $g^*_{\mu\nu}$ is the Einstein metric with its determinant g_*, $R_* \equiv g_*^{\mu\nu}R^*_{\mu\nu}$ is the Ricci scalar, ψ_m collectively denotes the matter content, and $A(\varphi)$ is the (conformal) coupling function that depends on the scalar field, φ. Henceforth, for simplicity, we assume that the potential, $V(\varphi)$, is a slowly varying function that changes on scales much larger than typical length scales of the system that we consider, thus, we set $V(\varphi) = 0$ in our calculation.

The field equations are derived with the least-action principle [97, 147] for $g^*_{\mu\nu}$

and φ,

$$R^*_{\mu\nu} = 2\partial_\mu\varphi\partial_\nu\varphi + \frac{8\pi G_*}{c^4}\left(T^*_{\mu\nu} - \frac{1}{2}T^* g^*_{\mu\nu}\right), \tag{7.2}$$

$$\Box_{g^*}\varphi = -\frac{4\pi G_*}{c^4}\alpha(\varphi)T_*, \tag{7.3}$$

with the energy-momentum tensor of matter fields, $T^{\mu\nu}_* \equiv 2c\,(-g_*)^{-1/2}\,\delta S_m/\delta g^*_{\mu\nu}$, and the field-dependent coupling strength between the scalar field and the trace of the energy-momentum tensor of matter fields, $\alpha(\varphi) \equiv \partial \ln A(\varphi)/\partial\varphi$.

Following Damour and Esposito-Farèse [147, 152], we consider a polynomial form for $\ln A(\varphi)$ up to quadratic order, that is $A(\varphi) = \exp(\beta_0\varphi^2/2)$, and denote $\alpha_0 \equiv \alpha(\varphi_0) = \beta_0\varphi_0$ with φ_0 the asymptotic value of φ at infinity. This particular scalar-tensor theory (henceforth, DEF theory) is completely characterized by two parameters (α_0, β_0) and for systems dominated by strong-field gravity, such as NSs, can give rise to potentially observable, nonperturbative physical phenomena [153, 169]. Weak-field Solar-system experiments, generally, only probe the α_0-dimension or the combination $\beta_0\alpha_0^2$ in the (α_0, β_0) parameter space (see Refs. [79, 368] and references therein). In GR, $\alpha_0 = \beta_0 = 0$.

Using a perfect-fluid description of the energy-momentum tensor for NSs in the Jordan frame, in 1993 Damour and Esposito-Farèse derived the Tolman-Oppenheimer-Volkoff (TOV) equations [153] for a NS in their scalar-tensor gravity theory. Interestingly, they discovered a *phase-transition* phenomenon when $\beta_0 \lesssim -4$, largely irrespective of the α_0 value (a nonzero α_0 tends to smooth the phase transition [152]). The phenomenon was named *spontaneous scalarization*. With a suitable (α_0, β_0), the "effective scalar coupling" that a NS develops, $\alpha_A \equiv \partial \ln m_A/\partial\varphi_0$ (the baryonic

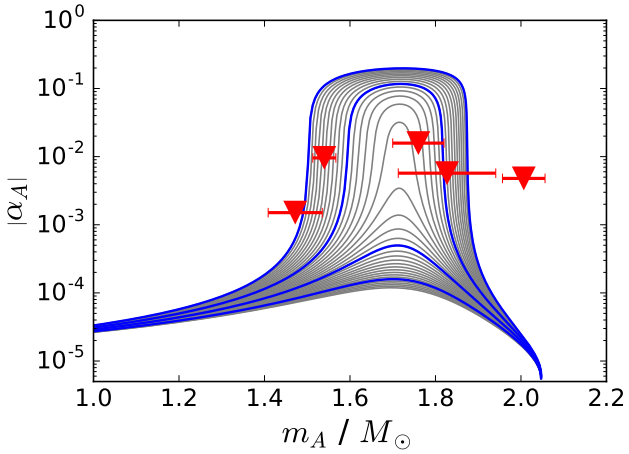

Figure 7.1: Illustration of spontaneous scalarization in the DEF gravity, in comparison to *individual* binary-pulsar limits, for a NS with EOS SLy4 and $|\alpha_0| = 10^{-5}$. The blue curves correspond to (from top to bottom) $\beta_0 = -4.5, -4.4, -4.3$, and -4.2; the grey curves in between differ in β_0 in steps of 0.01. We indicate with triangles the 90% CL upper limits on the effective scalar coupling $|\alpha_A|$ from the individual pulsars listed in Table 7.1. We can clearly see a scalarization window at $m_A \sim 1.7\, M_\odot$.

mass of NS is fixed while taking the derivative), could be $\mathcal{O}(1)$ when the NS mass, m_A, is within a certain EOS-dependent range [2]. For masses below and above this range, the effective scalar coupling is much smaller [3]. In Fig. 7.1 we show an example of spontaneous scalarization for a NS with the realistic EOS SLy4, and compare it to existing *individual* binary-pulsar constraints.

In general, if two compact bodies in a binary have effective scalar couplings, α_A and α_B, they produce gravitational dipolar radiation $\propto (\Delta\alpha)^2$, with $\Delta\alpha \equiv \alpha_A - \alpha_B$,

[2]For black holes, the effective scalar coupling equals to zero. Therefore, the tests performed with binary black holes [122] do not directly apply to the DEF theory.

[3]For sufficiently negative β_0 ($\lesssim -4.6$), NSs do not de-scalarize before reaching their maximum mass, i.e. spontaneous scalarization is found for all NSs above a certain critical mass, which depends on the actual value of β_0 and the EOS [152, 153].

which is at a lower post-Newtonian (PN) order than the canonical quadrupolar radiation in GR [152] [4]. In Ref. [276], Damour and Esposito-Farèse for the first time compared limits on the DEF gravity arising from Solar system and binary pulsar experiments with expected limits from ground-based GW detectors like LIGO and Virgo. The analysis in Ref. [276] is based on soft (by now excluded [248, 369]), medium and stiff EOSs, and for the LIGO/Virgo experiment it assumes a BNS merger with PSR B1913+16 like masses ($1.44\,M_\odot$ and $1.39\,M_\odot$), as well as a $1.4\,M_\odot$-$10\,M_\odot$ NS-BH merger. Damour and Esposito-Farèse come to the conclusion that binary-pulsar experiments would generally be expected to put more stringent constraints on the parameters (α_0, β_0) than ground-based detectors, such as LIGO and Virgo. Since then, several analyses have followed [247–249, 370, 371], but typically those studies did not probe a large set of NS masses and EOSs. Considering advances in our knowledge of NSs and more sensitive current and future ground-based detectors, we revisit this study here. Quite interestingly, as pointed out in a first study in Ref. [171], the constraints on the parameters (α_0, β_0) from binary pulsars depend quite crucially on the EOSs and the masses of the NSs, in particular in the parameter space that allows for spontaneous scalarization. By taking into account this dependence when setting bounds from pulsar timing, we shall find that current

[4] In this work, generally we denote with nPN the $\mathcal{O}(v^{2n}/c^{2n})$ corrections to the leading Newtonian dynamics (equations of motion). Therefore, the gravitational dipolar radiation reaction is at 1.5 PN, and the quadrupolar radiation is at 2.5 PN. In the GW phasing, when there is no potential confusion we sometimes refer to the quadrupolar (dipolar) radiation as 0 PN (-1 PN), as typically done in the literature.

and future GW detectors on the Earth might still be able to exclude certain specific regions of the parameter space (α_0, β_0) that are not probed by binary pulsars yet.

Twenty years after the discovery of spontaneous scalarization, Barausse *et al.* [169] found another interesting nonperturbative phenomenon in a certain parameter space of the DEF theory. This time the scalarization does not take place for a NS in isolation, but for NSs in a merging binary. Indeed, modeling the BNS evolution in numerical relativity, Barausse *et al.* found that the two NSs can scalarize even if initially, at large separation, they are not scalarized. This phenomenon is called *dynamical scalarization*, and its onset is determined by the binary compactness instead of the NS compactness. Reference [169] also demonstrated that a spontaneously scalarized NS can generate scalar hair on its initially unscalarized NS companion in a binary system through a process known as *induced scalarization*. Dynamical and induced scalarization cause BNSs to merge earlier [169, 171, 172] than in GR, resulting in a significant modification to the GW phasing that is potentially detectable by ground-based GW interferometers [3, 169, 170, 175].

Finally, it is important to note that cosmological solutions in the strictly massless limit of the DEF theory are known to evolve away from GR when β_0 is negative [175, 272, 273, 302]; to be consistent with current Solar-system observations, such cosmologies require significant fine tuning of initial conditions.[5] Various modifications to the theory have been considered to cure this fine-tuning problem, for example, by adding higher order polynomial terms to $\ln A(\varphi)$ [302] or including a

[5]For cosmologies in the scalar-tensor theories with a positive β_0, we refer readers to Refs. [272, 273, 372].

mass term $V(\varphi) = 2m_\varphi\varphi^2$ in the action [95, 152, 161, 303]. To date, none of these proposals have produced scalar-tensor theories that: (i) satisfy cosmological and weak-field gravity constraints, (ii) generate an asymptotic field φ_0 that is stable over timescales relevant to binary pulsars and GW sources, and (iii) give rise to the nonperturbative phenomena present in DEF theory. As is commonly done in the literature [3, 147, 152, 153, 169–172, 175], we will ignore these cosmological concerns in this work and focus only on (massless) DEF theory.

7.3 Constraints from binary pulsars

Until now, binary pulsars have provided the most stringent limits to the DEF theory [152, 247–249, 375]. These limits were usually obtained with individual pulsar systems and with representative EOSs [249] [6]. Here, by contrast, we combine observational results from multiple pulsar systems employing Markov-chain Monte Carlo (MCMC) simulations [380]. In particular, we pick the five NS-WD binaries that are the most constraining systems in testing spontaneous scalarization: PSRs J0348+0432 [248], J1012+5307 [373], J1738+0333 [247], J1909−3744 [374], and J2222−0137 [375]. We choose these five binaries basing on the binary nature (namely, NS-WD binaries), the timing precision that has been achieved, and the NS masses. These aspects are important to the study here, and see Refs. [89, 294, 305] for more discussion. For convenience, we list the parameters of these binaries in Table 7.1, and notice that it is the combination of their $\dot{P}_b^{\rm int}$ and the NS mass that

[6] An exception is Ref. [294], where, for individual binary pulsars, the most conservative limits in the (α_0, β_0) parameter space across different EOSs are presented.

Table 7.1: Binary parameters of the five NS-WD systems that we use to constrain the DEF theory [247, 248, 373–375]. The observed time derivatives of the orbit period P_b are corrected using the latest Galactic potential of Ref. [376]. For PSRs J0348+0432, J1012+5307 and J1738+0333, the mass ratios were obtained combining radio timing and optical high-resolution spectroscopy, while the companion masses are determined from the Balmer lines of the WD spectra based on WD models [248, 377–379]. For PSRs J1909−3744 and J2222−0137, the masses were calculated from the Shapiro delay, where the range of the Shapiro delay gives directly the companion mass, and the pulsar mass is then being derived from the mass function, using the shape of the observed Shapiro delay to determine the orbital inclination [374, 375]. The masses below are based on GR as the underlying gravity theory. However, since the companion WD is a weakly self-gravitating body, they are practically the same in the DEF theory (with a difference $\lesssim 10^{-4}$). We give in parentheses the standard 1-σ errors in units of the least significant digit(s).

Pulsar	J0348+0432 [248]	J1012+5307 [373]	J1738+0333 [247]
Orbital period, P_b (d)	0.102424062722(7)	0.60467271355(3)	0.3547907398724(13)
Eccentricity, e	$2.6(9) \times 10^{-6}$	$1.2(3) \times 10^{-6}$	$3.4(11) \times 10^{-7}$
Observed $\dot{P}_b$, $\dot{P}_b^{\rm obs}$ (fs s^{-1})	−273(45)	−50(14)	−17.0(31)
Intrinsic $\dot{P}_b$, $\dot{P}_b^{\rm int}$ (fs s^{-1})	−274(45)	−5(9)	−27.72(64)
Mass ratio, $q \equiv m_p/m_c$	11.70(13)	10.5(5)	8.1(2)
Pulsar mass, $m_p^{\rm obs}$ ($M_\odot$)	...	...	...
WD mass, $m_c^{\rm obs}$ ($M_\odot$)	$0.1715^{+0.0045}_{-0.0030}$	0.174(7)	$0.1817^{+0.0073}_{-0.0054}$

Pulsar	J1909−3744 [374]	J2222−0137 [375]
Orbital period, P_b (d)	1.533449474406(13)	2.44576454(18)
Eccentricity, e	$1.14(10) \times 10^{-7}$	0.00038096(4)
Observed $\dot{P}_b$, $\dot{P}_b^{\rm obs}$ (fs s^{-1})	−503(6)	200(90)
Intrinsic $\dot{P}_b$, $\dot{P}_b^{\rm int}$ (fs s^{-1})	−6(15)	−60(90)
Mass ratio, $q \equiv m_p/m_c$	...	...
Pulsar mass, $m_p^{\rm obs}$ ($M_\odot$)	1.540(27)	1.76(6)
WD mass, $m_c^{\rm obs}$ ($M_\odot$)	0.2130(24)	1.293(25)

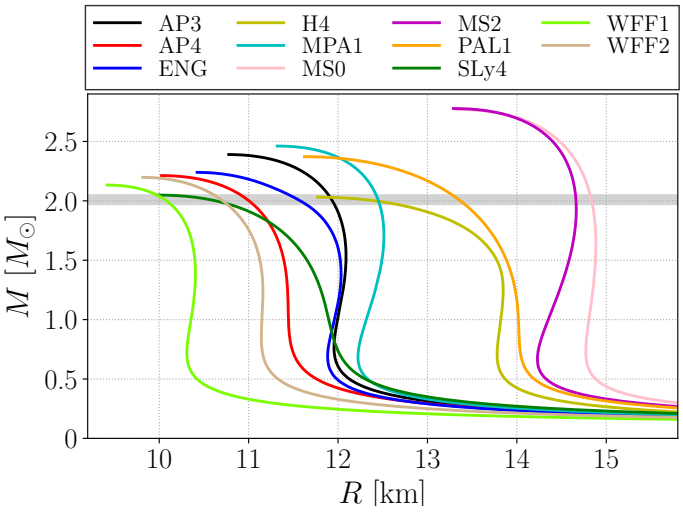

Figure 7.2: The mass-radius relation of NSs (in GR) for the 11 EOSs that are adopted in the study. The mass constraint (with 1-σ uncertainty) from PSR J0348+0432 [248] is depicted in grey. The color coding for different EOSs is kept consistent for all figures in this work.

makes them particularly suitable for the test of spontaneous scalarization. We obtain the limits using 11 different EOSs that have the maximum NS mass above $2\,M_\odot$ [381]. The names of these EOSs are AP3, AP4, ENG, H4, MPA1, MS0, MS2, PAL1, SLy4, WFF1, and WFF2 (see Refs. [381, 382] for reviews). Figure 7.2 shows the mass-radius relation of NSs in GR for these EOSs. As evidenced by the spread of the curves in the figure, we believe that these EOSs are sufficient to cover the different EOS-dependent properties of spontaneous scalarization, and at the same time satisfy the two-solar-mass limit from pulsar-timing observations [248, 369].

Markov-chain Monte Carlo techniques allow us to preform parameter estimation within the Bayesian framework. These methods provide the posterior distributions of the underlying parameters that are consistent with observations. In Bayesian analysis, given data $\mathcal{D}$ and a hypothesis $\mathcal{H}$ (here, the DEF theory), the

marginalized posterior distribution of (α_0, β_0) is given by [380],

$$P\left(\alpha_0, \beta_0 | \mathcal{D}, \mathcal{H}, \mathcal{I}\right) = \int \frac{P\left(\mathcal{D} | \alpha_0, \beta_0, \boldsymbol{\Xi}, \mathcal{H}, \mathcal{I}\right) P\left(\alpha_0, \beta_0, \boldsymbol{\Xi} | \mathcal{H}, \mathcal{I}\right)}{P\left(\mathcal{D} | \mathcal{H}, \mathcal{I}\right)} \mathrm{d}\boldsymbol{\Xi}\,, \tag{7.4}$$

where $\mathcal{I}$ is all other relevant prior background knowledge and $\boldsymbol{\Xi}$ collectively denotes all other unknown parameters besides (α_0, β_0), which are marginalized over to obtain the marginalized posterior distributions for just (α_0, β_0) [see below for more details]. In the above equation, given $\mathcal{H}$ and $\mathcal{I}$, $P\left(\alpha_0, \beta_0, \boldsymbol{\Xi} | \mathcal{H}, \mathcal{I}\right)$ is the prior on $(\alpha_0, \beta_0, \boldsymbol{\Xi})$, $P\left(\mathcal{D} | \alpha_0, \beta_0, \boldsymbol{\Xi}, \mathcal{H}, \mathcal{I}\right) \equiv \mathcal{L}$ is the likelihood, and $P\left(\mathcal{D} | \mathcal{H}, \mathcal{I}\right)$ is the model evidence. As said, we use MCMC techniques to explore the posterior in Eq. (7.4). We discuss below our choices for the priors and the likelihood function [see Eq. (7.9)]. We assume that observations with different binary pulsars are independent.

We now explain how we employ the MCMC technique to get the posterior by combining binary pulsar systems. Let us assume that N pulsars ($N = 1, 2, 5$, see below) are used to constrain the (α_0, β_0) parameter space. To obtain a complete description of the gravitational dipolar radiation of these systems in the DEF theory, we need $N + 2$ free parameters in the MCMC runs, which are $\boldsymbol{\theta} = \left\{\alpha_0, \beta_0, \tilde{\rho}_c^{(i)}\right\}$, where $\tilde{\rho}_c^{(i)}$ $(i = 1, \cdots, N)$ is the Jordan-frame central matter density of pulsar i [7]. As an initial value to the TOV solver, we also need the value of the scalar field in the center of a NS, $\varphi_c^{(i)}$, but the latter is fixed iteratively by requiring that all pulsars have a common asymptotic value of φ, $\varphi_0 \equiv \alpha_0/\beta_0$. Given $\tilde{\rho}_c^{(i)}$ and $\varphi_c^{(i)}$ for pulsar

[7] Actually, in the full calculation we need some other quantities, as well, for example, the orbital period, P_b, and the orbital eccentricity, e. Those quantities are observationally very well determined (see Table 7.1), thus we use their central values and find that our constraints on (α_0, β_0) do not change on a relevant scale when we take into account the errors on those quantities.

i, we integrate the modified TOV equations (see Eq. (7) in Ref. [153] or Eq. (3.6) in Ref. [152]) with initial conditions given by Eq. (3.14) in Ref. [152]. During the integration, we use tabulated data of EOSs, and linearly interpolate them in the logarithmic space of the matter density, $\tilde{\rho}$, the pressure, $\tilde{p}$, and the number density, $\tilde{n}$ [381]. Note that only one quantity among $\{\tilde{\rho}, \tilde{p}, \tilde{n}\}$ is free, while the others are determined by the EOS. The end products of the integration provide us, for each pulsar, the gravitational mass, $m_A^{(i)}$, the baryonic mass, $\bar{m}_A^{(i)}$, the NS radius, $R^{(i)}$, and the effective scalar coupling, $\alpha_A^{(i)}$ [152].

For the MCMC runs we use a uniform prior on $\log_{10}|\alpha_0|$ for $|\alpha_0| \in [5 \times 10^{-6}, 3.4 \times 10^{-3}]$, where 3.4×10^{-3} is the limit obtained from the Cassini spacecraft [180, 368]. We pick the parameter β_0 uniformly in the range $[-5, -4]$, which corresponds to a sufficiently large parameter space where the scalarization phenomena can take place [153, 169]. During the exploration of the parameter space, we restrict the values of (α_0, β_0) to this rectangle region, as well, in order to avoid overusing computational time in uninteresting regions. The initial central matter densities, $\left\{\tilde{\rho}_c^{(i)}\right\}$, are picked around their GR values, but they are allowed to explore a very large range in the simulations. As we discuss below, we perform convergence tests and verify that when evolving the chains all parameters in $\boldsymbol{\theta}$ quickly lose memory of their initial values.

During the MCMC runs, we evolve the $N + 2$ free parameters according to an affine-invariant ensemble sampler, which was implemented in the emcee package [383, 384] [8]. At every step, we solve the N sets of modified TOV equations on

[8] http://dan.iel.fm/emcee

the fly, using for the companion masses of the binary pulsars the values listed in Table 7.1 [9].

Then, for the decay of the binary's orbital period, which enters the likelihood function [see Eq. (7.9)], we use the dipolar contribution from the scalar field and the quadrupolar contribution from the tensor field as given by the following, well known, formulae [147, 385],

$$\dot{P}_b^{\rm dipole} = -\frac{2\pi G_*}{c^3} g(e) \left(\frac{2\pi}{P_b}\right) \frac{m_p m_c}{m_p + m_c} \left(\alpha_A - \alpha_0\right)^2 , \tag{7.5}$$

$$\dot{P}_b^{\rm quad} = -\frac{192\pi G_*^{5/3}}{5c^5} f(e) \left(\frac{2\pi}{P_b}\right)^{5/3} \frac{m_p m_c}{\left(m_p + m_c\right)^{1/3}} , \tag{7.6}$$

with

$$g(e) \equiv \left(1 + \frac{e^2}{2}\right) \left(1 - e^2\right)^{-5/2} , \tag{7.7}$$

$$f(e) \equiv \left(1 + \frac{73}{24} e^2 + \frac{37}{96} e^4\right) \left(1 - e^2\right)^{-7/2} . \tag{7.8}$$

We find that higher order terms, as well as the subdominant scalar quadrupolar radiation, give negligible contributions to this study. Notice that in Eq. (7.5), we have replaced the effective scalar coupling of the WD companion with the linear

[9] The masses in PSRs J0348+0432, J1012+5307, and J1738+0333 are based on a combination of radio timing of the pulsars and optical spectroscopic observation of the WDs. The derivation of the masses only depends on the well-understood WD atmosphere model in combination with gravity at Newtonian order, and the mass ratio q, which is free of any explicit strong-field effects [368]. Therefore, even within the DEF theory, these masses are valid [247, 248]. For PSRs J1909−3744 and J2222−0137, the masses are derived from the range and shape of the Shapiro delay [152, 249]. Since for the weakly self-gravitating WD companion $|\alpha_B| \approx |\alpha_0| \ll 1$, these masses are practically identical to the GR masses in Table 7.1.

matter-scalar coupling constant, since for a weakly self-gravitating WD $\alpha_A \simeq \alpha_0$ in the β_0 range of interest.[10] Furthermore, we can approximate the bare gravitational constant G_* in the above equations with the Newtonian gravitational constant $G_N = G_*(1+\alpha_0^2)$, since $|\alpha_0| \ll 1$ (*e.g.*, from the Cassini spacecraft [180, 368]).

We construct the logarithmic likelihood for the MCMC runs as,

$$\ln \mathcal{L} \propto -\frac{1}{2}\sum_{i=1}^{N}\left[\left(\frac{\dot{P}_b^{\rm int}-\dot{P}_b^{\rm th}}{\sigma_{\dot{P}_b}^{\rm obs}}\right)^2+\left(\frac{m_p/m_c-q}{\sigma_q^{\rm obs}}\right)^2\right], \tag{7.9}$$

where for PSRs J1909−3744 and J2222−0137 we replace the second term in the squared brackets with $\left[\left(m_p-m_p^{\rm obs}\right)/\sigma_{m_p}^{\rm obs}\right]^2$. In Eq. (7.9), the predicted orbital decay from the theory is $\dot{P}_b^{\rm th} \equiv \dot{P}_b^{\rm dipole}+\dot{P}_b^{\rm quad}$, and $\sigma_X^{\rm obs}$ is the observational uncertainty for $X \in \left\{\dot{P}_b^{\rm int}, q, m_p\right\}$, as given in Table 7.1. Note that $\dot{P}_b^{\rm th}$ and m_p implicitly depend on $(\alpha_0, \beta_0, \boldsymbol{\Xi})$, through direct integration of TOV equations in the DEF theory.

For each EOS, we perform four separate MCMC runs:

(i) 1 pulsar: PSR J0348+0432 (J0348);

(ii) 1 pulsar: PSR J1738+0333 (J1738);

(iii) combining 2 pulsars: PSRs J0348+0432 and J1738+0333 (2PSRs);

(iv) combining 5 pulsars: PSRs J0348+0432, J1012+5307, J1738+0333, J1909−3744 and J2222−0137 (5PSRs).

We pick J0348 and J1738 due to their mass difference (2.01 $M_\odot$ and 1.46 $M_\odot$ respectively), and their high timing precision (see Table 7.1), which leads to interesting differences in the constraints on the DEF parameters, especially on β_0. For each run,

[10] In this context, see footnote "d" in Ref. [370], concerning WDs and very large (positive) β_0.

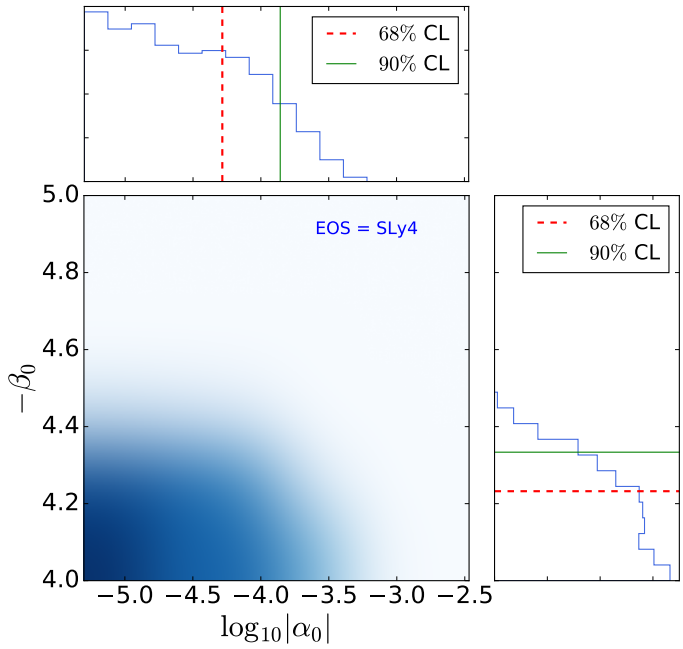

Figure 7.3: The marginalized 2-d distribution of $(\log_{10}|\alpha_0|, -\beta_0)$ from MCMC runs on the five pulsars listed in Table 7.1, for the EOS SLy4. The marginalized 1-d distributions and the extraction of upper limits are illustrated in upper and right panels.

we accumulate sufficient MCMC samples to guarantee the convergence of MCMC runs. By using the Gelman-Rubin statistic [386], we find that, for each EOS, 200,000 samples for cases J0348 and J1738, and 400,000 samples for cases 2PSRs and 5PSRs, are enough, respectively. We discard the first half chain points of these 44 runs (4 cases $\times$ 11 EOSs) as the BURN-IN phase [384, 387], while we use the remaining samples to do inference on the parameters (α_0, β_0).

As an example, we show in Fig. 7.3 the marginalized 2-d distribution in the parameter space of $(\log_{10}|\alpha_0|, -\beta_0)$ for the case 5PSRs and the EOS SLy4. As mentioned above, we distribute the initial values of $\log_{10}|\alpha_0|$ and $-\beta_0$ uniformly in the rectangle region of Fig. 7.3. We see that after MCMC simulations, the region

Table 7.2: Limits on the parameters of the massless mono-scalar-tensor DEF theory for different EOSs when applying the MCMC analysis to the five pulsars J0348+0432, J1012+5307, J1738+0333, J1909−3744, and J2222−0137. Results at 68% and 90% CLs are listed. $|\alpha_A|^{\max}$ is the maximum effective scalar coupling that a NS could still possess without violating the limits, and $m_A^{\max}$ is the corresponding (gravitational) mass at this maximum effective scalar coupling (see Figure 7.5).

68% confidence level				
EOS	$\lvert\alpha_0\rvert$	$-\beta_0$	$m_A^{\max}/M_\odot$	$\lvert\alpha_A\rvert^{\max}$
AP3	6.5×10^{-5}	4.21	1.83	1.1×10^{-3}
AP4	5.5×10^{-5}	4.24	1.71	1.2×10^{-3}
ENG	6.0×10^{-5}	4.21	1.80	1.0×10^{-3}
H4	5.7×10^{-5}	4.24	1.91	1.3×10^{-3}
MPA1	5.7×10^{-5}	4.22	1.92	1.1×10^{-3}
MS0	7.7×10^{-5}	4.28	2.26	2.7×10^{-3}
MS2	7.9×10^{-5}	4.26	2.24	2.1×10^{-3}
PAL1	7.3×10^{-5}	4.21	1.99	1.2×10^{-3}
SLy4	5.2×10^{-5}	4.23	1.71	1.1×10^{-3}
WFF1	5.3×10^{-5}	4.21	1.58	9.1×10^{-4}
WFF2	5.5×10^{-5}	4.24	1.68	1.2×10^{-3}
90% confidence level				
EOS	$\lvert\alpha_0\rvert$	$-\beta_0$	$m_A^{\max}/M_\odot$	$\lvert\alpha_A\rvert^{\max}$
AP3	1.5×10^{-4}	4.29	1.85	6.9×10^{-3}
AP4	1.4×10^{-4}	4.31	1.73	1.0×10^{-2}
ENG	1.6×10^{-4}	4.30	1.81	8.2×10^{-3}
H4	1.7×10^{-4}	4.33	1.92	2.8×10^{-2}
MPA1	1.6×10^{-4}	4.30	1.93	8.4×10^{-3}
MS0	2.0×10^{-4}	4.38	2.26	1.0×10^{-1}
MS2	2.4×10^{-4}	4.36	2.26	8.0×10^{-2}
PAL1	2.0×10^{-4}	4.29	2.00	8.2×10^{-3}
SLy4	1.4×10^{-4}	4.33	1.72	2.2×10^{-2}
WFF1	1.3×10^{-4}	4.30	1.60	6.9×10^{-3}
WFF2	1.4×10^{-4}	4.32	1.70	1.4×10^{-2}

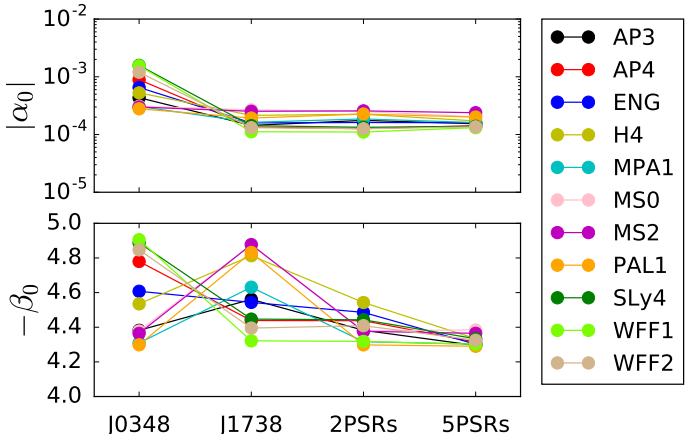

Figure 7.4: Marginalized upper limits on $|\alpha_0|$ (*upper*) and $-\beta_0$ (*lower*) at 90% CL. These limits are obtained from PSRs J0348+0432 (J0348), J1738+0333 (J1738), a combination of them (2PSRs), and a combination of PSRs J0348+0432, J1012+5307, J1738+0333, J1909−3744 and J2222−0137 (5PSRs).

with large $|\alpha_0|$ or large (negative) β_0 is no longer populated, and only a small corner is consistent with the observational results of the five NS-WD binary pulsars.

Furthermore, we extract the upper limits of $\log_{10}|\alpha_0|$ and $-\beta_0$ from their marginalized 1-d distributions at 68% and 90% CLs. We summarize the upper limits at 90% CL from all 44 runs in Fig. 7.4. It is interesting to observe the following facts. First, for all EOSs, J1738 gives a more constraining limit on α_0 than J0348. This result might be due to the fact that the $\sigma_{\dot{P}_b}^{\rm obs}$ of J1738 is about two orders of magnitude smaller than that of J0348, thus giving a tighter limit on α_0^2 by roughly the same order of magnitude. Second, the constraints on β_0 from J0348 and J1738 are extremely EOS-dependent. This should be a consequence of the masses of the NSs, which are (in GR) $1.46\,M_\odot$ for J1738, and $2.01\,M_\odot$ for J0348. For EOSs that favour spontaneous scalarization at around 1.4–1.5 $M_\odot$, J1738 gives a better limit,

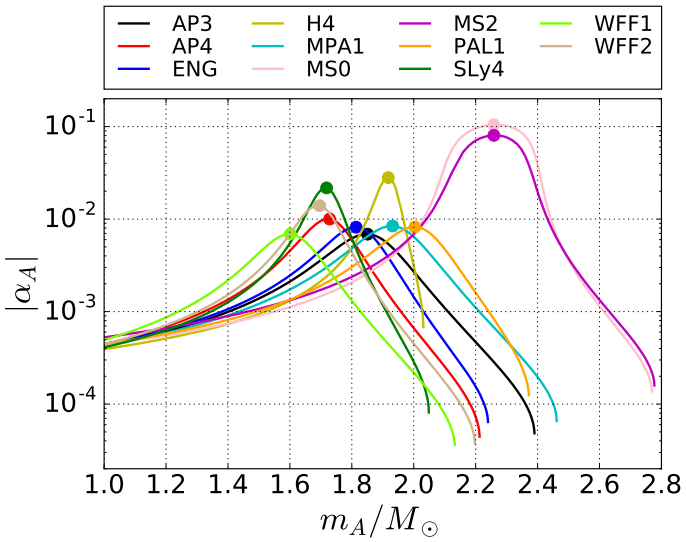

Figure 7.5: The effective scalar coupling $|\alpha_A|$ that an isolated NS could still develop after taking into account the 95% CL constraints from the five pulsars (see Table 7.2). The point of the maximum $|\alpha_A|$ is marked with a dot, and the values (and the corresponding masses) are listed in Table 7.2.

while for EOSs that favour spontaneous scalarization at around $2\,M_\odot$, J0348 gives a better limit. This trend is also consistent with Fig. 7.5 (to be introduced below). Third, by combining two pulsars (2PSRs), NSs are limited to scalarize at neither 1.4–1.5 $M_\odot$ nor $\sim 2\,M_\odot$. Therefore, almost for all EOSs, β_0 is well constrained. This result demonstrates the power of properly using multiple pulsars with different NS masses to constrain the DEF parameter space for *any* EOS. Fourth, we obtain the most stringent constraints with five pulsars (5PSRs). This is especially true for β_0, which is constrained at the level of ~ -4.2 (68% CL) and ~ -4.3 (90% CL) for all EOSs. Finally, we list in Table 7.2 the marginalized 1-d limits for 5PSRs. We shall use them in the next section when combining binary pulsars with laser-interferometer GW observations.

Considering the results that we have obtained when combining the five pulsars (5PSRs), one could wonder whether isolated NSs can still be strongly scalarized. To address this question, we use the limits on (α_0, β_0) and calculate the effective scalar coupling that a NS can still develop as a function of the NS mass, for the 11 EOSs used in this work. The results at 90% CL are summarized in Fig. 7.5, while in Table 7.2 we list the maximally allowed effective scalar couplings at 68% and 90% CLs, and their corresponding (gravitational) NS masses (marked as dots in Fig. 7.5).

Figure 7.5 clearly shows the *nonperturbative* nature of the scalarization phenomenon. The (absolute values of the) maximally allowed effective scalar coupling for NSs can be as large as $\mathcal{O}(10^{-2})$ and even 0.1 if the limits at 90% CL are used, while those values are $\lesssim 10^{-3}$ if one uses the limits at 68% CL (not shown in Fig. 7.5, but listed in Table 7.2). Furthermore, quite remarkably Fig. 7.5 shows that there are *scalarization windows* (this feature could also be seen in Fig. 7.1 for the EOS SLy4). What we mean is the following. The NS masses for the five most constraining pulsars are $1.46\,M_\odot$ (PSR J1738+0333) $1.54\,M_\odot$ (PSR J1909−3744), $1.76\,M_\odot$ (PSR J2222−0137), $1.83\,M_\odot$ (PSR 1012+5307), and $2.01\,M_\odot$ (PSR J0348+0432). For these specific masses, using the 11 EOSs that can give rise to spontaneous scalarization, we have constrained stringently the DEF parameters. However, some EOSs can still allow NS to scalarize strongly (*i.e.*, acquire large effective scalar couplings) for other values of the masses. As Fig. 7.5 shows, using limits at 90% CL, NSs with EOSs AP4, SLy4, and WFF2 can still have $|\alpha_A| \gtrsim \mathcal{O}(10^{-2})$ if the NS masses are in the range $m_A = 1.70$–$1.73\,M_\odot$, and NSs with EOS H4 can still be scalarized to $|\alpha_A| \sim 0.03$ with $m_A \simeq 1.92\,M_\odot$, and NSs with EOSs MS0 and MS2 can still be

strongly scalarized to $|\alpha_A| \simeq 0.1$ with $m_A \simeq 2.26\,M_\odot$. Those scalarization windows could be closed in the future if binary pulsars with these masses are discovered and their gravitational dipolar radiation is constrained by pulsar timing. As we shall discuss in Sec. 7.4, the presence of scalarization windows also opens the interesting possibility to close these gaps with future GW observations from BNSs, if the NS's masses lie in the scalarization window.

7.4 Projected sensitivities for laser-interferometer gravitational-wave detectors

Having determined constraints on the DEF's parameter space from binary pulsars (see Table 7.2) and found scalarization windows, we now address the question of whether present and future laser-interferometer GW observations on the ground can still improve these limits and close the gaps. Two scenarios are considered: (i) asymmetric BNS systems, equipped with separation-independent effective scalar couplings, whose gravitational dipolar radiation during the inspiral can modify the GW phasing [240, 276], and (ii) BNS systems that dynamically develop scalarization during the late stage of the inspiral, leading to significant, nonperturbative changes in the GW signal [3, 169, 171, 172]. A complete description of BNSs in the DEF theory should include both effects. However, complete waveform models from the theory are still not available, so here we investigate the two scenarios separately to obtain some conservative understanding of the whole picture.

7.4.1 Dipole radiation for binary neutron-star inspirals

The presence of a scalar field can significantly modify the inspiral of an asymmetric BNS system, due to the additional energy radiated off by the scalar degree of freedom. The most prominent effect is a modification of the phase evolution in GW signals. For two NSs with effective scalar couplings α_A and α_B respectively, one finds for the evolution of the orbital frequency, Ω, up to 2.5 PN order [2, 28, 240],

$$\frac{\dot{\Omega}}{\Omega^2} = \frac{\eta}{1+\alpha_A\alpha_B}\left[(\Delta\alpha)^2\mathcal{V}^3 + \frac{96}{5}\kappa\mathcal{V}^5 + \mathcal{O}(\mathcal{V}^6)\right], \tag{7.10}$$

where $\Delta\alpha \equiv \alpha_A - \alpha_B$, $\eta \equiv m_A m_B/M^2$, and the (dimensionless) "characteristic" velocity,

$$\mathcal{V} \equiv \left[G_*\left(1+\alpha_A\alpha_B\right)M\Omega\right]^{1/3}/c\,. \tag{7.11}$$

The quantity κ is given in Refs. [147, 248]. In GR one has $\alpha_A = \alpha_B = 0$ and $\kappa = 1$. Note that there is also a subdominant contribution from the scalar quadrupolar waves at 2.5 PN order, which however can be absorbed by a $\lesssim 1\%$ change in the mass parameters. Here we assume that α_A and α_B are constant during the inspiral, and their values are obtained from isolated NSs. This assumption is valid as long as the induced or dynamical scalarization mechanisms are not triggered.

For an asymmetric compact binary where $\alpha_A \neq \alpha_B$, the most prominent deviation from the GR phase evolution is determined by the dipole term in Eq. (7.10), *i.e.*, the contribution $\propto \mathcal{V}^3$. To leading order, the offset in the number of GW cycles in band until merger due to the dipole term is given by

$$\Delta\mathcal{N}_{\rm dipole} \simeq -\frac{25}{21504\,\pi}\,\eta^{-1}\,\mathcal{V}_{\rm in}^{-7}\,(\Delta\alpha)^2\,, \tag{7.12}$$

Table 7.3: The number of GW cycles in GR, $\mathcal{N}_{\rm GR}$, for a BNS merger with masses $(1.25\,M_\odot, 1.7\,M_\odot)$ for frequencies $f > f_{\rm in}$, and its change due to the dipole radiation in the DEF's theory, $\Delta\mathcal{N}_{\rm dipole}$, assuming $|\Delta\alpha| \equiv |\alpha_A - \alpha_B| \simeq 0.0199$, which comes from the maximally allowed effective scalar couplings for the EOS SLy4 at 90% CL (see Figure 7.5). The limits on the contributions from leading-order spin-orbit and spin-spin terms, $|\Delta\mathcal{N}_\beta|$ and $|\Delta\mathcal{N}_\sigma|$, are listed where the (dimensionless) spins of the double pulsar (when it merges in 86 Myr) are used. For $|\Delta\mathcal{N}_\beta|$ and $|\Delta\mathcal{N}_\sigma|$, we also give in parentheses when *both* NSs are spinning at the maximal spin that we have ever observed (in an eclipsing binary pulsar J1748−2446ad).

Detector	$f_{\rm in}$ (Hz)	$\mathcal{N}_{\rm GR}$	$\Delta\mathcal{N}_{\rm dipole}$	$\lvert\Delta\mathcal{N}_\beta\rvert$	$\lvert\Delta\mathcal{N}_\sigma\rvert$
aLIGO	10	1.5×10^4	-3.7×10^1	<0.76 $(<3.5\times10^1)$	$<1.8\times10^{-6}$ (<0.43)
CE	5	4.8×10^4	-1.9×10^2	<1.2 $(<5.6\times10^1)$	$<2.3\times10^{-6}$ (<0.55)
ET	1	7.0×10^5	-8.1×10^3	<3.5 $(<1.6\times10^2)$	$<3.9\times10^{-6}$ (<0.93)

where $\mathcal{V}_{\rm in}$ corresponds to $\mathcal{V}$ in Eq. (7.11) when the merging system enters the band of the GW detector, *i.e.*, when $\Omega = \pi f_{\rm in}$ (see Refs. [240, 276] for details). In the above equation we have used the approximation $\kappa \simeq 1$ and the fact that $\mathcal{V}_{\rm in}$ is much smaller than $\mathcal{V}$ just before merger. Within the approximation of Eq. (7.12) one can use $\mathcal{V}_{\rm in} \simeq (G_{\rm N} M \pi f_{\rm in})^{1/3}/c$, *i.e.*, replacing the effective gravitational constant $G_*\,(1+\alpha_A\alpha_B)$ in Eq. (7.11) by the Newtonian gravitational constant $G_{\rm N} \equiv G_*\,(1+\alpha_0^2)$ [147, 152]. Again, we stress that Eq. (7.12) is based on the assumption that the effective scalar couplings of the two NSs, α_A and α_B, remain unchanged during the inspiral in the detector's sensitive frequency band. It therefore neglects the phenomenon of induced scalarization, which can occur in a BNS system, when the unscalarized NS is sufficiently exposed to the scalar field of the scalarized companion [170]. This can reduce the dipolar radiation considerably on short ranges if α_A approaches α_B, and lead to a characteristic change in the late phase evolution of the merging BNSs. Studies on the dynamically changing effective scalar couplings are performed in the next subsection.

To obtain a rough understanding of the effects of dipolar radiation, let us calculate the dephasing from GR by an asymmetric BNS inspiral with $m_A = 1.25\,M_\odot$ and $m_B = 1.7\,M_\odot$. According to Fig. 7.5, at present, binary-pulsar experiments cannot exclude $|\alpha_A|$ as large as 10^{-2}–10^{-1} for NSs of a certain mass range, which depends on the EOS. For the EOS SLy4 we find from the corresponding (dark green) curve in Fig. 7.5 $|\alpha_A| \simeq 0.0007$ and $|\alpha_B| \simeq 0.0206$, hence $|\Delta\alpha| \equiv |\alpha_A - \alpha_B| \simeq 0.0199$.

In our study we consider the Advanced LIGO (aLIGO) detectors at design sensitivity [63], and future ground-based detectors, such as the Cosmic Explorer (CE), and the Einstein Telescope (ET). We use the starting frequencies, $f_{\rm in} = 10\,{\rm Hz}$ for aLIGO, $f_{\rm in} = 5\,{\rm Hz}$ for CE, and $f_{\rm in} = 1\,{\rm Hz}$ for ET [367, 388, 389]. In Table 7.3 we list the number of GW cycles as predicted by GR, $\mathcal{N}_{\rm GR}$, and the change in the number of cycles caused by the existence of a dipole radiation for a BNS signal, $\Delta\mathcal{N}_{\rm dipole}$. From Table 7.3 we can already see that, given the BNS parameters, current bounds by pulsars still leave room for significant time-domain phasing modifications in BNS mergers, in particular if one of the NSs falls into the scalarization window of $\sim 1.7\,M_\odot$ (for EOSs AP4, SLy4, and WFF2) to $\sim 1.9\,M_\odot$ (for the EOS H4), or if one NS's mass significantly exceeds $2\,M_\odot$ (for EOSs MS0 and MS2). As reference points, we list in Table 7.3 also the changes in the number of GW cycles from spin-orbit and spin-spin effects. Indeed, from the leading-order spin-orbit (1.5 PN) and spin-spin (2 PN) contributions to the GW phasing [259, 364], one has

$$\Delta\mathcal{N}_\beta \simeq \frac{5}{64\pi}\eta^{-1}\mathcal{V}_{\rm in}^{-2}\beta\,, \tag{7.13}$$

$$\Delta\mathcal{N}_\sigma \simeq -\frac{5}{32\pi}\eta^{-1}\mathcal{V}_{\rm in}^{-1}\sigma\,, \tag{7.14}$$

where

$$\beta = \frac{1}{12} \sum_{i=A,B} \left(113 \frac{m_i^2}{M^2} + 75\eta \right) \hat{\boldsymbol{L}} \cdot \boldsymbol{\chi}_i \,, \tag{7.15}$$

$$\sigma = \frac{\eta}{48} \left[-247 \boldsymbol{\chi}_A \cdot \boldsymbol{\chi}_B + 721 \left(\hat{\boldsymbol{L}} \cdot \boldsymbol{\chi}_A \right) \left(\hat{\boldsymbol{L}} \cdot \boldsymbol{\chi}_B \right) \right] . \tag{7.16}$$

The (dimensionless) spins of a BNS system, $\boldsymbol{\chi}_A$ and $\boldsymbol{\chi}_B$, are likely to be small in magnitude. The parameters β and σ are maximized when two spins are aligned with the direction of the orbital angular momentum, $\hat{\boldsymbol{L}}$. The limits on $|\Delta\mathcal{N}_\beta|$ and $|\Delta\mathcal{N}_\sigma|$ are listed in Table 7.3 where we have used the (dimensionless) spins of the double pulsar system that is the only double NS system where two spins are precisely measured. When the double pulsar evolves to the time of its merger in 86 Myr from now, one has $|\boldsymbol{\chi}_A| \simeq 0.014$ and $|\boldsymbol{\chi}_B| \simeq 0.00002$ [390], assuming a canonical moment of inertia $10^{38}\,\mathrm{kg\,m^2}$ for NSs. As we can see from Table 7.3, if the spins of BNSs to be discovered by GW detectors are comparable to that of the double pulsar, the inclusion of spins only affects the number of GW cycles at percentage level at most. In addition, because ground-based detectors could observe BNSs from a population different from the one observed with pulsar timing, we also give $|\Delta\mathcal{N}_\beta|$ and $|\Delta\mathcal{N}_\sigma|$ in Table 7.3 when the (dimensionless) spin of the fastest rotating pulsar ever observed, PSR J1748−2446ad ($P = 1.4\,\mathrm{ms}$) [391], is used for *both* NSs [11]. Even in this extreme case with $|\boldsymbol{\chi}_A| = |\boldsymbol{\chi}_B| \simeq 0.26$ (assuming a canonical mass $1.4\,M_\odot$), $|\Delta\mathcal{N}_{\rm dipole}|$ is still larger (or comparable in the case of the Advanced LIGO) than the *upper limits* of $|\Delta\mathcal{N}_\beta|$ and $|\Delta\mathcal{N}_\sigma|$.

[11] Notice that PSR J1748−2446ad is *not* in a double NS binary. Its companion is probably a bloated main-sequence star that recycles the pulsar to a large spin [391].

The dephasing quantity, $\Delta\mathcal{N}_{\rm dipole}$, is nevertheless a crude indicator for realistic detectability. In reality, one has to consider various degeneracy between binary parameters, the waveform templates that are used for detection and parameter estimation, the power spectral density (PSD) of noises in GW detectors, $S_n(f)$, the signal-to-noise ratio (SNR) of an event ρ, and so on. In order to obtain more quantitative estimates of the constraints on dipolar radiation that can be expected from GW detectors, one would need to compute Bayes factors between two alternatives [392] or apply cutting-edge parameter-estimation techniques, for example the MCMC or nested sampling [78]. However, given the limited scope of our analysis, for simplicity, here, we adopt the Fisher-matrix approach [240, 266, 393, 394], although we are aware of the fact that for events with mild SNR ($\rho \sim 10$), the Fisher matrix can have pitfalls [395]. In Appendix J we review the main Fisher-matrix tools that we use.

We summarize in Fig. 7.6 their dimensionless noise spectral density $\sqrt{fS_n(f)}$ [367, 388, 389], and show in the figure also an hypothetical BNS signal. For all the studies, we fix the luminosity distance to $D_L = 200\,\mathrm{Mpc}$ for aLIGO, CE, and ET. Indeed, within such a distance, aLIGO alone is supposed to observe 0.2–200 BNS events annually at design sensitivity [229]. With the four-site network incorporating LIGO-India at design sensitivity, the number of detectable BNS events will double [229]. Therefore, it is a realistic setting to discuss BNS events for aLIGO; to be conservative, we only consider a two-detector network for aLIGO in our study. CE and ET have better sensitivities, thus will have larger SNRs for these events; besides, they will be able to detect a larger number of BNSs, including those with

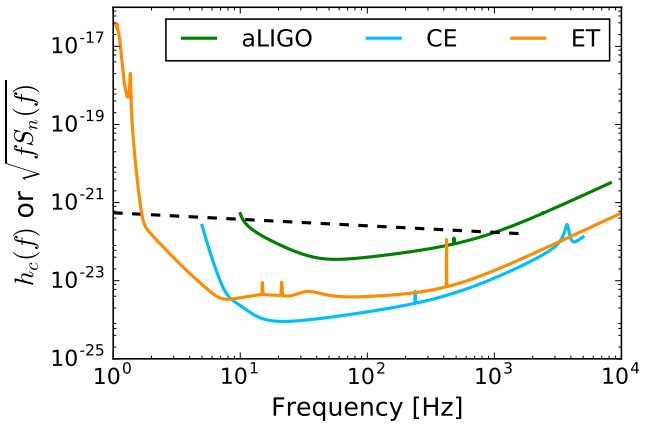

Figure 7.6: Dimensionless noise spectral density $\sqrt{fS_n(f)}$ of aLIGO, CE and ET GW detectors. The quantity $S_n(f)$ is the one-side design PSD [367, 388, 389]. The dashed line describes the (dimensionless) pattern-averaged characteristic strain $h_c(f) \equiv 2f\left|\tilde{h}(f)\right|$ for a BNS with rest-frame masses $(1.25\,M_\odot, 1.63\,M_\odot)$ at 200 Mpc ($z \simeq 0.0438$), up to the innermost-stable circular orbit given by Eq. (J.3).

unfavourable orientations. Using the standard cosmological model [396], the redshift associated to $D_L = 200\,\mathrm{Mpc}$ is $z \simeq 0.0438$, and we take it into account in our Fisher-matrix calculation, even if it generates a small effect. Moreover, we always report masses in the rest frame of a BNS system.

The Fisher matrix is constructed as usual from the Fourier-domain waveform $\tilde{h}(f)$ [240, 393, 394],

$$\Gamma_{ab} \equiv \left(\partial_a \tilde{h}(f) \,\middle|\, \partial_b \tilde{h}(f)\right) , \tag{7.17}$$

with $\partial_a \tilde{h}(f)$ being the partial derivative to the parameter labeled "a" (see Appendix J for definitions and notations). We use the waveform parameters $\left\{\ln \mathcal{A}, \ln \eta, \ln \mathcal{M}, t_c, \Phi_c, (\Delta\alpha)^2\right\}$ to construct the 6×6 Fisher matrix, Γ_{ab}. The inverse of the Fisher matrix is the correlation matrix for these parameters, from where

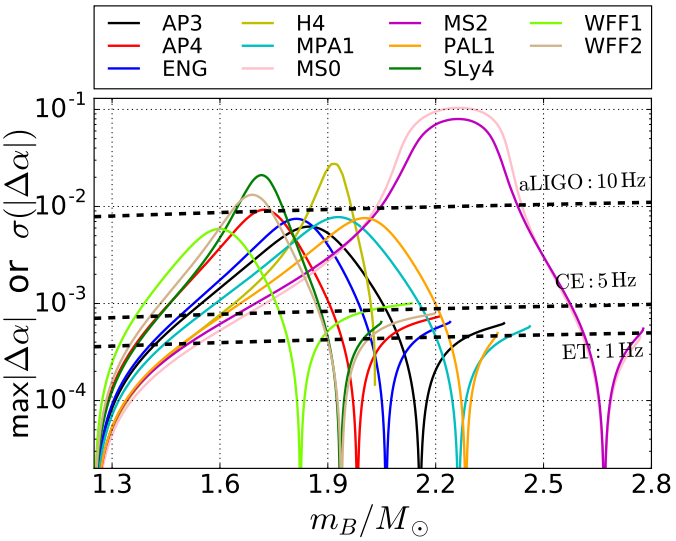

Figure 7.7: The sensitivities of aLIGO, CE, and ET to $|\Delta\alpha|$ (namely the uncertainty, $\sigma(|\Delta\alpha|)$, obtained from the inverse Fisher matrix) are depicted with dashed lines, as a function of m_B, for a pattern-averaged BNS inspiral signal with rest-frame component masses ($m_A = 1.25\,M_\odot$, m_B). The starting frequencies of GW detectors are labeled. Luminosity distance $D_L = 200\,\mathrm{Mpc}$ is assumed. The sensitivity to $|\Delta\alpha|$ from GW detectors scales with SNR as $\rho^{-1/2}$. The maximum available values of $|\Delta\alpha|$ for 11 EOSs, saturating the limits from binary pulsars at 90% CL, are shown in solid lines. If a sensitivity curve (dashed) is below a solid curve, the corresponding GW detector has the potential to improve the limit from binary pulsars for this particular EOS, with BNSs of suitable masses.

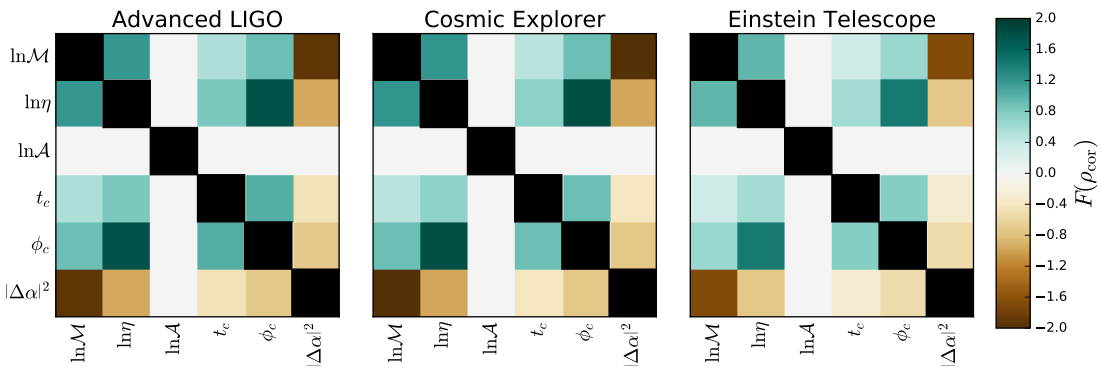

Figure 7.8: The correlations between six parameters, obtained from the inverse Fisher matrix in the matched-filter analysis for a BNS with rest-frame masses $(1.25\,M_\odot, 1.63\,M_\odot)$. $F(\rho_{\rm cor}) \equiv \log_{10}\left[(1+\rho_{\rm cor})\,/\,(1-\rho_{\rm cor})\right] - \rho_{\rm cor}\log_{10} 2$ is a function defined in Ref. [363] such that it *counts* 9's in the limit of large correlations [*e.g.*, $F(0.99) \simeq +2$, $F(-0.9) \simeq -1$, and $F(0) = 0$]. On diagonal, $F(\rho_{\rm cor} = 1)$ diverges and is plotted in black.

we can read their uncertainties and correlations [240, 266, 393, 394].

In Fig. 7.7 we plot in dashed lines the uncertainties in $|\Delta\alpha|$ obtained with three GW detectors (aLIGO, CE, and ET) for an asymmetric BNS with rest-frame masses $m_A = 1.25\,M_\odot$ and $m_B > 1.25\,M_\odot$, located at $D_L = 200\,$Mpc. For a BNS of masses, for example, $(1.25\,M_\odot, 1.63\,M_\odot)$ which are the most probable masses for the newly discovered asymmetric double-NS binary pulsar PSR J1913+1102 [397], we find that aLIGO, CE, and ET can detect its merger at 200 Mpc with $\rho = 10.6$, 450, and 153, respectively, after averaging over pattern functions and assuming two detectors in each case. The characteristic strain of such a BNS is illustrated in the frequency domain in Fig. 7.6. In the large SNR limit, the uncertainties in $|\Delta\alpha|$ scale with the SNR as $\rho^{-1/2}$. In Fig. 7.8, we give the correlations between parameters obtained from the matched-filter analysis. We find that due to its low-frequency

sensitivity ET can break some degeneracy between parameters better than aLIGO and CE do.

In Fig. 7.7, we show with solid lines the maximum values of $|\Delta\alpha|$ at 90% CL from pulsars for 11 EOSs (calculated from Fig. 7.5). If for some NS's mass range a solid line (which is associated to a certain EOS) is above a dashed line (associated to a certain detector), then for NSs described by that EOS, the corresponding GW detector has potential to further improve the DEF's parameters with the observation of a BNS within that mass range. From the figure we can see that, with the expected design sensitivity curves of aLIGO, CE, and ET [367, 388, 389],

- aLIGO has potential to further improve the current limits from binary pulsars with a discovery of a BNS of suitable masses, if the EOS of NSs is one of (or similar to) H4, MS0, MS2, SLy4, and WFF2;
- CE and ET, due to their low-frequency sensitivity and better PSD curves, are able to significantly improve current limits from binary pulsars on the DEF's parameters, no matter what the real EOS of NSs is.

We stress that those conclusions are obtained with a Fisher-matrix analysis, and should be made more robust in the future using more sophisticated tools, notably Bayesian analysis.

Constraints outside the spontaneous-scalarization regime

With the results above it is fairly straightforward to calculate the limits from aLIGO, CE and ET on $|\alpha_0|$ when β_0 is outside the spontaneous scalarization regime,

i.e., $\beta_0 \gtrsim -4$, and compare them to existing limits from the Solar system and pulsars [276]. For completeness, we present the relevant results here. Shibata et al. [171] have shown that for small α_0 there exists a simple relation between α_A, α_0 and m_A as long as spontaneous scalarization does not set in (see Eq. (44) in Ref. [171]), which in our notation reads [12]

$$\alpha_A \simeq \mathcal{A}^{(A)}_{\beta_0}(m_A, \beta_0; \mathrm{EOS})\, \alpha_0 \ . \tag{7.18}$$

With this equation at hand one can directly convert the limits from ground-based GW detectors of Fig. 7.7, for any given $\beta_0 \gtrsim -4$, into limits for $|\alpha_0|$ via

$$|\alpha_0| = \left| \frac{\Delta\alpha}{\mathcal{A}^{(A)}_{\beta_0} - \mathcal{A}^{(B)}_{\beta_0}} \right| \ . \tag{7.19}$$

Figure 7.9 gives the results for two different mass configurations and the EOS AP4. A more stiff EOS would generally lead to less constraining limits for ground-based GW detectors and binary pulsars. As one can see, in the range $\beta_0 \gtrsim -4$ current Solar system and pulsar tests are already clearly more constraining than what aLIGO is expected to obtain. For CE and ET, only inspirals with a very massive component will provide constraints that are better than present limits, for a limited range of β_0 (see also aLIGO [398] and ET [398, 399] limits from a NS-BH inspiral for the special case of $\beta_0 = 0$, i.e. the Jordan-Fierz-Brans-Dicke gravity). By the time CE or ET is operational, however, the expected limits from GAIA [400] and SKA [89] will have left little room for ground-based GW observatories in the regime. The space-based

[12] In principle, there is still a weak dependence on α_0 in $\mathcal{A}^{(A)}_{\beta_0}$. However, this dependence becomes very small for $|\alpha_0| \lesssim 10^{-2}$, as it scales with α_0^2. Therefore the α_0-dependence is absolutely negligible for the parameter space explored here.

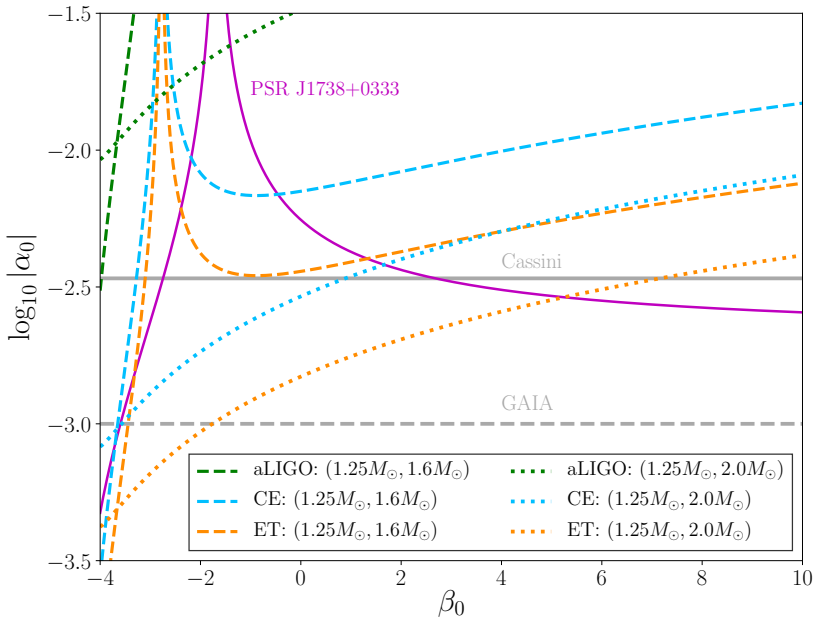

Figure 7.9: Upper limits on $|\alpha_0|$ as a function of β_0 for aLIGO (green), CE (blue), and ET (orange) [276]. The dashed lines correspond to a $1.25\,M_\odot/1.6\,M_\odot$ BNS merger, and the dotted lines correspond to a $1.25\,M_\odot/2.0\,M_\odot$ BNS merger. The chosen EOS is AP4. For comparison we have plotted Solar system limits (grey) and the limits from PSR J1738+0333 (magenta), which currently gives the best limit for $\beta_0 \gtrsim 3$. The limit from Cassini [180] and the limit expected from GAIA [400] are also shown.

GW observatories LISA [266, 364] and DECIGO/BBO [365] could in principle also provide limits on the DEF theory from an inspiral of a NS into an intermediate mass black hole, provided such BHs exist. However, the resulting limits on $|\alpha_0|$ are not expected to be better than limits from future ground-based GW observatories [266]. It is worthy to mention that for very large (positive) β_0, say, $\beta_0 \gtrsim 10^2$–10^3, massive NSs might develop instabilities [156, 304], which is beyond the scope of Fig. 7.9.

7.4.2 Dynamical scalarization

In addition to the nonlinear gravitational self-interaction testable with binary pulsars, GW detectors probe the nonlinear interactions between coalescing NSs. Dynamical scalarization stems from the interplay between these two regimes of strong gravity and thus offers a promising means of complementing pulsar timing constraints on scalar-tensor theories.

Numerical relativity simulations have demonstrated that dynamical scalarization can significantly alter the late-time behavior of a BNS system. If this transition occurs before merger, the sudden growth of effective scalar couplings impacts the system's gravitational binding energy and energy flux so as to shorten the time to merger [169, 171, 172].

The prospective detectability of this effect was investigated in Refs. [175, 271] using Bayesian model selection. The authors sought to recover injected inspiral waveforms containing dynamical scalarization with template banks constructed from similar waveforms. The injected signals and template banks used PN waveforms augmented with various non-analytic models of dynamical scalarization. To mimic the abrupt activation of the dipole emission at the onset of dynamical scalarization, Ref. [271] added a $-1\,\mathrm{PN}$ correction modulated by a Heaviside function to a GR waveform, *i.e.*, signals of the form

$$\tilde{h}(f) = \tilde{h}_{\mathrm{GR}}(f) e^{i\Psi_{-1\,\mathrm{PN}}(f)\Theta(f-f_*)}\,, \tag{7.20}$$

where $\Psi_{-1\,\mathrm{PN}}(f) = bf^{-7/3}$, and b and f_* are parameters of the model. Injected

Table 7.4: Frequency $f_{\rm DS}$ at which dynamical scalarization occurs for various equal-mass binaries, given in Hz. Results are given for theories that saturate the constraints given in Table 7.2 at 68% and 90% CLs. Binary systems are specified by their component NS masses, given in units of $M_\odot$. We highlight systems that scalarize at frequencies below 50 Hz with boldface.

68% confidence level				
EOS	1.3–1.3	1.5–1.5	1.7–1.7	1.9–1.9
AP3	838	354	123	84
AP4	577	183	57	199
ENG	858	358	118	102
H4	1301	650	235	51
MPA1	955	436	162	67
MS0	1503	854	422	165
MS2	1471	843	426	177
PAL1	1350	693	287	95
SLy4	674	217	66	356
WFF1	386	118	128	841
WFF2	519	154	57	302
90% confidence level				
EOS	1.3–1.3	1.5–1.5	1.7–1.7	1.9–1.9
AP3	694	246	**50**	**20**
AP4	461	105	**8**	109
ENG	694	236	**39**	**24**
H4	1131	513	131	**<1**
MPA1	809	325	84	**11**
MS0	1320	700	302	81
MS2	1290	687	306	88
PAL1	1190	570	193	**32**
SLy4	508	106	**<1**	197
WFF1	251	**33**	**35**	608
WFF2	391	72	**<1**	181

signals were recovered with a template bank of waveforms of the same form. In Ref. [175], the authors injected waveforms constructed in Ref. [170] by integrating the 2.5 PN equations of motion combined with a semi-analytic model of scalarization, then performed parameter estimation using both templates that included -1 PN and 0 PN scalar-tensor effects throughout the entire inspiral and those that modeled their sudden activation as in Ref. [271]

Combined, these analyses provide a loose criterion for whether a dynamically scalarizing BNS system could be distinguished from the corresponding system in GR by aLIGO. The key characteristic of such systems is the frequency $f_{\rm DS}$ at which dynamical scalarization occurs. To be distinguishable from a GR waveform, a significant portion of the dynamically scalarized signal's SNR must occur after $f_{\rm DS}$, or equivalently, $f_{\rm DS}$ must be sufficiently lower than the merger frequency. Using waveforms of the form of Eq. (7.20), the authors found in Ref. [271] that dynamical scalarization can only be observed with aLIGO if $f_{\rm DS} \lesssim 50$–100 Hz. In only one injection considered in Ref. [175] was dynamical scalarization detectable, occurring at $f_{\rm DS} \approx 80$ Hz. Understandably, these analyses rely on some initial assumptions that may bias these estimates away from the real detectability criteria, such as the limited range of masses and EOS considered and ignoring any degeneracies introduced by the merger and ringdown portions of the waveform or by the inclusion of spins. Ignoring these subtleties for the moment, we investigate whether the pulsar-timing constraints described in Sec. 7.3 can exclude the possibility of observing dynamical scalarization with aLIGO using the conservative detectability criterion from Refs. [175, 271] that scalarization must occur by $f_{\rm DS} \lesssim 50$ Hz.

We consider binary systems composed of NSs with masses ranging from $1.3\,M_\odot$ to $1.9\,M_\odot$. We compute $f_{\rm DS}$ within the "post-Dickean" (PD) framework, a resummation of the PN expansion formulated in Ref. [3]. This model introduces new dynamical degrees of freedom that capture the nonperturbative growth of the scalar field using a semi-analytic feedback loop. This approach provides a mathematically consistent backing to previous models of dynamical scalarization [170]. The model incorporates a certain flexibility in the choice of resummed quantities; we adopt the $\left(m^{(\rm RE)}, F^{(\tilde{\varphi})}\right)$ scheme outlined in Table I of Ref. [3] because it was found to give the best agreement with numerical computations of quasi-equilibrium configurations [172]. For clarity, we dress quantities defined in the PD framework with tildes and leave quantities defined in the PN framework unadorned; in the limit that no resummation is performed, the PD quantities reduce to their PN analogs.

Within the PD framework, the effective scalar coupling of each NS is promoted to a function of both the asymptotic scalar field φ_0 and the local scalar field in which the body is immersed, i.e. $\tilde{\alpha}_A = \tilde{\alpha}_A(\varphi_0, \varphi_A)$. Unlike in the PN treatment, this coupling evolves as the BNS coalesces. Similarly, the inertial mass of each body $\tilde{m}_A(\varphi_0, \varphi_A)$ evolves in the PD framework. However this mass varies by no more than 0.01%, so in practice, one can simply use the PN mass m_A in place of $\tilde{m}_A$.

We define the mass-averaged scalar coupling of the system as

$$\bar{\alpha} \equiv \frac{\tilde{m}_A\tilde{\alpha}_A + \tilde{m}_B\tilde{\alpha}_B}{\tilde{m}_A + \tilde{m}_B}, \tag{7.21}$$

where precise definitions of $\tilde{m}_A$ and $\tilde{\alpha}_A$ are given in Eqs. (A3) and (A4) in Ref. [3]. Note that for equal-mass binaries, we have $\tilde{\alpha}_A = \tilde{\alpha}_B = \bar{\alpha}$.

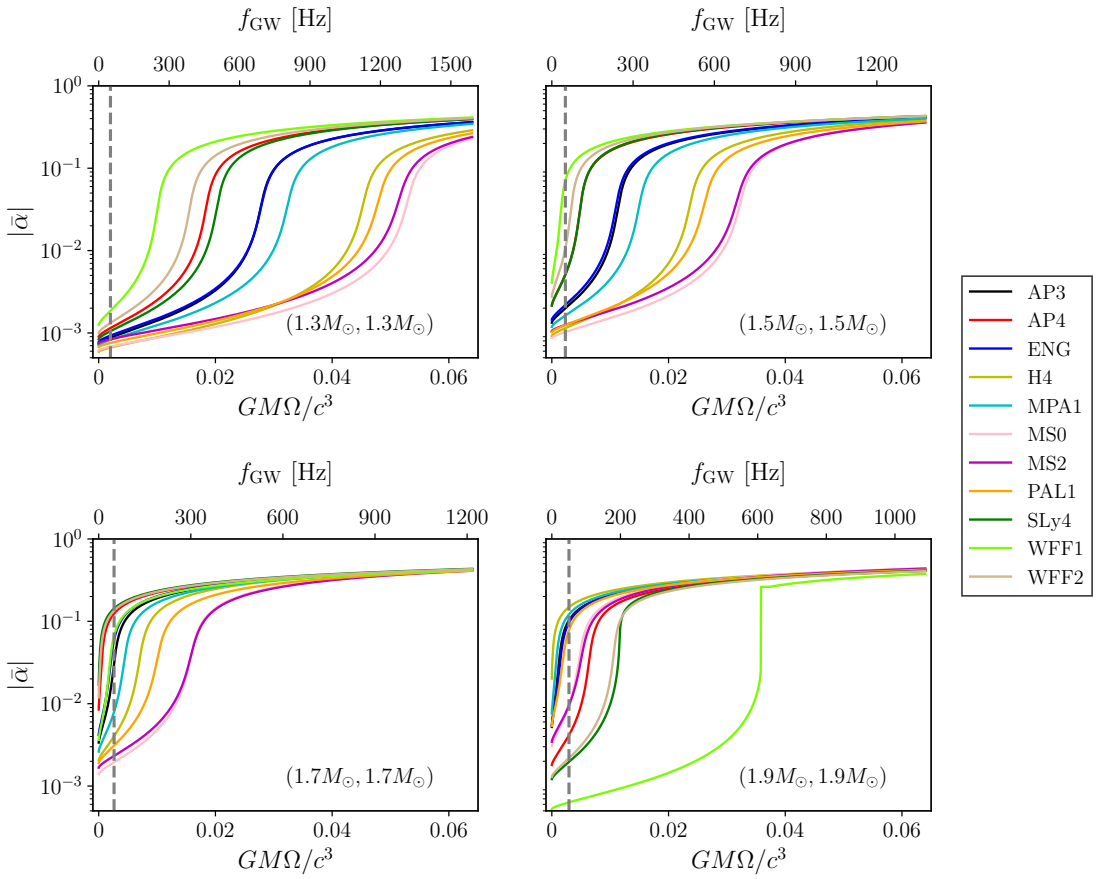

Figure 7.10: Mass-averaged scalar coupling as a function of orbital angular frequency for equal-mass BNS systems with masses $(1.3\,M_\odot, 1.3\,M_\odot)$, $(1.5\,M_\odot, 1.5\,M_\odot)$, $(1.7\,M_\odot, 1.7\,M_\odot)$, and $(1.9\,M_\odot, 1.9\,M_\odot)$. We use the limits on (α_0, β_0) at 90% CLs, given in Table 7.2, for each EOS. The corresponding GW frequency is given along the top axis, with $f_{\rm GW} = \Omega/\pi$. Dashed vertical lines highlight the conservative detectability criterion for aLIGO that $f_{\rm DS} \lesssim 50\,{\rm Hz}$, derived in Refs. [175, 271].

Table 7.5: Frequency $f_{\rm DS}$ (in Hz) at which dynamical scalarization occurs for various unequal-mass binaries with the EOS MPA1. Results are given for theories that saturate the constraints given in Table 7.2 at 68% and 90% CLs. Binary systems are specified by their component NS masses, given in units of $M_\odot$. We highlight systems that scalarize at frequencies below 50 Hz with boldface.

68% confidence level								
	1.2	1.3	1.4	1.5	1.6	1.7	1.8	1.9
1.2	1340	1130	942	767	611	471	364	304
1.3	...	955	795	649	515	399	306	258
1.4	...	...	661	538	427	329	253	212
1.5	...	...	...	436	347	268	206	172
1.6	...	...	...	...	274	212	163	136
1.7	...	...	...	...	...	162	126	105
1.8	...	...	...	...	...	...	96	80
1.9	...	...	...	...	...	...	...	67
90% confidence level								
	1.2	1.3	1.4	1.5	1.6	1.7	1.8	1.9
1.2	1160	973	788	618	458	315	194	119
1.3	...	809	653	511	380	262	158	99
1.4	...	...	529	415	305	210	129	79
1.5	...	...	...	325	240	165	101	62
1.6	...	...	...	...	178	120	73	**46**
1.7	...	...	...	...	...	84	51	**31**
1.8	...	...	...	...	...	...	**32**	**19**
1.9	...	...	...	...	...	...	...	**11**

Following the work of Ref. [3], we compute the mass-averaged scalar coupling as a function of frequency for binaries on quasi-circular orbits to 1 PD order. The average scalar coupling is plotted in Fig. 7.10 for equal-mass binaries for theories that saturate the pulsar-timing constraints at 90% CLs, as given in Table 7.2. Scalarization occurs earlier for larger mass systems, with an ordering (by EOS) determined by the magnitude of

$$\beta_A = \left(\frac{\mathrm{d}\alpha_A}{\mathrm{d}\varphi}\right)_{\varphi=\varphi_0} . \tag{7.22}$$

To compute this quantity, one takes the difference in effective scalar couplings of NSs (of equal baryonic mass) with infinitesimally different asymptotic scalar fields φ_0; however, for non-spontaneously scalarized stars, β_A is given approximately by

$$\beta_A \approx \frac{\beta_0 |\alpha_A|}{|\alpha_0|} , \tag{7.23}$$

provided that $|\alpha_A|$ is sufficiently small. Binaries with spontaneously scalarized stars begin with an appreciable effective scalar coupling at large separations that continues to grow as they coalesce. In light of this remark, we note that there is no observational distinction between spontaneous (or induced) scalarization and dynamical scalarization that occurs at sufficiently low frequencies; for example, compare the scalarization of $(1.7\,M_\odot, 1.7\,M_\odot)$ systems composed of NSs with the EOSs SLy4, AP4, and WFF1 (the dark green, red, and beige curves in the lower left panel of Fig. 7.10, respectively).

The sharp feature for the WFF1 EOS in the $(1.9\,M_\odot, 1.9\,M_\odot)$ system occurs because of the relatively low mass at which spontaneous scalarization occurs for this particular EOS. We provide a more detailed analysis of this phenomenon in

Appendix K. Similarly abrupt transitions occur for other EOSs in more massive binary systems with individual masses $\gtrsim 2\,M_\odot$.

We adopt the method introduced in Ref. [172] to extract $f_{\rm DS}$. The average effective scalar coupling can be closely fit by the piecewise function

$$\left(1+\bar{\alpha}^2\right)^{10/3} = 1 + a_1\,(x - x_{\rm DS})\,\Theta\,(x - x_{\rm DS}) \tag{7.24}$$

where Θ is the Heaviside function, a_1 and $x_{\rm DS}$ are fitting parameters, and $x \equiv (G_* M\Omega/c^3)^{2/3}$. In practice, we identify $x_{\rm DS}$ with the peak in the second derivative of the lefthand side of Eq. (7.24) with respect to x. The gravitational wave frequency at which dynamical scalarization occurs is then given by $f_{\rm DS} = \Omega_{\rm DS}/\pi$. In Ref. [3], the PD prediction was found to reproduce numerical-relativity results to within an error of $\lesssim 10\%$ with this fitting procedure.

The dynamical scalarization frequencies for the configurations considered in Fig. 7.10 are given in Table 7.4 for theories constrained at the 68% and 90% CLs. Systems containing spontaneously scalarized stars (*i.e.*, those with appreciable effective scalar coupling even in isolation) are demarcated as scalarizing below 1 Hz; as noted above, these systems would be indistinguishable to GW detectors from those that dynamically scalarize below 1 Hz. For clarity, we highlight the systems in Table 7.4 that scalarize (dynamically or spontaneously) below 50 Hz. Recall that, under our definition, induced scalarization occurs in binaries comprised of one initially scalarized star and one initially unscalarized star; this asymmetry cannot be achieved in equal-mass systems like those discussed above.

We next consider the onset of dynamical scalarization in unequal-mass sys-

tems. For the sake of compactness, we show in Table 7.5 the dynamical scalarization frequencies for binaries with NS masses of $1.2\,M_\odot$ to $1.9\,M_\odot$ with just the MPA1 EOS. We find that the total mass plays a more important role in determining the onset of dynamical scalarization than the mass ratio. Fixing the total mass, we find that scalarization occurs earlier in more asymmetric binaries of lower mass (*e.g.*, $M \lesssim 3.2 M_\odot$ for the MPA1 EOS). None of the systems listed in Table 7.5 undergo induced scalarization. As before, we highlight the systems in Table 7.5 that scalarize below 50 Hz.

To summarize, Tables 7.4 and 7.5 demonstrate that binary-pulsar constraints cannot entirely rule out the possibility of dynamical scalarization occurring at frequencies $f_{\rm DS} \lesssim 50$ Hz at 90% CL. Initial detectability studies — Refs. [175, 271] discussed above — suggest that this early scalarization should be observable with aLIGO (although these conclusions should be confirmed with future work in light of the limitations of these works; see above). Thus, failure to detect dynamical scalarization in future GW observations could provide tighter constraints on the parameters (α_0, β_0) in DEF theory than pulsar timing. However, as can be seen from Table 7.4, the prospects of producing such complementary constraints depend critically on the observed NS masses and the EOS of NSs.

7.5 Conclusions

In this work, we have studied the scalarization phenomena [153, 169] in the massless mono-scalar-tensor theory of gravity of DEF with pulsar timing and laser-

interferometer GW detectors on the Earth. We now summarize the key conclusions of our analysis.

1. The spontaneous scalarization phenomenon [153] occurs at different NS mass ranges for different EOSs [171]. Therefore, in a well-timed relativistic binary-pulsar system with a specific NS mass, the scalar-tensor gravity might be stringently constrained for some EOSs whose spontaneous-scalarization phenomenon occurs near that specific NS mass. However, in general, strong scalarization could still take place if NSs are described by an EOS whose scalarization occurs at a mass different from the one observed.

2. Combining two well-timed binary-pulsar systems with quite different NS masses, one could in principle constrain the scalar-tensor theory with whatever EOS Nature provides us. Using MCMC simulations, we showed in Sec. 7.3 that, combining five binary pulsars [247, 248, 373–375] that best constrain gravitational dipolar radiation, we can already bound the *scalarization parameter*, β_0, to be $\gtrsim -4.28$ at 68% CL and $\gtrsim -4.38$ at 90% CL, for any of the eleven EOSs that we have considered.

3. Nevertheless, because of the limited distribution of masses of the five chosen binary pulsars, we found that if the EOS of NSs were similar to one of AP4, SLy4, or WFF2, NSs with masses of $m_A \simeq 1.70$–$1.73\,M_\odot$ could still develop an effective scalar coupling $\gtrsim \mathcal{O}(10^{-2})$. This is also true for the EOS H4 with $m_A \simeq 1.92\,M_\odot$, and for the EOSs MS0 and MS2 with $m_A \simeq 2.26\,M_\odot$ (see Fig. 7.5).

4. Using the upper limits on the effective scalar coupling of NSs from binary pulsars, we found that for BNSs in the frequency bands of aLIGO, CE, and ET, we could still have a large time-domain dephasing in the number of GW cycles, on the orders of $\mathcal{O}(10^1)$, $\mathcal{O}(10^2)$, and $\mathcal{O}(10^3)$, respectively (see Table 7.3).

5. We performed a Fisher-matrix study of BNS inspiral signals using aLIGO, CE, and ET. We found that for BNSs at a luminosity distance $D_L = 200\,\mathrm{Mpc}$, where we expect to observe those sources, aLIGO can still improve the limits from binary pulsars for a couple of EOSs with BNSs of suitable masses. CE (whose bandwith starts at 5 Hz) can improve the current limits for all EOSs, while ET (whose bandwith starts at 1 Hz) will provide us with even more significant improvements over current constraints for all EOSs. This is mainly due its better low-frequency sensitivity. Our conclusions for aLIGO differ from the one obtained in Refs. [276, 370, 371], where the authors concluded that pulsar timing would do better than aLIGO in constraining scalar-tensor theories. The main reason of this difference comes from a better understanding and larger span of the NS masses and EOSs during the past two decades [248, 369], and the different PSD for aLIGO used in Refs. [240, 276]. If we restricted the analysis to the same NS masses and the same EOS used in Ref. [276], we would recover the same conclusions as in Ref. [276] (see Fig. 7.7).

6. We investigated dynamical scalarization in equal-mass and unequal-mass BNS systems. With the criterion that the dynamical scalarization transition frequency must fall below $\sim 50\,\mathrm{Hz}$ [175, 271] to be detectable, we found aLIGO

could be able to observe this phenomenon given the constraints obtained from binary-pulsar timing, even away from the scalarization windows. We found that the prospects for observing dynamical scalarization with GW detectors depends critically on the NS EOS—for example, dynamical scalarization of NSs with the MS0 EOS could not be detected with aLIGO. Producing new constraints on scalar-tensor theories from GW searches for dynamical scalarization requires waveform models that can faithfully reproduce this nonperturbative phenomenon; ultimately, these conclusions should be revisited once such models are developed.

Our comparisons between binary pulsars and GWs made use of the *current* limits of the former and the *expected* limits of the latter. It shows that advanced and next-generation ground-based GW detectors have potential to further improve the current limits set by pulsar timing. Nevertheless, the binary-pulsar limits will also improve over time, especially if suitable systems filling the scalarization windows are discovered in future pulsar surveys. Better mass measurements of currently known pulsars will also help in narrowing down the constraints, especially with PSRs J1012+5307 [373] and J1913+1102 [397], whose observational uncertainties in masses are still large, and they might have the right masses to close the windows below $2\,M_\odot$. To reach this goal, the next generation of radio telescopes, such as FAST and SKA will play a particularly important role [366, 401].

7.6 Acknowledgments

We thank Paulo Freire, Ian Harry, Jan Steinhoff, Thomas Tauris, and Nicolás Yunes for helpful discussions. We are grateful to Jim Lattimer for providing us with tabulated data for neutron-star equations of state. The Markov-chain Monte Carlo runs were performed on the Vulcan cluster at the Max Planck Institute for Gravitational Physics in Potsdam.

Chapter 8: Distinguishing boson stars from black holes and neutron stars from tidal interactions in inspiraling binary systems

Authors: *Noah Sennett, Tanja Hinderer, Jan Steinhoff, Alessandra Buonanno, and Serguei Ossokine*[1]

Abstract: Binary systems containing boson stars—self-gravitating configurations of a complex scalar field— can potentially mimic black holes or neutron stars as gravitational-wave sources. We investigate the extent to which tidal effects in the gravitational-wave signal can be used to discriminate between these standard sources and boson stars. We consider spherically symmetric boson stars within two classes of scalar self-interactions: an effective-field-theoretically motivated quartic potential and a solitonic potential constructed to produce very compact stars. We compute the tidal deformability parameter characterizing the dominant tidal imprint in the gravitational-wave signals for a large span of the parameter space of each boson star model, covering the entire space in the quartic case, and an extensive portion of interest in the solitonic case. We find that the tidal deformability for boson stars with a quartic self-interaction is bounded below by $\Lambda_{\rm min} \approx 280$ and for those with a solitonic interaction by $\Lambda_{\rm min} \approx 1.3$. We summarize our results as ready-to-use

[1]Originally published as Phys. Rev. **D96**, 024002 (2017).

fits for practical applications. Employing a Fisher matrix analysis, we estimate the precision with which Advanced LIGO and third-generation detectors can measure these tidal parameters using the inspiral portion of the signal. We discuss a novel strategy to improve the distinguishability between black holes/neutrons stars and boson stars by combining tidal deformability measurements of each compact object in a binary system, thereby eliminating the scaling ambiguities in each boson star model. Our analysis shows that current-generation detectors can potentially distinguish boson stars with quartic potentials from black holes, as well as from neutron-star binaries if they have either a large total mass or a large (asymmetric) mass ratio. Discriminating solitonic boson stars from black holes using only tidal effects during the inspiral will be difficult with Advanced LIGO, but third-generation detectors should be able to distinguish between binary black holes and these binary boson stars.

8.1 Introduction

Observations of gravitational waves (GWs) by Advanced LIGO [63], soon to be joined by Advanced Virgo [64], KAGRA [233], and LIGO-India [402], open a new window to the strong-field regime of general relativity (GR). A major target for these detectors are the GW signals produced by the coalescences of binary systems of compact bodies. Within the standard astrophysical catalog, only black holes (BHs) and neutron stars (NSs) are sufficiently compact to generate GWs detectable by current-generation ground-based instruments. To test the dynamical, non-linear

regime of gravity with GWs, one compares the relative likelihood that an observed signal was produced by the coalescence of BHs or NSs as predicted by GR against the possibility that it was produced by the merger of either: (a) BHs or NSs in alternative theories of gravity or (b) exotic compact objects in GR. Here, we pursue tests within the second class. Several possible exotic objects have been proposed that could mimic BHs or NSs, such as: quark stars [403]—stars whose interiors attain such high temperature and pressure that baryonic matter transitions to a phase of ultra-dense quark matter; boson stars (BSs) [404, 405]—self-gravitating configurations of a complex scalar field or fields; gravastars [406, 407]—localized vacuum regions of non-zero cosmological constant contained within a finite radius; and axion stars [408, 409]—self-gravitating configurations of a real scalar field whose self-interaction takes the same form as the QCD axion.

The coalescence of a binary system can be classified into three phases— the inspiral, merger, and ringdown— each of which can be modeled with different tools. The inspiral describes the early evolution of the binary and can be studied within the post-Newtonian (PN) approximation, a series expansion in powers of the relative velocity v/c (see Ref. [30] and references within). As the binary shrinks and eventually merges, strong, highly-dynamical gravitational fields are generated; the merger is only directly computable using numerical relativity (NR). Finally, during ringdown, the resultant object relaxes to an equilibrium state through the emission of GWs whose (complex) frequencies are given by the object's quasinormal modes (QNMs), calculable through perturbation theory (see Ref. [410] and references within). Complete GW signals are built by synthesizing results from these three regimes from

first principles with the effective-one-body (EOB) formalism [38, 45] or phenomenologically, through frequency-domain fits [411, 412] of inspiral, merger and ringdown waveforms.

An understanding of how exotic objects behave during each of these phases is necessary to determine whether GW detectors can distinguish them from conventional sources (i.e., BHs or NSs). Significant work in this direction has already been completed. The structure of spherically-symmetric compact objects is imprinted in the PN inspiral through tidal interactions that arise at 5PN order (i.e., as a $(v/c)^{10}$ order correction to the Newtonian dynamics). Tidal interactions are characterized by the object's tidal deformability, which has recently been computed for gravastars [413, 414] and "mini" BSs [415]. During the completion of this work, an independent investigation on the tidal deformability of several classes of exotic compact objects, including examples of the BS models considered here, was performed in Ref. [416]; details of the similarities and differences to this work are discussed in Sec. 8.7 below. Additional signatures of exotic objects include the magnitude of the spin-induced quadrupole moment and the absence of tidal heating. The possibility of discriminating BHs from exotic objects with these two effects was discussed in Refs. [417] and [418], respectively—we will not consider these effects in this work. The merger of BSs has been studied using NR in head-on collisions [419, 420] and following circular orbits [421]. The QNMs have been computed for BSs [422–424] and gravastars [425–427].

In this work, we compute the tidal deformability of two models of BSs: "massive" BSs [428] characterized by a quartic self-interaction and non-topological soli-

tonic BSs [429]. The self-interactions investigated here allow for the formation of compact BSs, in contrast to the "mini" BSs considered in Ref. [415]. We perform an extensive analysis of the BS parameter space within these models, thereby going beyond previous work in Ref. [416], which was limited to a specific choice of parameter characterizing the self-interaction for each model. Special consideration must be given to the choice of the numerical method because BSs are constructed by solving stiff differential equations—we employ relaxation methods to overcome this problem [430]. Our new findings show that for massive BSs, the tidal deformability Λ (defined below) is bounded below by $\Lambda_{\rm min} \approx 280$ for stable configurations, while for solitonic BSs the deformability can reach $\Lambda_{\rm min} \approx 1.3$. For comparison, the deformability of NSs is $\Lambda_{\rm NS} \gtrsim \mathcal{O}(10)$ and for BHs $\Lambda_{\rm BH} = 0$. We compactly summarize our results as fits for convenient use in future gravitational wave data analysis studies. In addition, we employ the Fisher matrix formalism to study the prospects for distinguishing BSs from NSs or BHs with current and future gravitational-wave detectors based on tidal effects during the inspiral. Prospective constraints on the combined tidal deformability parameters of both objects in a binary were also shown for two fiducial cases in Ref. [416]. Our findings are consistent with the conclusions drawn in Ref. [416]; we discuss a new type of analysis that can strengthen the claims made therein on the distinguishability of BSs from BHs and NSs by combining information on each body in a binary system.

The paper is organized as follows. Section 8.2 introduces the BS models investigated herein. We provide the necessary formalism for computing the tidal deformability in Sec. 8.3, and describe the numerical methods we employ in Sec. 8.4.

In Sec. 8.5, we compute the tidal deformability, providing results that range from the weak-coupling limit to the strong-coupling limit as well as numerical fits for the tidal deformability. Finally, in Sec. 8.6 we discuss the prospects of testing the existence of stellar-mass BSs using GW detectors and provide some concluding remarks in Sec. 8.7.

We use the signature $(-,+,+,+)$ for the metric and natural units $\hbar = G = c = 1$, but explicitly restore factors of the Planck mass $m_{\rm Planck} = \sqrt{\hbar c/G}$ in places to improve clarity. The convention for the curvature tensor is such that $\nabla_\beta\nabla_\alpha a_\mu - \nabla_\beta\nabla_\beta a_\mu = R^\nu{}_{\mu\alpha\beta}a_\nu$, where ∇_α is the covariant derivative and a_μ is a generic covector.

8.2 Boson star basics

Boson stars—self-gravitating configurations of a (classical) complex scalar field—have been studied extensively in the literature, both as potential dark matter candidates and as tractable toy models for testing generic properties of compact objects in GR. Boson stars are described by the Einstein-Klein-Gordon action

$$S = \int d^4x\sqrt{-g}\left[\frac{R}{16\pi} - \nabla^\alpha\Phi\nabla_\alpha\Phi^* - V(|\Phi|^2)\right], \tag{8.1}$$

where * denotes complex conjugation. The only experimentally confirmed elementary scalar field is the Higgs boson [431, 432], which is an unlikely candidate to form a BS because it readily decays to W and Z bosons. However, other massive scalar fields have been postulated in many theories beyond the Standard Model, e.g., bosonic superpartners predicted by supersymmetric extensions [433].

The Einstein equations derived from the action (8.1) are given by

$$R_{\alpha\beta} - \frac{1}{2} g_{\alpha\beta} R = 8\pi T^{\Phi}_{\alpha\beta}, \tag{8.2}$$

with

$$T^{\Phi}_{\alpha\beta} = \nabla_\alpha \Phi^* \nabla_\beta \Phi + \nabla_\beta \Phi^* \nabla_\alpha \Phi - g_{\alpha\beta}(\nabla^\gamma \Phi^* \nabla_\gamma \Phi + V(|\Phi|^2)). \tag{8.3}$$

The accompanying Klein-Gordon equation is

$$\nabla^\alpha \nabla_\alpha \Phi = \frac{dV}{d|\Phi|^2} \Phi, \tag{8.4}$$

along with its complex conjugate.

The earliest proposals for a BS contained a single non-interacting scalar field [434–436], that is

$$V\left(|\Phi|^2\right) = \mu^2 |\Phi|^2, \tag{8.5}$$

where μ is the mass of the boson. The free Einstein-Klein-Gordon action also describes the second-quantized theory of a real scalar field; thus, this class of BS can also be interpreted as a gravitationally bound Bose-Einstein condensate [436]. The maximum mass for BSs with the potential given in Eq. (8.5) is $M_{\max} \approx 0.633 m^2_{\text{Planck}}/\mu$, or in units of solar mass, $M_{\max}/M_\odot \approx 85\text{peV}/\mu$. The corresponding compactness for this BS is $C_{\max} \approx 0.08$ [434], where the compactness C of a body is given by the ratio between its mass M and radius R.[2] Because this maximum mass scales

[2]Formally, BSs have no surface, so the notion of a radius (and hence compactness) is inherently ambiguous. One common convention is to define the radius as that of a shell containing a fixed fraction of the total mass of the star (e.g., R_{99} where $m(r = R_{99}) = 0.99\, m(r = \infty)$). To avoid

more slowly with μ than the Chandrasekhar limit for a degenerate fermionic star $M_{\rm CH} \sim m_{\rm Planck}^3/m_{\rm Fermion}^2$, this class of BSs is referred to as *mini BSs*. The tidal deformability was computed in this model in Ref. [415]

Since the seminal work of the 1960s [434–436], BSs with various scalar self-interactions have been studied. We consider two such models in this work, both which reduce to mini BSs in the weak-coupling limit. The first BS model we consider is *massive BSs* [428], with a potential given by

$$V_{\rm massive}(|\Phi|^2) = \mu^2|\Phi|^2 + \frac{\lambda}{2}|\Phi|^4, \tag{8.6}$$

which is repulsive for $\lambda \geq 0$. In the strong-coupling limit $\lambda \gg \mu^2/m_{\rm Planck}^2$, spherically symmetric BSs obtain a maximum mass of $M_{\rm max} \approx 0.044\sqrt{\lambda} m_{\rm Planck}^3/\mu^2$ [428]. In units of the solar mass $M_\odot$ this reads $M_{\rm max}/M_\odot \approx \sqrt{\lambda}(0.3{\rm GeV}/\mu)^2$. Such configurations are roughly as compact as NSs, with an effective compactness of $C_{\rm max} \approx 0.158$ [437, 438]. This BS model is a natural candidate from an effective-field-theoretical perspective because the potential in Eq. (8.6) contains all renormalizable self-interactions for a scalar field, i.e., other interactions that scale as higher powers of $|\Phi|$ are expected to be suppressed far from the Planck scale. The "natural" values of $\lambda \sim 1$ and $\mu \ll m_{\rm Planck}$ yield the strong-coupling limit of the potential (8.6). Because it is the most theoretically plausible BS model, we investigate the strong-coupling regime of this interaction in detail in Section 8.5.1.

The second class of BS that we consider is the *solitonic BS* model [429], char-

this ambiguity, our results are given in terms of quantities that can be extracted directly from the asymptotic geometry of the BS: the total mass M and dimensionless tidal deformability Λ (defined below).

acterized by the potential

$$V_{\rm solitonic}(|\Phi|^2) = \mu^2|\Phi|^2\left(1-\frac{2|\Phi|^2}{\sigma_0^2}\right)^2. \tag{8.7}$$

This potential admits a false vacuum solution at $|\Phi| = \sigma_0/\sqrt{2}$. One can construct spherically symmetric BSs whose interior closely resembles this false vacuum state and whose exterior is nearly vacuum $|\Phi| \approx 0$; the transition between the false vacuum and true vacuum occurs over a surface of width $\Delta r \sim \mu^{-1}$. In the strong-coupling limit $\sigma_0 \ll m_{\rm Planck}$, the maximum mass of non-rotating BSs is $M_{\rm max} \approx 0.0198 m_{\rm Planck}^4/(\mu\sigma_0^2)$, or $M_{\rm max}/M_\odot \approx (\mu/\sigma_0)^2(0.7{\rm PeV}/\mu)^3$ [429]. The corresponding compactness $C_{\rm max} \approx 0.349$ approaches that of a BH $C_{\rm BH} = 1/2$ [429].[3] The main motivation for considering the potential (8.7) is as a model of very compact objects that could even possess a light-ring when $C > 1/3$. In this work, we will only consider solitonic BSs as potential BH mimickers, as NSs could be mimicked by the more natural massive BS model.

In this work, we restrict our attention to only non-rotating BSs. Axisymmetric (rotating) BSs have been constructed for the models we consider [440–443], but these solutions are significantly more complex than those that are spherically symmetric (non-rotating). The energy density of a rotating BS forms a toroidal topology, vanishing at the star's center. Because its angular momentum is quantized, a rotating BS cannot be constructed in the slow-rotation limit, i.e. by adding infinitesimal rotation to a spherically symmetric solution [444].

[3] This compactness is still lower than the theoretical Buchdahl limit of $C \leq 4/9$ for isotropic perfect fluid stars that respect the strong energy condition [439].

8.3 Tidal perturbations of spherically-symmetric boson stars

We consider linear tidal perturbations of a non-rotating BSs. We work within the adiabatic limit, that is we assume that the external tidal field varies on timescales much longer than any oscillation period of the star or relaxation timescale to reach a microphysical equilibrium. These conditions are typically satisfied during the inspiral of compact binaries. Close to merger, the assumptions concerning the separation of timescales can break down and the tides can become dynamical [292, 299, 445, 446]; we ignore these complications here. The computation of the tidal deformability of NSs in general relativity was first addressed in Refs. [308, 447] and was extended in Refs. [307, 359].

8.3.1 Background configuration

Here we review the equations describing a spherically symmetric BS [404, 428, 434], which is the background configuration that we use to compute the tidal perturbations in the following subsection. We follow the presentation in Ref. [424]. The metric written in polar-areal coordinates reads

$$ds_0^2 = -e^{v(r)}dt^2 + e^{u(r)}dr^2 + r^2(d\theta^2 + \sin^2\theta d\varphi^2). \tag{8.8}$$

As an ansatz for the background scalar field, we use the decomposition

$$\Phi_0(t, r) = \phi_0(r)e^{-i\omega t}. \tag{8.9}$$

Inserting Eqs. (8.8) and (8.9) into Eqs. (8.2)–(8.4) gives

$$e^{-u}\left(-\frac{u'}{r}+\frac{1}{r^2}\right)-\frac{1}{r^2}=-8\pi\rho, \tag{8.10a}$$

$$e^{-u}\left(\frac{v'}{r}+\frac{1}{r^2}\right)-\frac{1}{r^2}=8\pi p_{\rm rad}, \tag{8.10b}$$

$$\phi_0''+\left(\frac{2}{r}+\frac{v'-u'}{2}\right)\phi_0'=e^{u}\left(U_0-\omega^2e^{-v}\right)\phi_0, \tag{8.10c}$$

where a prime denotes differentiation with respect to r, $U_0 = U(\phi_0)$, $U(\phi) = dV/d|\Phi|^2$. Because the coefficients in Eq. (8.10c) are real numbers, we can restrict $\phi_0(r)$ to be a real function without loss of generality. We have also defined the effective density and pressures

$$\rho \equiv -T^{\Phi t}_{\ \ t}=\omega^2e^{-v}\phi_0^2+e^{-u}(\phi_0')^2+V_0, \tag{8.11}$$

$$p_{\rm rad} \equiv T^{\Phi r}_{\ \ r}=\omega^2e^{-v}\phi_0^2+e^{-u}(\phi_0')^2-V_0, \tag{8.12}$$

$$p_{\rm tan} \equiv T^{\Phi \theta}_{\ \ \theta}=\omega^2e^{-v}\phi_0^2-e^{-u}(\phi_0')^2-V_0, \tag{8.13}$$

where $V_0 = V(\phi_0)$. Note that BSs behave as anisotropic fluid stars with pressure anisotropy given by

$$\Sigma = p_{\rm rad}-p_{\rm tan}=2e^{-u}(\phi_0')^2. \tag{8.14}$$

An additional relation derived from Eqs. (8.2)–(8.9) that will be used to simplify the perturbation equations discussed in the next subsection is

$$p_{\rm rad}'=-\frac{(p_{\rm rad}+\rho)}{2r}\left[e^{u}\left(1+8\pi r^2p_{\rm rad}\right)-1\right]-\frac{2\Sigma}{r}. \tag{8.15}$$

We restrict our attention to ground-state configurations of the BS, in which $\phi_0(r)$ has no nodes. The background fields exhibit the following asymptotic behavior

$$\lim_{r\to 0} m(r) \sim r^3, \qquad \lim_{r\to\infty} m(r) \sim M, \tag{8.16a}$$

$$\lim_{r\to 0} v(r) \sim v^{(c)}, \qquad \lim_{r\to\infty} v(r) \sim 0, \tag{8.16b}$$

$$\lim_{r\to 0} \phi_0(r) \sim \phi_0^{(c)}, \qquad \lim_{r\to\infty} \phi_0(r) \sim \frac{1}{r} e^{-r\sqrt{\mu^2-\omega^2}}, \tag{8.16c}$$

where M is the BS mass, $v^{(c)}$ and $\phi_0^{(c)}$ are constants, and $m(r)$ is defined such that

$$e^{-u(r)} = \left(1 - \frac{2m(r)}{r}\right). \tag{8.17}$$

8.3.2 Tidal perturbations

We now consider small perturbations to the metric and scalar field defined such that

$$g_{\alpha\beta} = g^{(0)}_{\alpha\beta} + h_{\alpha\beta}, \tag{8.18}$$

$$\Phi = \Phi_0 + \delta\Phi. \tag{8.19}$$

We restrict our attention to static perturbations in the polar sector, which describe the effect of an external electric-type tidal field. Working in the Regge-Wheeler gauge [448], the perturbations take the form

$$h_{\alpha\beta}dx^\alpha dx^\beta = \sum_{l\geq|m|} Y_{lm}(\theta,\varphi)\left[e^v h_0(r)dt^2 + e^u h_2(r)dr^2 + r^2 k(r)(d\theta^2 + r\sin^2\theta d\varphi^2)\right], \tag{8.20a}$$

and

$$\delta\Phi = \sum_{l\geq|m|} \frac{\phi_1(r)}{r} Y_{lm}(\theta,\varphi)e^{-i\omega t}, \tag{8.20b}$$

where Y_{lm} are scalar spherical harmonics.

We insert the perturbed metric and scalar field from Eqs. (8.18)–(8.20) into the Einstein and Klein-Gordon equations, Eqs. (8.2) and (8.4), and expand to first order in the perturbations. For the metric functions, the (θ, ϕ)-component of the Einstein equations gives $h_2 = h_0$, and the (r, r)- and (r, θ)-components can be used to algebraically eliminate k and k' in favor of h_0 and its derivatives. Finally, the (t, t)-component leads to the following second-order differential equation:

$$\begin{aligned}
&h_0'' + \frac{e^u h_0'}{r}\left(1 + e^{-u} - 8\pi r^2 V_0\right) \\
&- \frac{32\pi e^u \phi_1}{r^2}\left[\phi_0'\left(-1 + e^{-u} - 8\pi r^2 p_{\rm rad}\right) + r\phi_0\left(U_0 - 2\omega^2 e^{-v}\right)\right] \\
&+ \frac{h_0 e^u}{r^2}\left[-16\pi r^2 V_0 - l(l+1) - e^u(1 - e^{-u} + 8\pi r^2 p_{\rm rad})^2 + 64\pi r^2 \omega^2 \phi_0^2 e^{-v}\right] = 0,
\end{aligned} \tag{8.21}$$

where we have also used the background equations (8.10a), (8.10b), and (8.15). From the linear perturbations to the Klein-Gordon equation, together with the results for the metric perturbations and the background equations, we obtain

$$\begin{aligned}
&\phi_1'' + \frac{e^u \phi_1'}{r}\left(1 - e^{-u} - 8\pi r^2 V_0\right) \\
&- e^u h_0\left[\phi_0'\left(-1 + e^{-u} - 8\pi r^2 p_{\rm rad}\right) + r\phi_0\left(U_0 - 2\omega^2 e^{-v}\right)\right] \\
&+ \frac{e^u \phi_1}{r^2}\left[8\pi r^2 V_0 - 1 + e^{-u} - l(l+1) - r^2\left(U_0 + 2W_0\phi_0^2\right)\right. \\
&\qquad \left. + r^2 e^{-v}\omega^2 - 32\pi e^{-u} r^2 \left(\phi_0'\right)^2\right] = 0,
\end{aligned} \tag{8.22}$$

where $W_0 = W(\phi_0)$ with $W(\phi) = dU/d|\Phi|^2$. These perturbation equations were also independently derived in Ref. [416] and are a special case of generic linear perturbations considered in the context of QNMs (see, e.g., Refs. [422–424]). As a check, we combined the three first-order and one algebraic constraint for the

spacetime perturbations from Ref. [424] into one second-order equation for h_0, which agrees with Eq. (8.21) in the limit of static perturbations. For the special case of mini BSs, the tidal perturbation equations were also obtained in Ref. [415].

The perturbations exhibit the following asymptotic behavior [424]

$$\lim_{r\to 0} h_0(r) \sim r^l, \tag{8.23a}$$

$$\lim_{r\to \infty} h_0(r) \sim c_1 \left(\frac{r}{M}\right)^{-(l+1)} + c_2 \left(\frac{r}{M}\right)^{l}, \tag{8.23b}$$

$$\lim_{r\to 0} \phi_1(r) \sim r^{l+1}, \tag{8.23c}$$

$$\lim_{r\to \infty} \phi_1(r) \sim r^{M\mu^2/\sqrt{\mu^2-\omega^2}} e^{-r\sqrt{\mu^2-\omega^2}}. \tag{8.23d}$$

8.3.3 Extracting the tidal deformability

The BS tidal deformability can be obtained in a similar manner as with NSs [307, 359, 447]. Working in the (nearly) vacuum region far from the center of the BS, the formalism developed for NSs remains (approximately) valid. For simplicity, we consider only $l = 2$ perturbations for the remainder of this section. The generalization of these results to arbitrary l is detailed in Ref. [307].

As shown in Eqs. (8.16) and (8.23), very far from the center of the BS, the system approaches vacuum exponentially. Neglecting the vanishingly small contributions from the scalar field, the metric perturbation reduces to the general form

$$h_0^{\rm vac} = c_1 \hat{Q}_{22}(x) + c_2 \hat{P}_{22}(x) + \mathcal{O}\left[(\phi_0)^1, (\phi_1)^1\right], \tag{8.24}$$

where we have defined $x \equiv r/M - 1$, $\hat{P}_{22}$ and $\hat{Q}_{22}$ are the associated Legendre functions of the first and second kind, respectively, normalized as in Ref. [307] such that

$\hat{P}_{22} \sim x^2$ and $\hat{Q}_{22} \sim 1/x^3$ when $x \to \infty$. The coefficients c_1 and c_2 are the same as in Eq. (8.23b).

In the BS's local asymptotic rest frame, the metric far from the star's center takes the form [449]

$$\begin{aligned} \bar{g}_{00} = &-1 + \frac{2M}{r} + \frac{3\mathcal{Q}_{ij}}{r^3}\left(n^i n^j - \frac{1}{3}\delta^{ij}\right) + \mathcal{O}\left(\frac{1}{r^4}\right) \\ &- \mathcal{E}_{ij}x^i x^j + \mathcal{O}\left(r^3\right) + \mathcal{O}\left[(\phi_0)^1, (\phi_1)^1\right], \end{aligned} \tag{8.25}$$

where $n^i = x^i/r$, $\mathcal{E}_{ij}$ is the external tidal field, and $\mathcal{Q}_{ij}$ is the induced quadrupole moment. Working to linear order in $\mathcal{E}_{ij}$, the tidal deformability $\lambda_{\rm Tidal}$ is defined such that

$$\mathcal{Q}_{ij} = -\lambda_{\rm Tidal}\mathcal{E}_{ij}. \tag{8.26}$$

For our purposes, it will be convenient to instead work with the dimensionless quantity

$$\Lambda \equiv \frac{\lambda_{\rm Tidal}}{M^5}. \tag{8.27}$$

Comparing Eqs. (8.24) and (8.25), one finds that the tidal deformability can be extracted from the asymptotic behavior of h_0 using

$$\Lambda = \frac{c_1}{3c_2}. \tag{8.28}$$

From Eq. (8.24), the logarithmic derivative

$$y \equiv \frac{d\log h_0}{d\log r} = \frac{rh_0'}{h_0}, \tag{8.29}$$

takes the form

$$y(x) = (1+x)\frac{3\Lambda\hat{Q}_{22}'(x) + \hat{P}_{22}'(x)}{3\Lambda\hat{Q}_{22}(x) + P_{22}(x)}, \tag{8.30}$$

or equivalently

$$\Lambda = -\frac{1}{3}\left(\frac{(1+x)\hat{P}'_{22}(x) - y(x)\hat{P}_{22}(x)}{(1+x)\hat{Q}'_{22}(x) - y(x)\hat{Q}_{22}(x)}\right). \tag{8.31}$$

Starting from a numerical solution to the perturbation equations (8.21) and (8.22), one obtains the deformability Λ by first computing y from Eq. (8.29) and then evaluating Eq. (8.31) at a particular extraction radius $x_{\rm Extract}$ far from the center of the BS. Details concerning the numerical extraction are described in Sec. 8.4 below.

8.4 Solving the background and perturbation equations

The background equations (8.10a)–(8.10c) and perturbation equations (8.21)–(8.22) form systems of coupled ordinary differential equations. These equations can be simplified by rescaling the coordinates and fields by μ (the mass of the boson field). To ease the comparison with previous work, we extend the definitions given in Ref. [424]: for massive BSs, we use

$$\begin{aligned} r &\to \frac{m^2_{\rm Planck}\tilde{r}}{\mu}, \qquad m(r) \to \frac{m^2_{\rm Planck}\tilde{m}(\tilde{r})}{\mu}, \\ \lambda &\to \frac{8\pi\mu^2\tilde{\lambda}}{m^2_{\rm Planck}}, \qquad \omega \to \frac{\mu\tilde{\omega}}{m^2_{\rm Planck}}, \\ \phi_0(r) &\to \frac{m_{\rm Planck}\tilde{\phi}_0(\tilde{r})}{(8\pi)^{1/2}}, \qquad \phi_1(r) \to \frac{m^2_{\rm Planck}\tilde{\phi}_1(\tilde{r})}{\mu(8\pi)^{1/2}}, \end{aligned} \tag{8.32}$$

while for solitonic BSs, we use

$$\begin{aligned} r &\to \frac{m^2_{\rm Planck}\tilde{r}}{\tilde{\sigma}_0\mu}, \qquad m(r) \to \frac{m^2_{\rm Planck}\tilde{m}(\tilde{r})}{\tilde{\sigma}_0\mu}, \\ \sigma_0 &\to \frac{m_{\rm Planck}\tilde{\sigma}_0}{(8\pi)^{1/2}}, \qquad \omega \to \frac{\tilde{\sigma}_0\mu\tilde{\omega}}{m^2_{\rm Planck}}, \\ \phi_0(r) &\to \frac{\sigma_0\tilde{\phi}_0(\tilde{r})}{(2)^{1/2}}, \qquad \phi_1(r) \to \frac{m^2_{\rm Planck}\tilde{\phi}_1(\tilde{r})}{(16\pi)^{1/2}\mu}, \end{aligned} \tag{8.33}$$

where factors of the Planck mass have been restored for clarity.

Finding solutions with the proper asymptotic behavior [Eqs. (8.16) and (8.23)] requires one to specify boundary conditions at both $\tilde{r} = 0$ and $\tilde{r} = \infty$. To impose these boundary conditions precisely, we integrate over a compactified radial coordinate

$$\zeta = \frac{\tilde{r}}{N + \tilde{r}}, \tag{8.34}$$

as is done in Ref. [450], where N is a parameter tuned so that exponential tails in the variables $\tilde{\phi}_0$ and $\tilde{\phi}_1$ [see Eqs. (8.16) and (8.23)] begin near the center of the domain $\zeta \in [0, 1]$. For massive BSs, we use N ranging from 20 to 60 depending on the body's compactness; for solitonic BSs we use N between 1 and 10.

Ground-state solutions to the background equations (8.10a)–(8.10c) can be completely parameterized by the central scalar field $\tilde{\phi}_0^{(c)}$ and frequency $\tilde{\omega}$. To determine the ground state frequency, we formally promote $\tilde{\omega}$ to an unknown constant function of $\tilde{r}$ and simultaneously solve both the background equations and

$$\tilde{\omega}'(\tilde{r}) = 0. \tag{8.35}$$

We impose the following boundary conditions on this combined system:

$$\begin{aligned} u(0) =& 0, \qquad \tilde{\phi}_0(0) = \tilde{\phi}_0^{(c)}, \qquad \tilde{\phi}_0'(0) = 0, \\ v(\infty) =& 0, \qquad \tilde{\phi}_0(\infty) = 0. \end{aligned} \tag{8.36}$$

Here, the inner boundary conditions ensure regularity at the origin, and the outer conditions guarantee asymptotic flatness.

The background and pertrubation equations are stiff, and therefore the shooting techniques usually used to solve two-point boundary value problems require

signficant fine-tuning to converge to a solution [424]. To avoid these difficulties, we use a standard relaxation algorithm that more easily finds a solution given a reasonable initial guess [430]. Once a solution is found for a particular choice of the central scalar field $\tilde{\phi}_0^{(c)}$ and scalar coupling (i.e., λ for massive BSs or σ_0 for solitonic BSs), this solution can be used as an initial guess to obtain nearby solutions. By iterating this process, one can efficiently generate many BS configurations.

After finding a background solution, we solve the perturbation equations (8.21) and (8.22). To improve numerical behavior of the perturbation equations near the boundaries, we factor out the dominant $\tilde{r}$ dependence and instead solve for

$$\bar{h}_0(\tilde{r}) \equiv h_0 \tilde{r}^{-2}, \tag{8.37}$$

$$\bar{\phi}_1(\tilde{r}) \equiv \tilde{\phi}_1 \tilde{r}^{-3}. \tag{8.38}$$

We employ the boundary conditions

$$\begin{aligned} \bar{h}_0(0) &= \bar{h}_0^{(c)}, \qquad \bar{h}_0'(0) = 0, \\ \bar{\phi}_1'(0) &= 0, \qquad \bar{\phi}_1(\infty) = 0, \end{aligned} \tag{8.39}$$

where the normalization $\bar{h}_0^{(c)}$ is an arbitrary non-zero constant.

Finally, we compute the tidal deformability using Eq. (8.31) in the nearly vacuum region $x \gg 1$. At very large distances, the exponential falloff of ϕ_0 and ϕ_1 is difficult to resolve numerically. This numerical error propagates through the computation of the tidal deformability in Eq. (8.31) for very large values of x. We find that extracting Λ at smaller radii provides more numerically stable results, with a typical variation of $\sim 0.1\%$ for different choices of extraction radius $x_{\rm Extract}$. For consistency, we extract Λ at the radius at which y attains its maximum.

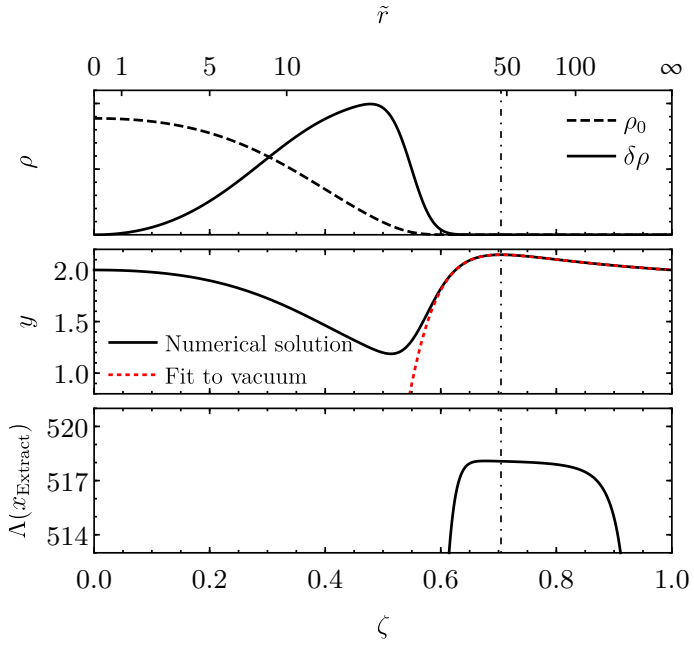

Figure 8.1: Perturbations of a massive BS as a function of rescaled coordinate $\tilde{r}$ and compactified coordinate ζ for a star of mass $M = 3.78 m^2_{\rm Planck}/\mu$ with coupling $\tilde{\lambda} = 300$. *Top panel:* The background density ρ_0 (dashed) and its first-order perturbation $\delta\rho$ (solid), rescaled to fit on the same plot. *Middle panel:* Logarithmic derivative y of the metric perturbation. The tidal deformability Λ is calculated using the numerically computed solution (black) at the peak of y (dot-dashed vertical line). Using this value for Λ, we plot corresponding expected behavior in vacuum (red) as given by Eq. (8.30). *Bottom panel:* Tidal deformability computed from Eq. (8.31) as a function of extraction radius $x_{\rm Extract}$.

Figure 8.1 demonstrates our procedure for computing the tidal deformability. The background and perturbation equations are solved for a massive BS with a coupling of $\tilde{\lambda} = 300$ using a compactified coordinate with $N = 20$. The profile of the effective density ρ, decomposed into its background value ρ_0 and first order correction $\delta\rho$, is shown in the top panel for a star of mass $3.78 m^2_{\rm Planck}/\mu$. Note that the magnitude of the perturbation is proportional to the strength of the external tidal field; to improve readability, we have scaled $\delta\rho$ to match the size of ρ_0.

The middle panel of Fig. 8.1 shows the computed logarithmic derivative y across the entire spacetime (black). We calculate the deformability with Eq. (8.31) using the peak value of y, located at the dot-dashed line. Comparing with the top panel, one sees that the scalar field is negligible in this region, justifying our use of formulae valid in vacuum. The bottom panel depicts the typical variation of Λ computed at different locations $x_{\rm Extract}$—our procedure yields consistent results provided one works reasonably close to the edge of the BS. As a check, we insert the computed value of Λ back into the vacuum solution for y given in Eq. (8.30), plotted in red in the middle panel. As expected, this curve closely matches the numerically computed solution at large radii, but deviates upon entering a region with non-negligible scalar field.

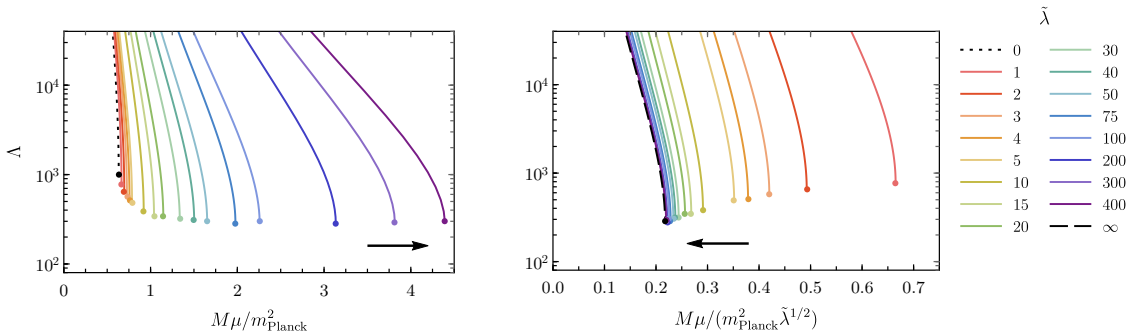

Figure 8.2: Dimensionless tidal deformability of a massive BS as a function of mass in units of (left) $m^2_{\rm Planck}/\mu$ and (right) $m^2_{\rm Planck}\tilde{\lambda}^{1/2}/\mu$. For each value of $\tilde{\lambda}$, the most compact stable configuration is highlighted with a colored dot. The arrows indicate the direction towards the strong-coupling regime, i.e. of increasing $\tilde{\lambda}$.

8.5 Results

8.5.1 Massive Boson Stars

The dimensionless tidal deformability of massive BSs is given as a function of the rescaled total mass $\tilde{M}$ [defined as in Eq. (8.32)] in the left panel of Fig. 8.2. The deformability in the weak-coupling limit $\tilde{\lambda} = 0$ is given by the dotted black curve; this limit corresponds to the mini BS model considered in Ref. [415].[4] One finds that the tidal deformability of the most massive stable star (colored dots) decreases from $\Lambda \sim 900$ in the weak-coupling limit towards $\Lambda \sim 280$ as $\tilde{\lambda}$ is increased. For large values of $\tilde{\lambda}$, the deformability exhibits a universal relation when written in terms of the rescaled mass $\tilde{M}/\tilde{\lambda}^{1/2}$ in the sense that the results for large $\tilde{\lambda}$ rapidly

[4] In Ref. [415], the authors computed the quantity $k_{\rm BS}$, related to the quantity Λ presented here by $k_{\rm BS} = \Lambda M^{10}$. The quantity k_2^E, computed in Ref. [416] for mini, massive, and solitonic BSs, is related to Λ by $k_2^E = (4\pi/5)^{1/2}\Lambda$.

approach a fixed curve as the coupling strength increases. This convergence towards the $\tilde{\lambda} = \infty$ relation is illustrated in the right panel of Fig. 8.2, in which the x-axis is rescaled by an additional factor of $\tilde{\lambda}^{1/2}$ relative to the left panel; in both panels, we have added black arrows to indicate the direction of increasing $\tilde{\lambda}$. Employing this rescaling of the mass, we compute the relation $\Lambda(\tilde{M}, \tilde{\lambda})$ in the strong-coupling limit $\tilde{\lambda} \to \infty$ below. The tidal deformability in this limit is plotted in Fig. 8.2 with a dashed black curve.

The gap in tidal deformability between BSs, for which the lowest values are $\Lambda \gtrsim 280$, and NSs, where for soft equations of state and large masses $\Lambda \gtrsim 10$, can be understood by comparing the relative size or compactness $C = M/R$ of each object. From the definitions (8.26) and (8.27), one expects the tidal deformability to scale as $\Lambda \propto 1/C^5$. In the strong-coupling limit, stable massive BSs can attain a compactness of $C_{\max} \approx 0.158$; note that in the exact strong-coupling limit $\tilde{\lambda} = \infty$, BSs develop a surface, and thus their compactness can be defined unambiguously. A NS of comparable compactness has a tidal deformability that is only ~ 0–25% larger than that of BSs. However, NS models predict stable stars with approximately twice the compactness that can be attained by massive BSs, and thus, their minimum tidal deformability is correspondingly much lower.

As argued in Sec. 8.2, the strong-coupling limit of massive BSs is the most plausible model investigated in this paper from an effective field theory perspective. We analyze the tidal deformability in this limit in greater detail. To study the strong-coupling limit of $\tilde{\lambda} \to \infty$, we employ a different set of rescalings introduced,

first in Ref. [428]:

$$
\begin{aligned}
r \to & \frac{m_{\rm Planck}^2 \tilde{\lambda}^{1/2} \hat{r}}{\mu}, \qquad m(r) \to \frac{m_{\rm Planck}^2 \tilde{\lambda}^{1/2} \hat{m}(\hat{r})}{\mu}, \\
\lambda \to & \frac{8\pi \mu^2 \tilde{\lambda}}{m_{\rm Planck}^2}, \qquad \omega \to \frac{\mu \hat{\omega}}{m_{\rm Planck}^2}, \\
\phi_0(r) \to & \frac{m_{\rm Planck} \hat{\phi}_0(\hat{r})}{(8\pi\tilde{\lambda})^{1/2}}, \qquad \phi_1(r) \to \frac{m_{\rm Planck}^2 \hat{\phi}_1(\hat{r})}{\mu (8\pi)^{1/2}},
\end{aligned}
\tag{8.40}
$$

where we have kept the previous notation for $\tilde{\lambda}$ to emphasize that it is the same quantity as defined in Eq. (8.32).

Keeping terms only at leading order in $\tilde{\lambda}^{-1} \ll 1$, Eqs. (8.10a)–(8.10c) become

$$
e^{-u}\left(-\frac{u'}{\hat{r}} + \frac{1}{\hat{r}^2}\right) - \frac{1}{\hat{r}^2} = -2\hat{\phi}_0^2 - \frac{3\hat{\phi}_0^4}{2}, \tag{8.41}
$$

$$
e^{-u}\left(\frac{v'}{\hat{r}} + \frac{1}{\hat{r}^2}\right) - \frac{1}{\hat{r}^2} = \frac{\hat{\phi}_0^4}{2}, \tag{8.42}
$$

$$
\hat{\phi}_0 = \left(\hat{\omega}^2 e^{-v} - 1\right)^{1/2}, \tag{8.43}
$$

where a prime denotes differentiation with respect to $\hat{r}$. Note that in particular, Eq. (8.10c) becomes an algebraic equation, reducing the system to a pair of first order differential equations.

Turning now to the perturbation equations, we use these rescalings and find that to leading order in $\tilde{\lambda}^{-1}$, Eqs. (8.21) and (8.22) become

$$
\begin{aligned}
& h_0'' + \frac{e^u h_0'}{\hat{r}}\left[\frac{\hat{r}^2}{2}\left(1 - e^{-2v}\hat{\omega}^4\right) + e^{-u} + 1\right] - \frac{e^u h_0}{\hat{r}^2}\left[+e^u(1-e^{-u})^2 + l(l+1)\right. \\
& \left. + \frac{\hat{r}^4 e^u}{4}\left(1 - e^{-v}\hat{\omega}^2\right)^4 + \hat{r}^2\left(e^u(1-e^{-v}\hat{\omega}^2)^2 + 10e^{-v}\hat{\omega}^2(1-e^{-v}\hat{\omega}^2) - 2\right)\right] = 0,
\end{aligned}
\tag{8.44}
$$

$$
\hat{\phi}_1 = \frac{h_0 \hat{r}\left(1 + \hat{\phi}_0^2\right)}{2\hat{\phi}_0}. \tag{8.45}
$$

As with the background fields, the equation for the scalar field $\hat{\phi}_1$ becomes algebraic in this limit. Note that the scalar perturbation diverges as one approaches the

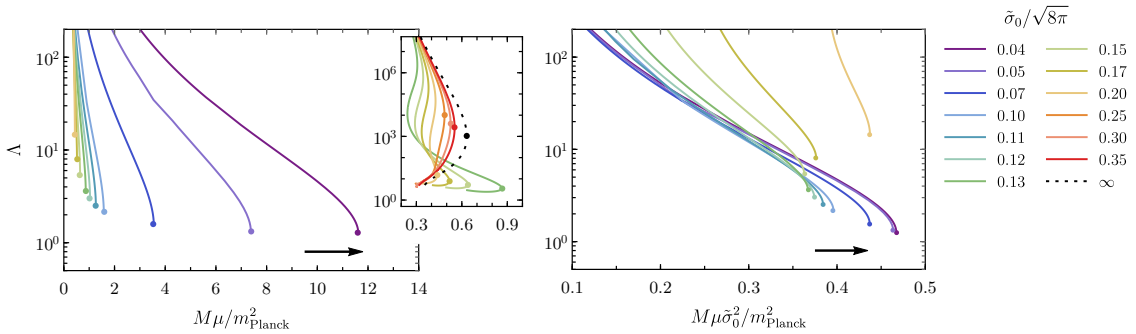

Figure 8.3: Dimensionless tidal deformability as a function BS mass in units of (left) $m^2_{\rm Planck}/\mu$ and (right) $m^2_{\rm Planck}/(\mu\tilde{\sigma}_0^2)$. For each value of $\tilde{\sigma}_0$, the most compact stable BS is highlighted with a colored dot. The inset plot in the left panel shows both stable and unstable configurations over a larger range of Λ to illustrate the weak-coupling limit $\tilde{\sigma}_0 \to \infty$ (dotted black). The arrows indicate the direction towards the strong-coupling regime, i.e. of decreasing $\tilde{\sigma}_0$; while not plotted explicitly, the strong-coupling limit $\tilde{\sigma}_0 \to 0$ corresponds the accumulation of curves in the right panel in the direction of the arrow.

surface of the BS, defined as the shell on which $\hat{\phi}_0$ vanishes. Nevertheless, the metric perturbation h_0 remains smooth over this surface.

We integrate the simplified background equations (8.41) and (8.42) and then the perturbation equation (8.44) using Runge-Kutta methods. We compute the tidal deformability using Eq. (8.31) evaluated at the surface of the BS, and plot the results in the right panel of Fig. 8.2 (dashed black).

8.5.2 Solitonic boson stars

The dimensionless tidal deformability of solitonic BSs is given as a function of the mass in Fig. 8.3. As in Fig. 8.2, the colored dots highlight the most massive stable configuration for different choices of the scalar coupling $\tilde{\sigma}_0$. To aid comparison

with the massive BS model, in the left panel we rescale the mass by an additional factor of $\tilde{\sigma}_0$ relative to the definition of $\tilde{M}$ in Eq. (8.33).

When the coupling $\tilde{\sigma}_0$ is strong, solitonic BSs can manifest two stable phases that can be smoothly connected through a sequence of unstable configurations [451]. The large plot in the left panel only shows stable configurations on the more compact branch of configurations. In the weak-coupling limit $\tilde{\sigma}_0 \to \infty$, solitonic BSs reduce to the free field model considered in Ref. [415]. To illustrate this limit, we show in the smaller inset the tidal deformability for both phases of BSs as well as the unstable configurations that bridge the two branches of solutions. The weak-coupling limit is depicted with a dotted black curve. We find that the tidal deformability of the less compact phase of BSs smoothly transitions from $\Lambda \to \infty$ in the strong-coupling limit ($\tilde{\sigma}_0 \to 0$)[5] to $\Lambda \sim 900$ in the weak-coupling limit ($\tilde{\sigma}_0 \to \infty$). Because their tidal deformability is so large, diffuse solitonic BSs of this kind would not serve as effective BH mimickers, and we will not discuss them for the remainder of this work. However, it should be noted that only this phase of stable configurations exists when $\sigma_0 \gtrsim 0.23\, m_{\rm Planck}$.

Focusing now on the more compact phase of solitonic BSs, one finds that the tidal deformability of the most massive stable star (colored dots) decreases towards $\Lambda \sim 1.3$ as $\tilde{\sigma}_0$ is decreased. As before, the relation between a rescaled mass and Λ approaches a finite limit in the strong coupling limit. We illustrate this in the right

[5] In the exact strong-coupling limit $\tilde{\sigma}_0 = 0$, this diffuse phase of solitonic BSs vanishes [429]. However, the tidal deformability of this branch of BS configurations can be made arbitrarily large by choosing $\tilde{\sigma}_0$ to be sufficiently small.

panel of Fig. 8.3 by rescaling the mass by an additional factor of $\tilde{\sigma}_0^{-1}$ relative to the definition in Eq. (8.33). While we do not examine the exact strong-coupling limit $\tilde{\sigma}_0 \to 0$ here, we find that the minimum deformability has converged to within a few percent of $\Lambda = 1.3$ for $0.03\, m_{\rm Planck} \leq \sigma_0 \leq 0.05\, m_{\rm Planck}$.

8.5.3 Fits for the relation between M and Λ

In this section we provide fits to our results for practical use in data analysis studies, focusing on the regime that is the most relevant region of the parameter space for BH and NS mimickers.

For massive BS, it is convenient to express the fit in terms of the variable

$$w = \frac{1}{1 + \tilde{\lambda}/8}, \tag{8.46}$$

which provides an estimate of the maximum mass in the weak-coupling limit $\tilde{M}_{\rm max} \approx 2/(\pi\sqrt{w})$ [452] and has a compact range $0 \leq w \leq 1$. A fit for massive BSs that is accurate[6] to $\sim 1\%$ for $\Lambda \leq 10^5$ and up to the maximum mass is given by

$$\begin{aligned}\sqrt{w}\tilde{M} = &\left[-0.529 + \frac{22.39}{\log\Lambda} - \frac{143.5}{(\log\Lambda)^2} + \frac{305.6}{(\log\Lambda)^3}\right] w \\ &+ \left[-0.828 + \frac{20.99}{\log\Lambda} - \frac{99.1}{(\log\Lambda)^2} + \frac{149.7}{(\log\Lambda)^3}\right] (1-w).\end{aligned} \tag{8.47}$$

The maximum mass where the BSs become unstable can be obtained from the extremum of this fit, which also determines the lower bound for Λ.

[6]The accuracy quoted here corresponds to the prediction for the mass at fixed Λ and coupling constant. The error in Λ at a fixed mass can be much larger, because Λ has a large gradient when varying the mass, which even diverges at the maximum mass. The applicability of our fits must be judged by the accuracy with which the masses can be measured from a GW signal.

In the solitonic case, a global fit for the tidal deformability for all possible values of σ_0 is difficult to obtain due to qualitative differences between the weak- and strong-coupling regimes. However, small values of σ_0 are most interesting, since they allow for the widest range for the tidal deformability and compactness. A fit for $\sigma_0 = 0.05\, m_{\rm Planck}$ accurate to better than 1% and valid for $\Lambda \leq 10^4$ (and again up to the maximum mass) reads

$$\log(\sigma_0 \tilde{M}) = -30.834 + \frac{1079.8}{\log\Lambda + 19} - \frac{10240}{(\log\Lambda + 19)^2}. \tag{8.48}$$

This fit is expected to be accurate for $0 \leq \sigma_0 \lesssim 0.05\, m_{\rm Planck}$, i.e., including the strong coupling limit $\sigma_0 = 0$, within a few percent. Notice that this fit remains valid through tidal deformabilities of the same magnitude as that of NSs.

8.6 Prospective constraints

8.6.1 Estimating the precision of tidal deformability measurements

Gravitational-wave detectors will be able to probe the structure of compact objects through their tidal interactions in binary systems, in addition to effects seen in the merger and ringdown phases. In this section, we discuss the possibility of distinguishing BSs from NSs and BHs using only tidal effects. We emphasize that our results in this section are based on several approximations and should be viewed only as estimates that provide lower bounds on the errors and can be used to identify promising scenarios for future studies with Bayesian data analysis and improved waveform models.

The parameter estimation method based on the Fisher information matrix is discussed in detail in Ref. [394]. This approximation yields only a lower bound on the errors that would be obtained from a Bayesian analysis. We assume that a detection criterion for a GW signal $h(t;\boldsymbol{\theta})$ has been met, where $\boldsymbol{\theta}$ are the parameters characterizing the signal: the distance D to the source, time of merger t_c, five positional angles on the sky, plane of the orbit, orbital phase at some given time ϕ_c, as well as a set of intrinsic parameters such as orbital eccentricity, masses, spins, and tidal parameters of the bodies. Given the detector output $s = h(t) + n$, where n is the noise, the probability $p(\boldsymbol{\theta}|s)$ that the signal is characterized by the parameters $\boldsymbol{\theta}$ is

$$p(\boldsymbol{\theta}|s) \propto p^{(0)} e^{-\frac{1}{2}(h(\boldsymbol{\theta})-s|h(\boldsymbol{\theta})-s)}, \tag{8.49}$$

where $p^{(0)}$ represents a priori knowledge. Here, the inner product $(\cdot|\cdot)$ is determined by the statistical properties of the noise and is given by

$$(h_1|h_2) = 2\int_0^\infty \frac{\tilde{h}_1^*(f)\tilde{h}_2(f) + \tilde{h}_2^*(f)\tilde{h}_1(f)}{S_n(f)} df, \tag{8.50}$$

where $S_n(f)$ is the spectral density describing the Gaussian part of the detector noise. For a measurement, one determines the set of best-fit parameters $\hat{\boldsymbol{\theta}}$ that maximize the probability distribution function (8.49). In the regime of large signal-to-noise ratio SNR $= \sqrt{(h|h)}$, for a given incident GW in different realizations of the noise, the probability distribution $p(\boldsymbol{\theta}|s)$ is approximately given by

$$p(\boldsymbol{\theta}|s) \propto p^{(0)} e^{-\frac{1}{2}\Gamma_{ij}\Delta\theta^i\Delta\theta^j}, \tag{8.51}$$

where

$$\Gamma_{ij} = \left(\frac{\partial h}{\partial\theta^i}\middle|\frac{\partial h}{\partial\theta^j}\right), \tag{8.52}$$

is the so-called Fisher information matrix. For a uniform prior $p^{(0)}$, the distribution (8.51) is a multivariate Gaussian with covariance matrix $\Sigma^{ij} = (\mathbf{\Gamma}^{-1})^{ij}$ and the root-mean-square measurement errors in θ^i are given by

$$\sqrt{\langle(\Delta\theta^i)^2\rangle} = \sqrt{(\mathbf{\Gamma}^{-1})^{ii}}, \tag{8.53}$$

where angular brackets denote an average over the probability distribution function (8.51).

We next discuss the model $\tilde{h}(f, \boldsymbol{\theta})$ for the signal. For a binary inspiral, the Fourier transform of the dominant mode of the signal has the form

$$\tilde{h}(f, \boldsymbol{\theta}) = \mathcal{A}(f, \boldsymbol{\theta}) e^{i\psi(f,\boldsymbol{\theta})}. \tag{8.54}$$

Using a PN expansion and the stationary-phase approximation (SPA), the phase ψ is computed from the energy balance argument by solving

$$\frac{d^2\psi}{d\Omega^2} = \frac{2}{d\Omega/dt} = 2\frac{(dE/d\Omega)}{\dot{E}_{\rm GW}}, \tag{8.55}$$

where E is the energy of the binary system, $\dot{E}_{\rm GW}$ is the energy flux in GWs, and $\Omega = \pi f$ is the orbital frequency. The result is of the form

$$\psi = \frac{3}{128(\pi\mathcal{M}f)^{5/2}}\left[1 + \alpha_{\rm 1PN}(\nu)x + \ldots + \left(\alpha^{\rm Newt}_{\rm tidal} + \alpha_{\rm 5PN}(\nu)\right)x^5 + \mathcal{O}(x^6)\right], \tag{8.56}$$

with $x = (\pi M f)^{2/3}$, $M = m_1 + m_2$, $\nu = m_1 m_2/M^2$, $\mathcal{M} = \nu^{3/5}M$, and the dominant tidal contribution is

$$\alpha^{\rm Newt}_{\rm tidal} = -\frac{39}{2}\tilde{\Lambda}. \tag{8.57}$$

Here, $\tilde{\Lambda}$ is the weighted average of the individual tidal deformabilities, given by

$$\tilde{\Lambda}(m_1, m_2, \Lambda_1, \Lambda_2) = \frac{16}{13}\left[\left(1 + 12\frac{m_2}{m_1}\right)\frac{m_1^5}{M^5}\Lambda_1 + (1 \leftrightarrow 2)\right]. \tag{8.58}$$

The phasing in Eq. (8.56) is known as the "TaylorF2 approximant." Specifically, we use here the 3.5PN point-particle terms [30] and the 1PN tidal terms [453]. At 1PN order, a second combination of tidal deformability parameters enters into the phasing in addition to $\tilde{\Lambda}$. This additional parameter vanishes for equal-mass binaries and will be difficult to measure with Advanced LIGO [454, 455]. For simplicity, we omit this term from our analysis.

The tidal correction terms in Eq. (8.56) enter with a high power of the frequency, indicating that most of the information on these effects comes from the late inspiral. This is also the regime where the PN approximation for the point-mass dynamics becomes inaccurate. To estimate the size of the systematic errors introduced by using the TaylorF2 waveform model in our analysis, we compare the model against predictions from a tidal EOB (TEOB) model. The accuracy of the TEOB waveform model has been verified for comparable-mass binaries through comparison with NR simulations; see, for example, Ref. [292]. For our comparison, we use the same TEOB model as in Ref. [292]. The point-mass part of this model—known as "SEOBNRv2"—has been calibrated with binary black hole (BBH) results from NR simulations. The added tidal effects are adiabatic quadrupolar tides including tidal terms at relative 2PN order in the EOB Hamiltonian and 1PN order in the fluxes and waveform amplitudes. The SPA phase for the TEOB model is computed by solving the EOB evolution equations to obtain $\Omega(t)$, numerically inverting this result for $t(\Omega)$, and solving Eq. (8.55) to arrive at $\psi(\Omega)$.

Figure 8.4 shows the difference in predicted phase from the TEOB model and the TaylorF2 model (8.56) for two nearly equal mass binary NS (BNS) systems.

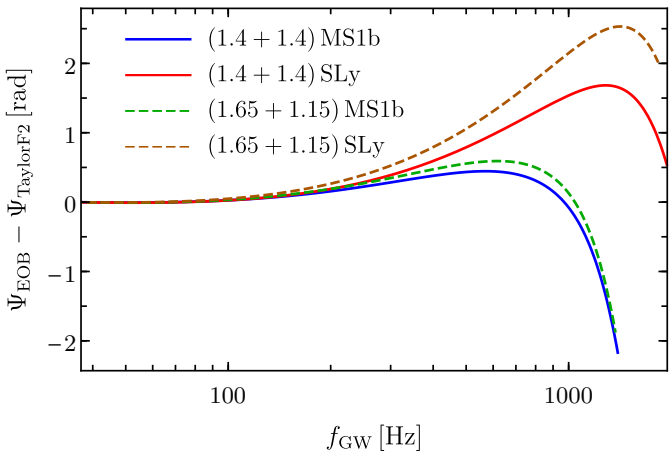

Figure 8.4: Dephasing between the TEOB and tidal TaylorF2 models for non-spinning BNS systems including adiabatic quadrupolar tidal effects. The curves end at the prediction for the merger from NR simulations described in Ref. [458]. The labels denote the masses (in units of $M_\odot$) and EoS of the NSs.

For our analysis, we consider two representative equations of state (EoS) for NSs: the relatively soft SLy model [456] and the stiff MS1b EoS [457]. Figure 8.4 illustrates that the dephasing between the TaylorF2 and TEOB waveforms remains small compared to the size of tidal effects, which is on the order of $\gtrsim 20$ rad for MS1b $(1.4 + 1.4)M_\odot$. Thus, we conclude that the TaylorF2 approximant is sufficiently accurate for our purposes and leave an investigation of the measurability of tidal parameters with more sophisticated waveform models for future work.

Besides the waveform model, the computation of the Fisher matrix also requires a model of the detector noise. We consider here the Advanced LIGO Zero-Detuned High Power configuration [389]. To assess the prospects for measurements with third-generation detectors we also use the ET-D [388] and Cosmic Explorer

[367] noise curves.

To compute the measurement errors we specialize to the restricted set of signal parameters $\boldsymbol{\theta} = \{\phi_c, t_c, \mathcal{M}, \nu, \tilde{\Lambda}\}$. The extrinsic parameters of the signal such as orientation on the sky enter only into the waveform's amplitude and can be treated separately; they are irrelevant for our purposes. Spin parameters are omitted because the TaylorF2 approximant inadequately captures these effects and one would instead need to use a more sophisticated model such as SEOBNR. We restrict our analysis to systems with low masses $M \lesssim 12M_\odot$ [259] for which the merger occurs at frequencies $f_{\rm merger} > 900$Hz so that the information is dominated by the inspiral signal. The termination conditions for the inspiral signal employed in our analysis are the predicted merger frequencies from NR simulations: for BNSs the formula from Ref. [458], and for BBH that from Ref. [459].

Ultimately, we need to convert our measurements of $\{\mathcal{M}, \nu, \tilde{\Lambda}\}$ into estimates of the individual masses and tidal deformabilities $\{m_1, m_2, \Lambda_1, \Lambda_2\}$. Comparing the dimensions of these two parameter spaces, one can immediately see that this transformation is underdetermined; any given measurement of $\{\mathcal{M}, \nu, \tilde{\Lambda}\}$ corresponds to a one-dimensional subspace of compatible choices for Λ_1 and Λ_2. However, this infinite range of Λ_1 and Λ_2 can be constrained through physically motivated assumptions on the relative size of Λ_1 and Λ_2. While we remain unable to estimate each body's tidal deformability precisely, we can at least place bounds on these quantities. The details of this analysis are presented below.

We adopt the convention that $m_1 \geq m_2$. For any realistic, stable self-gravitating body, we expect an increase in mass to also increase the body's compactness. Be-

cause the tidal deformability scales as $\Lambda \propto 1/C^5$, we assume that $\Lambda_1 \leq \Lambda_2$ provided that both bodies are the same type of compact object (e.g. NS, massive BS, solitonic BS, etc.). Furthermore, we assume that both tidal deformabilities are non-negative, as is the case for all compact objects we consider here.

Next, we consider the combinations of tidal deformabilities Λ_1, Λ_2 that are consistent with a particular set of measurements $\{\mathcal{M}^*, \nu^*, \tilde{\Lambda}^*\}$, or equivalently, a particular set of measurements $\{m_1^*, m_2^*, \tilde{\Lambda}^*\}$. Employing the assumption that $\Lambda_1 \leq \Lambda_2$, one finds that the deformability of the more massive object Λ_1 takes its maximal value when it is exactly equal to Λ_2, i.e. when $\tilde{\Lambda}^* = \tilde{\Lambda}(m_1^*, m_2^*, \Lambda_1, \Lambda_1)$. Conversely, Λ_2 takes its maximal value when Λ_1 vanishes exactly so that $\tilde{\Lambda}^* = \tilde{\Lambda}(m_1^*, m_2^*, 0, \Lambda_2)$. Substituting the expression for $\tilde{\Lambda}$ from Eq. (8.58) and using that $m_{1,2} = M(1 \pm \sqrt{1-4\nu})/2$ leads to the following bounds on the individual deformabilities

$$\Lambda_1 \leq g_1(\nu)\tilde{\Lambda}, \qquad \Lambda_2 \leq g_2(\nu)\tilde{\Lambda}, \tag{8.59}$$

where the functions g_i are given by

$$g_1(\nu) \equiv \frac{13}{16(1+7\nu-31\nu^2)}, \tag{8.60a}$$

$$g_2(\nu) \equiv \frac{13}{8\left[1+7\nu-31\nu^2-\sqrt{1-4\nu}\,(1+9\nu-11\nu^2)\right]}, \tag{8.60b}$$

and where we have dropped the asterisks for simplicity. Thus, the expected measurement precision of ν and $\tilde{\Lambda}$ provide an estimate of the precision with which Λ_1 and Λ_2 can be measured through

$$\Delta\Lambda_1 \leq \left[\left(g_1(\nu)\Delta\tilde{\Lambda}\right)^2 + \left(g_1'(\nu)\tilde{\Lambda}\Delta\nu\right)^2\right]^{1/2}, \tag{8.61a}$$

$$\Delta\Lambda_2 \leq \left[\left(g_2(\nu)\Delta\tilde{\Lambda}\right)^2 + \left(g_2'(\nu)\tilde{\Lambda}\Delta\nu\right)^2\right]^{1/2}, \tag{8.61b}$$

For simplicity, we have assumed in Eq. (8.61) that the statistical uncertainty in ν and $\tilde{\Lambda}$ is uncorrelated. Note that for BBH signals, this assumption is unnecessary because $\tilde{\Lambda} = 0$, and thus the second terms in Eqs. (8.61a) and (8.61b) vanish.

In the following subsections, we outline two tests to distinguish conventional GW sources from BSs and discuss the prospects of successfully differentiating the two with current- and third-generation detectors. First, we investigate whether one could accurately identify each body in a binary as a BH/NS rather than a BS. This test is only applicable to objects whose tidal deformability is significantly smaller than that of a BS, e.g., BHs and very massive NSs. For bodies whose tidal deformabilities are comparable to that of BSs, we introduce a novel analysis designed to test the slightly weaker hypothesis: can the binary system of BHs or NSs be distinguished from a binary BS (BBS) system? For both tests, we will assume that the true waveforms we observe are produced by BBH or BNS systems and then assess whether the resulting measurements are also consistent with the objects being BSs. In our analyses we consider only a single detector and assume that the sources are optimally oriented; to translate our results to a sky- and inclination-averaged ensemble of signals, one should divide the expected SNR by a factor of $\sqrt{2}$ and thus multiply the errors on $\Delta\tilde{\Lambda}$ by the same factor.

We consider two fiducial sets of binary systems in our analysis. First, we consider BBHs at a distance of 400 Mpc (similar to the distances at which GW150914 and GW151226 were observed [73, 184]) with total masses in the range $8M_\odot \leq M \leq 12M_\odot$. This range is determined by the assumption that the lowest BH mass is $4M_\odot$ and the requirement that the merger occurs at frequencies above ~ 900 Hz so the

information in the signal is dominated by the inspiral. The SNRs for these systems range from approximately 20 to 49 given the sensitivity of Advanced LIGO. The second set of systems that we consider are BNSs at a distance of 200 Mpc and with total masses $2M_\odot \leq M \leq M_{\rm max}$, where $M_{\rm max}$ is twice the maximum NS mass for each equation of state. The lower limit on this mass range comes from astrophysical considerations on NS formation [460]. The BNS distance was chosen to describe approximately one out of every ten events within the expected BNS range of ~ 300 Mpc for Advanced LIGO and translates to SNR $\sim 12-22$ for the SLy equation of state.

8.6.2 Distinguishability with a single deformability measurement

A key finding from Sec. 8.5 is that the tidal deformability is bounded below by $\Lambda \gtrsim 280$ for massive BSs and $\Lambda \gtrsim 1.3$ for solitonic BSs. By comparison, the deformability of BHs vanishes exactly, i.e. $\Lambda = 0$, whereas for nearly-maximal mass NSs, the deformability can be of order $\Lambda \approx \mathcal{O}(10)$. Thus, a BH or high-mass NS could be distinguished from a massive BS provided that a measurement error of $\Delta\Lambda \approx 200$ can be reached with GW detectors. Similarly, to distinguish a BH from a solitonic BS requires a measurement precision of $\Delta\Lambda \approx 1$.

The results for the measurement errors with Advanced LIGO for BBH systems at 400 Mpc are shown in Fig. 8.5, for a starting frequency of 10 Hz. The left panel shows the error in the combination $\tilde{\Lambda}$ that is directly computed from the Fisher matrix as a function of total mass M and mass ratio $q = m_1/m_2$. As discussed above,

the ranges of M and q we consider stem from our assumptions on the minimum BH mass and a high merger frequency. The right panel of Fig. 8.5 shows the inferred bound on the less well-measured individual deformability in the regime of unequal masses. We omit the region where the objects have nearly equal masses $q \to 1$ because in this regime, the 68% confidence interval $\nu + 2\Delta\nu$ exceeds the physical bound $\nu \leq 1/4$. Inferring the errors on the parameters of the individual objects requires a more sophisticated analysis [394] than that considered here. The coloring ranges from small errors in the blue shaded regions to large errors in the orange shaded regions; the labeled black lines are representative contours of constant $\Delta\Lambda$. Note that the errors on the individual deformability Λ_2 are always larger than those on the combination $\tilde{\Lambda}$.

We find that the tidal deformability of our fiducial BBH systems can be measured to within $\Delta\Lambda \lesssim 100$ by Advanced LIGO, which indicates that BHs can be readily distinguished from massive BSs. However, even for ideal BBHs—high mass, low mass-ratio binaries—the tidal deformability of each BH can only be measured within $\Delta\Lambda \gtrsim 15$ by Advanced LIGO. Therefore one cannot distinguish BHs from solitonic BSs using estimates of each bodies' deformability alone. Given these findings, we also estimate the precision with which the tidal deformability could be measured with third-generation instruments. Compared to Advanced LIGO, the measurement errors in the tidal deformability decrease by factors of ~ 13.5 and ~ 23.5 with Einstein telescope and Cosmic Explorer, respectively. Thus, the more massive BH in the binary would be marginally distinguishable from a solitonic BS with future GW detectors, as $\Delta\Lambda_1 \leq \Delta\tilde{\Lambda} \lesssim 1$. These findings are consistent with

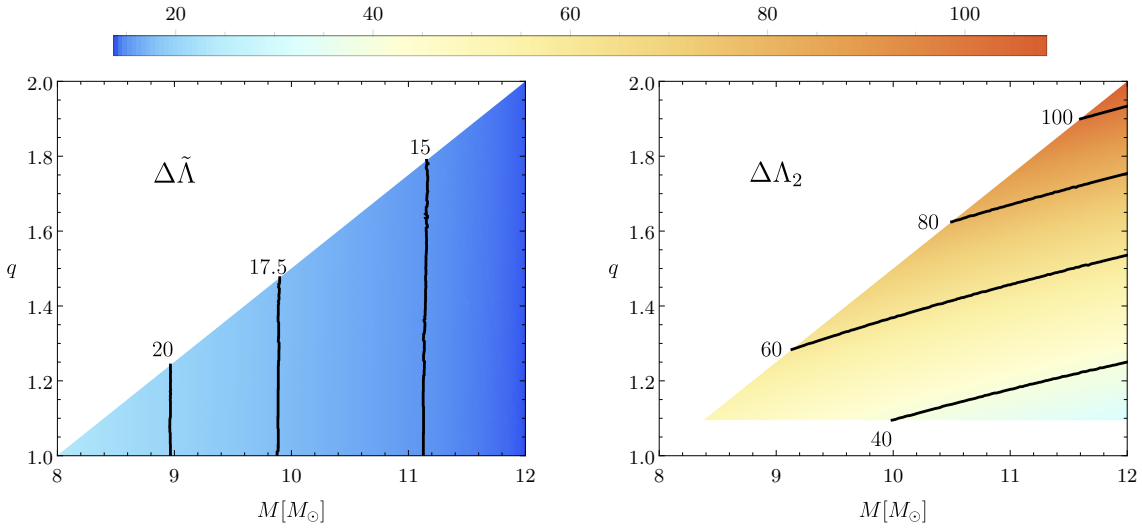

Figure 8.5: Estimated measurement error with Advanced LIGO of (left) the weighted average tidal parameter $\tilde{\Lambda}$ and (right) the less well-constrained individual tidal parameter Λ_2 for BBH systems at 400 Mpc. The black lines are contours of constant $\Delta\tilde{\Lambda}$ and $\Delta\Lambda_2$ in the left and right plots, respectively.

the conclusions of Cardoso et al [416], although these authors considered only equal-mass binaries at distances $D = 100$Mpc with total masses up to $50M_\odot$. However, we find that in an unequal-mass BBH case, the less massive body could not be differentiated from a solitonic BS even with third-generation detectors.

Next, we consider the measurements of a BNS system, shown in Fig. 8.6 assuming the SLy EoS. We restrict our analysis to systems with individual masses $1M_\odot \leq m_{\rm NS} \leq m_{\rm max}$, where $m_{\rm max} \approx 2.05M_\odot$ is the maximum mass for this EoS. Similar to Fig. 8.5, the left panel in Fig. 8.6 shows the results for the measurement error in the combination $\tilde{\Lambda}$ directly computed from the Fisher matrix, and the right panel shows the error for the larger of the individual deformabilities. The slight

warpage of the contours of constant $\Delta\tilde{\Lambda}$ compared to those in Fig. 8.5, best visible for the $\Delta\tilde{\Lambda} = 50$ contour, is due to an additional dependence of the merger frequency on $\tilde{\Lambda}$ for BNSs that is absent for BBHs, and a small difference in the Fisher matrix elements when evaluated for $\tilde{\Lambda} \neq 0$. We see that the deformability of NSs of nearly maximal mass in BNS systems can be measured to within $\Delta\Lambda \lesssim 200$, and thus can be distinguished from massive BSs. However, the measurement precision worsens as one decreases the NS mass, rendering lighter NSs indistinguishable from massive BSs using only each bodies deformability alone. In the next subsection, we discuss how combining the measurements of Λ for each object in a binary system can improve distinguishability from BSs even when the criteria discussed above are not met.

For completeness, we also computed how well third-generation detectors could measure the tidal deformabilities in BNS systems. As in the BBH case, we find that measurement errors in Λ decrease by factors of ~ 13.5 and ~ 23.5 with the Einstein Telescope and Cosmic Explorer, respectively. However, the conclusions reached above concerning the distinguishability of BHs or NSs and BSs remain unchanged.

8.6.3 Distinguishability with a pair of deformability measurements

In the previous subsection we determined that compact objects whose tidal deformability is much smaller than that of BSs could be distinguished as such with Advanced LIGO, e.g., BHs versus massive BSs. In this subsection, we present a more refined analysis to distinguish compact objects from BSs when the deformabilities

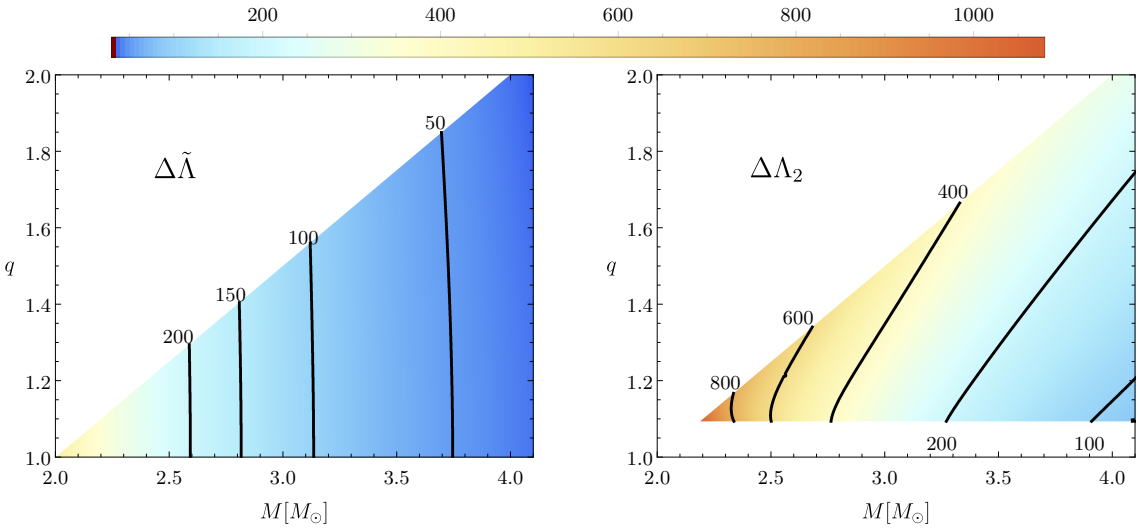

Figure 8.6: Estimated measurement error with Advanced LIGO of (left) the weighted average tidal parameter $\tilde{\Lambda}$ and (right) the less well-constrained individual tidal parameter Λ_2 for BNS systems at 200 Mpc with the SLy equation of state. The black lines are contours of constant $\Delta\tilde{\Lambda}$ and $\Delta\Lambda_2$ in the left and right plots, respectively.

of each are of approximately the same size. In particular, we focus on the prospects of distinguishing NSs between one and two solar masses from massive BSs and distinguishing BHs from solitonic BSs. Throughout this section, we only consider the possibility that a single species of BS exists in nature; differentiation between multiple, distinct complex scalar fields goes beyond the scope of this work. We show that combining the tidal deformability measurements of each body in a binary system can break the degeneracy in the BS model associated with choosing the boson mass μ. Utilizing the mass and deformability measurements of both bodies allows one to distinguish the binary system from a BBS system.

In Figs. 8.2 and 8.3, the tidal deformability of BSs was given as a function of mass rescaled by the boson mass and self-interaction strength. By simultaneously adjusting these two parameters of the BS model, one can produce stars with the same (unrescaled) mass and deformability. This degeneracy presents a significant obstacle in distinguishing BSs from other compact objects with comparable deformabilities. For example, the boson mass can be tuned for any value of the coupling λ (σ_0) so that the massive (solitonic) BS model admits stars with the exact same mass and tidal deformability as a solar mass NS. However, combining two tidal deformability measurements can break this degeneracy and improve the distinguishability between BSs and BHs or NSs. As an initial investigation into this type of analysis, we pose the following question: given a measurement (m_1, Λ_1) of a compact object in a binary, can the observation (m_2, Λ_2) of the companion exclude the possibility that both are BSs? We stress that our analysis is preliminary and that only qualitative conclusions should be drawn from it; a more thorough study goes beyond the scope

of this work.

From the Fisher matrix estimates for the errors in $(\mathcal{M}, \nu, \tilde{\Lambda})$ we obtain bounds on the uncertainty in the measurement (m_i, Λ_i) for each body in a binary, which we approximate as being characterized by a bivariate normal distribution with covariance matrix $\mathbf{\Sigma} = \mathrm{diag}(\Delta m_i, \Delta\Lambda_i)$. Figure 8.7 depicts such potential measurements by Advanced LIGO of (m_1, Λ_1) and (m_2, Λ_2), shown in black, for a $(1.55 + 1.35)M_\odot$ BNS system at a distance of 200 Mpc with two representative equations of state for the NSs: the SLy and MS1b models discussed above. The dashed black curves in Figure 8.7 show the $\Lambda(m)$ relation for these fiducial NSs. Figure 8.8 shows the corresponding measurements in a 6.5–4.5$M_\odot$ BBH measured at 400 Mpc made by Advanced LIGO, Einstein Telescope, and Cosmic Explorer in blue, red, and black, respectively.

The strategy to determine if the objects could be BSs is the following. Consider first the measurement (m_2, Λ_2) of the less massive body. For each point $\mathbf{x} = (m, \Lambda)$ within the 1σ ellipse, we determine the combinations of theory parameters $(\mu, \lambda)[\mathbf{x}]$ or $(\mu, \sigma_0)[\mathbf{x}]$ that could give rise to such a BS, assuming the massive or solitonic BS model, respectively. As discussed above, in general, λ or σ_0 can take any value by appropriately rescaling μ. Finally, we combine all mass-deformability curves from Figs. 8.2 or 8.3 that pass through the 1σ ellipise, that is we consider the model parameters $(\mu, \lambda) \in \bigcup_{\mathbf{x}}(\mu, \lambda)[\mathbf{x}]$ or $(\mu, \sigma_0) \in \bigcup_{\mathbf{x}}(\mu, \sigma_0)[\mathbf{x}]$ for massive and solitonic BS, respectively. These portions of BS parameter space are shown as the shaded regions in Figs. 8.7 and 8.8. If the tidal deformability measurements (m_1, Λ_1) of the more massive body—indicated by the other set of crosses—lie outside of these

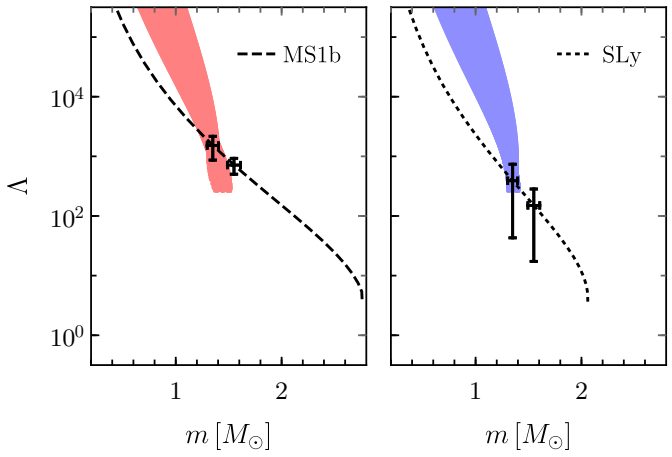

Figure 8.7: Dimensionless tidal deformability as a function of mass. Black points indicate hypothetical measurements of a $(1.55 + 1.35)M_\odot$ binary NS system with the (left) MS1b and (right) SLy EoS; the error bars are estimated for a system observed at 200 Mpc. The shaded regions depict all possible massive BSs (i.e., all possible values of the boson mass μ and coupling λ) consistent with the measurement of the smaller compact object. For the MS1b EoS, the tidal deformabilities of the binary are $\Lambda_{1.55} = 714$ and $\Lambda_{1.35} = 1516$. For the SLy EoS, the tidal deformabilites are $\Lambda_{1.55} = 150$ and $\Lambda_{1.35} = 390$.

shaded regions, one can conclude that the measurements are inconsistent with both objects being BSs.

Figure 8.7 demonstrates that an asymmetric BNS with masses 1.55–1.35$M_\odot$ can be distinguished from a BBS with Advanced LIGO by using this type of analysis. When considered individually, either NS measurement shown here would be consistent with a possible massive BS; by combining these measurements we improve our ability to differentiate the binary systems. This type of test can better distinguish BBSs from conventional GW sources than the analysis performed in the previous section because it utilizes measurements of both the mass and tidal deformability

rather than just using the deformability alone. However the power of this type of test hinges on the asymmetric mass ratio in the system; with an equal-mass system, this procedure provides no more information than that described in Section 8.6.2.

A similar comparison between a BBH with masses 6.5–4.5$M_\odot$ and a binary solitonic BS system is illustrated in Fig. 8.8. For simplicity, the yellow shaded region depicts all possible solitonic BSs for a particular choice of coupling $\sigma_0 = 0.05\, m_{\rm Planck}$ that are consistent with the measurement of the smaller mass by Advanced LIGO (rather than all possible values of the coupling σ_0). We see that in contrast to the massive BS case, after fixing the boson mass μ with the measurement of one body, the measurement of the companion remains within that shaded region. As with the more simplistic analysis performed in Section 8.6.2, we again find that Advanced LIGO will be unable to distinguish solitonic BSs from BHs.

In the previous section, we showed that third-generation GW detectors will be able to distinguish marginally at least one object in a BBH system from a solitonic BS and thus determine whether a GW signal was generated by a BBS system. Using the analysis introduced in this section, we can now strengthen this conclusion. We repeat the procedure described above for a 6.5–4.5$M_\odot$ BBH at 400 Mpc but instead use the 3σ error estimates in the measurements of the bodies' mass and tidal deformability. In Fig. 8.8, all possible solitonic BSs consistent with the measurement of the smaller mass are shown in green and pink for Einstein Telescope and Cosmic Explorer, respectively. We see that while the deformability measurements of each BH considered individually are consistent with either being solitonic BSs, they cannot both be BSs. Thus, we can conclude with much greater confidence

that third-generation detectors will be able to distinguish BBH systems from binary systems of solitonic BSs.

To summarize, the precision expected from Advanced LIGO is potentially sufficient to differentiate between massive BSs and NSs or BHs, particularly in systems with larger mass asymmetry. Advanced LIGO is not sensitive enough to discriminate between solitonic BSs and BHs, but next-generation detectors like the Einstein Telescope or Cosmic Explorer should be able to distinguish between BBS and BBH systems. However, we emphasize again that our conclusions are based on several approximations and further studies are needed to make these precise. We also note that we have deliberately restricted our analysis to the parameter space where waveforms are inspiral-dominated in Advanced LIGO. Tighter constraints on BS parameters are expected for binaries where information can also be extracted from the merger and ringdown portion, provided that waveform models that include this regime are available.

8.7 Conclusions

Gravitational waves can be used to test whether the nature of BHs and NSs is consistent with GR and to search for exotic compact objects outside of the standard astrophysical catalog. A compact object's structure is imprinted in the GW signal produced by its coalescence with a companion in a binary system. A key target for such tests is the characteristic ringdown signal of the final remnant. However, the small SNR of that part of the GW signal complicates such efforts. Complementary

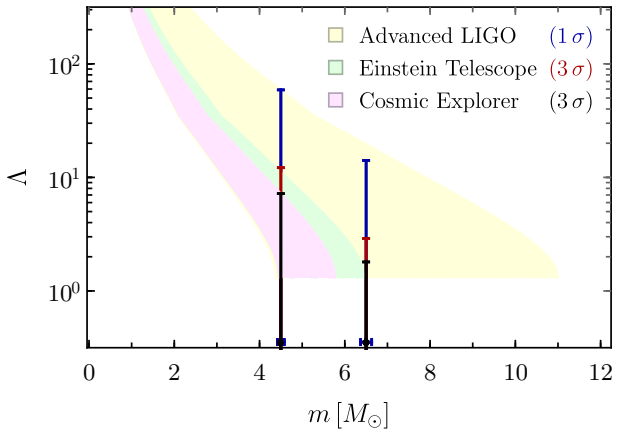

Figure 8.8: Dimensionless tidal deformability as a function of mass. Hypothetical measurements of a $(6.5+4.5)M_\odot$ binary BH system with error bars estimated for a system observed at 400 Mpc by Advanced LIGO, the Einstein Telescope, and Cosmic Explorer are given in blue, red, and black, respectively. The shaded regions depict all possible solitonic BSs with coupling $\sigma_0 = 0.05\, m_{\rm Planck}$ that are consistent with the measurements of the smaller compact object by each detector.

information can be obtained by measuring a small but cumulative signature due to tidal effects in the inspiral that depend on the compact object's structure through its tidal deformability. This quantity may be measurable from the late inspiral and could be used to distinguish BHs or NSs from exotic compact objects.

In this work, we computed the tidal deformability Λ for two models of BSs: *massive BSs*, characterized by a quartic self-interaction, and *solitonic BSs*, whose scalar self-interaction is designed to produce very compact objects. For the quartic interaction, our results span the entire two-dimensional parameter space of such a model in terms of the mass of the boson and the coupling constant in the potential. For the solitonic case, our results span the portion of interest for BH mimickers. We presented fits to our results for both cases that can be used in future data

analysis studies. We find that the deformability of massive BSs is markedly larger than that of BHs and very massive NSs; in particular, we showed that the tidal deformability $\Lambda \gtrsim 280$ irrespective of the boson mass and the strength of the quartic self-interaction. The tidal deformability of solitonic BSs is bounded below by $\Lambda \gtrsim 1.3$.

To determine whether ground-based GW detectors can distinguish NSs and BHs from BSs, we first computed a lower bound on the expected measurement errors in Λ using the Fisher matrix formalism. We considered BBH systems located at 400 Mpc and BNS systems at 200 Mpc with generic mass ratios that merge above 900 Hz. We found that, with Advanced LIGO, BBHs could be distinguished from binary systems composed of massive BSs and that BNSs could be distinguished provided that the NSs were of nearly-maximal mass or of sufficiently different masses (i.e. a high mass ratio binary). We also demonstrated that the prospects for distinguishing solitonic BSs from BHs based only on tidal effects are bleak using current-generation detectors; however, third-generation detectors will be able to discriminate between BBH and BBS systems. We presented two different analyses to determine whether an observed GW was produced by BSs: the first relied on the minimum tidal deformability being larger than that of a NS or BH, while the second combined mass and deformability measurements of each body in a binary system to break degeneracies arising from the (unknown) mass of the fundamental boson field.

Work by Cardoso et al. [416] also investigated the tidal deformabilities of BSs and the prospects of distinguishing them from BHs and NSs. Despite the topic being similar, the work in this chapter is complementary: Cardoso et al. [416] performed

a broad survey of tidal effects for different classes of exotic objects and BHs in modified theories of gravity, while our work focuses on an in-depth analysis of BSs. Additionally, these authors computed the deformability of BSs to both axial and polar tidal perturbations with $l = 2, 3$, whereas our results are restricted to the $l = 2$ polar case. The $l = 2$ effects are expected to leave the dominant tidal imprint in the GW signal, with the $l = 3$ corrections being suppressed by a relative factor of $125\Lambda_3/(351\Lambda_2)(M\Omega)^{4/3} \sim 4(M\Omega)^{4/3}$ [461] using the values from Table I of Ref. [416], where Ω is the orbital frequency of the binary. For reference, $M\Omega \sim 5 \times 10^{-3}$ for a binary with $M = 12M_\odot$ at 900Hz.

We also cover several aspects that were not considered in Ref. [416], where the study of BSs was limited to a single example for a particular choice of theory parameters for each potential (quartic and solitonic). Here, we analyzed the entire parameter space of self-interaction strengths for the quartic potential and the regime of interest for BH mimickers in the solitonic case. Furthermore, we developed fitting formulae for immediate use in future data analysis studies aimed at constraining the BS parameters with GW measurements. Cardoso et al. [416] also discussed prospective constraints obtained from the Fisher matrix formalism for a range of future detectors, including the space-based detector LISA that we did not consider here. However, their analysis was limited to equal-mass systems, to bounds on $\tilde{\Lambda}$, and to the specific examples within each BS models. We went beyond this study by delineating a strategy for obtaining constraints on the BS parameter space from a pair of measurements and considering binaries with generic mass ratio. We also restricted our results to the regime where the signals are dominated by the inspiral.

Although this choice significantly reduces the parameter space of masses surveyed compared to Cardoso et al., we imposed this restriction because full waveforms that include the late inspiral, merger and ringdown are not currently available. Another difference is that we took BBH or BNS signals to be the "true" signals around which the errors were computed and used results from NR for the merger frequency to terminate the inspiral signals, whereas the authors of Ref. [416] chose BS signals for this purpose and terminated them at the Schwarzschild ISCO.

The purpose of this work was to compute the tidal properties of BSs that could mimic BHs and NSs for GW detectors and to estimate the prospects of discriminating between such objects with these properties. Our analysis hinged on a number of simplifying assumptions. For example, the Fisher matrix approximation that we employed only yields lower bounds on estimates of statistical uncertainty. Additionally, we considered only a restricted set of waveform parameters, whereas including spins could also worsen the expected measurement accuracy. On the other hand, improved measurement precision is expected if one uses full inspiral-merger-ringdown waveforms or if one combines results from multiple GW events. Our conclusions should be revisited using Bayesian data analysis tools and more sophisticated waveform models, such as the EOB model. Tidal effects are a robust feature for any object, meaning that the only change needed in existing tidal waveform models is to insert the appropriate value of the tidal deformability parameter for the object under consideration. However, the merger and ringdown signals are more difficult to predict, and further developments and NR simulations are needed to model them for BSs or other exotic objects.

8.8 Acknowledgments

N.S. acknowledges support from NSF Grant No. PHY-1208881. We thank Ben Lackey for useful discussions. We are grateful to Vitor Cardoso and Paolo Pani for helpful comments on this manuscript.

Chapter 9: Parameterized tests of general relativity with generic frequency-domain waveform models

Authors: *Noah Sennett*[1]

Abstract: Theory-agnostic and theory-specific gravitational-wave tests of gravity rely on "generalized" waveform models that introduce parameterized deviations to pre-established waveform models in general relativity (GR). We develop a new flexible theory-agnostic (`FTA`) framework that allows such deviations to be added to the inspiral of any frequency-domain, non-precessing baseline waveform. This infrastructure is well-adapted to testing GR with LIGO and Virgo observations and to investigating the systematic biases that may arise in such tests through the particular construction of generalized waveforms. As part of the LIGO Scientific Collaboration, we use this infrastructure to bound phenomenological deviations from GR in the phase evolution of BBH and BNS events observed during the first two observing runs of the Advanced LIGO and Virgo detectors; by comparing the results of these tests with those conducted with other generalized waveforms, we verify that

[1]Contains results prepared separately in: Phys. Rev. **D102**, 044056 (2020) [8]; Phys. Rev. Lett. **123**, 011102 (2019) [9]; Phys. Rev. **D100**, 104036 (2019) [10]; Sennett, Buonanno, Gergely, Isi, and Sathyaprakash, "Constraining Jordan-Fierz-Brans-Dicke gravity with GW170817," (in prep) [11].

waveform systematics have not significantly affect these tests. We also employ the `FTA` framework to design and carry out tests of specific alternative theories of gravity. Using GW170817, the first observed BNS, we place the first GW bounds on Jordan-Fierz-Brans-Dicke gravity, finding that the scalar-tensor coupling $\alpha_0 \lesssim 4 \times 10^{-1}$. Additionally, using two low mass BBH events—GW151226 and GW170608—we constrain a higher-order curvature corrections that arise naturally from a class of effective-field-theory-inspired extensions of GR, ruling out new physics that enters on distance scales between 70 and 200 km.

9.1 Introduction

Theory-agnostic tests of general relativity (GR) with gravitational-waves (GWs) often utilize waveform models that have been "generalized" from an existing GR template. The basic strategy for such tests is as follows. One first constructs a generalized waveform model by introducing deviations to a GR waveform model controlled by some set of parameters $\{\delta\hat{\varphi}_n\}$. These deviations are defined such that there exists some choice of parameters $\{\delta\hat{\varphi}_n^{(\mathrm{GR})}\}$ for which the generalized waveform model exactly reproduces the underlying GR waveform, i.e. the generalized model restricted to the hypersurface of parameter space $\delta\hat{\varphi}_n = \delta\hat{\varphi}_n^{(\mathrm{GR})}$ can be identified with the GR model. Without loss of generality, one can reparameterize the deviations such that that the GR prediction corresponds with zero, i.e. $\delta\hat{\varphi}_n^{(\mathrm{GR})} = 0$; we adopt this convention throughout the remainder of this chapter.

Then, given a detected GW, one performs standard parameter estimation using

this generalized waveform model to assess the consistency of the observed signal with the predictions of GR. This consistency can be quantified in a number of ways. One oft-used technique is to examine the posterior distribution of binary parameters and measure the proximity of this distribution's mode to the GR hypersurface of the generalized model. As a specific example, the LIGO and Virgo collaborations adopt this method for certain tests of GR performed on observed binary coalescences, testing whether the GR predictions $\delta\hat{\varphi}_n = 0$ fall within the 90% credible regions of the marginalized posterior distributions for $\delta\hat{\varphi}_n$ [9, 10, 73, 122]. Another way to quantify the consistency between observation and GR prediction is through the relative odds between two competing hypotheses: the detected signal does (does not) agree with the predictions of GR $\mathcal{H}_{\rm GR}$ ($\mathcal{H}_{\text{non-GR}}$) [120, 176, 462]. This approach offers a more easily quantified p-value, but such estimates require proper context for correct interpretation. Due to the different dimensionality of the hypotheses ($\delta\hat{\varphi}_n = 0$ vs. $\delta\hat{\varphi}_n \neq 0$) and biases inherited from experimental design optimized for GW detection in GR, one can only assess the significance of the aforementioned odds ratio for a particular detection by comparing against a theoretical background distribution estimated independently.

The overarching framework outlined above subsumes a large swath of tests of GR that have been performed with GWs [9, 10, 73, 122, 187]. And yet, these tests are not all exactly the same; they differ in either (i) the choice of generalized waveform model and/or (ii) how this model is applied to data. In this work, we develop a framework to examine how the details of the construction of generalized waveform models systematically affect the tests of GR in which they are employed.

This infrastructure allows one to add generic corrections to the inspiral portion of any non-precessing, frequency-domain waveform, thereby allowing theory-agnostic tests of GR to be performed with a broader range of generalized waveform models than previously possible. Accordingly, this framework is denoted as the flexible theory-agnostic (`FTA`) approach. In addition to this original use, the easily adaptable design of the `FTA` framework also allows for easy construction of waveform models for theory-specific tests.

This work is organized as follows. Section 9.2 details the construction of the `FTA` infrastructure. Section 9.3 presents the results of theory-agnostic tests conducted as part of the LIGO Scientific Collaboration employing the `FTA` framework on binary black hole (BBH) and binary neutron star (BNS) events detected during their first and second observing runs. In Sec. 9.4, we use the `FTA` construction to test Jordan-Fierz-Brans-Dicke gravity (JFBD) with GW170817—the first GW observation of a BNS. These results represent the first (albeit weak) GW constraints on this very well-known alternative theory of gravity. Similarly, in Sec. 9.5, we test the higher-order curvature extension of GR recently proposed in Ref. [351] with the lowest-mass BBH observations during the first and second observing runs of LIGO and Virgo. Using the `FTA` infrastructure, we rule out the appearance of new physics in this theory entering at the scale of 70-200 km.

9.2 The FTA construction of generalized waveform models

The construction of any generalized waveform model begins with a baseline model in GR, which we express in the Fourier domain as $h_{\rm GR}(f;\boldsymbol{\theta})$ for the binary parameters $\boldsymbol{\theta}$ (e.g. masses, spins, etc.). Restricting our attention to the dominant $\ell = m = 2$ mode of signals from non-precessing systems, the complex phase $\psi_{\rm GR}$ of the waveform can be well approximated during the early inspiral by [30, 259]

$$\psi^{(\rm GR)}(f;\boldsymbol{\theta}) \sim \frac{3}{128\eta v^5}\left[\sum_{n=0}^{7}\psi_n^{(\rm GR)}(\boldsymbol{\theta})v^n + \sum_{n=5}^{6}\psi_{n(l)}^{(\rm GR)}(\boldsymbol{\theta})v^n\log v\right], \tag{9.1}$$

where $v \equiv (GM\pi f/c^3)^{1/3}$ is the standard post-Newtonian (PN) parameter, M is the total mass of the binary, η is its symmetric mass ratio, and $\psi_n^{(\rm GR)}$ and $\psi_{n(l)}^{(\rm GR)}$ are the $(n/2)$-PN coefficients, which depend on the binary parameters. Note that the logarithmic terms in Eq. (9.1) arise from so-called "hereditary contribution" to the inspiral, i.e. terms that depend on the full past history of the binary; see Chapter 3.4 for an detailed discussion of such terms.

To generalize this waveform model, one must add parameterized deviations to the baseline waveform $h_{\rm GR}(f)$. Though not the only possible option, a compelling choice to test the inspiral behavior of the signal is to consider corrections to the phase that take a similar PN form

$$\delta\psi\left(f;\boldsymbol{\theta},\{\delta\hat{\varphi}_n,\delta\hat{\varphi}_{n(l)}\}\right) \sim \frac{3}{128\eta v^5}\left[\sum_{n=-2}^{7}\delta\psi_n(\boldsymbol{\theta},\delta\hat{\varphi}_n)v^n + \sum_{n=5}^{6}\delta\psi_{n(l)}(\boldsymbol{\theta},\delta\hat{\varphi}_{n(l)})v^n\log v\right], \tag{9.2}$$

where $\delta\psi_n$ and $\delta\psi_{n(l)}$ are deviations to the $(n/2)$-PN phase coefficients that, in addition to $\boldsymbol{\theta}$, each depend on the corresponding deviation parameter $\delta\hat{\varphi}_n$ or $\delta\hat{\varphi}_{n(l)}$,

respectively. We include possible deviations at "pre-Newtonian" orders ($n < 0$) as these are predicted in many alternative theories of gravity, e.g. through the emission of dipole radiation. Parameterized deviations of this form can be mapped onto the predictions of any hypothetical alternative theory provided that (i) the theory admits a weak-field, slow-velocity PN expansion as in GR and (ii) the deviations from GR are parametrically smaller than the PN expansion parameter v^2/c^2; note that this excludes theories that admit non-perturbative phenomena like dynamical scalarization, for which the PN expansion breaks down. [2]

In the `FTA` framework, we adopt the following definitions for $\delta\psi_n$ and $\delta\psi_{n(l)}$

$$\delta\psi_n(\boldsymbol{\theta}, \hat{\varphi}_n) \equiv \hat{\varphi}_n \psi_n^{(\mathrm{GR})}(\boldsymbol{\theta}), \qquad \delta\psi_{n(l)}(\boldsymbol{\theta}, \hat{\varphi}_{n(l)}) \equiv \hat{\varphi}_{n(l)} \psi_{n(l)}^{(\mathrm{GR})}(\boldsymbol{\theta}), \tag{9.3}$$

that is, each deviation parameter represents a fractional deviation to the corresponding PN coefficient in GR. We handle PN orders for which the GR coefficient vanishes slightly differently (e.g. at 0.5PN order); for those cases, we let $\hat{\varphi}_n$ instead represent

[2] Despite the generality of Eq. (9.2), in most practical settings, the majority of the deviation parameters are explicitly set to zero when performing tests of GR. Our null hypothesis for these tests is that GR is correct, and accordingly that the deviation parameters recovered using a generalized waveform are consistent with zero. Under this assumption, each independent deviation parameter allowed to vary freely would tend to worsen the statistical significance of the conclusions that can be made. Fortunately, if this assumption is incorrect, many deviations from GR can still be identified with a reduced number of deviation parameters; for example, Ref. [121] showed that a signal containing deviations at several PN orders will lead to measurement of non-zero deviation using a model with only single deviation parameter. Because of the scientific cost of introducing new free parameters, deviations to the GW amplitude are neglected, as GW detectors are more sensitive to the evolution of a signal's phase than its amplitude.

an *absolute* deviation at that order.

While Eq. (9.2) unambiguously details how to generalize GR waveforms containing only the inspiral, additional care must be taken for waveforms that contain later portions of the GW signal. For the FTA approach, we require that the parameterized deviation observe the following properties:

1. The early inspiral (low frequency) waveform has a phase $\psi(f;\boldsymbol{\theta}) = \psi^{(\mathrm{GR})}(f;\boldsymbol{\theta}) + \delta\psi(f;\boldsymbol{\theta})$, where $\delta\psi$ takes the form of Eq. (9.2).

2. The post-inspiral (high frequency) waveform has a phase $\psi(f;\boldsymbol{\theta}) = \psi^{\mathrm{GR}}(f;\boldsymbol{\theta}) + \Delta\psi(\boldsymbol{\theta})$ that exactly reproduces the underlying GR model up to some constant shift (which represents the total dephasing from the GR model accumulated over the complete inspiral).

3. The waveform is C^2 smooth over all frequencies.

We construct $\delta\psi(f;\boldsymbol{\theta})$ starting from the total "PN-like" phase correction given by $\{\delta\hat{\varphi}_n, \delta\hat{\varphi}_{n(l)}\}$

$$\delta\psi^{(\mathrm{PN})}(f;\boldsymbol{\theta}) \equiv \frac{3}{128\eta v^5}\left[\sum_{n=-2}^{7}\psi_n^{(\mathrm{GR})}(\boldsymbol{\theta})\delta\hat{\varphi}_n v^n + \sum_{n=5}^{6}\psi_{n(l)}^{(\mathrm{GR})}(\boldsymbol{\theta})\delta\hat{\varphi}_{n(l)} v^n \log v\right]. \quad (9.4)$$

To smoothly apply this correction over only the inspiral, we use a windowing function $W(f; f_{\mathrm{win}}, \Delta f_{\mathrm{win}})$ given by

$$W(f; f_{\mathrm{win}}, \Delta f_{\mathrm{win}}) \equiv \left[1 + \exp\left(\frac{f - f_{\mathrm{win}}}{\Delta f_{\mathrm{win}}}\right)\right]^{-1}, \quad (9.5)$$

which smoothly transitions between one and zero at f_{win} over a frequency range of $\sim \Delta f_{\mathrm{win}}$. We construct the total phase correction by combining this windowing

function with the second derivative of $\delta\psi^{(\mathrm{PN})}$ and re-integrating with appropriate integration constants to ensue C^2 smoothness

$$\delta\psi(f; f_{\mathrm{win}}, \Delta f_{\mathrm{win}}) = \int_{f_{\mathrm{ref}}}^{f}\int_{f_{\mathrm{ref}}}^{f'} \delta\psi^{(\mathrm{PN})}(f'')W(f''; f_{\mathrm{win}}, \Delta f_{\mathrm{win}}), \tag{9.6}$$

where f_{ref} is an arbitrarily chosen reference frequency at which the phase of the original waveform model vanishes, i.e. $\psi_{\mathrm{GR}}(f_{\mathrm{ref}}) = 0$.

9.3 Theory-agnostic inspiral tests with LIGO/Virgo events

One of the primary scientific objectives of the LIGO Scientific and Virgo Collaborations is to test the accuracy of the predictions of GR in the highly dynamical, strong-field regime of gravity reached during the coalescence of BHs and/or NSs. Several types of theory-agnostic tests are performed on observed GW events; amongst those are tests of the inspiral portion of those signals, for which the `FTA` infrastructure has been employed. These tests provide a consistency check on the inspiral dynamics of the sources that generated the observed GW signals. To date, no statistically significant deviations from GR have been uncovered with these tests.

The overarching design of these tests closely follows the description laid out in Sec. 9.1: using a generalized waveform model, one performs parameter estimation to measure (or constrain) the parameterized deviations $\{\hat{\varphi}_n, \hat{\varphi}_{n(l)}\}$ most consistent with an observed GW event. Consistency with GR is indicated by measurements of the parameterized deviations consistent with zero. Due to limitations in the sensitivity of current detectors, we do not allow the full set of parameterized deviations $\{\hat{\varphi}_n, \hat{\varphi}_{n(l)}\}$ to vary freely in our model; each additional free parameter in

one's model worsens the measurement errors on the deviation parameters (see, e.g. Refs. [120, 122]). Instead, we allow only one deviation parameter to vary and set the remainder to zero, repeating this test for each such deviation parameter.

During the first and second observing runs of the Advanced LIGO and Virgo detectors, ten GW events from BBHs [463] and one GW event from a BNS [186] were observed. However, not all of these events are amenable to tests of the inspiral dynamics of the corresponding sources. The inspiral ends at comparatively lower frequencies for high-mass sources; because the detectors were only sensitive above 20-30 Hz during the first two observing runs, the inspiral portion of these signals was severely truncated. Following the criteria laid out in Ref. [10], we consider only events for which the inspiral was recovered with SNR > 6, which are the BBHs GW150914 [184], GW151226 [182], GW170104 [123], GW170608 [183], GW170814 [185] and the BNS GW170817 [186].

The particular choice of generalized waveform used in each test is based off of the type source observed. For the BBH events listed above, we performed the aforementioned parameterized test of GR using the aligned-spin effective-one-body (EOB) model `SEOBNRv4` [45]. A fast, frequency-domain surrogate model is constructed from `SEOBNRv4` using reduced-order modeling techniques [464], and then finally, we apply the `FTA` procedure to construct a generalized waveform. For the BNS, we instead use a baseline GR waveform model that includes additional physical effects absent in pure vacuum binaries, such as the tidal interactions between the stars during the late inspiral. We employ the `NRTidal` model introduced in Refs. [465–467], which allows one to convert a BBH waveform model to a BNS

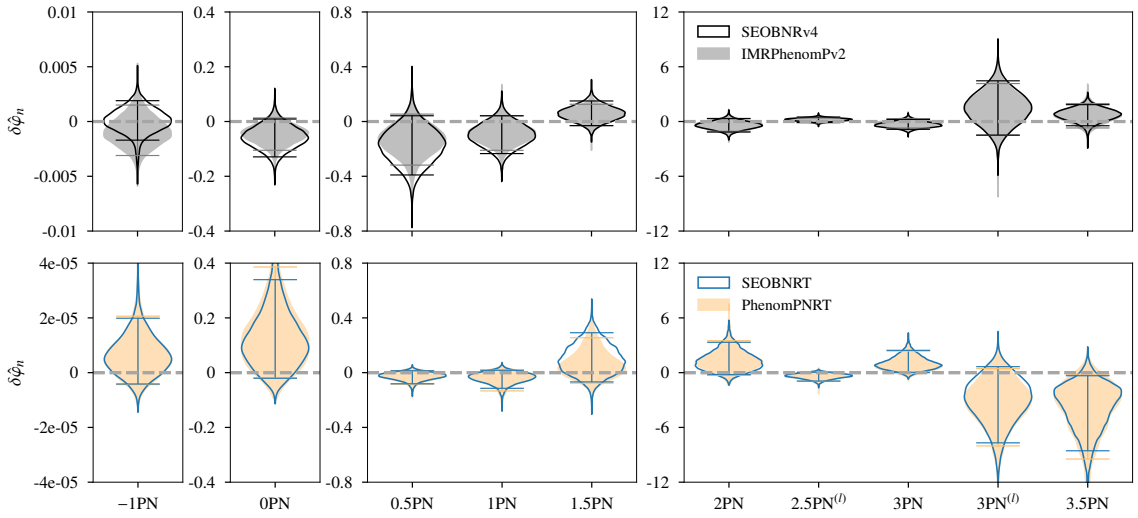

Figure 9.1: Marginalized posterior distributions of fractional deviations to PN coefficients. *(Top)*: Combined posterior distributions from all BBHs observed during first and second observing run of LIGO and Virgo with sufficiently measurable inspiral; adapted from Ref. [10]. *(Bottom)*: Posterior distribution from GW170817; adapted from Ref. [9].

waveform by adding an analytic tidal term to the frequency-domain phase evolution fit from PN and NR results. This tidal correction is added prior to generalizing the model using the `FTA` framework; this tidal model is denoted as `SEOBNRT`. Note that `SEOBNRT` is parameterized by two additional quantities relative to the BBH waveform `SEOBNRv4`: the tidal deformabilities of each NS. Because of this difference in dimensionality of their respective parameter spaces, one must take care when directly comparing constraints measured with BBH and BNS waveform models; for example, degeneracies between the tidal deformabilities and deviation parameters $\delta\hat{\varphi}_n$ produce features in the posterior distributions recovered for BNS signals that are absent for BBH signals.

As part of the LIGO Scientific Collaboration, we performed theory-agnostic

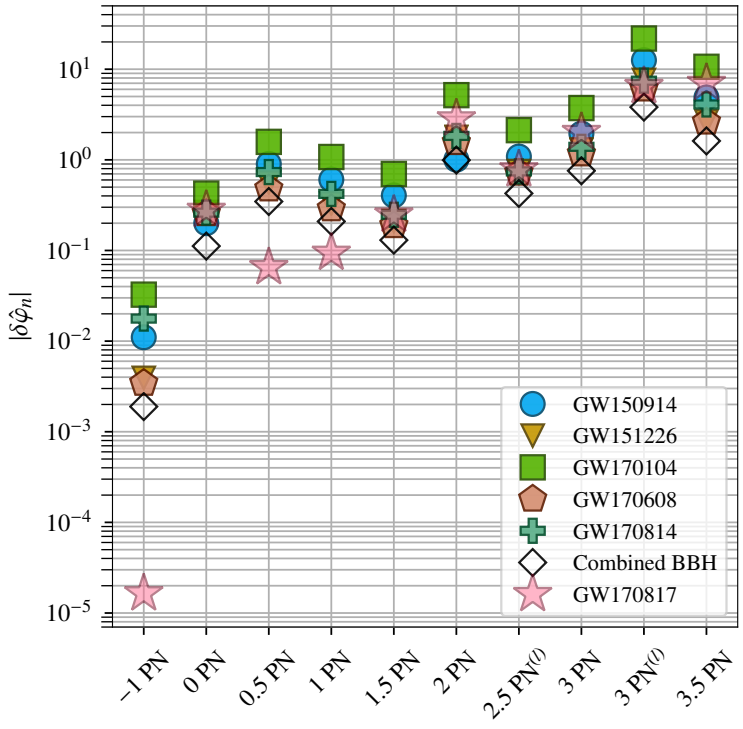

Figure 9.2: 90% upper bounds on $|\delta\hat{\varphi}_n|$ from individual BBH observations, combining these BBH observations, and the BNS observation GW170817. Plot adapted from Refs. [9] and [10].

tests of the inspiral dynamics for the restricted set of BBH and BNS observations listed above with generalized `SEOBNRv4` and `SEOBNRT` waveform models, respectively. These tests were carried out using the `LALInference` software package [78], a component of the LIGO Algorithm Library Suite (LALSuite) [468]. Figures 9.1 and 9.2 summarize the results of the tests; these figures have been adapted from analogous plots in Refs. [9] and [10]. The top panel of Fig. 9.1 shows the marginalized posterior distributions on $\delta\hat{\varphi}_n$ combined across all BBH events. Assuming all of the observed signals are statistically independent, the combined posterior distribution is simply given by the product of the posterior distributions across all events (suitably normalized). The results using `SEOBNRv4` in conjunction with the `FTA` framework are shown in solid black lines; the 90% credible regions are demarcated with horizontal lines. To compare, we also show the posteriors recovered using a different baseline GR waveform—`IMRPhenomPv2` [412, 469, 470]—generalized using a procedure other than `FTA` [120, 176] in gray. Whereas the aforementioned EOB models are constructed by resumming PN calculations and calibrating against NR, the `IMRPhenomPv2` model is a phenomenological fit to a combination of PN, EOB, and NR results; additionally, this latter model includes precession, whereas the EOB models we consider do not. Despite the different baseline waveform and generalization procedure, we recover consistent measurements with both the EOB and phenomenological waveform models, indicating that waveform systematics do not significantly affect these tests. Additionally, because the measured $\delta\hat{\varphi}_n$ are consistent with zero at a 90% confidence level, our tests indicate that the BBH inspirals observed are consistent with GR. We can convert this consistency check into a more quantitative measure

in Fig. 9.2; here we plot the 90% upper bounds on $|\delta\hat{\varphi}_n|$ measured using `SEOBNRv4` for each event

Similarly, the bottom panel of Fig. 9.1 shows the marginalized posterior distributions on the deviation parameters for GW170817. For comparison, we plot the measurements recovered with `SEOBNRT` in blue and with an alternative model `PhenomPNRT`—-constructed by applying the `NRTidal` model to `IMRPhenomPv2` and then generalizing using the procedure of Ref. [120, 176]—in orange. Again, we find good agreement between the two waveform models, indicating that waveform systematics do not significantly bias the measurement of deviation parameters. Consistency with GR at a 90% confidence level is found for all deviation parameters except for at 3PN and 3.5PN, where the GR value falls at the 95^{th} percentile of the marginalized posterior. At present, we have no reason to believe that these offsets have anything other than a statistical origin. The upper bounds on each deviation parameter are also shown in Fig. 9.2. Note in particular the significant improvement in the constraint on -1PN deviations made possible with GW10817. We use this particularly strong constraint in the following section to place constraints on a JFBD—a well-known alternative to GR.

9.4 Constraints on Jordan-Fierz-Brans-Dicke gravity from GW170817

Jordan-Fierz-Brans-Dicke gravity is one of the most well-known alternatives to Einstein's theory of general relativity [177–179]. Initially formulated in the mid-20th century, JFBD was the very first ST theory—a theory in which gravity is mediated

by both a tensor (the metric) and a scalar. Since then, significant work has been done to extend this notion beyond JFBD to broader, more generic classes of ST theories (e.g. Horndeski theories [90], Beyond Horndeski theories [93], Degenerate Higher-Order Scalar-Tensor theories [471, 472], etc.). Yet, despite its simplicity, JFBD remains relevant today, though more as a pedagogical archetype of modified gravity than as a truly viable alternative to GR. In this vein, constraining JFBD with a particular experiment offers an easily understood benchmark of its sensitivity to deviations from GR. In this work, we present the first bounds on JFBD from the measurement of gravitational waves by the Advanced LIGO [63] and Virgo [64] detectors.

The action for JFBD written in the Jordan frame is given by

$$S = \int d^4x \frac{\sqrt{-\tilde{g}}}{16\pi} \left(\phi \tilde{R} - \frac{\omega_{\rm BD}}{\phi} \tilde{g}^{\mu\nu} \partial_\mu \phi \partial_\nu \phi \right) + S_m[\tilde{g}_{\mu\nu}, \psi], \tag{9.7}$$

where ϕ is a massless scalar field, $\omega_{\rm BD}$ is a dimensionless coupling constant[3], and S_m represents the action for matter fields ψ minimally coupled to the metric $\tilde{g}_{\mu\nu}$. Alternatively, the action can be rewritten in the Einstein frame by performing the conformal transformation $g_{\mu\nu} \equiv \phi \tilde{g}_{\mu\nu}$

$$S = \int d^4x \frac{\sqrt{-g}}{16\pi} \left(R - 2 g^{\mu\nu} \partial_\mu \varphi \partial_\nu \varphi \right) + S_m[e^{-2\alpha_0 \varphi} g_{\mu\nu}, \psi], \tag{9.8}$$

where we have defined the dimensionless parameter $\alpha_0 \equiv (3 + 2\omega_{\rm BD})^{-1/2}$ and introduced the scalar field $\varphi \equiv \log(\phi)/(2\alpha_0)$; note that α_0 is non-negative and that we have implicitly assumed that $\omega_{\rm BD} > -3/2$. In the limit that $\alpha_0 \to 0$ ($\omega_{\rm BD} \to \infty$),

[3] JFBD is also commonly known as simply Brans-Dicke gravity (BD); following the standard convention in the literature, we adopt this abbreviation when denoting the coupling constant $\omega_{\rm BD}$.

the scalar field decouples from the metric and matter, and JFBD reduces to GR with an additional free, massless scalar. Doppler tracking of the Cassini spacecraft through the Solar System [180] provides the best current constraints on this parameter: $\alpha_0 < 4 \times 10^{-3}$ ($\omega_{\rm BD} > 4 \times 10^4$).

The recent advent of GW astronomy offers a new avenue to test gravity in the relativistic regime. The majority of GWs observed by LIGO and Virgo thus far were generated by the coalescence of BBHs; several tests of GR have already been conducted using these observations [10, 73, 122, 187]. However, Hawking famously showed that stationary BHs in JFBD must have a trivial scalar profile, and thus are indistinguishable from the analogous solutions in GR [23]. Although there are some possible scenarios that evade this no-hair theorem (see Ref. [98] for details), binary systems composed of BHs are generally expected to behave identically in JFBD and GR, and thus GWs from such systems are unable to constrain this ST theory.

Unlike BHs, NSs source a non-trivial scalar field in JFBD, and thus BNS systems can be used to constrain α_0. Using this fact, precise timing of binary pulsars constrains $\alpha_0 \lesssim 10^{-2}$ [329]. In this section, we use the first GW observation of a coalescing BNS—GW170817 [186]—to constrain $\alpha_0 \lesssim 4 \times 10^{-1}$ at a 68% confidence level. Though the constraint from GW170817 is not as strong as those previously quoted from other experiments, this result represents the first bound directly from the highly dynamical (orbital velocities $v \sim 10^{-1}$) and strong-field (Newtonian potential $\Phi_{\rm Newt} = M/R \sim 10^{-1}$) regime of gravity.

This section is organized as follows. In Section 9.4.1, we detail the GW signature of JFBD in BNSs. Then, in Section 9.4.2, we present two Bayesian analyses

to constrain α_0 with GW170817: the first directly uses the theory-agnostic analyses presented in Section 9.3, while the second is tailored specifically to test JFBD.

9.4.1 Gravitational-wave signature of Jordan-Fierz-Brans-Dicke gravity

The predominant differences in GWs produced in JFBD as compared to GR stem from the fact that only the latter respects the *strong equivalence principle*. This principle extends the universality of free fall by test particles implied by the Einstein equivalence principle introduced in Chapter 1 to also include self-gravitating bodies; unlike in GR, the motion of a body through spacetime depends on its internal gravitational interactions (i.e. its composition) in ST theories like JFBD. This section details how this violation of the strong equivalence principle impacts the GWs produced by binary systems in JFBD. This alternative theory of gravity falls within the class of ST theories examined in Chapter 3, and thus we can employ PN predictions computed there to the task at hand. Though those results were computed at next-to-next-to-leading PN order (and even higher order PN calculations have been completed recently [210, 473]), we will assume that α_0 is sufficiently small that we can neglect all but the leading-order PN effects when describing the signature of JFBD in a gravitational waveform.

The dominant effect on the inspiral from the new scalar introduced in JFBD is the emission of dipole radiation, which enters into the phase evolution at -1PN

order. In the notation of the FTA framework, this contribution is given by

$$\hat{\varphi}_{-2} = -\frac{5(\alpha_1 - \alpha_2)^2}{168} + \mathcal{O}\left(\alpha_0^4\right), \tag{9.9}$$

where α_A is the *scalar charge* of body A, defined as

$$\alpha_A \equiv -\frac{d \log m_A(\varphi)}{d\varphi}, \tag{9.10}$$

where $m_A(\varphi)$ is the gravitational mass of body A measured in the Einstein frame. That a body's mass depends on the local value of the scalar field is unsurprising given the form of Eq. (9.8); a shift in φ modulates the physical metric $e^{-2\alpha_0\varphi} g_{\mu\nu}$ that effects gravity upon the matter fields ψ, and thus also modulates any body's gravitational mass. This dependence is an explicit manifestation of violation of the strong equivalence principle. Note that in the limit that a body has no self-gravity (i.e. the test-body limit), the functional form of $m_A(\varphi)$ simplifies significantly to

$$m_A^{(\text{test body})}(\varphi) = e^{-\alpha_0\varphi} m_A^{(\text{test body})}(\varphi = 0), \tag{9.11}$$

and thus its scalar charge reduces to

$$\alpha_A^{(\text{test body})} = \alpha_0. \tag{9.12}$$

9.4.1.1 Isolated neutron star solutions in Jordan-Fierz-Brans-Dicke gravity

As strongly self-gravitating bodies, violations of the strong equivalence principle are particularly pronounced in NSs. This violation manifests as a scalar charge that differs significantly from the test-body charge α_0. As the scalar charges of a

binary's constituents—or rather their difference, the scalar dipole—control the dominant effect on the GW signal in JFBD, we devote the remainder of this subsection to computing these quantities for various NSs.

We consider spherically symmetric, static solutions sourced by a perfect fluid as a model for an isolated, non-rotating NS. Under these assumptions, the field equations for Eq. (9.8) reduce to the Tolman-Oppenheimer-Volkoff (TOV) equations, given in the Einstein frame in Ref. [153]. These solutions are parameterized by three degrees of freedom; for our purposes, these are most clearly manifested as the (i) background scalar field φ_0, i.e. the scalar field far from the NS, (ii) the NS equation of state (EOS), and (iii) the NS mass[4]. In fact, though, the asymptotic scalar field φ_0 can be set to zero without loss of generality by rescaling the Jordan-frame bare gravitational constant $\tilde{G}$ accordingly, i.e. $\varphi_0 \to 0 \Rightarrow \tilde{G} \to \tilde{G} e^{2\alpha_0 \varphi_0}$. The remaining degrees of freedom can be mapped to boundary conditions for the matter and scalar field at the origin with a numerical shooting method [430]. These conditions are parameterized by the central pressure P_c and scalar field φ_c, which serve as the inputs for numerically integrating the TOV equations. The details for extracting the mass and scalar charge from the numerical solutions of the NS interior are given in Ref. [153].

[4]We define the NS mass as the tensor mass m_T introduced in Ref. [474] because—as shown in that reference—it obeys the same conservation laws as the ADM mass in GR

Table 9.1: One-dimensional polynomial fits of the normalized NS coupling α_A/α_0 as a function of NS mass m_A (in units of $M_\odot$) for various equations of state.

EOS	$[\alpha_A/\alpha_0](m_A)$
sly[456]	$-0.726798 - 0.749029m_A + 1.270944m_A^2 - 0.72871m_A^3 + 0.161002m_A^4$
eng[475]	$-0.817884 - 0.393375m_A + 0.772615m_A^2 - 0.435306m_A^3 + 0.095059m_A^4$
H4[476]	$-0.613880 - 1.210074m_A + 1.836631m_A^2 - 1.056595m_A^3 + 0.228102m_A^4$

9.4.1.2 Polynomial fits of the neutron star scalar charge

Ultimately, we would like to combine the numerical calculations of NS scalar charge outlined above with their anticipated effect on the GW signal (9.9) to constrain JFBD. However, evaluating the scalar charge directly for every point visited by the stochastic sampling algorithms used for parameter estimation would require an unreasonable amount of computational resources. Instead, in this subsection, we compute polynomial fits for the scalar charge, which, after having been derived, can be evaluated quickly and with little computational overhead.

We first construct solutions for various choices of EOS, NS mass, and ST coupling α_0. We interpolate tabulated EOS data for the sly [456], eng [475], and H4 [476] EOSs; sly is a soft EOS (compact stars) whereas H4 is relatively stiff (diffuse stars). Then, we numerically construct NSs with masses ranging between $m_A \in [0.5\,M_\odot, 2.0\,M_\odot]$ and scalar coupling $\alpha_0 \in [0.001, 1.0]$ and compute their scalar charge.

We calculate two types of polynomial fits of the scalar charge for each EOS. For the first, we factor out the dominant linear dependence of α_A on α_0, fitting their quotient as a fourth-order polynomial in m_A. We compute the polynomial fits

Table 9.2: Two-dimensional polynomial fits of NS coupling α_A as functions of of Brans-Dicke parameter α_0 and NS mass m_A (in units of $M_\odot$) for various equations of state.

EOS	$\alpha_A(\alpha_0, m_A)$
sly[456]	$\alpha_0(-0.92569 + 0.22258\alpha_0 m_A + 0.13329 m_A^2 - 0.15151\alpha_0 m_A^2)$
eng[475]	$\alpha_0(-0.97423 + 0.15584 m_A + 0.18527\alpha_0 m_A - 0.11739\alpha_0 m_A^2 + 0.024333 m_A^3)$
H4[476]	$\alpha_0(-0.93341 + 0.19073\alpha_0 m_A + 0.10270 m_A^2 - 0.11284\alpha_0 m_A^2)$

with least-squares regression; the fits are given in Table 9.1 for each EOS that we consider. These fits match all of our data sets within 5% relative error, with the greatest discrepancy arising for masses close to $2\,M_\odot$.

Although these (effectively) one-dimensional polynomial fits are crucial for some of the analysis contained in this chapter, it is possible to construct two-dimensional fits that are simpler (fewer terms) and more accurate using more sophisticated methods. We compute these fits using the greedy-multivariate-rational regression method developed in Ref. [477]. This method relies on a greedy algorithm to construct a multivariate fit: during each iteration, it adds a polynomial term to the current fit (up to a pre-specified maximum degree) so as to best improve the agreement with the inputted data. This process is repeated until sufficient accuracy is achieved, and then terms are systematically removed from the polynomial until the accuracy goal is saturated. Using this method, we construct fits that agree to within 1% relative error for each EOS—these are listed in Table 9.2.

9.4.2 Constraining α_0 with GW170817

Next, we use the tools introduced in the previous subsections to place constraints on the ST coupling α_0 in JFBD with GW170817—the first GW event from a coalescing BNS. We present two complementary analyses based off of the `FTA` infrastructure to achieve this result. These two methods follow the same overall approach, but adopt different statistical assumptions, utilize different waveform models, and use different numerical fits for the NS scalar charge α_A. In both approaches, we employ a generalized waveform model that allows for additional contribution to the phase evolution at -1PN order, so as to reproduce the behavior seen in Eq. (9.9); however, the parameterization of this -1PN deviation from GR differs in each approach. Ultimately, both analyses provide a bound on α_0 of the same order of magnitude.

The first approach we adopt directly uses the theory-agnostic constraints on a -1PN deviation discussed in Section 9.3 and originally published in Ref. [9]. Recall that this analysis used a generalization of the `SEOBNRT` baseline waveform model in which -1PN deviations were parameterized by the deviation parameter $\delta\hat{\varphi}_{-2}$. By assuming a particular NS EOS, we can use the polynomial fit in Table 9.1 in conjunction with Eq. (9.9) to map a measured value of $\delta\hat{\varphi}_{-2}$ to an inferred value on α_0; schematically, this mapping takes the form $\alpha_0(\delta\hat{\varphi}_{-2}, m_1, m_2; \text{EOS})$. Note that this mapping is infeasible using the multivariate fit in Table 9.2 because of the nonlinear dependence of α_A on α_0. Though the exact NS EOS remains unknown, we can repeat this analysis for the three candidate EOSs detailed earlier, and then

use the variance in bounds on α_0 recovered each time as an estimate of systematic error arising from our ignorance of the true NS EOS.

In practice, one does not measure the masses and deviation parameter $\delta\hat{\varphi}_{-2}$ with perfect accuracy, but instead uses Bayesian inference to reconstruct the posterior distribution $P(\boldsymbol{\theta}|d)$ on these parameters given some assumed prior distribution $P(\boldsymbol{\theta})$. So, rather than map a single point from one parameterization to another, one instead maps the appropriate distributions to their counterparts in the new parameterization. These prior and posterior distributions transform respectively as

$$P(\alpha_0, m_1, m_2) = \left|\frac{\partial\alpha_0}{\partial\delta\hat{\varphi}_{-2}}\right|^{-1} P(\delta\hat{\varphi}_{-2}, m_1, m_2), \tag{9.13}$$

and

$$P(\alpha_0, m_1, m_2|d) = \left|\frac{\partial\alpha_0}{\partial\delta\hat{\varphi}_{-2}}\right|^{-1} P(\delta\hat{\varphi}_{-2}, m_1, m_2|d), \tag{9.14}$$

where the first term on the righthand side is the inverse of the Jacobian of the aforementioned transformation.

In the analysis of Section 9.3 (and Ref. [9]), a flat prior (i.e. a uniform distribution over a bounded region) was assumed on the component masses and deviation parameter $\delta\hat{\varphi}_{-2}$. These choices reflect the theory-agnostic nature of that test; without a preferred alternative, this choice represents the simplest prior in terms of these binary parameters. Figure 9.3 depicts with dashed lines how this choice of prior distribution maps to an assumed prior on α_0 through Eq. (9.13); here the different colors correspond to different assumed EOSs. Similarly, Fig. 9.4 shows the corresponding marginalized posteriors on α_0, transformed from the posterior on $\delta\hat{\varphi}_{-2}$ and component masses (which, when marginalized, is shown in the bottom panel of

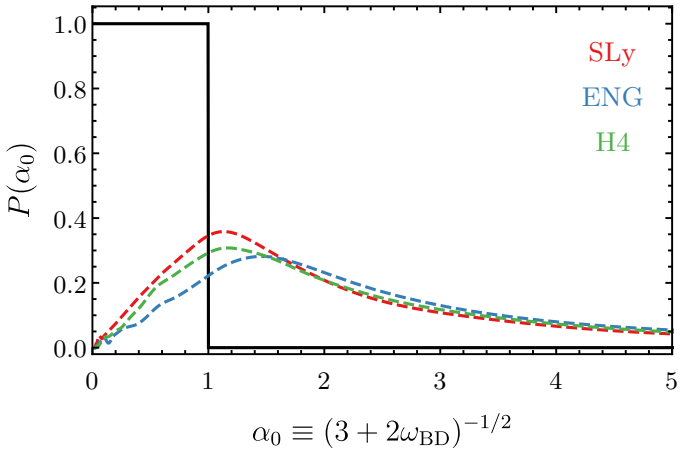

Figure 9.3: Marginalized prior distributions on the JFBD parameter α_0 used in the two analyses discussed in this chapter. The dashed colored curves depict the prior distribution equivalent to the flat prior distribution on component masses and deviation parameter $\delta\hat{\varphi}_{-2}$ assumed in the theory-agnostic analysis of Section 9.3. The solid black dashed curve depicts the flat prior on α_0 assumed in the second analysis presented in this section.

Fig. 9.1) via Eq. (9.14). This analysis provides a bound of $\alpha_0 \lesssim 2 \times 10^{-1}$ at a 68% confidence level; note that the systematic error arising from our ignorance of the NS EOS does not impact our estimate at this level of precision.

The second approach we employ to constrain α_0 relies instead on a waveform model design specifically to test JFBD. Using the `FTA` infrastructure, we construct a generalized waveform model from `SEOBNRT` in which the deviation parameter is precisely α_0. The appropriate form of the -1PN correction to the phase evolution is obtained by inserting the polynomial fit for $\alpha_A(\alpha_0, m_A)$ found in Table 9.2 for a particular choice of EOS into Eq. (9.9). Additionally, unlike the previous theory-agnostic analysis in which the tidal parameters were allowed to vary freely, for this analysis, we express these parameters as functions of the respective NS masses and

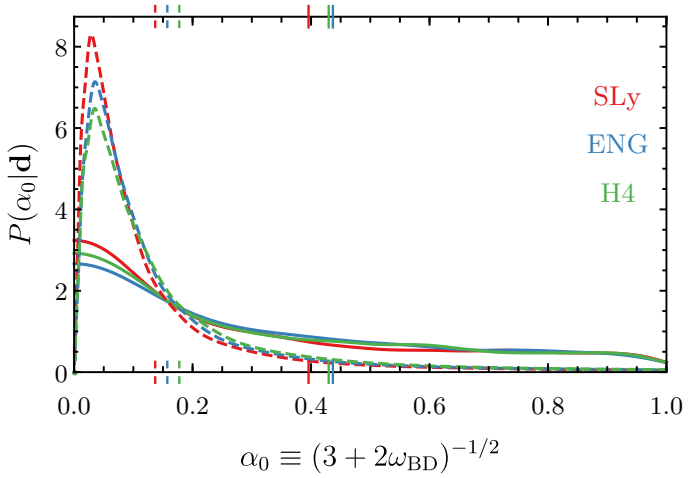

Figure 9.4: Marginalized posterior distributions on the JFBD parameter α_0 recovered from GW170817 from both analyses discussed in the text. The dashed colored curves show the posterior recovered directly from the theory-agnostic analysis of Section 9.3. The solid colored curves depict the posterior using the theory-specific test of JFBD assuming a flat prior for α_0. For both analyses, different colors correspond to different assumed EOSs. Colored ticks on the horizontal axes represent the 68% upper bounds on α_0 for each analysis.

assumed EOS.[5] This step reduces the dimensionality of the waveform model by two parameters while ensuring that all matter effects are handled self consistently. We assume a flat prior on $\alpha_0 \in [0, 1]$ for this analysis; beyond this upper bound, our assumption that JFBD effects, which scale as α_0^2, are subdominant to the PN effects in GR is no longer valid. This prior distribution is depicted in Fig. 9.3 with a solid black curve. Using the generalized waveform described above, we perform parameter estimation to construct the marginalized posterior distribution on α_0, shown in Fig. 9.4 with solid colored curves corresponding to the assumed EOS. We obtain the upper bound of $\alpha_0 \lesssim 4 \times 10^{-1}$ where, as before, the systematic error due to ignorance of the true NS EOS does not contribute at this level of precision.

Comparing the bounds set by the two analyses, we see that the theory-agnostic test provides a stronger bound on α_0. At first glance, this result may appear counterintuitive, as Fig. 9.3 shows that this test assumed a marginalized prior on α_0 with greater support away from zero. The predominant cause for this discrepancy stems from how the tidal parameters are handled by each waveform model. For the theory-agnostic test, these parameters are allowed to vary freely, independent of the masses of the NSs. However, in the theory-specific test, the tidal parameters are linked directly to the component masses. This latter restriction significantly affects the recovered posterior distribution on the component masses, placing much greater

[5] We use polynomial fits to the tidal parameters as a function of NS mass that are constructed in GR, not in JFBD. However, the differences between these two relations scale as α_0^2, and thus can be neglected in favor of the simpler GR relation by the same reasoning that the other sub-dominant PN effects (e.g. at 0PN order, 0.5PN order, etc.) can be ignored.

weight near equal-mass configurations than in the previous case. As can be seen in Eq. (9.9), in very symmetric configurations, the total deviation from the baseline GR waveform remains small even when α_0 is relatively large; as a result, the JFBD parameter is more poorly measured when the tidal parameters cannot vary freely, and thus we recover a weaker bound with this theory-specific test.

9.5 Constraints on higher-order curvature corrections from GW151226 and GW170608

The previous two sections demonstrate two very different ways in which the `FTA` framework can be used to test GR with GW observations. These investigations represent two opposite ends of the spectrum of theory-agnostic (Sec. 9.3) vs. theory-specific (Sec. 9.4) tests. In this final section, we again use the `FTA` framework, but this time to perform tests that fall between these two extremes. Using the powerful tools of effective field theory (EFT), we place constraints on higher-order curvature corrections expected to arise in many possible UV-completions of GR. The assumptions made in constructing the extensions of GR are minimal; the most conspicuous of them is that we restrict our attention to theories for which deviations from GR are conceivably observable with ground-based GW detectors.

In the interest of brevity, we limit our discussion concerning the construction of the EFT in this thesis and instead direct interested readers to Ref. [181]. We consider the most general extension to GR under the following assumptions: (i) locality, causality, Lorentz invariance, unitarity and diffeomorphism invariance are

preserved by new physics; (ii) no new particle lighter than the cutoff scale of the theory is introduced; (iii) the extension to GR impacts phenomena observable with the LIGO and Virgo detectors. The resulting EFT takes the form

$$S_{\rm eff} = 2M_{\rm pl}^2 \int d^4x\sqrt{-g}\left(-R + \frac{\mathcal{C}^2}{\Lambda^6} + \frac{\tilde{\mathcal{C}}^2}{\tilde{\Lambda}^6} + \frac{\mathcal{C}\,\tilde{\mathcal{C}}}{\Lambda_-^6}\right) + \dots\,, \tag{9.15}$$

where $M_{\rm pl} = \sqrt{\hbar c/G}$ is the Planck mass,

$$\mathcal{C} \equiv R_{\alpha\beta\gamma\delta}\,R^{\alpha\beta\gamma\delta}\,, \quad \tilde{\mathcal{C}} \equiv R_{\alpha\beta\gamma\delta}\,\epsilon^{\alpha\beta}{}_{\mu\nu}\,R^{\mu\nu\gamma\delta}\,, \tag{9.16}$$

$\Lambda, \tilde{\Lambda}, \tilde{\Lambda}_- \sim \mathcal{O}(\mathrm{km}^{-1})$ are various cutoff scales of the EFT, the dots in Eq. (9.15) denote terms with powers in the Riemann tensor beyond four, and the Levi-Civita tensor $\epsilon^{\mu\nu\rho\sigma}$ is defined such that $\epsilon^{0123} = 1/\sqrt{-g}$. The cutoff scales are taken to be no greater than km^{-1}, as this is approximately the maximum mass scale (shortest distance scale) to which ground-based GW detectors would be sensitive; for reference, the Schwarzschild radius of a one solar-mass BH is ~ 3km.

Naively, one might expect corrections to gravity occurring on distance scales of kilometers to be already strongly constrained by existing laboratory and Solar System tests. However, the curvature scales involved in those experiments are much smaller than those reached near solar-mass BHs, and thus the possibility remains that new physics could remain at the km^{-1} scale that only emerges in the high-curvature regime. This possibility can be formalized into an assumption of a "soft UV completion" of the theory, which states that all EFT effects saturate at the cutoff scale, i.e. they do not continue to grow as some power of E/Λ_c at energies E above the cutoff Λ_c—see Ref. [181] for more detail.

9.5.1 Gravitational-wave signature of higher-order curvature corrections

Having established the assumptions and action (9.15) describing our EFT, we next turn to the signature of this extension to GR in the inspiral signal of a BBH. For simplicity, we restrict our attention to only the $\mathcal{C}^2$ term in (9.15), as this provides the dominant (lowest PN order) effect in the waveform. Furthermore, we assume that $\Lambda \lesssim 1/M$, where M is the total mass of the binary; other effects are known to play an important role in the regime wherein $\Lambda \gtrsim 1/M$ (such as tidal effects) [478], but we have checked that these are not observable for the BBH systems that we consider.

During the early inspiral, the dynamics of a binary system of two objects with mass m_1 and m_2 can be characterized by an effective action that in center-of-mass frame takes the form [181]

$$S = \int dt \left(m_1 + m_2 + \frac{1}{2}\mu(t)|\mathbf{v}|^2 - V\left(r(t)\right) + \frac{1}{2}Q_{ij}(t)R^{i0j0} + \dots \right), \tag{9.17}$$

where μ is the reduced mass of the system, $|\mathbf{v}|$ is the relative velocity between the inspiraling objects, $V(r(t))$ is the potential energy, $Q_{ij}(t)$ is the mass quadrupole moment of the system and the dots represent higher-order multipole moments.

As shown in Ref. [181], the leading-order PN corrections to the gravitational potential of a non-spinning or slowly-spinning binary system take the form

$$V^{\Lambda} = \frac{2}{\pi^6}\frac{m_1 m_2}{r}\left(\frac{2\pi}{\Lambda r}\right)^6 \frac{4(m_1^2 + m_2^2)}{r^2}\,. \tag{9.18}$$

The non-GR terms in the action (9.15) also modify the emission of GW radiation.

The leading-order effect manifests as a correction to the Newtonian quadrupole moment $Q_{ij}^{\rm Newt}$ of the binary system

$$Q_{ij}^{\Lambda} = \left[1 + \frac{21}{2\pi^6}\left(\frac{2\pi}{\Lambda r}\right)^6 \left(\frac{2(m_1+m_2)}{r}\right)^2\right] Q_{ij}^{\rm Newt}\,. \tag{9.19}$$

In the following subsections, we compute the effect of these corrections on the conservative and dissipative sectors independently. We then use the balance equation to relate the two and to compute the leading-order correction to the GW phase.

9.5.1.1 Conservative dynamics

Working on the orbital timescale, the various time-dependent quantities in the action (9.17) can be treated as constant and the radiative terms can be neglected. Restricting to quasi-circular orbits and varying the action (9.17) with respect to $\mathbf{r}(t)$, the equations of motion of the binary system can be written as:

$$\mu\Omega^2 r = \frac{dV}{dr} = \frac{dV_{\rm Newt}}{dr} + \frac{dV_{\Lambda}}{dr} + \dots\,, \tag{9.20}$$

where $\dots$ denote higher PN corrections. This relation can be inverted to get a relation between the orbital radius r and the orbital frequency Ω. To leading order in $1/\Lambda$ one gets

$$r = \frac{M}{(M\Omega)^{2/3}}\left(1 - \frac{1536\,(m_1^2+m_2^2)}{M^8\Lambda^6}\,(M\Omega)^{16/3}\right)\,. \tag{9.21}$$

Using the equations above one finds that the binding energy (per unit total mass) is given by

$$E = \frac{1}{2}\nu|\mathbf{v}|^2 + V(r)/M = -\frac{1}{2}\nu v^2 - 2560\nu(1-2\nu)\left(\frac{d_\Lambda}{M}\right)^6 v^{18}, \tag{9.22}$$

where $M = m_1 + m_2$ is the total mass of the system, $\nu = m_1 m_2/M^2$ is the symmetric mass ratio and we have defined $v \equiv (M\Omega)^{1/3}$. For convenience we have also introduced the parameter $d_\Lambda \equiv 1/\Lambda$. Restoring the higher PN corrections in GR we have

$$E^\Lambda(v) = E^{\rm GR} - 2560\nu\,(1-2\nu)\left(\frac{d_\Lambda}{M}\right)^6 v^{18}\,. \tag{9.23}$$

where $E^{\rm GR}$ denotes the PN expression for the binding energy in GR.

9.5.1.2 Dissipative dynamics

The renormalized quadrupole moment (9.19) leads to corrections to the GW flux. As in GR, Eq. (9.17) predicts a leading-order GW flux given by the quadrupole formula

$$\mathcal{F} = \frac{1}{5} < \dddot{Q}_{ij}\dddot{Q}^{ij} >\,, \tag{9.24}$$

where $< \cdots >$ indicates the average over an orbit. The resulting GW flux can be written as

$$\mathcal{F}(v) = \mathcal{F}^{\rm GR}(v) + \mathcal{F}^\Lambda(v)\,, \tag{9.25}$$

where $\mathcal{F}^{\rm GR}(v)$ is the PN expression for the flux in GR and the leading-order correction to the flux $\mathcal{F}^\Lambda(v)$ reads

$$\mathcal{F}^\Lambda(v) = \left(\frac{393216}{5}\nu^3 - \frac{24576}{5}\nu^2\right)\left(\frac{d_\Lambda}{M}\right)^6 v^{26}\,. \tag{9.26}$$

9.5.1.3 Gravitational waveform in the stationary phase approximation

We are now in the position to compute the leading-order correction to the gravitational-wave phase due to the non-GR corrections computed above. In the PN regime one can compute the Fourier representation of the GW waveform using the stationary phase approximation (see e.g. [259, 479]). In this approximation the waveform in the frequency domain can be written as [259]

$$\begin{aligned} \tilde{h}(f) &= \frac{A(t_f)}{\sqrt{\dot{F}(t_f)}} e^{i[\psi_f(t_f)-\pi/4]}\,, \\ \psi_f(t) &\equiv 2\pi f t - \phi(t)\,, \end{aligned} \tag{9.27}$$

where $A(t)$ is the amplitude of the time-domain waveform, $\phi(t)$ is the orbital phase of the binary and $\pi F(t) = d\phi(t)/dt$ defines the instantaneous GW frequency $F(t)$. The quantity t_f is the saddle point where $d\psi_f(t)/dt = 0$, i.e. the time when $F(t)$ is equal to the Fourier variable f. In the adiabatic approximation ψ_f and t_f are given by

$$t_f = t_{\rm ref} + M\int_{v_f}^{v_{\rm ref}} \frac{E'(v)}{\mathcal{F}(v)} dv\,, \tag{9.28}$$

$$\psi_f(t_f) = 2\pi f t_{\rm ref} - \phi_{\rm ref} + 2\int_{v_f}^{v_{\rm ref}} (v_f^3 - v^3)\frac{E'(v)}{\mathcal{F}(v)} dv\,, \tag{9.29}$$

where we defined $v_f \equiv (\pi M f)^{1/3}$, $t_{\rm ref}$ and $\phi_{\rm ref}$ are integration constants and $v_{\rm ref}$ is and arbitrary reference velocity, commonly taken to be the velocity at the last stable orbit.

Using the PN expansions of the energy and flux and expanding the ratio $E'(v)/\mathcal{F}(v)$ at consistent PN order, the integral in Eq. (9.29) can be solved explicitly.

We find that the leading-order to the GW phase is given by

$$\psi(f) = \psi^{\rm GR}(f) + \frac{3}{128\nu v_f^5}\left(\frac{234240}{11} - \frac{522240}{11}\nu\right)\left(\frac{d_\Lambda}{M}\right)^6 v_f^{16}\,, \tag{9.30}$$

where $\psi^{\rm GR}(f)$ represents the GW phase in GR. An important conclusion of this calculation is that although the non-GR corrections enter formally at 8PN order, when $d_\Lambda v^2/M \equiv (\Lambda r)^{-1} \sim 1$ the corrections are numerically of 2PN order in magnitude.

9.5.1.4 On the validity of the post-Newtonian waveform model

By construction, the EFT action (9.15) is valid only for orbital separations $r \gtrsim d_\Lambda$; below this separation, terms containing higher powers of Λ^{-1} can impact the binary dynamics. Therefore, one must be careful to only employ this model in this limited regime of validity. For the purposes of parameter estimation, this lower limit on orbital separations r is more conveniently expressed as an upper limit on the frequency content of the signal. However, the conversion between these limits in not unique because r is not a gauge-invariant quantity. A natural choice is to first relate r to the orbital frequency Ω through the relation $r = (M/\Omega^2)^{1/3} + \mathcal{O}(v^2/c^2)$. Then, because the dominant contribution to the GW signal comes at twice the orbital frequency during the adiabatic inspiral, we can define a cutoff frequency $f_\Lambda \equiv 1/\pi\sqrt{M/d_\Lambda^3}$, such that the waveform model given by Eqs. (9.27) and (9.30) is expected to be valid for GW frequencies $f \ll f_\Lambda$.

Additionally, because we employ the PN approximation to compute our waveform, we must also impose that the typical velocity of the system $v \ll 1$. Again, there is no single well-defined point at which the PN approximation is no longer

valid, but a reasonable benchmark is the innermost stable circular orbit (ISCO) of an equivalent BH with mass M. We use this point as a canonical cutoff point for the PN approximation, restricting our waveforms to frequencies below $f_{\rm ISCO} = 1/(6\sqrt{6}\pi M)$.

Combining these two conditions, our model is only valid for frequencies $f < f_{\rm cutoff} \simeq \min[f_{\rm ISCO}, f_\Lambda]$.

9.5.2 Constraining d_Λ with GW151226 and GW170608

Having calculated the impact of higher-order curvature corrections on the phase evolution of the inspiral, we now establish a statistical framework to constrain such deviations from GR with GW observations. As before, the first step is to construct a generalized waveform that can represent these deviations. We use the `FTA` framework to add deviations of the form given in Eq. (9.30) to a PN waveform model in GR. As a baseline waveform model, we use the `TaylorF2` waveform approximant, an inspiral-only PN model given in the frequency domain that is valid for spinning, non-precessing systems up to 3.5PN order.[6] However, unlike the approach in Secs. 9.3 and 9.4, we use Bayesian model selection to constrain the effective distance-scale of new physics d_Λ.

As discussed in Chapter 1, the goal of Bayesian model selection is to calculate the odds ratio between two competing (1.26) hypotheses by computing the Bayes factor—the ratio of evidences—for either proposal. Here, the two hypotheses we

[6] As a check of consistency, we also repeat this analysis using the inspiral-merger-ringdown model `IMRPhenomPv2` (restricted to non-precessing systems) and find similar results. For this separate analysis, we do not impose the frequency cutoff of $f_{\rm ISCO}$ required by the PN approximation.

consider are: (i) $\mathcal{H}_{\text{non-GR}}$: higher-order curvature corrections enter at some fixed scale $d_\Lambda = d_\Lambda^* \sim$ km ; and (ii) $\mathcal{H}_{\text{GR}}$: higher-order curvature corrections are not present or (equivalently) appear at infinitesimal distance scales $d_\Lambda = 0$. The odds ratio between these hypotheses is given by

$$\mathcal{O}_{\text{GR}}^{\text{non-GR}} = \frac{p(\mathcal{H}_{\text{non-GR}})}{p(\mathcal{H}_{\text{GR}})} \text{BF}_{\text{GR}}^{\text{non-GR}}, \tag{9.31}$$

where the Bayes factor BF is determined by

$$\text{BF}_{\text{GR}}^{\text{non-GR}} \equiv \frac{p(d|\mathcal{H}_{\text{non-GR}})}{p(d|\mathcal{H}_{\text{GR}})} \tag{9.32}$$

given a particular GW observation d. Normally, one must be careful when using Bayesian model selection to perform tests of GR because the null and alternative hypothesis typically have parameter spaces of different dimensions. We avoid this particular obstacle by fixing d_Λ in $\mathcal{H}_{\text{non-GR}}$ to some particular value; we perform this test repeatedly for different values of d_Λ to scan the full parameter space. To remain agnostic, we always assume prior odds $p(\mathcal{H}_{\text{non-GR}})/p(\mathcal{H}_{\text{GR}})$ of unity.

The evidence for each hypothesis is computed as the marginalization of the likelihood over the space of binary parameters

$$P(d|\mathcal{H}) = \int d\boldsymbol{\theta} P(d|\boldsymbol{\theta}, \mathcal{H}). \tag{9.33}$$

The total likelihood is given by the (normalized) product of likelihoods for the signal d_i observed at each detector i

$$P(d|\boldsymbol{\theta}, \mathcal{H}) \propto \prod_i P_i(d_i|\boldsymbol{\theta}, \mathcal{H}), \tag{9.34}$$

where $P_i(d_i|\boldsymbol{\theta},\mathcal{H})$ takes the same form as introduced in Chapter 1:

$$P_i(d_i|\boldsymbol{\theta},\mathcal{H}) \propto e^{(d_i-h(\boldsymbol{\theta})|d_i-h(\boldsymbol{\theta}))}, \tag{9.35}$$

with the inner product weighted by the power spectral density $S_n^i(f)$ of each detector

$$(a|b) \equiv 2\int_{f_{\rm low}}^{f_{\rm high}} \frac{a(f)b^*(f)+a^*(f)b(f)}{S_n^i(f)}\,. \tag{9.36}$$

The evidence for each hypothesis is evaluated using the nested sampling algorithm implemented in the `LALInference` code package [78].

We consider the bounds that can be set by GW151226 [182] and GW170608 [183], the two lowest mass (i.e. longest) BBH events detected by LIGO and Virgo during the first two observing runs. Because of their low mass, the vast majority of the SNR of these signals is concentrated in their inspiral phase, which minimizes the measurement biases inherited from using a inspiral-only waveform model. For each event, we use $f_{\rm low} = 20$ Hz, as this is the lowest frequency for which $S_n(f)$ has been released for these events.[7] We choose $f_{\rm high}$ so as to respect the range of validity of the waveform, i.e. $f_{\rm high} < f_{\rm ISCO}$ and $f_{\rm high} < f_\Lambda$. The first of these conditions restricts the waveform to the PN regime; it is automatically imposed in the LALSuite implementation of the `TaylorF2` waveform mode, as the integrand of Eq. (9.36) always evaluates to zero for frequencies above $f_{\rm ISCO}$. The second condition restricts the waveform to the regime in which the EFT is valid. However, because the frequency at which this approximation breaks down is unknown *a priori*, there remains

[7] This research has made use of data, software and/or web tools obtained from the Gravitational Wave Open Science Center (https://www.gw-openscience.org), a service of LIGO Laboratory, the LIGO Scientific Collaboration and the Virgo Collaboration.

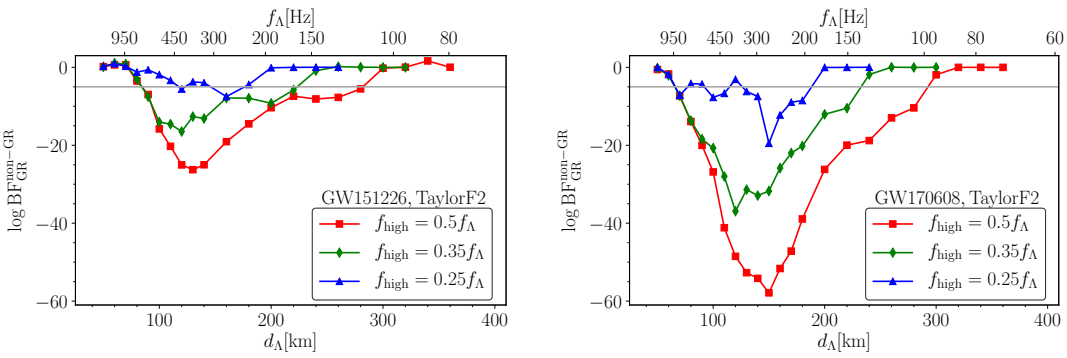

Figure 9.5: The log Bayes factors of non-GR versus GR hypotheses with (left) GW151226 and (right) GW170608 for different choices of d_Λ (in km). The corresponding $f_\Lambda \equiv 1/\pi\sqrt{M_{\mathrm{tot}}/d_\Lambda^3}$ shown on the top x-axis. Different choices of cutoff criteria f_{high} are shown in different colors.

some ambiguity in how to choose f_{high}; this ambiguity comprises a source of systematic error in our analysis. To gauge the impact of this ambiguity, we perform our analysis with the different choices of cutoff frequency $f_{\mathrm{high}} \in [0.25 f_\Lambda, 0.35 f_\Lambda, 0.5 f_\Lambda]$. Smaller choices for f_{high} represent more conservative usage of our EFT, whereas larger choices assume that it remains valid over a larger range of scales. For simplicity, we compute $f_\Lambda \equiv 1/\pi\sqrt{M_{\mathrm{tot}}/d_\Lambda^3}$ by fixing the total BH mass to the median value for the total BH mass obtained from parameter estimation with a full IMR waveform model in GR as given in Refs. [182, 183].

Figure 9.5 depicts the logarithm of the Bayes factors in opposition of versus in support of GR from GW151226 (left) and GW170608 (right) as a function of d_Λ. Results computed using different cutoff criteria are depicted with different colors—red, green, and blue corresponding to the least to most conservative cutoff, respectively. For each event, the value of f_Λ corresponding to d_Λ is shown on the top

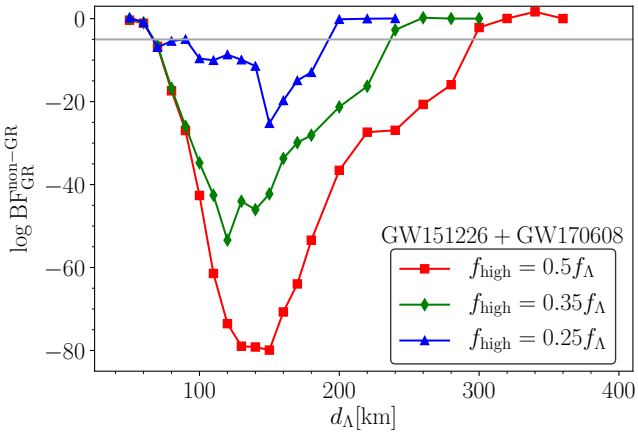

Figure 9.6: Same as Fig. 9.5 but computed by combining information from both GW151226 and GW170608.

axis. We observe that $\log \mathrm{BF}^{\text{non-GR}}_{\mathrm{GR}} < 0$ across a range of values of d_Λ, indicating that the non-GR hypothesis is disfavored in those regions. These regions largely overlap across the two events due to their similar total mass; however, one obtains slightly stronger evidence in support of GR from GW170608 due to the event's larger SNR relative to GW151226.

The qualitative features of our results can be understood in terms of two effects. First, the Bayes factor asymptotically approaches $B^{\mathrm{non-GR}}_{\mathrm{GR}} \sim 1$ as d_Λ tends to zero because the non-GR contribution to the waveform scales with d^6_Λ. Second, the Bayes factor also asymptotically approaches $B^{\mathrm{non-GR}}_{\mathrm{GR}} \sim 1$ for large d_Λ because this limit corresponds to a very small cutoff frequency f_{high}. By restricting ourselves to only the very low-frequency content of the observed GW, we no longer have sufficient data to distinguish the signal from noise regardless of which model (non-GR vs. GR) we assume, and thus neither hypothesis is preferred. Assuming

statistical independence between the two observed events, we can compute Bayes factor using both observations by simply multiplying the Bayes factors from each event individually; this combined result is shown in Fig. 9.6.

The Bayes factors discussed above indicate the odds for/against higher-order curvature corrections at a given scale d_Λ. These can be translated into a constraint on d_Λ by setting some significance threshold beyond which one unequivocally accepts either hypothesis. We adopt as our threshold $|\log \mathrm{BF}| \gtrsim 5$, shown as a horizontal gray line in Figs. 9.5 and 9.6. We note that this threshold is substantially larger than standard choices suggested in the literature [480]. We adopt this conservative threshold because we find that systematic effects—such as changing the choice of prior distributions—can shift $\log \mathrm{BF}$ by as much as ± 3; we suspect that these systematic errors also cause the small fluctuations seen in Figs. 9.5 and 9.6. Imposing this significance threshold, we rule out the existence of higher-order curvature contributions on the distance scales of $d_\Lambda \sim [70, 200]$ km using the most conservative cutoff criteria we considered; relaxing this cutoff criteria increases the width of the excluded region of parameter space.

Chapter 10: Conclusions and future work

In this thesis, I have presented work directed towards extending and improving tests of GR with GWs. This is an incredibly multi-faceted endeavor; even when focusing on just one portion of only a single type of GW observation—the inspiral of a coalescing compact binary system—I addressed this central objective from a variety of directions, employing an assortment of different techniques. In this final chapter, I wish to reiterate the common threads that connect the work described in the previous chapters of this thesis. Then, inspired by this summary, I conclude by addressing directions for future research.

One key theme of this thesis was modeling the behavior of binary inspirals and the GW signals they produce in alternative theories of gravity. Not only are these modeling efforts necessary for any theory-specific test of GR, they can also provide a conceptual foundation for more theory-agnostic approaches as well. I carried out work of this nature in great detail in Chapters 2 and 3 for two particular scalar extensions of GR: Einstein-Maxwell-dilaton gravity (EMd) [1] and massless scalar-tensor (ST) theories [2], respectively. These theories represent perturbative deviations from GR, in the sense that there exists a limit in which the scalar degrees of freedom smoothly decouple from gravity and matter, and binaries behave as

in GR. By contrast, in Chapters 4 and 5, I examine a ST theory in which non-perturbative deviations from GR manifest in the form of scalarization of NSs [3, 4]. In the strong-coupling regime, NSs (either in isolation or in binary systems) can undergo a phase transition during which the scalar field is spontaneously excited; I study in particular detail the behavior of binary systems during the onset of this transition.

Another focus of this thesis was modeling specific phenomenology known to occur across a range of alternatives to GR and then understanding how this can be connected to specific examples of such theories. In contrast to the previous chapters, this type of approach embodies a more bottom-up philosophy. Taking lessons learned in these earlier chapters, Chapter 6 presented a theory-agnostic description of scalarization and offered a simple yet robust parameterization suitable for GW searches for such non-perturbative effects [5]. Chapter 7 described how the generic signatures of spontaneous and dynamical scalarization could be translated to bounds on a specific ST theory that manifests such phenomena [6]. Chapter 8 examined a different type of signature for new strong-field physics: the tidal deformations of compact objects close to the merger of a binary system [7]. This phenomenon is known to occur for mundane sources (e.g. NSs) as well as exotic alternatives (e.g. "BH mimickers"); here I estimated the extent to which such observations can be used to distinguish boson stars from NSs and BHs.

Finally, in Chapter 9, I developed tools to test non-GR phenomenology in observed GWs not linked to any particular alternative theory. The primary result of this work was the introduction of the flexible theory-agnostic (`FTA`) framework

that allowed one to adapt any frequency-domain waveform model for use in such tests. As a member of the LIGO Scientific Collaboration, I used this framework to perform theory-agnostic tests on BBH and BNS inspirals observed with Advanced LIGO and Virgo [9, 10]. However, I then circled back to the efforts presented at the start of the thesis by using the `FTA` infrastructure to perform theory-specific tests for two specific alternatives to GR. [11, 138]

A crucial takeaway from the previous discussion is that many of the exact same tools can be used for theory-specific and theory-agnostic (or top-down and bottom-up) tests of GR. This fact has been used often to convert the bounds from theory-agnostic tests (e.g. those produced by the LIGO and Virgo collaborations) to constraints on particular modified theories of gravity; see, for example Refs. [187, 481]. However, theory-specific and theory-agnostic analyses test slightly different statistical hypotheses, and within a fully Bayesian framework, converting results from one to the other requires care. To my knowledge, this issue has not been studied in detail in the context of GW tests of GR, and thus offers an interesting new avenue for future work. The ultimate goal of such a study would be to understand how to systematically translate results between theory-specific and theory-agnostic (as well as top-down and bottom-up) tests. I provide some speculative starting points for such an investigation below, using the theory-agnostic and theory-agnostic tests presented in Chapter 9 as prototypical examples.

Recall that in Chapter 9 a theory-agnostic test of dipole radiation (or equivalently, an anomalous -1PN contribution to the GW phase evolution) employed the same type of generalized waveform model as a theory-specific test of Jordan-Fierz-

Brans-Dicke gravity (JFBD). In fact, there exists an invertible map between the -1PN deviation parameter $\delta\hat{\varphi}_{-2}$ used in the former and the JFBD parameter α_0 used in the latter that allows the two waveform models to be identified. Thus, within a Bayesian context, the likelihood function $P(d|\boldsymbol{\theta})$ in either test would be identical [see Eq. (1.23)]; the only difference between these two tests are the choice of prior functions $P(\boldsymbol{\theta})$. Note that any choice of prior distribution can be identified with a family of parameterizations in which that prior is uniform over its support, i.e. one can always find a reparameterization $\boldsymbol{\theta} \to \boldsymbol{\theta}'$ such that the Jacobian

$$\left|\frac{\partial\theta'^a}{\partial\theta^b}\right| \propto \frac{1}{P(\boldsymbol{\theta})} \tag{10.1}$$

over the support of $P(\boldsymbol{\theta})$, and thus

$$P(\boldsymbol{\theta}') \propto \left|\frac{\partial\theta'^a}{\partial\theta^b}\right| P(\boldsymbol{\theta}) = \text{constant}. \tag{10.2}$$

In the theory-agnostic test of dipole radiation presented in Chapter 9, the parameterization corresponding to a flat prior used $\delta\hat{\varphi}_{-2}$, whereas in the (second) test of JFBD, this parameterization used α_0. So, an open question for future study is how should one choose the prior—or equivalently, preferred parameterization—for tests of GR?

One approach, in line with a top-down philosophy, would be to choose a preferred parameterization that leaves "physical" parameters unbiased by the prior. For example, in a theory-specific test, these parameters could be the fundamental masses and couplings that enter at the level of the action. In contrast, a more theory-agnostic approach could follow the principles of effective field theory and include all relevant operators in an action up to some dimension. Then, the

masses/couplings of each operator would serve as the natural parameters to test GR. Similar approaches have been adopted for cosmological tests of modified gravity for theories in which the current accelerated expansion of the Universe is caused by a single scalar field [482–486]. However, these models have been used primarily to study Friedmann-Lemaître-Robertson-Walker solutions and their linear perturbations, whereas modeling the inspiral of compact objects could require greater understanding of nonlinear interactions. In the most ambitious scenario, one could hope to formulate GW tests of GR with an approach like the Standard Model Extension [487–489], which provides a complete effective-field-theoretical framework for studying CPT and Lorentz violations on curved backgrounds.

Another approach, more in line with a bottom-up philosophy, would be to choose a parameterization based off of our understanding of waveform models in GR and the characteristics of our detectors. For example, adopting a Jeffreys prior [490] would eliminate the parameterization-dependence of one's statistical analysis; with this prior, the likelihood function $P(d|\boldsymbol{\theta})$ takes the same form for any parameterization $\boldsymbol{\theta}$. This prior assigns greater weight to regions of parameter space in which detectors are most sensitive, as determined by the determinant of the Fisher information matrix $\Gamma_{ij}(\boldsymbol{\theta})$. For the generalized waveforms conventionally used for GW tests of GR—such as all of those used in Chapter 9—one can always reparameterize the deviation parameters of the waveform such that Jeffreys prior appears flat (i.e. is uniform over some finite bounded region of parameter space). Though not tied directly to any underlying physical parameter, this new parameterization offers more appealing statistical properties (e.g. parameterization-independence) than

that currently used in standard theory-agnostic tests.

Appendix A: The 1PN two-body Lagrangian in Einstein-Maxwell-dilaton theory

In this appendix, we derive the 1PN two-body Lagrangian in EMd theory using the Fokker action method [207] (see also Refs. [208–210]). To derive the Lagrangian, we expand the EMd action in Eq. (2.2), together with the matter action for point particles in Eq. (2.3) and the mass expansion from Eq. (2.7). After that, we obtain the field equations for the potentials, solve them, and plug the solutions back into the action to get the Lagrangian. Throughout, we work in the harmonic gauge $g^{\mu\nu}\Gamma^{\lambda}_{\mu\nu} = 0$ and the Lorenz gauge $\partial_\mu A^\mu = 0$. Also, in this appendix and the next, we explicitly write c and G for bookkeeping.

A.1 Expanding the metric and connection coefficients

Before expanding the EMd action, we start by expanding the metric in powers of v/c [491],

$$\begin{aligned} g_{00} &= -1 + 2V - 2V^2 + \dots, \\ g_{0i} &= -4V_i + \dots, \\ g_{ij} &= \delta_{ij} + 2V\delta_{ij} + \dots, \end{aligned} \tag{A.1}$$

where the potentials $V \sim \mathcal{O}(1/c^2)$, and $V_i \sim \mathcal{O}(1/c^3)$. The inverse metric satisfies $g^{\mu\lambda} g_{\lambda\nu} = \delta^{\mu}{}_{\nu}$.

The connection coefficients in terms of the metric are given by

$$\Gamma^{\mu}{}_{\nu\lambda} = \frac{1}{2} g^{\mu\rho} \left(\partial_\lambda g_{\rho\nu} + \partial_\nu g_{\rho\lambda} - \partial_\rho g_{\nu\lambda} \right) . \tag{A.2}$$

Plugging the metric expansion in terms of the potentials yields the connection coefficients to $\mathcal{O}(1/c^4)$

$$\begin{aligned}
\Gamma^{0}{}_{00} &= -\partial_0 V \,, \\
\Gamma^{0}{}_{0i} &= -\partial_i V \,, \\
\Gamma^{i}{}_{00} &= -\partial_i V + 2\partial_i V^2 - 4\partial_0 V_i \,, \\
\Gamma^{0}{}_{ij} &= 2\left(\partial_j V_i - \partial_i V_j \right) + \delta_{ij} \partial_0 V \,, \\
\Gamma^{i}{}_{0j} &= 2\left(\partial_i V_j - \partial_j V_i \right) + \delta_{ij} \partial_0 V \,, \\
\Gamma^{i}{}_{jk} &= -(1+2V) \left(\delta_{ij} \partial_k V + \delta_{ik} \partial_j V - \delta_{jk} \partial_i V \right) .
\end{aligned} \tag{A.3}$$

A.2 Expanding the action

The action of EMd theory is given by Eq. (2.2). We can divide that action into four pieces

$$S = S_g + S_\varphi + S_{\rm em} + S_m \,, \tag{A.4}$$

where S_g is the gravitational action, S_φ is the dilaton action, $S_{\rm em}$ is the electromagnetic action with the dilaton coupling, and S_m is the matter action.

In the Einstein frame, the gravitational action is the same as in GR. The

Einstein-Hilbert gravitational action can be written in the Landau-Lifshitz form

$$S_g = \frac{c^4}{16\pi G}\int dtd^3\boldsymbol{x}\,\sqrt{-g}g^{\mu\nu}\left(\Gamma^{\rho}_{\mu\lambda}\Gamma^{\lambda}_{\nu\rho} - \Gamma^{\rho}_{\mu\nu}\Gamma^{\lambda}_{\rho\lambda}\right). \tag{A.5}$$

Substituting the connection coefficients from Eq. (A.3) in terms of the potentials leads to

$$S_g = \frac{c^4}{16\pi G}\int dtd^3\boldsymbol{x}\Big[-2\partial_i V\partial_i V - 16\partial_i V\partial_0 V_i - 6\partial_0 V\partial_0 V + 8\partial_i V_j\partial_i V_j - 8\partial_i V_j\partial_j V_i\Big]. \tag{A.6}$$

Imposing the harmonic gauge condition $g^{\mu\nu}\Gamma^{\lambda}_{\mu\nu} = 0$ gives $\partial_0 V + \partial_i V_i = 0$. Applying that condition in the action and integrating by parts yields

$$S_g = \frac{c^4}{16\pi G}\int dtd^3\boldsymbol{x}\Big[-2\partial_i V\partial_i V + 2\partial_0 V\partial_0 V + 8\partial_i V_j\partial_i V_j\Big]. \tag{A.7}$$

The dilaton action is given by

$$S_\varphi = -\frac{c^4}{8\pi G}\int dtd^3\boldsymbol{x}\sqrt{-g}g^{\mu\nu}\partial_\mu\varphi\partial_\nu\varphi\,. \tag{A.8}$$

Since φ is of order $1/c^2$, then to $\mathcal{O}(1/c^2)$

$$S_\varphi = -\frac{c^4}{8\pi G}\int dtd^3\boldsymbol{x}\left(-\partial_0\varphi\partial_0\varphi + \partial_i\varphi\partial_i\varphi\right). \tag{A.9}$$

The electromagnetic action including the dilaton coupling is given by

$$S_{\rm em} = \frac{-1}{16\pi}\int dtd^3\boldsymbol{x}\sqrt{-g}e^{-2a\varphi}F_{\mu\nu}F^{\mu\nu}\,, \tag{A.10}$$

with the electromagnetic field $F_{\mu\nu} = \nabla_\mu A_\nu - \nabla_\nu A_\mu = \partial_\mu A_\nu - \partial_\nu A_\mu$ and the vector potential $A_\mu = (A_0, A_i)$. The component $A_0 = \mathcal{O}(1) + \mathcal{O}(1/c^2) + \ldots$, while the components $A_i = \mathcal{O}(1/c) + \ldots$. Therefore, expanding $F_{\mu\nu}F^{\mu\nu}$ to $\mathcal{O}(1/c^2)$ leads to

$$F_{\mu\nu}F^{\mu\nu} = -2\partial_i A_0\partial_i A_0 + 2\partial_j A_i\partial_j A_i + 4\partial_0 A_i\partial_i A_0 - 2\partial_i A_j\partial_j A_i\,. \tag{A.11}$$

Because the last two terms in Eq. (A.11) are of order $1/c^2$, we can use integration by parts and the Lorentz gauge condition ($\partial_\mu A^\mu = 0$) to replace these last two terms by $2\partial_0 A_0 \partial_0 A_0$. Since $\sqrt{-g} = 1+2V$, and $e^{-2a\varphi} \simeq 1-2a\varphi+\ldots$, the action becomes

$$S_{\rm em} = \frac{1}{8\pi}\int dt d^3\boldsymbol{x}\big[(1+2V-2a\varphi)\partial_i A_0\partial_i A_0 - \partial_j A_i \partial_j A_i - \partial_0 A_0 \partial_0 A_0\big]. \tag{A.12}$$

The matter action S_m for point particles at monopolar order (dipole/spin and higher multipoles neglected) is given by

$$S_m = -\sum_A \int dt\left[\mathfrak{m}_A(\varphi)c^2\sqrt{-g_{\mu\nu}\,v_A^\mu v_A^\nu/c^2} - \frac{1}{c}q_A A_\mu \frac{dx^\mu}{dt}\right], \tag{A.13}$$

where the field-dependent mass of each body has the expansion given by Eq. (2.7)

$$\mathfrak{m}(\varphi) = m\left[1+\alpha\varphi+\frac{1}{2}(\alpha^2+\beta)\varphi^2+\mathcal{O}\left(1/c^6\right)\right]. \tag{A.14}$$

Defining the mass density ρ_g in terms of the constant masses

$$\rho_g \equiv \sum_A m_A \delta^3(\boldsymbol{x}-\boldsymbol{x}_A), \tag{A.15}$$

and defining the electric charge density by

$$\rho_e \equiv \sum_A q_A \delta^3(\boldsymbol{x}-\boldsymbol{x}_A), \tag{A.16}$$

then the matter action to $\mathcal{O}(1/c^2)$ can be written as

$$\begin{aligned} S_m = \int dt d^3\boldsymbol{x}\Bigg[&\rho_g\left(-c^2+\frac{1}{2}v^2+Vc^2+\frac{1}{8}\frac{v^4}{c^2}+\frac{3}{2}Vv^2-\frac{1}{2}V^2c^2-4V_i v^i c\right)\\ &+\rho_g\alpha\varphi\left(-c^2+\frac{1}{2}v^2+Vc^2\right)-\frac{1}{2}c^2\rho_g(\alpha^2+\beta)\varphi^2+\rho_e\left(A_0+\frac{1}{c}A_i v^i\right)\Bigg]. \end{aligned} \tag{A.17}$$

The parameters α and β will be assigned a subscript when multiplied by the delta functions in ρ_g.

A.3 The field equations

Combining the expansion of the action from the previous subsection, the total action at 1PN order is given by

$$\begin{aligned} S = \int dt d^3\boldsymbol{x} \Bigg\{ & \frac{c^4}{16\pi G}\left[-2\partial_i V \partial_i V + 2\partial_0 V \partial_0 V + 8\partial_i V_j \partial_i V_j\right] \\ & + \rho_g \left[-c^2 + \frac{1}{2}v^2 + Vc^2 + \frac{1}{8}\frac{v^4}{c^2} + \frac{3}{2}Vv^2 - \frac{1}{2}V^2c^2 - 4V_i v^i c\right] \\ & - \frac{c^4}{8\pi G}\left(-\partial_0\varphi\partial_0\varphi + \partial_i\varphi\partial_i\varphi\right) + \rho_g\alpha\varphi\left(-c^2 + \frac{1}{2}v^2 + Vc^2\right) \\ & - \frac{1}{2}c^2\rho_g(\alpha^2+\beta)\varphi^2 + \rho_e\left(A_0 + \frac{1}{c^2}A_i v^i\right) \\ & + \frac{1}{8\pi}\left[(1+2V-2a\varphi)\partial_i A_0\partial_i A_0 - \partial_j A_i \partial_j A_i - \partial_0 A_0 \partial_0 A_0\right]\Bigg\}. \end{aligned} \tag{A.18}$$

Varying the action with respect to the potentials V_i, A_i, V, φ, and A_0 respectively yields the field equations

$$\nabla^2 V_i = -\frac{4\pi G}{c^3}\rho_g v^i\,, \tag{A.19}$$

$$\nabla^2 A_i = -\frac{4\pi}{c}\rho_e v^i\,, \tag{A.20}$$

$$\Box V = -\frac{4\pi G}{c^2}\rho_g - \frac{4\pi G}{c^4}\rho_g\left(\frac{3}{2}v^2 - Vc^2\right) - \frac{4\pi G}{c^2}\rho_g\alpha\varphi - \frac{G}{c^4}\partial_i A_0\partial_i A_0\,, \tag{A.21}$$

$$\Box\varphi = -\frac{4\pi G}{c^4}\rho_g\left[-\alpha + \frac{1}{2}\alpha v^2 + \alpha V - (\alpha^2+\beta)\varphi\right] + \frac{Ga}{c^4}\partial_i A_0\partial_i A_0\,, \tag{A.22}$$

$$\Box A_0 = 4\pi\rho_e - 2V\nabla^2 A_0 - 2\partial_i V\partial_i A_0 + 2a\varphi\nabla^2 A_0 + 2a\partial_i\varphi\partial_i A_0\,, \tag{A.23}$$

where $\Box = -\partial_0^2 + \nabla^2$ is the flat d'Alembertian.

The first two equations can be solved directly for V_i, and A_i

$$V_i = \frac{G}{c^3}\left(\frac{m_1 v_1^i}{|\boldsymbol{x}-\boldsymbol{x}_1|} + \frac{m_2 v_2^i}{|\boldsymbol{x}-\boldsymbol{x}_2|}\right), \tag{A.24}$$

$$A_i = \frac{1}{c}\left(\frac{q_1 v_1^i}{|\boldsymbol{x}-\boldsymbol{x}_1|} + \frac{q_2 v_2^i}{|\boldsymbol{x}-\boldsymbol{x}_2|}\right). \tag{A.25}$$

To solve the other three equations, we first rewrite the terms $\partial_i A_0 \partial_i A_0$, $\partial_i \varphi \partial_i A_0$, and $\partial_i V \partial_i A_0$ using the identity

$$\nabla^2(\chi\xi) = \chi\nabla^2\xi + \xi\nabla^2\chi + 2\partial_i\chi\partial_i\xi\,, \tag{A.26}$$

where χ and ξ are any scalar functions. Using that identity, Eqs. (A.21), (A.22), and (A.23) can be written as

$$\Box V = -\frac{4\pi G}{c^2}\rho_g - \frac{4\pi G}{c^4}\rho_g\left(\frac{3}{2}v^2 - Vc^2\right) - \frac{4\pi G}{c^2}\rho_g\alpha\varphi - \frac{G}{2c^4}\nabla^2(A_0)^2 + \frac{G}{c^4}A_0\nabla^2 A_0\,, \tag{A.27}$$

$$\Box\varphi = -\frac{4\pi G}{c^4}\rho_g\left[-c^2\alpha + \frac{1}{2}\alpha v^2 + c^2\alpha V - c^2(\alpha^2+\beta)\varphi\right] - \frac{Ga}{c^4}A_0\nabla^2 A_0 + \frac{Ga}{2c^4}\nabla^2(A_0)^2\,, \tag{A.28}$$

$$\Box A_0 = 4\pi\rho_e - \nabla^2(VA_0) - V\nabla^2 A_0 + A_0\nabla^2 V + a\nabla^2(\varphi A_0) + a\varphi\nabla^2 A_0 - aA_0\nabla^2\varphi\,. \tag{A.29}$$

At this point, one could split the fields into separate PN orders, followed by further simplifications of the action through partial integrations and use of the field equations. Eventually one would only need an explicit expression for the leading order solution to the field equations here in order to obtain the 1PN Fokker action. This is essentially the "n+2" method from Ref. [209]. However, at this order this does overall not provide a big simplification, and we need a solution for the 1PN scalar field for Figs. 2.4 and 2.5. We therefore proceed by solving the 1PN field equations and straightforwardly insert the solution into the complete action.

To solve those three equations, we first solve for the leading order terms of V, φ, and A_0, and then insert that solution back into the right hand side of the

equations. Equation (A.27) yields

$$
\begin{aligned}
V = & \frac{G}{c^2}\left(\frac{m_1}{|\boldsymbol{x}-\boldsymbol{x}_1|}+\frac{m_2}{|\boldsymbol{x}-\boldsymbol{x}_2|}\right)+\frac{G}{2c^4}\left(m_1\frac{\partial^2}{\partial t^2}|\boldsymbol{x}-\boldsymbol{x}_1|+m_2\frac{\partial^2}{\partial t^2}|\boldsymbol{x}-\boldsymbol{x}_2|\right) \\
& +\frac{3G}{2c^4}\left(\frac{m_1 v_1^2}{|\boldsymbol{x}-\boldsymbol{x}_1|}+\frac{m_2 v_2^2}{|\boldsymbol{x}-\boldsymbol{x}_2|}\right)-\frac{G^2}{c^4}m_1 m_2\left(\frac{1}{r|\boldsymbol{x}-\boldsymbol{x}_1|}+\frac{1}{r|\boldsymbol{x}-\boldsymbol{x}_2|}\right) \\
& -\frac{G^2}{c^4}\alpha_1\alpha_2 m_1 m_2\left(\frac{1}{r|\boldsymbol{x}-\boldsymbol{x}_1|}+\frac{1}{r|\boldsymbol{x}-\boldsymbol{x}_2|}\right)-\frac{G}{2c^4}\left(\frac{q_1}{|\boldsymbol{x}-\boldsymbol{x}_1|}+\frac{q_2}{|\boldsymbol{x}-\boldsymbol{x}_2|}\right)^2 \\
& +\frac{G}{c^4}q_1 q_2\left(\frac{1}{r|\boldsymbol{x}-\boldsymbol{x}_1|}+\frac{1}{r|\boldsymbol{x}-\boldsymbol{x}_2|}\right), \qquad \text{(A.30)}
\end{aligned}
$$

where $r \equiv |\boldsymbol{x}_1 - \boldsymbol{x}_2|$ and

$$
\frac{\partial^2}{\partial t^2}|\boldsymbol{x}-\boldsymbol{x}_1| = \frac{v_1^2}{|\boldsymbol{x}-\boldsymbol{x}_1|} - \boldsymbol{n}_1\cdot\boldsymbol{a}_1 - \frac{(\boldsymbol{n}_1\cdot\boldsymbol{v}_1)^2}{|\boldsymbol{x}-\boldsymbol{x}_1|}, \qquad \text{(A.31)}
$$

with $\boldsymbol{n}_1 \equiv (\boldsymbol{x}-\boldsymbol{x}_1)/|\boldsymbol{x}-\boldsymbol{x}_1|$, and $\boldsymbol{a}_1 = d\boldsymbol{v}_1/dt$ is the acceleration.

Solving Eq. (A.28) and using Eq. (A.31), we get

$$
\begin{aligned}
\varphi = & -\frac{G}{c^2}\left(\frac{\alpha_1 m_1}{|\boldsymbol{x}-\boldsymbol{x}_1|}+\frac{\alpha_2 m_2}{|\boldsymbol{x}-\boldsymbol{x}_2|}\right)+\frac{G}{2c^4}\alpha_1 m_1\left(\boldsymbol{n}_1\cdot\boldsymbol{a}_1+\frac{(\boldsymbol{n}_1\cdot\boldsymbol{v}_1)^2}{|\boldsymbol{x}-\boldsymbol{x}_1|}\right) \\
& +\frac{G}{2c^4}\alpha_2 m_2\left(\boldsymbol{n}_2\cdot\boldsymbol{a}_2+\frac{(\boldsymbol{n}_2\cdot\boldsymbol{v}_2)^2}{|\boldsymbol{x}-\boldsymbol{x}_2|}\right)+\frac{a}{2}\left(\frac{q_1}{|\boldsymbol{x}-\boldsymbol{x}_1|}+\frac{q_2}{|\boldsymbol{x}-\boldsymbol{x}_2|}\right)^2 \\
& +\frac{G^2}{c^4}m_1 m_2\left(\frac{\alpha_1+\alpha_2(\alpha_1^2+\beta_1)}{r|\boldsymbol{x}-\boldsymbol{x}_1|}+\frac{\alpha_2+\alpha_1(\alpha_2^2+\beta_2)}{r|\boldsymbol{x}-\boldsymbol{x}_2|}\right) \\
& -\frac{Ga}{c^4}q_1 q_2\left(\frac{1}{r|\boldsymbol{x}-\boldsymbol{x}_1|}+\frac{1}{r|\boldsymbol{x}-\boldsymbol{x}_2|}\right). \qquad \text{(A.32)}
\end{aligned}
$$

The solution of Eq. (A.29) for A_0 is given by

$$
\begin{aligned}
A_0 = & -\left(\frac{q_1}{|\boldsymbol{x}-\boldsymbol{x}_1|}+\frac{q_2}{|\boldsymbol{x}-\boldsymbol{x}_2|}\right)-\frac{q_1}{2c^2}\left(\frac{v_1^2}{|\boldsymbol{x}-\boldsymbol{x}_1|}-\boldsymbol{n}_1\cdot\boldsymbol{a}_1-\frac{(\boldsymbol{n}_1\cdot\boldsymbol{v}_1)^2}{|\boldsymbol{x}-\boldsymbol{x}_1|}\right) \\
& -\frac{q_2}{2c^2}\left(\frac{v_2^2}{|\boldsymbol{x}-\boldsymbol{x}_2|}-\boldsymbol{n}_2\cdot\boldsymbol{a}_2-\frac{(\boldsymbol{n}_2\cdot\boldsymbol{v}_2)^2}{|\boldsymbol{x}-\boldsymbol{x}_2|}\right) \\
& +\frac{G}{c^2}\left((1+a\alpha_1)\frac{m_1}{|\boldsymbol{x}-\boldsymbol{x}_1|}+(1+a\alpha_2)\frac{m_2}{|\boldsymbol{x}-\boldsymbol{x}_2|}\right)\left(\frac{q_1}{|\boldsymbol{x}-\boldsymbol{x}_1|}+\frac{q_2}{|\boldsymbol{x}-\boldsymbol{x}_2|}\right) \\
& +\frac{G}{c^2}\left((1+a\alpha_2)\frac{q_1 m_2}{r|\boldsymbol{x}-\boldsymbol{x}_1|}+(1+a\alpha_1)\frac{q_2 m_1}{r|\boldsymbol{x}-\boldsymbol{x}_2|}\right) \\
& -\frac{G}{c^2}\left((1+a\alpha_1)\frac{m_1 q_2}{r|\boldsymbol{x}-\boldsymbol{x}_1|}+(1+a\alpha_2)\frac{m_2 q_1}{r|\boldsymbol{x}-\boldsymbol{x}_2|}\right). \qquad \text{(A.33)}
\end{aligned}
$$

A.4 The 1PN Lagrangian

The total action, after using the field equations and integrating by parts, can be written as

$$S = \int dt d^3\boldsymbol{x} \Bigg[\rho_g \left(-c^2 + \frac{1}{2}v^2 + \frac{v^4}{8c^2} + \frac{1}{2}Vc^2 + \frac{3}{4}Vv^2 - 2V_i v^i c \right) + \rho_e \left(\frac{1}{2}A_0 + \frac{1}{2c}A_i v^i \right) + \frac{1}{2}\rho_g \alpha\varphi \left(-c^2 + \frac{1}{2}v^2 \right) + \frac{1}{2}\rho_e A_0 V - \frac{1}{2}a\rho_e A_0 \varphi + \frac{G}{4c^2}\rho_g (1 + a\alpha) A_0^2 \Bigg]. \tag{A.34}$$

Substituting the potentials gives acceleration terms that can be eliminated using integration by parts in the action

$$\int dt \, (\boldsymbol{n} \cdot \boldsymbol{a}_1) = \int dt \left(-\frac{v_1^2}{r} + \frac{(\boldsymbol{n} \cdot \boldsymbol{v}_1)^2}{r} - \frac{(\boldsymbol{n} \cdot \boldsymbol{v}_1)(\boldsymbol{n} \cdot \boldsymbol{v}_2)}{r} + \frac{\boldsymbol{v}_1 \cdot \boldsymbol{v}_2}{r} \right), \tag{A.35}$$

where $\boldsymbol{n} \equiv (\boldsymbol{x}_1 - \boldsymbol{x}_2)/|\boldsymbol{x}_1 - \boldsymbol{x}_2|$, and $\boldsymbol{a}_1 = \dot{\boldsymbol{v}}_1$. Finally, integrating over space term by term and simplifying leads to the 1PN Lagrangian

$$L = -m_1 c^2 - m_2 c^2 + L_0 + \frac{1}{c^2} L_1 \,, \tag{A.36}$$

with

$$\begin{aligned} L_0 =& \frac{1}{2}m_1 v_1^2 + \frac{1}{2}m_2 v_2^2 + G(1 + \alpha_1\alpha_2)\frac{m_1 m_2}{r} - \frac{q_1 q_2}{r}, \\ L_1 =& \frac{1}{8}m_1 v_1^4 + \frac{1}{8}m_2 v_2^4 + \frac{q_1 q_2}{2r}\left[\boldsymbol{v_1} \cdot \boldsymbol{v_2} + (\boldsymbol{n} \cdot \boldsymbol{v_1})(\boldsymbol{n} \cdot \boldsymbol{v_2}) \right] \\ &+ \frac{G m_1 m_2}{2r}\left[(3 - \alpha_1\alpha_2)(v_1^2 + v_2^2) - (7 - \alpha_1\alpha_2)(\boldsymbol{v_1} \cdot \boldsymbol{v_2}) - (1 + \alpha_1\alpha_2)(\boldsymbol{n} \cdot \boldsymbol{v_1})(\boldsymbol{n} \cdot \boldsymbol{v_2}) \right] \\ &- \frac{G^2 m_1 m_2}{2r^2}\left[(1 + 2\alpha_1\alpha_2)(m_1 + m_2) + m_1\alpha_1^2(\alpha_2^2 + \beta_2) + m_2\alpha_2^2(\alpha_1^2 + \beta_1) \right] \\ &+ \frac{G q_1 q_2}{r^2}\left[m_1(1 + a\alpha_1) + m_2(1 + a\alpha_2) \right] - \frac{G}{2r^2}\left[m_1 q_2^2(1 + a\alpha_1) + m_2 q_1^2(1 + a\alpha_2) \right]. \end{aligned} \tag{A.37}$$

Appendix B: Energy flux to next-to-leading PN order in Einstein-Maxwell-dilaton theory

In this appendix, we derive the next-to-leading order scalar, vector, and tensor energy fluxes for general orbits. The derivation follows the one used in Ref. [147] in the context of ST theory.

B.1 Scalar energy flux

The scalar field in a radiative coordinate system can be written as

$$\varphi(\boldsymbol{X}^{\mu}) = \varphi_0 + \frac{1}{R}\psi(U, \boldsymbol{N}) + \mathcal{O}\left(\frac{1}{R^2}\right), \tag{B.1}$$

where $R \equiv |\boldsymbol{X}|$, $U \equiv T - R/c$, $\boldsymbol{N} \equiv \boldsymbol{X}/R$, and the Einstein-frame radiative scalar multipole moments are defined by

$$\psi(U, \boldsymbol{N}) = G \sum_{\ell \geq 0} \frac{1}{\ell! c^{\ell+2}} N^{L} \Psi_{L}^{(\ell)}(U). \tag{B.2}$$

In this notation, an uppercase index denotes a multi-index, such as $N^{L} = N^{i_1} N^{i_2} \ldots N^{i_\ell}$. A superscript in parentheses denotes derivative, such as $\Psi^{(\ell)}(U) = d^{\ell}\Psi/dU^{\ell}$.

Next, to relate the radiative moments to the source moments, one defines 'algorithmic' moments that serve as functional parameters for a general external metric. Based on the arguments in Refs. [147, 492], the radiative moments coincide

with the algorithmic ones to $\mathcal{O}(1/c^3)$, and the algorithmic moments agree with the source moments K_L to order $\mathcal{O}(1/c^4)$

$$\Psi_L = \Psi_L^{(\mathrm{alg})} + \mathcal{O}(1/c^3), \tag{B.3}$$

$$\Psi_L^{(\mathrm{alg})} = K_L + \mathcal{O}(1/c^4). \tag{B.4}$$

The source moments are defined by

$$K_L = \int d^3x \left[\widehat{x}_L S + \frac{1}{2(2\ell+3)c^2} \boldsymbol{x}^2 \widehat{x}_L \frac{\partial^2 S}{\partial t^2} \right], \tag{B.5}$$

where the hat on x_L denotes a symmetric trace-free projection on the ℓ indices. The source function S is defined by the field equation for φ as

$$\Box\varphi = -\frac{4\pi G}{c^2} S. \tag{B.6}$$

The scalar energy flux

$$\mathcal{F}_S = -cR^2 \oint T_{0i}^S N^i d\Omega, \tag{B.7}$$

where the scalar part of the stress-energy tensor is given by

$$T_{\mu\nu}^S = \frac{c^4}{4\pi G} \left[\nabla_\mu\varphi\nabla_\nu\varphi - \frac{1}{2} g_{\mu\nu} (\nabla\varphi)^2 \right]. \tag{B.8}$$

In the far zone,

$$T_{0i}^S \simeq \frac{c^4}{4\pi G} \partial_0\varphi\partial_i\varphi \simeq -\frac{c^4}{4\pi G} N_i (\partial_0\varphi)^2, \tag{B.9}$$

where, in the last step, we used the relation

$$\partial_i\varphi = -N_i\partial_0\varphi + \mathcal{O}(r/R^2). \tag{B.10}$$

The scalar flux becomes

$$\begin{aligned}\mathcal{F}_S &= \frac{c^3}{4\pi G}\int d\Omega \left(\frac{\partial\psi}{\partial U}\right)^2 \\ &= G\sum_{\ell\geq 0}\frac{1}{c^{2\ell+1}(\ell!)^2}\int\frac{d\Omega}{4\pi}N^L N^P \Psi_L^{(\ell+1)}(U)\Psi_P^{(\ell+1)}(U).\end{aligned} \tag{B.11}$$

To integrate over the solid angle, we use the integration formula given by Eq. (A 29a) in Ref. [493], which yields

$$\begin{aligned}\mathcal{F}_S &= G\sum_{\ell\geq 0}\frac{1}{c^{2\ell+1}\ell!(2\ell+1)!!}\Psi_L^{(\ell+1)}(U)\Psi_L^{(\ell+1)}(U) \\ &= G\left[\frac{\Psi^{(1)}\Psi^{(1)}}{c} + \frac{\Psi_i^{(2)}\Psi_i^{(2)}}{c^3} + \frac{\Psi_{ij}^{(3)}\Psi_{ij}^{(3)}}{c^5} + \dots\right],\end{aligned} \tag{B.12}$$

where the first term is the monopole flux, the second is the dipole flux, and the third is the quadrupole flux. In terms of the source function S, those multipole moments needed for the calculation of the next-to-leading order flux are given by

$$\Psi = \int d^3x \left[S + \frac{1}{6c^2}\frac{d}{dt}(x^2 S)\right], \tag{B.13}$$

$$\Psi_i = \int d^3x \left[x^i S + \frac{1}{10c^2}\frac{d}{dt}\left(x^2 x^i S\right)\right], \tag{B.14}$$

$$\Psi_{ij} = \int d^3x \left(x^i x^j - \frac{1}{3}x^2\delta_{ij}\right) S. \tag{B.15}$$

The 1PN field equation for φ is given by Eq. (A.28)

$$\Box\varphi = -\frac{4\pi G}{c^2}\rho_g\left[-\alpha + \frac{1}{2c^2}\alpha v^2 + \alpha V - (\alpha^2+\beta)\varphi\right] - \frac{Ga}{c^4}A_0\nabla^2 A_0 + \frac{Ga}{2c^4}\nabla^2(A_0)^2\,. \tag{B.16}$$

The last term in that equation can be moved to the left hand side by a redefinition of the field, and since $A_0^2 \sim 1/R^2$, we can neglect that term to $\mathcal{O}(1/R)$. The other terms are expressed in terms of delta functions. Hence, we can write the source

function S as

$$S(\boldsymbol{x},t)=\sum_A \sigma_A \delta^3(\boldsymbol{x}-\boldsymbol{x}_A), \tag{B.17}$$

with

$$\sigma_1 = -m_1\alpha_1\left(1-\frac{v_1^2}{2c^2}\right)+\frac{m_1m_2}{c^2r}\left(\alpha_1+\alpha_1^2\alpha_2+\beta_1\alpha_2\right)-\frac{aq_1q_2}{c^2r}\,, \tag{B.18}$$

and similarly for σ_2, where $\boldsymbol{r}\equiv\boldsymbol{x}_1-\boldsymbol{x}_2$. In the center-of-mass coordinates, we define

$$\begin{aligned}
&\boldsymbol{v}\equiv\frac{d\boldsymbol{r}}{dt}\,, \qquad \boldsymbol{a}\equiv\frac{d\boldsymbol{v}}{dt}\,,\\
&\boldsymbol{x}_1=\frac{m_2}{M}\boldsymbol{r}+\mathcal{O}\left(\frac{1}{c^2}\right),\\
&\boldsymbol{x}_2=-\frac{m_1}{M}\boldsymbol{r}+\mathcal{O}\left(\frac{1}{c^2}\right).
\end{aligned} \tag{B.19}$$

Thus, σ_1 can be written as

$$\sigma_1 = -m_1\alpha_1+\frac{\nu}{2c^2}m_1\alpha_1v^2+\frac{M^2\nu}{c^2r}\left[\alpha_1+\alpha_1^2\alpha_2+\beta_1\alpha_2-\frac{aq_1q_2}{M\mu}\right]. \tag{B.20}$$

The multipole moments can now be written in terms of σ after integrating the delta functions

$$\Psi^{(1)}=\frac{d\sigma_1}{dt}-\frac{m_1\alpha_1}{6c^2}\frac{d^2}{dt^2}x_1^2+1\leftrightarrow 2, \tag{B.21}$$

$$\Psi_i^{(2)}=\frac{d^2}{dt^2}(x_1^i\sigma_1)-\frac{m_1\alpha_1}{10c^2}\frac{d^4}{dt^4}x_1^2x_1^i+1\leftrightarrow 2, \tag{B.22}$$

$$\Psi_{ij}^{(3)}=-m_1\alpha_1\frac{d^3}{dt^3}\left(x_1^ix_1^j-\frac{1}{3}x_1^2\delta_{ij}\right)+1\leftrightarrow 2, \tag{B.23}$$

where, in the higher order terms, we used $\sigma_1=-m_1\alpha_1$.

For the monopole and quadrupole fluxes, the multipole moments in the center-of-mass coordinates can be written as

$$\Psi^{(1)}=\frac{d}{dt}(\sigma_1+\sigma_2)-\frac{\nu}{6c^2}\left(m_2\alpha_1+m_1\alpha_2\right)\frac{d^3r^2}{dt^3}\,, \tag{B.24}$$

$$\Psi_{ij}^{(3)}=-\nu(m_2\alpha_1+m_1\alpha_2)\frac{d^3}{dt^3}\left(r^ir^j-\frac{1}{3}r^2\delta_{ij}\right). \tag{B.25}$$

Differentiating, and using the relations

$$\begin{aligned}\frac{d^2\boldsymbol{r}}{dt^2} &= -\frac{G_{12}M}{r^2}\boldsymbol{n} + \mathcal{O}\left(\frac{1}{c^2}\right),\\ \frac{d\boldsymbol{n}}{dt} &= \frac{\boldsymbol{v} - \dot{r}\boldsymbol{n}}{r},\end{aligned} \tag{B.26}$$

where

$$G_{12} \equiv G\left(1 + \alpha_1\alpha_2 - \frac{q_1q_2}{M\mu}\right), \tag{B.27}$$

we get

$$\begin{aligned}\Psi^{(1)} =& -\frac{2}{3}\frac{G_{12}M\mu}{c^2r^2}\dot{r}\left(X_2\alpha_1 + X_1\alpha_2\right)\\ &-\frac{M\mu}{c^2r^2}\dot{r}\left[\alpha_1 + \alpha_2 + \alpha_1^2\alpha_2 + \alpha_2^2\alpha_1 + \beta_1\alpha_2 + \beta_2\alpha_1 - \frac{2aq_1q_2}{M\mu}\right],\\ \Psi^{(3)}_{ij} =& -\frac{G_{12}M\mu}{r^2}\left(X_1\alpha_2 + X_2\alpha_1\right)\left[6\dot{r}n^in^j - 4(n^iv^j + n^jv^i) + \frac{2}{3}\dot{r}\delta_{ij}\right].\end{aligned} \tag{B.28}$$

Squaring leads to the monopole and quadrupole scalar fluxes

$$\begin{aligned}\mathcal{F}_S^{\rm Mon} =& G\frac{\Psi^{(1)}\Psi^{(1)}}{c}\\ =& \frac{G}{c^5}\left(\frac{G_{12}M\mu}{r^2}\right)^2\dot{r}^2\Bigg[\frac{2}{3}\left(X_2\alpha_1 + X_1\alpha_2\right)\\ &+ \tfrac{1}{1+\alpha_1\alpha_2-\frac{q_1q_2}{M\mu}}\left(\alpha_1 + \alpha_2 + \alpha_1^2\alpha_2 + \alpha_2^2\alpha_1 + \beta_1\alpha_2 + \beta_2\alpha_1 - \frac{2aq_1q_2}{M\mu}\right)\Bigg]^2.\end{aligned} \tag{B.29}$$

$$\begin{aligned}\mathcal{F}_S^{\rm Quad} =& G\frac{\Psi^{(3)}_{ij}\Psi^{(3)}_{ij}}{c^5}\\ =& \frac{G}{30c^5}\left(\frac{G_{12}M\mu}{r^2}\right)^2\left(X_1\alpha_2 + X_2\alpha_1\right)^2\left(32v^2 - \frac{88}{3}\dot{r}^2\right).\end{aligned} \tag{B.30}$$

For the dipole flux, we need to write $\boldsymbol{x}_1$ and $\boldsymbol{x}_2$ in the center-of-mass coordinates to 1PN order. From the boost invariance of the Lagrangian, we obtain

[147]

$$\boldsymbol{x}_1 = \frac{\mu_2}{\mu_1+\mu_2}\boldsymbol{r} + \mathcal{O}\left(\frac{1}{c^4}\right),$$
$$\boldsymbol{x}_2 = -\frac{\mu_1}{\mu_1+\mu_2}\boldsymbol{r} + \mathcal{O}\left(\frac{1}{c^4}\right), \tag{B.31}$$

where

$$\begin{aligned}\mu_1 &\equiv m_1\left(1+\frac{v_1^2}{2c^2}-\frac{G_{12}m_2}{2c^2r}\right)+\mathcal{O}\left(\frac{1}{c^4}\right)\\ &= M\left(X_1+X_2\frac{\nu v^2}{2c^2}-\frac{G_{12}M\nu}{2c^2r}\right)+\mathcal{O}\left(\frac{1}{c^4}\right),\end{aligned} \tag{B.32}$$

and similarly for μ_2. This leads to the dipole moment Ψ_i in the center-of-mass coordinates

$$\Psi_i^{(2)} = \frac{d^2}{dt^2}\left(\frac{\mu_2}{\mu_1+\mu_2}r^i\sigma_1\right) - \frac{d^2}{dt^2}\left(\frac{\mu_1}{\mu_1+\mu_2}r^i\sigma_2\right) + \frac{\mu}{10c^2}\left(X_1^2\alpha_2 - X_2^2\alpha_1\right)\frac{d^4}{dt^4}(r^2r^i). \tag{B.33}$$

To calculate the dipole flux, we also need the 1PN acceleration, which can be derived from the 1PN Lagrangian, and we obtain

$$\begin{aligned}\frac{d^2\boldsymbol{r}}{dt^2} =& -\frac{G_{12}M}{r^2}\boldsymbol{n}\Bigg\{1+\frac{v^2}{c^2}\left[3\nu+\frac{1-\alpha_1\alpha_2+q_1q_2/2M\mu}{1+\alpha_1\alpha_2-q_1q_2/M\mu}\right]-\frac{3}{2c^2}\nu\dot{r}^2-2\nu\frac{G_{12}M}{c^2r}\\ &-\frac{G_{12}M}{c^2r}\frac{1}{\left(1+\alpha_1\alpha_2-\frac{q_1q_2}{M\mu}\right)^2}\Bigg[2\nu\left(1+\alpha_1\alpha_2-\frac{q_1q_2}{M\mu}\right)^2+X_2\frac{q_1^2}{M\mu}(1+a\alpha_2)\\ &+X_1\frac{q_2^2}{M\mu}(1+a\alpha_1)-2a\frac{q_1q_2}{M\mu}\left(X_1\alpha_1+X_2\alpha_2\right)-\frac{q_1q_2}{M\mu}(5-\alpha_1\alpha_2)\\ &+4(1+\alpha_1\alpha_2)+X_2\beta_1\alpha_2^2+X_1\beta_2\alpha_1^2\Bigg]\Bigg\}\\ &-\frac{G_{12}M}{c^2r^2}\dot{r}\boldsymbol{v}\left[2\nu-\frac{4-q_1q_2/M\mu}{1+\alpha_1\alpha_2-q_1q_2/M\mu}\right]+\mathcal{O}\left(\frac{1}{c^4}\right).\end{aligned} \tag{B.34}$$

Finally, we obtain the dipole scalar flux

$$\mathcal{F}_S^{\rm dip} = \frac{G}{3c^3}\left(\frac{G_{12}M\mu}{r^2}\right)^2\left\{(\alpha_1-\alpha_2)^2+f^S_{\dot{r}^2}\frac{\dot{r}^2}{c^2}+f^S_{v^2}\frac{v^2}{c^2}+f^S_{1/r}\frac{G_{12}M}{c^2r}\right\}, \tag{B.35}$$

with the coefficients

$$
\begin{aligned}
f^S_{\dot{r}^2} = \frac{-1}{1+\alpha_1\alpha_2-\frac{q_1q_2}{M\mu}}\Bigg\{ & 8(\alpha_1-\alpha_2)^2 - 2\nu(\alpha_1-\alpha_2)^2(1+\alpha_1\alpha_2) \\
& + (\alpha_1-\alpha_2)(1+\alpha_1\alpha_2)\left[X_1(\alpha_1+3\alpha_2) - X_2(\alpha_2+3\alpha_1)\right] \\
& - \frac{q_1q_2}{M\mu}\left[2(1-\nu)(\alpha_1-\alpha_2)^2 + (X_1-X_2)\,(\alpha_1-\alpha_2)(2a+\alpha_1+\alpha_2)\right] \\
& + 2(\alpha_1-\alpha_2)\,(X_1\alpha_1\beta_2 - X_2\alpha_2\beta_1)\Bigg\}, \qquad \text{(B.36a)}
\end{aligned}
$$

$$
\begin{aligned}
f^S_{v^2} = \frac{2}{5\left(1+\alpha_1\alpha_2-\frac{q_1q_2}{M\mu}\right)}\Bigg\{ & 5(\alpha_1-\alpha_2)^2(1-\alpha_1\alpha_2) + 5(\alpha_1-\alpha_2)\,(X_1\alpha_1\beta_2 - X_2\alpha_2\beta_1) \\
& + (\alpha_1-\alpha_2)(1+\alpha_1\alpha_2)\left[-\frac{25}{2}(1-\nu)(\alpha_1-\alpha_2) + \frac{11}{2}\left(X_2^2\alpha_1 - X_1^2\alpha_2\right)\right. \\
& \qquad \left. + \frac{35}{2}\,(X_1\alpha_1 - X_2\alpha_2)\right] \\
& + \frac{q_1q_2}{2M\mu}(\alpha_1-\alpha_2)\left[5(1-5\nu)(\alpha_1-\alpha_2) - 10a\,(X_1-X_2) - 11\left(X_2^2\alpha_1 - X_1^2\alpha_2\right)\right] \\
& - \frac{5q_1q_2}{2M\mu}(\alpha_1-\alpha_2)\left[2\,(X_1\alpha_1 - X_2\alpha_2) + 3\,(X_1\alpha_2 - X_2\alpha_1)\right]\Bigg\}, \qquad \text{(B.36b)}
\end{aligned}
$$

$$
\begin{aligned}
f^S_{1/r} = -\frac{2}{5}\Bigg\{ & 5\nu(\alpha_1-\alpha_2)^2 + 5(\alpha_1^2-\alpha_2^2)\,(X_1-X_2) + 6(\alpha_1-\alpha_2)\left(X_2^2\alpha_1 - X_1^2\alpha_2\right) \\
& + \frac{5(\alpha_1-\alpha_2)^2}{\left(1+\alpha_1\alpha_2-\frac{q_1q_2}{M\mu}\right)^2}\left[-\frac{q_1q_2}{M\mu}\,(5-\alpha_1\alpha_2+2aX_1\alpha_1+2aX_2\alpha_2)\right. \\
& \qquad \left. + X_2\frac{q_1^2}{M\mu}(1+a\alpha_2) + X_1\frac{q_2^2}{M\mu}(1+a\alpha_1)\right] \\
& + \frac{5(\alpha_1-\alpha_2)^2}{\left(1+\alpha_1\alpha_2-\frac{q_1q_2}{M\mu}\right)^2}\left[4(1+\alpha_1\alpha_2) + X_2\alpha_2^2\beta_1 + X_1\alpha_1^2\beta_2\right]\Bigg\}. \qquad \text{(B.36c)}
\end{aligned}
$$

This flux reduces to the ST dipole flux derived in Ref. [147] in the limit where the electric charges are zero.

B.2 Vector energy flux

The calculation of the vector flux is similar to that of the scalar flux. The vector potential can be written in terms of radiative multipole moments as [494]

$$A_0(\boldsymbol{X},T) = \frac{1}{R}\sum_{\ell\geq 0}\frac{1}{\ell! c^\ell} N^L Q_L^{(\ell)}(U),$$
$$A_i(\boldsymbol{X},T) = \frac{1}{R}\sum_{\ell\geq 1}\frac{1}{\ell! c^\ell}\left[N_{L-1}Q_{iL-1}^{(\ell)}(U) - \frac{\ell}{(\ell+1)c}\varepsilon_{iab}N_{aL-1}M_{bL-1}^{(\ell)}\right]. \tag{B.37}$$

As was done in the previous subsection, the radiative moments can be related to the source moments using algorithmic moments. At leading order, the three agree, and we can express the electric and magnetic multipole moments directly in terms of the source moments

$$Q_L(U) = \int d^3x\left[\widehat{x}_L\rho + \frac{1}{2(2\ell+3)c^2}x^2\widehat{x}_L\frac{d^2\rho}{dt^2} - \frac{2\ell+1}{(\ell+1)(2\ell+1)c^2}\widehat{x}_{aL}\frac{dJ_a}{dt}\right], \quad \ell\geq 0\,, \tag{B.38}$$

$$M_L(U) = \int d^3x\left[\widehat{x}_{\langle L-1}m_{i_\ell\rangle} + \frac{1}{2(2\ell+3)c^2}x^2\widehat{x}_{\langle L-1}\frac{d}{dt^2}m_{i_\ell\rangle}\right], \quad \ell\geq 1\,, \tag{B.39}$$

where the magnetization density $\boldsymbol{m} = \boldsymbol{x}\times\boldsymbol{J}$. The source functions ρ and J_i are defined by

$$\Box A_0 = 4\pi\rho\,, \qquad \Box A_i = -\frac{4\pi}{c}J_i. \tag{B.40}$$

The vector flux

$$\mathcal{F}_V = -cR^2\oint N^i T_{0i}^{\rm EM}d\Omega, \tag{B.41}$$

where the electromagnetic part of the stress-energy tensor is given by

$$T_{\mu\nu}^{\rm EM} = \frac{1}{8\pi}e^{-2a\varphi}\left(2F_{\mu\alpha}F_\nu{}^\alpha - \frac{1}{2}g_{\mu\nu}F^2\right). \tag{B.42}$$

In the far zone,

$$\begin{aligned} T_{0i}^{\rm EM} &= \frac{1}{4\pi} F_{0j} F_i{}^j \\ &= \frac{1}{4\pi} \left(\partial_0 A_j - \partial_j A_0\right) \left(\partial_i A_j - \partial_j A_i\right). \end{aligned} \tag{B.43}$$

The vector flux becomes

$$\mathcal{F}_V = \frac{R^2}{4\pi c} \int d\Omega \left[\frac{\partial A_i}{\partial U} \frac{\partial A_i}{\partial U} - N^i N^j \frac{\partial A_i}{\partial U} \frac{\partial A_j}{\partial U} \right]. \tag{B.44}$$

The vector potential A_i, to the required order, has the multipole expansion

$$A_i = \frac{1}{R} \left[\frac{1}{c} Q_i^{(1)} - \frac{1}{2c^2} \varepsilon_{ijk} N^j M_k^{(1)} + \frac{1}{2c^2} N^j Q_{ij}^{(2)} \right], \tag{B.45}$$

which leads to

$$\begin{aligned} \frac{R^2}{4\pi c} \int d\Omega \left(\frac{\partial A_i}{\partial U} \right)^2 =& \frac{Q_i^{(2)} Q_i^{(2)}}{c^3} + \frac{M_i^{(2)} M_i^{(2)}}{6c^5} + \frac{Q_{ij}^{(3)} Q_{ij}^{(3)}}{12c^5} + \mathcal{O}\left(\frac{1}{c^7}\right) \\ =& \sum_{\ell \geq 1} \frac{1}{c^{2\ell+1} \ell! (2\ell+1)!!} \left[\frac{2\ell+1}{\ell} Q_L^{(\ell+1)} Q_L^{(\ell+1)} \right. \\ & \left. + \frac{\ell}{c^2(\ell+1)} M_L^{(\ell+1)} M_L^{(\ell+1)} \right], \end{aligned} \tag{B.46}$$

and

$$\begin{aligned} \frac{R^2}{4\pi c} \int d\Omega N^i N^j \frac{\partial A_i}{\partial U} \frac{\partial A_j}{\partial U} =& \frac{Q_i^{(2)} Q_i^{(2)}}{3c^3} + \frac{Q_{ij}^{(3)} Q_{ij}^{(3)}}{30c^5} + \mathcal{O}\left(\frac{1}{c^7}\right) \\ =& \sum_{\ell \geq 1} \frac{1}{c^{2\ell+1} \ell! (2\ell+1)!!} Q_L^{(\ell+1)} Q_L^{(\ell+1)}. \end{aligned} \tag{B.47}$$

Hence, the vector flux

$$\begin{aligned} \mathcal{F}_V &= \sum_{\ell \geq 1} \frac{1}{c^{2\ell+1} \ell! (2\ell+1)!!} \left[\frac{\ell+1}{\ell} Q_L^{(\ell+1)} Q_L^{(\ell+1)} + \frac{\ell}{c^2(\ell+1)} M_L^{(\ell+1)} M_L^{(\ell+1)} \right] \\ &= \frac{2 Q_i^{(2)} Q_i^{(2)}}{3c^3} + \frac{M_i^{(2)} M_i^{(2)}}{6c^5} + \frac{Q_{ij}^{(3)} Q_{ij}^{(3)}}{20c^5} + \ldots. \end{aligned} \tag{B.48}$$

The first two terms give the dipole flux, and the third term is the quadrupole flux. There is no monopole flux because of the conservation of the total electric charge.

The 1PN field equations are given by Eqs. (A.20) and (A.29), which are

$$\Box A_i = -\frac{4\pi}{c}\rho_e v^i\,, \tag{B.49}$$

$$\begin{aligned}\Box A_0 =\ & 4\pi\rho_e - V\nabla^2 A_0 + A_0\nabla^2 V + a\varphi\nabla^2 A_0 \\ & - aA_0\nabla^2\varphi - \nabla^2(VA_0) + a\nabla^2(\varphi A_0).\end{aligned} \tag{B.50}$$

The last two terms in the above equation are of order $1/R^2$, and hence do not contribute to the next-to-leading order flux. The source functions ρ and J^i are then given by

$$\rho = \rho_e = q_1\delta^3(\boldsymbol{x}-\boldsymbol{x}_1) + q_2\delta^3(\boldsymbol{x}-\boldsymbol{x}_2), \tag{B.51}$$

$$J^i = \rho_e v^i = q_1 v_1^i\delta^3(\boldsymbol{x}-\boldsymbol{x}_1) + q_2 v_2^i\delta^3(\boldsymbol{x}-\boldsymbol{x}_2). \tag{B.52}$$

The function ρ is simply the electric charge density because the higher order terms from the field equation cancel when summed over the two bodies.

For the dipole flux, we need Q_i and M_i to $\mathcal{O}(1/c^2)$

$$\begin{aligned}Q_i =& \int d^3x\left[x_i\rho_e + \frac{1}{10c^2}\rho_e\frac{d^2}{dt^2}\left(x^2x^i\right) - \frac{3}{10c^2}\frac{d}{dt}\left(\widehat{x}_{ij}J_j\right)\right] \\ =& \left(q_1\frac{\mu_2}{\mu_1+\mu_2} - q_2\frac{\mu_1}{\mu_1+\mu_2}\right)r^i + \frac{1}{10c^2}\left(q_1\frac{m_2^3}{M^3} - q_2\frac{m_1^3}{M^3}\right)\frac{d^2}{dt^2}\left(r^ir^2\right) \\ & - \frac{3}{10c^2}\left(q_1\frac{m_2^3}{M^3} - q_2\frac{m_1^3}{M^3}\right)\frac{d}{dt}\left(r^ir^j - \frac{1}{3}r^2\delta^{ij}\right)v^j\,,\end{aligned} \tag{B.53}$$

$$\begin{aligned}M_i =& q_1\varepsilon_{ijk}x_1^jv_1^k + q_2\varepsilon_{ijk}x_2^jv_2^k \\ =& \left(q_1\frac{m_2^2}{M^2} + q_2\frac{m_1^2}{M^2}\right)\varepsilon_{ijk}r^jv^k\,.\end{aligned} \tag{B.54}$$

Differentiating and using the 1PN acceleration from Eq. (B.34), we obtain the next-to-leading order vector dipole flux

$$\mathcal{F}_V^{\rm Dip} = \frac{2}{3c^3}\left(\frac{G_{12}M\mu}{r^2}\right)^2\left[\left(\frac{q_1}{m_1}-\frac{q_2}{m_2}\right)^2 + f^V_{v^2}\frac{v^2}{c^2} + f^V_{\dot r^2}\frac{\dot r^2}{c^2} + f^V_{1/r}\frac{G_{12}M}{c^2 r}\right], \quad \text{(B.55)}$$

with the coefficients

$$f^V_{v^2} = \frac{2}{5}\left(X_2^2\frac{q_1}{m_1} - X_1^2\frac{q_2}{m_2}\right)\left(\frac{q_1}{m_1}-\frac{q_2}{m_2}\right) + \frac{2}{M}(X_1-X_2)(q_1+q_2)\left(\frac{q_1}{m_1}-\frac{q_2}{m_2}\right) + \frac{1}{1+\alpha_1\alpha_2-\frac{q_1q_2}{M\mu}}\left(\frac{q_1}{m_1}-\frac{q_2}{m_2}\right)^2\left(2+6\nu+2\alpha_1\alpha_2(3\nu-1)+\frac{q_1q_2}{M\mu}(1-6\nu)\right), \quad \text{(B.56a)}$$

$$f^V_{\dot r^2} = -\left(\frac{q_1}{m_1}-\frac{q_2}{m_2}\right)^2\left[3\nu + \frac{(X_1-X_2)(q_1+q_2)}{M\left(\frac{q_1}{m_1}-\frac{q_2}{m_2}\right)} + \frac{8-4\nu(1+\alpha_1\alpha_2)-2\frac{q_1q_2}{M\mu}(1-2\nu)}{1+\alpha_1\alpha_2-\frac{q_1q_2}{M\mu}}\right], \quad \text{(B.56b)}$$

$$f^V_{1/r} = -2\left(\frac{q_1}{m_1}-\frac{q_2}{m_2}\right)^2\left[2\nu + \frac{2}{5}\frac{X_2^2q_1/m_1 - X_1^2q_2/m_2}{q_1/m_1-q_2/m_2} - \frac{q_1q_2}{M\mu}\frac{5-\alpha_1\alpha_2+2a\left(X_1\alpha_1+X_2\alpha_2\right)}{\left(1+\alpha_1\alpha_2-\frac{q_1q_2}{M\mu}\right)^2} + \frac{(X_1-X_2)(q_1+q_2)}{M\left(\frac{q_1}{m_1}-\frac{q_2}{m_2}\right)} + \frac{4(1+\alpha_1\alpha_2)+X_2\frac{q_1^2}{M\mu}(1+a\alpha_2)+X_1\frac{q_2^2}{M\mu}(1+a\alpha_1)+X_2\alpha_2^2\beta_1+X_1\alpha_1^2\beta_2}{\left(1+\alpha_1\alpha_2-\frac{q_1q_2}{M\mu}\right)^2}\right]. \quad \text{(B.56c)}$$

For the quadrupole flux,

$$Q^{(3)}_{ij} = \int d^3x\left(x_ix_j-\frac{1}{3}x^2\delta_{ij}\right)\rho_e = \left(X_2^2q_1+X_1^2q_2\right)\frac{d^3}{dt^3}\left(r^ir^j-\frac{1}{3}r^2\delta^{ij}\right), \quad \text{(B.57)}$$

which leads to

$$\mathcal{F}_V^{\rm Quad} = \frac{Q^{(3)}_{ij}Q^{(3)}_{ij}}{30c^5} = \frac{1}{30c^5}\left(\frac{G_{12}M\mu}{r^2}\right)^2\left(X_2\frac{q_1}{M}+X_1\frac{q_2}{m_2}\right)^2\left(32v^2-\frac{88}{3}\dot r^2\right). \quad \text{(B.58)}$$

B.3 Tensor energy flux

The metric in radiative coordinates

$$G_{\mu\nu}(\boldsymbol{X}^{\mu}) = \eta_{\mu\nu} + \frac{1}{R} H_{\mu\nu}(U, \boldsymbol{N}) + \mathcal{O}\left(\frac{1}{R^2}\right), \tag{B.59}$$

where the radiative multipole moments M_L and S_L are defined by

$$H_{ij}^{\mathrm{TT}}(U, \boldsymbol{N}) = 4G \sum_{\ell \geq 2} \frac{1}{\ell! c^{\ell+2}} \left[N_{L-2} M_{ijL-2}^{(\ell)}(U) - \frac{2\ell}{(\ell+1)c} N_{hL-2} \varepsilon_{hk(i} S_{j)kL-2}^{(\ell)} \right]^{\mathrm{TT}}. \tag{B.60}$$

The radiative multipoles agree with the source multipoles I_L and J_L up to order

$$M_L = I_L + \mathcal{O}(1/c^3), \qquad S_L = J_L + \mathcal{O}(1/c^2), \tag{B.61}$$

where [147, 494]

$$I_L(t) = \int d^3x \left[\widehat{x}_L \sigma + \frac{1}{2(2\ell+3)c^2} x^2 \widehat{x}_L \frac{\partial^2 \sigma}{\partial t^2} - \frac{4(2\ell+1)}{(\ell+1)(2\ell+3)c^2} \widehat{x}_{Ls} \frac{\partial \sigma^s}{\partial t} \right], \tag{B.62}$$

$$J_L(t) = \int d^3x \, \varepsilon_{hk\langle i_\ell} \widehat{x}_{L-1\rangle h} \sigma^k. \tag{B.63}$$

In terms of the multipole moments, the tensor flux is given by

$$\begin{aligned} F_g &= \frac{c^3}{32\pi G} \int d\Omega \left(\frac{\partial H_{ij}^{\mathrm{TT}}}{\partial U} \right)^2 \\ &= G \sum_{\ell \geq 2} \frac{1}{c^{2\ell+1} \ell! (2\ell+1)!!} \left[\frac{(\ell+1)(\ell+2)}{\ell(\ell-1)} M_L^{(\ell+1)}(U) M_L^{(\ell+1)}(U) \right. \\ &\qquad \left. + \frac{4\ell(\ell+2)}{c^2(\ell-1)(\ell+1)} S_L^{\ell+1}(U) S_L^{(\ell+1)}(U) \right] \\ &= \frac{G}{5c^5} M_{ij}^{(3)} M_{ij}^{(3)} + \frac{G}{189c^7} M_{ijk}^{(4)} M_{ijk}^{(4)} + \frac{16G}{45c^7} S_{ij}^{(3)} S_{ij}^{(3)} + \mathcal{O}\left(1/c^9\right), \end{aligned} \tag{B.64}$$

where the first term is the mass quadrupole flux, the second is the mass octopole, and the third is the current quadrupole.

The source functions σ and σ^i are given by

$$\sigma \equiv \frac{T^{00}+T^{ss}}{c^2}, \qquad \sigma^i \equiv \frac{T^{0i}}{c}, \tag{B.65}$$

and from the 1PN field equations (A.27) and (A.19)

$$\Box V = -\frac{4\pi G}{c^2}\sigma, \qquad \Box V^i = -\frac{4\pi G}{c^3}\sigma^i, \tag{B.66}$$

with

$$\sigma^i = m_1 v_1^i \delta^3(\boldsymbol{x}-\boldsymbol{x}_1) + m_2 v_2^i \delta^3(\boldsymbol{x}-\boldsymbol{x}_2), \tag{B.67}$$

$$\sigma = \left[m_1 + \frac{3}{2c^2}m_1 v_1^2 - \frac{G_{12}m_1 m_2}{c^2 r}\right]\delta(\boldsymbol{x}-\boldsymbol{x}_1) + 1 \leftrightarrow 2. \tag{B.68}$$

The multipole moments needed for the next-to-leading order flux are M_{ij}, M_{ijk}, and S_{ij}, which are given by

$$M_{ij} = \left(m_1 + \frac{3}{2c^2}m_1 v_1^2 - \frac{G_{12}m_1 m_2}{c^2 r}\right)\widehat{x}_1^{ij} + \frac{m_1}{14c^2}\frac{d^2}{dt^2}x_1^2\widehat{x}_1^{ij} - \frac{20m_1}{21c^2}\frac{d}{dt}v_1^k\widehat{x}_1^{ijk} + 1 \leftrightarrow 2, \tag{B.69}$$

$$M_{ijk} = m_1\widehat{x}_1^{ijk} + m_2\widehat{x}_2^{ijk}, \tag{B.70}$$

$$S_{ij} = m_1\varepsilon^{hk\langle j}x_1^{i\rangle}x_1^h v_1^k + 1 \leftrightarrow 2. \tag{B.71}$$

In the center-of-mass coordinates, this becomes

$$M_{ij} = \mu\left[1 + \frac{3}{2c^2}(1-3\nu)v^2 - \frac{G_{12}M}{c^2 r}(1-2\nu)\right] + \frac{\mu}{14c^2}(1-3\nu)\frac{d^2}{dt^2}r^2\widehat{r}^{ij} - \frac{20\mu}{21c^2}(1-3\nu)\frac{d}{dt}v^k\widehat{r}^{ijk}, \tag{B.72}$$

$$M_{ijk} = \mu\left[\frac{m_2^2}{M^2} - \frac{m_1^2}{M^2}\right]\widehat{r}^{ijk}, \tag{B.73}$$

$$S_{ij} = \mu\left[\frac{m_2^2}{M^2} - \frac{m_1^2}{M^2}\right]\varepsilon^{hk\langle j}r^{i\rangle}r^h v^k, \tag{B.74}$$

where

$$\widehat{r}^{ij} = r^i r^j - \frac{1}{3} r^2 \delta_{ij}, \tag{B.75}$$

$$\widehat{r}^{ijk} = r^i r^j r^k - \frac{r^2}{5} \left(r^i \delta^{jk} + r^j \delta^{ik} + r^k \delta^{ij} \right), \tag{B.76}$$

$$\varepsilon^{hk\langle j} r^{i\rangle} r^h v^k = \left[\frac{1}{2} \varepsilon^{hkj} r^i + \frac{1}{2} \varepsilon^{hki} r^j - \frac{1}{3} \varepsilon^{hkm} r^m \right] r^h v^k. \tag{B.77}$$

Taking the time derivatives of the multipole moments and squaring, we obtain the tensor flux

$$\begin{aligned} \mathcal{F}_T = \frac{8G}{15c^5} \left(\frac{G_{12} M \mu}{r^2} \right)^2 \left[12v^2 - 11\dot{r}^2 \right] + \frac{8G}{420c^7} \left(\frac{G_{12} M \mu}{r^2} \right)^2 \Bigg[& f^T_{v^4} v^4 + f^T_{v^2 \dot{r}^2} v^2 \dot{r}^2 \\ & + f^T_{\dot{r}^4} \dot{r}^4 + f^T_{v^2/r} \frac{G_{12} M v^2}{r} + f^T_{\dot{r}^2/r} \frac{G_{12} M \dot{r}^2}{r} + f^T_{1/r^2} \frac{G_{12}^2 M^2}{r^2} \Bigg], \end{aligned} \tag{B.78}$$

with the coefficients

$$f^T_{v^4} = \left[\frac{785 + 113\alpha_1\alpha_2 - 281 \frac{q_1 q_2}{M\mu}}{1 + \alpha_1\alpha_2 - \frac{q_1 q_2}{M\mu}} - 852\nu \right], \tag{B.79a}$$

$$f^T_{v^2 \dot{r}^2} = -2 \left[\frac{1487 + 255\alpha_1\alpha_2 - 563 \frac{q_1 q_2}{M\mu}}{1 + \alpha_1\alpha_2 - \frac{q_1 q_2}{M\mu}} - 1392\nu \right], \tag{B.79b}$$

$$f^T_{\dot{r}^4} = 3 \left[\frac{687 + 127\alpha_1\alpha_2 - 267 \frac{q_1 q_2}{M\mu}}{1 + \alpha_1\alpha_2 - \frac{q_1 q_2}{M\mu}} - 620\nu \right], \tag{B.79c}$$

$$f^T_{1/r^2} = 16(1 - 4\nu), \tag{B.79d}$$

$$\begin{aligned} f^T_{v^2/r} = -\frac{8}{\left(1 + \alpha_1\alpha_2 - \frac{q_1 q_2}{M\mu} \right)^2} \Bigg[& 20(1 + \alpha_1\alpha_2)(17 - \nu) + 4\alpha_1\alpha_2(1 + \alpha_1\alpha_2)(22 - 5\nu) \\ & + 84 \frac{q_1^2}{M\mu} X_2 (1 + a\alpha_2) + 84 \frac{q_2^2}{M\mu} X_1 (1 + a\alpha_1) + \frac{q_1^2 q_2^2}{M^2 \mu^2} (67 - 20\nu) \\ & - 168 \frac{a q_1 q_2}{M\mu} \left(X_1 \alpha_1 + X_2 \alpha_2 \right) - \frac{q_1 q_2}{M\mu} (491 - 40\nu) \\ & - \alpha_1\alpha_2 \frac{q_1 q_2}{M\mu} (71 - 40\nu) + 84 \left(X_1 \alpha_1^2 \beta_2 + X_2 \alpha_2^2 \beta_1 \right) \Bigg], \end{aligned} \tag{B.79e}$$

$$\begin{aligned} f^T_{\dot{r}^2/r} = \frac{8}{\left(1 + \alpha_1\alpha_2 - \frac{q_1 q_2}{M\mu} \right)^2} \Bigg[& (1 + \alpha_1\alpha_2)(367 - 15\nu) + 3\alpha_1\alpha_2(1 + \alpha_1\alpha_2)(29 - 5\nu) \end{aligned}$$

$$+84\frac{q_1^2}{M\mu}X_2(1+a\alpha_2)+84\frac{q_2^2}{M\mu}X_1(1+a\alpha_1)+\frac{q_1^2q_2^2}{M^2\mu^2}(73-15\nu)$$
$$-168\frac{aq_1q_2}{M\mu}\left(X_1\alpha_1+X_2\alpha_2\right)-\frac{2q_1q_2}{M\mu}(262-15\nu)$$
$$-2\frac{q_1q_2}{M\mu}\alpha_1\alpha_2(38-15\nu)+84\left(X_1\alpha_1^2\beta_2+X_2\alpha_2^2\beta_1\right)\Bigg]. \tag{B.79f}$$

This flux reduces to the one derived in Ref. [151], in the context of ST theory, when the electric charges are zero and after converting the notation to the Jordan-Fierz frame.

B.4 Energy flux for circular orbits

In this section, we express the energy flux for circular orbits in terms of the gauge-independent parameter x, which is defined by

$$x\equiv\left(\frac{G_{12}M\Omega}{c^3}\right)^{2/3}, \tag{B.80}$$

where Ω is the orbital frequency. To do that, we need to find the relation between r and Ω to 1PN order (Kepler's third law). We start by writing the Lagrangian (2.31) in the center-of-mass coordinates

$$L=-Mc^2+\frac{1}{2}\mu v^2+\frac{G_{12}M\mu}{r}$$
$$+\frac{1}{c^2}\Bigg\{\frac{1}{8}(1-3\nu)\mu v^4+\frac{G_{12}M\mu}{2r}\left[\left(\frac{3-\alpha_1\alpha_2}{1+\alpha_1\alpha_2-\frac{q_1q_2}{M\mu}}+\nu\right)v^2+\nu\dot{r}^2\right]$$
$$-\frac{M^2\mu}{2r^2}\Bigg[(1+\alpha_1\alpha_2)^2+X_2\alpha_2^2\beta_1+X_1\alpha_1^2\beta_2-2\frac{q_1q_2}{M\mu}\left(1+a\alpha_1X_1+a\alpha_2X_2\right)$$
$$+\frac{q_2^2}{M\mu}X_1(1+a\alpha_1)+\frac{q_1^2}{M\mu}X_2(1+a\alpha_2)\Bigg]\Bigg\}. \tag{B.81}$$

Applying the Euler-Lagrange equation and using $\dot{r}=0$ and $v=r\Omega$ leads to

$$\Omega^2=\frac{G_{12}M}{r^3}\left[1-3f_\gamma\gamma+\mathcal{O}\left(\frac{1}{c^4}\right)\right], \tag{B.82}$$

where the parameter γ is defined by

$$\gamma \equiv \frac{G_{12}M}{c^2 r}\,, \tag{B.83}$$

and the the coefficient f_γ is defined by

$$\begin{aligned} f_\gamma \equiv \frac{1}{6G_{12}^2}\Big[&G_{12}^2(1-2\nu)+G_{12}(3-\alpha_1\alpha_2)+2(1+\alpha_1\alpha_2)^2+2X_2\alpha_2^2\beta_1+2X_1\alpha_1^2\beta_2 \\ &+2\frac{q_2^2}{M\mu}X_1(1+a\alpha_1)+2\frac{q_1^2}{M\mu}X_2(1+a\alpha_2)-4\frac{q_1q_2}{M\mu}\left(1+aX_1\alpha_1+aX_2\alpha_2\right)\Big]. \end{aligned} \tag{B.84}$$

Substituting x instead of Ω and inverting Eq. (B.82), we obtain

$$\gamma = x\left[1+f_\gamma x+\mathcal{O}\left(1/c^4\right)\right]. \tag{B.85}$$

To express the flux for circular orbits in terms of γ, we set $\dot{r}=0$ and $v=r\Omega$ and then use Eqs. (B.82) to obtain

$$\mathcal{F}_S = \frac{Gc^5}{3G_{12}^2}\nu^2\gamma^4(\alpha_1-\alpha_2)^2+\frac{Gc^5}{3G_{12}^2}\nu^2\gamma^5\left[f^S_{v^2}+f^S_{1/r}+\frac{16}{5}\left(X_1\alpha_2+X_2\alpha_1\right)^2\right], \tag{B.86a}$$

$$\mathcal{F}_V = \frac{2Gc^5}{3G_{12}^2}\nu^2\gamma^4\left(\frac{q_1}{m_1}-\frac{q_2}{m_2}\right)^2+\frac{2Gc^5}{3G_{12}^2}\nu^2\gamma^5\left[\frac{8}{5}\left(X_2\frac{q_1}{m_1}+X_1\frac{q_2}{m_2}\right)^2+f^V_{v^2}+f^V_{1/r}\right], \tag{B.86b}$$

$$\mathcal{F}_T = \frac{32Gc^5}{5G_{12}^2}\nu^2\gamma^5+\frac{2Gc^5}{105G_{12}^2}\nu^2\gamma^6\left(f^T_{v^4}+f^T_{v^2/r}+f^T_{1/r^2}+1008f_\gamma\right). \tag{B.86c}$$

Using Eq. (B.85) to express the energy flux in terms of x instead of γ leads to Eq. (2.43a).

Appendix C: Translating between scalar-tensor theory notations

This appendix contains the conversion between notation introduced in Table 3.1 and that employed by Damour and Esposito-Farèse [495, 496]. Note that these authors defined α_A with a relative minus sign compared to Eq. (3.11) and defined G_* as the bare gravitational constant in the Einstein frame.

Weak-field parameters:

$$G \rightarrow \tilde{G} = G_* A_0^2 \left(1 + \alpha_0^2\right), \tag{C.1}$$

$$\zeta \rightarrow \frac{\alpha_0^2}{1+\alpha_0^2}, \tag{C.2}$$

$$\lambda_1 \rightarrow -\frac{\alpha_0 \beta_0}{\left(1+\alpha_0^2\right) A_0^2}, \tag{C.3}$$

$$\lambda_2 \rightarrow -\frac{\alpha_0^2 \left(\alpha_0 \beta_0' - 3\beta_0^2\right)}{\left(1+\alpha_0^2\right)^2 A_0^4}. \tag{C.4}$$

Strong-field parameters:

$$s_A \rightarrow \frac{1}{2} - \frac{\alpha_A}{2\alpha_0}, \tag{C.5}$$

$$s_A' \rightarrow \frac{\beta_0 \alpha_A}{2\alpha_0^2 A_0^2} + \frac{\beta_A}{4\alpha_0^2}, \tag{C.6}$$

$$s_A'' \rightarrow \frac{\alpha_A \beta_0'}{2\alpha_0^2 A_0^4} + \frac{\beta_A'}{8\alpha_0^3} - \frac{\beta_0^2 \alpha_A}{\alpha_0^3 A_0^4} + \frac{\beta_0 \alpha_A}{2\alpha_0^2 A_0^2} - \frac{3\beta_0 \beta_A}{4\alpha_0^3 A_0^2}. \tag{C.7}$$

Binary parameters:

$$\alpha \rightarrow \frac{1+\alpha_1\alpha_2}{1+\alpha_0^2}, \tag{C.8}$$

$$\gamma \rightarrow \gamma_{12} = -\frac{2\alpha_1\alpha_2}{1+\alpha_1\alpha_2}, \tag{C.9}$$

$$\beta_1 \rightarrow \beta_{22}^1 = \frac{\beta_1\alpha_2^2}{2(1+\alpha_1\alpha_2)^2}, \tag{C.10}$$

$$\beta_2 \rightarrow \beta_{11}^2 = \frac{\beta_2\alpha_1^2}{2(1+\alpha_1\alpha_2)^2}, \tag{C.11}$$

$$\delta_1 \rightarrow \frac{\alpha_1^2}{(1+\alpha_1\alpha_2)^2}, \tag{C.12}$$

$$\delta_2 \rightarrow \frac{\alpha_2^2}{(1+\alpha_1\alpha_2)^2}, \tag{C.13}$$

$$\chi_1 \rightarrow -\frac{1}{4}\epsilon_{222}^1 = -\frac{\beta_1'\alpha_2^3}{4(1+\alpha_1\alpha_2)^3}, \tag{C.14}$$

$$\chi_2 \rightarrow -\frac{1}{4}\epsilon_{111}^2 = -\frac{\beta_2'\alpha_1^3}{4(1+\alpha_1\alpha_2)^3}. \tag{C.15}$$

Our conversions agree with those presented in Table II of Ref. [497] with one exception: we find $G\alpha = \tilde{G}_{12}$ rather than $G\alpha = G_{12}$.

Appendix D: Explicit formulas for the Fourier-domain phasing of waveforms in scalar-tensor theories

This appendix gathers explicit formulae for the coefficients entering our results that were too voluminous to be kept in the main text.

In the dipole-driven case of Section 3.5.1, we obtained for the flux

$$\mathcal{F}^{\rm DD}(x) = \frac{4\mathcal{S}_-^2\zeta\eta^2 x^4}{3G\alpha}\left[1 + f_2^{\rm DD}x + f_3^{\rm DD}x^{3/2} + f_4^{\rm DD}x^2 + \mathcal{O}(5)\right] \tag{D.1}$$

with the coefficients

$$\begin{aligned} f_2^{\rm DD} =& -\frac{14}{5} + \frac{4\mathcal{S}_+^2}{5\mathcal{S}_-^2} - \frac{4}{3}\beta_+ + \frac{4\mathcal{S}_+\beta_-}{\mathcal{S}_-\gamma} + \frac{4\beta_+}{\gamma} - \frac{2}{3}\gamma + \frac{24}{5\mathcal{S}_-^2\zeta} \\ &+ \frac{12\gamma}{5\mathcal{S}_-^2\zeta} - \frac{4}{3}\eta + \frac{4}{3}\beta_-\psi - \frac{4\beta_-\psi}{\gamma} - \frac{4\mathcal{S}_+\beta_+\psi}{\mathcal{S}_-\gamma}, \end{aligned} \tag{D.2}$$

$$f_3^{\rm DD} = 2\pi + \pi\gamma, \tag{D.3}$$

$$\begin{aligned} f_4^{\rm DD} =& -\frac{29}{28} - \frac{97\mathcal{S}_+^2}{28\mathcal{S}_-^2} - \frac{4\mathcal{S}_+\beta_-}{3\mathcal{S}_-} - \frac{4}{3}\beta_-^2 + \frac{2}{15}\beta_+ - \frac{32\mathcal{S}_+^2\beta_+}{15\mathcal{S}_-^2} - \frac{4}{3}\beta_+^2 + \frac{4\beta_-^2}{\gamma^2} + \frac{4\mathcal{S}_+^2\beta_-^2}{\mathcal{S}_-^2\gamma^2} \\ &+ \frac{16\mathcal{S}_+\beta_-\beta_+}{\mathcal{S}_-\gamma^2} + \frac{4\beta_+^2}{\gamma^2} + \frac{4\mathcal{S}_+^2\beta_+^2}{\mathcal{S}_-^2\gamma^2} - \frac{4\mathcal{S}_+\beta_-}{\mathcal{S}_-\gamma} - \frac{8\beta_-^2}{3\gamma} - \frac{36\beta_+}{5\gamma} + \frac{16\mathcal{S}_+^2\beta_+}{5\mathcal{S}_-^2\gamma} - \frac{16\mathcal{S}_+\beta_-\beta_+}{3\mathcal{S}_-\gamma} \\ &- \frac{8\beta_+^2}{3\gamma} + \frac{2}{5}\gamma - \frac{16\mathcal{S}_+^2\gamma}{15\mathcal{S}_-^2} + \frac{1}{2}\gamma^2 + \frac{2}{3}\delta_+ - \frac{1247}{70\mathcal{S}_-^2\zeta} - \frac{64\beta_+}{5\mathcal{S}_-^2\zeta} - \frac{2143\gamma}{140\mathcal{S}_-^2\zeta} - \frac{32\beta_+\gamma}{5\mathcal{S}_-^2\zeta} \\ &- \frac{16\gamma^2}{5\mathcal{S}_-^2\zeta} + \frac{55}{6}\eta - \frac{7\mathcal{S}_+^2\eta}{3\mathcal{S}_-^2} + \frac{16}{3}\beta_-^2\eta + \frac{40}{3}\beta_+\eta - \frac{48\beta_-^2\eta}{\gamma^2} - \frac{32\mathcal{S}_+\beta_-\beta_+\eta}{\mathcal{S}_-\gamma^2} + \frac{32\beta_+^2\eta}{\gamma^2} \\ &- \frac{16\mathcal{S}_+^2\beta_+^2\eta}{\mathcal{S}_-^2\gamma^2} - \frac{56\mathcal{S}_+\beta_-\eta}{3\mathcal{S}_-\gamma} + \frac{80\beta_-^2\eta}{3\gamma} - \frac{56\beta_+\eta}{3\gamma} + \frac{32\mathcal{S}_+\beta_-\beta_+\eta}{3\mathcal{S}_-\gamma} - \frac{16\beta_+^2\eta}{\gamma} - \frac{4}{3}\gamma\eta \end{aligned}$$

$$
\begin{aligned}
&-\frac{1}{3}\gamma^2\eta-\frac{4}{3}\delta_+\eta-\frac{14\eta}{\mathcal{S}_-^2\zeta}-\frac{7\gamma\eta}{\mathcal{S}_-^2\zeta}+\frac{2}{3}\eta^2+\frac{4\mathcal{S}_+\chi_-}{\mathcal{S}_-\gamma}-\frac{8\mathcal{S}_+\eta\chi_-}{\mathcal{S}_-\gamma}-\frac{4}{3}\chi_++\frac{4\chi_+}{\gamma}+\frac{8}{3}\eta\chi_+\\
&-\frac{8\eta\chi_+}{\gamma}+\frac{11\mathcal{S}_+\psi}{2\mathcal{S}_-}-\frac{2}{15}\beta_-\psi+\frac{32\mathcal{S}_+^2\beta_-\psi}{15\mathcal{S}_-^2}+\frac{4\mathcal{S}_+\beta_+\psi}{3\mathcal{S}_-}+\frac{8}{3}\beta_-\beta_+\psi-\frac{8\mathcal{S}_+\beta_-^2\psi}{\mathcal{S}_-\gamma^2}\\
&-\frac{8\beta_-\beta_+\psi}{\gamma^2}-\frac{8\mathcal{S}_+^2\beta_-\beta_+\psi}{\mathcal{S}_-^2\gamma^2}-\frac{8\mathcal{S}_+\beta_+^2\psi}{\mathcal{S}_-\gamma^2}+\frac{36\beta_-\psi}{5\gamma}-\frac{16\mathcal{S}_+^2\beta_-\psi}{5\mathcal{S}_-^2\gamma}+\frac{8\mathcal{S}_+\beta_-^2\psi}{3\mathcal{S}_-\gamma}\\
&+\frac{4\mathcal{S}_+\beta_+\psi}{\mathcal{S}_-\gamma}+\frac{16\beta_-\beta_+\psi}{3\gamma}+\frac{8\mathcal{S}_+\beta_+^2\psi}{3\mathcal{S}_-\gamma}+\frac{3\mathcal{S}_+\gamma\psi}{\mathcal{S}_-}+\frac{2}{3}\delta_-\psi+\frac{64\beta_-\psi}{5\mathcal{S}_-^2\zeta}\\
&+\frac{32\beta_-\gamma\psi}{5\mathcal{S}_-^2\zeta}-\frac{16}{3}\beta_-\eta\psi+\frac{20\beta_-\eta\psi}{3\gamma}+\frac{20\mathcal{S}_+\beta_+\eta\psi}{3\mathcal{S}_-\gamma}+\frac{4}{3}\chi_-\psi-\frac{4\chi_-\psi}{\gamma}-\frac{4\mathcal{S}_+\chi_+\psi}{\mathcal{S}_-\gamma}.
\end{aligned}
\tag{D.4}
$$

Note that f_3^{d} is determined entirely by tail terms of the form of Eq. (3.36); this is the only hereditary contribution to the flux.

For the ratio $\rho(x)$, we obtained

$$
\rho^{\mathrm{DD}}(x)=\frac{3}{8\mathcal{S}_-^2\zeta\eta x^4}\left[1+\rho_2^{\mathrm{DD}}x+\rho_3^{\mathrm{DD}}x^{3/2}+\rho_4^{\mathrm{DD}}x^2+\mathcal{O}(5)\right] \tag{D.5}
$$

with the coefficients

$$
\begin{aligned}
\rho_2^{\mathrm{DD}}=&\frac{13}{10}-\frac{4\mathcal{S}_+^2}{5\mathcal{S}_-^2}+\frac{8}{3}\beta_+-\frac{4\mathcal{S}_+\beta_-}{\mathcal{S}_-\gamma}-\frac{4\beta_+}{\gamma}-\frac{2}{3}\gamma\\
&-\frac{24}{5\mathcal{S}_-^2\zeta}-\frac{12\gamma}{5\mathcal{S}_-^2\zeta}+\frac{7}{6}\eta-\frac{8}{3}\beta_-\psi+\frac{4\beta_-\psi}{\gamma}+\frac{4\mathcal{S}_+\beta_+\psi}{\mathcal{S}_-\gamma},
\end{aligned}
\tag{D.6}
$$

$$
\rho_3^{\mathrm{DD}}=-2\pi-\pi\gamma, \tag{D.7}
$$

$$
\begin{aligned}
\rho_4^{\mathrm{DD}}=&-\frac{7629}{1400}+\frac{129\mathcal{S}_+^2}{700\mathcal{S}_-^2}+\frac{16\mathcal{S}_+^4}{25\mathcal{S}_-^4}+\frac{4\mathcal{S}_+\beta_-}{3\mathcal{S}_-}+\frac{80}{9}\beta_-^2+\frac{181}{15}\beta_+-\frac{16\mathcal{S}_+^2\beta_+}{15\mathcal{S}_-^2}+\frac{80}{9}\beta_+^2\\
&+\frac{12\beta_-^2}{\gamma^2}+\frac{12\mathcal{S}_+^2\beta_-^2}{\mathcal{S}_-^2\gamma^2}+\frac{48\mathcal{S}_+\beta_-\beta_+}{\mathcal{S}_-\gamma^2}+\frac{12\beta_+^2}{\gamma^2}+\frac{12\mathcal{S}_+^2\beta_+^2}{\mathcal{S}_-^2\gamma^2}-\frac{62\mathcal{S}_+\beta_-}{5\mathcal{S}_-\gamma}+\frac{32\mathcal{S}_+^3\beta_-}{5\mathcal{S}_-^3\gamma}\\
&-\frac{40\beta_-^2}{3\gamma}-\frac{46\beta_+}{5\gamma}+\frac{16\mathcal{S}_+^2\beta_+}{5\mathcal{S}_-^2\gamma}-\frac{80\mathcal{S}_+\beta_-\beta_+}{3\mathcal{S}_-\gamma}-\frac{40\beta_+^2}{3\gamma}-\frac{77}{5}\gamma+\frac{16\mathcal{S}_+^2\gamma}{15\mathcal{S}_-^2}+\frac{44}{9}\beta_+\gamma\\
&-\frac{205}{36}\gamma^2+\frac{1}{3}\delta_++\frac{576}{25\mathcal{S}_-^4\zeta^2}+\frac{576\gamma}{25\mathcal{S}_-^4\zeta^2}+\frac{144\gamma^2}{25\mathcal{S}_-^4\zeta^2}-\frac{653}{350\mathcal{S}_-^2\zeta}+\frac{192\mathcal{S}_+^2}{25\mathcal{S}_-^4\zeta}+\frac{96\mathcal{S}_+\beta_-}{5\mathcal{S}_-^3\zeta}\\
&+\frac{64\beta_+}{5\mathcal{S}_-^2\zeta}+\frac{192\mathcal{S}_+\beta_-}{5\mathcal{S}_-^3\gamma\zeta}+\frac{192\beta_+}{5\mathcal{S}_-^2\gamma\zeta}+\frac{3827\gamma}{700\mathcal{S}_-^2\zeta}+\frac{96\mathcal{S}_+^2\gamma}{25\mathcal{S}_-^4\zeta}-\frac{16\beta_+\gamma}{5\mathcal{S}_-^2\zeta}+\frac{16\gamma^2}{5\mathcal{S}_-^2\zeta}+\frac{71}{24}\eta
\end{aligned}
$$

$$
\begin{aligned}
&+\frac{\mathcal{S}_+^2\eta}{3\mathcal{S}_-^2}-\frac{320}{9}\beta_-^2\eta-\frac{245}{9}\beta_+\eta-\frac{16\beta_-^2\eta}{\gamma^2}-\frac{96\mathcal{S}_+\beta_-\beta_+\eta}{\mathcal{S}_-\gamma^2}-\frac{32\beta_+^2\eta}{\gamma^2}-\frac{48\mathcal{S}_+^2\beta_+^2\eta}{\mathcal{S}_-^2\gamma^2}\\
&+\frac{26\mathcal{S}_+\beta_-\eta}{3\mathcal{S}_-\gamma}-\frac{32\beta_-^2\eta}{3\gamma}+\frac{26\beta_+\eta}{3\gamma}+\frac{160\mathcal{S}_+\beta_-\beta_+\eta}{3\mathcal{S}_-\gamma}+\frac{64\beta_+^2\eta}{\gamma}+\frac{110}{9}\gamma\eta+\frac{4}{3}\gamma^2\eta\\
&+\frac{16}{3}\delta_+\eta+\frac{2\eta}{\mathcal{S}_-^2\zeta}+\frac{\gamma\eta}{\mathcal{S}_-^2\zeta}+\frac{55}{72}\eta^2-\frac{4\mathcal{S}_+\chi_-}{\mathcal{S}_-\gamma}+\frac{8\mathcal{S}_+\eta\chi_-}{\mathcal{S}_-\gamma}+\frac{16}{3}\chi_+-\frac{4\chi_+}{\gamma}-\frac{32}{3}\eta\chi_+\\
&+\frac{8\eta\chi_+}{\gamma}-\frac{11\mathcal{S}_+\psi}{2\mathcal{S}_-}-\frac{181}{15}\beta_-\psi+\frac{16\mathcal{S}_+^2\beta_-\psi}{15\mathcal{S}_-^2}-\frac{4\mathcal{S}_+\beta_+\psi}{3\mathcal{S}_-}-\frac{160}{9}\beta_-\beta_+\psi-\frac{24\mathcal{S}_+\beta_-^2\psi}{\mathcal{S}_-\gamma^2}\\
&-\frac{24\beta_-\beta_+\psi}{\gamma^2}-\frac{24\mathcal{S}_+^2\beta_-\beta_+\psi}{\mathcal{S}_-^2\gamma^2}-\frac{24\mathcal{S}_+\beta_+^2\psi}{\mathcal{S}_-\gamma^2}+\frac{46\beta_-\psi}{5\gamma}-\frac{16\mathcal{S}_+^2\beta_-\psi}{5\mathcal{S}_-^2\gamma}+\frac{40\mathcal{S}_+\beta_-^2\psi}{3\mathcal{S}_-\gamma}\\
&+\frac{62\mathcal{S}_+\beta_+\psi}{5\mathcal{S}_-\gamma}-\frac{32\mathcal{S}_+^3\beta_+\psi}{5\mathcal{S}_-^3\gamma}+\frac{80\beta_-\beta_+\psi}{3\gamma}+\frac{40\mathcal{S}_+\beta_+^2\psi}{3\mathcal{S}_-\gamma}-\frac{3\mathcal{S}_+\gamma\psi}{\mathcal{S}_-}-\frac{44}{9}\beta_-\gamma\psi+\frac{1}{3}\delta_-\psi\\
&-\frac{64\beta_-\psi}{5\mathcal{S}_-^2\zeta}-\frac{96\mathcal{S}_+\beta_+\psi}{5\mathcal{S}_-^3\zeta}-\frac{192\beta_-\psi}{5\mathcal{S}_-^2\gamma\zeta}-\frac{192\mathcal{S}_+\beta_+\psi}{5\mathcal{S}_-^3\gamma\zeta}+\frac{16\beta_-\gamma\psi}{5\mathcal{S}_-^2\zeta}+\frac{11}{9}\beta_-\eta\psi+\frac{10\beta_-\eta\psi}{3\gamma}\\
&+\frac{10\mathcal{S}_+\beta_+\eta\psi}{3\mathcal{S}_-\gamma}-\frac{16}{3}\chi_-\psi+\frac{4\chi_-\psi}{\gamma}+\frac{4\mathcal{S}_+\chi_+\psi}{\mathcal{S}_-\gamma}. \qquad \text{(D.8)}
\end{aligned}
$$

In the quadrupole-driven case of Section 3.5.2, we obtained for the dipolar part of the flux

$$
\mathcal{F}_{\rm dip}(x)=\frac{4\mathcal{S}_-^2\zeta\eta^2x^4}{3G\alpha}\left[1+f_2^{\rm d}x+f_3^{\rm d}x^{3/2}+f_4^{\rm d}x^2+\mathcal{O}(5)\right] \qquad \text{(D.9)}
$$

with coefficients given by

$$
f_2^{\rm d}=-\frac{14}{5}-\frac{4}{3}\beta_++\frac{4\mathcal{S}_+\beta_-}{\mathcal{S}_-\gamma}+\frac{4\beta_+}{\gamma}-\frac{2}{3}\gamma-\frac{4}{3}\eta+\frac{4}{3}\beta_-\psi-\frac{4\beta_-\psi}{\gamma}-\frac{4\mathcal{S}_+\beta_+\psi}{\mathcal{S}_-\gamma}, \qquad \text{(D.10)}
$$

$$
f_3^{\rm d}=2\pi+\pi\gamma, \qquad \text{(D.11)}
$$

$$
\begin{aligned}
f_4^{\rm d}=&-\frac{29}{28}-\frac{4\mathcal{S}_+\beta_-}{3\mathcal{S}_-}-\frac{4}{3}\beta_-^2+\frac{2}{15}\beta_+-\frac{4}{3}\beta_+^2+\frac{4\beta_-^2}{\gamma^2}+\frac{16\mathcal{S}_+\beta_-\beta_+}{\mathcal{S}_-\gamma^2}+\frac{4\beta_+^2}{\gamma^2}-\frac{4\mathcal{S}_+\beta_-}{\mathcal{S}_-\gamma}\\
&-\frac{8\beta_-^2}{3\gamma}-\frac{36\beta_+}{5\gamma}-\frac{16\mathcal{S}_+\beta_-\beta_+}{3\mathcal{S}_-\gamma}-\frac{8\beta_+^2}{3\gamma}+\frac{2}{5}\gamma+\frac{1}{2}\gamma^2+\frac{2}{3}\delta_++\frac{55}{6}\eta+\frac{16}{3}\beta_-^2\eta\\
&+\frac{40}{3}\beta_+\eta-\frac{48\beta_-^2\eta}{\gamma^2}-\frac{32\mathcal{S}_+\beta_-\beta_+\eta}{\mathcal{S}_-\gamma^2}+\frac{32\beta_+^2\eta}{\gamma^2}-\frac{56\mathcal{S}_+\beta_-\eta}{3\mathcal{S}_-\gamma}+\frac{80\beta_-^2\eta}{3\gamma}-\frac{56\beta_+\eta}{3\gamma}\\
&+\frac{32\mathcal{S}_+\beta_-\beta_+\eta}{3\mathcal{S}_-\gamma}-\frac{16\beta_+^2\eta}{\gamma}-\frac{4}{3}\gamma\eta-\frac{1}{3}\gamma^2\eta-\frac{4}{3}\delta_+\eta+\frac{2}{3}\eta^2+\frac{4\mathcal{S}_+\chi_-}{\mathcal{S}_-\gamma}-\frac{8\mathcal{S}_+\eta\chi_-}{\mathcal{S}_-\gamma}
\end{aligned}
$$

$$
\begin{aligned}
&- \frac{4}{3}\chi_+ + \frac{4\chi_+}{\gamma} + \frac{8}{3}\eta\chi_+ - \frac{8\eta\chi_+}{\gamma} + \frac{11\mathcal{S}_+\psi}{2\mathcal{S}_-} - \frac{2}{15}\beta_-\psi + \frac{4\mathcal{S}_+\beta_+\psi}{3\mathcal{S}_-} + \frac{8}{3}\beta_-\beta_+\psi \\
&- \frac{8\mathcal{S}_+\beta_-^2\psi}{\mathcal{S}_-\gamma^2} - \frac{8\beta_-\beta_+\psi}{\gamma^2} - \frac{8\mathcal{S}_+\beta_+^2\psi}{\mathcal{S}_-\gamma^2} + \frac{36\beta_-\psi}{5\gamma} + \frac{8\mathcal{S}_+\beta_-^2\psi}{3\mathcal{S}_-\gamma} + \frac{4\mathcal{S}_+\beta_+\psi}{\mathcal{S}_-\gamma} + \frac{16\beta_-\beta_+\psi}{3\gamma} \\
&+ \frac{8\mathcal{S}_+\beta_+^2\psi}{3\mathcal{S}_-\gamma} + \frac{3\mathcal{S}_+\gamma\psi}{\mathcal{S}_-} + \frac{2}{3}\delta_-\psi - \frac{16}{3}\beta_-\eta\psi + \frac{20\beta_-\eta\psi}{3\gamma} + \frac{20\mathcal{S}_+\beta_+\eta\psi}{3\mathcal{S}_-\gamma} + \frac{4}{3}\chi_-\psi \\
&- \frac{4\chi_-\psi}{\gamma} - \frac{4\mathcal{S}_+\chi_+\psi}{\mathcal{S}_-\gamma}.
\end{aligned} \tag{D.12}
$$

For the non-dipolar part, we obtained

$$
\mathcal{F}_{\text{non-dip}}(x) = \frac{32\eta^2\xi x^5}{5G\alpha}\left[1 + f_2^{\text{nd}}x + \mathcal{O}(3)\right] \tag{D.13}
$$

with the coefficient

$$
\begin{aligned}
f_2^{\text{nd}} =& - \frac{1247}{336\xi} - \frac{8\beta_+}{3\xi} - \frac{2143\gamma}{672\xi} - \frac{4\beta_+\gamma}{3\xi} - \frac{2\gamma^2}{3\xi} - \frac{485\mathcal{S}_+^2\zeta}{672\xi} - \frac{4\mathcal{S}_+^2\beta_+\zeta}{9\xi} + \frac{5\mathcal{S}_+^2\beta_-^2\zeta}{6\gamma^2\xi} \\
&+ \frac{5\mathcal{S}_+^2\beta_+^2\zeta}{6\gamma^2\xi} + \frac{2\mathcal{S}_+^2\beta_+\zeta}{3\gamma\xi} - \frac{2\mathcal{S}_+^2\gamma\zeta}{9\xi} - \frac{35\eta}{12\xi} - \frac{35\gamma\eta}{24\xi} - \frac{35\mathcal{S}_+^2\zeta\eta}{72\xi} - \frac{10\mathcal{S}_+^2\beta_+^2\zeta\eta}{3\gamma^2\xi} \\
&+ \frac{8\beta_-\psi}{3\xi} + \frac{4\beta_-\gamma\psi}{3\xi} + \frac{4\mathcal{S}_+^2\beta_-\zeta\psi}{9\xi} - \frac{5\mathcal{S}_+^2\beta_-\beta_+\zeta\psi}{3\gamma^2\xi} - \frac{2\mathcal{S}_+^2\beta_-\zeta\psi}{3\gamma\xi}.
\end{aligned} \tag{D.14}
$$

For the non-dipolar ratio $\rho_{\text{non-dip}}(x)$, we obtain

$$
\rho_{\text{non-dip}}(x) = \frac{5}{64\eta\xi x^5}\left[1 + \rho_2^{\text{nd}}x + \rho_3^{\text{nd}}x^{3/2} + \rho_4^{\text{nd}}x^2 + \mathcal{O}(5)\right] \tag{D.15}
$$

with the coefficients

$$
\begin{aligned}
\rho_2^{\text{nd}} =& \frac{743}{336\xi} + \frac{4\beta_+}{\xi} + \frac{743\gamma}{672\xi} + \frac{2\beta_+\gamma}{\xi} + \frac{317\mathcal{S}_+^2\zeta}{672\xi} + \frac{2\mathcal{S}_+^2\beta_+\zeta}{3\xi} - \frac{5\mathcal{S}_+^2\beta_-^2\zeta}{6\gamma^2\xi} - \frac{5\mathcal{S}_+^2\beta_+^2\zeta}{6\gamma^2\xi} \\
&- \frac{2\mathcal{S}_+^2\beta_+\zeta}{3\gamma\xi} + \frac{11\eta}{4\xi} + \frac{11\gamma\eta}{8\xi} + \frac{11\mathcal{S}_+^2\zeta\eta}{24\xi} + \frac{10\mathcal{S}_+^2\beta_+^2\zeta\eta}{3\gamma^2\xi} - \frac{4\beta_-\psi}{\xi} - \frac{2\beta_-\gamma\psi}{\xi} \\
&- \frac{2\mathcal{S}_+^2\beta_-\zeta\psi}{3\xi} + \frac{5\mathcal{S}_+^2\beta_-\beta_+\zeta\psi}{3\gamma^2\xi} + \frac{2\mathcal{S}_+^2\beta_-\zeta\psi}{3\gamma\xi},
\end{aligned} \tag{D.16}
$$

$$
\rho_3^{\text{nd}} = - f_3^{\text{ST}} - \frac{4\pi}{\xi}, \tag{D.17}
$$

$$
\rho_4^{\text{nd}} = - \frac{81}{8} - f_4^{\text{ST}} + 4\beta_-^2 + 3\beta_+ + 4\beta_+^2 - 14\gamma + 4\beta_+\gamma - \frac{19}{4}\gamma^2 + \delta_+ + \frac{57}{8}\eta - 16\beta_-^2\eta
$$

$$
\begin{aligned}
&- 19\beta_+\eta - \frac{48\beta_-^2\eta}{\gamma} + \frac{48\beta_+^2\eta}{\gamma} + 11\gamma\eta + \gamma^2\eta + 4\delta_+\eta - \frac{1}{8}\eta^2 + \frac{1555009}{112896\xi^2} + \frac{64\beta_-^2}{9\xi^2} \\
&+ \frac{1247\beta_+}{63\xi^2} + \frac{64\beta_+^2}{9\xi^2} + \frac{2672321\gamma}{112896\xi^2} + \frac{64\beta_-^2\gamma}{9\xi^2} + \frac{565\beta_+\gamma}{21\xi^2} + \frac{64\beta_+^2\gamma}{9\xi^2} + \frac{2275691\gamma^2}{150528\xi^2} \\
&+ \frac{16\beta_-^2\gamma^2}{9\xi^2} + \frac{1013\beta_+\gamma^2}{84\xi^2} + \frac{16\beta_+^2\gamma^2}{9\xi^2} + \frac{2143\gamma^3}{504\xi^2} + \frac{16\beta_+\gamma^3}{9\xi^2} + \frac{4\gamma^4}{9\xi^2} + \frac{604795\mathcal{S}_+^2\zeta}{112896\xi^2} \\
&- \frac{14\mathcal{S}_+^2\beta_-^2\zeta}{27\xi^2} + \frac{4379\mathcal{S}_+^2\beta_+\zeta}{1512\xi^2} - \frac{14\mathcal{S}_+^2\beta_+^2\zeta}{27\xi^2} - \frac{6235\mathcal{S}_+^2\beta_-^2\zeta}{1008\gamma^2\xi^2} - \frac{40\mathcal{S}_+^2\beta_-^2\beta_+\zeta}{3\gamma^2\xi^2} \\
&- \frac{6235\mathcal{S}_+^2\beta_+^2\zeta}{1008\gamma^2\xi^2} - \frac{40\mathcal{S}_+^2\beta_+^3\zeta}{9\gamma^2\xi^2} - \frac{1987\mathcal{S}_+^2\beta_-^2\zeta}{224\gamma\xi^2} - \frac{1247\mathcal{S}_+^2\beta_+\zeta}{252\gamma\xi^2} - \frac{20\mathcal{S}_+^2\beta_-^2\beta_+\zeta}{3\gamma\xi^2} \\
&- \frac{1987\mathcal{S}_+^2\beta_+^2\zeta}{224\gamma\xi^2} - \frac{20\mathcal{S}_+^2\beta_+^3\zeta}{9\gamma\xi^2} + \frac{4235377\mathcal{S}_+^2\gamma\zeta}{677376\xi^2} + \frac{32\mathcal{S}_+^2\beta_-^2\gamma\zeta}{27\xi^2} + \frac{91\mathcal{S}_+^2\beta_+\gamma\zeta}{18\xi^2} \\
&+ \frac{32\mathcal{S}_+^2\beta_+^2\gamma\zeta}{27\xi^2} + \frac{257\mathcal{S}_+^2\gamma^2\zeta}{108\xi^2} + \frac{32\mathcal{S}_+^2\beta_+\gamma^2\zeta}{27\xi^2} + \frac{8\mathcal{S}_+^2\gamma^3\zeta}{27\xi^2} + \frac{235225\mathcal{S}_+^4\zeta^2}{451584\xi^2} + \frac{16\mathcal{S}_+^4\beta_-^2\zeta^2}{81\xi^2} \\
&+ \frac{29\mathcal{S}_+^4\beta_+\zeta^2}{84\xi^2} + \frac{16\mathcal{S}_+^4\beta_+^2\zeta^2}{81\xi^2} + \frac{25\mathcal{S}_+^4\beta_-^4\zeta^2}{36\gamma^4\xi^2} + \frac{25\mathcal{S}_+^4\beta_-^2\beta_+^2\zeta^2}{6\gamma^4\xi^2} + \frac{25\mathcal{S}_+^4\beta_+^4\zeta^2}{36\gamma^4\xi^2} \\
&+ \frac{10\mathcal{S}_+^4\beta_-^2\beta_+\zeta^2}{3\gamma^3\xi^2} + \frac{10\mathcal{S}_+^4\beta_+^3\zeta^2}{9\gamma^3\xi^2} - \frac{1529\mathcal{S}_+^4\beta_-^2\zeta^2}{2016\gamma^2\xi^2} - \frac{20\mathcal{S}_+^4\beta_-^2\beta_+\zeta^2}{9\gamma^2\xi^2} - \frac{1529\mathcal{S}_+^4\beta_+^2\zeta^2}{2016\gamma^2\xi^2} \\
&- \frac{20\mathcal{S}_+^4\beta_+^3\zeta^2}{27\gamma^2\xi^2} - \frac{26\mathcal{S}_+^4\beta_-^2\zeta^2}{27\gamma\xi^2} - \frac{485\mathcal{S}_+^4\beta_+\zeta^2}{504\gamma\xi^2} - \frac{26\mathcal{S}_+^4\beta_+^2\zeta^2}{27\gamma\xi^2} + \frac{485\mathcal{S}_+^4\gamma\zeta^2}{1512\xi^2} \\
&+ \frac{16\mathcal{S}_+^4\beta_+\gamma\zeta^2}{81\xi^2} + \frac{4\mathcal{S}_+^4\gamma^2\zeta^2}{81\xi^2} + \frac{6235\eta}{288\xi^2} - \frac{256\beta_-^2\eta}{9\xi^2} + \frac{140\beta_+\eta}{9\xi^2} + \frac{2825\gamma\eta}{96\xi^2} - \frac{256\beta_-^2\gamma\eta}{9\xi^2} \\
&+ \frac{140\beta_+\gamma\eta}{9\xi^2} + \frac{5065\gamma^2\eta}{384\xi^2} - \frac{64\beta_-^2\gamma^2\eta}{9\xi^2} + \frac{35\beta_+\gamma^2\eta}{9\xi^2} + \frac{35\gamma^3\eta}{18\xi^2} + \frac{6755\mathcal{S}_+^2\zeta\eta}{864\xi^2} \\
&- \frac{64\mathcal{S}_+^2\beta_-^2\zeta\eta}{27\xi^2} + \frac{175\mathcal{S}_+^2\beta_+\zeta\eta}{54\xi^2} + \frac{40\mathcal{S}_+^2\beta_+^2\zeta\eta}{9\xi^2} - \frac{175\mathcal{S}_+^2\beta_-^2\zeta\eta}{36\gamma^2\xi^2} + \frac{320\mathcal{S}_+^2\beta_-^2\beta_+\zeta\eta}{9\gamma^2\xi^2} \\
&+ \frac{835\mathcal{S}_+^2\beta_+^2\zeta\eta}{42\gamma^2\xi^2} + \frac{160\mathcal{S}_+^2\beta_+^3\zeta\eta}{9\gamma^2\xi^2} + \frac{283\mathcal{S}_+^2\beta_-^2\zeta\eta}{24\gamma\xi^2} - \frac{35\mathcal{S}_+^2\beta_+\zeta\eta}{9\gamma\xi^2} + \frac{160\mathcal{S}_+^2\beta_-^2\beta_+\zeta\eta}{9\gamma\xi^2} \\
&+ \frac{4745\mathcal{S}_+^2\beta_+^2\zeta\eta}{252\gamma\xi^2} + \frac{80\mathcal{S}_+^2\beta_+^3\zeta\eta}{9\gamma\xi^2} + \frac{3745\mathcal{S}_+^2\gamma\zeta\eta}{576\xi^2} - \frac{128\mathcal{S}_+^2\beta_-^2\gamma\zeta\eta}{27\xi^2} + \frac{70\mathcal{S}_+^2\beta_+\gamma\zeta\eta}{27\xi^2} \\
&+ \frac{35\mathcal{S}_+^2\gamma^2\zeta\eta}{27\xi^2} + \frac{2425\mathcal{S}_+^4\zeta^2\eta}{3456\xi^2} - \frac{64\mathcal{S}_+^4\beta_-^2\zeta^2\eta}{81\xi^2} + \frac{35\mathcal{S}_+^4\beta_+\zeta^2\eta}{81\xi^2} - \frac{50\mathcal{S}_+^4\beta_-^2\beta_+^2\zeta^2\eta}{3\gamma^4\xi^2} \\
&- \frac{50\mathcal{S}_+^4\beta_+^4\zeta^2\eta}{9\gamma^4\xi^2} - \frac{80\mathcal{S}_+^4\beta_-^2\beta_+\zeta^2\eta}{9\gamma^3\xi^2} - \frac{40\mathcal{S}_+^4\beta_+^3\zeta^2\eta}{9\gamma^3\xi^2} - \frac{559\mathcal{S}_+^4\beta_-^2\zeta^2\eta}{216\gamma^2\xi^2} \\
&+ \frac{160\mathcal{S}_+^4\beta_-^2\beta_+\zeta^2\eta}{27\gamma^2\xi^2} + \frac{3025\mathcal{S}_+^4\beta_+^2\zeta^2\eta}{756\gamma^2\xi^2} + \frac{80\mathcal{S}_+^4\beta_+^3\zeta^2\eta}{27\gamma^2\xi^2} + \frac{64\mathcal{S}_+^4\beta_-^2\zeta^2\eta}{27\gamma\xi^2} - \frac{35\mathcal{S}_+^4\beta_+\zeta^2\eta}{54\gamma\xi^2}
\end{aligned}
$$

$$+\frac{40\mathcal{S}_+^4\beta_+^2\zeta^2\eta}{27\gamma\xi^2}+\frac{35\mathcal{S}_+^4\gamma\zeta^2\eta}{162\xi^2}+\frac{1225\eta^2}{144\xi^2}+\frac{1225\gamma\eta^2}{144\xi^2}+\frac{1225\gamma^2\eta^2}{576\xi^2}+\frac{1225\mathcal{S}_+^2\zeta\eta^2}{432\xi^2}$$
$$+\frac{175\mathcal{S}_+^2\beta_+^2\zeta\eta^2}{9\gamma^2\xi^2}+\frac{175\mathcal{S}_+^2\beta_+^2\zeta\eta^2}{18\gamma\xi^2}+\frac{1225\mathcal{S}_+^2\gamma\zeta\eta^2}{864\xi^2}+\frac{1225\mathcal{S}_+^4\zeta^2\eta^2}{5184\xi^2}+\frac{100\mathcal{S}_+^4\beta_+^4\zeta^2\eta^2}{9\gamma^4\xi^2}$$
$$+\frac{175\mathcal{S}_+^4\beta_+^2\zeta^2\eta^2}{54\gamma^2\xi^2}-\frac{1655}{2592\xi}+\frac{32\beta_-^2}{9\xi}+\frac{239\beta_+}{252\xi}+\frac{32\beta_+^2}{9\xi}-\frac{39239\gamma}{4032\xi}+\frac{16\beta_-^2\gamma}{9\xi}$$
$$-\frac{73\beta_+\gamma}{56\xi}+\frac{16\beta_+^2\gamma}{9\xi}-\frac{2647\gamma^2}{504\xi}-\frac{8\beta_+\gamma^2}{9\xi}-\frac{8\gamma^3}{9\xi}-\frac{485\mathcal{S}_+^2\zeta}{448\xi}+\frac{16\mathcal{S}_+^2\beta_-^2\zeta}{27\xi}+\frac{199\mathcal{S}_+^2\beta_+\zeta}{168\xi}$$
$$+\frac{16\mathcal{S}_+^2\beta_+^2\zeta}{27\xi}+\frac{5\mathcal{S}_+^2\beta_-^2\zeta}{4\gamma^2\xi}-\frac{10\mathcal{S}_+^2\beta_-^2\beta_+\zeta}{3\gamma^2\xi}+\frac{5\mathcal{S}_+^2\beta_+^2\zeta}{4\gamma^2\xi}-\frac{10\mathcal{S}_+^2\beta_+^3\zeta}{9\gamma^2\xi}+\frac{2\mathcal{S}_+^2\beta_-^2\zeta}{9\gamma\xi}$$
$$+\frac{\mathcal{S}_+^2\beta_+\zeta}{\gamma\xi}+\frac{2\mathcal{S}_+^2\beta_+^2\zeta}{9\gamma\xi}-\frac{653\mathcal{S}_+^2\gamma\zeta}{504\xi}-\frac{8\mathcal{S}_+^2\beta_+\gamma\zeta}{27\xi}-\frac{8\mathcal{S}_+^2\gamma^2\zeta}{27\xi}-\frac{5239\eta}{224\xi}-\frac{128\beta_-^2\eta}{9\xi}$$
$$+\frac{31\beta_+\eta}{9\xi}-\frac{8881\gamma\eta}{1344\xi}-\frac{64\beta_-^2\gamma\eta}{9\xi}+\frac{31\beta_+\gamma\eta}{18\xi}-\frac{37\gamma^2\eta}{18\xi}-\frac{3425\mathcal{S}_+^2\zeta\eta}{4032\xi}-\frac{64\mathcal{S}_+^2\beta_-^2\zeta\eta}{27\xi}$$
$$+\frac{31\mathcal{S}_+^2\beta_+\zeta\eta}{54\xi}+\frac{5\mathcal{S}_+^2\beta_-^2\zeta\eta}{36\gamma^2\xi}+\frac{80\mathcal{S}_+^2\beta_-^2\beta_+\zeta\eta}{9\gamma^2\xi}-\frac{175\mathcal{S}_+^2\beta_+^2\zeta\eta}{36\gamma^2\xi}+\frac{40\mathcal{S}_+^2\beta_+^3\zeta\eta}{9\gamma^2\xi}$$
$$+\frac{32\mathcal{S}_+^2\beta_-^2\zeta\eta}{9\gamma\xi}+\frac{\mathcal{S}_+^2\beta_+\zeta\eta}{9\gamma\xi}-\frac{40\mathcal{S}_+^2\beta_+^2\zeta\eta}{9\gamma\xi}-\frac{37\mathcal{S}_+^2\gamma\zeta\eta}{54\xi}-\frac{295\eta^2}{72\xi}-\frac{35\gamma\eta^2}{144\xi}-\frac{35\mathcal{S}_+^2\zeta\eta^2}{432\xi}$$
$$-\frac{5\mathcal{S}_+^2\beta_+^2\zeta\eta^2}{9\gamma^2\xi}+4\chi_+-8\eta\chi_+-3\beta_-\psi-8\beta_-\beta_+\psi-4\beta_-\gamma\psi+\delta_-\psi+\beta_-\eta\psi$$
$$-\frac{1247\beta_-\psi}{63\xi^2}-\frac{128\beta_-\beta_+\psi}{9\xi^2}-\frac{565\beta_-\gamma\psi}{21\xi^2}-\frac{128\beta_-\beta_+\gamma\psi}{9\xi^2}-\frac{1013\beta_-\gamma^2\psi}{84\xi^2}$$
$$-\frac{32\beta_-\beta_+\gamma^2\psi}{9\xi^2}-\frac{16\beta_-\gamma^3\psi}{9\xi^2}-\frac{4379\mathcal{S}_+^2\beta_-\zeta\psi}{1512\xi^2}+\frac{28\mathcal{S}_+^2\beta_-\beta_+\zeta\psi}{27\xi^2}+\frac{40\mathcal{S}_+^2\beta_-^3\zeta\psi}{9\gamma^2\xi^2}$$
$$+\frac{6235\mathcal{S}_+^2\beta_-\beta_+\zeta\psi}{504\gamma^2\xi^2}+\frac{40\mathcal{S}_+^2\beta_-\beta_+^2\zeta\psi}{3\gamma^2\xi^2}+\frac{1247\mathcal{S}_+^2\beta_-\zeta\psi}{252\gamma\xi^2}+\frac{20\mathcal{S}_+^2\beta_-^3\zeta\psi}{9\gamma\xi^2}$$
$$+\frac{1987\mathcal{S}_+^2\beta_-\beta_+\zeta\psi}{112\gamma\xi^2}+\frac{20\mathcal{S}_+^2\beta_-\beta_+^2\zeta\psi}{3\gamma\xi^2}-\frac{91\mathcal{S}_+^2\beta_-\gamma\zeta\psi}{18\xi^2}-\frac{64\mathcal{S}_+^2\beta_-\beta_+\gamma\zeta\psi}{27\xi^2}$$
$$-\frac{32\mathcal{S}_+^2\beta_-\gamma^2\zeta\psi}{27\xi^2}-\frac{29\mathcal{S}_+^4\beta_-\zeta^2\psi}{84\xi^2}-\frac{32\mathcal{S}_+^4\beta_-\beta_+\zeta^2\psi}{81\xi^2}-\frac{25\mathcal{S}_+^4\beta_-^3\beta_+\zeta^2\psi}{9\gamma^4\xi^2}$$
$$-\frac{25\mathcal{S}_+^4\beta_-\beta_+^3\zeta^2\psi}{9\gamma^4\xi^2}-\frac{10\mathcal{S}_+^4\beta_-^3\zeta^2\psi}{9\gamma^3\xi^2}-\frac{10\mathcal{S}_+^4\beta_-\beta_+^2\zeta^2\psi}{3\gamma^3\xi^2}+\frac{20\mathcal{S}_+^4\beta_-^3\zeta^2\psi}{27\gamma^2\xi^2}$$
$$+\frac{1529\mathcal{S}_+^4\beta_-\beta_+\zeta^2\psi}{1008\gamma^2\xi^2}+\frac{20\mathcal{S}_+^4\beta_-\beta_+^2\zeta^2\psi}{9\gamma^2\xi^2}+\frac{485\mathcal{S}_+^4\beta_-\zeta^2\psi}{504\gamma\xi^2}+\frac{52\mathcal{S}_+^4\beta_-\beta_+\zeta^2\psi}{27\gamma\xi^2}$$
$$-\frac{16\mathcal{S}_+^4\beta_-\gamma\zeta^2\psi}{81\xi^2}-\frac{140\beta_-\eta\psi}{9\xi^2}-\frac{140\beta_-\gamma\eta\psi}{9\xi^2}-\frac{35\beta_-\gamma^2\eta\psi}{9\xi^2}-\frac{175\mathcal{S}_+^2\beta_-\zeta\eta\psi}{54\xi^2}$$

$$
\begin{aligned}
&+\frac{175\mathcal{S}_+^2\beta_-\beta_+\zeta\eta\psi}{18\gamma^2\xi^2}-\frac{160\mathcal{S}_+^2\beta_-\beta_+^2\zeta\eta\psi}{9\gamma^2\xi^2}+\frac{35\mathcal{S}_+^2\beta_-\zeta\eta\psi}{9\gamma\xi^2}+\frac{175\mathcal{S}_+^2\beta_-\beta_+\zeta\eta\psi}{36\gamma\xi^2}\\
&-\frac{80\mathcal{S}_+^2\beta_-\beta_+^2\zeta\eta\psi}{9\gamma\xi^2}-\frac{70\mathcal{S}_+^2\beta_-\gamma\zeta\eta\psi}{27\xi^2}-\frac{35\mathcal{S}_+^4\beta_-\zeta^2\eta\psi}{81\xi^2}+\frac{100\mathcal{S}_+^4\beta_-\beta_+^3\zeta^2\eta\psi}{9\gamma^4\xi^2}\\
&+\frac{40\mathcal{S}_+^4\beta_-\beta_+^2\zeta^2\eta\psi}{9\gamma^3\xi^2}+\frac{175\mathcal{S}_+^4\beta_-\beta_+\zeta^2\eta\psi}{108\gamma^2\xi^2}-\frac{80\mathcal{S}_+^4\beta_-\beta_+^2\zeta^2\eta\psi}{27\gamma^2\xi^2}+\frac{35\mathcal{S}_+^4\beta_-\zeta^2\eta\psi}{54\gamma\xi^2}\\
&-\frac{239\beta_-\psi}{252\xi}-\frac{64\beta_-\beta_+\psi}{9\xi}+\frac{73\beta_-\gamma\psi}{56\xi}-\frac{32\beta_-\beta_+\gamma\psi}{9\xi}+\frac{8\beta_-\gamma^2\psi}{9\xi}-\frac{199\mathcal{S}_+^2\beta_-\zeta\psi}{168\xi}\\
&-\frac{32\mathcal{S}_+^2\beta_-\beta_+\zeta\psi}{27\xi}+\frac{10\mathcal{S}_+^2\beta_-^3\zeta\psi}{9\gamma^2\xi}-\frac{5\mathcal{S}_+^2\beta_-\beta_+\zeta\psi}{2\gamma^2\xi}+\frac{10\mathcal{S}_+^2\beta_-\beta_+^2\zeta\psi}{3\gamma^2\xi}-\frac{\mathcal{S}_+^2\beta_-\zeta\psi}{\gamma\xi}\\
&-\frac{4\mathcal{S}_+^2\beta_-\beta_+\zeta\psi}{9\gamma\xi}+\frac{8\mathcal{S}_+^2\beta_-\gamma\zeta\psi}{27\xi}-\frac{31\beta_-\eta\psi}{9\xi}-\frac{31\beta_-\gamma\eta\psi}{18\xi}-\frac{31\mathcal{S}_+^2\beta_-\zeta\eta\psi}{54\xi}\\
&-\frac{5\mathcal{S}_+^2\beta_-\beta_+\zeta\eta\psi}{18\gamma^2\xi}-\frac{40\mathcal{S}_+^2\beta_-\beta_+^2\zeta\eta\psi}{9\gamma^2\xi}-\frac{\mathcal{S}_+^2\beta_-\zeta\eta\psi}{9\gamma\xi}-4\chi_-\psi. \qquad \text{(D.18)}
\end{aligned}
$$

The result for the dipolar ratio $\rho_{\rm dip}(x)$ is

$$
\rho_{\rm dip}(x)=-\frac{25\mathcal{S}_-^2\zeta}{1536\eta\xi^2x^6}\left[1+\rho_2^{\rm d}x+\rho_3^{\rm d}x^{3/2}+\rho_4^{\rm d}x^2+\mathcal{O}(5)\right] \qquad \text{(D.19)}
$$

with the coefficients

$$
\begin{aligned}
\rho_2^{\rm d}=&\frac{2623}{840\xi}+\frac{2\mathcal{S}_+\beta_-}{\mathcal{S}_-\xi}+\frac{22\beta_+}{3\xi}+\frac{4\mathcal{S}_+\beta_-}{\mathcal{S}_-\gamma\xi}+\frac{4\beta_+}{\gamma\xi}+\frac{3743\gamma}{1680\xi}+\frac{8\beta_+\gamma}{3\xi}+\frac{\gamma^2}{3\xi}+\frac{407\mathcal{S}_+^2\zeta}{560\xi}\\
&+\frac{8\mathcal{S}_+^2\beta_+\zeta}{9\xi}-\frac{5\mathcal{S}_+^2\beta_-^2\zeta}{3\gamma^2\xi}-\frac{5\mathcal{S}_+^2\beta_+^2\zeta}{3\gamma^2\xi}+\frac{2\mathcal{S}_+^3\beta_-\zeta}{3\mathcal{S}_-\gamma\xi}-\frac{2\mathcal{S}_+^2\beta_+\zeta}{3\gamma\xi}+\frac{\mathcal{S}_+^2\gamma\zeta}{9\xi}+\frac{13\eta}{3\xi}\\
&+\frac{13\gamma\eta}{6\xi}+\frac{13\mathcal{S}_+^2\zeta\eta}{18\xi}+\frac{20\mathcal{S}_+^2\beta_+^2\zeta\eta}{3\gamma^2\xi}-\frac{22\beta_-\psi}{3\xi}-\frac{2\mathcal{S}_+\beta_+\psi}{\mathcal{S}_-\xi}-\frac{4\beta_-\psi}{\gamma\xi}-\frac{4\mathcal{S}_+\beta_+\psi}{\mathcal{S}_-\gamma\xi}\\
&-\frac{8\beta_-\gamma\psi}{3\xi}-\frac{8\mathcal{S}_+^2\beta_-\zeta\psi}{9\xi}+\frac{10\mathcal{S}_+^2\beta_-\beta_+\zeta\psi}{3\gamma^2\xi}+\frac{2\mathcal{S}_+^2\beta_-\zeta\psi}{3\gamma\xi}-\frac{2\mathcal{S}_+^3\beta_+\zeta\psi}{3\mathcal{S}_-\gamma\xi}, \qquad \text{(D.20)}\\
\rho_3^{\rm d}=&-2f_3^{\rm ST}+2\pi+\pi\gamma-\frac{8\pi}{\xi}, \qquad \text{(D.21)}\\
\rho_4^{\rm d}=&-\frac{1949}{280}-2f_4^{\rm ST}-\frac{20\mathcal{S}_+\beta_-}{3\mathcal{S}_-}+\frac{8}{9}\beta_-^2-\frac{59}{15}\beta_++\frac{8}{9}\beta_+^2+\frac{4\beta_-^2}{\gamma^2}+\frac{16\mathcal{S}_+\beta_-\beta_+}{\mathcal{S}_-\gamma^2}+\frac{4\beta_+^2}{\gamma^2}\\
&-\frac{10\mathcal{S}_+\beta_-}{\mathcal{S}_-\gamma}+\frac{8\beta_-^2}{3\gamma}-\frac{66\beta_+}{5\gamma}+\frac{16\mathcal{S}_+\beta_-\beta_+}{3\mathcal{S}_-\gamma}+\frac{8\beta_+^2}{3\gamma}-\frac{133}{15}\gamma+\frac{44}{9}\beta_+\gamma-\frac{121}{36}\gamma^2\\
&+\frac{5}{3}\delta_++\frac{2251}{120}\eta-\frac{32}{9}\beta_-^2\eta-\frac{65}{9}\beta_+\eta-\frac{48\beta_-^2\eta}{\gamma^2}-\frac{32\mathcal{S}_+\beta_-\beta_+\eta}{\mathcal{S}_-\gamma^2}+\frac{32\beta_+^2\eta}{\gamma^2}-\frac{58\mathcal{S}_+\beta_-\eta}{3\mathcal{S}_-\gamma}
\end{aligned}
$$

$$
- \frac{128\beta_-^2\eta}{3\gamma} - \frac{58\beta_+\eta}{3\gamma} - \frac{32\mathcal{S}_+\beta_-\beta_+\eta}{3\mathcal{S}_-\gamma} + \frac{32\beta_+^2\eta}{\gamma} + \frac{104}{9}\gamma\eta + \frac{2}{3}\gamma^2\eta + \frac{8}{3}\delta_+\eta + \frac{55}{72}\eta^2
$$
$$
+ \frac{1555009}{37632\xi^2} + \frac{64\beta_-^2}{3\xi^2} + \frac{1247\beta_+}{21\xi^2} + \frac{64\beta_+^2}{3\xi^2} + \frac{2672321\gamma}{37632\xi^2} + \frac{64\beta_-^2\gamma}{3\xi^2} + \frac{565\beta_+\gamma}{7\xi^2}
$$
$$
+ \frac{64\beta_+^2\gamma}{3\xi^2} + \frac{2275691\gamma^2}{50176\xi^2} + \frac{16\beta_-^2\gamma^2}{3\xi^2} + \frac{1013\beta_+\gamma^2}{28\xi^2} + \frac{16\beta_+^2\gamma^2}{3\xi^2} + \frac{2143\gamma^3}{168\xi^2} + \frac{16\beta_+\gamma^3}{3\xi^2}
$$
$$
+ \frac{4\gamma^4}{3\xi^2} + \frac{604795\mathcal{S}_+^2\zeta}{37632\xi^2} - \frac{14\mathcal{S}_+^2\beta_-^2\zeta}{9\xi^2} + \frac{4379\mathcal{S}_+^2\beta_+\zeta}{504\xi^2} - \frac{14\mathcal{S}_+^2\beta_+^2\zeta}{9\xi^2} - \frac{6235\mathcal{S}_+^2\beta_-^2\zeta}{336\gamma^2\xi^2}
$$
$$
- \frac{40\mathcal{S}_+^2\beta_-^2\beta_+\zeta}{\gamma^2\xi^2} - \frac{6235\mathcal{S}_+^2\beta_+^2\zeta}{336\gamma^2\xi^2} - \frac{40\mathcal{S}_+^2\beta_+^3\zeta}{3\gamma^2\xi^2} - \frac{5961\mathcal{S}_+^2\beta_-^2\zeta}{224\gamma\xi^2} - \frac{1247\mathcal{S}_+^2\beta_+\zeta}{84\gamma\xi^2}
$$
$$
- \frac{20\mathcal{S}_+^2\beta_-^2\beta_+\zeta}{\gamma\xi^2} - \frac{5961\mathcal{S}_+^2\beta_+^2\zeta}{224\gamma\xi^2} - \frac{20\mathcal{S}_+^2\beta_+^3\zeta}{3\gamma\xi^2} + \frac{4235377\mathcal{S}_+^2\gamma\zeta}{225792\xi^2} + \frac{32\mathcal{S}_+^2\beta_-^2\gamma\zeta}{9\xi^2}
$$
$$
+ \frac{91\mathcal{S}_+^2\beta_+\gamma\zeta}{6\xi^2} + \frac{32\mathcal{S}_+^2\beta_+^2\gamma\zeta}{9\xi^2} + \frac{257\mathcal{S}_+^2\gamma^2\zeta}{36\xi^2} + \frac{32\mathcal{S}_+^2\beta_+\gamma^2\zeta}{9\xi^2} + \frac{8\mathcal{S}_+^2\gamma^3\zeta}{9\xi^2} + \frac{235225\mathcal{S}_+^4\zeta^2}{150528\xi^2}
$$
$$
+ \frac{16\mathcal{S}_+^4\beta_-^2\zeta^2}{27\xi^2} + \frac{29\mathcal{S}_+^4\beta_+\zeta^2}{28\xi^2} + \frac{16\mathcal{S}_+^4\beta_+^2\zeta^2}{27\xi^2} + \frac{25\mathcal{S}_+^4\beta_-^4\zeta^2}{12\gamma^4\xi^2} + \frac{25\mathcal{S}_+^4\beta_-^2\beta_+^2\zeta^2}{2\gamma^4\xi^2}
$$
$$
+ \frac{25\mathcal{S}_+^4\beta_+^4\zeta^2}{12\gamma^4\xi^2} + \frac{10\mathcal{S}_+^4\beta_-^2\beta_+\zeta^2}{\gamma^3\xi^2} + \frac{10\mathcal{S}_+^4\beta_+^3\zeta^2}{3\gamma^3\xi^2} - \frac{1529\mathcal{S}_+^4\beta_-^2\zeta^2}{672\gamma^2\xi^2} - \frac{20\mathcal{S}_+^4\beta_-^2\beta_+\zeta^2}{3\gamma^2\xi^2}
$$
$$
- \frac{1529\mathcal{S}_+^4\beta_+^2\zeta^2}{672\gamma^2\xi^2} - \frac{20\mathcal{S}_+^4\beta_+^3\zeta^2}{9\gamma^2\xi^2} - \frac{26\mathcal{S}_+^4\beta_-^2\zeta^2}{9\gamma\xi^2} - \frac{485\mathcal{S}_+^4\beta_+\zeta^2}{168\gamma\xi^2} - \frac{26\mathcal{S}_+^4\beta_+^2\zeta^2}{9\gamma\xi^2}
$$
$$
+ \frac{485\mathcal{S}_+^4\gamma\zeta^2}{504\xi^2} + \frac{16\mathcal{S}_+^4\beta_+\gamma\zeta^2}{27\xi^2} + \frac{4\mathcal{S}_+^4\gamma^2\zeta^2}{27\xi^2} + \frac{6235\eta}{96\xi^2} - \frac{256\beta_-^2\eta}{3\xi^2} + \frac{140\beta_+\eta}{3\xi^2} + \frac{2825\gamma\eta}{32\xi^2}
$$
$$
- \frac{256\beta_-^2\gamma\eta}{3\xi^2} + \frac{140\beta_+\gamma\eta}{3\xi^2} + \frac{5065\gamma^2\eta}{128\xi^2} - \frac{64\beta_-^2\gamma^2\eta}{3\xi^2} + \frac{35\beta_+\gamma^2\eta}{3\xi^2} + \frac{35\gamma^3\eta}{6\xi^2}
$$
$$
+ \frac{6755\mathcal{S}_+^2\zeta\eta}{288\xi^2} - \frac{64\mathcal{S}_+^2\beta_-^2\zeta\eta}{9\xi^2} + \frac{175\mathcal{S}_+^2\beta_+\zeta\eta}{18\xi^2} + \frac{40\mathcal{S}_+^2\beta_+^2\zeta\eta}{3\xi^2} - \frac{175\mathcal{S}_+^2\beta_-^2\zeta\eta}{12\gamma^2\xi^2}
$$
$$
+ \frac{320\mathcal{S}_+^2\beta_-^2\beta_+\zeta\eta}{3\gamma^2\xi^2} + \frac{835\mathcal{S}_+^2\beta_+^2\zeta\eta}{14\gamma^2\xi^2} + \frac{160\mathcal{S}_+^2\beta_+^3\zeta\eta}{3\gamma^2\xi^2} + \frac{283\mathcal{S}_+^2\beta_-^2\zeta\eta}{8\gamma\xi^2} - \frac{35\mathcal{S}_+^2\beta_+\zeta\eta}{3\gamma\xi^2}
$$
$$
+ \frac{160\mathcal{S}_+^2\beta_-^2\beta_+\zeta\eta}{3\gamma\xi^2} + \frac{4745\mathcal{S}_+^2\beta_+^2\zeta\eta}{84\gamma\xi^2} + \frac{80\mathcal{S}_+^2\beta_+^3\zeta\eta}{3\gamma\xi^2} + \frac{3745\mathcal{S}_+^2\gamma\zeta\eta}{192\xi^2} - \frac{128\mathcal{S}_+^2\beta_-^2\gamma\zeta\eta}{9\xi^2}
$$
$$
+ \frac{70\mathcal{S}_+^2\beta_+\gamma\zeta\eta}{9\xi^2} + \frac{35\mathcal{S}_+^2\gamma^2\zeta\eta}{9\xi^2} + \frac{2425\mathcal{S}_+^4\zeta^2\eta}{1152\xi^2} - \frac{64\mathcal{S}_+^4\beta_-^2\zeta^2\eta}{27\xi^2} + \frac{35\mathcal{S}_+^4\beta_+\zeta^2\eta}{27\xi^2}
$$
$$
- \frac{50\mathcal{S}_+^4\beta_-^2\beta_+^2\zeta^2\eta}{\gamma^4\xi^2} - \frac{50\mathcal{S}_+^4\beta_+^4\zeta^2\eta}{3\gamma^4\xi^2} - \frac{80\mathcal{S}_+^4\beta_-^2\beta_+\zeta^2\eta}{3\gamma^3\xi^2} - \frac{40\mathcal{S}_+^4\beta_+^3\zeta^2\eta}{3\gamma^3\xi^2} - \frac{559\mathcal{S}_+^4\beta_-^2\zeta^2\eta}{72\gamma^2\xi^2}
$$
$$
+ \frac{160\mathcal{S}_+^4\beta_-^2\beta_+\zeta^2\eta}{9\gamma^2\xi^2} + \frac{3025\mathcal{S}_+^4\beta_+^2\zeta^2\eta}{252\gamma^2\xi^2} + \frac{80\mathcal{S}_+^4\beta_+^3\zeta^2\eta}{9\gamma^2\xi^2} + \frac{64\mathcal{S}_+^4\beta_-^2\zeta^2\eta}{9\gamma\xi^2} - \frac{35\mathcal{S}_+^4\beta_+\zeta^2\eta}{18\gamma\xi^2}
$$

$$+\frac{40\mathcal{S}_+^4\beta_+^2\zeta^2\eta}{9\gamma\xi^2}+\frac{35\mathcal{S}_+^4\gamma\zeta^2\eta}{54\xi^2}+\frac{1225\eta^2}{48\xi^2}+\frac{1225\gamma\eta^2}{48\xi^2}+\frac{1225\gamma^2\eta^2}{192\xi^2}+\frac{1225\mathcal{S}_+^2\zeta\eta^2}{144\xi^2}$$
$$+\frac{175\mathcal{S}_+^2\beta_+^2\zeta\eta^2}{3\gamma^2\xi^2}+\frac{175\mathcal{S}_+^2\beta_+^2\zeta\eta^2}{6\gamma\xi^2}+\frac{1225\mathcal{S}_+^2\gamma\zeta\eta^2}{288\xi^2}+\frac{1225\mathcal{S}_+^4\zeta^2\eta^2}{1728\xi^2}+\frac{100\mathcal{S}_+^4\beta_+^4\zeta^2\eta^2}{3\gamma^4\xi^2}$$
$$+\frac{175\mathcal{S}_+^4\beta_+^2\zeta^2\eta^2}{18\gamma^2\xi^2}-\frac{142951}{6480\xi}+\frac{2143\mathcal{S}_+\beta_-}{84\mathcal{S}_-\xi}+\frac{32\beta_-^2}{3\xi}+\frac{361\beta_+}{140\xi}+\frac{64\mathcal{S}_+\beta_-\beta_+}{3\mathcal{S}_-\xi}+\frac{32\beta_+^2}{3\xi}$$
$$+\frac{1247\mathcal{S}_+\beta_-}{42\mathcal{S}_-\gamma\xi}+\frac{64\beta_-^2}{3\gamma\xi}+\frac{1247\beta_+}{42\gamma\xi}+\frac{128\mathcal{S}_+\beta_-\beta_+}{3\mathcal{S}_-\gamma\xi}+\frac{64\beta_+^2}{3\gamma\xi}-\frac{47343\gamma}{1120\xi}+\frac{16\mathcal{S}_+\beta_-\gamma}{3\mathcal{S}_-\xi}$$
$$-\frac{84\beta_+\gamma}{5\xi}-\frac{5177\gamma^2}{280\xi}-\frac{16\beta_+\gamma^2}{3\xi}-\frac{8\gamma^3}{3\xi}-\frac{4171\mathcal{S}_+^2\zeta}{672\xi}+\frac{16\mathcal{S}_+^3\beta_-\zeta}{9\mathcal{S}_-\xi}+\frac{28\mathcal{S}_+^2\beta_+\zeta}{45\xi}$$
$$-\frac{20\mathcal{S}_+^3\beta_-^3\zeta}{3\mathcal{S}_-\gamma^3\xi}-\frac{20\mathcal{S}_+^2\beta_-^2\beta_+\zeta}{\gamma^3\xi}-\frac{20\mathcal{S}_+^3\beta_-\beta_+^2\zeta}{\mathcal{S}_-\gamma^3\xi}-\frac{20\mathcal{S}_+^2\beta_+^3\zeta}{3\gamma^3\xi}+\frac{11\mathcal{S}_+^2\beta_-^2\zeta}{6\gamma^2\xi}-\frac{32\mathcal{S}_+^3\beta_-\beta_+\zeta}{3\mathcal{S}_-\gamma^2\xi}$$
$$+\frac{11\mathcal{S}_+^2\beta_+^2\zeta}{6\gamma^2\xi}+\frac{485\mathcal{S}_+^3\beta_-\zeta}{84\mathcal{S}_-\gamma\xi}+\frac{62\mathcal{S}_+^2\beta_-^2\zeta}{9\gamma\xi}+\frac{1611\mathcal{S}_+^2\beta_+\zeta}{140\gamma\xi}+\frac{64\mathcal{S}_+^3\beta_-\beta_+\zeta}{9\mathcal{S}_-\gamma\xi}+\frac{62\mathcal{S}_+^2\beta_+^2\zeta}{9\gamma\xi}$$
$$-\frac{12091\mathcal{S}_+^2\gamma\zeta}{2520\xi}-\frac{16\mathcal{S}_+^2\beta_+\gamma\zeta}{9\xi}-\frac{8\mathcal{S}_+^2\gamma^2\zeta}{9\xi}-\frac{10513\eta}{144\xi}+\frac{35\mathcal{S}_+\beta_-\eta}{3\mathcal{S}_-\xi}-\frac{128\beta_-^2\eta}{3\xi}+\frac{11\beta_+\eta}{3\xi}$$
$$-\frac{128\mathcal{S}_+\beta_-\beta_+\eta}{3\mathcal{S}_-\xi}+\frac{70\mathcal{S}_+\beta_-\eta}{3\mathcal{S}_-\gamma\xi}-\frac{256\beta_-^2\eta}{3\gamma\xi}+\frac{70\beta_+\eta}{3\gamma\xi}-\frac{256\mathcal{S}_+\beta_-\beta_+\eta}{3\mathcal{S}_-\gamma\xi}-\frac{22697\gamma\eta}{672\xi}$$
$$-\frac{4\beta_+\gamma\eta}{\xi}-\frac{47\gamma^2\eta}{6\xi}-\frac{12793\mathcal{S}_+^2\zeta\eta}{2016\xi}-\frac{4\mathcal{S}_+^2\beta_+\zeta\eta}{3\xi}+\frac{160\mathcal{S}_+^2\beta_-^2\beta_+\zeta\eta}{3\gamma^3\xi}+\frac{80\mathcal{S}_+^3\beta_-\beta_+^2\zeta\eta}{\mathcal{S}_-\gamma^3\xi}$$
$$+\frac{80\mathcal{S}_+^2\beta_+^3\zeta\eta}{3\gamma^3\xi}+\frac{143\mathcal{S}_+^2\beta_-^2\zeta\eta}{6\gamma^2\xi}+\frac{64\mathcal{S}_+^3\beta_-\beta_+\zeta\eta}{3\mathcal{S}_-\gamma^2\xi}-\frac{157\mathcal{S}_+^2\beta_+^2\zeta\eta}{6\gamma^2\xi}+\frac{35\mathcal{S}_+^3\beta_-\zeta\eta}{9\mathcal{S}_-\gamma\xi}$$
$$-\frac{128\mathcal{S}_+^2\beta_-^2\zeta\eta}{9\gamma\xi}+\frac{53\mathcal{S}_+^2\beta_+\zeta\eta}{9\gamma\xi}-\frac{128\mathcal{S}_+^3\beta_-\beta_+\zeta\eta}{9\mathcal{S}_-\gamma\xi}-\frac{40\mathcal{S}_+^2\beta_+^2\zeta\eta}{3\gamma\xi}-\frac{47\mathcal{S}_+^2\gamma\zeta\eta}{18\xi}-\frac{575\eta^2}{36\xi}$$
$$-\frac{35\gamma\eta^2}{8\xi}-\frac{35\mathcal{S}_+^2\zeta\eta^2}{24\xi}-\frac{10\mathcal{S}_+^2\beta_+^2\zeta\eta^2}{\gamma^2\xi}+\frac{4\mathcal{S}_+\chi_-}{\mathcal{S}_-\gamma}-\frac{8\mathcal{S}_+\eta\chi_-}{\mathcal{S}_-\gamma}+\frac{8}{3}\chi_++\frac{4\chi_+}{\gamma}-\frac{16}{3}\eta\chi_+$$
$$-\frac{8\eta\chi_+}{\gamma}+\frac{11\mathcal{S}_+\psi}{2\mathcal{S}_-}+\frac{59}{15}\beta_-\psi+\frac{20\mathcal{S}_+\beta_+\psi}{3\mathcal{S}_-}-\frac{16}{9}\beta_-\beta_+\psi-\frac{8\mathcal{S}_+\beta_-^2\psi}{\mathcal{S}_-\gamma^2}-\frac{8\beta_-\beta_+\psi}{\gamma^2}$$
$$-\frac{8\mathcal{S}_+\beta_+^2\psi}{\mathcal{S}_-\gamma^2}+\frac{66\beta_-\psi}{5\gamma}-\frac{8\mathcal{S}_+\beta_-^2\psi}{3\mathcal{S}_-\gamma}+\frac{10\mathcal{S}_+\beta_+\psi}{\mathcal{S}_-\gamma}-\frac{16\beta_-\beta_+\psi}{3\gamma}-\frac{8\mathcal{S}_+\beta_+^2\psi}{3\mathcal{S}_-\gamma}+\frac{3\mathcal{S}_+\gamma\psi}{\mathcal{S}_-}$$
$$-\frac{44}{9}\beta_-\gamma\psi+\frac{5}{3}\delta_-\psi-\frac{25}{9}\beta_-\eta\psi+\frac{22\beta_-\eta\psi}{3\gamma}+\frac{22\mathcal{S}_+\beta_+\eta\psi}{3\mathcal{S}_-\gamma}-\frac{1247\beta_-\psi}{21\xi^2}-\frac{128\beta_-\beta_+\psi}{3\xi^2}$$
$$-\frac{565\beta_-\gamma\psi}{7\xi^2}-\frac{128\beta_-\beta_+\gamma\psi}{3\xi^2}-\frac{1013\beta_-\gamma^2\psi}{28\xi^2}-\frac{32\beta_-\beta_+\gamma^2\psi}{3\xi^2}-\frac{16\beta_-\gamma^3\psi}{3\xi^2}$$
$$-\frac{4379\mathcal{S}_+^2\beta_-\zeta\psi}{504\xi^2}+\frac{28\mathcal{S}_+^2\beta_-\beta_+\zeta\psi}{9\xi^2}+\frac{40\mathcal{S}_+^2\beta_-^3\zeta\psi}{3\gamma^2\xi^2}+\frac{6235\mathcal{S}_+^2\beta_-\beta_+\zeta\psi}{168\gamma^2\xi^2}+\frac{40\mathcal{S}_+^2\beta_-\beta_+^2\zeta\psi}{\gamma^2\xi^2}$$

$$+\frac{1247\mathcal{S}_+^2\beta_-\zeta\psi}{84\gamma\xi^2}+\frac{20\mathcal{S}_+^2\beta_-^3\zeta\psi}{3\gamma\xi^2}+\frac{5961\mathcal{S}_+^2\beta_-\beta_+\zeta\psi}{112\gamma\xi^2}+\frac{20\mathcal{S}_+^2\beta_-\beta_+^2\zeta\psi}{\gamma\xi^2}-\frac{91\mathcal{S}_+^2\beta_-\gamma\zeta\psi}{6\xi^2}$$
$$-\frac{64\mathcal{S}_+^2\beta_-\beta_+\gamma\zeta\psi}{9\xi^2}-\frac{32\mathcal{S}_+^2\beta_-\gamma^2\zeta\psi}{9\xi^2}-\frac{29\mathcal{S}_+^4\beta_-\zeta^2\psi}{28\xi^2}-\frac{32\mathcal{S}_+^4\beta_-\beta_+\zeta^2\psi}{27\xi^2}-\frac{25\mathcal{S}_+^4\beta_-^3\beta_+\zeta^2\psi}{3\gamma^4\xi^2}$$
$$-\frac{25\mathcal{S}_+^4\beta_-\beta_+^3\zeta^2\psi}{3\gamma^4\xi^2}-\frac{10\mathcal{S}_+^4\beta_-^3\zeta^2\psi}{3\gamma^3\xi^2}-\frac{10\mathcal{S}_+^4\beta_-\beta_+^2\zeta^2\psi}{\gamma^3\xi^2}+\frac{20\mathcal{S}_+^4\beta_-^3\zeta^2\psi}{9\gamma^2\xi^2}+\frac{1529\mathcal{S}_+^4\beta_-\beta_+\zeta^2\psi}{336\gamma^2\xi^2}$$
$$+\frac{20\mathcal{S}_+^4\beta_-\beta_+^2\zeta^2\psi}{3\gamma^2\xi^2}+\frac{485\mathcal{S}_+^4\beta_-\zeta^2\psi}{168\gamma\xi^2}+\frac{52\mathcal{S}_+^4\beta_-\beta_+\zeta^2\psi}{9\gamma\xi^2}-\frac{16\mathcal{S}_+^4\beta_-\gamma\zeta^2\psi}{27\xi^2}-\frac{140\beta_-\eta\psi}{3\xi^2}$$
$$-\frac{140\beta_-\gamma\eta\psi}{3\xi^2}-\frac{35\beta_-\gamma^2\eta\psi}{3\xi^2}-\frac{175\mathcal{S}_+^2\beta_-\zeta\eta\psi}{18\xi^2}+\frac{175\mathcal{S}_+^2\beta_-\beta_+\zeta\eta\psi}{6\gamma^2\xi^2}-\frac{160\mathcal{S}_+^2\beta_-\beta_+^2\zeta\eta\psi}{3\gamma^2\xi^2}$$
$$+\frac{35\mathcal{S}_+^2\beta_-\zeta\eta\psi}{3\gamma\xi^2}+\frac{175\mathcal{S}_+^2\beta_-\beta_+\zeta\eta\psi}{12\gamma\xi^2}-\frac{80\mathcal{S}_+^2\beta_-\beta_+^2\zeta\eta\psi}{3\gamma\xi^2}-\frac{70\mathcal{S}_+^2\beta_-\gamma\zeta\eta\psi}{9\xi^2}-\frac{35\mathcal{S}_+^4\beta_-\zeta^2\eta\psi}{27\xi^2}$$
$$+\frac{100\mathcal{S}_+^4\beta_-\beta_+^3\zeta^2\eta\psi}{3\gamma^4\xi^2}+\frac{40\mathcal{S}_+^4\beta_-\beta_+^2\zeta^2\eta\psi}{3\gamma^3\xi^2}+\frac{175\mathcal{S}_+^4\beta_-\beta_+\zeta^2\eta\psi}{36\gamma^2\xi^2}-\frac{80\mathcal{S}_+^4\beta_-\beta_+^2\zeta^2\eta\psi}{9\gamma^2\xi^2}$$
$$+\frac{35\mathcal{S}_+^4\beta_-\zeta^2\eta\psi}{18\gamma\xi^2}-\frac{361\beta_-\psi}{140\xi}-\frac{32\mathcal{S}_+\beta_-^2\psi}{3\mathcal{S}_-\xi}-\frac{2143\mathcal{S}_+\beta_+\psi}{84\mathcal{S}_-\xi}-\frac{64\beta_-\beta_+\psi}{3\xi}-\frac{32\mathcal{S}_+\beta_+^2\psi}{3\mathcal{S}_-\xi}$$
$$-\frac{1247\beta_-\psi}{42\gamma\xi}-\frac{64\mathcal{S}_+\beta_-^2\psi}{3\mathcal{S}_-\gamma\xi}-\frac{1247\mathcal{S}_+\beta_+\psi}{42\mathcal{S}_-\gamma\xi}-\frac{128\beta_-\beta_+\psi}{3\gamma\xi}-\frac{64\mathcal{S}_+\beta_+^2\psi}{3\mathcal{S}_-\gamma\xi}+\frac{84\beta_-\gamma\psi}{5\xi}$$
$$-\frac{16\mathcal{S}_+\beta_+\gamma\psi}{3\mathcal{S}_-\xi}+\frac{16\beta_-\gamma^2\psi}{3\xi}-\frac{28\mathcal{S}_+^2\beta_-\zeta\psi}{45\xi}-\frac{16\mathcal{S}_+^3\beta_+\zeta\psi}{9\mathcal{S}_-\xi}+\frac{20\mathcal{S}_+^2\beta_-^3\zeta\psi}{3\gamma^3\xi}+\frac{20\mathcal{S}_+^3\beta_-^2\beta_+\zeta\psi}{\mathcal{S}_-\gamma^3\xi}$$
$$+\frac{20\mathcal{S}_+^2\beta_-\beta_+^2\zeta\psi}{\gamma^3\xi}+\frac{20\mathcal{S}_+^3\beta_+^3\zeta\psi}{3\mathcal{S}_-\gamma^3\xi}+\frac{16\mathcal{S}_+^3\beta_-^2\zeta\psi}{3\mathcal{S}_-\gamma^2\xi}-\frac{11\mathcal{S}_+^2\beta_-\beta_+\zeta\psi}{3\gamma^2\xi}+\frac{16\mathcal{S}_+^3\beta_+^2\zeta\psi}{3\mathcal{S}_-\gamma^2\xi}$$
$$-\frac{1611\mathcal{S}_+^2\beta_-\zeta\psi}{140\gamma\xi}-\frac{32\mathcal{S}_+^3\beta_-^2\zeta\psi}{9\mathcal{S}_-\gamma\xi}-\frac{485\mathcal{S}_+^3\beta_+\zeta\psi}{84\mathcal{S}_-\gamma\xi}-\frac{124\mathcal{S}_+^2\beta_-\beta_+\zeta\psi}{9\gamma\xi}-\frac{32\mathcal{S}_+^3\beta_+^2\zeta\psi}{9\mathcal{S}_-\gamma\xi}$$
$$+\frac{16\mathcal{S}_+^2\beta_-\gamma\zeta\psi}{9\xi}-\frac{11\beta_-\eta\psi}{3\xi}-\frac{35\mathcal{S}_+\beta_+\eta\psi}{3\mathcal{S}_-\xi}-\frac{70\beta_-\eta\psi}{3\gamma\xi}-\frac{70\mathcal{S}_+\beta_+\eta\psi}{3\mathcal{S}_-\gamma\xi}+\frac{4\beta_-\gamma\eta\psi}{\xi}$$
$$+\frac{4\mathcal{S}_+^2\beta_-\zeta\eta\psi}{3\xi}-\frac{80\mathcal{S}_+^2\beta_-\beta_+^2\zeta\eta\psi}{3\gamma^3\xi}-\frac{80\mathcal{S}_+^3\beta_+^3\zeta\eta\psi}{3\mathcal{S}_-\gamma^3\xi}-\frac{5\mathcal{S}_+^2\beta_-\beta_+\zeta\eta\psi}{\gamma^2\xi}-\frac{53\mathcal{S}_+^2\beta_-\zeta\eta\psi}{9\gamma\xi}$$
$$-\frac{35\mathcal{S}_+^3\beta_+\zeta\eta\psi}{9\mathcal{S}_-\gamma\xi}-\frac{8}{3}\chi_-\psi-\frac{4\chi_-\psi}{\gamma}-\frac{4\mathcal{S}_+\chi_+\psi}{\mathcal{S}_-\gamma}. \tag{D.22}$$

Appendix E: Post-Dickean expansion of mass and scalar charge

The exact form of the mass m and the scalar charge α defined in Eq. (4.79) depend on how the mass is resummed, that is, on our choice of $m(\phi,\xi)$ and $F(\phi)$. For example, using the expressions in $m^{(\mathrm{RJ})}$ and $F^{(\phi)}$ given in Table 4.1, the mass and scalar charge are given at 1PD order by

$$m_A^{(\mathrm{RJ},\phi)} = m_A(\xi), \tag{E.1}$$

$$\begin{aligned}\alpha_A^{(\mathrm{RJ},\phi)} =& \mu_0\left(1-2\phi_0\frac{d\log m_A}{d\xi}\right)+\frac{B\mu_0}{2}\left(1-2\phi_0\frac{d\log m_A}{d\xi}\right)\left(1-2\phi_0\frac{d\log m_B}{d\xi}\right)\frac{Gm_B}{\phi_0 rc^2}\\ &-4{\mu_0}^3\left(\frac{d\log m_A}{d\xi}\right)\left(1-2\phi_0\frac{d\log m_B}{d\xi}\right)\frac{Gm_B}{rc^2}+\mathcal{O}\left(\frac{1}{c^4}\right),\end{aligned} \tag{E.2}$$

where $A\neq B$, while the choice of $m^{(\mathrm{RE})}$ and $F^{(\bar{\varphi})}$ gives

$$m_A^{(\mathrm{RE},\varphi)} = \sqrt{\phi_0}m_A^{(E)}(\xi)\left(1+\frac{Gm_B^{(E)}\mu_0\alpha_B}{\sqrt{\phi_0}rc^2}\right)+\mathcal{O}\left(\frac{1}{c^4}\right), \tag{E.3}$$

$$\alpha_A^{(\mathrm{RE},\varphi)} = -\frac{d\log m_A^{(E)}(\xi)}{d\xi}. \tag{E.4}$$

Note that the expressions in Eqs. (E.2) and (E.3) receive higher-order corrections, while Eqs. (E.1) and (E.4) are exact. In general, whenever the function $m(\phi,\xi)$ can be factored into

$$m(\phi,\xi) = m_\phi(\phi)m_\xi(\xi), \tag{E.5}$$

the quantities

$$\tilde{m}(\xi) \equiv m_\xi(\xi), \tag{E.6}$$

$$q \equiv -\frac{d\log m_\xi}{d\xi} = \left(\frac{d\log m_\phi}{d\phi} - \frac{D\log m(\phi,\xi)}{D\phi}\right) \Big/ \frac{dF}{d\phi}, \tag{E.7}$$

are exact at all orders in the PD expansion. These quantities represent the resummed piece of the mass and scalar charge; for the resummation schemes defined in Table 4.1, these quantities are listed in Table E.1. When using a particular resummation scheme, it is most convenient to work with these variables instead of m and α so as to avoid the additional bookkeeping required to track the PD corrections to the mass and scalar charge.

Table E.1: Resummed piece of the mass m and scalar charge α for the resummation schemes given in Table 4.1. We denote the differential operator $\frac{D}{D\phi}$ with the abbreviation D.

Resummation Scheme		$\tilde{m}(\xi)$	$q(\xi)$
$m^{(-)}$	$F^{(-)}$		
RJ	ϕ	m	$-D\log m$
RJ	$\tilde{\varphi}$	m	$-2\phi\left(\frac{B\log\phi}{2}\right)^{1/2} D\log m$
RE	ϕ	$m^{(E)}$	$\frac{1}{2\phi} - D\log m$
RE	$\tilde{\varphi}$	$m^{(E)}$	$\left(\frac{B\log\phi}{2}\right)^{1/2}(1 - 2\phi D\,\log m)$

Appendix F: Two-body potentials at post-Dickean order

The sources defined in Eqs. (4.53)–(4.56) computed at 1PD order are

$$\sigma = m_1 \left(1 + \frac{3v_1^2}{2c^2} - \frac{Gm_2(1-5\mu_0\alpha_2)}{\phi_0 r c^2}\right)\delta^{(3)}(x-x_1) + \mathcal{O}\left(\frac{1}{c^4}\right) + (1 \rightleftharpoons 2)\,, \tag{F.1}$$

$$\sigma_s = \frac{m_1\alpha_1}{\mu_0}\left(1 - \frac{v_1^2}{2c^2} - \frac{Gm_2(6\mu_0 + B\alpha_2 - 6\mu_0^2\alpha_2)}{2\mu_0\phi_0 r c^2}\right)\delta^{(3)}(x-x_1) + \mathcal{O}\left(\frac{1}{c^4}\right) + (1 \rightleftharpoons 2)\,, \tag{F.2}$$

$$\sigma^i = \frac{m_1 v_1^i}{c}\delta^{(3)}(x-x_1) + \mathcal{O}\left(\frac{1}{c^3}\right) + (1 \rightleftharpoons 2)\,, \tag{F.3}$$

$$\sigma^{ii} = \frac{m_1 v_1^2}{c^2}\delta^{(3)}(x-x_1) + \mathcal{O}\left(\frac{1}{c^4}\right) + (1 \rightleftharpoons 2)\,, \tag{F.4}$$

where $r = |\mathbf{x}_1 - \mathbf{x}_2|$ and we have suppressed the expansions in m_i and α_i using the notation of Eq. (4.79). Hence, the two body potentials needed to compute the equations of motion and scalar mass in Secs. 4.5 and 4.7 are given by

$$U \equiv \int \frac{\sigma(t,\mathbf{x}')}{|\mathbf{x}-\mathbf{x}'|}d^3x' = \frac{m_1}{r_1}\left(1 + \frac{3v_1^2}{2c^2} - \frac{Gm_2(1-5\mu_0\alpha_2)}{\phi_0 r c^2}\right) + \mathcal{O}\left(\frac{1}{c^4}\right) + (1 \rightleftharpoons 2)\,, \tag{F.5}$$

$$U_s \equiv \int \frac{\sigma_s(t,\mathbf{x}')}{|\mathbf{x}-\mathbf{x}'|}d^3x' = \frac{m_1\alpha_1}{\mu_0 r_1}\left(1 - \frac{v_1^2}{2c^2} - \frac{Gm_2(6\mu_0 + B\alpha_2 - 6\mu_0^2\alpha_2)}{2\mu_0\phi_0 r c^2}\right) + \mathcal{O}\left(\frac{1}{c^4}\right) + (1 \rightleftharpoons 2)\,, \tag{F.6}$$

$$
\begin{aligned}
M_s &\equiv \int \sigma_s(t,\mathbf{x}')d^3x' = {\mu_0}^{-1} m_1\alpha_1 + \mathcal{O}\left(\frac{1}{c^2}\right) + (1 \rightleftharpoons 2)\,, \\
\dot{M}_s &= \mathcal{O}\left(\frac{1}{c^3}\right),
\end{aligned}
\tag{F.7}
$$

$$
V^i \equiv \int \frac{\sigma^i(t,\mathbf{x}')}{|\mathbf{x}-\mathbf{x}'|}d^3x' = \frac{m_1}{r_1}\frac{v_1^i}{c} + \mathcal{O}\left(\frac{1}{c^3}\right) + (1 \rightleftharpoons 2)\,, \tag{F.8}
$$

$$
V_s^i \equiv \int \frac{\sigma_s(t,\mathbf{x}')v'^i}{|\mathbf{x}-\mathbf{x}'|}d^3x' = \frac{m_1\alpha_1}{\mu_0 r_1}\frac{v_1^i}{c} + \mathcal{O}\left(\frac{1}{c^3}\right) + (1 \rightleftharpoons 2)\,, \tag{F.9}
$$

$$
\Phi_1 \equiv \int \frac{\sigma^{ii}(t,\mathbf{x}')}{|\mathbf{x}-\mathbf{x}'|}d^3x' = \frac{m_1}{r_1}\frac{v_1^2}{c^2} + \mathcal{O}\left(\frac{1}{c^3}\right) + (1 \rightleftharpoons 2)\,, \tag{F.10}
$$

$$
\Phi_1^{ij} \equiv \int \frac{\sigma^{ij}(t,\mathbf{x}')}{|\mathbf{x}-\mathbf{x}'|}d^3x' = \frac{m_1}{r_1}\frac{v_1^i v_1^j}{c^2} + \mathcal{O}\left(\frac{1}{c^3}\right) + (1 \rightleftharpoons 2)\,, \tag{F.11}
$$

$$
\Phi_2^s \equiv \int \frac{\sigma_s(t,\mathbf{x}')U(t,\mathbf{x}')}{|\mathbf{x}-\mathbf{x}'|}d^3x' = \frac{m_1 m_2\alpha_1}{\mu_0 r_1 r} + \mathcal{O}\left(\frac{1}{c^2}\right) + (1 \rightleftharpoons 2)\,, \tag{F.12}
$$

$$
\Phi_{2s} \equiv \int \frac{\sigma(t,\mathbf{x}')U_s(t,\mathbf{x}')}{|\mathbf{x}-\mathbf{x}'|}d^3x' = \frac{m_1 m_2\alpha_2}{\mu_0 r_1 r} + \mathcal{O}\left(\frac{1}{c^2}\right) + (1 \rightleftharpoons 2)\,, \tag{F.13}
$$

$$
\Phi_{2s}^s \equiv \int \frac{\sigma_s(t,\mathbf{x}')U_s(t,\mathbf{x}')}{|\mathbf{x}-\mathbf{x}'|}d^3x' = \frac{m_1 m_2\alpha_1\alpha_2}{{\mu_0}^2 r_1 r} + \mathcal{O}\left(\frac{1}{c^2}\right) + (1 \rightleftharpoons 2)\,, \tag{F.14}
$$

$$
\begin{aligned}
X &\equiv \int \sigma(t,\mathbf{x}')|\mathbf{x}-\mathbf{x}'|d^3x' = m_1 r_1 + \mathcal{O}\left(\frac{1}{c^2}\right) + (1 \rightleftharpoons 2)\,, \\
\ddot{X} &= \frac{d^2 m_1}{dt^2}r_1 + 2\frac{dm_1}{dt}\frac{dr_1}{dt} + m_1\frac{d^2 r_1}{dt^2} + \mathcal{O}\left(\frac{1}{c^2}\right) + (1 \rightleftharpoons 2)\,, \\
&= m_1\left(\mathbf{a}_1\cdot\mathbf{n}_1 + \frac{v_1^2}{r_1} - \frac{(\mathbf{v}_1\cdot\mathbf{n}_1)^2}{r_1}\right) + \mathcal{O}\left(\frac{1}{c^2}\right) + (1 \rightleftharpoons 2)\,,
\end{aligned}
\tag{F.15}
$$

$$
\begin{aligned}
X_s &\equiv \int \sigma_s(t,\mathbf{x}')|\mathbf{x}-\mathbf{x}'|d^3x' = {\mu_0}^{-1} m_1\alpha_1 r_1 + \mathcal{O}\left(\frac{1}{c^2}\right) + (1 \rightleftharpoons 2)\,. \\
\ddot{X}_s &= {\mu_0}^{-1}\left[\frac{d^2(m_1\alpha_1)}{dt^2}r_1 + 2\frac{d(m_1\alpha_1)}{dt}\frac{dr_1}{dt} + m_1\alpha_1\frac{d^2 r_1}{dt^2}\right] + (1 \rightleftharpoons 2)\,, \\
&= \frac{m_1\alpha_1}{\mu_0}\left(\mathbf{a}_1\cdot\mathbf{n}_1 + \frac{v_1^2}{r_1} - \frac{(\mathbf{v}_1\cdot\mathbf{n}_1)^2}{r_1}\right) + \mathcal{O}\left(\frac{1}{c^2}\right) + (1 \rightleftharpoons 2)\,,
\end{aligned}
\tag{F.16}
$$

where the time derivatives of the masses and scalar charges are pushed to higher PD order because

$$
\frac{dm_A}{dt} = \frac{Dm_A}{D\phi}v_A^\mu\partial_\mu\phi(x_A) \sim \mathcal{O}\left(\frac{1}{c^3}\right), \tag{F.17}
$$

where $v_A^\mu \equiv u_A^\mu/u_A^0$.

Appendix G: A closer look at the dynamical scalarization model of *Palenzuela et. al.*

Another analytic model of dynamical scalarization was proposed in Ref. [173]. This model augments the PN equations of motion with a feedback mechanism that simulates the non-perturbative growth of the scalar field around each body (see Sec. 4.8.2 for more detail). This prescription is uniquely defined when working at leading order but becomes ambiguous when extended to higher PN orders. The construction given in Ref. [173] uses the 2.5PN equations of motion (given in Ref. [497]) and a Newtonian order feedback mechanism [Eqs. (4.142) and (4.143)]. The authors also set to zero all derivatives of the scalar charge [the first of which is given in Eq. (4.93)].

While this particular set of choices leads to predictions consistent with numerical-relativity, we would like to explore other realizations of this model for two reasons. First, we want to understand the impact of these algorithmic decisions; if a particular choice greatly impacts the model's performance, understanding its physical significance is important. Second, we would like to track the changes to the model at each order so as to check the best way to improve the results of Ref. [173] with future PN calculations. We address these two concerns by investigating the effects

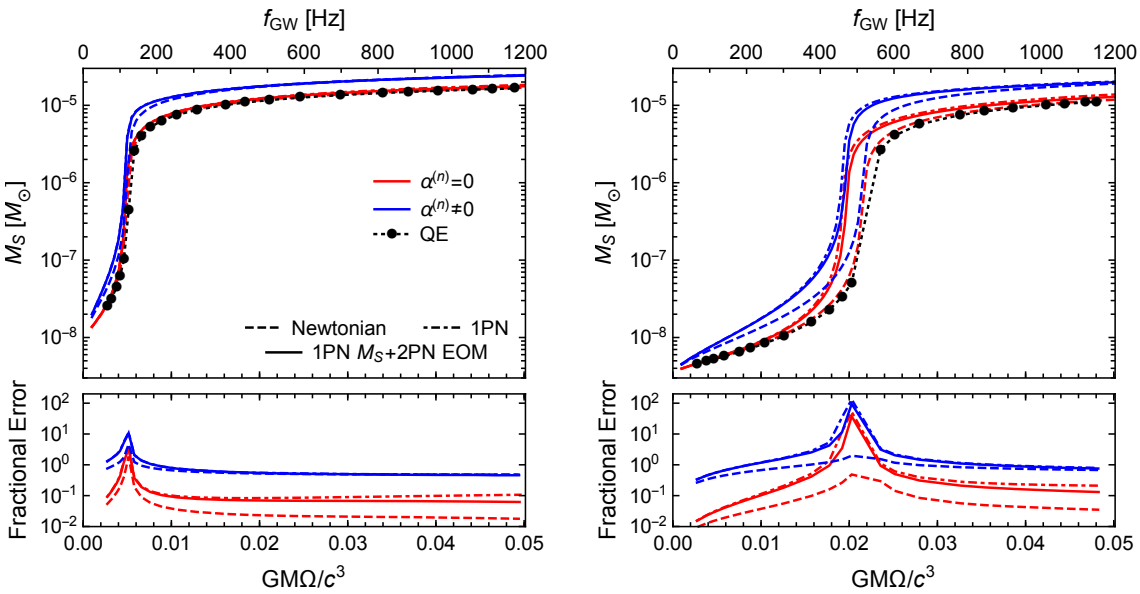

Figure G.1: Scalar mass predicted by the model of Ref. [173] for a $(1.35 + 1.35)M_\odot$ neutron-star binary system on a circular orbit as a function of the orbital frequency and gravitational wave frequency. The scalar mass at Newtonian and 1PN order computed without (with) the derivatives of scalar charge is plotted in red (blue) using the Newtonian, 1PN, and 2PN equations of motion (dashed, dot-dashed, and solid lines, respectively) and the Newtonian order feedback mechanism given in Eq. (4.142). We also plot the quasi-equilibrium configurations (QE) reported in Ref. [174] (dotted). The bottom panels depict the magnitude of the fractional error between the PD and quasi-equilibrium results. We use the APR4 equation of state with (left) $B = 9$, $\tilde{\varphi}_0 = 3.33 \times 10^{-11}$ and (right) $B = 8.4$, $\tilde{\varphi}_0 = 3.45 \times 10^{-11}$.

of including derivatives of the scalar charge and using a higher-order feedback mechanism. The authors of Ref. [173] briefly mention these two modifications and argue that they do not significantly impact the model; we expand on this discussion here, offering a precise, quantitative description of their effects.

Including derivatives of the scalar charge: The derivatives of the scalar charge enter this model through the equations of motion [see Eqs. (4.89) and (4.90)] and the feedback mechanism [see Eqs. (G.2) and (G.3)] beginning at 1PN order. The

decision to set these derivatives to zero was made in Ref. [173] to ensure that $\bar{m}(\phi)$ and $\bar{\alpha}(\phi)$ were evaluated at each star rather than expanded about the background value ϕ_0. However, this procedure is problematic, as simply setting the derivatives of $\bar{\alpha}$ to zero does not properly resum these expansions. For example, $\bar{\alpha}$ itself appears in every term of the Einstein-frame mass [analogous to Eq. (4.15)]

$$\bar{m}^{(E)}(\tilde{\varphi}) = m^{(E)}(\tilde{\varphi}_0)\left[1 + \bar{\alpha}\Delta - \frac{1}{2}(\bar{\alpha}^2 - \bar{\alpha}')\Delta^2 + \cdots\right], \tag{G.1}$$

where $\Delta \equiv (\tilde{\varphi} - \tilde{\varphi}_0)$. Removing the derivatives of $\bar{\alpha}$ eliminates most of the terms in the expansions of $\bar{m}(\phi)$ and $\bar{\alpha}(\phi)$ but leaves certain higher-order terms proportional to powers of the scalar charge. A fully consistent treatment should absorb these extraneous terms into the definitions of $\bar{m}(\phi)$ and $\bar{\alpha}(\phi)$; instead, this model's treatment of $\bar{m}$ and $\bar{\alpha}$ as unexpanded quantities ensures that the surviving terms in the expansion are effectively double counted.

Even without a mathematically rigorous motivation, the choice to drop the derivatives of the charge still yields predictions in qualitative agreement with numerical relativity. However, there are many other equally valid ways to alter the coefficients in expansions like that of Eq. (G.1) — for example, the coefficients containing $\bar{\alpha}'$ could be halved rather than set to zero. To provide some bound on the effect of these choices, in Fig. G.1 we compare the total scalar mass predicted by the model of Ref. [173] when all derivatives of the scalar charge are dropped (red) and when all are kept (blue). We restrict to circular orbits using the Newtonian, 1PN, and 2PN equations of motion (dashed, dot-dashed, and solid lines, respectively) — the exact prescription used in Ref. [173] is the solid, red curve.

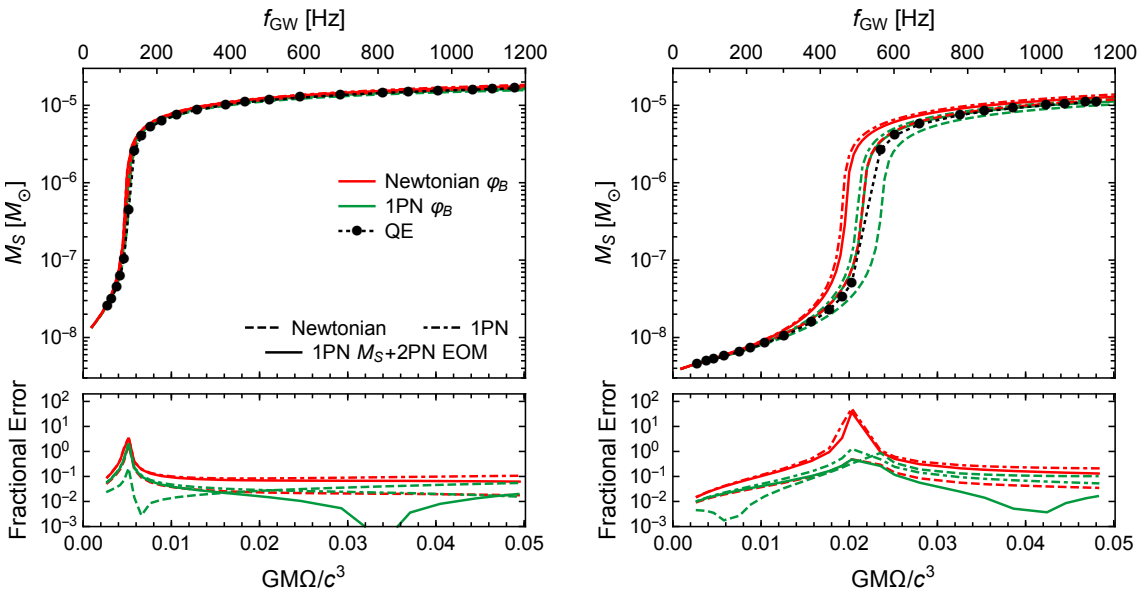

Figure G.2: Same as Fig. G.1 but also including the predictions of the model of Ref. [173] computed using the 1PN extension of the feedback model (green) given in Eq. (G.2). The derivatives of the scalar charge were dropped in computing all of the plotted curves.

The inclusion of these terms increases the scalar mass by approximately 20 – 50% both before and after scalarization. This result is consistent with our previous observation that higher-order terms left in the PN expansion should produce extraneous contributions when the mass and charge are resummed. In addition, we note that the model of Ref. [173] overestimates the scalar mass compared to the PD approximation at the same order. Combining these two observations, we argue that double counting can become a significant issue when using a simple feedback mechanism like that of Ref. [173], and that while simply dropping particular terms from the PN expansion can help remedy these issues, it is not the ideal solution. Instead, the corresponding resummation should be accounted for in a more systematic way, as is done with the PD approach.

Extending the feedback mechanism to 1PN order: The feedback mechanism used in Ref. [173] contains only the leading order contributions to the scalar field despite being paired with the 2.5PN equations of motion computed.[1] The impact of using approximants of such different order is unclear, but the mismatch may lead to certain unintuitive predictions. We consider instead using the natural 1PN extension of the feedback mechanism

$$\varphi_B^{(1)} = \tilde{\varphi}_0 + \frac{G\bar{m}_2\bar{\alpha}_2}{\phi_0 r c^2} + \frac{G\bar{m}_2}{\phi_0 r c^4}\left[-\frac{1}{2}\bar{\alpha}_2(\mathbf{v}_2\cdot\mathbf{n})^2 - \left(\frac{3}{2}\bar{\alpha}_2 + \frac{3}{2}\bar{\alpha}_1\bar{\alpha}_2^2 - \bar{\alpha}_1\bar{\alpha}_2'\right)\frac{G\bar{m}_1}{\phi_0 r}\right], \tag{G.2}$$

$$\varphi_B^{(2)} = (1 \rightleftharpoons 2), \tag{G.3}$$

where $\bar{m}_i$, $\bar{\alpha}_i$, and $\bar{\alpha}_i'$ are evaluated at $\varphi_B^{(i)}$.

We compare the total scalar mass computed using the Newtonian (red) and 1PN feedback models (green) with equations of motion at Newtonian, 1PN, and 2PN order in Fig. G.2, making the additional choice to set all derivatives of the scalar charge to zero, as was done in Ref. [173]. The inclusion of higher-order effects in these two aspects of the model produces competing shifts in the predicted onset of DS: the choice of 1PN feedback system over the Newtonian system pushes this transition point to higher frequency, while the 1PN terms in the equations of motion push the transition to lower frequency. These two effects nearly cancel each other in

[1] The authors of Ref. [173] considered the effect of adding to this feedback mechanism the order $\mathcal{O}(1/r^2)$ terms from the field felt by a static test mass far from an isolated body. These terms were shown to have negligible impact on their model. Here, we consider the 1PN corrections to the scalar field felt by each body in a comparable-mass binary system, which comprise a more comprehensive set of $\mathcal{O}(1/r^2)$ corrections.

such a way that the predictions when working consistently at Newtonian order (i.e. Newtonian order feedback and equations of motion) are very close to those when working consistently at 1PN order. We observe that working consistently at one order generally improves the agreement with the quasi-equilibrium configuration calculations of Ref. [174]. The most accurate model depicted in Fig. G.2 uses the 1PN feedback model in conjunction with the 2PN equations of motion, but in line with the previous observation, we suspect that adding the 2PN corrections to Eqs. (G.2) and (G.3) will improve these predictions; we leave the calculation and implementation of these higher-order terms for future work.

To recap, some of the technical aspects in the construction of the model proposed in Ref. [173] are ambiguous; the prescription for these options is only precisely specified when working at Newtonian order. These choices arise because the model splices a non-linear feedback mechanism on to independently computed PN equations of motion. We find that the model is most accurate when one uses a feedback mechanism and equations of motion of the same order and when one drops some of the higher-order terms in the PN expansions (e.g. the derivatives of the charge) to minimize double counting.

The PD formalism avoids these issues by performing a resummation of the post-Newtonian expansion at the level of the action. By carrying through this resummation consistently, a non-linear feedback mechanism analogous to Eqs. (G.2) and (G.3) organically arises alongside the equations of motion. Thus, the PD model gives results at a consistent order while also avoiding double counting.

Appendix H: Effective action for compact objects away from critical point

A crucial assumption made in the construction of the effective action (6.7) is the near-criticality of the scalar mode q. The power counting used in the main text to formulate this relatively simple effective theory is not valid without this assumption. For example, if $c_{(2)} > 0$ (i.e., the object does not spontaneously scalarize), then away from the critical point one finds $q \sim \phi^{\rm IR}(y) \sim \mathcal{O}(R/r)$ and must include terms like $[\phi^{\rm IR}(y)]^2$ to the action to work consistently at the given order in R/r. For scalarized compact objects $c_{(2)} < 0$ far from the critical point, the scalar field $\phi^{\rm IR}(y)$ and mode q reach values too large for our polynomial expansion around zero to be valid. If one expands the fields around their true (nonzero) equilibrium values instead, the effective action no longer respects the spontaneously broken scalar-inversion symmetry of the underlying theory.

In this appendix, we relax this assumption that the scalar mode q is nearly critical. We construct an effective action valid in this broader context, and then show that the model (6.7) is recovered as one approaches the critical point. We still ignore derivative couplings involving $\partial_\mu \phi^{\rm IR}(y)$ since they belong to multipoles above the monopole ($\ell > 0$) and we are only interested in a monopolar mode q. The

most generic effective action in the scalar-inversion-symmetric (unbroken) phase then reads

$$S_{\rm CO}^{\rm unbroken} = \int d\tau \left[\frac{c_{\dot{q}^2}}{2} \dot{q}^2 - c_{(0,0)} - V - V^{\phi} - V^{q\phi} + c_A A_\mu^{\rm IR}(y) \dot{y}^\mu \right], \tag{H.1}$$

$$V = \frac{c_{(0,2)}}{2} q^2 + \frac{c_{(0,4)}}{4!} q^4 + \dots, \tag{H.2}$$

$$V^{\phi} = \frac{c_{(2,0)}}{2} [\phi^{\rm IR}(y)]^2 + \frac{c_{(4,0)}}{4!} [\phi^{\rm IR}(y)]^4 + \text{time derivatives} + \dots, \tag{H.3}$$

$$\begin{aligned} V^{q\phi} = &-\phi^{\rm IR}(y) q + \frac{c_{(1,3)}}{3!} \phi^{\rm IR}(y) q^3 + \frac{c_{(2,2)}}{4} [\phi^{\rm IR}(y)]^2 q^2 \\ &+ \frac{c_{(3,1)}}{3!} [\phi^{\rm IR}(y)]^3 q + \text{time derivatives} + \dots, \end{aligned} \tag{H.4}$$

where the subscripts in $c_{(i,j)}$ indicate the powers of $\phi^{\rm IR}$ and q, respectively; the coefficients $c_{(n)}$ in the main text correspond to $c_{(0,n)}$ in this notation. All terms must be even polynomials in $\phi^{\rm IR}$, q due to scalar-inversion symmetry and must contain an even number of time derivatives due to time-reversal symmetry. Higher time derivatives that would appear in V can always be removed by appropriate redefinition of q [498]; we assume that such field redefinition has been done. This allows for an interpretation of V as an ordinary potential for the mode q in the absence of an external driving field $\phi^{\rm IR}$.

To fix all coefficients in the action, one needs to match against the exact solution for an isolated body in a generic time-dependent external scalar field. In general, this is a complicated endeavor, and we do not attempt it here.[1] Instead, we explore what information can be gleaned from the sequences of equilibrium solutions

[1] Note that our assumption of time-reversal symmetry needs to be imposed on the exact solution as well, so, in the case of a BH, one must impose somewhat unphysical (reflecting) boundary conditions at the horizon.

considered in the main text. Using only this restricted class of solutions, we do not expect to find a unique match for all coefficients in the effective action above, but rather a series of relations relating them to the exact solutions.

Solutions for compact objects in equilibrium are manifestly time independent, and thus cannot inform the terms containing time derivatives in the effective action; we omit these terms from the action below for brevity. We perform the same procedure outlined in the main text to match the IR fields of the effective theory (H.1) to the IR projection of the UV solutions (6.11) and find $c_A = \mathcal{E}$, $\phi_0 = \phi^{\rm IR}(y)$, and

$$Q(\phi_0) = -\frac{\partial V^{q\phi}(q,\phi^{\rm IR})}{\partial \phi^{\rm IR}} - \frac{dV^{\phi}(\phi^{\rm IR})}{d\phi^{\rm IR}}, \tag{H.5}$$

$$\mathcal{M}(\phi_0) = c_{(0,0)} + V + V^{\phi} + V^{q\phi}. \tag{H.6}$$

Together with the equation of motion for q,

$$0 = \frac{dV(q)}{dq} + \frac{\partial V^{q\phi}(q,\phi^{\rm IR})}{\partial q}, \tag{H.7}$$

we see that

$$d\mathcal{M} = \left[\frac{dV(q)}{dq} + \frac{\partial V^{q\phi}(q,\phi^{\rm IR})}{\partial q}\right] dq + \left[\frac{\partial V^{q\phi}(q,\phi^{\rm IR})}{\partial \phi^{\rm IR}} + \frac{dV^{\phi}(\phi^{\rm IR})}{d\phi^{\rm IR}}\right] d\phi^{\rm IR} \tag{H.8}$$

$$= -Q\, d\phi_0, \tag{H.9}$$

in agreement with the first law of BH thermodynamics [333, 334]. We see that ϕ_0 and Q are conjugate variables, and therefore we can construct the "gravitational free energy" $\mathbb{M}(Q)$ via a Legendre transformation of $\mathcal{M}(\phi_0)$,

$$\mathbb{M}(Q) \equiv \mathcal{M}(\phi_0) + \phi_0 Q, \tag{H.10}$$

such that $\phi_0 = d\mathbb{M}/dQ$. As in the main text, from a sequence of exact compact-object solutions in the full theory, one obtains $\mathcal{M}(\phi_0)$ and $Q(\phi_0)$ and then can compute $\mathbb{M}(Q)$ numerically from Eq. (H.10).

To aid comparison, we also define

$$\mathbb{V}(Q) \equiv \mathbb{M}(Q) - c_{(0,0)}, \tag{H.11}$$

which represents the component of the "free energy" due to the scalar charge Q. It admits an expansion around $Q = 0$

$$\mathbb{V}(Q) = \frac{C_{(2)}}{2} Q^2 + \frac{C_{(4)}}{4!} Q^4 + \ldots, \tag{H.12}$$

whose coefficients can be extracted numerically. Unlike V, this quantity does not correspond to the potential of any dynamical variable, but instead simply represents the energetics of a sequence of equilibrium solutions. While these two quantities are not directly related in general, in the vicinity of the critical point it is possible to reconstruct the potential V from the energetics $\mathbb{V}$ (as we found in the main text). In the remainder of this appendix, we demonstrate this connection explicitly by expressing the $C_{(n)}$ in terms of the coefficients in the effective action $c_{(i,j)}$, and then take the limit that q becomes unstable $c_{(0,2)} \to 0$, i.e., approaches the critical point.

Working perturbatively in $\phi_0 = \phi^{\rm IR}$, we solve the equation of motion (H.7) for q, relate this solution to Q and $\mathcal{M}$ via Eqs. (H.5) and (H.6), and then insert these solutions into Eq. (H.11) and read off the coefficients $C_{(n)}$ from the expansion in

Eq. (H.12). We find that

$$C_{(2)} = \frac{c_{(0,2)}}{1 - c_{(0,2)}c_{(2,0)}}, \tag{H.13}$$

$$C_{(4)} = \frac{1}{(1 - c_{(0,2)}c_{(2,0)})^4}\left[c_{(0,4)} + 4c_{(0,2)}c_{(1,3)} + 6c_{(0,2)}^2 c_{(2,2)} + 4c_{(0,2)}^3 c_{(3,1)} + c_{(0,2)}^4 c_{(4,0)}\right].$$

We see that, in general, an instability in the mode q cannot be inferred directly from $\mathbb{V}(Q)$, i.e., $C_{(2)} < 0 \not\Rightarrow c_{(0,2)} < 0$ and $c_{(0,2)} < 0 \not\Rightarrow C_{(2)} < 0$. However, close to the critical point $c_{(0,2)} \approx 0$, we find

$$C_{(2)} = c_{(0,2)} + \mathcal{O}(c_{(0,2)}^2), \tag{H.14}$$

$$C_{(4)} = c_{(0,4)} + \mathcal{O}(c_{(0,2)}), \tag{H.15}$$

which confirms the link between the dynamical mode potential $V(q)$ and the energetics of equilibrium solutions $\mathbb{V}(Q)$, close to the critical point.

The relation between the mode q and the scalar charge Q along a sequence of equilibrium solutions reads

$$q = \frac{Q}{1 - c_{(0,2)}c_{(2,0)}} + \frac{Q^3}{3!(1 - c_{(0,2)}c_{(2,0)})^4}\Big[c_{(1,3)} + c_{(2,0)}c_{(0,4)} + 3c_{(0,2)}(c_{(2,2)} + c_{(2,0)}c_{(1,3)})$$
$$+ 3c_{(0,2)}^2(c_{(3,1)} + c_{(2,0)}c_{(2,2)}) + c_{(0,2)}^3(c_{(4,0)} + c_{(2,0)}c_{(3,1)})\Big] + \ldots \tag{H.16}$$

Note that Eq. (H.16) does not lead to $Q = q$ as in the main text when $c_{(0,2)} = 0$. But full agreement with the main text (ignoring higher orders in $c_{(0,2)}$ throughout) is achieved if we redefine

$$q \to q + \frac{q^3}{3!}\left[c_{(1,3)} + c_{(2,0)}c_{(0,4)}\right] + \mathcal{O}(c_{(0,2)}, Q^5). \tag{H.17}$$

Appendix I: Numerical calculation of the effective point-particle action $V(q)$

In this appendix, we detail the numerical calculation of equilibrium BH solutions in EMS theory used to construct $V(q)$ through the matching procedure discussed in the main text. We consider the class of theories in Eq. (6.1) and restrict our attention to static, spherically symmetric configurations. Starting with the ansatz for vector potential and metric

$$A = \lambda(r)\, dt, \tag{I.1}$$

$$ds^2 = -N(r)e^{-2\delta(r)}dt^2 + \frac{dr^2}{N(r)} + r^2(d\theta^2 + \sin^2\theta d\varphi^2), \tag{I.2}$$

where $N(r) \equiv 1 - 2m(r)/r$ and $m(r)$ is the Misner-Sharp mass (not to be confused with $m(q)$ introduced in the main text), the field equations reduce to

$$\lambda' = -\frac{e^{-\delta}}{f(\phi)}\frac{\mathcal{E}}{r^2}, \tag{I.3a}$$

$$m' = \frac{1}{2}r^2 N\phi'^2 + \frac{\mathcal{E}^2}{2f(\phi)r^2}, \tag{I.3b}$$

$$\delta' + r\phi'^2 = 0, \tag{I.3c}$$

$$(e^{-\delta}r^2 N\phi')' = -e^{-\delta}\frac{f'(\phi)\mathcal{E}^2}{2(f(\phi))^2 r^2}, \tag{I.3d}$$

where $' = d/dr$ and $\mathcal{E}$ is the electric charge of the BH. Here, the field equation for the electric potential λ was already integrated once, introducing the electric charge

$\mathcal{E}$ as an integration constant. We impose the following boundary conditions at the horizon

$$\begin{aligned} m(r_H) =& \frac{r_H}{2}, \quad \delta(r_H) = \delta_H, \quad \phi(r_H) = \phi_H, \\ \phi'(r_H) =& -\frac{f'(\phi_H)}{2f(\phi_H)r_H}\left(\frac{\mathcal{E}^2}{f(\phi_H)r_H^2 - \mathcal{E}^2}\right). \end{aligned} \tag{I.4}$$

Note that δ_H represents a simple rescaling of the time coordinate, and thus can be chosen arbitrarily; we ultimately rescale t such that $\delta(r = \infty) = 0$. For computational simplicity, we rescale all dimensional quantities by the horizon radius r_H, i.e., $\tilde{r} \equiv r/r_H$, $\tilde{m} \equiv m/r_H$, and $\tilde{\mathcal{E}} = \mathcal{E}/r_H$, and then compactify the domain over which they are solved using the variable

$$x \equiv \frac{r - r_H}{r + br_H} = \frac{\tilde{r} - 1}{\tilde{r} + b}, \tag{I.5}$$

where the constant b is chosen to adequately resolve the solution.

As discussed in the main text, we consider sequences of BH solutions with fixed electric charge $\mathcal{E}$ and entropy $\mathcal{S}$ (or horizon area), which is equivalent to fixed $\tilde{\mathcal{E}}$ and r_H. Fixing these two parameters, we generate a sequence of solutions by solving Eqs. (I.3) and (I.4) for several values of ϕ_H. We then extract the mass $\mathcal{M}$, asymptotic field ϕ_0, and scalar charge Q from the asymptotic behavior of the solution

$$m(r) \to \mathcal{M} + \mathcal{O}\left(\frac{1}{r}\right), \quad \phi(r) \to \phi_0 + \frac{Q}{r} + \mathcal{O}\left(\frac{1}{r^2}\right), \tag{I.6}$$

allowing us to implicitly construct the functions $\mathcal{M}(\phi_0)$ and $Q(\phi_0)$ used in the main text to compute the effective potential $V(q)$.

Appendix J: Ingredients for the Fisher matrix analysis

For a GW detector with the one-side PSD, $S_n(f)$, the SNR of a Fourier-domain waveform, $\tilde{h}(f)$, is

$$\rho = \left(\tilde{h}(f)\middle|\,\tilde{h}(f)\right)^{1/2}\,, \tag{J.1}$$

where the inner product is defined to be [393, 394],

$$\left(\tilde{h}_1(f)\middle|\,\tilde{h}_2(f)\right) \equiv 2\int_{f_{\rm min}}^{f_{\rm max}} \frac{\tilde{h}_1^*(f)\tilde{h}_2(f)+\tilde{h}_1(f)\tilde{h}_2^*(f)}{S_n(f)}{\rm d}f\,. \tag{J.2}$$

For all calculations in Sec. 7.4.1, we use the design zero-detuned high-power noise PSD, starting from 10 Hz for aLIGO [389], the target noise PSD, starting from 5 Hz for CE [367], and the ET-D noise PSD, starting from 1 Hz for ET [388]. Thus, in Eq. (J.2) we choose $f_{\rm min} = 10\,{\rm Hz}$, $5\,{\rm Hz}$, and $1\,{\rm Hz}$ for aLIGO, CE, and ET, respectively. Somewhat arbitrarily, we choose for $f_{\rm max}$ twice the innermost stable circle orbit (ISCO) frequency computed from the binary's binding energy at 2 PN order. It reads [499],

$$f_{\rm max} = \frac{c^3}{\pi GM}\left[\frac{3}{14\eta}\left(1-\sqrt{1-\frac{14}{9}\eta}\right)\right]^{3/2}\,. \tag{J.3}$$

Because the three detectors do not have good sensitivity at high frequency, say $\gtrsim$ kHz, the choice of $f_{\rm max}$ influences the result very marginally.

For the nonspinning BNS inspiraling waveform in the Fourier domain, we use a

restricted waveform with the leading-order term in amplitude, $\mathcal{A}$, and up to 3.5 PN terms in the phase, $\Psi(f)$ [240, 259, 266],

$$\tilde{h}(f) = \mathcal{A} f^{-7/6} e^{i\Psi(f)} \,, \tag{J.4}$$

$$\begin{aligned}\Psi(f) =& 2\pi f t_c - \Phi_c - \frac{\pi}{4} + \frac{3}{128\eta}\mathfrak{u}^{-5/3}\left\{1 - \frac{5}{168}(\Delta\alpha)^2\mathfrak{u}^{-2/3} + \left(\frac{3715}{756} + \frac{55}{9}\eta\right)\mathfrak{u}^{2/3}\right.\\ &-16\pi\mathfrak{u} + \left(\frac{15293365}{508032} + \frac{27145}{504}\eta + \frac{3085}{72}\eta^2\right)\mathfrak{u}^{4/3}\\ &+\pi\left(\frac{38645}{756} - \frac{65}{9}\eta\right)(1 + \ln\mathfrak{u})\,\mathfrak{u}^{5/3} + \left[\frac{11583231236531}{4694215680} - \frac{640}{3}\pi^2 - \frac{6848}{21}\gamma_{\rm E}\right.\\ &\left.-\frac{6848}{63}\ln(64\mathfrak{u}) + \left(-\frac{15737765635}{3048192} + \frac{2255}{12}\pi^2\right)\eta + \frac{76055}{1728}\eta^2 - \frac{127825}{1296}\eta^3\right]\mathfrak{u}^2\\ &\left.+\pi\left(\frac{77096675}{254016} + \frac{378515}{1512}\eta - \frac{74045}{756}\eta^2\right)\mathfrak{u}^{7/3}\right\} \,,\end{aligned} \tag{J.5}$$

where $\mathfrak{u} \equiv \pi G M f/c^3$, $\mathcal{A} \propto \mathcal{M}^{5/6}/D_L$ with the chirp mass $\mathcal{M} \equiv \eta^{3/5} M$ and the luminosity distance D_L, t_c and Φ_c are reference time and phase respectively, and $\gamma_{\rm E} = 0.577216\ldots$ is the Euler constant. Note that in Eq. (J.5) the gothic $\mathfrak{u}$ is equal to $\eta^{-3/5}u$ where $u \equiv \pi G\mathcal{M} f/c^3$, as defined in Ref. [240]. We include in Eq. (J.5) only the leading dipole term for the scalar contribution. Furthermore, since the spins of BNS systems are supposed to be small, we do not include them in the analysis (see Table 7.3 where we give a rough estimation of the spin terms in the GW phasing).

To calculate the Fisher matrix (7.17), we need to compute partial derivatives of the frequency-domain waveform (J.4). They read (notice that, when calculating

derivatives, $\mathfrak{u}$ depends on both η and $\mathcal{M}$),

$$\frac{\partial\tilde{h}(f)}{\partial\ln\mathcal{A}} =\tilde{h}(f)\,, \tag{J.6}$$

$$\begin{aligned}\frac{\partial\tilde{h}(f)}{\partial\ln\eta} =&\frac{i}{\eta}\mathfrak{u}^{-5/3}\left\{-\frac{1}{3584}\Delta\alpha^2\mathfrak{u}^{-2/3}+\left(-\frac{743}{16128}+\frac{11}{128}\eta\right)\mathfrak{u}^{2/3}+\frac{9}{40}\pi\mathfrak{u}\right.\\&+\left(-\frac{3058673}{5419008}+\frac{5429}{21504}\eta+\frac{617}{512}\eta^2\right)\mathfrak{u}^{4/3}\\&+\pi\left(-\frac{7729}{4032}-\frac{38645}{32256}\ln\mathfrak{u}+\frac{13}{128}\eta\right)\mathfrak{u}^{5/3}+\left[-\frac{11328104339891}{166905446400}+\frac{321}{35}\gamma_{\rm E}\right.\\&\left.+6\pi^2+\frac{107}{35}\ln\left(64\mathfrak{u}\right)+\left(\frac{3147553127}{130056192}-\frac{451}{512}\pi^2\right)\eta+\frac{15211}{18432}\eta^2-\frac{25565}{6144}\eta^3\right]\mathfrak{u}^2\\&\left.+\pi\left(-\frac{15419335}{1548288}-\frac{75703}{32256}\eta-\frac{14809}{10752}\eta^2\right)\mathfrak{u}^{7/3}\right\}\tilde{h}(f)\,,\end{aligned} \tag{J.7}$$

$$\begin{aligned}\frac{\partial\tilde{h}(f)}{\partial\ln\mathcal{M}} =&\frac{i}{\eta}\mathfrak{u}^{-5/3}\left\{-\frac{5}{128}+\frac{5}{3072}\Delta\alpha^2\mathfrak{u}^{-2/3}+\left(-\frac{3715}{32256}-\frac{55}{384}\eta\right)\mathfrak{u}^{2/3}+\frac{\pi}{4}\mathfrak{u}\right.\\&+\left(-\frac{15293365}{65028096}-\frac{27145}{64512}\eta-\frac{3085}{9216}\eta^2\right)\mathfrak{u}^{4/3}+\pi\left(\frac{38645}{32256}-\frac{65}{384}\eta\right)\mathfrak{u}^{5/3}\\&+\left[\frac{10052469856691}{600859607040}-\frac{5}{3}\pi^2-\frac{107}{42}\gamma_{\rm E}+\left(-\frac{15737765635}{390168576}+\frac{2255}{1536}\pi^2\right)\eta\right.\\&\left.-\frac{107}{126}\ln\left(64\mathfrak{u}\right)+\frac{76055}{221184}\eta^2-\frac{127825}{165888}\eta^3\right]\mathfrak{u}^2\\&\left.+\pi\left(\frac{77096675}{16257024}+\frac{378515}{96768}\eta-\frac{74045}{48384}\eta^2\right)\mathfrak{u}^{7/3}\right\}\tilde{h}(f)\,,\end{aligned} \tag{J.8}$$

$$\frac{\partial\tilde{h}(f)}{\partial t_c} =i2\pi f\tilde{h}(f)\,, \tag{J.9}$$

$$\frac{\partial\tilde{h}(f)}{\partial\Phi_c} =-i\tilde{h}(f)\,, \tag{J.10}$$

$$\frac{\partial\tilde{h}(f)}{\partial(\Delta\alpha)^2} =-i\frac{5}{7168\eta}\mathfrak{u}^{-7/3}\tilde{h}(f)\,. \tag{J.11}$$

Appendix K: Dynamical scalarization in ultra-relativistic binary neutron stars

In this appendix, we discuss the sharp feature observed in the averaged effective scalar coupling of a very massive BNS that undergoes dynamical scalarization (see the $1.9\,M_\odot$–$1.9\,M_\odot$ case in Fig. 7.10). We find that generically NSs of very high mass can scalarize more abruptly than their less massive counterparts.

From Fig. 7.5, we observe that very massive NSs exhibit very small effective scalar couplings α_A. In these stars, the effective scalar coupling is nonperturbatively suppressed below the non-relativistic (low-mass) limit $\alpha_A \approx \alpha_0$. The cores of these stars are ultra-relativistic, with a negative trace of the stress-energy tensor $T_* = \epsilon_* - 3p_* < 0$. The mass at which NSs become ultra-relativistic in this sense depends on the EOS and can be read off from Fig. 7.7 as the mass at which the best constraint on $|\alpha|$ drops to zero. Recall that spontaneous scalarization stems from a large, positive source on the righthand side of Eq. (7.3) that grows with φ. In ultra-relativistic stars, this source term becomes negative, causing the star to spontaneously "de-scalarize".

When placed in a binary system, ultra-relativistic NSs can dynamically scalarize, but the transition occurs very abruptly (*e.g.*, the $1.9\,M_\odot$–$1.9\,M_\odot$ system with

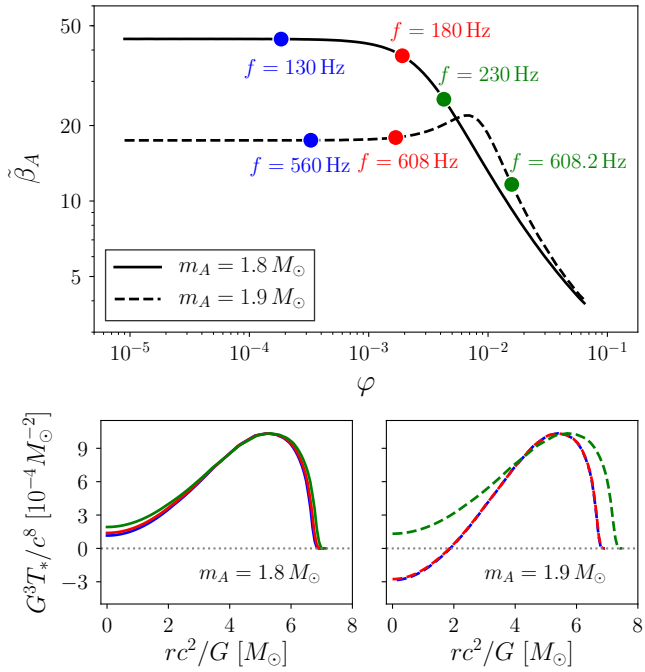

Figure K.1: (*Top*) Evolution of $\tilde{\beta}_A$ for NSs with (dashed) and without (solid) ultra-relativistic cores as a function of the background scalar field. The blue, red, and green annotations indicate the scalar field at each star at frequencies before, during, and after dynamical scalarization in an equal-mass binary system respectively. (*Bottom*) Profile of the trace of the stress-energy tensor within each NS at each of the annotated points in the top panel.

the EOS WFF1 shown in Fig. 7.10). As the system scalarizes, the massive NSs transition to a state in which T_* is everywhere positive. Figure K.1 depicts this transition in comparison to dynamical scalarization in less massive systems. The top panel shows $\tilde{\beta}_A$—the PD equivalent of the quantity defined in Eq. (7.22)—for $1.8\,M_\odot$ (solid) and $1.9\,M_\odot$ (dashed) stars with the EOS WFF1 plotted as a function of scalar field. The highlighted points indicate the field at each NS in an equal-mass binary before (blue), during (red), and after (green) dynamical scalarization. The bottom panels depict the profile of T_* within each star at each of these points.

The top panel of Fig. K.1 demonstrates why dynamical scalarization occurs abruptly for ultra-relativistic NSs. Recall that β_A (and consequently $\tilde{\beta}_A$) quantifies how easily a NS can scalarize, with larger values indicating that the star is more susceptible to dynamical scalarization. As expected, when immersed in a weak scalar field (*i.e.*, during the early inspiral), $\tilde{\beta}_A$ is significantly smaller for ultra-relativistic stars than less massive stars, indicating that the latter will dynamically scalarize at a lower frequency. However, unlike for less massive stars, $\tilde{\beta}_A$ increases slightly as the scalar field reaches larger values ($\varphi \sim 0.002$ in Fig. K.1) for ultra-relativistic NSs. This triggers a run-away process in a binary system as a small increase in the scalar field produced by one star causes the other star to scalarize more easily, which in turn allows the second star to produce a larger scalar field for the first. For the ultra-relativistic BNS depicted in the top panel of Fig. K.1, this transition is completed after an evolution of only 0.2 Hz.

Bibliography

[1] M. Khalil, N. Sennett, J. Steinhoff, J. Vines, and A. Buonanno, "Hairy binary black holes in Einstein-Maxwell-dilaton theory and their effective-one-body description," Phys. Rev. **D98**, 104010 (2018), arXiv:1809.03109 .

[2] N. Sennett, S. Marsat, and A. Buonanno, "Gravitational waveforms in scalar-tensor gravity at 2PN relative order," Phys. Rev. **D94**, 084003 (2016), arXiv:1607.01420 .

[3] N. Sennett and A. Buonanno, "Modeling dynamical scalarization with a resummed post-Newtonian expansion," Phys. Rev. **D93**, 124004 (2016), arXiv:1603.03300 .

[4] N. Sennett, L. Shao, and J. Steinhoff, "Effective action model of dynamically scalarizing binary neutron stars," Phys. Rev. **D96**, 084019 (2017), arXiv:1708.08285 .

[5] M. Khalil, N. Sennett, J. Steinhoff, and A. Buonanno, "Theory-agnostic framework for dynamical scalarization of compact binaries," Phys. Rev. D **100**, 124013 (2019), arXiv:1906.08161 [gr-qc] .

[6] L. Shao, N. Sennett, A. Buonanno, M. Kramer, and N. Wex, "Constraining nonperturbative strong-field effects in scalar-tensor gravity by combining pulsar timing and laser-interferometer gravitational-wave detectors," Phys. Rev. **X7**, 041025 (2017), arXiv:1704.07561 .

[7] N. Sennett, T. Hinderer, J. Steinhoff, A. Buonanno, and S. Ossokine, "Distinguishing Boson Stars from Black Holes and Neutron Stars from Tidal Interactions in Inspiraling Binary Systems," Phys. Rev. **D96**, 024002 (2017), arXiv:1704.08651 .

[8] N. Sennett, R. Brito, A. Buonanno, V. Gorbenko, and L. Senatore, "Gravitational-Wave Constraints on an Effective Field-Theory Extension of General Relativity," Phys. Rev. D **102**, 044056 (2020), arXiv:1912.09917 [gr-qc] .

[9] B. P. Abbott *et al.* (LIGO Scientific, Virgo), "Tests of General Relativity with GW170817," Phys. Rev. Lett. **123**, 011102 (2019), arXiv:1811.00364 .

[10] B. P. Abbott *et al.* (LIGO Scientific, Virgo), "Tests of General Relativity with the Binary Black Hole Signals from the LIGO-Virgo Catalog GWTC-1," Phys. Rev. **D100**, 104036 (2019), arXiv:1903.04467 .

[11] N. Sennett, A. Buonanno, L. Gergely, M. Isi, and B. Sathyaprakash, "Constraining Jordan-Fierz-Brans-Dicke gravity with GW170817," (2019, *in prep.*).

[12] A. Einstein, "On the General Theory of Relativity," Sitzungsber. Preuss. Akad. Wiss. Berlin (Math. Phys.) **1915**, 778–786 (1915), [Addendum: Sitzungsber. Preuss. Akad. Wiss. Berlin (Math. Phys.)1915,799(1915)].

[13] A. Einstein, "The Field Equations of Gravitation," Sitzungsber. Preuss. Akad. Wiss. Berlin (Math. Phys.) **1915**, 844–847 (1915).

[14] H. Minkowski, "Raum un Zeit," Phys. Z. **10**, 104–111 (1908).

[15] C. W. Misner, K. S. Thorne, and J. A. Wheeler, *Gravitation* (W. H. Freeman, San Francisco, 1973).

[16] K. Schwarzschild, "Über das Gravitationsfeld eines Massenpunktes nach der Einsteinschen Theorie," Sitzungsberichte der Königlich Preußischen Akademie der Wissenschaften (Berlin), 1916, Seite 189-196 (1916).

[17] K. S. Thorne, "Nonspherical Gravitational Collapse: A Short Review," in *Magic Without Magic: John Archibald Wheeler: A Collection of Essays in Honor of His Sixtieth Birthday*, edited by J. R. Klauder (W. H. Freeman, San Francisco, 1972).

[18] Y. B. Zel'dovich and I. D. Novikov, "The Hypothesis of Cores Retarded during Expansion and the Hot Cosmological Model," Sov. Astr. **10**, 602 (1967).

[19] S. Hawking, "Gravitationally collapsed objects of very low mass," Mon. Not. Roy. Astron. Soc. **152**, 75 (1971).

[20] M. Sasaki, T. Suyama, T. Tanaka, and S. Yokoyama, "Primordial black holes—perspectives in gravitational wave astronomy," Class. Quant. Grav. **35**, 063001 (2018), arXiv:1801.05235 .

[21] J. E. Chase, "Event horizons in static scalar-vacuum space-times," Commun. Math. Phys. **19**, 276–288 (1970).

[22] J. D. Bekenstein, "Transcendence of the law of baryon-number conservation in black hole physics," Phys. Rev. Lett. **28**, 452–455 (1972).

[23] S. W. Hawking, "Black holes in the Brans-Dicke theory of gravitation," Commun. Math. Phys. **25**, 167–171 (1972).

[24] M. S. Volkov and D. V. Galtsov, "NonAbelian Einstein Yang-Mills black holes," JETP Lett. **50**, 346–350 (1989), [Pisma Zh. Eksp. Teor. Fiz.50,312(1989)].

[25] R. Penrose, "Gravitational collapse and space-time singularities," Phys. Rev. Lett. **14**, 57–59 (1965).

[26] A. Einstein, "Approximative Integration of the Field Equations of Gravitation," Sitzungsber. Preuss. Akad. Wiss. Berlin (Math. Phys.) **1916**, 688–696 (1916).

[27] A. Einstein, "Über Gravitationswellen," Sitzungsber. Preuss. Akad. Wiss. Berlin (Math. Phys.) **1918**, 154–167 (1918).

[28] M. Maggiore, *Gravitational Waves. Vol. I: Theory and Experiments*, Oxford Master Series in Physics (Oxford University Press, 2007).

[29] E. Poisson, A. Pound, and I. Vega, "The Motion of point particles in curved spacetime," Living Rev. Rel. **14**, 7 (2011), arXiv:1102.0529 .

[30] L. Blanchet, "Gravitational Radiation from Post-Newtonian Sources and Inspiralling Compact Binaries," Living Rev. Rel. **17**, 2 (2014), arXiv:1310.1528 .

[31] T. Damour, "The problem of motion in Newtonian and Einsteinian gravity." in *Three hundred years of gravitation* (1987) pp. 128–198.

[32] P. C. Peters and J. Mathews, "Gravitational radiation from point masses in a Keplerian orbit," Phys. Rev. **131**, 435–439 (1963).

[33] S. F. Portegies Zwart and S. McMillan, "Black hole mergers in the universe," Astrophys. J. **528**, L17 (2000), arXiv:astro-ph/9910061 .

[34] M. L. Lidov, "The evolution of orbits of artificial satellites of planets under the action of gravitational perturbations of external bodies," Planet. Space Sci. **9**, 719–759 (1962).

[35] Y. Kozai, "Secular perturbations of asteroids with high inclination and eccentricity," AJ **67**, 591–598 (1962).

[36] B. P. Abbott *et al.* (LIGO Scientific, Virgo), "Search for Eccentric Binary Black Hole Mergers with Advanced LIGO and Advanced Virgo during their First and Second Observing Runs," Astrophys. J. **883**, 149 (2019), arXiv:1907.09384 [astro-ph.HE] .

[37] L. D. Landau and E. M. Lifshitz, *The Classical Theory of Fields*, 4th ed. (Butterworth-Heinemann, 1980).

[38] A. Buonanno and T. Damour, "Effective one-body approach to general relativistic two-body dynamics," Phys. Rev. **D59**, 084006 (1999), arXiv:gr-qc/9811091 .

[39] A. Buonanno and T. Damour, "Transition from inspiral to plunge in binary black hole coalescences," Phys. Rev. **D62**, 064015 (2000), arXiv:gr-qc/0001013 .

[40] L. Barack, T. Damour, and N. Sago, "Precession effect of the gravitational self-force in a Schwarzschild spacetime and the effective one-body formalism," Phys. Rev. **D82**, 084036 (2010), arXiv:1008.0935 .

[41] D. Bini and T. Damour, "Gravitational self-force corrections to two-body tidal interactions and the effective one-body formalism," Phys. Rev. **D90**, 124037 (2014), arXiv:1409.6933 .

[42] S. Akcay and M. van de Meent, "Numerical computation of the effective-one-body potential q using self-force results," Phys. Rev. **D93**, 064063 (2016), arXiv:1512.03392 .

[43] D. Bini, T. Damour, and A. Geralico, "Spin-orbit precession along eccentric orbits: improving the knowledge of self-force corrections and of their effective-one-body counterparts," Phys. Rev. **D97**, 104046 (2018), arXiv:1801.03704 .

[44] A. Taracchini *et al.*, "Effective-one-body model for black-hole binaries with generic mass ratios and spins," Phys. Rev. **D89**, 061502 (2014), arXiv:1311.2544 .

[45] A. Bohé *et al.*, "Improved effective-one-body model of spinning, nonprecessing binary black holes for the era of gravitational-wave astrophysics with advanced detectors," Phys. Rev. **D95**, 044028 (2017), arXiv:1611.03703 .

[46] R. L. Arnowitt, S. Deser, and C. W. Misner, "Dynamical Structure and Definition of Energy in General Relativity," Phys. Rev. **116**, 1322–1330 (1959).

[47] R. Arnowitt, S. Deser, and C. Misner, "The dynamics of general relativity," in *Gravitation: An Introduction to Current Research*, edited by L. Witten (John Wiley & Sons, Inc., New York, 1962).

[48] F. Pretorius, "Evolution of binary black hole spacetimes," Phys. Rev. Lett. **95**, 121101 (2005), arXiv:gr-qc/0507014 .

[49] M. Campanelli, C. O. Lousto, P. Marronetti, and Y. Zlochower, "Accurate evolutions of orbiting black-hole binaries without excision," Phys. Rev. Lett. **96**, 111101 (2006), arXiv:gr-qc/0511048 .

[50] J. G. Baker, J. Centrella, D.-I. Choi, M. Koppitz, and J. van Meter, "Gravitational wave extraction from an inspiraling configuration of merging black holes," Phys. Rev. Lett. **96**, 111102 (2006), arXiv:gr-qc/0511103 .

[51] J. A. Font, "Numerical Hydrodynamics and Magnetohydrodynamics in General Relativity," Living Rev. Rel. **11**, 7 (2008).

[52] L. Lehner and F. Pretorius, "Numerical Relativity and Astrophysics," Ann. Rev. Astron. Astrophys. **52**, 661–694 (2014), arXiv:1405.4840 .

[53] M. Shibata, "Constraining nuclear equations of state using gravitational waves from hypermassive neutron stars," Phys. Rev. Lett. **94**, 201101 (2005), arXiv:gr-qc/0504082 .

[54] M. Shibata, K. Taniguchi, and K. Uryu, "Merger of binary neutron stars with realistic equations of state in full general relativity," Phys. Rev. **D71**, 084021 (2005), arXiv:gr-qc/0503119 .

[55] C. V. Vishveshwara, "Scattering of Gravitational Radiation by a Schwarzschild Black-hole," Nature **227**, 936–938 (1970).

[56] S. Chandrasekhar and S. L. Detweiler, "The quasi-normal modes of the Schwarzschild black hole," Proc. Roy. Soc. Lond. **A344**, 441–452 (1975).

[57] J. Weber, "Detection and Generation of Gravitational Waves," Phys. Rev. **117**, 306–313 (1960).

[58] J. Weber, *General Relativity and Gravitational Waves* (Interscience Publishers, New York, 1961).

[59] P. Astone *et al.* (International Gravitational Event), "Methods and results of the IGEC search for burst gravitational waves in the years 1997 - 2000," Phys. Rev. **D68**, 022001 (2003), arXiv:astro-ph/0302482 .

[60] L. Stodolsky, "Matter and light wave interferometry in gravitational fields," Gen. Relativ. Gravit. **11**, 391–405 (1979).

[61] S. Dimopoulos, P. W. Graham, J. M. Hogan, M. A. Kasevich, and S. Rajendran, "An Atomic Gravitational Wave Interferometric Sensor (AGIS)," Phys. Rev. **D78**, 122002 (2008), arXiv:0806.2125 .

[62] P. W. Graham, J. M. Hogan, M. A. Kasevich, and S. Rajendran, "A New Method for Gravitational Wave Detection with Atomic Sensors," Phys. Rev. Lett. **110**, 171102 (2013), arXiv:1206.0818 .

[63] J. Aasi *et al.* (LIGO Scientific), "Advanced LIGO," Class. Quant. Grav. **32**, 074001 (2015), arXiv:1411.4547 .

[64] F. Acernese *et al.* (Virgo), "Advanced Virgo: a second-generation interferometric gravitational wave detector," Class. Quant. Grav. **32**, 024001 (2015), arXiv:1408.3978 .

[65] B. J. Meers, "Recycling in Laser Interferometric Gravitational Wave Detectors," Phys. Rev. **D38**, 2317–2326 (1988).

[66] J. Mizuno, K. Strain, P. Nelson, J. Chen, R. Schilling, A. Rüdiger, W. Winkler, and K. Danzmann, "Resonant sideband extraction: a new configuration for interferometric gravitational wave detectors," Phys. Lett. A **175**, 273 – 276 (1993).

[67] S. A. Hughes and K. S. Thorne, "Seismic gravity gradient noise in interferometric gravitational wave detectors," Phys. Rev. **D58**, 122002 (1998), arXiv:gr-qc/9806018 .

[68] S. Klimenko, I. Yakushin, A. Mercer, and G. Mitselmakher, "Coherent method for detection of gravitational wave bursts," *Proceedings, 18th International Conference on General Relativity and Gravitation (GRG18) and 7th Edoardo Amaldi Conference on Gravitational Waves (Amaldi7), Sydney, Australia, July 2007*, Class. Quant. Grav. **25**, 114029 (2008), arXiv:0802.3232 .

[69] S. Klimenko *et al.*, "Method for detection and reconstruction of gravitational wave transients with networks of advanced detectors," Phys. Rev. **D93**, 042004 (2016), arXiv:1511.05999 .

[70] R. Lynch, S. Vitale, R. Essick, E. Katsavounidis, and F. Robinet, "Information-theoretic approach to the gravitational-wave burst detection problem," Phys. Rev. **D95**, 104046 (2017), arXiv:1511.05955 .

[71] N. J. Cornish and T. B. Littenberg, "BayesWave: Bayesian Inference for Gravitational Wave Bursts and Instrument Glitches," Class. Quant. Grav. **32**, 135012 (2015), arXiv:1410.3835 .

[72] B. J. Owen, "Search templates for gravitational waves from inspiraling binaries: Choice of template spacing," Phys. Rev. **D53**, 6749–6761 (1996), arXiv:gr-qc/9511032 .

[73] B. P. Abbott *et al.* (LIGO Scientific, Virgo), "Binary Black Hole Mergers in the first Advanced LIGO Observing Run," Phys. Rev. **X6**, 041015 (2016), [erratum: Phys. Rev.X8,no.3,039903(2018)], arXiv:1606.04856 .

[74] T. Dal Canton and I. W. Harry, "Designing a template bank to observe compact binary coalescences in Advanced LIGO's second observing run," (2017), arXiv:1705.01845 .

[75] N. Metropolis, A. W. Rosenbluth, M. N. Rosenbluth, A. H. Teller, and E. Teller, "Equation of state calculations by fast computing machines," J. Chem. Phys. **21**, 1087–1092 (1953).

[76] W. K. Hastings, "Monte carlo sampling methods using markov chains and their applications," Biometrika **57**, 97–109 (1970).

[77] J. Skilling, "Nested sampling for general bayesian computation," Bayesian Anal. **1**, 833–859 (2006).

[78] J. Veitch *et al.*, "Parameter estimation for compact binaries with ground-based gravitational-wave observations using the LALInference software library," Phys. Rev. **D91**, 042003 (2015), arXiv:1409.7215 .

[79] C. M. Will, "The Confrontation between General Relativity and Experiment," Living Rev. Rel. **17**, 4 (2014), arXiv:1403.7377 .

[80] M. N. R. Wohlfarth, "Gravity a la Born-Infeld," Class. Quant. Grav. **21**, 1927 (2004), [Erratum: Class. Quant. Grav.21,5297(2004)], arXiv:hep-th/0310067 .

[81] T. Biswas, A. Mazumdar, and W. Siegel, "Bouncing universes in string-inspired gravity," JCAP **0603**, 009 (2006), arXiv:hep-th/0508194 .

[82] M. Banados and P. G. Ferreira, "Eddington's theory of gravity and its progeny," Phys. Rev. Lett. **105**, 011101 (2010), [Erratum: Phys. Rev. Lett.113,no.11,119901(2014)], arXiv:1006.1769 .

[83] K. S. Stelle, "Renormalization of Higher Derivative Quantum Gravity," Phys. Rev. **D16**, 953–969 (1977).

[84] D. Lovelock, "The Einstein tensor and its generalizations," J. Math. Phys. **12**, 498–501 (1971).

[85] D. Lovelock, "The four-dimensionality of space and the einstein tensor," J. Math. Phys. **13**, 874–876 (1972).

[86] M. Ostrogradsky, "Sur les intégrales des équations générales de la dynamique," Mem. Ac. St. Petersbourg **VI 4**, 385 (1850).

[87] T. Clifton, P. G. Ferreira, A. Padilla, and C. Skordis, "Modified Gravity and Cosmology," Phys. Rept. **513**, 1–189 (2012), arXiv:1106.2476 .

[88] N. Yunes and X. Siemens, "Gravitational-Wave Tests of General Relativity with Ground-Based Detectors and Pulsar Timing-Arrays," Living Rev. Rel. **16**, 9 (2013), arXiv:1304.3473 .

[89] E. Berti *et al.*, "Testing General Relativity with Present and Future Astrophysical Observations," Class. Quant. Grav. **32**, 243001 (2015), arXiv:1501.07274 .

[90] G. W. Horndeski, "Second-order scalar-tensor field equations in a four-dimensional space," Int. J. Theor. Phys. **10**, 363–384 (1974).

[91] M. Zumalacárregui and J. García-Bellido, "Transforming gravity: from derivative couplings to matter to second-order scalar-tensor theories beyond the Horndeski Lagrangian," Phys. Rev. **D89**, 064046 (2014), arXiv:1308.4685 .

[92] J. Gleyzes, D. Langlois, F. Piazza, and F. Vernizzi, "Exploring gravitational theories beyond Horndeski," JCAP **1502**, 018 (2015), arXiv:1408.1952 .

[93] J. Gleyzes, D. Langlois, F. Piazza, and F. Vernizzi, "Healthy theories beyond Horndeski," Phys. Rev. Lett. **114**, 211101 (2015), arXiv:1404.6495 .

[94] J. Alsing, E. Berti, C. M. Will, and H. Zaglauer, "Gravitational radiation from compact binary systems in the massive Brans-Dicke theory of gravity," Phys. Rev. **D85**, 064041 (2012), arXiv:1112.4903 .

[95] S. S. Yazadjiev, D. D. Doneva, and D. Popchev, "Slowly rotating neutron stars in scalar-tensor theories with a massive scalar field," Phys. Rev. **D93**, 084038 (2016), arXiv:1602.04766 .

[96] S. S. Yazadjiev, D. D. Doneva, and K. D. Kokkotas, "Tidal Love numbers of neutron stars in $f(R)$ gravity," Eur. Phys. J. **C78**, 818 (2018), arXiv:1803.09534 .

[97] C. M. Will, *Theory and Experiment in Gravitational Physics* (Cambridge University Press, Cambridge, 1993).

[98] T. P. Sotiriou, "Black Holes and Scalar Fields," Class. Quant. Grav. **32**, 214002 (2015), arXiv:1505.00248 .

[99] O. Sarbach, E. Barausse, and J. A. Preciado-López, "Well-posed Cauchy formulation for Einstein-æther theory," Class. Quant. Grav. **36**, 165007 (2019), arXiv:1902.05130 .

[100] D. Blas, O. Pujolas, and S. Sibiryakov, "Consistent Extension of Horava Gravity," Phys. Rev. Lett. **104**, 181302 (2010), arXiv:0909.3525 .

[101] P. Horava, "Quantum Gravity at a Lifshitz Point," Phys. Rev. **D79**, 084008 (2009), arXiv:0901.3775 .

[102] T. Jacobson and D. Mattingly, "Einstein-Aether waves," Phys. Rev. **D70**, 024003 (2004), arXiv:gr-qc/0402005 .

[103] K. Yagi, D. Blas, E. Barausse, and N. Yunes, "Constraints on Einstein-Æther theory and Hor**a**va gravity from binary pulsar observations," Phys. Rev. **D89**, 084067 (2014), [Erratum: Phys. Rev.D90,no.6,069901(2014)], arXiv:1311.7144 .

[104] O. Ramos and E. Barausse, "Constraints on Hor**a**va gravity from binary black hole observations," Phys. Rev. **D99**, 024034 (2019), arXiv:1811.07786 .

[105] C. Eling and T. Jacobson, "Black Holes in Einstein-Aether Theory," Class. Quant. Grav. **23**, 5643–5660 (2006), [Erratum: Class. Quant. Grav.27,049802(2010)], arXiv:gr-qc/0604088 .

[106] L. Barack *et al.*, "Black holes, gravitational waves and fundamental physics: a roadmap," Class. Quant. Grav. **36**, 143001 (2019), arXiv:1806.05195 .

[107] C. de Rham and G. Gabadadze, "Generalization of the Fierz-Pauli Action," Phys. Rev. **D82**, 044020 (2010), arXiv:1007.0443 .

[108] C. de Rham, G. Gabadadze, and A. J. Tolley, "Resummation of Massive Gravity," Phys. Rev. Lett. **106**, 231101 (2011), arXiv:1011.1232 .

[109] C. de Rham, "Massive Gravity," Living Rev. Rel. **17**, 7 (2014), arXiv:1401.4173 .

[110] A. I. Vainshtein, "To the problem of nonvanishing gravitation mass," Phys. Lett. **39B**, 393–394 (1972).

[111] C. M. Will, "Bounding the mass of the graviton using gravitational wave observations of inspiralling compact binaries," Phys. Rev. **D57**, 2061–2068 (1998), arXiv:gr-qc/9709011 .

[112] M. Maggiore and M. Mancarella, "Nonlocal gravity and dark energy," Phys. Rev. **D90**, 023005 (2014), arXiv:1402.0448 .

[113] Y. Dirian, S. Foffa, M. Kunz, M. Maggiore, and V. Pettorino, "Non-local gravity and comparison with observational datasets. II. Updated results and Bayesian model comparison with ΛCDM," JCAP **1605**, 068 (2016), arXiv:1602.03558 .

[114] A. Kehagias and M. Maggiore, "Spherically symmetric static solutions in a nonlocal infrared modification of General Relativity," JHEP **08**, 029 (2014), arXiv:1401.8289 .

[115] E. Belgacem, Y. Dirian, S. Foffa, and M. Maggiore, "Gravitational-wave luminosity distance in modified gravity theories," Phys. Rev. **D97**, 104066 (2018), arXiv:1712.08108 .

[116] E. Belgacem, Y. Dirian, S. Foffa, and M. Maggiore, "Modified gravitational-wave propagation and standard sirens," Phys. Rev. **D98**, 023510 (2018), arXiv:1805.08731 .

[117] K. G. Arun, B. R. Iyer, M. S. S. Qusailah, and B. S. Sathyaprakash, "Probing the non-linear structure of general relativity with black hole binaries," Phys. Rev. **D74**, 024006 (2006), arXiv:gr-qc/0604067 .

[118] N. Yunes and F. Pretorius, "Fundamental Theoretical Bias in Gravitational Wave Astrophysics and the Parameterized Post-Einsteinian Framework," Phys. Rev. **D80**, 122003 (2009), arXiv:0909.3328 .

[119] C. K. Mishra, K. G. Arun, B. R. Iyer, and B. S. Sathyaprakash, "Parametrized tests of post-Newtonian theory using Advanced LIGO and Einstein Telescope," Phys. Rev. **D82**, 064010 (2010), arXiv:1005.0304 .

[120] T. G. F. Li, W. Del Pozzo, S. Vitale, C. Van Den Broeck, M. Agathos, J. Veitch, K. Grover, T. Sidery, R. Sturani, and A. Vecchio, "Towards a generic test of the strong field dynamics of general relativity using compact binary coalescence," Phys. Rev. **D85**, 082003 (2012), arXiv:1110.0530 .

[121] J. Meidam *et al.*, "Parametrized tests of the strong-field dynamics of general relativity using gravitational wave signals from coalescing binary black holes: Fast likelihood calculations and sensitivity of the method," Phys. Rev. **D97**, 044033 (2018), arXiv:1712.08772 .

[122] B. P. Abbott *et al.* (LIGO Scientific, Virgo), "Tests of general relativity with GW150914," Phys. Rev. Lett. **116**, 221101 (2016), [Erratum: Phys. Rev. Lett.121,no.12,129902(2018)], arXiv:1602.03841 .

[123] B. P. Abbott *et al.* (LIGO Scientific, Virgo), "GW170104: Observation of a 50-Solar-Mass Binary Black Hole Coalescence at Redshift 0.2," Phys. Rev. Lett. **118**, 221101 (2017), arXiv:1706.01812 .

[124] K. G. Arun and C. M. Will, "Bounding the mass of the graviton with gravitational waves: Effect of higher harmonics in gravitational waveform templates," Class. Quant. Grav. **26**, 155002 (2009), arXiv:0904.1190 .

[125] A. Stavridis and C. M. Will, "Bounding the mass of the graviton with gravitational waves: Effect of spin precessions in massive black hole binaries," Phys. Rev. **D80**, 044002 (2009), arXiv:0906.3602 .

[126] S. Mirshekari, N. Yunes, and C. M. Will, "Constraining Generic Lorentz Violation and the Speed of the Graviton with Gravitational Waves," Phys. Rev. **D85**, 024041 (2012), arXiv:1110.2720 .

[127] T. Baker, E. Bellini, P. G. Ferreira, M. Lagos, J. Noller, and I. Sawicki, "Strong constraints on cosmological gravity from GW170817 and GRB 170817A," Phys. Rev. Lett. **119**, 251301 (2017), arXiv:1710.06394 .

[128] P. Creminelli and F. Vernizzi, "Dark Energy after GW170817 and GRB170817A," Phys. Rev. Lett. **119**, 251302 (2017), arXiv:1710.05877 .

[129] J. Sakstein and B. Jain, "Implications of the Neutron Star Merger GW170817 for Cosmological Scalar-Tensor Theories," Phys. Rev. Lett. **119**, 251303 (2017), arXiv:1710.05893 .

[130] J. M. Ezquiaga and M. Zumalacárregui, "Dark Energy After GW170817: Dead Ends and the Road Ahead," Phys. Rev. Lett. **119**, 251304 (2017), arXiv:1710.05901 .

[131] D. Langlois, R. Saito, D. Yamauchi, and K. Noui, "Scalar-tensor theories and modified gravity in the wake of GW170817," Phys. Rev. **D97**, 061501 (2018), arXiv:1711.07403 .

[132] A. Dima and F. Vernizzi, "Vainshtein Screening in Scalar-Tensor Theories before and after GW170817: Constraints on Theories beyond Horndeski," Phys. Rev. **D97**, 101302 (2018), arXiv:1712.04731 .

[133] S. Boran, S. Desai, E. O. Kahya, and R. P. Woodard, "GW170817 Falsifies Dark Matter Emulators," Phys. Rev. **D97**, 041501 (2018), arXiv:1710.06168 .

[134] C. de Rham and S. Melville, "Gravitational Rainbows: LIGO and Dark Energy at its Cutoff," Phys. Rev. Lett. **121**, 221101 (2018), arXiv:1806.09417 .

[135] K. Chatziioannou, N. Yunes, and N. Cornish, "Model-Independent Test of General Relativity: An Extended post-Einsteinian Framework with Complete Polarization Content," Phys. Rev. **D86**, 022004 (2012), [Erratum: Phys. Rev.D95,no.12,129901(2017)], arXiv:1204.2585 .

[136] M. Isi and A. J. Weinstein, "Probing gravitational wave polarizations with signals from compact binary coalescences," (2017), arXiv:1710.03794 .

[137] T. B. Littenberg, J. B. Kanner, N. J. Cornish, and M. Millhouse, "Enabling high confidence detections of gravitational-wave bursts," Phys. Rev. **D94**, 044050 (2016), arXiv:1511.08752 .

[138] N. Sennett, R. Brito, A. Buonanno, V. Gorbenko, and L. Senatore, "Constraints on an effective field theory extension to General Relativity using gravitational-wave observations," (2019, *in prep.*).

[139] A. De Rujula, S. L. Glashow, and U. Sarid, "Charged dark matter," Nucl. Phys. **B333**, 173–194 (1990).

[140] M. L. Perl and E. R. Lee, "The search for elementary particles with fractional electric charge and the philosophy of speculative experiments," Am. J. Phys. **65**, 698–706 (1997).

[141] S. D. McDermott, H.-B. Yu, and K. M. Zurek, "Turning off the Lights: How Dark is Dark Matter?" Phys. Rev. **D83**, 063509 (2011), arXiv:1011.2907 .

[142] L. Ackerman, M. R. Buckley, S. M. Carroll, and M. Kamionkowski, "Dark Matter and Dark Radiation," Phys. Rev. **D79**, 023519 (2009), arXiv:0810.5126 .

[143] J. L. Feng, H. Tu, and H.-B. Yu, "Thermal Relics in Hidden Sectors," JCAP **0810**, 043 (2008), arXiv:0808.2318 .

[144] J. L. Feng, M. Kaplinghat, H. Tu, and H.-B. Yu, "Hidden Charged Dark Matter," JCAP **0907**, 004 (2009), arXiv:0905.3039 .

[145] E. Barausse, N. Yunes, and K. Chamberlain, "Theory-Agnostic Constraints on Black-Hole Dipole Radiation with Multiband Gravitational-Wave Astrophysics," Phys. Rev. Lett. **116**, 241104 (2016), arXiv:1603.04075 .

[146] H. W. Zaglauer, "Neutron stars and gravitational scalars," Astrophys. J. **393**, 685–696 (1992).

[147] T. Damour and G. Esposito-Farese, "Tensor multiscalar theories of gravitation," Class. Quant. Grav. **9**, 2093–2176 (1992).

[148] T. P. Sotiriou and V. Faraoni, "Black holes in scalar-tensor gravity," Phys. Rev. Lett. **108**, 081103 (2012), arXiv:1109.6324 .

[149] S. Mirshekari and C. M. Will, "Compact binary systems in scalar-tensor gravity: Equations of motion to 2.5 post-Newtonian order," Phys. Rev. **D87**, 084070 (2013), arXiv:1301.4680 .

[150] R. N. Lang, "Compact binary systems in scalar-tensor gravity. II. Tensor gravitational waves to second post-Newtonian order," Phys. Rev. **D89**, 084014 (2014), arXiv:1310.3320 .

[151] R. N. Lang, "Compact binary systems in scalar-tensor gravity. III. Scalar waves and energy flux," Phys. Rev. **D91**, 084027 (2015), arXiv:1411.3073 .

[152] T. Damour and G. Esposito-Farese, "Tensor - scalar gravity and binary pulsar experiments," Phys. Rev. **D54**, 1474–1491 (1996), arXiv:gr-qc/9602056 .

[153] T. Damour and G. Esposito-Farese, "Nonperturbative strong field effects in tensor - scalar theories of gravitation," Phys. Rev. Lett. **70**, 2220–2223 (1993).

[154] I. Z. Stefanov, S. S. Yazadjiev, and M. D. Todorov, "Phases of 4D scalar-tensor black holes coupled to Born-Infeld nonlinear electrodynamics," Mod. Phys. Lett. **A23**, 2915–2931 (2008), arXiv:0708.4141 .

[155] D. D. Doneva, S. S. Yazadjiev, K. D. Kokkotas, and I. Z. Stefanov, "Quasinormal modes, bifurcations and non-uniqueness of charged scalar-tensor black holes," Phys. Rev. **D82**, 064030 (2010), arXiv:1007.1767 .

[156] C. Palenzuela and S. L. Liebling, "Constraining scalar-tensor theories of gravity from the most massive neutron stars," Phys. Rev. **D93**, 044009 (2016), arXiv:1510.03471 .

[157] R. F. P. Mendes and N. Ortiz, "Highly compact neutron stars in scalar-tensor theories of gravity: Spontaneous scalarization versus gravitational collapse," Phys. Rev. **D93**, 124035 (2016), arXiv:1604.04175 .

[158] C. A. R. Herdeiro, E. Radu, N. Sanchis-Gual, and J. A. Font, "Spontaneous Scalarization of Charged Black Holes," Phys. Rev. Lett. **121**, 101102 (2018), arXiv:1806.05190 .

[159] P. G. S. Fernandes, C. A. R. Herdeiro, A. M. Pombo, E. Radu, and N. Sanchis-Gual, "Spontaneous Scalarisation of Charged Black Holes: Coupling Dependence and Dynamical Features," Class. Quant. Grav. **36**, 134002 (2019), arXiv:1902.05079 .

[160] P. Chen, T. Suyama, and J. Yokoyama, "Spontaneous scalarization: asymmetron as dark matter," Phys. Rev. **D92**, 124016 (2015), arXiv:1508.01384 .

[161] F. M. Ramazanoglu and F. Pretorius, "Spontaneous Scalarization with Massive Fields," Phys. Rev. **D93**, 064005 (2016), arXiv:1601.07475 .

[162] L. Sagunski, J. Zhang, M. C. Johnson, L. Lehner, M. Sakellariadou, S. L. Liebling, C. Palenzuela, and D. Neilsen, "Neutron star mergers as a probe of modifications of general relativity with finite-range scalar forces," Phys. Rev. **D97**, 064016 (2018), arXiv:1709.06634 .

[163] D. D. Doneva and S. S. Yazadjiev, "New Gauss-Bonnet Black Holes with Curvature-Induced Scalarization in Extended Scalar-Tensor Theories," Phys. Rev. Lett. **120**, 131103 (2018), arXiv:1711.01187 .

[164] H. O. Silva, J. Sakstein, L. Gualtieri, T. P. Sotiriou, and E. Berti, "Spontaneous scalarization of black holes and compact stars from a Gauss-Bonnet coupling," Phys. Rev. Lett. **120**, 131104 (2018), arXiv:1711.02080 .

[165] G. Antoniou, A. Bakopoulos, and P. Kanti, "Evasion of No-Hair Theorems and Novel Black-Hole Solutions in Gauss-Bonnet Theories," Phys. Rev. Lett. **120**, 131102 (2018), arXiv:1711.03390 .

[166] G. Antoniou, A. Bakopoulos, and P. Kanti, "Black-Hole Solutions with Scalar Hair in Einstein-Scalar-Gauss-Bonnet Theories," Phys. Rev. **D97**, 084037 (2018), arXiv:1711.07431 .

[167] D. D. Doneva and S. S. Yazadjiev, "Neutron star solutions with curvature induced scalarization in the extended Gauss-Bonnet scalar-tensor theories," JCAP **1804**, 011 (2018), arXiv:1712.03715 .

[168] Y. Brihaye and B. Hartmann, "Spontaneous scalarization of charged black holes at the approach to extremality," Phys. Lett. **B792**, 244–250 (2019), arXiv:1902.05760 .

[169] E. Barausse, C. Palenzuela, M. Ponce, and L. Lehner, "Neutron-star mergers in scalar-tensor theories of gravity," Phys. Rev. **D87**, 081506 (2013), arXiv:1212.5053 .

[170] C. Palenzuela, E. Barausse, M. Ponce, and L. Lehner, "Dynamical scalarization of neutron stars in scalar-tensor gravity theories," Phys. Rev. **D89**, 044024 (2014), arXiv:1310.4481 .

[171] M. Shibata, K. Taniguchi, H. Okawa, and A. Buonanno, "Coalescence of binary neutron stars in a scalar-tensor theory of gravity," Phys. Rev. **D89**, 084005 (2014), arXiv:1310.0627 .

[172] K. Taniguchi, M. Shibata, and A. Buonanno, "Quasiequilibrium sequences of binary neutron stars undergoing dynamical scalarization," Phys. Rev. **D91**, 024033 (2015), arXiv:1410.0738 .

[173] C. Palenzuela, E. Barausse, M. Ponce, and L. Lehner, "Dynamical scalarization of neutron stars in scalar-tensor gravity theories," Phys. Rev. D **89**, 044024 (2014).

[174] K. Taniguchi, M. Shibata, and A. Buonanno, "Quasiequilibrium sequences of binary neutron stars undergoing dynamical scalarization," Phys. Rev. D **91**, 024033 (2015).

[175] L. Sampson, N. Yunes, N. Cornish, M. Ponce, E. Barausse, A. Klein, C. Palenzuela, and L. Lehner, "Projected Constraints on Scalarization with Gravitational Waves from Neutron Star Binaries," Phys. Rev. **D90**, 124091 (2014), arXiv:1407.7038 .

[176] M. Agathos, W. Del Pozzo, T. G. F. Li, C. Van Den Broeck, J. Veitch, and S. Vitale, "TIGER: A data analysis pipeline for testing the strong-field dynamics of general relativity with gravitational wave signals from coalescing compact binaries," Phys. Rev. **D89**, 082001 (2014), arXiv:1311.0420 .

[177] P. Jordan, *Schwerkraft und Weltall* (F. Vieweg, Braunschweig, 1955).

[178] M. Fierz, "On the physical interpretation of P.Jordan's extended theory of gravitation," Helv. Phys. Acta **29**, 128–134 (1956).

[179] C. Brans and R. H. Dicke, "Mach's principle and a relativistic theory of gravitation," Phys. Rev. **124**, 925–935 (1961).

[180] B. Bertotti, L. Iess, and P. Tortora, "A test of general relativity using radio links with the Cassini spacecraft," Nature **425**, 374–376 (2003).

[181] S. Endlich, V. Gorbenko, J. Huang, and L. Senatore, "An effective formalism for testing extensions to General Relativity with gravitational waves," JHEP **09**, 122 (2017), arXiv:1704.01590 .

[182] B. P. Abbott *et al.* (LIGO Scientific, Virgo), "GW151226: Observation of Gravitational Waves from a 22-Solar-Mass Binary Black Hole Coalescence," Phys. Rev. Lett. **116**, 241103 (2016), arXiv:1606.04855 .

[183] B. P. Abbott *et al.* (LIGO Scientific, Virgo), "GW170608: Observation of a 19-solar-mass Binary Black Hole Coalescence," Astrophys. J. **851**, L35 (2017), arXiv:1711.05578 .

[184] B. P. Abbott *et al.* (LIGO Scientific, Virgo), "Observation of Gravitational Waves from a Binary Black Hole Merger," Phys. Rev. Lett. **116**, 061102 (2016), arXiv:1602.03837 .

[185] B. P. Abbott *et al.* (LIGO Scientific, Virgo), "GW170814: A Three-Detector Observation of Gravitational Waves from a Binary Black Hole Coalescence," Phys. Rev. Lett. **119**, 141101 (2017), arXiv:1709.09660 .

[186] B. Abbott *et al.* (LIGO Scientific, Virgo), "GW170817: Observation of Gravitational Waves from a Binary Neutron Star Inspiral," Phys. Rev. Lett. **119**, 161101 (2017), arXiv:1710.05832 .

[187] N. Yunes, K. Yagi, and F. Pretorius, "Theoretical Physics Implications of the Binary Black-Hole Mergers GW150914 and GW151226," Phys. Rev. **D94**, 084002 (2016), arXiv:1603.08955 .

[188] G. W. Gibbons and K.-i. Maeda, "Black Holes and Membranes in Higher Dimensional Theories with Dilaton Fields," Nucl. Phys. **B298**, 741–775 (1988).

[189] D. Garfinkle, G. T. Horowitz, and A. Strominger, "Charged black holes in string theory," Phys. Rev. **D43**, 3140 (1991), [Erratum: Phys. Rev.D45,3888(1992)].

[190] J. H. Horne and G. T. Horowitz, "Rotating dilaton black holes," Phys. Rev. **D46**, 1340–1346 (1992), arXiv:hep-th/9203083 .

[191] V. P. Frolov, A. I. Zelnikov, and U. Bleyer, "Charged Rotating Black Hole From Five-dimensional Point of View," Annalen Phys. **44**, 371–377 (1987).

[192] G. W. Gibbons, "Vacuum Polarization and the Spontaneous Loss of Charge by Black Holes," Commun. Math. Phys. **44**, 245–264 (1975).

[193] D. M. Eardley and W. H. Press, "Astrophysical processes near black holes," Ann. Rev. Astron. Astrophys. **13**, 381–422 (1975).

[194] V. Cardoso, C. F. B. Macedo, P. Pani, and V. Ferrari, "Black holes and gravitational waves in models of minicharged dark matter," JCAP **1605**, 054 (2016), arXiv:1604.07845 .

[195] S. Davidson, S. Hannestad, and G. Raffelt, "Updated bounds on millicharged particles," JHEP **05**, 003 (2000), arXiv:hep-ph/0001179 .

[196] C. Burrage, J. Jaeckel, J. Redondo, and A. Ringwald, "Late time CMB anisotropies constrain mini-charged particles," JCAP **0911**, 002 (2009), arXiv:0909.0649 .

[197] M. Ahlers, "The Hubble diagram as a probe of mini-charged particles," Phys. Rev. **D80**, 023513 (2009), arXiv:0904.0998 .

[198] K. Kadota, T. Sekiguchi, and H. Tashiro, "A new constraint on millicharged dark matter from galaxy clusters," (2016), arXiv:1602.04009 .

[199] E. W. Hirschmann, L. Lehner, S. L. Liebling, and C. Palenzuela, "Black Hole Dynamics in Einstein-Maxwell-Dilaton Theory," Phys. Rev. **D97**, 064032 (2018), arXiv:1706.09875 .

[200] M. Zilhão, V. Cardoso, C. Herdeiro, L. Lehner, and U. Sperhake, "Collisions of charged black holes," Phys. Rev. **D85**, 124062 (2012), arXiv:1205.1063 .

[201] M. Zilhão, V. Cardoso, C. Herdeiro, L. Lehner, and U. Sperhake, "Collisions of oppositely charged black holes," Phys. Rev. **D89**, 044008 (2014), arXiv:1311.6483 .

[202] F.-L. Julié, "On the motion of hairy black holes in Einstein-Maxwell-dilaton theories," JCAP **1801**, 026 (2018), arXiv:1711.10769 .

[203] E. E. Flanagan, "The Conformal frame freedom in theories of gravitation," Class. Quant. Grav. **21**, 3817 (2004), arXiv:gr-qc/0403063 .

[204] D. M. Eardley, "Observable effects of a scalar gravitational field in a binary pulsar," Astrophys. J. **196**, L59–L62 (1975).

[205] A. Taracchini, A. Buonanno, G. Khanna, and S. A. Hughes, "Small mass plunging into a Kerr black hole: Anatomy of the inspiral-merger-ringdown waveforms," Phys. Rev. **D90**, 084025 (2014), arXiv:1404.1819 .

[206] J. S. Read, B. D. Lackey, B. J. Owen, and J. L. Friedman, "Constraints on a phenomenologically parameterized neutron-star equation of state," Phys. Rev. **D79**, 124032 (2009), arXiv:0812.2163 .

[207] A. D. Fokker, "Ein invarianter Variationssatz für die Bewegung mehrerer elektrischer Massenteilchen," Z. Phys. **58**, 386–393 (1929).

[208] T. Damour and G. Esposito-Farese, "Testing gravity to second postNewtonian order: A Field theory approach," Phys. Rev. **D53**, 5541–5578 (1996), arXiv:gr-qc/9506063 .

[209] L. Bernard, L. Blanchet, A. Bohé, G. Faye, and S. Marsat, "Fokker action of nonspinning compact binaries at the fourth post-Newtonian approximation," Phys. Rev. **D93**, 084037 (2016), arXiv:1512.02876 .

[210] L. Bernard, "Dynamics of compact binary systems in scalar-tensor theories: I. Equations of motion to the third post-Newtonian order," (2018), arXiv:1802.10201 .

[211] L. Blanchet and B. R. Iyer, "Third postNewtonian dynamics of compact binaries: Equations of motion in the center-of-mass frame," Class. Quant. Grav. **20**, 755 (2003), arXiv:gr-qc/0209089 .

[212] N. Yunes and S. A. Hughes, "Binary Pulsar Constraints on the Parameterized post-Einsteinian Framework," Phys. Rev. **D82**, 082002 (2010), arXiv:1007.1995 .

[213] W. Del Pozzo, J. Veitch, and A. Vecchio, "Testing General Relativity using Bayesian model selection: Applications to observations of gravitational waves from compact binary systems," Phys. Rev. **D83**, 082002 (2011), arXiv:1101.1391 .

[214] N. Cornish, L. Sampson, N. Yunes, and F. Pretorius, "Gravitational Wave Tests of General Relativity with the Parameterized Post-Einsteinian Framework," Phys. Rev. **D84**, 062003 (2011), arXiv:1105.2088 .

[215] S. Gossan, J. Veitch, and B. S. Sathyaprakash, "Bayesian model selection for testing the no-hair theorem with black hole ringdowns," Phys. Rev. **D85**, 124056 (2012), arXiv:1111.5819 .

[216] T. Damour, B. R. Iyer, and B. S. Sathyaprakash, "Frequency domain P approximant filters for time truncated inspiral gravitational wave signals from compact binaries," Phys. Rev. **D62**, 084036 (2000), arXiv:gr-qc/0001023 .

[217] "LIGO-T1800042-v5: Updated Advanced LIGO sensitivity design curve," `https://dcc.ligo.org/LIGO-T1800044/public`.

[218] R. Coquereaux and G. Esposito-Farese, "The Theory of Kaluza-Klein-Jordan-Thiry revisited," Ann. Inst. H. Poincare Phys. Theor. **52**, 113–150 (1990).

[219] F.-L. Julié, "Reducing the two-body problem in scalar-tensor theories to the motion of a test particle : a scalar-tensor effective-one-body approach," Phys. Rev. **D97**, 024047 (2018), arXiv:1709.09742 .

[220] T. Damour and A. Nagar, "Effective One Body description of tidal effects in inspiralling compact binaries," Phys. Rev. **D81**, 084016 (2010), arXiv:0911.5041 .

[221] F.-L. Julié and N. Deruelle, "Two-body problem in Scalar-Tensor theories as a deformation of General Relativity : an Effective-One-Body approach," Phys. Rev. **D95**, 124054 (2017), arXiv:1703.05360 .

[222] T. Damour, P. Jaranowski, and G. Schäfer, "Fourth post-Newtonian effective one-body dynamics," Phys. Rev. **D91**, 084024 (2015), arXiv:1502.07245 .

[223] A. Buonanno, "Reduction of the two-body dynamics to a one-body description in classical electrodynamics," Phys. Rev. **D62**, 104022 (2000), arXiv:hep-th/0004042 .

[224] T. Damour, "Gravitational scattering, post-Minkowskian approximation and Effective One-Body theory," Phys. Rev. **D94**, 104015 (2016), arXiv:1609.00354 .

[225] J. Vines, "Scattering of two spinning black holes in post-Minkowskian gravity, to all orders in spin, and effective-one-body mappings," Class. Quant. Grav. **35**, 084002 (2018), arXiv:1709.06016 .

[226] Y. Pan, A. Buonanno, L. T. Buchman, T. Chu, L. E. Kidder, H. P. Pfeiffer, and M. A. Scheel, "Effective-one-body waveforms calibrated to numerical relativity simulations: coalescence of non-precessing, spinning, equal-mass black holes," Phys. Rev. **D81**, 084041 (2010), arXiv:0912.3466 .

[227] P. Jai-akson, A. Chatrabhuti, O. Evnin, and L. Lehner, "Black hole merger estimates in Einstein-Maxwell and Einstein-Maxwell-dilaton gravity," Phys. Rev. **D96**, 044031 (2017), arXiv:1706.06519 .

[228] V. Ferrari, M. Pauri, and F. Piazza, "Quasinormal modes of charged, dilaton black holes," Phys. Rev. **D63**, 064009 (2001), arXiv:gr-qc/0005125 .

[229] B. P. Abbott *et al.* (KAGRA, LIGO Scientific, Virgo), "Prospects for Observing and Localizing Gravitational-Wave Transients with Advanced LIGO, Advanced Virgo and KAGRA," Living Rev. Rel. **21**, 3 (2018), arXiv:1304.0670 .

[230] B. P. Abbott *et al.* (LIGO Scientific, Virgo), "GW150914: The Advanced LIGO Detectors in the Era of First Discoveries," Phys. Rev. Lett. **116**, 131103 (2016), arXiv:1602.03838 .

[231] B. P. Abbott *et al.* (LIGO Scientific, Virgo), "The Rate of Binary Black Hole Mergers Inferred from Advanced LIGO Observations Surrounding GW150914," Astrophys. J. **833**, L1 (2016), arXiv:1602.03842 .

[232] T. Accadia *et al.* (Virgo), "Virgo: a laser interferometer to detect gravitational waves," JINST **7**, P03012 (2012).

[233] Y. Aso, Y. Michimura, K. Somiya, M. Ando, O. Miyakawa, T. Sekiguchi, D. Tatsumi, and H. Yamamoto (KAGRA), "Interferometer design of the KAGRA gravitational wave detector," Phys. Rev. **D88**, 043007 (2013), arXiv:1306.6747 .

[234] B. Iyer, T. Souradeep, C. S. Unnikrishnan, S. Dhurandhar, S. Raja, and A. Sengupta, "LIGO-India, Proposal of the Consortium for Indian Initiative in Gravitational-wave Observations (IndIGO)," LIGO-India Tech. rep. (2011), (unpublished).

[235] P. Amaro-Seoane *et al.*, "eLISA/NGO: Astrophysics and cosmology in the gravitational-wave millihertz regime," GW Notes **6**, 4–110 (2013), arXiv:1201.3621 .

[236] Y. Xie, W.-T. Ni, P. Dong, and T.-Y. Huang, "Second post-Newtonian approximation of scalar-tensor theory of gravity," Adv. Space Res. **43**, 171–180 (2009), arXiv:0704.2991 .

[237] L. Blanchet, G. Faye, B. R. Iyer, and S. Sinha, "The Third post-Newtonian gravitational wave polarisations and associated spherical harmonic modes for inspiralling compact binaries in quasi-circular orbits," Class. Quant. Grav. **25**, 165003 (2008), [Erratum: Class. Quant. Grav.29,239501(2012)], arXiv:0802.1249 .

[238] G. Faye, S. Marsat, L. Blanchet, and B. R. Iyer, "The third and a half post-Newtonian gravitational wave quadrupole mode for quasi-circular inspiralling compact binaries," Class. Quant. Grav. **29**, 175004 (2012), arXiv:1204.1043 .

[239] G. Faye, L. Blanchet, and B. R. Iyer, "Non-linear multipole interactions and gravitational-wave octupole modes for inspiralling compact binaries to third-and-a-half post-Newtonian order," Class. Quant. Grav. **32**, 045016 (2015), arXiv:1409.3546 .

[240] C. M. Will, "Testing scalar - tensor gravity with gravitational wave observations of inspiraling compact binaries," Phys. Rev. **D50**, 6058–6067 (1994), arXiv:gr-qc/9406022 .

[241] P. Jordan, *Schwerkraft und Weltall* (F. Vieweg, Braunschweig, 1955).

[242] D. M. Eardley, "Observable effects of a scalar gravitational field in a binary pulsar," **196**, L59–L62 (1975).

[243] C. M. Will and H. W. Zaglauer, "Gravitational Radiation, Close Binary Systems, and the Brans-dicke Theory of Gravity," Astrophys. J. **346**, 366 (1989).

[244] H. M. Antia, S. M. Chitre, and D. O. Gough, "Temporal Variations in the Sun's Rotational Kinetic Energy," Astron. Astrophys. (2007), 10.1051/0004-6361:20078209, [Astron. Astrophys.477,657(2008)], arXiv:0711.0799 .

[245] N. D. R. Bhat, M. Bailes, and J. P. W. Verbiest, "Gravitational-radiation losses from the pulsar-white-dwarf binary PSR J1141-6545," Phys. Rev. **D77**, 124017 (2008), arXiv:0804.0956 .

[246] J. Antoniadis, C. G. Bassa, N. Wex, M. Kramer, and R. Napiwotzki, "A white dwarf companion to the relativistic pulsar PSR J1141-6545," Mon. Not. Roy. Astron. Soc. **412**, 580 (2011), arXiv:1011.0926 .

[247] P. C. C. Freire, N. Wex, G. Esposito-Farese, J. P. W. Verbiest, M. Bailes, B. A. Jacoby, M. Kramer, I. H. Stairs, J. Antoniadis, and G. H. Janssen, "The relativistic pulsar-white dwarf binary PSR J1738+0333 II. The most stringent test of scalar-tensor gravity," Mon. Not. Roy. Astron. Soc. **423**, 3328 (2012), arXiv:1205.1450 .

[248] J. Antoniadis *et al.*, "A Massive Pulsar in a Compact Relativistic Binary," Science **340**, 6131 (2013), arXiv:1304.6875 .

[249] N. Wex, "Testing Relativistic Gravity with Radio Pulsars," (2014), arXiv:1402.5594 .

[250] L. Shao *et al.*, "Testing Gravity with Pulsars in the SKA Era," *Advancing Astrophysics with the Square Kilometre Array (AASKA14): Giardini Naxos, Italy, 2014*, PoS **AASKA14**, 042 (2015), arXiv:1501.00058 .

[251] L. Blanchet, "Radiative gravitational fields in general relativity. 2. Asymptotic behaviour at future null infinity," Proc. Roy. Soc. Lond. **A409**, 383–399 (1987).

[252] L. Blanchet and T. Damour, "Hereditary effects in gravitational radiation," Phys. Rev. **D46**, 4304–4319 (1992).

[253] L. Blanchet and T. Damour, "Radiative gravitational fields in general relativity I. general structure of the field outside the source," Phil. Trans. Roy. Soc. Lond. **A320**, 379–430 (1986).

[254] C. M. Will and A. G. Wiseman, "Gravitational radiation from compact binary systems: Gravitational wave forms and energy loss to second postNewtonian order," Phys. Rev. D **54**, 4813–4848 (1996).

[255] M. E. Pati and C. M. Will, "PostNewtonian gravitational radiation and equations of motion via direct integration of the relaxed Einstein equations. 1. Foundations," Phys. Rev. D **62**, 124015 (2000).

[256] L. Blanchet and G. Schaefer, "Gravitational wave tails and binary star systems," Class. Quant. Grav. **10**, 2699–2721 (1993).

[257] D. Christodoulou, "Nonlinear nature of gravitation and gravitational wave experiments," Phys. Rev. Lett. **67**, 1486–1489 (1991).

[258] K. G. Arun, L. Blanchet, B. R. Iyer, and M. S. S. Qusailah, "The 2.5PN gravitational wave polarisations from inspiralling compact binaries in circular orbits," Class. Quant. Grav. **21**, 3771–3802 (2004), [Erratum: Class. Quant. Grav.22,3115(2005)], arXiv:gr-qc/0404085 .

[259] A. Buonanno, B. Iyer, E. Ochsner, Y. Pan, and B. S. Sathyaprakash, "Comparison of post-Newtonian templates for compact binary inspiral signals in gravitational-wave detectors," Phys. Rev. **D80**, 084043 (2009), arXiv:0907.0700 .

[260] K. S. Thorne, "Multipole Expansions of Gravitational Radiation," Rev. Mod. Phys. **52**, 299–339 (1980).

[261] L. Blanchet, T. Damour, B. R. Iyer, C. M. Will, and A. Wiseman, "Gravitational radiation damping of compact binary systems to second postNewtonian order," Phys. Rev. Lett. **74**, 3515–3518 (1995), arXiv:gr-qc/9501027 .

[262] K. Thorne, "Gravitational radiation," in *Three hundred years of gravitation*, edited by S. Hawking and W. Israel (Cambridge University Press, Cambridge, 1987) pp. 330–458.

[263] N. Yunes, P. Pani, and V. Cardoso, "Gravitational Waves from Quasicircular Extreme Mass-Ratio Inspirals as Probes of Scalar-Tensor Theories," Phys. Rev. **D85**, 102003 (2012), arXiv:1112.3351 .

[264] P. D. Scharre and C. M. Will, "Testing scalar tensor gravity using space gravitational wave interferometers," Phys. Rev. **D65**, 042002 (2002), arXiv:gr-qc/0109044 .

[265] C. M. Will and N. Yunes, "Testing alternative theories of gravity using LISA," Class. Quant. Grav. **21**, 4367 (2004), arXiv:gr-qc/0403100 .

[266] E. Berti, A. Buonanno, and C. M. Will, "Estimating spinning binary parameters and testing alternative theories of gravity with LISA," Phys. Rev. **D71**, 084025 (2005), arXiv:gr-qc/0411129 .

[267] K. Yagi and T. Tanaka, "Constraining alternative theories of gravity by gravitational waves from precessing eccentric compact binaries with LISA," Phys. Rev. **D81**, 064008 (2010), [Erratum: Phys. Rev.D81,109902(2010)], arXiv:0906.4269 .

[268] J. R. Gair, M. Vallisneri, S. L. Larson, and J. G. Baker, "Testing General Relativity with Low-Frequency, Space-Based Gravitational-Wave Detectors," Living Rev. Rel. **16**, 7 (2013), arXiv:1212.5575 .

[269] T. G. F. Li, W. Del Pozzo, S. Vitale, C. Van Den Broeck, M. Agathos, J. Veitch, K. Grover, T. Sidery, R. Sturani, and A. Vecchio, "Towards a generic test of the strong field dynamics of general relativity using compact binary coalescence: Further investigations," *Gravitational waves. Numerical relativity - data analysis. Proceedings, 9th Edoardo Amaldi Conference, Amaldi 9, and meeting, NRDA 2011, Cardiff, UK, July 10-15, 2011*, J. Phys. Conf. Ser. **363**, 012028 (2012), arXiv:1111.5274 .

[270] L. Sampson, N. Cornish, and N. Yunes, "Gravitational Wave Tests of Strong Field General Relativity with Binary Inspirals: Realistic Injections and Optimal Model Selection," Phys. Rev. **D87**, 102001 (2013), arXiv:1303.1185 .

[271] L. Sampson, N. Cornish, and N. Yunes, "Mismodeling in gravitational-wave astronomy: The trouble with templates," Phys. Rev. **D89**, 064037 (2014), arXiv:1311.4898 .

[272] T. Damour and K. Nordtvedt, "General relativity as a cosmological attractor of tensor scalar theories," Phys. Rev. Lett. **70**, 2217–2219 (1993).

[273] T. Damour and K. Nordtvedt, "Tensor - scalar cosmological models and their relaxation toward general relativity," Phys. Rev. **D48**, 3436–3450 (1993).

[274] S. DeDeo and D. Psaltis, "Towards New Tests of Strong-field Gravity with Measurements of Surface Atomic Line Redshifts from Neutron Stars," Phys. Rev. Lett. **90**, 141101 (2003), arXiv:astro-ph/0302095 .

[275] H. Sotani and K. D. Kokkotas, "Probing strong-field scalar-tensor gravity with gravitational wave asteroseismology," Phys. Rev. **D70**, 084026 (2004), arXiv:gr-qc/0409066 .

[276] T. Damour and G. Esposito-Farese, "Gravitational wave versus binary - pulsar tests of strong field gravity," Phys. Rev. **D58**, 042001 (1998), arXiv:gr-qc/9803031 .

[277] S. DeDeo and D. Psaltis, "Testing strong-field gravity with quasiperiodic oscillations," (2004), submitted to: Phys. Rev. D, arXiv:astro-ph/0405067 [astro-ph] .

[278] D. D. Doneva, S. S. Yazadjiev, N. Stergioulas, K. D. Kokkotas, and T. M. Athanasiadis, "Orbital and epicyclic frequencies around rapidly rotating compact stars in scalar-tensor theories of gravity," Phys. Rev. **D90**, 044004 (2014), arXiv:1405.6976 .

[279] K. Just, Z. Phys. **157** (1959).

[280] A. Akmal, V. R. Pandharipande, and D. G. Ravenhall, "The Equation of state of nucleon matter and neutron star structure," Phys. Rev. **C58**, 1804–1828 (1998), arXiv:nucl-th/9804027 .

[281] T. Damour and J. H. Taylor, "Strong field tests of relativistic gravity and binary pulsars," Phys. Rev. **D45**, 1840–1868 (1992).

[282] G. Esposito-Farèse, "Motion in alternative theories of gravity," *Mass and Motion in General Relativity*, Fundam. Theor. Phys. **162**, 461–489 (2011).

[283] W. Scherrer, "Zur theorie der elementarteilchen," Verh. Schweiz. Naturf. Ges. **121**, 86–87 (1941).

[284] Y. Thiry, J. Math. Pures et Appl. **30**, 275–396 (1951).

[285] R. Epstein and R. V. Wagoner, "Post-Newtonian generation of gravitational waves," Astrophys. J. **197**, 717 (1975).

[286] R. V. Wagoner and C. M. Will, "Post-Newtonian gravitational radiation from orbiting point masses," Astrophys. J. **210**, 764 (1976).

[287] C. M. Will and A. G. Wiseman, "Gravitational radiation from compact binary systems: Gravitational wave forms and energy loss to second postNewtonian order," Phys. Rev. **D54**, 4813–4848 (1996), arXiv:gr-qc/9608012 .

[288] M. E. Pati and C. M. Will, "PostNewtonian gravitational radiation and equations of motion via direct integration of the relaxed Einstein equations. 1. Foundations," Phys. Rev. **D62**, 124015 (2000), arXiv:gr-qc/0007087 .

[289] M. E. Pati and C. M. Will, "PostNewtonian gravitational radiation and equations of motion via direct integration of the relaxed Einstein equations. 2. Two-body equations of motion to second postNewtonian order, and radiation reaction to 3.5 postNewtonia order," Phys. Rev. **D65**, 104008 (2002), arXiv:gr-qc/0201001 .

[290] A. Buonanno, Y.-b. Chen, and M. Vallisneri, "Detection template families for gravitational waves from the final stages of binary–black-hole inspirals: Nonspinning case," Phys. Rev. **D67**, 024016 (2003), [Erratum: Phys. Rev.D74,029903(2006)], arXiv:gr-qc/0205122 .

[291] G. "Schäfer, "The gravitational quadrupole radiation reaction force and the canonical formalism of ADM," Annals Phys. **161**, 81–100 (1985).

[292] T. Hinderer *et al.*, "Effects of neutron-star dynamic tides on gravitational waveforms within the effective-one-body approach," Phys. Rev. Lett. **116**, 181101 (2016), arXiv:1602.00599 .

[293] J. Steinhoff, private communication.

[294] M. Kramer, "Pulsars as probes of gravity and fundamental physics," Int. J. Mod. Phys. **D25**, 1630029 (2016), arXiv:1606.03843 .

[295] D. Psaltis, "Probes and Tests of Strong-Field Gravity with Observations in the Electromagnetic Spectrum," Living Rev. Rel. **11**, 9 (2008), arXiv:0806.1531 .

[296] T. Baker, D. Psaltis, and C. Skordis, "Linking Tests of Gravity On All Scales: from the Strong-Field Regime to Cosmology," Astrophys. J. **802**, 63 (2015), arXiv:1412.3455 .

[297] B. P. Abbott *et al.* (LIGO Scientific, Virgo), "Upper Limits on the Rates of Binary Neutron Star and Neutron Star–Black Hole Mergers From Advanced Ligo's First Observing run," Astrophys. J. **832**, L21 (2016), arXiv:1607.07456 .

[298] J. E. Vines and É. É. Flanagan, "Post-1-Newtonian quadrupole tidal interactions in binary systems," Phys. Rev. **D88**, 024046 (2013), arXiv:1009.4919 .

[299] J. Steinhoff, T. Hinderer, A. Buonanno, and A. Taracchini, "Dynamical Tides in General Relativity: Effective Action and Effective-One-Body Hamiltonian," Phys. Rev. **D94**, 104028 (2016), arXiv:1608.01907 .

[300] P. Jordan, "Formation of the Stars and Development of the Universe," Nature **164**, 637–640 (1949).

[301] M. Abernathy *et al.* (ET Science Team), "Einstein gravitational wave telescope: Conceptual design study," (2011).

[302] D. Anderson, N. Yunes, and E. Barausse, "The Effect of Cosmological Evolution on Solar System Constraints and on the Scalarization of Neutron Stars in Massless Scalar-Tensor Theories," Phys. Rev. **D94**, 104064 (2016), arXiv:1607.08888 .

[303] T. A. de Pirey Saint Alby and N. Yunes, "Cosmological Evolution and Solar System Consistency of Massive Scalar-Tensor Gravity," Phys. Rev. **D96**, 064040 (2017), arXiv:1703.06341 .

[304] R. F. P. Mendes, "Possibility of setting a new constraint to scalar-tensor theories," Phys. Rev. **D91**, 064024 (2015), arXiv:1412.6789 .

[305] L. Shao and N. Wex, "Tests of gravitational symmetries with radio pulsars," Sci. China Phys. Mech. Astron. **59**, 699501 (2016), arXiv:1604.03662 .

[306] P. Ajith *et al.*, "Phenomenological template family for black-hole coalescence waveforms," Class. Quant. Grav. **24**, S689–S700 (2007), arXiv:0704.3764 .

[307] T. Damour and A. Nagar, "Relativistic tidal properties of neutron stars," Phys. Rev. **D80**, 084035 (2009), arXiv:0906.0096 .

[308] É. É. Flanagan and T. Hinderer, "Constraining neutron star tidal Love numbers with gravitational wave detectors," Phys. Rev. **D77**, 021502 (2008), arXiv:0709.1915 .

[309] S. Chakrabarti, T. Delsate, and J. Steinhoff, "New perspectives on neutron star and black hole spectroscopy and dynamic tides," (2013), arXiv:1304.2228 .

[310] D. M. Eardley, "Observable effects of a scalar gravitational field in a binary pulsar," Astrophys. J. **196**, L59–L62 (1975).

[311] M. E. Peskin and D. V. Schroeder, *An Introduction to quantum field theory* (Addison-Wesley, Boston, 1995).

[312] S. Weinberg, "Effective field theory, past and future," Int. J. Mod. Phys. **A31**, 1630007 (2016).

[313] T. Jacobson, "Primordial black hole evolution in tensor scalar cosmology," Phys. Rev. Lett. **83**, 2699–2702 (1999), arXiv:astro-ph/9905303 .

[314] M. W. Horbatsch and C. P. Burgess, "Cosmic Black-Hole Hair Growth and Quasar OJ287," JCAP **1205**, 010 (2012), arXiv:1111.4009 .

[315] W. D. Goldberger and I. Z. Rothstein, "An Effective field theory of gravity for extended objects," Phys. Rev. **D73**, 104029 (2006), arXiv:hep-th/0409156 .

[316] T. Damour, P. Jaranowski, and G. Schafer, "Nonlocal-in-time action for the fourth post-Newtonian conservative dynamics of two-body systems," Phys. Rev. **D89**, 064058 (2014), arXiv:1401.4548 .

[317] K. Taniguchi and M. Shibata, "Binary Neutron Stars in Quasi-equilibrium," Astrophys. J. Suppl. **188**, 187 (2010), arXiv:1005.0958 .

[318] L. D. Landau, "Theory of phase transformations. I," Zh. Eksp. Teor. Fiz. **7**, 19–32 (1937).

[319] S. W. Hawking and R. Penrose, "The Singularities of gravitational collapse and cosmology," Proc. Roy. Soc. Lond. **A314**, 529–548 (1970).

[320] F. Englert and R. Brout, "Broken Symmetry and the Mass of Gauge Vector Mesons," Phys. Rev. Lett. **13**, 321–323 (1964).

[321] P. W. Higgs, "Broken Symmetries and the Masses of Gauge Bosons," Phys. Rev. Lett. **13**, 508–509 (1964).

[322] G. S. Guralnik, C. R. Hagen, and T. W. B. Kibble, "Global Conservation Laws and Massless Particles," Phys. Rev. Lett. **13**, 585–587 (1964).

[323] A. Coates, M. W. Horbartsch, and T. P. Sotiriou, "Gravitational Higgs Mechanism in Neutron Star Interiors," Phys. Rev. **D95**, 084003 (2017), arXiv:1606.03981 .

[324] F. M. Ramazanoğlu, "Spontaneous growth of gauge fields in gravity through the Higgs mechanism," Phys. Rev. **D98**, 044013 (2018), arXiv:1804.03158 .

[325] F. M. Ramazanoğlu, "Spontaneous growth of vector fields in gravity," Phys. Rev. **D96**, 064009 (2017), arXiv:1706.01056 .

[326] F. M. Ramazanoğlu, "Spontaneous tensorization from curvature coupling and beyond," Phys. Rev. **D99**, 084015 (2019), arXiv:1901.10009 .

[327] F. M. Ramazanoğlu, "Spontaneous growth of spinor fields in gravity," Phys. Rev. **D98**, 044011 (2018), arXiv:1804.00594 .

[328] P. Zimmerman, "Gravitational self-force in scalar-tensor gravity," Phys. Rev. **D92**, 064051 (2015), arXiv:1507.04076 .

[329] D. Anderson, P. Freire, and N. Yunes, "Binary Pulsar constraints on massless scalar-tensor theories using Bayesian statistics," (2019), arXiv:1901.00938 .

[330] B. P. Abbott *et al.* (LIGO Scientific, Virgo), "Properties of the binary neutron star merger GW170817," Phys. Rev. **X9**, 011001 (2019), arXiv:1805.11579 .

[331] Y. S. Myung and D.-C. Zou, "Instability of Reissner-Nordström black hole in Einstein-Maxwell-scalar theory," (2018), arXiv:1808.02609 .

[332] F. M. Ramazanoğlu, "Regularization of instabilities in gravity theories," Phys. Rev. **D97**, 024008 (2018), arXiv:1710.00863 .

[333] G. W. Gibbons, R. Kallosh, and B. Kol, "Moduli, scalar charges, and the first law of black hole thermodynamics," Phys. Rev. Lett. **77**, 4992–4995 (1996), arXiv:hep-th/9607108 .

[334] M. Cárdenas, F.-L. Julié, and N. Deruelle, "Thermodynamics sheds light on black hole dynamics," (2017), arXiv:1712.02672 .

[335] J. L. Blázquez-Salcedo, D. D. Doneva, J. Kunz, and S. S. Yazadjiev, "Radial perturbations of the scalarized Einstein-Gauss-Bonnet black holes," Phys. Rev. **D98**, 084011 (2018), arXiv:1805.05755 .

[336] M. Minamitsuji and T. Ikeda, "Scalarized black holes in the presence of the coupling to Gauss-Bonnet gravity," Phys. Rev. **D99**, 044017 (2019), arXiv:1812.03551 .

[337] H. O. Silva, C. F. B. Macedo, T. P. Sotiriou, L. Gualtieri, J. Sakstein, and E. Berti, "Stability of scalarized black hole solutions in scalar-Gauss-Bonnet gravity," Phys. Rev. **D99**, 064011 (2019), arXiv:1812.05590 .

[338] Y. S. Myung and D.-C. Zou, "Stability of scalarized charged black holes in the Einstein–Maxwell–Scalar theory," Eur. Phys. J. **C79**, 641 (2019), arXiv:1904.09864 .

[339] Y. S. Myung and D.-C. Zou, "Quasinormal modes of scalarized black holes in the Einstein–Maxwell–Scalar theory," Phys. Lett. **B790**, 400–407 (2019), arXiv:1812.03604 .

[340] L. D. Landau, Ukr. J. Phys **53**, 25–35 (2008), (English translation).

[341] M. W. Choptuik, "Universality and scaling in gravitational collapse of a massless scalar field," Phys. Rev. Lett. **70**, 9–12 (1993).

[342] A. M. Abrahams and C. R. Evans, "Critical behavior and scaling in vacuum axisymmetric gravitational collapse," Phys. Rev. Lett. **70**, 2980–2983 (1993).

[343] C. R. Evans and J. S. Coleman, "Observation of critical phenomena and self-similarity in the gravitational collapse of radiation fluid," Phys. Rev. Lett. **72**, 1782–1785 (1994), arXiv:gr-qc/9402041 .

[344] M. W. Choptuik, T. Chmaj, and P. Bizon, "Critical behavior in gravitational collapse of a Yang-Mills field," Phys. Rev. Lett. **77**, 424–427 (1996), arXiv:gr-qc/9603051 .

[345] S. E. Gralla and P. Zimmerman, "Critical Exponents of Extremal Kerr Perturbations," Class. Quant. Grav. **35**, 095002 (2018), arXiv:1711.00855 .

[346] S. E. Gralla and P. Zimmerman, "Scaling and Universality in Extremal Black Hole Perturbations," JHEP **06**, 061 (2018), arXiv:1804.04753 .

[347] W. D. Goldberger and A. Ross, "Gravitational radiative corrections from effective field theory," Phys. Rev. **D81**, 124015 (2010), arXiv:0912.4254 .

[348] A. Kuntz, F. Piazza, and F. Vernizzi, "Effective field theory for gravitational radiation in scalar-tensor gravity," JCAP **1905**, 052 (2019), arXiv:1902.04941 .

[349] H. Witek, L. Gualtieri, P. Pani, and T. P. Sotiriou, "Black holes and binary mergers in scalar Gauss-Bonnet gravity: scalar field dynamics," Phys. Rev. **D99**, 064035 (2019), arXiv:1810.05177 .

[350] V. Cardoso, S. Chakrabarti, P. Pani, E. Berti, and L. Gualtieri, "Floating and sinking: The Imprint of massive scalars around rotating black holes," Phys. Rev. Lett. **107**, 241101 (2011), arXiv:1109.6021 .

[351] S. Endlich and R. Penco, "A Modern Approach to Superradiance," JHEP **05**, 052 (2017), arXiv:1609.06723 .

[352] L. K. Wong, A.-C. Davis, and R. Gregory, "Effective field theory for black holes with induced scalar charges," (2019), arXiv:1903.07080 .

[353] S. Reyes and D. A. Brown, "Constraints on non-linear tides due to p-g mode coupling from the neutron-star merger GW170817," (2018), arXiv:1808.07013 .

[354] B. P. Abbott *et al.* (LIGO Scientific, Virgo), "Constraining the p-Mode–g-Mode Tidal Instability with GW170817," Phys. Rev. Lett. **122**, 061104 (2019), arXiv:1808.08676 .

[355] E. Gaertig, K. Glampedakis, K. D. Kokkotas, and B. Zink, "The f-mode instability in relativistic neutron stars," Phys. Rev. Lett. **107**, 101102 (2011), arXiv:1106.5512 .

[356] N. Andersson and K. D. Kokkotas, "The R mode instability in rotating neutron stars," Int. J. Mod. Phys. **D10**, 381–442 (2001), arXiv:gr-qc/0010102 .

[357] K. Yagi and N. Yunes, "Approximate Universal Relations for Neutron Stars and Quark Stars," Phys. Rept. **681**, 1–72 (2017), arXiv:1608.02582 .

[358] K. Yagi and N. Yunes, "I-Love-Q," Science **341**, 365–368 (2013), arXiv:1302.4499 .

[359] T. Binnington and E. Poisson, "Relativistic theory of tidal Love numbers," Phys. Rev. **D80**, 084018 (2009), arXiv:0906.1366 .

[360] B. Kol and M. Smolkin, "Black hole stereotyping: Induced gravito-static polarization," JHEP **02**, 010 (2012), arXiv:1110.3764 .

[361] T. Kaluza, "On the Problem of Unity in Physics," Sitzungsber. Preuss. Akad. Wiss. Berlin (Math. Phys.) **1921**, 966–972 (1921).

[362] P. Jordan, *Schwerkraft und Weltall:*, Die Wissenschaft, Bd. 107 (Braunschweig, 1952).

[363] L. Shao, "Testing the strong equivalence principle with the triple pulsar PSR J0337+1715," Phys. Rev. **D93**, 084023 (2016), arXiv:1602.05725 .

[364] E. Berti, A. Buonanno, and C. M. Will, "Testing general relativity and probing the merger history of massive black holes with LISA," Class. Quant. Grav. **22**, S943–S954 (2005), arXiv:gr-qc/0504017 .

[365] K. Yagi and T. Tanaka, "DECIGO/BBO as a probe to constrain alternative theories of gravity," Prog. Theor. Phys. **123**, 1069–1078 (2010), arXiv:0908.3283 .

[366] L. Shao *et al.*, "Testing Gravity with Pulsars in the SKA Era," *Proceedings, Advancing Astrophysics with the Square Kilometre Array (AASKA14): Giardini Naxos, Italy, June 9-13, 2014*, PoS **AASKA14**, 042 (2015), arXiv:1501.00058 .

[367] B. P. Abbott *et al.* (LIGO Scientific), "Exploring the Sensitivity of Next Generation Gravitational Wave Detectors," Class. Quant. Grav. **34**, 044001 (2017), arXiv:1607.08697 .

[368] T. Damour, "Binary Systems as Test-beds of Gravity Theories," (2007), arXiv:0704.0749 .

[369] P. Demorest, T. Pennucci, S. Ransom, M. Roberts, and J. Hessels, "Shapiro Delay Measurement of A Two Solar Mass Neutron Star," Nature **467**, 1081–1083 (2010), arXiv:1010.5788 .

[370] G. Esposito-Farèse, "Binary pulsar tests of strong field gravity and gravitational radiation damping," in *Proceedings of the Tenth Marcel Grossmann Meeting. On recent developments in theoretical and experimental general relativity, gravitation and relativistic field theories* (2004) pp. 647–666, arXiv:gr-qc/0402007 .

[371] G. Esposito-Farèse, "Tests of scalar-tensor gravity," *Phi in the Sky: The Quest for Cosmological Scalar Fields*, AIP Conf. Proc. **736**, 35–52 (2004), arXiv:gr-qc/0409081 .

[372] D. Anderson and N. Yunes, "Solar System constraints on massless scalar-tensor gravity with positive coupling constant upon cosmological evolution of the scalar field," Phys. Rev. **D96**, 064037 (2017), arXiv:1705.06351 .

[373] K. Lazaridis *et al.*, "Generic tests of the existence of the gravitational dipole radiation and the variation of the gravitational constant," Mon. Not. R. Astron. Soc. **400**, 805–814 (2009), arXiv:0908.0285 .

[374] D. J. Reardon *et al.*, "Timing analysis for 20 millisecond pulsars in the Parkes Pulsar Timing Array," Mon. Not. Roy. Astron. Soc. **455**, 1751–1769 (2016), arXiv:1510.04434 .

[375] I. Cognard *et al.*, "A Massive-born Neutron Star with a Massive White Dwarf Companion," Astrophys. J. **844**, 128 (2017), arXiv:1706.08060 .

[376] P. J. McMillan, "The mass distribution and gravitational potential of the Milky Way," Mon. Not. Roy. Astron. Soc. **465**, 76–94 (2017), arXiv:1608.00971 .

[377] P. J. Callanan, P. M. Garnavich, and D. Koester, "The mass of the neutron star in the binary millisecond pulsar PSR J1012 + 5307," Mon. Not. Roy. Astron. Soc. **298**, 207–211 (1998).

[378] J. Antoniadis, T. M. Tauris, F. Ozel, E. Barr, D. J. Champion, and P. C. C. Freire, "The millisecond pulsar mass distribution: Evidence for bimodality and constraints on the maximum neutron star mass," (2016), arXiv:1605.01665 .

[379] J. Antoniadis, M. H. van Kerkwijk, D. Koester, P. C. C. Freire, N. Wex, T. M. Tauris, M. Kramer, and C. G. Bassa, "The relativistic pulsar-white dwarf binary PSR J1738+0333 I. Mass determination and evolutionary history," Mon. Not. Roy. Astron. Soc. **423**, 3316 (2012), arXiv:1204.3948 .

[380] W. Del Pozzo and A. Vecchio, "On tests of general relativity with binary radio pulsars," Mon. Not. Roy. Astron. Soc. **462**, L21–L25 (2016), arXiv:1606.02852 .

[381] J. M. Lattimer, "The nuclear equation of state and neutron star masses," Ann. Rev. Nucl. Part. Sci. **62**, 485–515 (2012), arXiv:1305.3510 .

[382] J. M. Lattimer and M. Prakash, "Neutron star structure and the equation of state," Astrophys. J. **550**, 426 (2001), arXiv:astro-ph/0002232 .

[383] J. Goodman and J. Weare, "Ensemble samplers with affine invariance," Comm. App. Math. and Comp. Sci. **5**, 65–80 (2010).

[384] D. Foreman-Mackey, D. W. Hogg, D. Lang, and J. Goodman, "emcee: The MCMC Hammer," Publ. Astron. Soc. Pac. **125**, 306–312 (2013), arXiv:1202.3665 .

[385] P. C. Peters, "Gravitational Radiation and the Motion of Two Point Masses," Phys. Rev. **136**, B1224–B1232 (1964).

[386] A. Gelman and D. B. Rubin, "Inference from Iterative Simulation Using Multiple Sequences," Statist. Sci. **7**, 457–472 (1992).

[387] S. Brooks, A. Gelman, G. Jones, and X. Meng, *Handbook of Markov Chain Monte Carlo* (CRC Press, 2011).

[388] S. Hild *et al.*, "Sensitivity Studies for Third-Generation Gravitational Wave Observatories," Class. Quant. Grav. **28**, 094013 (2011), arXiv:1012.0908 .

[389] D. Shoemaker (LIGO Collaboration), "Advanced LIGO anticipated sensitivity curves," (2010), LIGO Document T0900288-v3.

[390] M. Kramer *et al.*, "Tests of general relativity from timing the double pulsar," Science **314**, 97–102 (2006), arXiv:astro-ph/0609417 .

[391] J. W. T. Hessels, S. M. Ransom, I. H. Stairs, P. C. C. Freire, V. M. Kaspi, and F. Camilo, "A radio pulsar spinning at 716-hz," Science **311**, 1901–1904 (2006), arXiv:astro-ph/0601337 .

[392] W. Del Pozzo, K. Grover, I. Mandel, and A. Vecchio, "Testing general relativity with compact coalescing binaries: comparing exact and predictive methods to compute the Bayes factor," Class. Quant. Grav. **31**, 205006 (2014), arXiv:1408.2356 .

[393] L. S. Finn, "Detection, measurement and gravitational radiation," Phys. Rev. **D46**, 5236–5249 (1992), arXiv:gr-qc/9209010 .

[394] C. Cutler and E. E. Flanagan, "Gravitational waves from merging compact binaries: How accurately can one extract the binary's parameters from the inspiral wave form?" Phys. Rev. **D49**, 2658–2697 (1994), arXiv:gr-qc/9402014 .

[395] M. Vallisneri, "Use and abuse of the Fisher information matrix in the assessment of gravitational-wave parameter-estimation prospects," Phys. Rev. **D77**, 042001 (2008), arXiv:gr-qc/0703086 .

[396] P. A. R. Ade *et al.* (Planck), "Planck 2015 results. XIII. Cosmological parameters," Astron. Astrophys. **594**, A13 (2016), arXiv:1502.01589 .

[397] P. Lazarus *et al.*, "Einstein@Home discovery of a Double-Neutron Star Binary in the PALFA Survey," Astrophys. J. **831**, 150 (2016), arXiv:1608.08211 .

[398] K. G. Arun and A. Pai, "Tests of General Relativity and Alternative theories of gravity using Gravitational Wave observations," Int. J. Mod. Phys. **D22**, 1341012 (2013), arXiv:1302.2198 .

[399] X. Zhang, J. Yu, T. Liu, W. Zhao, and A. Wang, "Testing Brans-Dicke gravity using the Einstein telescope," Phys. Rev. **D95**, 124008 (2017), arXiv:1703.09853 .

[400] F. Mignard and S. A. Klioner, "Gaia: Relativistic modelling and testing," in *Relativity in Fundamental Astronomy: Dynamics, Reference Frames, and Data Analysis*, IAU Symposium, Vol. 261, edited by S. A. Klioner, P. K. Seidelmann, and M. H. Soffel (2010) pp. 306–314.

[401] R. Nan, D. Li, C. Jin, Q. Wang, L. Zhu, W. Zhu, H. Zhang, Y. Yue, and L. Qian, "The Five-Hundred-Meter Aperture Spherical Radio Telescope (FAST) Project," Int. J. Mod. Phys. **D20**, 989–1024 (2011), arXiv:1105.3794 .

[402] B. Iyer *et al.* (LIGO Collaboration), "LIGO-India, Proposal of the Consortium for Indian Initiative in Gravitational-wave Observations," (2011), LIGO Document M1100296-v2.

[403] N. Itoh, "Hydrostatic Equilibrium of Hypothetical Quark Stars," Prog. Theor. Phys. **44**, 291 (1970).

[404] F. E. Schunck and E. W. Mielke, "General relativistic boson stars," Class. Quant. Grav. **20**, R301–R356 (2003), arXiv:0801.0307 .

[405] S. L. Liebling and C. Palenzuela, "Dynamical Boson Stars," Living Rev. Rel. **15**, 6 (2012), arXiv:1202.5809 .

[406] P. O. Mazur and E. Mottola, "Gravitational condensate stars: An alternative to black holes," (2001), arXiv:gr-qc/0109035 .

[407] P. O. Mazur and E. Mottola, "Gravitational vacuum condensate stars," Proc. Nat. Acad. Sci. **101**, 9545–9550 (2004), arXiv:gr-qc/0407075 .

[408] J. Eby, M. Leembruggen, J. Leeney, P. Suranyi, and L. C. R. Wijewardhana, "Collisions of Dark Matter Axion Stars with Astrophysical Sources," JHEP **04**, 099 (2017), arXiv:1701.01476 .

[409] A. Iwazaki, "A Possible origin of gamma-ray bursts and axionic boson stars," Phys. Lett. **B455**, 192–196 (1999), arXiv:astro-ph/9903251 .

[410] K. D. Kokkotas and B. G. Schmidt, "Quasinormal modes of stars and black holes," Living Rev. Rel. **2**, 2 (1999), arXiv:gr-qc/9909058 .

[411] P. Ajith *et al.*, "A Template bank for gravitational waveforms from coalescing binary black holes. I. Non-spinning binaries," Phys. Rev. **D77**, 104017 (2008), [Erratum: Phys. Rev. **D79**, 129901 (2009)], arXiv:0710.2335 .

[412] S. Khan, S. Husa, M. Hannam, F. Ohme, M. Pürrer, X. Jiménez Forteza, and A. Bohé, "Frequency-domain gravitational waves from nonprecessing black-hole binaries. II. A phenomenological model for the advanced detector era," Phys. Rev. **D93**, 044007 (2016), arXiv:1508.07253 .

[413] P. Pani, "I-Love-Q relations for gravastars and the approach to the black-hole limit," Phys. Rev. **D92**, 124030 (2015), [Erratum: Phys. Rev.D95,no.4,049902(2017)], arXiv:1506.06050 .

[414] N. Uchikata, S. Yoshida, and P. Pani, "Tidal deformability and I-Love-Q relations for gravastars with polytropic thin shells," Phys. Rev. **D94**, 064015 (2016), arXiv:1607.03593 .

[415] R. F. P. Mendes and H. Yang, "Tidal deformability of dark matter clumps," (2016), arXiv:1606.03035 .

[416] V. Cardoso, E. Franzin, A. Maselli, P. Pani, and G. Raposo, "Testing strong-field gravity with tidal Love numbers," Phys. Rev. **D95**, 084014 (2017), [Addendum: Phys. Rev.D95,no.8,089901(2017)], arXiv:1701.01116 .

[417] N. V. Krishnendu, K. G. Arun, and C. K. Mishra, "Testing the binary black hole nature of a compact binary coalescence," Phys. Rev. Lett. **119**, 091101 (2017), arXiv:1701.06318 .

[418] A. Maselli, P. Pani, V. Cardoso, T. Abdelsalhin, L. Gualtieri, and V. Ferrari, "Probing Planckian corrections at the horizon scale with LISA binaries," (2017), arXiv:1703.10612 .

[419] C. Palenzuela, I. Olabarrieta, L. Lehner, and S. L. Liebling, "Head-on collisions of boson stars," Phys. Rev. **D75**, 064005 (2007), arXiv:gr-qc/0612067 .

[420] V. Cardoso, S. Hopper, C. F. B. Macedo, C. Palenzuela, and P. Pani, "Gravitational-wave signatures of exotic compact objects and of quantum corrections at the horizon scale," Phys. Rev. **D94**, 084031 (2016), arXiv:1608.08637 .

[421] C. Palenzuela, L. Lehner, and S. L. Liebling, "Orbital Dynamics of Binary Boson Star Systems," Phys. Rev. **D77**, 044036 (2008), arXiv:0706.2435 .

[422] S. Yoshida, Y. Eriguchi, and T. Futamase, "Quasinormal modes of boson stars," Phys. Rev. **D50**, 6235–6246 (1994).

[423] S. H. Hawley and M. W. Choptuik, "Boson stars driven to the brink of black hole formation," Phys. Rev. **D62**, 104024 (2000), arXiv:gr-qc/0007039 .

[424] C. F. B. Macedo, P. Pani, V. Cardoso, and L. C. B. Crispino, "Astrophysical signatures of boson stars: quasinormal modes and inspiral resonances," Phys. Rev. **D88**, 064046 (2013), arXiv:1307.4812 .

[425] C. B. M. H. Chirenti and L. Rezzolla, "How to tell a gravastar from a black hole," Class. Quant. Grav. **24**, 4191–4206 (2007), arXiv:0706.1513 .

[426] P. Pani, E. Berti, V. Cardoso, Y. Chen, and R. Norte, "Gravitational wave signatures of the absence of an event horizon. I. Nonradial oscillations of a thin-shell gravastar," Phys. Rev. **D80**, 124047 (2009), arXiv:0909.0287 .

[427] C. Chirenti and L. Rezzolla, "Did GW150914 produce a rotating gravastar?" Phys. Rev. **D94**, 084016 (2016), arXiv:1602.08759 .

[428] M. Colpi, S. L. Shapiro, and I. Wasserman, "Boson Stars: Gravitational Equilibria of Selfinteracting Scalar Fields," Phys. Rev. Lett. **57**, 2485–2488 (1986).

[429] R. Friedberg, T. D. Lee, and Y. Pang, "Scalar Soliton Stars and Black Holes," Phys. Rev. **D35**, 3658 (1987).

[430] W. Press, *Numerical Recipes in C: The Art of Scientific Computing*, Numerical Recipes in C book set No. v. 1 (Cambridge University Press, 1992).

[431] S. Chatrchyan *et al.* (CMS), "Observation of a new boson at a mass of 125 GeV with the CMS experiment at the LHC," Phys. Lett. **B716**, 30–61 (2012), arXiv:1207.7235 .

[432] G. Aad *et al.* (ATLAS), "Observation of a new particle in the search for the Standard Model Higgs boson with the ATLAS detector at the LHC," Phys. Lett. **B716**, 1–29 (2012), arXiv:1207.7214 .

[433] L. Roszkowski, "Supersymmetric dark matter: A Review," in *1993 Aspen Winter Physics Conference Elementary Particle Physics: Particle Physics from Supercolliders to the Planck Scale Aspen, Colorado, January 10-16, 1993* (1993) arXiv:hep-ph/9302259 .

[434] D. J. Kaup, "Klein-Gordon Geon," Phys. Rev. **172**, 1331–1342 (1968).

[435] D. A. Feinblum and W. A. McKinley, "Stable States of a Scalar Particle in Its Own Gravational Field," Phys. Rev. **168**, 1445 (1968).

[436] R. Ruffini and S. Bonazzola, "Systems of selfgravitating particles in general relativity and the concept of an equation of state," Phys. Rev. **187**, 1767–1783 (1969).

[437] F. S. Guzman, "Accretion disc onto boson stars: A Way to supplant black holes candidates," Phys. Rev. **D73**, 021501 (2006), arXiv:gr-qc/0512081 .

[438] P. Amaro-Seoane, J. Barranco, A. Bernal, and L. Rezzolla, "Constraining scalar fields with stellar kinematics and collisional dark matter," JCAP **1011**, 002 (2010), arXiv:1009.0019 .

[439] H. A. Buchdahl, "General Relativistic Fluid Spheres," Phys. Rev. **116**, 1027 (1959).

[440] S. Yoshida and Y. Eriguchi, "Rotating boson stars in general relativity," Phys. Rev. **D56**, 762–771 (1997).

[441] F. D. Ryan, "Spinning boson stars with large selfinteraction," Phys. Rev. **D55**, 6081–6091 (1997).

[442] B. Kleihaus, J. Kunz, and M. List, "Rotating boson stars and Q-balls," Phys. Rev. **D72**, 064002 (2005), arXiv:gr-qc/0505143 .

[443] P. Grandclement, C. Somé, and E. Gourgoulhon, "Models of rotating boson stars and geodesics around them: new type of orbits," Phys. Rev. **D90**, 024068 (2014), arXiv:1405.4837 .

[444] Y. Kobayashi, M. Kasai, and T. Futamase, "Does a boson star rotate?" Phys. Rev. **D50**, 7721–7724 (1994).

[445] K. D. Kokkotas and G. Schäfer, "Tidal and tidal resonant effects in coalescing binaries," Mon. Not. Roy. Astron. Soc. **275**, 301 (1995), arXiv:gr-qc/9502034 .

[446] D. Lai, "Resonant oscillations and tidal heating in coalescing binary neutron stars," Mon. Not. Roy. Astron. Soc. **270**, 611 (1994), arXiv:astro-ph/9404062 .

[447] T. Hinderer, "Tidal Love numbers of neutron stars," Astrophys. J. **677**, 1216–1220 (2008), arXiv:0711.2420 .

[448] T. Regge and J. A. Wheeler, "Stability of a Schwarzschild singularity," Phys. Rev. **108**, 1063–1069 (1957).

[449] K. S. Thorne, "Tidal stabilization of rigidly rotating, fully relativistic neutron stars," Phys. Rev. **D58**, 124031 (1998), arXiv:gr-qc/9706057 .

[450] C.-W. Lai, *A Numerical study of boson stars*, Ph.D. thesis, British Columbia U. (2004), arXiv:gr-qc/0410040 .

[451] B. Kleihaus, J. Kunz, and S. Schneider, "Stable Phases of Boson Stars," Phys. Rev. **D85**, 024045 (2012), arXiv:1109.5858 .

[452] E. W. Mielke and F. E. Schunck, "Boson stars: Alternatives to primordial black holes?" Nucl. Phys. **B564**, 185–203 (2000), arXiv:gr-qc/0001061 .

[453] J. Vines, É. É. Flanagan, and T. Hinderer, "Post-1-Newtonian tidal effects in the gravitational waveform from binary inspirals," Phys. Rev. **D83**, 084051 (2011), arXiv:1101.1673 .

[454] M. Favata, "Systematic parameter errors in inspiraling neutron star binaries," Phys. Rev. Lett. **112**, 101101 (2014), arXiv:1310.8288 .

[455] L. Wade, J. D. E. Creighton, E. Ochsner, B. D. Lackey, B. F. Farr, T. B. Littenberg, and V. Raymond, "Systematic and statistical errors in a bayesian approach to the estimation of the neutron-star equation of state using advanced gravitational wave detectors," Phys. Rev. **D89**, 103012 (2014), arXiv:1402.5156 .

[456] F. Douchin and P. Haensel, "A unified equation of state of dense matter and neutron star structure," Astron. Astrophys. **380**, 151 (2001), arXiv:astro-ph/0111092 .

[457] H. Müller and B. D. Serot, "Relativistic mean field theory and the high density nuclear equation of state," Nucl. Phys. **A606**, 508–537 (1996), arXiv:nucl-th/9603037 .

[458] S. Bernuzzi, T. Dietrich, and A. Nagar, "Modeling the complete gravitational wave spectrum of neutron star mergers," Phys. Rev. Lett. **115**, 091101 (2015), arXiv:1504.01764 .

[459] A. Taracchini, Y. Pan, A. Buonanno, E. Barausse, M. Boyle, T. Chu, G. Lovelace, H. P. Pfeiffer, and M. A. Scheel, "Prototype effective-one-body model for nonprecessing spinning inspiral-merger-ringdown waveforms," Phys. Rev. **D86**, 024011 (2012), arXiv:1202.0790 .

[460] K. Belczynski, G. Wiktorowicz, C. Fryer, D. Holz, and V. Kalogera, "Missing Black Holes Unveil The Supernova Explosion Mechanism," Astrophys. J. **757**, 91 (2012), arXiv:1110.1635 .

[461] T. Hinderer, B. D. Lackey, R. N. Lang, and J. S. Read, "Tidal deformability of neutron stars with realistic equations of state and their gravitational wave signatures in binary inspiral," Phys. Rev. **D81**, 123016 (2010), arXiv:0911.3535 .

[462] A. Zimmerman, C.-J. Haster, and K. Chatziioannou, "On combining information from multiple gravitational wave sources," Phys. Rev. **D99**, 124044 (2019), arXiv:1903.11008 .

[463] B. P. Abbott *et al.* (LIGO Scientific, Virgo), "GWTC-1: A Gravitational-Wave Transient Catalog of Compact Binary Mergers Observed by LIGO and Virgo during the First and Second Observing Runs," Phys. Rev. **X9**, 031040 (2019), arXiv:1811.12907 .

[464] M. Pürrer, "Frequency domain reduced order models for gravitational waves from aligned-spin compact binaries," Class. Quant. Grav. **31**, 195010 (2014), arXiv:1402.4146 .

[465] T. Dietrich, S. Bernuzzi, and W. Tichy, "Closed-form tidal approximants for binary neutron star gravitational waveforms constructed from high-resolution numerical relativity simulations," Phys. Rev. **D96**, 121501 (2017), arXiv:1706.02969 .

[466] T. Dietrich *et al.*, "Matter imprints in waveform models for neutron star binaries: Tidal and self-spin effects," Phys. Rev. **D99**, 024029 (2019), arXiv:1804.02235 .

[467] T. Dietrich, A. Samajdar, S. Khan, N. K. Johnson-McDaniel, R. Dudi, and W. Tichy, "Improving the NRTidal model for binary neutron star systems," Phys. Rev. **D100**, 044003 (2019), arXiv:1905.06011 .

[468] LIGO Scientific Collaboration and Virgo Collaboration, "LALSuite software," (2018).

[469] S. Husa, S. Khan, M. Hannam, M. Pürrer, F. Ohme, X. Jiménez Forteza, and A. Bohé, "Frequency-domain gravitational waves from nonprecessing black-hole binaries. I. New numerical waveforms and anatomy of the signal," Phys. Rev. **D93**, 044006 (2016), arXiv:1508.07250 .

[470] M. Hannam, P. Schmidt, A. Bohé, L. Haegel, S. Husa, F. Ohme, G. Pratten, and M. Pürrer, "Simple Model of Complete Precessing Black-Hole-Binary Gravitational Waveforms," Phys. Rev. Lett. **113**, 151101 (2014), arXiv:1308.3271 .

[471] D. Langlois and K. Noui, "Degenerate higher derivative theories beyond Horndeski: evading the Ostrogradski instability," JCAP **1602**, 034 (2016), arXiv:1510.06930 .

[472] D. Langlois, "Degenerate Higher-Order Scalar-Tensor (DHOST) theories," in *Proceedings, 52nd Rencontres de Moriond on Gravitation (Moriond Gravitation 2017): La Thuile, Italy, March 25-April 1, 2017* (2017) pp. 221–228, arXiv:1707.03625 .

[473] L. Bernard, "Dynamics of compact binary systems in scalar-tensor theories: II. Center-of-mass and conserved quantities to 3PN order," Phys. Rev. **D99**, 044047 (2019), arXiv:1812.04169 .

[474] D. L. Lee, "Conservation laws, gravitational waves, and mass losses in the Dicke-Brans-Jordan theory of gravity," Phys. Rev. **D10**, 2374–2383 (1974).

[475] L. Engvik, G. Bao, M. Hjorth-Jensen, E. Osnes, and E. Ostgaard, "Asymmetric nuclear matter and neutron star properties," Astrophys. J. **469**, 794 (1996), arXiv:nucl-th/9509016 .

[476] B. D. Lackey, M. Nayyar, and B. J. Owen, "Observational constraints on hyperons in neutron stars," Phys. Rev. **D73**, 024021 (2006), arXiv:astro-ph/0507312 .

[477] L. London and E. Fauchon-Jones, "On modeling for Kerr black holes: Basis learning, QNM frequencies, and spherical-spheroidal mixing coefficients," (2018), arXiv:1810.03550 .

[478] V. Cardoso, M. Kimura, A. Maselli, and L. Senatore, "Black holes in an Effective Field Theory extension of GR," (2018), arXiv:1808.08962 .

[479] T. Damour, B. R. Iyer, and B. S. Sathyaprakash, "Improved filters for gravitational waves from inspiralling compact binaries," Phys. Rev. **D57**, 885–907 (1998), arXiv:gr-qc/9708034 .

[480] H. Jeffreys, *The Theory of Probability* (Clarendon Press, Oxford, England, 1961).

[481] R. Nair, S. Perkins, H. O. Silva, and N. Yunes, "Fundamental Physics Implications for Higher-Curvature Theories from Binary Black Hole Signals in the LIGO-Virgo Catalog GWTC-1," Phys. Rev. Lett. **123**, 191101 (2019), arXiv:1905.00870 .

[482] P. Creminelli, G. D'Amico, J. Noreña, and F. Vernizzi, "The effective theory of quintessence: the w ¡ -1 side unveiled," Journal of Cosmology and Astroparticle Physics **2009**, 018–018 (2009).

[483] G. Gubitosi, F. Piazza, and F. Vernizzi, "The effective field theory of dark energy," Journal of Cosmology and Astroparticle Physics **2013**, 032–032 (2013).

[484] J. Gleyzes, D. Langlois, F. Piazza, and F. Vernizzi, "Essential building blocks of dark energy," Journal of Cosmology and Astroparticle Physics **2013**, 025–025 (2013).

[485] J. Bloomfield, É. É. Flanagan, M. Park, and S. Watson, "Dark energy or modified gravity? an effective field theory approach," Journal of Cosmology and Astroparticle Physics **2013**, 010–010 (2013).

[486] E. Bellini and I. Sawicki, "Maximal freedom at minimum cost: linear large-scale structure in general modifications of gravity," JCAP **1407**, 050 (2014), arXiv:1404.3713 .

[487] D. Colladay and V. A. Kostelecky, "CPT violation and the standard model," Phys. Rev. **D55**, 6760–6774 (1997), arXiv:hep-ph/9703464 .

[488] D. Colladay and V. A. Kostelecky, "Lorentz violating extension of the standard model," Phys. Rev. **D58**, 116002 (1998), arXiv:hep-ph/9809521 .

[489] V. A. Kostelecky, "Gravity, Lorentz violation, and the standard model," Phys. Rev. **D69**, 105009 (2004), arXiv:hep-th/0312310 .

[490] H. Jeffreys, "An invariant form for the prior probability in estimation problems," Proc. R. Soc. Lond. A **186** (1946), 10.1098/rspa.1946.0056.

[491] T. Damour, M. Soffel, and C. Xu, "General relativistic celestial mechanics. 1. Method and definition of reference systems," Phys. Rev. **D43**, 3273–3307 (1991).

[492] L. Blanchet and T. Damour, "Postnewtonian Generation of Gravitational Waves," Ann. Inst. H. Poincare Phys. Theor. **50**, 377–408 (1989).

[493] L. Blanchet and T. Damour, "Radiative gravitational fields in general relativity i. general structure of the field outside the source," Phil. Trans. R. Soc. Lond. A **320**, 379–430 (1986).

[494] T. Damour and B. R. Iyer, "Multipole analysis for electromagnetism and linearized gravity with irreducible cartesian tensors," Phys. Rev. **D43**, 3259–3272 (1991).

[495] T. Damour and G. Esposito-Farèse, "Tensor multiscalar theories of gravitation," Class. Quant. Grav. **9**, 2093–2176 (1992).

[496] T. Damour and G. Esposito-Farèse, "Tensor-scalar gravity and binary-pulsar experiments," Phys. Rev. D **54**, 1474–1491 (1996).

[497] S. Mirshekari and C. M. Will, "Compact binary systems in scalar-tensor gravity: Equations of motion to 2.5 post-Newtonian order," Phys. Rev. D **87**, 084070 (2013).

[498] T. Damour and G. Schäfer, "Redefinition of position variables and the reduction of higher order Lagrangians," J. Math. Phys. **32**, 127–134 (1991).

[499] M. Favata, "Conservative self-force correction to the innermost stable circular orbit: comparison with multiple post-Newtonian-based methods," Phys. Rev. **D83**, 024027 (2011), arXiv:1008.4622 .